ASH UTILIZATION WITH SILICA AND METALS RECOVERY

Sol Shcherban
The International Association of Sciences, Inc., 110 Bennett Ave., # 3H
New York, NY 10033

Keywords: coal fly ash, utilization, silica and metals recovery

ABSTRACT

The annual generation of electric power in the United States results in production of over 43 million tons of fly ash. Only about 22% of this amount is presently utilized. Neither of the used ash applications requires the recovery of metals and other valuable components (i). In the process of studying, there is another group of methods based on direct recovery of metals from ash (ii). This paper continues presentation of new technologies for ash processing with silica pre-extraction process (SP-process) and recovery of metals. Silica in ash represent about 40-65% of the total, therefore the possibility of silica recovering and converting into a wide variety of pure chemical silicate products with the predetermined properties is one of the main advantages of new technologies. For technical and economic features these perspective technologies present the third new group of methods of ash utilization (iii).

INTRODUCTION

In 1993, approximately 43.4 million metric tons of coal combustion fly ash were produced by the electric utilities in the United States [1]. Only about 22% of this amount was used mainly for cement, concrete products, and other [2]. For these applications, ash is used in an unsophisticated way without recovery of same components (i). The low level of ash utilization shows that such applications are insufficient for the complete utilization of fly ash, which is why there is a constant need for finding new ways to increase utilization of fly ash. For a significant increase in ash utilization, it is necessary to expand the assortment of useful products which can be produced from ash.

Aluminum is one of the major ash components. Many chemo-metallurgical methods were proposed for recovery of alumina from high-silica alumina-containing ores and industrial by-products including ashes (ii). As applied to ashes, these methods have two fundamentally important deficiencies which make them non- or low- profitable. One of them consists of great outlet streams of raw materials and intermediate products which leads to high capital and operating costs of alumina production [3-5]. As it will be shown below, no less important is the second deficiency - withdrawal of silica from the technological process in the form of solid residue. Conversion of silica into solid residue restricts the possibility of its utilization while silica represents the largest component of ash (40-65% of the total).

This paper continues to present new technologies for ash processing which makes it possible to reduce the outlet streams of raw materials and intermediate products, and to put out the most part of silica in the form of chemical silicate products (iii). The earlier papers described the background and main operations of new technologies [6,7]. The purpose of this paper is to expose main features of new technologies with silica pre-extraction process and to evaluate their possible influence on the economic showings.

EXPERIMENTAL

Object of research.
It is important to distinguish the varieties of ashes for choosing methods of the metal recovery, depending on chemical and mineralogical compositions of ash. As object of present consideration, ashes with low content of calcium and magnesium compounds were chosen. Ashes of some typical United States' coals of West Virginia, Ohio, and Illinois as well as ashes of Ekibastuz (Kazakhstan, Russia), Donetzk, Kuznetzk, Podmoscow (Ukraine and Russia) coals are suitable for this consideration. The chemical analysis of ashes and traditional raw materials used by aluminum industry are given in Table 1.

Prospects for ash using for alumina production. Strategy.
There are serious reasons to be doubtful about prospects of ashes to compete with traditional aluminum raw materials if ash is used as a monomineral material like bauxite for aluminum production only. The comparatively low content of alumina, high content of silica, and presence of aluminum mainly in the form of chemically stable mullite [6,7] result in great outlet streams of materials which have to be processed by the most power-consuming operations as roasting, sintering, and other (Table 2). Finally, this leads to the high capital and operating costs of alumina production from ash [3-5].

However, available industrial experience of alumina production shows that high silica materials can be processed profitably if they are used as polymineral raw materials for production of alumina and salable by-products as soda, potash and alkali for nephelines or sulfates for alunites. But ashes do not contain any considerable quantities of alkali (Table 1) whose availability creates a profitable technology of nephelines processing. Therefore, silica- the largest component of ash, can be used as a salable by- product for ashes. The foregoing shows:

-ash can not be processed profitably as a monomineral raw material used for aluminum production only

-to make aluminum production competitive, it is necessary to utilize silica that represents the largest component of the ash

-it is important to develop less power-consuming technologies by means of lowering outlet streams of raw materials and intermediate products.

Methods of ash utilization
Taking into account the principal importance of silica utilization, it is useful to examine all of the methods from the viewpoint of silica recovery and utilization. From this standpoint, all of the methods can be subdivided into three groups (Figure 1):

(i) Ash uses without recovery of components from ash (cement, concrete products, road base and subbase, structural fills, embankments, filler, grouting, waste stabilization and other)[2].
(ii) Direct metallurgical processing of ash for alumina (aluminum) production without recovery of silica.
(iii) Ash processing with silica recovery and utilization [6,7].

Chemo-metallurgical methods of the group (ii).
Many methods of this group are known for recovering aluminum from high-silica alumina containing ores, concentrates, and industrial by-products. Technically suitable for ashes are those that allow to convert the compounds of aluminum, mainly mullite or metakaolinite (in low-temperature formed ashes) into acid- or alkali- soluble compounds by roasting, sintering or high-temperature hydrochemical processes [3-5].

Acid methods
One of the main advantages of acid methods is the possibility of separating the great quantities of silica in the beginning of process by leaching. But this very important advantage can be realized only in the process of direct acid leaching which is suitable for low-temperature formed ashes containing aluminum in the form of metakaolinite. In other methods, the great outlet streams of ash and auxiliary agents (limestone[8], lime, acid or other) have to be sent to the most power-consuming roasting and sintering processes which proceed to the process of leaching (Figure 1 /i/).

Alkaline methods
The current world aluminum production is based only on the alkaline technologies owing to the following advantages of these methods:
- purity and physical properties of alumina correspond to the requirements of the electrolysis process
- comparatively small stream of pulps and liquors because of high solubility of alumina in the solutions
- lack of necessity of corrosion protection for equipment and solution purification from iron

As applied to ashes, the main deficiencies of both acid and alkaline methods are the following:

1. The great streams of ash, furnace charges, cakes, pulps and liquors (Table 2).

2. Withdrawal of silica from technological process in the form of solid residue (Table 3). Contrary to silica obtained from the silicate solutions, composition and physical properties of solid residue are predetermined by the conditions of leaching therefore they can not be changed. This restricts the areas of solid residue using mainly by cement production. As has been mentioned above this application do not provide the further augmentation of ash utilization.

Ash processing for alumina production with silica recovery and utilization (Figure1, /iii/).

A great difference in solubility of mullite and compounds of free silica (Figure 2) was used for the extraction of the major part of silica from fly ash by silica pre-extraction process (SSP) [6,7]. Silica dissolved in alkaline and soda-alkaline solutions can be converted into a wide variety of valuable pure silicate products (Table 3). Extraction of the largest part of silica from fly ash decreases the outlet streams of ash, limestone, furnace charge, cake, and mud by 1.5-5.0 times (Table 2), and accordingly reduces the capital and operating costs of alumina production from fly ash.

SUMMARY

The major deficiencies of the chemo-metallurgical methods which make them non- or low-profitable for ash processing are the great outlet streams of ash and the intermediate products, and putting out silica in the form of solid residue. The deficiencies can be eliminated by means of new technologies of ash processing with the silica pre-extraction process (SPP). The main advantages of this process can be summarized in the following:

- ash is used as a polymineral source from which all of the major components including alumina, silica and iron [6] can be recovered and utilized

- silica is put out from the technological process in the form of salable chemical silicate products

- the possibility to produce a variety of valuable chemical silicate products becomes a decisive factor for improving economic showings of new technologies

- the major part of silica (50-75%) can be extracted from ash at the beginning of the technological process. This results in outlet streams decreasing and accordingly in reduction of capital and operating costs.

REFERENCES

1. 1993 Coal Combustion Byproducts Production and Consumption, American Coal Ash Association, Inc.,Washington, D.C.,1994.

2. Tyson S. and Blackstock T. Coal Combustion Fly Ash - Overview of Applications and Opportunities in the USA. Paper Presented at the 211th ACS National Meeting, New Orleans, LA, March 24-28, 1996, Volume 41, No.2, pp. 587-591.

3. O'Connor D.J. Alumina extraction from non bauxitic materials. Aluminum-Verlag 6mbH, Dusseldorf. p.320-345.

4. Kirbay C., and Barclay J.A. 'Alumina from nonbauxitic resources'. 'Trav. Com. int. etude bauxites, alumine et alum', 1981, No.16, 1-12.

5. Bengston K.B., Chuberka P., Nunn R.F., Phillips W.A., Malm L. and San Jose A.V. 'Some technical and economic comparisons of six processes for the production of alumina from non-bauxitic ores' 'Trav. Com. int. etude bauxites, alumine et alum.',1981, No.16, 109-132.

6. Shcherban S., Rayzman V. and Pevzner I. Technologies of Coal Fly Ash Processing into Metallurgical and Silicate Chemical Products.' Paper Presented at 210th ACS National Meeting Chicago, IL August 20-25, 1995, Volume 40, No.4, pp. 863-867.

7. Shcherban S.A. and Rayzman V.L. 'Alkaline Technologies of Coal Fly Ash Processing into Metallurgical and Silicate Chemical Products', 1995 International Ash Utilization Symposium, October 23-25, Lexington, Kentucky, Proceedings, XI.

8. Torma A.E. 'Extraction of Alumina from Fly Ash', Metal. 37, Jahrgang. Heft 6, June 1983, pp. 589-592.

Table 1. CHEMICAL ANALYSIS OF FLY ASH AND RAW MATERIALS USED BY ALUMINUM INDUSTRY (Wt. %).

Materials	Al_2O_3	SiO_2	Fe_2O_3	TiO_2	CaO	MgO	Na_2O	K_2O
Ash of Ekibastuz coal	28.4	59.6	5.10	1.83	1.31	0.65	0.33	0.59
Ash of WV	30.00	60.00	4.00	1.60	0.60	0.60	0.50	1.50
Bauxite:								
-low silica	41.0-60.0	0.4-8.0	0.3-30	1.0-4.0				
-high silica	43-57	12-19	6-22	2-3.5			$Na_2O + K_2O$	
Nepheline Concentrate	28-30	43-44	2-4		2-3		19 - 20	
Nepheline (Russia)	27.5	40-41	4-5			SO_3	13	
Alunite (Azerbaijan)	22	41	4			20	5	

Table 2. APPROXIMATE OUTLET STREAMS OF RAW MATERIALS AND INTERMEDIATE PRODUCTS DURING PROCESS OF ALUMINA PRODUCTION.

Material	Outlet stream, t/t Al_2O_3		Decreasing of outlet streams, times
	Direct metallurgical ash processing (S-L.S)*	Ash processing with silica preextraction (S-L.S SP)**	
Raw material	3.99 (ash)	2.63 (concentrate)	1.51
Limestone	10.27	2.06	4.98
Furnace charge	15.3	6.26	2.44
Cake	10.00	4.61	2.16
Mud	8.30	2.82	2.94

* S-L.S - soda- limestone sintering process
**S-L.S SP - soda- limestone sintering process with silica pre-extraction

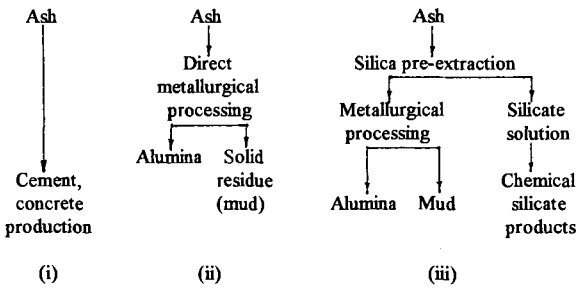

Figure1. Comparison of methods for ash utilization.
(i)-Ash uses without recovery of components. (ii)-Direct metallurgical processing of ash. (iii)-Ash processing with silica pre-extraction.

Table 3. COMPARISON OF SILICON CONTAINING PRODUCTS AND SOLID RESIDUE AFTER ALKALINE PROCESSING OF ASH BY THE DIRECT RECOVERY OF ALUMINA (ii) AND PROCESS WITH SILICA PRE-EXTRACTION (iii).

Method of coal ash processing	Silicon containing products and residue after ash processing		
	Products from solutions	Solid residue. Principal compound	Commercial uses
(ii) Direct recovery of alumina:			
- Lime-Soda Sintering		β - mud (β - Ca_2SiO_4)	cement
- Lime Sintering		γ - mud (γ -Ca_2SiO_4)	cement
- Hydrochemical high-caustic, high-temperature leaching		calcium-silica mud ($Ca[H_2SiO_4]$)	cement
(iii) Ash processing with silica pre-extraction - Sintering with silica pre-extraction process	a) Chemical silicate products*: SAS, SSS,SMS,CMS, SSM, SA, SC and other (45-75% of the SiO_2 total)		glasses, glazes,ceramics, enamels, color cements, zeolite, fillers, plasticizers, cosmetics, detergents and other silicon containing products
		b) β -mud (β - Ca_2SiO_4) (55-25% of the SiO_2 total)	cement

* SAS- silica alkaline solution; SSS- soda-silicate solution; SMC- sodium hydrometasilicate; CMS- calcium hydrometasilicate; SSM- soda-silicate-mixtures; SA- silica amorphous; SC- silica crystalline

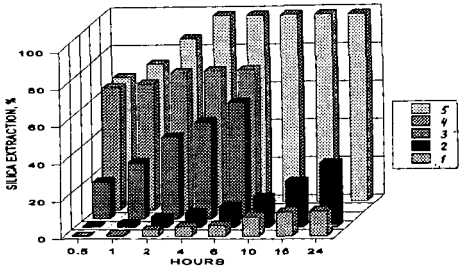

Figure 2. Efficiency of major ash compounds dissolution in alkaline solution: 1-mullite, 2-quartz, 3-ash glassy phase, 4-ash cristobalite, 5-syntetic cristobalite

CHEMICAL VAPOR DEPOSITION: STABLE CARBONS FROM LOW-RANK COALS

Ramesh K. Sharma, Ronald W. Kulas, and Edwin S. Olson
University of North Dakota
Energy & Environmental Research Center
PO Box 9018
Grand Forks, ND 58202

Keywords: Chemical vapor deposition, lignite, activation

ABSTRACT

A chemical vapor deposition (CVD) technique has been used to increase the oxidative stability of activated carbons. Activated carbons prepared from Gascoyne lignite (North Dakota) by thermal or potassium hydroxide activations were subjected to BCl_3 in helium at 727°C with or without benzene for a limited period of time, followed by annealing in helium at 900°C for three days. Untreated and acid-washed coal samples were used to assess the magnitude of the effect of mineral matter in the coal on the boron coating. The oxidative stability of the boron-modified carbons was determined from the decomposition curves obtained from the thermogravimetric analysis.

Modification of the as-received, KOH-treated carbon yielded oxidatively stable carbons up to an initial temperature of 520°C, compared to about 350°C for the starting material. Similar results were obtained for the carbonized Gascoyne lignite. Sulfurous acid washing of the Gascoyne significantly enhanced the thermal stability (600°C) of the boron-modified carbon.

INTRODUCTION

A major limitation in the use of carbons is their oxidative instability in air at high temperatures, usually greater than 400°C. At higher temperatures, the carbon reacts with oxygen in the air to produce CO and CO_2. Some high-surface-area carbons could be utilized as catalysts or catalyst supports or in separation technologies at higher temperatures if they could be stabilized against oxidative degradation.

The application of a protective layer on the carbon surface could block oxygen from reacting with the surface carbons, or it could inhibit the reaction of oxygen with the surface carbon. Previous work demonstrated that boron atoms substituted for carbon atoms on the surface of a carbon fiber, composite, or graphite inhibits the oxidation reaction (1). Diffusion of boron via solid contact was attempted but gave low incorporation. Recently, a CVD reaction was used to form a protective layer on carbon fibers (2). This procedure resulted in a high concentration (25%) of boron, corresponding to the formula BC_3. A similar reaction of boron trichloride and benzene vapors on a hot activated carbon surface could form a similar boron carbide protective coating. In this paper, we report the preparation and performance of the protective layer formed in this manner on sorbent and catalytic carbons.

EXPERIMENTAL

Preparation of CVD Carbons

As-received Coal Corporation of Victoria (CCV) lignite carbon was dried at 110°C overnight. The predried carbon (1.62 g) was packed in a quartz tube. The tube was placed in a vertical furnace and attached to a gas inlet. The outlet was attached to a bubbler filled with NaOH solution to trap HCl or BCl_3. The carbon was heated to 727°C, and vapors of BCl_3 diluted with vapors of helium saturated with benzene were passed through the carbon. The CVD was carried out for 4 hours.

In some cases, benzene was not used, and vapors of BCl_3 diluted with nitrogen were used for carbide deposition.

The vapor-deposited carbon was annealed by heating in a gentle flow of helium at 900°C for 72 hours. The annealed carbon was grayish with a silvery mirror. The weight of the annealed carbon was 1.6 g.

TGA Determinations of Stability in Air at High Temperatures

Determinations of stability in air were conducted in a Dupont Thermal Analyst 2100 system with the TGA 951 analyzer module. Samples (50 mg) were heated at a rate of 25°C/min in an air stream.

RESULTS

Boron-Deposition on KOH-Activated Carbon

Several carbons and chars were treated to increase their stability in air or hydrogen atmospheres. Initially, the chemically activated carbon produced by the KOH method was utilized. This carbon was prepared in Australia (CCV) from Gascoyne, North Dakota, lignite by pyrolysis in KOH. The CCV carbon had a high surface area (N_2-BET = 1325 m^2/g) but was not as thermally stable as a carbon prepared by steam activation. The thermogravimetric analysis (TGA) tests in air showed that the CCV carbon began to react with air at 351°C (Table 1), and at 660°C, the carbon was completely consumed. The decomposition curve was smooth, and the derivative peak was symmetrical, indicating a consistency in the oxidation mechanism. The residue present after the TGA experiment indicated an ash content of 7.3%. Much of the residue is potassium remaining from the earlier activation procedure. It is difficult to wash out all the potassium salts, and they can be the cause of the lower stability of the CCV lignite. The potassium salts will catalyze the gasification–combustion reactions that occur as the carbon is heated in air (or another reactive atmosphere).

Chemical vapor deposition was performed by passing a helium stream containing boron trichloride and benzene vapors through the CCV carbon at 727°C for 4 hours. The carbon was further treated by annealing at 900°C in the helium stream for 72 hours. The TGA test with the resulting carbon demonstrated an increased stability; the oxidation was not initiated until 507°C and was completed at 854°C. The decomposition curve was a little less symmetrical, indicating two different types of material or mechanisms were involved in the gasification–combustion reaction with air. In this experiment, an ash representing 11.2% of the material remained after the TGA experiment was completed. Thus a substantial amount of boron had been added.

A control experiment was performed by heating the CCV carbon in a helium stream with no reagent gases at 727°C, followed by annealing at 900°C. The TGA test on this sample exhibited an initial oxidation at 381°C, and the oxidation proceeded more slowly than the oxidation of the original CCV carbon, but this was higher than the oxidation rate of the CVD carbons. The ash content was 7.2%, similar to that of untreated CCV carbon. Thus the annealing procedure appeared to increase the stability by only a small factor, probably due to removal of the more reactive carbon material.

The presumed reaction is substitution of boron on the benzene or benzene decomposition products to form a graphitic layer with substitutional boron (2). It seemed possible that boron could form a protective coating on an activated carbon in the absence of the benzene by reacting directly with the carbon surface. Thus a second CVD experiment was performed with the CCV carbon, in which a helium stream containing only the boron trichloride was passed through the heated (727°C) carbon. The carbon was annealed as before. The TGA test of the carbon produced by this method showed an initial oxidation temperature of 518°C, but the decomposition occurred more rapidly, being complete at 777°C. In this case, the ash weight was 4.4%, indicating that some of the potassium present in the carbon must have been lost. The chlorine liberated from the boron trichloride may have formed potassium chloride which devolatilized at the high temperatures.

Boron Deposition on Gascoyne Char

Several reactions were performed with a Gascoyne carbon that was produced by carbonizing a cleaned lignite under conditions similar to those used in the CVD procedure. The lignite was washed with sulfurous acid to exchange out the calcium and alkali metals associated with the carboxylate groups of the coal. The exchanged coal was carbonized at 727°C and then 900°C to produce the carbon precursor for the CVD experiments. The control experiment on the carbon from the acid-exchanged Gascoyne gave an initial oxidation temperature of 527°C. The ash content of the untreated carbon was 5.8%.

A CVD carbon was then prepared from the 900°C-annealed carbon using a helium stream containing boron trichloride and benzene vapors at 727°C. The resulting carbon was annealed at 900°C. The TGA of this CVD carbon showed a remarkable improvement in stability, with an initial oxidation temperature of 600°C and complete oxidation at 890°C (See Figure 1). The ash content of this material was 12.85%, indicating a substantial amount of boron was incorporated.

Treatment of the 900°C-annealed carbon with boron trichloride vapor in helium (no benzene) was performed at 727°C for 4 hours, followed by annealing at 900°C to give the CVD carbon. The TGA test with this CVD carbon showed an initial oxidation temperature of 522°C, similar to that obtained from the 900°C-annealed precursor carbon. The ash content obtained in this test was 8.8%, indicating that boron was incorporated, even though benzene was not added to condense with the boron.

The addition of a carbon vapor source (benzene) to the boron trichloride generated an effective protective boron carbide coating on the surface of the lignite-derived carbons. The lower stability of the CVD carbons produced by boron trichloride vapor alone compared to the carbons produced by boron trichloride-benzene CVD carbon suggests that the carbon structures are different in these two types of samples, but we do not yet understand what boron forms are present. Although aromatic volatile compounds released during carbonization of a lignite might decompose to provide the carbon needed for the boron carbide layer, the type of volatile carbon species released in the gasification of an activated carbon at 727°C (CO, CO_2, CH_4) may react with the boron differently or not at all. On the other hand, condensation of the boron and carbon species generated from decomposition of the benzene and boron trichloride gases does form a protective edge structure or layer. Boron carbide has also been deposited on carbon fibers in a high-temperature (1200°-1500°C) reaction of boron trichloride vapor with hydrogen (3).

Carbonization of an as-received Gascoyne lignite was also studied to determine whether the mineral content of the resulting carbon affects the oxidation of the carbon. For the control (non-CVD), the lignite was first carbonized at 400°C, then 727°C, and finally 900°C. The initial oxidation temperature was similar to that obtained from similar thermal activation of the acid-washed lignite discussed above. When the char produced at 400°C was treated with boron trichloride vapor in helium for 2 hours at 727°C and then annealed at 900°C, the TGA test on this CVD carbon gave an initial oxidation temperature of 503°C. Thus, the stability actually decreased as a result of the boron treatment. The ash content of this boron-CVD carbon was quite high (16.0%). It is likely that much of the ash represents reactions of the mineral matter with the BCl_3 to form calcium and sodium chloride.

When the boron trichloride vapor treatment was continued for 4 hours, the resulting CVD carbon showed an initial oxidation temperature of 516°C and final burnout at 826°C. This is still somewhat less stable than the carbons produced without boron CVD.

CONCLUSIONS

The stability of activated carbons to air oxidation was remarkably improved by CVD with boron trichloride and benzene vapors. A boron carbide layer on a lignite-derived carbon was able to increase the stability to air oxidation so that the carbon could be used in an air stream at 600°C without decomposition. A very high surface area carbon was stabilized significantly by the CVD of boron carbide.

REFERENCES

1. Jones, L.E.; Thrower, P.A. *Carbon* **1991**, *29*, 251.
2. Fecko, D.L.; Jones, L.E.; Thrower, P.A. *Carbon* **1993**, *31*, 637.
3. Vincent, H.; Vincent, C.; Scharff, J.P.; Mourichoux, H.; Bouix, J. *Carbon* **1992**, *30*, 495.

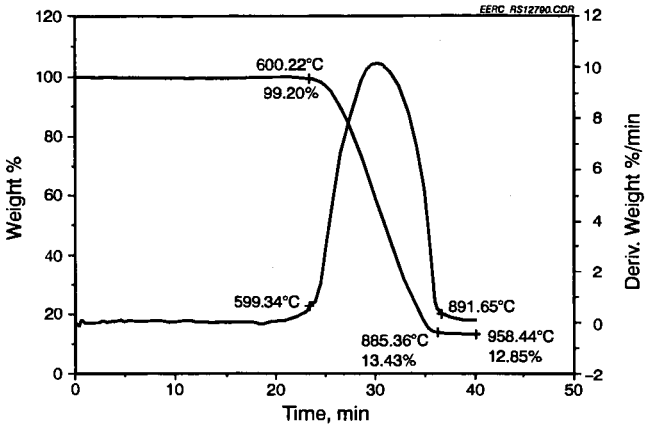

Figure 1. TGA of CVD-Gascoyne Activated Carbon

TABLE 1

Chemical Vapor Deposition on Carbons

Carbon/Char, g	CVD Method	Activation	Init. Oxid. Temp.
CCV-Lig	-	-	351
CCV-Lig	BCl_3+He/727°C/4 hr	900°C/He/72 hr	519
CCV-Lig	BCl_3+benzene+He/727C/4 hr	900°C/He/72 hr	507
CCV-Lig	-	727°C/He/4 hr 900°C/He/72 hr	381
Gascoyne/carb. 400°C	BCl_3+He/727°C/4 hr	900°C/He/72 hr	516
Gascoyne/carb. 400°C	BCl_3+He/727°C/2 hr	900°C/He/72 hr	503
Gascoyne/carb. 400°C	-	727°C/He/4 hr 900°C/He/72 hr	532
Gascoyne/carb. 400°C/727°C/4 hr/ 900°C/72 hr	BCl_3+He/727°C/4 hr	900°C/He/72 hr	536
Gascoyne H_2SO_3-Cl/carb. 400°C		He/727°C/4 hr 900°C/He/72 hr	527
Gascoyne H_2SO_3-Cl/ carb./4 hr/727°C/4 hr 900°C/72 hr	BCl_3+He/727°C/4 hr	900°C/He/72 hr	522
Gascoyne H_2SO_3-Cl carb./4 hr/727°C/4 hr 900°C/72 hr	BCl_3+benzene+He/727°C/4 hr	900°C/He/72 hr	600

H_2SO_3-Cl = H_2SO_3 - Cleaned

QUANTITATIVE DETERMINATION OF THE FLUID AND INERT COMPONENTS DURING COAL CARBONISATION BY HIGH TEMPERATURE IN-SITU ^{1}H NMR

M. Mercedes Maroto-Valer, John M. Andrésen and Colin E. Snape

University of Strathclyde, Department of Pure and Applied Chemistry, 295 Cathedral Street, Glasgow G1 1XL, Scotland, UK

Keywords: Thermoplasticity, inert material, high temperature ^{1}H NMR.

Although high temperature in-situ ^{1}H NMR has successfully been used previously to investigate the development of plasticity during coal carbonisation, the proportions of rigid and fluid material have rarely been determined. This has been achieved here using a high temperature Doty NMR probe operating at a frequency of 100 MHz. At maximum fluidity, the mobile phase accounts for up to 45% of the total hydrogen. Indeed, the fluid component increases both in terms of concentration and mobility up to maximum fluidity. Decreasing the particle size below 150 μm suppresses softening, but at maximum fluidity, the concentration of inert component is independent of the particle size.

INTRODUCTION

Although standard empirical tests such as Gieseler plastometer and Audibert-Arnu dilatometer are widely used to ascertain the plasticity behaviour of coking coals [1], these tests do not easily relate to the actual structural changes that occur. High temperature in-situ ^{1}H NMR has successfully been used to investigate the motion of coals in-situ during carbonisation, where parameters reflecting the spin-spin relaxation times T_2s, have been correlated with plasticity [2]. There are usually two contributions to the ^{1}H NMR signals of coals: a mobile component with a Lorentzian decay, and an inert component with a Gaussian distribution [3]. Coal being a macromolecular network contains a substantial inert component which does not soften and forms the broad constituent of the NMR signal.

In the late 70's, Sanada and coworkers conducted the first high temperature ^{1}H NMR study on coal and pitches at the early stages of carbonisation [4]. The development of plasticity in coals was monitored by changes in the half width of the spectra. However, due to experimental factors including the relatively small sample size and low magnetic field used (37.5 MHz for ^{1}H), the spectra could not be deconvoluted to derive the proportion of inert material present. This limitation was overcome from 1983 onwards by Lynch et al [2,3,5,6], who have referred to the technique as "Proton Magnetic Resonance Thermal Analysis" (PMRTA). They have used mainly the empirical parameter, M2t16, corresponding to the spectrum truncated at 16 kHz which was found to be the optimum frequency for gauging changes in fluidity [6]. However, in-situ ^{1}H NMR has not been used widely to determine the overall concentrations of fluid and inert material during coal carbonisation, due to the possiblity of truncating broad Gaussian signals when signal to noise levels tend to be low at high temperatures. This has been achieved here using a high temperature Doty NMR probe operating at a frequency of 100 MHz. Three Australian bituminous coals with different plastic properties have been investigated and both the oncentration and mobility of the fluid components have been monitored. Furthermore, for one of the coals investigated the effect of the particle size has been studied for fractions below 212 μm.

EXPERIMENTAL

Table 1 lists the proximate and maceral analysis as well as the Gieseler plastometer results for the three coals investigated. The coals were ground to -212 μm. Sample AUS-1 was also ground to give <45 and 212-45 μm fractions.

In the high temperature measurements, the 90° pulse width varied with temperature between 2.2 μs at ambient to 3.0 μs at 600°C. The solid echo pulse sequence (90° - τ - 90°) with a refocusing of 5 μs was used in order to minimise the loss of signal due to the dead time of the NMR coil. About 40-70 mg of sample was packed in a zirconia container which was placed horizontally in the stator. A flow of 12 dm^3 min^{-1} of dry nitrogen was used to transfer heat to the samples and to remove the volatiles escaping trough a small ventilation hole in the container. Spectra were obtained at a number of different temperatures and the free induction decays (FIDs) were transferred from the spectrometer to a PC for processing and fitted to Lorentzian and Gaussian components, as appropriate. The spectra obtained in the fluidity range could best be fitted to either one Gaussian and one Lorentzian component or two Gaussian components.

RESULTS AND DISCUSSION

General aspects Figure 1 shows the ^1H NMR spectra for sample AUS-1 obtained at 25°C, 453°C - maximum fluidity and 529°C - after resolidification. Figure 2 compares the peak widths at half height, $\Delta H_{1/2}$, measured in-situ at temperatures up to 600°C for the three coals and Figure 3 shows the deconvoluted spectra for two of the coals at the temperature of maximum fluidity. The coals behave in a similar way with a constant $\Delta H_{1/2}$ corresponding to single Gaussian component before the onset of thermoplasticity (300-350°C). The maximum fluidity at 430-480°C is reflected by the minimum in $\Delta H_{1/2}$, corresponding to a maximum in T_2. During the fluidity range, the peak width of the plastic phase is only between 20 and 30% of that for the initial coal. Comparable observations in peak half width have been reported earlier by Sanada [4,7] and by Lynch et al. Using the M_{2T16} parameter [5,6]. As expected, the fluid component has its highest contribution to the total NMR signal at maximum fluidity.

After the onset of resolidification, (470-510°C) the average peak width increases to reach a value similar to that of the initial coal with only a single Gaussian component being observed. The inert component represented by a Gaussian distribution has a relativerly constant T_2 of ≈20 μs throughout the temperature range studied (Table 2).

Proportions of rigid and fluid material For the coals investigated, Table 2 lists the proportions of these components at maximum fluidity and their associated spin-spin relaxation times (T_2s). The data (<212 μ fractions indicate that the extent of fluidity development for AUS-4 is much less than for AUS-1 and AUS-8 (Table 2). It generates a lower concentration of fluid material that has considerably less mobility than that for the other coals (Table 2). Indeed, the spectrum at maximum fluidity for AUS-4 can be fitted using only two Gaussian components, without including the Lorentzian for the most fluid material. Further, Figure 2 indicates that maximum fluidity is attained at a lower temperature for AUS-1 and AUS-8 than AUS-4, consistent with the Gieseler plastometer data. For AUS-8, the concentration of inert material only accounts for 56% of the total hydrogen observed (Table 2).

Figure 4 shows the evolution of the fluid component for sample AUS-1. During the plastic stage, the T_2 or mobility of the Lorentzian component increases, together with its contribution to the total signal. This reaches a maximum at 450°C and then decreases during the resolidification process. Thus, the

development of fluidity and subsequent resolidification in the coals follow the same trend involving changes in both concentration and mobility of the plastic phase.

Particle size For AUS-1, the particle size has a significant effect on the development of fluidity. Table 3 lists the proportions of rigid and mobile material and their T_2s at maximum fluidity for the three different particle size fractions studied. The mobility of the narrowest component is suppressed for the <45μm fraction, and there is still a noticeable difference between the <212 and 212-45 μm fractions. The suppression of fluidity with decreasing particle size is represented by a reduction in the mobility of the fluid material, rather than a reduction in its concentration. This reduction in fluidity may be ascribed to either an oxidation effect or a combination of reduced voidage between the coal particles and the fact that fluid material will escape easier from smaller particles. Careful grinding of the coal and high temperature NMR analysis of the resultant fractions strongly suggests that the latter is the prime cause of the fluidity loss. Furthermore, it has been shown that fluidity is essentially a reversible phenomenon provided that the sample is cooled rapidly from the temperature of maximum fluidity.

CONCLUSIONS

The results have confirmed the ability of high temperature ^{1}H NMR to follow coal carbonisation in-situ. The approach used here is able to describe the carbonisation process in terms of the proportions of rigid and fluid material as well as the mobility of the latter. Decreasing the particle size below 150 μm suppresses softening, but at maximum fluidity, the proportion of inert material is independent of the particle size.

ACKNOWLEDGEMENTS

The authors thank the European Coal & Steel Community (Contract Nos.: 7220-EC/870 and 7220-EB/845) and the Basque Government (studentship for M.M. Maroto-Valer) for financial support.

LITERATURE CITED

1 D.W. van Krevelen, Coal, 3rd Revised Edn, Elsevier, Amsterdam, 1993, Chs.23- 24.
2 L.J. Lynch, D.S. Webster, R. Sakurovs, W.A. Barton and T.P. Maher, Fuel, 1988, **67**, 579.
3 T.J. Parks, L.F. Cross and L.J. Lynch, Carbon, 1991, **7** , 921.
4 K. Miyazawa, T. Yokono and Y. Sanada, Carbon,1979, **17**, 223.
5 L.J. Lynch and D.S. Webster, Amrican Chemical Sociey Symposium Series, 1983, **230**, 353.
6. R. Sakurovs, L.J. Lynch and W.A. Barton, Amer. Chem. Soc. Adv.in Chem. Series, 1993, **229**,229.
7. T. Yokono, T. Obara, Y. Sanada and K. Miyazawa, Carbon, 1984, **2**, 169.

Table 1 Proximate analysis, vitrinite reflectance, atomic H/C and temperature of maximum fluidity determined by Gieseler and NMR for the coals investigated.

	VM (db)	Ro (max)	atomic H/C	Tem. max / °C
AUS-1	23.1	1.20	0.60	451 (453) [a]
AUS-4	19.63	1.46	0.61	472 (470)
AUS-8	33.94	0.86	0.74	460 (460)

[a] Values in brackets were determined by ^{1}H NMR.

Table 2 Deconvolution into two components identified in the ^{1}H NMR spectra obtained at maximum fluidity for the three coals investigated.

	% rigid	T_2 rigid / μs	% mobile	T_2 mobile / μs
AUS-1*	62	20.7	38	82
AUS-4**	81	20.9	19	68
AUS-8*	56	22.2	44	92

* Deconvoluted into one Gaussian and one Lorentzian components.

** Deconvoluted into two Gaussian components.

Table 3 Deconvolution into two components of the ^{1}H NMR spectra obtained at maximum fluidity for AUS-1 as a function of the particle size.

	%rigid	T_2 rigid / μs	% mobile	T_2 mobile / μs
<45μm	63	18.5	37	48
<212μm	62	20.7	38	82
45μm - 212μm	68	23.3	32	111

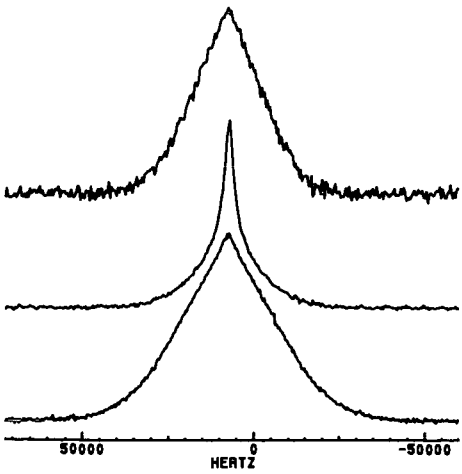

Figure 1 ^{1}H NMR spectra for AUS-1 at 25°C (bottom), maximum fluidity at 453°C (middle), and resolidification at 529°C (top).

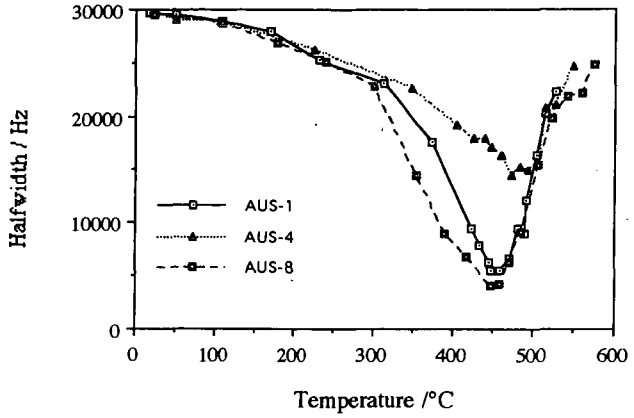

Figure 2 Variation in the average peak half-width for the three coals investigated (<212 μm). The peak half-width is dominated by the contribution from the mobile component close to maximium fluidity.

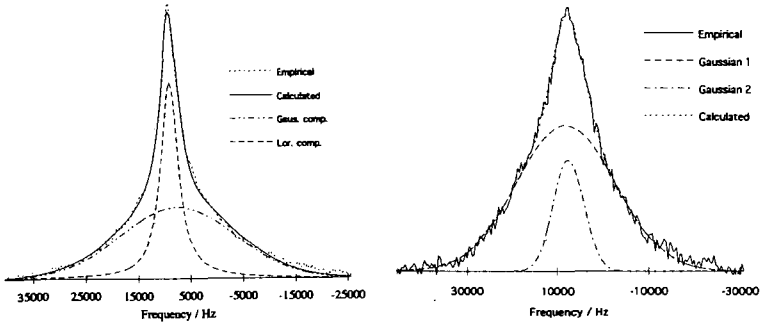

Figure 3 Deconvoluted ^1H NMR spectra at maximum fluidity for AUS-1 (rigth), and AUS-4 (left).

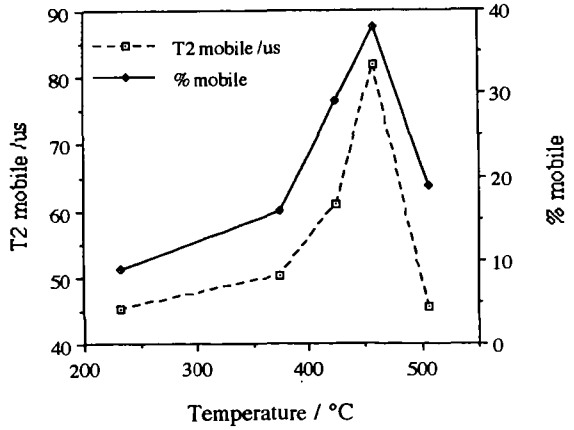

Figure 4 Evolution of the fluid component for AUS-1 with temperature.

EVAPORATIVE LIGHT SCATTERING DETECTION IN QUANTITATIVE HPLC OF PAC MIXTURES AND COAL-TAR PITCHES

Vicente L. Cebolla, Luis Membrado, Jesús Vela, Ana C. Ferrando, and Clemente Romero
Departamento de Procesos Químicos
Instituto de Carboquímica, CSIC
P.O. Box 589, 50080 Zaragoza, Spain

Keywords: evaporative light scattering detector, HPLC, polycyclic aromatic compounds

INTRODUCTION

The term Polycyclic Aromatic Compounds (PACs) include a wide variety of classes of compounds. In turn, the number of possible PACs for each class is of astronomical proportion (1, 2). Environmental and fossil-fuel samples are composed of very complex mixtures of unknown PACs. The strategy for their analysis depends, among others, on the nature of matrix and PAC concentration, and involves cleanup/prefractionation steps and HPLC analysis. Therefore, HPLC detectors must be calibrated with pure reference standards for every substance to be quantified. However, only a relatively small fraction of PACs can unambiguously be identified and are commercially available (2). An ideal detector for chromatography of complex mixtures should provide uniform response factors for each separated compound or class of compounds. None of the conventional HPLC detectors (UV, Refractive Index, fluorescence) meet this requirement, neither for mixtures of unknown but well-separated pure peaks nor for compound-class fractionation of fossil fuels (where other additional problems can occur, such as presence of very heavy and polar PACs, quenching problems using fluorescence detection, need of tedious absolute calibrations, etc.)

It has been reported that the Evaporative Light Scattering Detector (ELSD) enables all types of non-volatile solutes to be detected (3, 4), although it has recently been reported that solutes having a lower volatility than the mobile phase can be analyzed working at mild temperatures (5). Detector response has been reported to be quite independent of the chemical composition of the solute. However, very different response factors were reported in the past in the case of semi-volatile PACs (6). This work intends: i) to evaluate the possibility of the application of ELSD in order to quantify PACs in complex mixtures, ii) to theoretically justify the responses of the studied PACs, and iii) to lay the groundwork for application to fossil-fuel characterization.

EXPERIMENTAL

The HPLC system consisted of: a Waters 510 pump, a 7725i Rheodyne injector, a PL-Gel Mixed-E (30 cm length, 3 μm particle size with mixed pore distribution), and a PL-EMD 950 ELSD. GPC-grade-Tetrahydrofuran (THF) stabilized with BHT was used as mobile phase. Flow rate was 1 ml/min. The output signal from the detector was fed into a Fluke Hydra 2620 multichannel data acquisition unit, and stored in an HP 100LX computer for data acquisition. Raw data were further reprocessed using an adequate spreadsheet in a 486 PC clone.

The operating mode of ELSD is as follows: the effluent from the chromatographic column enters a Venturi nebulizer and is converted into an aerosol by a stream of air (12 l min^{-1}). Venturi consists of a stainless steel capillary tube (0.25 mm i.d., 1.59 mm o.d.) carrying the column effluent, which is surrounded by a larger tube (2 mm i.d.). The fine droplets formed are then carried out through a temperature controlled drift tube which causes evaporation of the mobile phase to form small particles of non-volatile solute. This cloud of solute passes through a white light in the broad-band 400-700 nm, which produces light scattering, which in turn is detected by a photomultiplier at a 60° angle. The evaporation temperature used was 30°C.

The amounts (μg) of the studied PACs reported throughout the text correspond to the mass effectively injected. The response factor of each standard is defined as its corresponding area, A (counts as μV s^{-1}) per mass unit, m (μg). Only absolute response factors are used throughout this paper.

RESULTS AND DISCUSSION

Quantification of PACs using ELSD

In a first step of the research, detector response (A) vs sample load (m) was evaluated for pure PACs, and binary mixtures of PACs. In each mixture injected, either coronene or 2-hydroxycarbazole was used as reference standard due to their adequate retention time using the above-mentioned column. Although adequate regression coefficients ($r = 0.999$) were obtained for the studied PACs using linear regressions, deviations from the theoretical linearity at low sample loads were evidenced by: i) significantly lower response factors for each pure PAC as sample load decreased (Table 1), ii) in the case of mixtures, greater differences between area percentages from the chromatogram and known mass percentages (hereafter referred as to A-m differences) at low sample loads (Table 1), and iii) a better fit of experimental data to logarithmic regressions ($\log A = \log a + b * \log m$, from $A = a * m^b$). Parameters from both types of regression for some different PACs are given in Table 2. Values of a and b are similar for the studied PACs despite their different chemical nature, suggesting similar responses. The physical meaning of b, and the agreement between the experimentally obtained and

theoretically calculated *b* values for the studied PACs are explained later in this work, as well as a theoretical justification of linearity deviation. This is inherent to ELSD regardless of the volatility/involatility of the PACs. Recent results reported by Dreux el al. (5) showed a similar behavior in the case of glucose analysis on an octadecyl bonded silica when using either ELSD or Refractive Index detector. They demonstrated that linearity deviation is even larger in the latter case. The sample load range in which ELSD behaves in a non-linear fashion depends on the considered PAC (Table 1, results at 20 and 40 μg). Results from Table 1 at 40 μg (in the linear zone of ELSD) show that the studied 3-6 ringed, semi-volatile polycyclic aromatic hydrocarbons (PAHs) can be analyzed using ELSD under the described mild conditions with A-m differences lower than 6 % w/w. The same can be said for other analyzed hydroxy-PAHs, and heteronuclear PACs. All these standards presented quite uniform response factors despite their different chemical natures. Therefore, ELSD can be used in this zone *for the analysis of complex mixtures of PACs in which there are unknown components, avoiding any calibration step*. This is an advantage with regard to the other conventional HPLC detectors, such as UV, Refractive Index and fluorescence. At low sample loads, ELSD needs a calibration step and can be useful for mixtures of known PACs, in the same manner than the other HPLC detectors. From the point of view of quantitative accuracy, *b* does not have to be equal or close to unity providing an accurate value is known (7).

Are low-sized PACs really underestimated using ELSD?

The chromatographic quantification of PACs and other related compounds (with b.p. and MW lower than 285°C and 300 u.m.a., respectively) using ELSD was questioned in the past (6, 8). However, our results show reasonably uniform response factors in the linear zone of ELSD in the case of PACs with these characteristics. A partial volatilization of all the studied PACs due to the nebulization and evaporation must be discarded, given the negligeable volatility, for instance, of coronene (Po = 1.63 * 10^{-9} mm Hg at 150°C) at the mild conditions used (30°C). Semi-volatile PAHs with 3-6 aromatic rings, small-sized N-heteronuclear PACs and hydroxy-PAHs present similar response factors to hardly volatile coronene, and therefore can be analyzed using mild working conditions.

The impossibility of analyzing PACs using ELSD was exclusively attributed to the supposed volatility of these compounds. Although this should not be discarded in some cases, results presented here suggest that the values of the corresponding response factors reported in the literature were estimated at low loads and/or higher temperatures than those used here. As well, there have been changes in the configuration of nebulizers in the newer models with respect to the older ones. Nebulization directly influences particle diameter, which in turn affects the sensitivity of ELSD for different solutes, as explained in the last section of this work.

It must be stressed that the volatility of a given compound cannot merely be predicted from its b.p. and MW (3). For instance, although acenaphthene and 2-naphthol have similar b.p. and MW, the former showed no signal from ELSD under the conditions used, while the latter gave a high response factor. Vapor pressure at a given temperature (if possible) is a better parameter to compare relative volatilities although it should be taken with caution because ELSD evaporates in an air flow.

However, there is a value of vapor pressure for a given temperature over which PACs cannot be analyzed using ELSD. Thus, two-ringed PACs (naphthalene, 2-methylnaphtalene), and low-sized, non-planar, hydrogenated PACs (acenaphthene, fluorene), showed either no signal or an important loss of response at 30°C, as expected given their high vapor pressures.

Agreement between theoretical and experimental data on evaporative light scattering response of PACs. Why are response factors of studied PACs reasonably uniform under the used working conditions?

The stages involved in evaporative light scattering detection are: nebulization of the HPLC effluent, evaporation of the mobile-phase droplet cloud, and scattering of incident light.

Nebulization depends on the mobile phase properties and flow rate, nebulizer geometry and nebulization conditions, through Mugele and Evans' droplet size distribution (9), and the equation of Nukiyama and Tanassawa, as reported by Van der Meeren et al. (10). Details of all calculations presented here are reported elsewhere (11). The droplet size distribution (in volume) under our working conditions is given in Figure 1.

After evaporating, the diameter of solute particles (d_s) can be related to the concentration, *C*, through

$$d_s = d_m (C / \rho_s)^{1/3}$$

where ρ_s is the solute density, and d is each value of the droplet diameter distribution after nebulization. *C* is function of both time and chromatographic conditions according to

$$C = \frac{X/10^9}{Q_l} \frac{\exp\left[-(t_r - t)^2 / (2sd^2)\right]}{(2\Pi)^{1/2} sd}$$

where X is the sample load, Q_t is the mobile phase flow rate and sd and t_r are the standard deviation and retention time of the chromatographic peak, respectively. This means that each point of a given chromatogram has its corresponding particle size distribution. The highest diameters in the distributions correspond to the maximum of each peak. Figure 2 shows nine size distributions corresponding to the first half of the chrysene peak. Figure 3 gives the particle size distributions at peak maxima in the cases of chrysene and coronene. Particle size distributions for the studied PACs are similar because their densities are not very different (between 1100 and 1300 kg m^3, approximately).

ELSD is a detector which presents different sensitivities with regard to the scattering domain of work (Rayleigh, Mie, reflexion-refraction). These domains are determined by the ratio of a characteristic dimension (e.g. diameter, d_e) of the solute particle to the wavelength(s) of the incident light beam (λ) (12). It is very important to work in similar d_e/λ ranges in order to have homogeneous response factors for the components of a complex mixture. Rayleigh scattering is predominant when d_e/λ is smaller than 0.1. In this domain, the intensity (I) of scattering increases very rapidly with increasing particle diameter (d_e^6). I is lower for particles in the Rayleigh domain than for other domains. Mie scattering becomes preponderant when d_e/λ is greater than 0.1. In this domain, I increases as the fourth power of diameter. For greater d_e/λ ratios (approximately 2), reflexion and refraction become dominant and sensitivity increases. (I is function of diameter squared). I from spherical particles can be calculated *for any size* using Mie's theory. Therefore, when I is expressed in function of the concentration, (13) through particle diameter ($d_e = d_m^* (C / \rho_s)^{1/3}$), then $I = f(C^2)$, $f(C^{1.33})$ or $f(C^{0.66})$, for Rayleigh, Mie or reflexion-refraction domains, respectively. In Table 2 it can be seen that experimentally obtained b values for PACs are between 1.29 and 1.47, that is, near to the theoretical value for Mie's domain. Calculations of d_e/λ from particle size distributions are in agreement with this. The highest d_e/λ for chrysene (at 40 µg, at the maximum of the peak, and for λ=400 nm) is 1.05. The homogeneous response of PACs is illustrated by the similar values of d_e/λ for chrysene and coronene (Figure 3).

Application of ELSD to HPLC-compound class fractionation and HPLC-GPC of fossil fuels

Besides the above-mentioned quantitative application of ELSD for analyzing mixtures of unknown PACs, this detector presents several advantages with respect to Refractive index detector, in the case of compound-class fractionation of fossil fuels, in general: possibility of using gradients of eluants and typical eluants of reversed phase, rapid stabilization with temperature, and adequate baseline (no negative peaks, no solvent fronting). More particularly, coal-tar pitches mainly consist of PAHs and their heteronuclear analogues (14). Therefore, the PACs studied in this work represent quite well a part of PACs found in coal-tar pitches. These are usually analyzed using HPLC-compound class characterization after a chromatographic prefractionation. According to our results, ELSD could be used to quantify this type of analysis. GPC-ELSD has been carried out to obtain comparative curves of size distribution for coal-tar pitches, using the same column as that used here (15). Given that no discrete peaks are obtained with this technique, more research is needed to understand the influence of nebulization and chromatographic conditions on particle diameter in order to perform semi or quantitative analyses.

ACKNOWLEDGEMENTS

The authors are grateful to Spanish DGICYT (Project PB93-0100) and ECSC (European Steel & Coal Community, Project 7220-EC/765) for their financial support

REFERENCES

1. Vo-Dinh, T. In "Chemical Analysis of Polycyclic Aromatic Compounds", ed. by Vo-Dinh, T. Chemical Analysis, vol. 101, John Wiley & Sons, New York, 1989, ch. 1.
2. Lafleur, A.L.; Monchamp, P.A.; Plummer, E.F.; Wornat, M.J. *Anal. Letters* **1987**, *20*, 1171
3. Charlesworth, J.M. *Anal. Chem.* **1978**, *50*, 1414.
4. Lafosse, M; Elfakir, C.; Morin-Allory, L.; Dreux, M. *J. High Resol. Chromatogr.* **1992**, *15*, 312.
5. Dreux, M.; Lafosse, M.; Morin-Allory, L. *LC-GC International* **1996**, march.
6. Coulombe, S. *J. Chromatogr. Sci.* **1988**, *26*, 1.
7. Scott, R.P.W. in "Quantitative Analysis using Chromatographic Techniques", ed. By Katz, E. Separation Science Series. John Wiley & Sons, New York, 1987, ch. 1, p. 24.
8. Bartle, K.D.; Taylor, N.; Mulligan, M.J.; Mills, D.G.; Gibson, C. *Fuel* **1983**, *62*, 1181.
9. Mourey, T.H.; Oppenheimer, L.E. *Anal. Chem.* **1984**, *56*, 2427.
10. Van der Meeren, P.; Vanderdeelen, J.; Baert, L. *Anal. Chem.* **1992**, *64*, 1056.
11. Cebolla, V.L.; Membrado, L.; Vela, J.; Ferrando, A.C., submitted to *J. Chromatogr. Sci.*
12. Kerker, M. "The scattering of light and other electromagnetic radiation", 2nd ed. Academic Press, Inc., New York, 1969.
13. Dreux, M.; Lafosse, M. *Analusis* **1992**, *20*, 587.
14. Alula, M.; Diack, M.; Gruber, R.; Kirsch, G.; Wilhelm; J.C.; Cagniant, D. *Fuel* **1989**, *68*, 1330.
15. Johnson, B.R.; Bartle, K.D.; Herod, A.A.; Kandiyoti, R. *Preprints Am. Chem. Soc., Div. Fuel Chem.* **1995**, *40* (3), 457.

Table 1. Response factors (A/m), and differences between area and mass percentages (Δ) of PAC standards in binary mixtures at several sample loads using either 2-hydroxycarbazole (HCBZ) or coronene (CRN) as references[1].

Standards	40 μg		20 μg		8 μg
	Δ[2]	A/m	Δ[2]	A/m	A/m
7,8-benzoquinoline	0.8	1.188	15.7	0.475	0.213
diphenyldisulfide	1.0	1.187‡	7.0	0.621‡	0.347
coronene	1.5	1.308	8.2	0.870	0.321
perylene	1.5	1.383	7.2	0.754	0.410
2-hydroxycarbazole	1.5	1.390‡	8.2	1.220‡	0.565
Benzo[a]pyrene	2.5	1.407	5.2	0.794	0.435
tianthrene	2.5	1.291	1.3	0.974	0.446
anthracene	2.6	1.002	7.0	0.733	0.536
acridine	2.6	1.523	4.7	1.138	0.319
phenoxazine	3.4	1.584‡	10.1	0.994‡	0.562
2-naphthol	4.2	1.301‡	3.4	0.782‡	0.243
9-phenanthrol	4.4	1.090‡	1.7	1.166‡	0.573
pyrene	4.7	1.478	5.1	1.147	0.563
fluoranthene	5.8	1.436	6.5	0.941	0.390
2,3-benzofluorene	6.1	0.850	8.3	0.638	0.320
9-hydroxyfluorene	6.7	1.454‡	5.8	1.083‡	0.550
carbazole	8.7	0.917‡	7.6	0.634‡	0.389
chrysene	9.7	0.857	9.2	0.647	0.345
phenanthrene	9.0	0.775	22.2	0.419	0.225

[2] Absolute value.[1] Superscript ‡ indicates that coronene was the reference; the remaining refer to HCBZ.

Table 2.- Fitting of ELSD response vs sample load for three studied PACs.

	2-hydroxycarbazole	coronene	chrysene
Linear regression			
slope	1.542	1.537	0.994
intercept	-6.887	-10.07	-3.66
r	0.9995	0.9923	0.999
error %[1] at 5 μg	17.0[2]	140.2	74.9
Logarithmic regression			
b	1.291	1.474	1.344
a	-0.340	-06677	-0.5897
r	0.9984	0.9999	0.9963
error %[1] at 5 μg	-2.9[2]	0.04	-10.5

[1] Error % between the corresponding experimental value and that predicted from the corresponding fitting curve. [2] In these cases, error % at 8 μg.

Figure 1

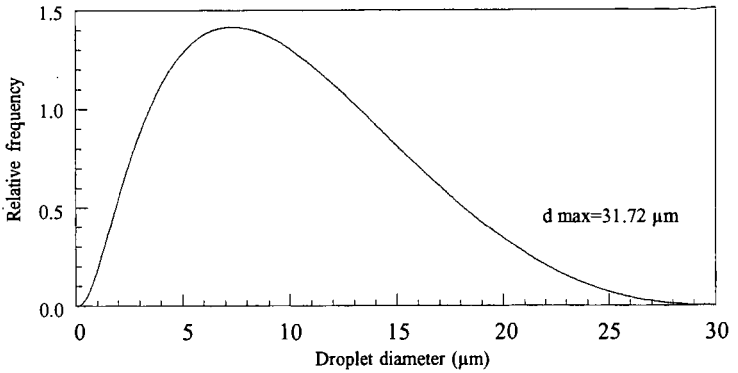

Droplet size distribution (in volume) from the nebulization of THF in a venturi.

Figure 2

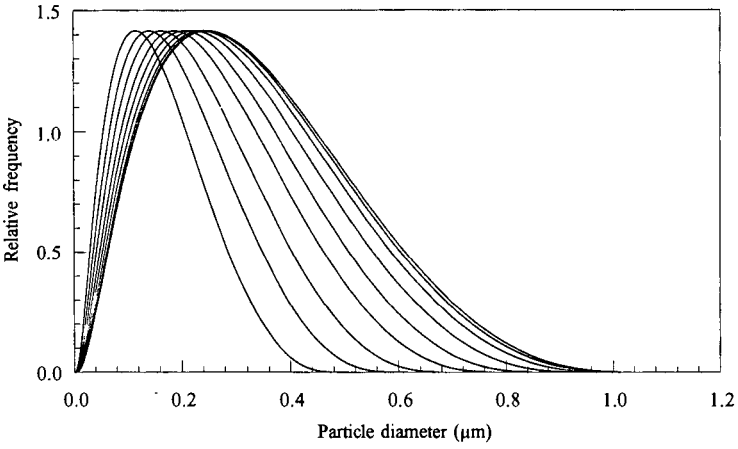

Nine particle size distributions (in volume) corresponding to chrysene elution (5 µg load) from t=tr - w/2 (start of peak) to t=tr (peak maximum)

Figure 3

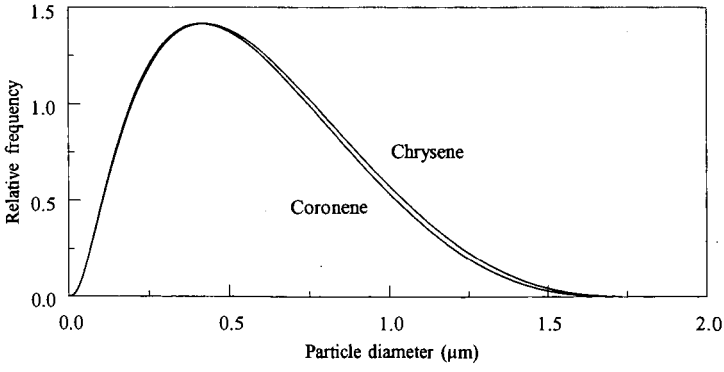

Particle size distributions at peak maxima (40 µg) for chrysene and coronene

ANALYSES OF PRODUCTS FROM AUTOCLAVE REACTIONS: DERIVATION OF REACTION PARAMETERS

Belma Demirel
Center for Applied Energy Research
3572 Iron Works Pike, Lexington, KY 40511-8433, USA
and
Jan Paul
Bilkent University, Chemistry
Bilkent 06533, Ankara, Turkey

Keywords: Hydrocracking, Decalins, Faujasites

ABSTRACT
This work presents energetics for high pressure hydroprocessing reactions derived from post analyses of liquid and gaseous products. Specifically, GC and GC/MS were used to follow the product distribution from the hydrocracking of methyldecalins over zeolite supported palladium and platinum catalysts as a function of temperature. Plain Arrhenius plots summarize key results and reveal possible connections in terms of 'activation energies' between hydrogen consumption and the amounts of different products. The total cycloalkane production and the consumption of hydrogen both show a simple temperature dependence with the same 'activation' energies. Methane production varies more rapidly with temperature but can still be described by a single exponential term. The final example, conversion to aromatics, displays a more complicated dependence with an accelerated yield at high temperature. This form of data analyses connects to a new routine for mass balance evaluations and it is now applied to model catalyst performance and to understand optimum reaction conditions. Other branches of this project include surface spectroscopic measurements of fresh, sulfided and used catalysts, characterization of partially hydrogenated naphthalenes and modeling of hydrogen activity at metal sulfides.

INTRODUCTION

The present work is twofold motivated. The overall project goal is to find optimum conditions for a two-stage conversion of polyaromatic feeds, modelled by 1-methylnaphthalene (1-MeNapht), to fuels [1]. The first step, hydrogenation to methyldecalins (MeDecs) is addressed elsewhere [2]. Within the above engineering framework several scientific challenges constitute a second motivation. One challenge is to improve mass-balance evaluations [3], another to identify surface intermediates by a combination of spectroscopic tools and quantum chemical calculations [4], and yet a third to derive energetics from product analyses. The present work addresses the third topic.

Conversion, product distribution and potential for commercialization were recently demonstrated for an optimized two-stage operation with an initial hydrogenation stage of 1-MeNapht to MeDecs over $NiMo/TiO_2$-Al_2O_3 and a second hydrocracking stage of MeDecs over Pd/Faujasite [5]. This work was extended with weight change measurements and physico-chemical characterization of surface sulfides formed by pretreatment in H_2S/H_2 and of carbonaceous residues formed during operation [6,7]. The extension represents an additional improvement over previous schemes for mass-balance evaluations based solely on analyses of liquid and gaseous phases.

MATERIALS AND METHODS

The catalysts were either prepared with surface impregnation techniques from aqueous solutions followed by calcination in air and sulfidation in H_2S/H_2 (400°C, 2h) or, for ion exchanged Faujusites, used as received from the manufacturer [5]. 1- MeNapht (98%,Aldrich) was used as received for the first reaction stage. The feed for the second stage, MeDecs, was synthesized with better than 95% selectivity [2]. The catalysts and feed were mixed (1:4 to 1:10) in a stirred batch autoclave, operated either as a closed or an open system under hydrogen (700-1500 psi). The liquid product was weighed and analyzed by GC/MS. The composition of the gaseous product was analyzed by GC. The mass of hydrocarbon gases was derived from the pressure change (closed systems) or from the volume of the gas product. The hydrogen amount was calculated from the pressure change before and after reaction (closed systems) or from the change in H:C ratio from feed to product (closed and open systems).

RESULTS AND DISCUSSION

The prime result is a novel compilation of performance data for a series of two-stage reactions of 1-methylnaphthalene conversion to gasoline components using different catalysts. These data clearly show the conversion and potential for an industrial process and the ratio between gaseous and liquid products [1,5].

The scientific results are exemplified by two figures showing the evolution of products as a function of temperature over Pt (Fig.1) and Pd (Fig.2) ion-exchanged Faujasites.

Figs.1 shows that the hydrogen consumption and the total production of cycloalkanes over Pt/Faujasite are well described by a single Arrhenius term with the same apparent activation energy, 30 kJ/mol. Methane production is again well described by a single exponential term but with a considerably larger 'activation energy' 150 kJ/mol. The conversion to aromatics displays a more complicated volcano shape vs. temperature and it is not meaningful to derive a single slope over the entire temperature range.

Hydrocracking of MeDecs over Pd/Faujasite (Fig.2) shows a similar behavior with the following 'activation energies': hydrogen consumption 29 kJ/mol, total cycloalkane production 27 kJ/mol and methane production 130 kJ/mol. Aromatics production again shows a more complex temperature dependence.

The simple temperature dependence of hydrogen consumption and cycloalkane production motivates the search for a simple reaction mechanism involving both functionalities. The apparent 'activation energy' is too low to be translated directly to a certain bond activation process and its origin from possibly counteracting enthalpy and entropy terms is not clear.

The mechanism is different for methane production with an 'activation energy' of 130-150 kJ/mol. This branch of hydrocracking resembles the hydrogenation of surface carbon in Fisher-Tropsch catalysis.

The separate temperature dependence of the aromatics production shows that these compounds are formed neither along the same route as methane nor the cycloalkanes. A bell curve is often the result of competing processes, in our case the onset of dehydrogenation and/or cleavage reactions.

CONCLUSIONS

Quantitative analyses of liquid products and off-gases from autoclave studies of hydrocracking of methyldecalins over Pd/Faujasite and Pt/Faujasite catalysts are presented. The data shows that the mechanism for cycloalkane production is closely related to the hydrogen activity i.e. most likely to the generation of adsorbed atomic hydrogen. It also shows that the route for methane production is separate from this mechanism as well as from the path leading to aromatic compounds.

ACKNOWLEDGEMENTS

We acknowledge collaborations with P.Nordlander at Rice and D.W.Goodman at Texas A&M within the framework of this project. B.Demirel would also like to express her sincere gratefulness to W.D.Wiser, Univ.of Utah, for his help and kindness during most of this project.

REFERENCES

1. Demirel B. and Wiser W.H., Hydrotreatment and Hydrocracking of Oil Fractions Oostende, Belgium, 1997, submitted
2. Demirel B. and Wiser W.H., ASC, Orlando, 1996
3. Demirel B. and Paul J., 7th NSC, Turku, 1996
4. Demirel B., Şafak S., Süzer Ş., Paul J., in progress
5. Demirel B., PhD Thesis, Univ.of Utah, 1996
6. Demirel B. and Paul J., MRS, Boston, 1996, submitted
7. Demirel B. and Paul J., Hydrotreatment and Hydrocracking of Oil Fractions Oostende, Belgium, 1997, submitted

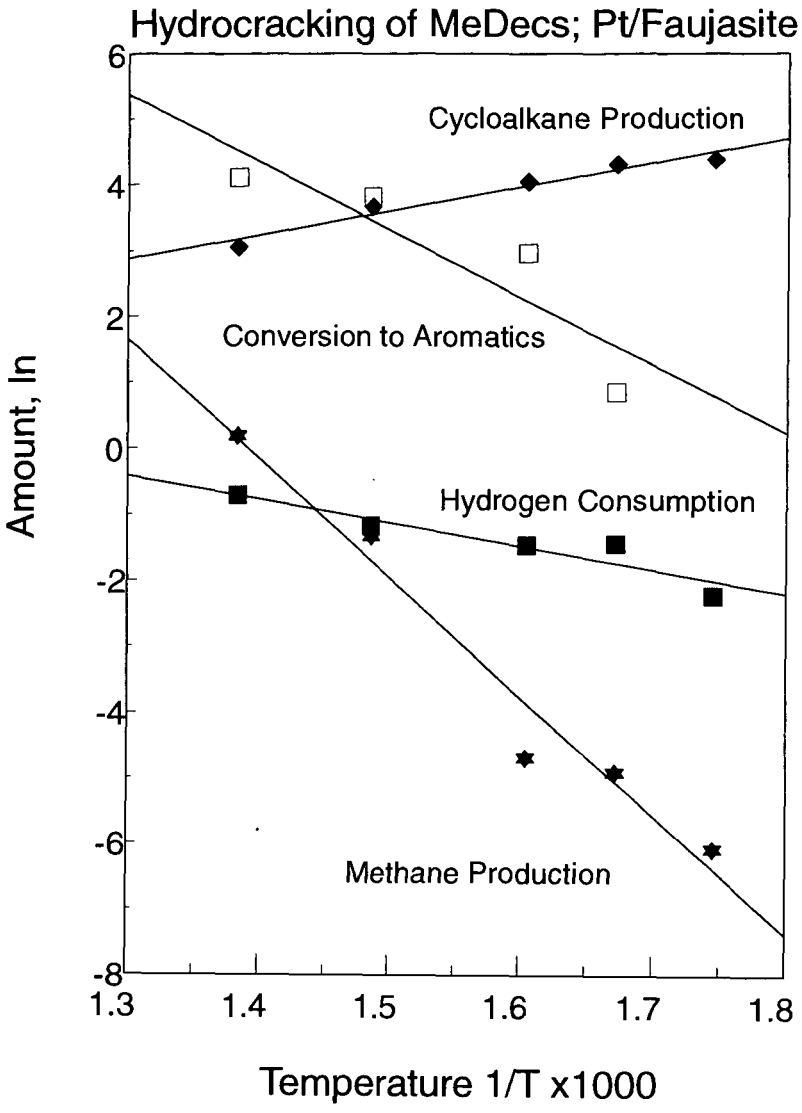

Figure 1.
Hydrocracking of Methyldecalins over Pt/Faujasite. 700 psi. 1h. 10:1 Feed to Catalyst Ratio.

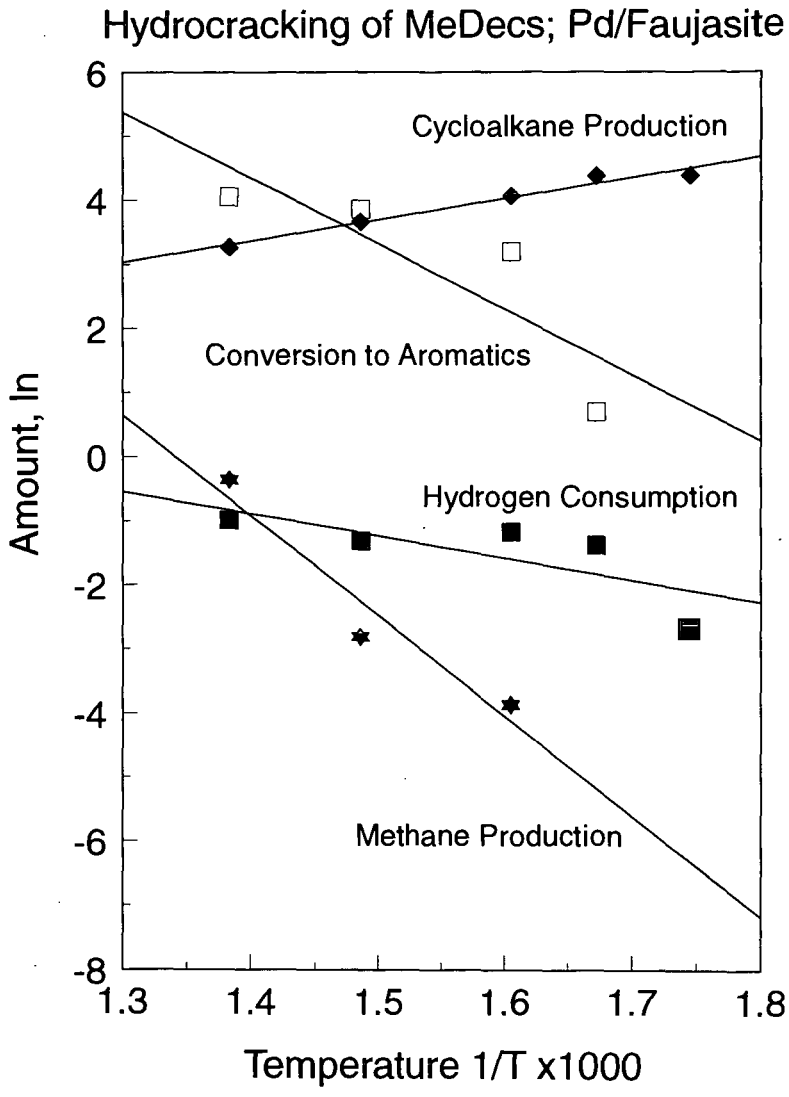

Figure 2.
Hydrocracking of Methyldecalins over Pd/Faujasite. 700 psi. 1h. 10:1 Feed to Catalyst Ratio.

REACTION BEHAVIORS OF MIXED PLASTICS IN LIQUID-PHASE CRACKING

Jyi-Perng A. Wann, Tohru Kamo, Hiroshi Yamaguchi*, and Yoshiki Sato
National Institute for Resources and Environment, Tsukuba, Ibaraki, 305 Japan
*Engineering Research Center, NKK Corp., Kawasaki, Kanagawa, 210 Japan

Keywords: PS, PE, Liquefaction

INTRODUCTION

The majority of waste plastics today is either incinerated or buried for landfills. However, incineration of waste plastics can cause damages in furnace and air pollution problems. Shortage of available landfill sites also has become a serious concern. The methods of waste plastic recycling therefore have been paid much attention with the viewpoint of effective environmental protection. Liquefaction of waste plastics is an attractive recycling method in terms of producing fuel oil or chemicals. To date, most of the waste plastic liquefaction investigations have been limited to the areas not involving the use of a solvent. Pilot-scaled plants, such as those in the Fuji Recycle Process in Japan [1] and the VCC Process in Germany [2], have been operated for some time. Although high conversion of waste plastics can be obtained at a temperature as low as 400 °C, problems such as wide molecular weight distribution in the produced oil and high coking tendency have been encountered. Liquid-phase cracking of waste plastics has the potential of overcoming these problems, yet few research has been reported on the liquefaction behaviors for the liquid-phase cracking [3-5]. Polyethylene (PE) has been regarded as one of the polymers difficult to liquefy, while the cracking of polystyrene (PS) is considered to proceed in a way different from that of PE. Hence, we investigated the cracking of PS, PE, and their mixtures using solvents of different hydrogen donation capability. Differences in the liquefaction behaviors between PS and PE, influences of the solvent type, synergistic effects for the liquefaction of PS/PE mixtures, and a property in the oil are presented in this paper.

EXPERIMENTAL

Pellet-sized high-density PE (Mitsui Petrochemical Co.) and PS (Dai-Nippon Ink Chemicals) of commercial grades were used. Reagent-grade tetralin (>97% purity) and n-decane (>99% purity) (Tokyo Chemical Industry Co.) were used without further purification. A total weight of 80 g of the plastic-solvent mixture was charged into a 300-mL autoclave reactor in each run. The wt./wt. ratio between the plastic and the solvent was 1/3 or 1/0. For the liquefaction of plastic mixtures, the wt./wt. ratio of PS to PE used was 3/1, 1/1, or 1/3. The reactor was charged with nitrogen to 40 kg/cm^2 (570 psig) at room temperature. The reaction was conducted at 440 °C for 60 min, with constant stirring at 1000 rpm. The volume and the composition of the produced gases were measured after reaction. The produced liquid, of which the weight was calculated based on the assumption of no weight loss for light products at room temperature, was distilled under a vacuum less than 1 torr. The recovered liquid, with the boiling point range lower than 538 °C, was further analyzed with a GC–FID system equipped with a capillary column. The oil yield was calculated with the following equation:

$$\text{Oil yield, (wt./wt. basis)} = \frac{\text{wt. (recovered liquid)} - \text{wt. (charged solvent)}}{\text{wt. (charged plastic)}}$$

Concentrations of, mainly, benzene, toluene, and some alkylbenzenes and n-alkanes, were measured by the FID-GC analysis.

RESULTS AND DISCUSSION

Cracking of PS

The yields of products from PS cracking at 440 °C, with and without solvent addition, are presented in Table 1. The results for corresponding solvent blank runs are also included for comparison. In the absence of a solvent, the yields of gas, oil, and residue were 0.3, 72.9, and 26.8%, respectively. Toluene, ethylbenzene, and cumene were the main liquid products from PS. Benzene, styrene, and n-propylbenzene were produced in relatively low quantities. We found that a much higher molar quantity of toluene was produced than that of methane. This suggests that the majority of the toluene may not come directly from the cracking of ethylbenzene.

When n-decane was used, the yields of gas, oil, and residue were 5.1, 83.8, and 11.1%, respectively. Under the reaction condition, n-decane was expected to be an

inert solvent, because only a small amount of n-alkanes in C5–C9 range was produced during the n-decane solvent blank run. Nevertheless, a slight increase in the total yield of gas, which includes ethane, propane, and n-butane that can be converted from n-decane, has been observed in the reaction with PS. The increased gas yield indicates that the presence of PS may have enhanced the decomposition of n-decane slightly. The higher oil yield, when compared to the case without the solvent addition, suggests that the occurrence of condensation reactions may be decreased by a dilution effect from n-decane solvent.

The highest oil yield of 95.8% was obtained when tetralin was the solvent. This could be due to both the effects of solvent dilution and hydrogen donation from tetralin solvent.

Cracking of PE

Table 2 shows the distribution of products from PE cracking at 440 °C. Without the solvent addition, the yields of gas, oil, and residue were 1.7, 53.9, and 44.4%, respectively. The characteristic distribution of n-alkanes in the produced oil indicates that the decomposition of PE proceed by radical chain reactions [1]. Very low oil yields of 1.6% and 0.8% were obtained for the cracking in n-decane and in tetralin, respectively. The decreased conversion of PE with n-decane may be due to a retardation effect resulting from solvent dilution to the induced cracking of PE. The lowest conversion of PE, obtained in tetralin, suggests that the combined effects of dilution and hydrogenation by tetralin may have further retarded the decomposition of PE.

Cracking of PS/PE Mixtures

No solvent addition. Figure 1 shows the yields of toluene, ethylbenzene, cumene, n-alkanes in C5–C9 range, and oil yield in the reaction without solvent addition. At each PE fraction (as expressed by PE/(PE+PS) in Figures 1–3) of 0.25, 0.50, and 0.75, the oil yield of the plastic mixtures was higher than that of each comprising plastic. The fairly constant yield of toluene and the slight decreased yield of ethylbenzene, as observed for the PE fractions from 0 to 0.50, suggests that cracking of PS may have been enhanced by the mixing from PE. The total yield of n-alkanes in C5–C9 range produced from PE was low but increased proportionally with the increasing amount of PE in the feed mixtures. This indicates that the presence of PS did not enhance the cracking of PE. Therefore, it is considered that the enhanced conversion of PS to oil could be mainly due to a dilution effect resulted from PE, similar to that from n-decane to the cracking of PS, as discussed earlier.

n-Decane as the solvent. Figure 2 shows the effect of n-decane on the distribution of products due to PE and PS mixing. The figure shows significant synergistic effects for oil yields in the mixtures. The yields of toluene, ethylbenzene, and cumene decrease almost linearly with the increased PE fraction in the feed mixtures. The trend for the products implies that cracking of PS may not be significantly enhanced by the presence of PE. The high synergistic effect for oil yield at the PE fraction of 0.75 could be mainly due to the enhanced contribution from PE cracking since the dilution effect from the solvent may be considered equal for all the fractions. The yield of C5–C9 n-alkanes was fairly constant in the PE fraction ranges from 0 to 0.75. This indicates that the n-alkanes may be produced from the decomposition of n-decane, PE, or the both.

Tetralin as the solvent. Figure 3 shows the effect of tetralin on the distribution of products due to PE and PS mixing. The yields of oil and each light aromatic compound from PS decreased monotonously with the increased PE fraction. The results also show that the effects of tetralin for oil yield increases in the mixtures were not as pronounced as in the aforementioned two cases. The nearly linear relationship between the yields of each products at each PE fraction indicates that the synergistic effects between PS and PE could be low in tetralin solvent. It may be a result of rapid stabilization by hydrogen donation from tetralin to the radicals produced from PS cracking.

CONCLUSIONS

The use of solvents can play important roles in the liquefaction of plastics. For the liquid-phase cracking of PS, it has been demonstrated that the oil yield can be

increased by the minimization of condensation reactions. On the other hand, the oil yield for PE cracking can be decreased as a result of retardation to radical chain reactions, due to the dilution or hydrogen donation effect from the solvents. Interactions between PS and PE also can be influenced by the solvents used. Liquid-phase cracking shows a promising direction for the processing of waste plastics by proper selection of reaction systems.

ACKNOWLEDGMENTS

One author, J.-P. Anthony Wann, would like to thank the financial supports of STA fellowship arranged by National Science Foundation, USA, and Science and Technology Agency, Japan. He is also grateful to the helpful discussion from Professor David M. Bodily of University of Utah.

REFERENCES

1. Kasutani, T., et al., Waste Plastics – Thermal and Chemical Recycling, Kagaku Kogyo Nippo Sha, Tokyo, Japan, 1994. p. 9.
2. Niemann K., "Feedstock Recycling of Post Consumer Waste Plastics," Proceedings Recycle '95 – Environmental Technologies, p. 5-3.1.
3. Palmer, S. R., Hippo, E. J., Tandon, D., and Blankenship, M., "Liquefaction of Coal/Waste Plastic Mixtures" Proc. 8th Int. Conf. of Coal Sci., 1995, Elsevier, Amsterdam, Vol. II, p. 1523.
4. Huffman, G. P., Feng, Zhen, Huggins, F. E., and Mahajan, V., "Direct Liquefaction of Waste Plastics and Coliquefaction of Waste Plastics with Coal," Proc. 8th Int. Conf. of Coal Sci., 1995, Elsevier, Amsterdam, Vol. II, p. 1513.
5. Burgtorf, J., and Kocker, H. Meier zu, "Hydrogenating Liquefaction of Plastic Wastes in Hydrogen-Donating and Non-Hydrogen-Donating Solvents," Ber.-Dtsch. Wiss. Ges. Erdoel, Erdgas Kohle, Tagungsber, 1994, p. 353.

Table 1. Yields of products from blank runs and from PS cracking at 440 °C

Reaction Environment:	Tetralin		n-Decane		No Solvent
wt.% of PS	Blank[1)]	440 °C	Blank[1)]	440 °C	440 °C
Gas	**0.0**	**0.7**	**2.1**	**5.1**	**0.3**
Oil		**95.8**		**83.8**	**72.9**
benzene	0.0	0.2	0.0	0.7	0.9
toluene	0.2	40.8	0.0	33.3	21.6
ethylbenzene	0.2	27.7	0.0	13.4	27.4
styrene	0.0	0.5	0.0	0.5	0.0
cumene	0.0	5.5	0.0	3.7	6.6
n-propylbenzene	0.0	1.5	0.0	1.6	1.3
total light aromatics	0.4	76.2	0.0	53.1	57.8
total C5–C9 n-alkanes	0.0	0.0	7.8	1.0	0.1
Residue		**3.5**		**11.1**	**26.8**

Note:1) data calculated on the basis of the initial weight of plastic

Table 2. Yields of products from PE cracking at 440 °C

Reaction Environment:	Tetralin	n-Decane	No Solvent
wt.% of PE			
Gas	**0.1**	**0.8**	**1.7**
Oil	**0.8**	**1.6**	**53.9**
total C5–C9 n-alkanes	0.0	3.2	6.8
Residue	**99.1**	**97.6**	**44.4**

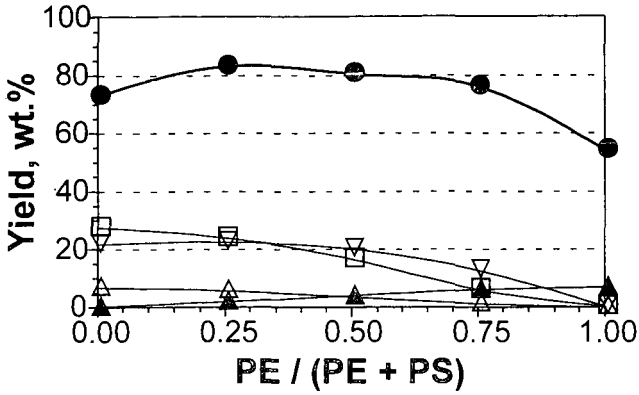

△cumene □ethylbenzene ▽toluene ▲C5-C9 n-alkanes ●oil

Figure 1. Effect of plastics mixing on yields of products without solvent

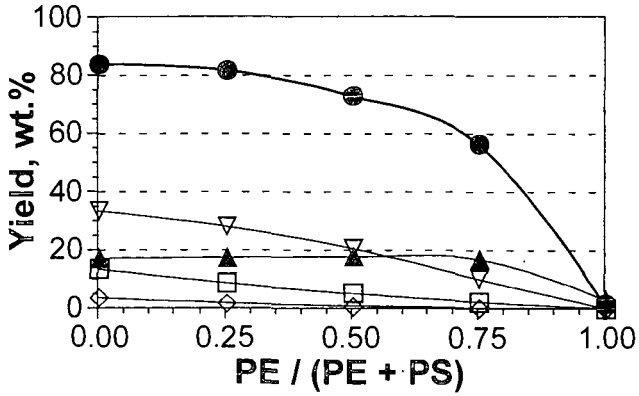

△cumene □ethylbenzene ▽toluene ▲C5-C9 n-alkanes ●oil

Figure 2. Effect of n-decane on yields of products due to PS-PE mixing

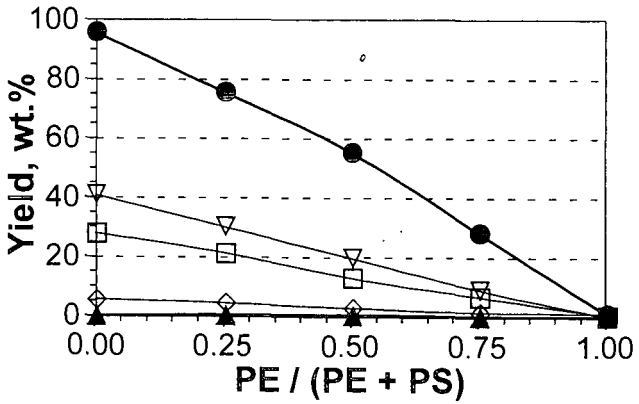

△cumene □ethylbenzene ▽toluene ▲C5-C9 n-alkanes ●oil

Figure 3. Effect of tetralin on yields of products due to PS-PE mixing

CATALYTIC CRACKING OF POLYSTYRENE

Rong Lin and Robert L. White
Department of Chemistry and Biochemistry
The University of Oklahoma, Norman, OK 73019

Keywords: catalytic cracking, polymer cracking, polymer recycling

Introduction

Plastics have become the most produced materials in the United States since the mid of 1970's. The significant increase in plastics production has resulted in a similar significant increase in plastics disposal. Polystyrene is widely used in consumer product packaging and to make disposable containers. About one billion pounds of polystyrene are used in single-use disposable applications.

One approach to deal with plastic waste is to convert it into useful products, such as fuel oil and chemicals[1,2], by tertiary recycling methods. The development of effective plastic waste recycling by catalytic cracking will require detailed knowledge of the relationship between catalyst structure and cracking product distributions[3-7]. In order to compare the polymer cracking properties of different catalysts, it is preferable to examine the effects of catalysts without complications due to reactions of primary cracking products with polymer residue. Secondary reactions can be minimized by limiting the contact between primary volatile products and the catalyst/polymer mixture. This can be accomplished by maintaining high catalyst to polymer ratios and providing efficient and rapid removal of volatile products. In this paper, the importance of catalyst acidity and HZSM-5 channel structure on the volatile catalytic cracking product distributions derived from polystyrene is assessed by comparing thermal analysis results obtained from samples prepared by coating silica-alumina, HZSM-5 zeolite, and sulfated zirconia catalysts with thin layers of polystyrene.

Experimental

Samples examined in this study were: high molecular weight polystyrene (HPS), low molecular weight polystyrene (LPS), and polystyrenes coated on silica-alumina, HZSM-5, and sulfated zirconia cracking catalysts (10-20% (wt/wt)). HPS and LPS were purchased from Aldrich Chemical Company (Milwaukee, WI). The silica-alumina catalyst was provided by Condea Chemie GmbH (Hamburg, Germany). The silica-alumina catalyst contained 11.8% by weight alumina and had a surface area of 282m^2/g. The HZSM-5 zeolite catalyst was obtained from Mobil Oil (Paulsboro, NJ) and was characterized by a 355 m^2/g surface area and a 1.5% alumina content. The sulfated zirconia catalyst was synthesized following procedures described previously. The sulfated zirconia catalyst had a surface area of 157 m^2/g and contained 9% by weight sulfate. Polystyrene-catalyst samples were prepared by dissolving polystyrene in cyclohexane, adding catalyst, and then rotoevaporating the mixture to remove solvent. The resulting polymer coated catalyst samples were dried for several hours at 90°C. The apparatus used for pyrolysis-GC/MS and TG-MS measurements have been described previously. Pyrolysis separations were achieved by using a HP 5890 capillary GC with a DB-5 column (0.25 μm film thickness). The gas chromatograph oven temperature program consisted of a 2 min isothermal period at -50 °C followed by a 10 °C/min ramp to 280 °C, and then another isothermal period at 280 °C for 5 minutes. For TG-MS studies, samples were heated from 50 °C to 600 °C in He at rates of 1, 10, 25, and 50 °C/min. For TG-GC/MS studies, a Valco Instruments, Inc. (Houston, TX) heated eight external volume sample injector was employed to divert small volumes (ca. 20 μL) of TG effluent into a 30 m DB-5 capillary column (0.25 μm film thickness) for GC/MS analysis. A 5 °C/min heating rate from 50 °C to 600 °C in 20 mL/min He was used to heat samples in the thermogravimetric analyzer. When samples reached 100 °C, TG effluent was sampled. Above 100 °C, TG effluent sampling was repeated at 3 min intervals during TG-GC/MS analysis. A 5 mL/min He carrier gas flow rate through the TG-GC/MS chromatographic column was employed and the column temperature was maintained at 100 °C during separations. TG-GC/MS column effluent was split prior to entering the mass spectrometer to maintain an ion source pressure of 5 x 10^{-5} torr.

Results and Discussion

Pyrolysis-GC/MS results obtained for polymers and polymer-catalyst samples pyrolyzed at 400°C were compared to investigate the effects of different catalysts and initial polymer molecular weight on cracking product distributions. Tables 1 and 2 contain the volatile product distributions derived from chromatograms for neat polymers and polymer-catalyst samples. Thermal degradation of neat polystyrene samples produced primarily styrene monomer along with substantial amounts of dimer and trimer. By examining the volatile product distributions for high molecular weight polystyrene (HPS) and low molecular weight polystyrene (LPS), it was found that the relative yield of trimer was about three times that of the dimer and the relative yield of styrene was greater for the HPS sample than for the LPS sample. However, in the presence of catalysts, the most abundant volatile product was benzene, and very little styrene was detected. Benzene comprised about 30% of the volatile material produced from the polymer-Si/Al and polymer-ZrO_2/SO_4 samples, and over 50% from the polymer-HZSM-5 zeolite samples. Other volatile products detected from the polymer-catalyst samples with relative yields over 1% included: alkyl benzenes, indanes, indenes, and naphthalenes. For both LPS and HPS samples, the relative yields of alkyl benzenes were greatest for samples containing Si/Al and ZrO_2/SO_4 catalysts, whereas polymer-HZSM-5 samples produced fewer alkyl benzenes but significantly larger quantities of indenes.

TG-MS was employed to correlate the evolution of volatile thermal decomposition products with sample weight loss and to calculate volatilization activation energies. Weight loss curves obtained by heating samples at 10 °C/min in He are shown in Figures 1 and 2. Compared to neat polymer thermal decompositions, all three catalysts lowered the temperature at which significant sample weight loss occurred. The catalytic effect was greatest for the samples containing the ZrO_2/SO_4 catalyst. By examining the weight loss curves, it was found that, for the same catalysts, the weight loss onset temperature was lower for the LPS polymer than for the HPS polymer. The polymer-ZrO_2/SO_4 samples exhibited two distinct steps in their weight loss curves. TG effluent mass spectra indicated that the low temperature weight loss step was caused by polystyrene decomposition. The high temperature step resulted from catalyst decomposition and corresponded to SO_2 evolution.

Neat polymer and polymer-catalyst samples were subjected to TG-MS analysis in He with heating rates of 1, 10, 25, and 50 °C/min to investigate the effects of catalysts on volatilization activation energies calculated by using the Friedman method. The activation energy for the neat HPS polymer was slightly higher than that for the neat LPS polymer. For samples containing the same catalyst, those containing the LPS polymer exhibited a lower volatilization activation energy than those containing the HPS polymer. The lowest volatilization activation energies were calculated for samples containing ZrO_2/SO_4 catalyst.

Mass spectra obtained during TG-MS analyses could not be used to profile the temperature dependent evolutions of the primary thermal decomposition products because species specific ions could not be identified. By placing a gas chromatograph between the thermogravimetric analyzer and mass spectrometer, it was possible to separate the primary volatile products generated in the thermogravimetric analyzer prior to mass analysis. Figures 3 and 4 contain plots of TG-GC/MS chromatographic peak areas (integrated total ion current) as a function of sample temperature for selected products. For all samples analyzed, benzene was by far the most abundant volatile product. All of the polymer-catalyst samples produced alkyl benzenes and indanes, however samples containing HZSM-5 catalyst produced significantly less than the other samples. Styrene and indenes were only detected from samples containing HZSM-5 catalyst.

Formation of the primary polystyrene catalytic cracking volatile products can be explained by consequences of initial electrophilic attack on polymer aromatic rings by protons. Most of the products detected by pyrolysis-GC/MS and TG-GC/MS can be derived from ortho ring protonation. The initial step in polystyrene cracking is protonation of polymer aromatic rings. Ortho protonation can easily lead to benzene evolution and the formation of a secondary macro cation, or may result in chain shortening, yielding a chain end cation and a saturated chain end.

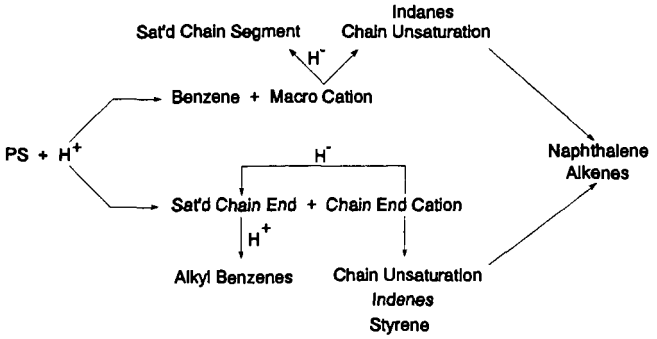

After protonation of chain end aromatic rings, β-scission can yield alkyl benzenes. Beta-scission and rearrangement of chain end cations can lead to chain unsaturation or the formation of styrene and indenes. Cyclization of the secondary macro cations can lead to the formation of indanes, or after rearrangements and β-scission of macro cations, chain unsaturation can be formed. Also, macro cations can undergo hydride abstraction leading to the formation of saturated chain segments. A consequence of chain unsaturation might be the formation of conjugated polyene segments that may subsequently cyclize to form naphthalenes.

Conclusions

Effects of different catalysts and initial molecular weights of polystyrene on catalytic cracking product distributions were studied. Benzene was produced by polystyrene catalytic cracking at temperatures as low as 130 °C for LPS-ZrO_2/SO_4 samples. This suggests that low temperature benzene evolution may result primarily from chain ends, which would be more abundant for the LPS polymer than for the HPS polymer. Chain end aromatic rings should be somewhat more susceptible to electrophilic attack because electron release from the polymer backbone into these rings should be slightly greater than for other aromatic rings in the polymer. Because the samples containing the LPS polymer had more chain ends than the HPS polymer, low temperature reaction rates for the LPS polymer would be consistently higher than for the HPS polymer, which would lead to the observed higher benzene evolution rates at low temperature for samples containing the LPS polymer. Benzene can be easily formed after aromatic ring protonation, but that formation of other volatile products is more difficult and may require additional reactions, such as macro cation rearrangement, hydride abstraction, or successive protonations.

Acknowledgment

Financial support for this work from the National Science Foundation (CTS-9509240) is gratefully acknowledged.

References

1. D.S. Scott, S.R. Czernik, J. Piskorz, D.Radlein, *Energy & Fuels*, 4, 407(1990).
2. Y. Ishihara, H. Nambu, T. Ikemura, T. Takesue, *J. Appl. Polym. Sci.*, 38, 1491(1989).
3. M. Yamamoto, I. Suzuko, S. Yamanaka, *Nippon Kagaku Kaishi*, 5, 802(1976).
4. T. Ogawa, T. Kuroki, S. Ide, T. Ikemura, *J. Appl. Polym. Sci.*, 27, 857(1981).
5. Cr.I. Simionescu, C. Vasile, P. Onu, M. Sabliovschi, G. Moroi, V. Barboiu, D. Ganju, M. Florea, *Thermochim Acta*, 134, 301(1988).
6. Z. Zhang, T. Hirose, S. Nishio, Y. Morioka, N. Azuma, A. Ueno, H. Ohkita, M. Okada, *Ind. Eng. Chem. Res.*, 34, 4514(1995).
7. G. Audisio, F. Bertini, P.L. Beltrame, P. Carniti, *Polym. Degrad. Stab.*, 29, 191(1990).

Table 1. LPS Decomposition Products at 400°C

Product	Neat LPS	LPS-Si/Al	LPS-ZrO_2/SO_4	LPS-HZSM-5
benzene		31	31	52
toluene	1	1	3	3
ethyl benzene		20	10	5
styrene	41	1		1
isopropyl benzene		6	6	
methyl styrene				
indane		10	10	7
indene		1		3
methyl indane		17	25	7
methyl indene				3
naphthalene		4	2	7
2-methyl naphthalene		4	2	6
1-methyl naphthalene		2	2	
dimer	11			
trimer	35			

Table 2. HPS Decomposition Products at 400°C

Product	Neat HPS	HPS-Si/Al	HPS-ZrO_2/SO_4	HPS-HZSM-5
benzene		30	33	60
toluene			3	2
ethyl benzene		14	12	2
styrene	68	4		2
isopropyl benzene		9	8	
methyl styrene				1
indane		15	9	3
indene		1		3
methyl indane		17	8	6
methyl indene				3
naphthalene		3	7	3
2-methyl naphthalene		2	5	3
1-methyl naphthalene		2	5	1
dimer	6			
trimer	16			

Table 3. Volatilization Activation Energies (kcal/mol)

Catalyst	LPS	HPS
none	46.4 ± 1.2	48.5 ± 0.8
Si-Al	33.8 ± 0.5	38.6 ± 0.5
ZrO_2/SO_4	24.4 ± 2.9	28.9 ± 1.9
HZSM-5	34.6 ± 0.5	36.0 ± 1.3

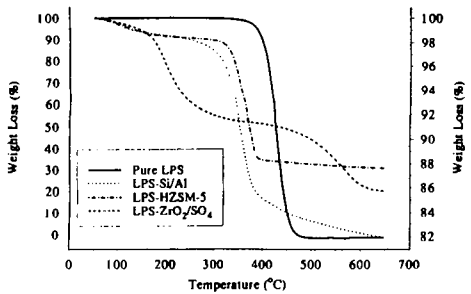

Figure 1. TG weight loss curves for neat LPS (left axis) and LPS-catalyst samples (right axis) obtained by heating samples at a rate of 10 °C/min.

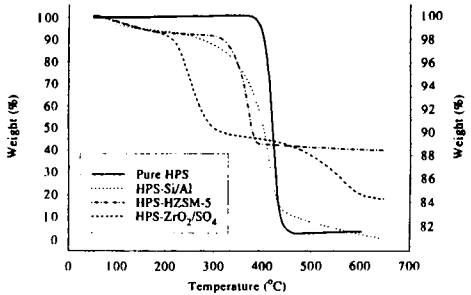

Figure 2. TG weight loss curves for neat HPS (left axis) and HPS-catalyst samples (right axis) obtained by heating samples at a rate of 10 °C/min.

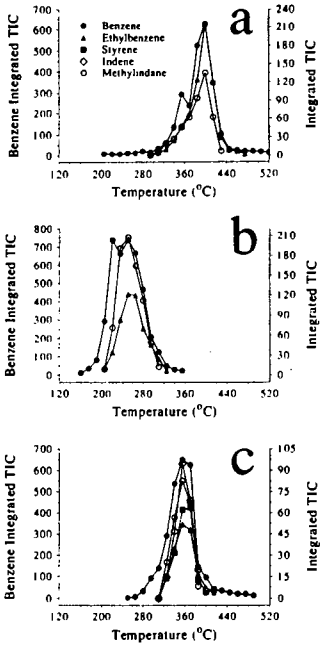

Figure 3. TG-GC/MS chromatographic peak areas derived from (a) LPS-Si/Al, (b) LPS-ZrO_2/SO_4; and (c) LPS-HZSM-5.

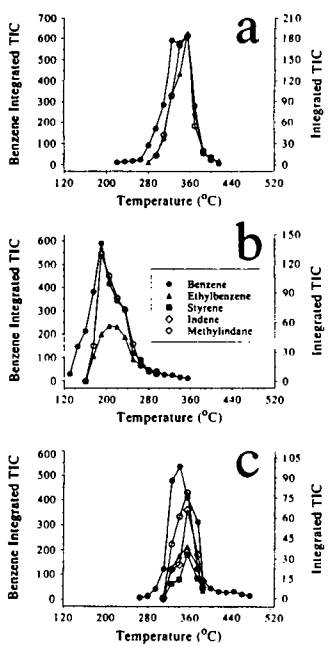

Figure 4. TG-GC/MS chromatographic peak areas derived from (a) HPS-Si/Al, (b) HPS-ZrO_2/SO_4; and (c) HPS-HZSM-5.

INFLUENCE OF METAL OXIDE MODIFICATION OF ALUMINA ON THE DISPERSION AND ACTIVITY OF VANADIA CATALYSTS

L. Jhansi Lakshmi and Elmer C. Alyea

Department of Chemistry and Biochemistry
University of Guelph, ON N1G 2W1

and

S.T. Srinivas, P.S. Sai Prasad and P. Kanta Rao

Physical and Inorganic Chemistry Division
Indian Institute of Chemical Technology
Hyderabad-5000 007, A.P., India

Alumina was modified with 10% MO_x (MO_x = TiO_2, ZrO_2, La_2O_3 or MgO) prior to its impregnation with 12 wt% vanadia. The catalysts were characterised by x-ray diffraction (XRD), electron spin resonance (ESR) and oxygen chemisorption. The activities of the catalysts were determined by methanol partial oxidation and their acid-base properties were evaluated for the decomposition of isopropanol. Metal oxide modification is found to influence significantly the surface coverage and the methanol partial oxidation activity of vanadia supported on alumina. With proper MO_x modification enhanced reducibility of vanadia could be attained, which in turn makes the partial oxidation more facile.

Keywords: modified alumina, vanadia, partial oxidation

INTRODUCTION

Vanadia supported on high surface area carriers like Al_2O_3, SiO_2, etc., has been widely studied for catalyzing a great variety of reactions such as partial oxidation, selective catalytic reduction of NO_x and oxidative dehydrogenation of light alkanes [1-5]. The oxides like TiO_2 and ZrO_2 when employed as supports for partial oxidation and hydroprocessing catalysts, were found to exhibit enhanced activities and selectivities in comparison with Al_2O_3-supported catalysts [2,6]. The disadvantages with these carriers are their low surface area, high surface acidity, low volume activity and phase transition at high temperatures making them unsuitable for industrial applications. By adding small quantities of these oxides to relatively high surface area, thermally stable supports such as alumina the aforesaid problems can be obviated. Recently there are reports in the literature [7-11] on the support modification with additives like alkali/alkaline earth metals, halides, rare earth oxides, phosphates and sulphates, which enhance the acidic or basic character or impart thermal stability to the carrier. Shen et al. [7,8] in their investigations on Al_2O_3 support modification with additives such as K_2O, MgO, La_2O_3, SnO_2 etc. have observed that these oxides influence the number and nature of acid sites on alumina support surface. Wei et al. [12] have observed increased reducibility of molybdena and higher hydrodesulphurisation activity on titania modified γ-Al_2O_3 supported hydroprocessing catalysts. Support modification is said to influence the nature of active sites by way of increasing the reducibility of the transition metal oxide resulting in enhanced activity and selectivity of the catalysts. However, the influence of support modification on the redox and acid-base properties of V_2O_5/Al_2O_3 is not yet thoroughly understood.

The aim of the present investigation is to elucidate the role of modification of the Al_2O_3 support with TiO_2, ZrO_2, La_2O_3 or MgO on the dispersion and methanol partial oxidation activity of vanadia catalysts.

EXPERIMENTAL

Four different modified supports, namely, TiAl, ZrAl, LaAl and MgAl were prepared by impregnating the γ-Al_2O_3 (Harshaw, Gamma phase, S.A. 196 m^2/g) support with 10 wt.% each of MO_x, (MO_x = TiO_2, ZrO_2, La_2O_3, MgO). The precursors used were Fluka A.R. grade $(C_{12}H_{28}O_4)Ti$ and $(C_{12}H_{28}O_4)Zr$ for TiO_2 and ZrO_2 respectively; and Loba Chemie, A.R. grade $Mg(NO_3)_2$, $6H_2O$ and $La(NO_3)_3$, $6H_2O$ for MgO and La_2O_3, respectively. The organometallic precursors of titania and zirconia were dissolved in methanol prior to impregnation on Al_2O_3. Lanthanum and magnesium hydroxides were precipitated by ammonia hydrolysis of their aqueous nitrate solutions. The excess solutions were evaporated to dryness on a water bath and the catalyst masses were further dried in an air oven at 110°C for 12 h. The modified supports were calcined at 550°C for 5 h. VMAl catalysts (M = Ti, Zr, La, Mg) were synthesized by

impregnation of aqueous solution containing a calculated amount of NH_4VO_3 (Fluka, A.R. grade), corresponding to 12 wt.% V_2O_5, on modified supports. Drying and calcination procedures were similar to those described above. Following the same procedure a 12 wt.% V_2O_5/Al_2O_3(VAl) was prepared as a reference.

XRD patterns were recorded on a Phillips PW 1051 diffractometer using Ni filtered CuK_a radiation. ESR spectra were recorded on a Bruker ER 200 D SRC X band spectrometer with 100 KHz modulation at ambient temperature. An all-glass high vacuum apparatus with a facility to reduce (at 500°C, in a flow of H_2) the samples *in situ* was used to carry out the low temperature (-78°C) oxygen chemisorption experiments. The details of the experimental procedure are described elsewhere [10]. BET surface area of the catalysts were determined by N_2 physisorption.

Activity studies for the partial oxidation of methanol were carried out in the temperature range 175-250°C taking 200 mg of the catalyst (0.5 mm size) packed in a fixed bed tubular glass reactor of 6 mm i.d. Purified air at a flow rate of 60 ml/min, saturated with methanol (by passing through a saturator maintained at 25°C), was introduced into the reactor. After a steady-state period of 30 min the products were analyzed on-line with a 10% Carbowax 20 M column (2 m long) using a flame ionization detector. The product stream comprised mainly formaldehyde, dimethyl ether with some traces of methyl formate, CO and CO_2. Oxidative decomposition of isopropanol was carried out in the same reactor under similar reaction and analysis conditions at a constant temperature of 175°C and at atmospheric pressure, using about 200 mg of catalyst. The products observed consisted mainly of propene and acetone with traces of diisopropyl ether.

RESULTS AND DISCUSSION

BET surface area, oxygen uptake, active site density and surface coverage values are shown in Table 1. It can be seen that the surface areas of the vanadia catalysts supported on MO_x modified alumina (VMAl) are significantly lower than vanadia on unmodified alumina (VAl), which in turn, is lower than the alumina support itself. This observation is expected due to the blockage of pores in the alumina as a result of the addition of the metal oxide as well as the active component. Oxygen uptakes of the VMAl catalysts are more when compared to the VAl catalyst except in the case of VMgAl. Among the four catalysts VTiAl is showing the highest oxygen uptake which may be due to a greater number of reducible vanadia sites. Both active site density and the surface coverage are high in VTiAl indicating that the V_2O_5 is highly dispersed on the TiO_2 modified Al_2O_3 support. Generally the strength of interaction between the support and the active component governs the dispersion and hence oxygen uptake capacity [13]. The increased oxygen uptakes of VTiAl, VZrAl and VLaAl catalysts may be due to reduced strength of metal oxide-support interaction. Modification of alumina might have caused a decrease in interaction between the support and active phase enabling increased reducibility of V_2O_5. Similar observations were made by Wei et al. in molybdena based hydroprocessing catalysts supported on TiO_2 modified Al_2O_3 [12].

The XRD patterns of the VAl and VMAl catalysts show that there are no lines corresponding to crystalline vanadia in all the catalysts. Vanadia may be existing as a highly dispersed phase. However, the presence of microcrystalline particles with size less than 40 A cannot be ruled out. The modified supports exhibited the peaks corresponding to their respective oxides with low intensities. The anatase phase of TiO_2 was observed in TiAl and lines corresponding to tetragonal and monoclinic phases of ZrO_2 were observed in ZrAl. LaAl and MgAl were x-ray amorphous.

Fig. 1 shows the ESR spectra of various catalysts recorded at ambient temperature. Clear hyperfine splitting (hfs) corresponding to V^{4+} can be seen in VTiAl and VZrAl indicating the isolation of vanadia species on the surface of the support. This is a significant observation since the hfs of vanadia species vanadia supported on unmodified Al_2O_3 has been reported to be recorded only at liquid nitrogen temperature [14]. The observance of hyperfine interaction only at -196°C implies that it is destroyed by spin-spin interaction at higher temperatures between neighboring V^{4+} ions. The resolution of peaks is not so discrete in the cases of VLaAl and VMgAl indicating possible agglomerisation of V^{4+} ions leading to dipolar broadening.

The conversions and selectivities towards formaldehyde and dimethylether on various catalysts in partial oxidation of methanol (carried out at a reaction temperature of 200°C) are plotted in Fig. 2. The activities of VMAl catalysts are in the order VTiAl > VZrAl > VLaAl > VMgAl. The O_2 uptakes of the catalysts also varied in a similar manner indicating that the active sites titrated by oxygen molecules are responsible for the observed activities of the catalysts. Active sites are the vacancies created by removal of labile oxygen atoms (by reduction) upon which the

dissociative chemisorption of oxygen takes place. Selectivity towards the dehydrogenation product, HCHO, has been improved over the VAl catalyst.

Deo and Wachs [2] in their investigation on partial oxidation activity on supported vanadia catalysts have reported that instead of the weakcning of the V=O bond, it is the weakening of the vandium-oxygen-support bridging bond that is responsible for the activity. Our results indicate that the increased oxygen uptake capacities of vanadia on TiO_2, ZrO_2 and La_2O_3 modified alumina catalysts are a consequence of reduced strength of metal-support interaction. Interaction of V_2O_5 with MgO appears to be stronger compared to the oxide support interaction in the cases of VAl and the other VMAl catalysts, which leads to reduced oxygen uptake and hence the partial oxidation activity.

Supported vanadia catalysts exhibit bifunctional character since they posses both acid-base and redox sites. The influence of MO_x modification on the acid-base properties of the catalysts have been examined by the isopropanol decomposition reaction. The results are incorporated in Table 1. Relatively higher decomposition rates have been obtained on VTiAl, VZrAl and VLaAl compared to VAl catalyst. But, when compared to VAl, the acetone selectivities of the above three catalysts have decreased by 15-25%. However, the sustained predominance of selectivity to acetone over selectivity to propylene indicates that in these catalysts the redox property is more dominant than their acid-base character. However, in the case of VMgAl the lower decomposition activity associated with maximum dehydrogenation selectivity could be mainly due to the generation of acid-base paired sites which act in a concerted manner as proposed by Bond et al. [15]. Low oxygen uptake, a consequence of low reducibility, further supports this observation.

Hence, it may be concluded that by choosing a suitable MO_x for the modification of γ-alumina, the desired redox property could be achieved which enhances the partial oxidation activity of the vanadia catalyst.

ACKNOWLEDGMENTS

LJL and STS thank the Council of Scientific and Industrial Research, New Delhi for the award of research associateships.

REFERENCES

1. Oyama, S.T. and Somorjai, G.A., J. Phys. Chem. **94**, 5022 (1990).
2. Deo, G. and Wachs, I.E., J. Catal. **146**, 325 (1994).
3. Owens, L. and Kung, H.H., J. Catal. **148**, 587 (1994).
4. Sobalik, Z., Markvart, M. and Lapina, O.B., Catal. Lett. **28**, 25 (1994).
5. Eon, J.G., Olier, R. and Volta, J.C., J. Catal. **145**, 318 (1994).
6. Weissmann, J.G., Appl. Catal. **94**, 45 (1993).
7. Shen, J., Cortright, R.D., Chen, Y. and Dumesic, J.A. J. Phys. Chem. **98**, 8067 (1994).
8. Shen, J., Cortright, R.D., Chen Y. and Dumesic, J.A., Catal. Lett. **26**, 247 (1994).
9. Trawlzynski, J. and Walendziewski, J., Appl. Catal. **119**, 59 (1994).
10. Lakshmi, L.J., Narsimha, K. and Kanta Rao, P., Appl. Catal. **94**, 61 (1993).
11. Corma, A., Fornes, V., Juan-Rajadell, M.I., and Lopez Nieto, J.M., Appl. Catal. **116**, 151 (1994).
12. Wei, Z., Xin, Q., Guo, X., Grange, P. and Delmon, B., Appl. Catal. **75**, 178 (1991).
13. Reddy, B.M., Narsimha, K., Sivaraj, Ch. and Kanta Rao, P., Appl. Catal. **55**, 1, (1991).
14. Nag, N.K., Chary, K.V.R., Reddy, B.M., Rama Rao, B. and Subrahmanyam, V.S., Appl. Catal. **9**, 225 (1984).
15. Bond, G.C., Flamerz, S. and Shukri, R., Faraday, Discuss. Chem. Soc. **87**, 65 (1989).

Table 1: Physico-chemical properties and the product distribution during the IPA decomposition on vanadia catalysts.

Catalyst	Surface area (m^2/g)	O_2 uptake uptake (μmol/g)	Surface coverage (%)	Active site density (nm^{-2})	IPA conv. (%)	Acetone sel. (%)	Propylene sel. (%)
1. VAl	168	56	9.9	0.40	7	100	--
2. VTiAl	122	133	32.3	1.21	23	74	26
3. VZrAl	129	89	20.4	0.83	19	83	17
4. VLaAl	153	58	10.8	0.44	12	98	2
5. VMgAl	115	22	5.7	0.28	4	99	1

[1] Surface coverage is defined as 100x active surface area/BET SA of reduced catalyst.
[2] Active site density is the number of 'O' atoms chemisorbed per unit area of catalyst.

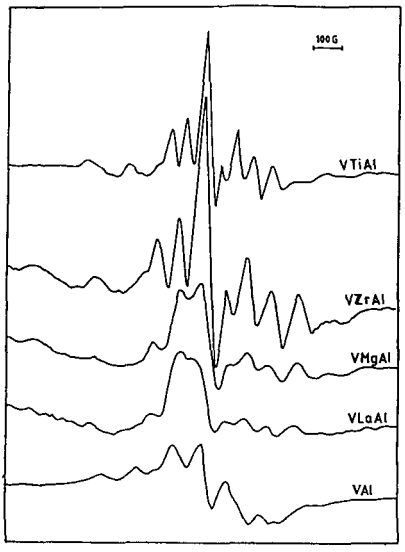

Figure 1. ESR patterns of the VAl and VMAl catalysts.

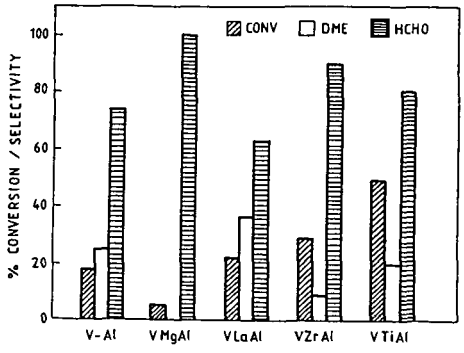

Figure 2. Methanol partial oxidation activity and selectivities on VAl and VMAl catalysts.

LIQUIDIZATION OF DEWATERED ORGANIC SLUDGE AND ANAEROBIC TREATMENT

Shigeki Sawayama, Seiichi Inoue, & Tomoko Ogi
Biomass Laboratory, National Institute for Resources and Environment, 16-3 Onogawa, Tsukuba, Ibaraki, 305, Japan

Keywords: Anaerobic digestion, Organic sludge, Thermochemical liquidization

ABSTRACT

Dewatered sewage sludge was thermochemically liquidized at 175 °C and the liquidized sludge was separated by centrifugation to 58% (w/w) supernatant and 42% precipitate. The amount of proteins in the liquidized sludge slightly decreased through the liquidization process, however, that of lipids increased. The supernatant separated from the sludge liquidized with dewatered sewage sludge was successfully anaerobically digested. Biogas yield from the supernatant from dewatered sewage sludge at organic loading concentrations of 1.9-2.2 g VS/l during 9 days' incubation was 440 ml/g-added VS and digestion ratio was 66% (w/w). Biogas yield in the case of dewatered sewage sludge was 257 ml /g-added VS and digestion ratio was 45%. Similar results were obtained in the case of the anaerobically digested with sewage sludge and dewatered sludge. Anaerobic digestion of the supernatants from the liquidized sludges resulted in high biogas productivity and high digestion ratio compared with these of the original sludges. Moreover, the precipitates contained lower moisture, therefore, they can be incinerated easier than the respective original sludges.

INTRODUCTION

Treatments of sewage sludge and anaerobically digested sludge have been important environmental issues to resolve. Anaerobic digestion of sewage sludge is commonly used for treatment of sewage sludge and energy is recovered in the form of methane (Fannin *et al.*, 1983). A thermal pretreatment system for anaerobic digestion of concentrated sewage sludge with 2-3% volatile solid (VS) has been studied to improve anaerobic digestibility and dewatering properties (Haug, 1977; Haug *et al.*, 1978; Haug *et al.*, 1983; Hiraoka *et al.*, 1984). The volume of concentrated sewage sludge for thermal pretreatment is huge, and therefore this process consumes a large amount of energy.

Dewatered sludges (VS of 12%) are clay like solids and are therefore not suitable for anaerobic digestion. An attempt at liquidization of dewatered sewage sludge by a thermochemical process was conducted (Dote *et al.*, 1993; Sawayama *et al.*, 1995). The volume of dewatered sewage sludge decreased markedly from that of concentrated sewage sludge (VS of 2-3%), suggesting that heat treatment of dewatered sewage sludge would require less energy than in the case of concentrated sewage sludge. As for anaerobically digested sludge, thermochemical liquidization can possibly improve anaerobic re-digestibility and the dewatering properties.

This paper deals with the thermochemical liquidization of dewatered sewage sludge and anaerobically digested and dewatered sludge, and the batch anaerobic digestion of the supernatants separated from the liquidized sludges.

METHODS

Liquidization of sludge

Dewatered sewage sludge, and anaerobically digested and dewatered sludge used in the experiment were obtained from an aerobic sewage treatment facility for domestic sewage in Ibaraki prefecture, Japan. The liquidization of the dewatered sludges were conducted as previously demonstrated (Dote *et al.*, 1993). After purging with nitrogen gas, the dewatered sludge was heated at 175°C in an electric furnace and held at 175°C for 1 h in a 1 *l* autoclave (4 MPa). The liquidized sludge was separated by centrifugation (1000 g, 10 min) to supernatant and precipitate.

Anaerobic digestion

Seed sludge for batch anaerobic digestion was obtained from the sewage sludge treatment facility in Ibaraki prefecture, Japan. Two liters of the seed sludge (VS concentration: approximately 1 %, w/w) was incubated in a 2 *l* conical flask at 35°C. A sample was added to the seed sludge at 1.6-2.2 g-VS/l and air in the digester was purged with nitrogen gas. Samples for anaerobic digestion included the original sludges (dewatered sewage sludge, and anaerobically digested and dewatered sludge), liquidized sludges and separated supernatants. The gas production yield from the digester was monitored by displacement of saturated sodium chloride solution.

Analyses of sludges and gas

Moisture content was determined by heating the sample at 105°C for 24 h before weighing, and VS and ash content were determined by heating at 600°C for 1 h. Digestion ratio was expressed as the ratio of the amount of VS decrease during 9 or 8 days' digestion to the amount of VS added.

The Kjeldahl-nitrogen method was used for protein analysis. After extraction, a gravimetric method was used for determination of lipids. The Somogyi method was used for carbohydrate analysis.

High heating value (HQ, MJ/kg) for VS of sludges is calculated using to Dulong's formula (Selvig & Gibson, 1945):

$$HQ=0.3383\times C+1.442(H-O/8)$$

where C, H and O are weight percentages of carbon, hydrogen and oxygen, respectively. Low heating value (LQ, MJ/kg) is calculated using the following equation:

$$LQ=HQ\times V-0.0251\times(9\times H+M)$$

where V is the ratio of volatile solid and M is the weight percentage of moisture.

The biogas composition was determined by gas chromatography. The digestion ratio was expressed as the ratio of decreased VS during 9 or 8 days of digestion versus added VS.

RESULTS AND DISCUSSION

Liquidization

Procedures of liquidization and anaerobic treatment for sewage sludge are shown in Fig. 1, and those of liquidization and anaerobic re-treatment for anaerobically digested and dewatered sludge are shown in Fig. 2. Dewatered sewage sludge (moisture, 84%, w/w; VS, 12%, w/w), and anaerobically digested and dewatered sludge (moisture; 84%, w/w, VS; 11%, w/w) were successfully liquidized by thermochemical reaction at 175°C with holding time of 1h. The protein content (33 %) in the sewage sludge was higher than that (28%) in the liquidized sludge. On the other hand, the lipid content (14%) in the liquidized sludge from the sewage sludge was approximately two times higher than that (7%) in the sewage sludge. It was reported that volatile acids would be produced through thermal treatment (170-230 °C) of sewage sludge (Fisher & Swanwick, 1971). These results suggest that proteins were converted to lipids through the liquidization process.

The liquidized sludge from the dewatered sewage sludge was separated by centrifugation to supernatant (58%, w/w) and precipitate (42%, w/w), and that from the anaerobically digested and dewatered sludge was separated to supernatant (46%, w/w) and precipitate (54%, w/w). The moisture content of the precipitates decreased from the both original sludges through centrifugation, therefore, thermal liquidization of organic sludges was considered to be a pretreatment for dewatering.

Anaerobic digestion

The supernatant separated from the sludge liquidized with the dewatered sewage sludge was successfully anaerobically digested. The digestion ratio (66%) of the supernatant was higher than that of the original sewage sludge (45%) after 9 days of incubation. The total biogas yield from the supernatant during 9 days' incubation was 440 ml /g-added VS (Fig. 3) and the total methane yield was 328 ml /g-added VS. The biogas productivity in the anaerobic treatment of the supernatant was improved by thermochemical treatment compared with those of the original sewage sludge and the liquidized sludge. There was no difference in methane contents of biogas (75-77%) among those three anaerobic experiments.

The digestion ratio (61%) of the supernatant from the sludge liquidized with the anaerobically digested and dewatered sludge was higher than that of the original sludge (27%) after 8 days of incubation. The total biogas yield from the supernatant after 8 days of incubation was 339 ml /g-added VS (Fig. 3) and the total methane yield was 253 ml /g-added VS. The biogas conversion ratio of the supernatant based on carbon was 36 %. The improvement in the digestion ratio of the anaerobically digested sludge by thermal pretreatment was more apparent than that of the sewage sludge. This effect was thought to be partly caused by degradation of the cell wall and membrane and to be the same effect caused by the thermal treatment of sewage sludge reported by Hauge *et al*, 1978.

Anaerobic treatment of the thermal treatment liquor (average COD; 6-10 g/*l*) has been studied (Pugh *et al.*, 1987; Kimata *et al.*, 1993). After this preliminary batch experiment, application of the anaerobic digestion method with granular sludge such as the UASB method could contribute to a faster digestion rate for the supernatant from liquidized sludge.

Low heating values of precipitates

The precipitate separated from the sludge liquidized with the dewatered sewage sludge was composed of 71% moisture, 19% VS and 10% ash. The precipitate obtained by centrifugation of the sludge liquidized with the anaerobically digested and dewatered sludge was composed of 76% moisture, 14% VS and 10% ash. This thermochemical liquidization process improved the dewaterability of the dewatered sludges.

The calculated low heating value of the precipitate separated from the sludge liquidized with the dewatered sewage sludge was 1.2 MJ/kg and that of the original sludge was -1.0 MJ/kg. The calculated low heating value of the precipitate separated from the sludge liquidized with the anaerobically digested and dewatered sludge was -0.4 MJ/kg and that of the original sludge was -1.6 MJ/kg. The precipitates separated from the liquidized sludges have higher heating values compared to those of the original dewatered sludges which means that incineration of the precipitate could save energy by using less fuel. A more suitable dewatering method for liquidized sludges would provide higher low heating values for their solid fractions.

ACKNOWLEDGMENT

We are grateful to Wastewater Treatment Office in Ibaraki prefecture for preparation of the sewage sludge and to Dr. Yutaka Dote in Department of Civil and Environmental Engineering, Miyazaki University for the useful discussions.

REFERENCES

Dote, Y., Yokoyama, S., Minowa, T., Masuta, T., Sato, K., Itoh, S. & Suzuki, A. (1993). Thermochemical liquidization of dewatered sewage sludge. *Biomass Bioenergy*, **4**, 243-248.

Fannin, K. F., Conrad, J. R., Srivastava, V. J., Jerger, D. E. & Chynoweth, D. P. (1983). Anaerobic processes. *J. Water Poll. Control Fed.*, **55**, 623-632.

Fisher, W. J. & Swanwick, J. D. (1971). High-temperature treatment of sewage sludges. *Water Poll. Control*, **70**, 355-373.

Haug, R. T. (1977). Sludge processing to optimize digestibility and energy production. *J. Water Poll. Control Fed.*, **49**, 1713-1721 .

Haug, R.T., Stuckey, D.C., Gossett, J.M., and McCarty, P.L. (1978). Effect of thermal pretreatment on digestibility and dewaterability of organic sludges. *J. Water Poll. Control Fed.*, **50**, 73-85.

Haug, R.T., LeBrun, T.J., and Tortorici, L.D. (1983). Thermal pretreatment of sludges - a field demonstration. *J. Water Poll. Control Fed.*, **55**, 23-34.

Hiraoka, M., Takeda, N., Sakai, S., and Yasuda, A.: Highly efficient anaerobic digestion with thermal pretreatment. *Water Sci. Technol.*, **17**, 529-539 (1984).

Kimata, T., Kawai, T., Tada, M., Tanaka, K., Shinabe, K. & Shimizu, K. (1993). Anaerobic treatment of thermal sludge conditioning liquor with granular sludge. *Water Environ. Res.*, **65**, 6-14.

Pugh, L. B., Kang S. J. & Spangler, J. L. (1987). Anaerobic fluidized bed and anaerobic filter/contact stabilization application for heat treatment liquor. *J. Water Poll. Control Fed.*, **59**, 1050-1058.

Sawayama, S., Inoue, S., Yagishita, T., Ogi, T. & Yokoyama, S. (1995). Thermochemical liquidization and anaerobic treatment of dewatered sewage sludge. *J. Ferment. Bioeng.*, **79**, 300-302.

Selvig, W. A. & Gibson, F. H. (1945). Calorific value of coal. In *Chemistry of Coal Utilization*. ed. H. H. Lowry. John Wiley & Sons, New York, pp. 132-144.

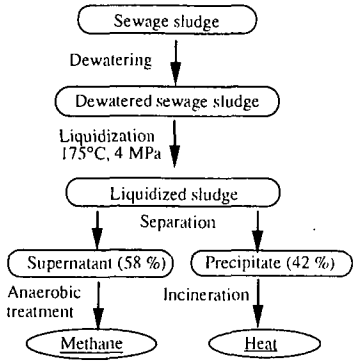

Fig. 1. Flow diagram of liquidization and anaerobic treatment of sewage sludge.

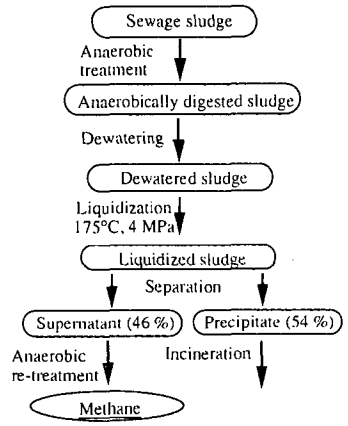

Fig. 2. Flow diagram of liquidization and anaerobic re-treatment of anaerobically digested sludge

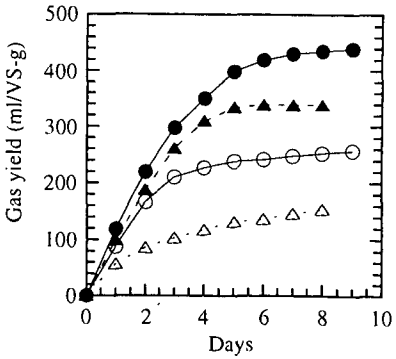

Fig. 3. Gas yield from anaerobic treatments from sewage sludge (open circle) and anaerobically digested sludge (open triangle), and supernatant (closed circle) from sewage sludge and supernatant (closed triangle) from anaerobically digested sludge.

IGNITABILITY OF VARIOUS COALS AS MEASURED BY LASER IGNITION

John C. Chen,[†] Subrahmanyam Musti,[*] Vinayak Kabadi[*]
Departments of [†]Mechanical and [*]Chemical Engineering
North Carolina A&T State University
Greensboro, NC 27411

KEYWORDS: Coal ignition, laser, coal reactivity

INTRODUCTION

We present a novel experiment designed to study the ignition and combustion of pulverized fuels in a room-temperature gas environment. The absence of hot furnace walls surrounding the test section allowed for optical detection of the reaction sequence. Our goals are to determine, by direct observation, the ignition mechanism (heterogeneous or homogeneous ignition) of a range of coals, and to quantify the differences in ignition reactivity between the fuels.

EXPERIMENT

The experiment is similar to one described in detail elsewhere,[1] so only a brief description is given here. Figure 1 presents a schematic of the laser ignition experiment; the inset shows the details around the test section. Sieve-sized particles were dropped through a tube into a laminar, upward-flow wind tunnel with a quartz test section (5 cm square cross-section). The gas was not preheated. The gas flow rate was set so that the particles emerged from the feeder tube, fell approximately 5 cm, then turned and traveled upward out of the tunnel. This ensured that the particles were moving slowly downward at the ignition point, chosen to be 2 cm below the feeder-tube exit. A single pulse from a Nd:YAG laser was focused through the test section, then defocused after exiting the test section, and two addition prisms folded the beam back through the ignition point. Heating the particles from two sides in this manner achieved more spatial uniformity and allowed for higher energy input than a single laser pass. For nearly every case, two to five particles were contained in the volume formed by the two intersecting beams, as determined by previous observation with high-speed video.[2]

The laser operated at 10 Hz and emitted a nearly collimated beam (6 mm diameter) in the near-infrared (1.06 μm wavelength). The laser pulse duration was ~100 μs and the pulse energy was fixed at 830 mJ per pulse, with pulse-to-pulse energy fluctuations of less than 3%. The laser pulse energy delivered to the test section was varied by a polarizer placed after the laser exit; variation from 150 to 750 mJ was achieved by rotating the polarizer. Increases in the laser pulse energy result in heating of the coal particles to higher temperatures. At the ignition point the beam diameter normal to its propagation direction was ~3 mm on each pass of the beam. An air-piston-driven laser gate (see Fig. 1) permitted the passage of a single pulse to the test section. The system allowed for control of the delay time between the firing of feeder and the passage of the laser pulse. Finally, ignition or nonignition was determined by examining the signal generated by a high-speed silicon photodiode connected to a digital oscilloscope, as described elsewhere.[1]

We report here the ignition behavior of four coals ranging in rank from subbituminous to medium-volatile bituminous. All samples were obtained from the Penn State University Coal Sample Bank, and the reported proximate and ultimate analyses are shown in Table 1. The coals were sieve-sized using a Ro-Tap shaker to -120/+140 mesh (106-125 μm diameter), and dried at 70°C under vacuum for at least 12 hours prior to each day's experiment.

RESULTS

Each day's experiment was conducted as follows: After choosing the coal and oxygen concentration to examine, the coal was loaded into the batch-wise feeder. The delay time between the triggering of the feeder and the appearance of the coal batch at the feeder tube exit was measured by visual observation in conjunction with a stop watch; typical values were ~2.9 s. The delay time was then programmed into the device which triggered the laser gate. The gas flow rate needed to achieve a drop distance of ~5 cm for the coal batch was also determined by visual observation. Finally, a laser pulse energy was chosen, and the experiment commenced. At each set of operating conditions (coal type and size, oxygen concentration, and laser energy), 20 attempts at ignition were made in order to measure the ignition frequency, or probability, which is the parameter sought from these studies. Mapping this ignition frequency over a range of laser pulse energy produces an ignition-frequency distribution.

Such a frequency distribution is shown in Fig. 2 for the Pittsburgh #8 coal. It can be seen that at each oxygen concentration, ignition frequency increases monotonically over a range of increasing laser pulse energy. Below this range the ignition frequency is zero, and higher energies result in 100% ignition frequency. This behavior is due to the fact that, within any coal sample, there exists a variation of reactivity among the particles.[3] Thus, in this experiment, in which a batch of perhaps several hundred particles of a sample is dropped into the test section but only a few are heated by the laser pulse, there is an increasing probability (or frequency) as the laser energy is increased that at least one of the heated particles is reactive enough to ignite under the given conditions.

The repeated distributions under 100% oxygen, measured on separate days, show the excellent repeatability of this experiment; the most important factor for reproducibility is the moisture content of the sample.

Figure 2 also shows the effect of oxygen concentration: As oxygen level is decreased from 100% to 75%, and then to 50%, the frequency distribution shifts to higher laser energies or, equivalently, higher particles temperatures, as expected. This is consistent with ignition theory since at decreased oxygen levels, higher temperatures are necessary to achieve the equality between heat generation by the particles (due to chemical reactions) and heat loss from the particles. This equality is the minimum requirement for ignition, and is termed 'critical ignition.' The shift in distribution can be viewed in two ways: First, for a fixed laser pulse energy, a decrease in oxygen level leads to a decrease in the ignition frequency, all else being the same; second, a decrease in oxygen implies that a higher laser pulse energy is needed, in order to achieve the same ignition frequency.

Finally, it should be noted that for the Pittsburgh #8, the decreases in oxygen concentration shift the distributions to higher laser energies in approximately equal increments (equal energy ranges), and with little or no effect on the slope of the distributions. This finding is in contrast to the results for the Sewell coal (Fig. 3).

Three major differences between the ignition behaviors of the Pittsburgh #8 and Sewell exist. First, decreasing oxygen concentrations has a stronger effect in shifting the distributions of the Sewell to higher laser pulse energies (or higher particle temperatures). Second, as oxygen level is decreased, the slope of the distribution is undoubtedly decreased for the Sewell, while little effect is observed for the Pittsburgh #8. Finally, a comparison of the distributions of the two coals under 100% oxygen shows that the Sewell reaches 100% ignition frequency in a significantly smaller range of laser energy ($\sim$150 mJ versus $\sim$250 mJ).

The results for the two remaining coals — the Illinois #6 and the Wyodak — are shown in Figs. 4 and 5. The two coals span similar ranges in going from 0 to 100% ignition frequency ($\sim$350 mJ), which are larger than both the Pittsburgh #8 or Sewell coals. Comparing the results for these two coals, it is also observed that the ignition-frequency distributions of the Illinois #6 are shifted to higher laser energies than the Wyodak, implying that the Illinois #6 is a less reactive coal, at least with regard to ignition.

DISCUSSION

Over the past three decades, many experiments have examined the ignition of pulverized coals under conditions which simulate pulverized fuel-firing conditions.[4,5,6,7,8,9] The common factor among these studies is the assumption of a single, average, kinetic rate-constant in describing the ignition reactivity of each coal. As we have shown previously,[3] it is necessary to account for the variation in reactivity among the particles within a sample in order to model the ignition distribution observed in this and nearly all previous ignition studies. Once such a model is implemented, the parameters may then be adjusted to fit the data and produce the desired ignition rate constant and reaction order with respect to oxygen for each coal.

Our previous experience in modeling ignition distribution data[3] provides some insight to explain the results described earlier. The model details will not be described here, but it is sufficient to note that the model accounts for particle-to-particle variations in reactivity by having a single preexponential factor and a Gaussian distribution of activation energies among the particles within a sample.

In light of this model, the differences in the range of laser energies over which the various coals achieved 100% ignition frequency is a direct result of the breadth of the Gaussian distribution of activation energies: A narrow distribution (small standard deviation) leads to a small laser-energy range since most particles have similar activation energies and, thus, reactivities. Indeed, in the limit that the standard deviation is zero (all particles have the same

activation energy), the ignition-frequency distribution would become a step function. Conversely, a broad distribution of reactivities leads to a relatively larger range of laser energy needed to achieve 100% frequency, as is the case for the Pittsburgh #8 compared to the Sewell. The fact that the Illinois #6 and Wyodak coals span a similar laser-energy range suggests that the spread of their reactivity distributions are similar. However, since the ignition-frequency distributions of the Illinois #6 are shifted to higher laser energies than the Wyodak, the interpretation is that the reactivity distribution of the Illinois #6 has a lower average activation energy, and therefore it is more reactive, as stated earlier.

Finally, with regard to the effect of oxygen concentration on the slope and shift of the ignition-frequency distributions observed for the Pittsburgh #8 and Sewell coals, the model interprets such differences to be the result of the variation in the reaction order with respect to oxygen concentration. We are presently at work on modeling the results reported here, with the goal of presenting kinetic rate parameters in the near future.

ACKNOWLEDGEMENT

The support of this project by the U.S. Department of Energy through Grant DE-FG22-94MT94012 is gratefully acknowledged. The assistance of Cynthia Marshall and Monique Jenkins with the experiments is also greatly appreciated.

REFERENCES

1 Chen, J.C., Taniguchi, M., Narato, K., and Ito, K. "Laser Ignition of Pulverized Coal," *Combust. Flame* 97, 107 (1994).

2 Chen, J.C., Taniguchi, M., Ito, K. "Observation of Laser Ignition and Combustion of Pulverized Coals," *Fuel*, 74(3), 323 (1995).

3 Chen, J. C. "Distributed Activation Energy Model of Heterogeneous Coal Ignition," *Combust. Flame*, in press (1996).

4 Essenhigh, R.H., Mahendra, K.M., and Shaw, D.W. *Combust. Flame*, 77, 3 (1989).

5 Cassel, H.M. and Liebman, I. *Combust. Flame*, 3, 467 (1959).

6 Karcz, H., Kordylewski, W., and Rybak, W. *Fuel*, 59, 799 (1980).

7 Fu, W. and Zeng, T. *Combust. Flame*, 88, 413 (1992).

8 Zhang, D., Wall, T.F., Harrie, D.J., Smith, I.W., Chen, J., and Stanmore, B.R. *Fuel*, 71, 1239 (1992).

9 Boukara, R., Gadiou, R., Gilot, P., Delfosse, L., and Prado, G. *Twenty-Fourth Symposium (International) on Combustion*, The Combustion Institute, Pittsburgh, PA, 1993, pp. 1127-1133.

Coal		Prox. Analy. (dry wt%)		Ultimate Analysis (dry, ash-free wt%)				
Penn State ID	Rank	Vol. Matter	Ash	C	H	N	S	O (diff.)
Pittsburgh #8 (DECS 23)	low-volatile A bituminous	39.4	9.44	82.0	5.63	1.49	4.27	6.66
Sewell (DECS 13)	medium-volatile bituminous	25.0	4.22	88.2	4.95	1.50	0.65	4.71
Illinois #6 (DECS 24)	high-volatile C bituminous	40.8	13.4	76.3	5.30	1.32	6.38	10.74
Wyodak (DECS 26)	subbituminous B	44.9	7.57	75.5	6.11	1.02	0.47	16.92

Table 1: Ultimate and proximate analyses of coals used in this study.

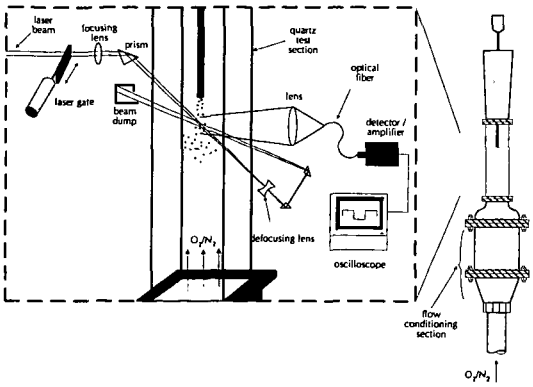

Fig. 1: Schematic of the laser ignition experiment.

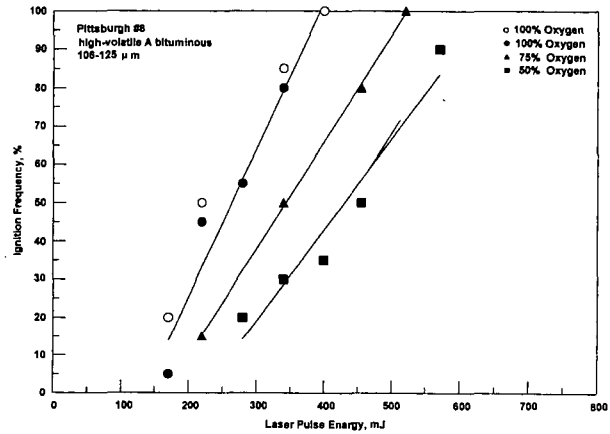

Fig. 2: Ignition-frequency distributions for the Pittsburgh #8 coal. Two data sets (open and filled circles) at 100% oxygen show reproducibility of experiment.

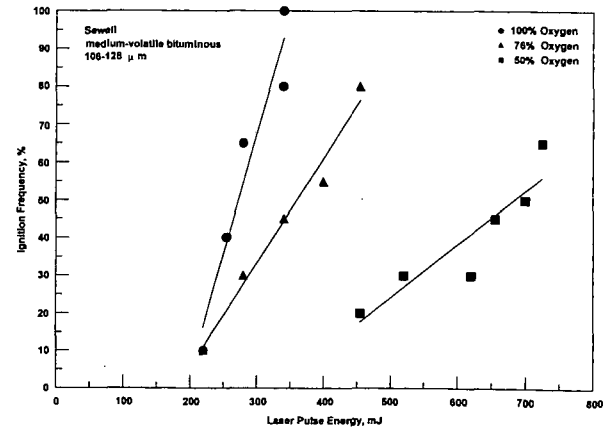

Fig. 3: Ignition-frequency distributions for the Sewell coal.

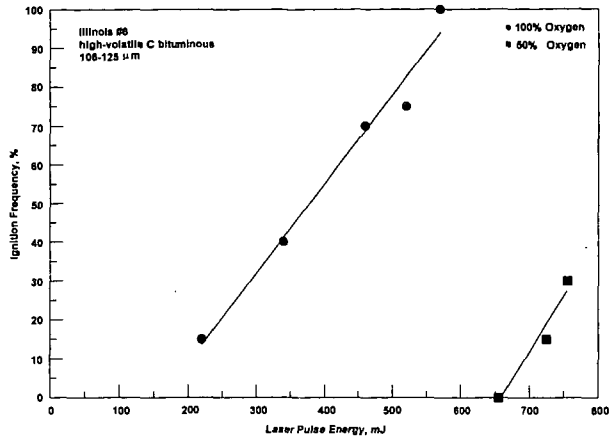

Fig. 4: Ignition-frequency distributions for the Illinois #6 coal.

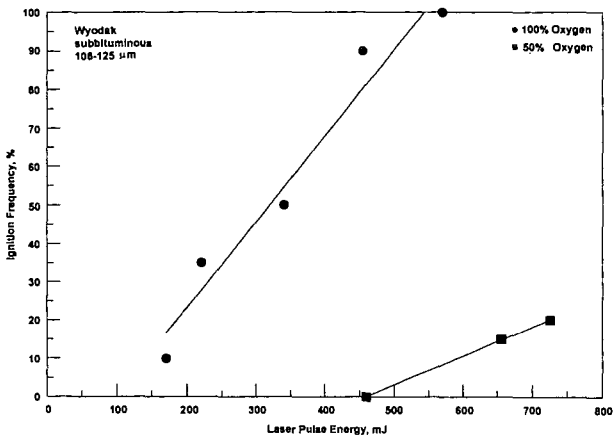

Fig. 5: Ignition-frequency distributions for the Wyodak coal.

MODELING OF SMOLDERING CELLULOSIC MATERIALS-EVAPORATION AND PYROLYSIS PROCESSES

Sung-Chul Yi and Young Chai Kim

Department of Chemical Engineering, Hanyang University, 17, Haengdang-dong, Sungdong-ku, Seoul, 133-791, Korea

Keywords: model, smoldering, cellulosic material

INTRODUCTION

Over 1600 people die each year [Miller, 1991] from fires started by smoking materials (cigarettes, matches, etc.), and many times that number are hurt and/or disfigured; most of those fires are established in upholstered furniture. As a result, Congress passed the Cigarette Safety Act of 1984. One of the tasks under the Act was to model mathematically the behavior of upholstered furniture and the cigarette, when a smoldering cigarette is dropped onto it. To do this, the heating of the substrate when subjected to a moving heat source must first be accurately modeled, and a criterion established for its ignition. In order to examine how changing one or more properties of the cigarette will influence its ignition propensity, it is also necessary to understand the behavior of a smoldering cigarette. This includes knowing how its external heat flux and burning velocity depend upon its physical and/or chemical properties.

Considerable effort has been expended in the study of the burning cellulosic material such as tobacco etc.. Egerton et al. [1963] studied the smoldering combustion in cigarettes. From the data of various experiments, they explained several aspects of the mechanism of smoldering. A theoretical and experimental investigation of the smoldering mechanism of a cylindrical cellulosic rod was carried out by Moussa et al. [1976]. They proposed a simple steady-state, 1-dimensional model of a burning cellulosic rod. Based on a postulated mechanism of smoldering, Muramatsu et al. [1979] developed one-dimensional model of the pyrolysis/distillation zone. Their model contains four general pyrolysis reactions, one distillation process and combined conductive and radiative heat transfer from the combustion zone.

The purpose of this paper is to present the results of a study using numerical techniques to compute the static burn rate, mass burn rate, heat flux and the amount of heat released in the natural smoldering cigarette. The study was made on cigarettes containing flue-cured and burley tobaccos since physical properties and kinetic data are readily available [Muramatsu et al. 1979].

MATHEMATICAL MODEL

A cigarette generally includes a filter attached to the end of the tobacco rod. The rod is a packed column of approximately 1 g of shredded tobacco, generally 8 mm in diameter and 70 mm long, wrapped in a thin porous paper. The shreds are nonuniformly packed in the tobacco rod which contains about 70 - 85 % void space.

Smoldering is a non-flaming combustion mode, characterized by thermal degradation and charring of the virgin tobacco, evolution of smoke, and emission of a visible glow. The temperature in the burning zone increases to the ignition temperature, and the temperature gradients are directly correlated to the basic processes which take place in the cigarette (i.e. distillation, pyrolysis, and combustion) and affect the absolute density [Baker, 1979] of the rod in the burning zone.

During natural burning the oxygen transport to the surface is restricted and the peripheral region with its large heat losses cannot maintain rapids surface oxidation. Muramatsu et al. have developed a model of the evaporation-pyrolysis processes with the following assumptions:

1) The solid phase and the gas phase inside the burning tobacco are the same temperature.
2) Heat loss from the outer surface of the element is caused by free convection and radiation.
3) Heat transfer inside the cigarette column is caused by thermal conduction characterized by a effective thermal conductivity.

Pyrolytic decomposition of tobacco can be expressed by the following simplified equation;

$aA(s) \rightarrow bB(g) + cC(s)$

The virgin tobacco and its water content are gradually consumed to form smoke, water vapor, and a residual char with final density ρ_f. In the steady state of combustion, the temperature is raised by the heat transferred from the burning zone. The temperature distribution of the tobacco column depends upon the thermal properties of the cigarette such as the effective thermal conductivity, specific heat and thermal diffusivity. The total density of the burning tobacco is given by

$$\rho_t = \rho_v + \rho_c + \rho_w \qquad (1)$$

where ρ is density, and the subscripts t, v, c, and w stand for total, unreacted tobacco, carbonaceous residue, and water, respectively. The conversion of virgin tobacco can be expressed by

$$\frac{\partial \rho_v}{\partial t} = \sum_{i=1}^{4} \frac{\partial \rho_{vi}}{\partial t} \tag{2}$$

and then the individual Arrhenius forms:

$$\frac{\partial \rho_{vi}}{\partial t} = -A_i \exp\left(\frac{-E_i}{RT}\right)\left(\frac{\rho_{vi}}{\rho_{vi}^o}\right)^n \rho_{vi}^o \tag{3}$$

and the char density is given by

$$\frac{\partial \rho_c}{\partial t} = -\frac{\rho_f}{\sum_{i=1}^{4} \rho_{vi}^o} \frac{\partial \rho_v}{\partial t} \tag{4}$$

where superscript o is the initial state. The loss of tobacco moisture from a tobacco rod is assumed to involve both the conversion of moisture to a water vapor as well as mass transfer of the moisture out of the tobacco rod. The evaporation rate of the water from tobacco can be expressed by the empirical equation,

$$\frac{\partial w}{\partial t} = -\left(\frac{S}{w}\right)\exp\left(\frac{-\theta}{T}\right)(w - w_{eq})^{\beta} \tag{5}$$

where w is water content in tobacco, S is surface area of a tobacco lamina, θ and β are empirical constants, and subscript eq is equilibrium state. The pyrolysis reaction of virgin tobacco in the region where water evaporation takes place is slow, and can be considered to be negligible. Thus

$$\frac{\partial \rho_w}{\partial t} = -N_o \alpha \exp\left(\frac{-\theta}{T}\right)(w - w_{eq})^{\beta} = \sum_{i=1}^{4} \rho_{vi}^o \frac{\partial w}{\partial t} \tag{6}$$

where N_s is total surface area of tobacco shreds per unit volume of a cigarette, α is experimental constant, and w_{eq} is related to the water vapor pressure, p_w, by

$$w_{eq} = \frac{p_w / p_{ws}}{a + b\left(p_w / p_{ws}\right) - c\left(p_w / p_{ws}\right)^2} \tag{7}$$

The saturated vapor pressure of water, p_{ws}, can be expressed by Calingart's equation [Calingert and Davis, 1925] as follows;

$$\log p_{ws} = 7.991 - \frac{1687}{T - 43} \tag{8}$$

The mass balance equation for the water vapor pressure, p_w, inside the tobacco rod is

$$\frac{\partial}{\partial t}\left(\frac{p_w}{RT}\right) = \frac{\partial}{\partial z}\left\{D_z \frac{\partial}{\partial z}\left(\frac{p_w}{RT}\right)\right\} - \frac{2D_r}{\Phi r \delta RT}\left(p_w - p_{w\infty}\frac{T}{T_\infty}\right) - \frac{\sum_{i=1}^{4} \rho_{vi}^o}{\Phi m}\frac{\partial w}{\partial t} \tag{9}$$

where the first term of left hand side is the net rate of accumulation of water vapor, the first term of right hand side (rhs) is the rate of accumulation water vapor by diffusion, the second term of rhs is the rate of loss of water vapor by diffusion through a cigarette paper of thickness, δ, and the last term is the rate of evaporation of water from the tobacco.

The heat balance equation for the element is given by

$$\frac{\partial\left(H_v \rho_v + H_c \rho_c + H_w \rho_w\right)}{\partial t} = \frac{\partial}{\partial z}\left(K_e \frac{\partial T}{\partial z}\right) + Q_p \frac{\partial \rho_v}{\partial t} + Q_w \frac{\partial \rho_w}{\partial t} - \frac{2}{r}\left\{h(T - T_\infty) + \sigma \varepsilon_s (T^4 - T_\infty^4)\right\} \tag{10}$$

where the thermal conductivity, K_e, depends upon the void fraction, φ and the temperature, T.

$$K_e = (1 - \phi^{2/3})K_s + \phi^{1/3}(1 + \frac{2}{3} h_r D_p / K_g)K_g \tag{11}$$

where $h_r = 5.422 x 10^{-12} \varepsilon_r T^3$

The cigarette weight after t time is;

$$M(t) = u\pi r^2 \int_0^u \rho_a(t, r, \%moisture, \ldots.)dt \tag{12}$$

The heat flux is then given by;

$$q = \frac{1}{x}\int_0^x \frac{2}{r}\left[h(T - T_\infty) + \sigma \varepsilon_s (T^4 - T_\infty^4)\right]dx \tag{13}$$

and the initial and boundary conditions are;

$$T = T_\infty @ x = -\infty$$

$$T = T_o @ x = x_o$$

$$\left(\frac{dT}{dx}\right)_{x=x_o} = \frac{u}{K_o}(T - T_\infty)(\rho_{vo}C_{pvo} + \rho_{wo}C_{pwo}) \qquad (14)$$

$$\rho_{ao} = \frac{M_o}{V}, \rho_{wo} = \rho_{ao}\frac{w_o}{1+w_o}, \rho_{co} = 0.0, \rho_{vo} = \rho_{ao} - \rho_{wo}$$

w_o refers to the moisture content in the tobacco. The values of physical parameters used to solve the simultaneous differential equations can be obtained elsewhere [Muramatsu et al., 1979]. Then, the set of simultaneous differential equations can be solved numerically by the LSODE.

RESULTS AND DISCUSSIONS

In this section, we examine the factors affecting the static burn rate, the mass burn rate, heat flux and the heat released at the boundary by convection and radiation. The results are expected to provide a tool for understanding the mechanism of smoldering and controlling the physical parameters in the design of cigarette.

The mass burn rate (MBR), static burn rate (SBR), heat flux and heat released shown in Table 1 as a function of cigarette moisture at constant circumference and initial density. The analysis reveals that the SBR and MBR decrease with increased cigarette moisture content and are linear functions within the range of 10 to 15 % moisture. Thus, increased moisture reduces the rate of combustion due to the extra heat needed to vaporize water from the tobacco. The approximate value of heat flux regardless of moisture content are 0.327 and 0.177 cal/cm^2 sec for burley and flue-cured, respectively. The total heat released from the cigarette rod, neglecting the contribution from the paper is a function of the moisture content of the rod. The calculated heat released values at 12 % moisture are 1734 cal for burley and 1344 cal for flue-cured tobaccos. These values agree well with the results of Muramatsu et al.[1979]. Therefore, an increase in the tobacco moisture content causes a decrease in the static burn rate, but an increase in the total heat released.

The packing density of the cigarette has an effect on the SBR and MBR. Table 2 shows the typical smoldering speed calculated for a cigarette containg burley and flue-cured tobaccos and indicate that increasing the density at constant moisture and circumference causes the SBR to decrease. However, results show that the increase of the rod density appears to increase the MBR only slighty.

Table 3 summarizes the effect of rod circumference on the SBR and MBR. The results show that the MBR increase as circumference increases.

CONCLUSIONS

A mathematical model of the natural smoldering of cellulosic material is presented. The following conclusions can be drawn;

1) A simple interpretation of the calculation is that the variations in tobacco moisture content, rod densuty and circumferences can explain variations in SBR, MBR, heat flux and total heat released.

2) The calculation illustrates that the circumference of the cigarette is the major physical factor affecting MBR, while rod densuty strongly affects the SBR, heat flux, and heat released.

3) A quantitative relationship between these parameters and the MBR, SBR, and heat flux has been developed. The results may be a useful predictive tool for use in cigarette design.

REFERENCES

Miller, A.L., NFPA Journal, Jan/Feb 86, (1991).
Egerton, A., Gugan, K., and Weinberg, F.J., Combust. Flame 7:63 (1963).
Moussa, N.A., Toong, T.Y., and Darris, C.A., Sixteenth Symposium (International) on Combustion, The Combustion Institute, Pittsburgh, 1447 (1977).
Muramatsu, M., S. Umemura, and T. Okada, Combust. Flame 36:245 (1979).
Baker, R.R., Thermochim Acta, 28 (1979).
Calingert, G., and Davis, D.S., Ind. Eng. Chem. 17:1287 (1925).

Table 1. Calculated values of moisture content vs. SBR, MBR, and heat released.

A. Burley

Moisture content (%)	Static burn rate (10^{-3} cm/sec)	Mass burn rate (mg/min)	Heat released (cal)
10.0	6.497	74.178	1644.1
10.9	6.330	72.001	1691.7
12.0	6.112	69.218	1734.5
13.0	5.905	66.590	1797.4
14.0	5.692	63.951	1865.2
15.0	5.479	61.311	1937.6

B. Flue-cured

Moisture content (%)	Static burn rate (10^{-3} cm/sec)	Mass burn rate (mg/min)	Heat released (cal)
11.0	4.676	60.365	1308.7
12.0	4.563	58.731	1344.4
13.1	4.430	56.813	1387.9
14.0	4.318	55.220	1425.8
15.0	4.190	53.406	1471.1
16.0	4.060	51.587	1519.3

Table 2. Initial density effect on the SBR, MBR, and heat released.

Initial density (g/cc)	Static burn rate (10^{-3} cm/sec)		Mass burn rate (mg/min)		Heat released (cal)	
	flue-cured	burley	flue-cured	burley	flue-cured	burley
0.213	5.901	7.630	52.270	67.933	1057.2	1424.5
0.228	5.520	7.142	53.459	69.479	1133.3	1489.4
0.313	3.970	5.149	58.149	75.548	1552.9	2053.0
0.341	3.620	4.709	59.143	76.845	1693.5	2242.0
0.370	3.340	4.338	59.981	77.924	1838.4	2431.2

Table 3. Circumference effect on the MBR and heat released.

Circumference (cm)	Mass burn rate (mg/min)		Heat released (cal)	
	flue-cured	burley	flue-cured	burley
2.10	35.888	46.197	1563.6	1788.3
2.20	40.544	51.886	1511.8	1758.0
2.30	45.468	58.011	1466.8	1711.9
2.40	50.662	64.401	1431.3	1702.8
2.512	56.813	72.001	1387.9	1691.7
2.60	61.867	78.244	1371.2	1662.2
2.70	67.868	85.669	1363.4	1656.2
2.80	74.129	93.420	1344.6	1637.9

AN ANALYSIS OF COAL PYROLYSIS RATES USING THERMOGRAVIMETRY

Atsushi Inaba
National Institute for Resources and Environment
Tsukuba 305, JAPAN

Hiroyasu Okuo and Toshinori Kojima
Seikei University
Tokyo 113, JAPAN

INTRODUCTION

The modeling of coal pyrolysis reactions has been pursued since the initial studies by Gavalas and Howard. Recently, a large number of models has been reported, such as the FG-VDC, CPD, Flashchain and DEAM models. In these models, the activation energy or their distribution plays an important role.

In this study, the weight loss of coals by thermogravimetry (TG) was analyzed to obtain pyrolysis activation energies and frequency factors.

EXPERIMENTAL

Miike, Akabira, and Taiheiyo coals pulverized by a mortar and pestle were used in this study. The results of ultimate and proximate analyses are shown in Table 1.

Pyrolysis was carried out in nitrogen at atmospheric pressure (100 cc/min flow rate) or under vacuum conditions (10-30 Pa total pressure) using a TG to temperatures up to 1073 K at heating rates between 3 K/min and 100 K/min.

RESULTS

Figures 1 and 2 show the weight loss curves for Miike coal at atmospheric pressure and under vacuum, respectively. In both cases, the weight loss curve was moved to the higher temperature zone as the heating rate increases. This phenomenon is also seen in the degradation of synthetic polymers having the simple chemical bonds, such as polyethylene and polypropylene.

The final weight loss of coals heated to 1073 K under vacuum was larger than those under atmospheric pressure, suggesting that mass transfer strongly influences weight loss in experiments under atmospheric pressure.

ANALYSIS

Coal pyrolysis is generally analyzed as a first order reaction of volatile matter in the coal residue. In this study, the final weight loss at 1073 K under vacuum conditions, 0.58, 0.52, and 0.55 for Mikke, Akabira, and Taiheiyo coals, respectively, was defined as the quantity of original volatile matter in the raw coals. These values were also used to model the experiments at atmospheric pressure.

Assuming a first order reaction and the Arrhenius Equation for the rate constant, Equation 1 is obtained.

$$(dV/dT)C = (A)\exp(-E/RT)(V^*-V) \quad (1)$$

where, A is frequency factor, E is activation energy, C is the heating rate, T is the temperature, and V^* is the original volatile matter in the raw coal.

By integration of Equation 1, Equation 2 is obtained.

$$\ln(C/T^2)=-(E/R)(1/T)+\ln[(AR/E)/\ln[V^*/(V^*-V)]] \quad (2)$$

Assuming that the rate constant, K, of the first order reaction is identical at the same extent of conversion at different heating rates, E at a specific extent of conversion can be obtained by plotting $\ln(C/T^2)$ vs. (1/T), where T is the temperature at which the same conversion is obtained at each heating rate. A is then calculated using Equation 2.

Figure 3 shows the plot of $\ln(C/T^2)$ vs. (1/T) of Miike coal pyrolyzed at atmospheric pressure for conversions from 0.2 to 0.6. Activation energies and frequency factors for the different conversions obtained by the above method are shown in Figures 4 and 5.

Figure 6 shows the relationship between A and E obtained for conversions between 0.2 and 0.6, which can be expressed as a line independent of coal and pressure. The rate constant of the first order reaction is defined by the combination of A and E. This suggests that coal degradation rate constant is the same for the conversions of 0.2 - 0.6 regardless of coals and pressure.

If the frequency factor is assumed to be constant during pyrolysis, a distribution of activation energies is obtained by Equation 3, which is a popular method for the analysis of the first order parallel reactions. In this study, the minimum frequency factors obtained by Figure 5 for the experiments under vacuum condition, which are 1.0×10^{12}, 1.5×10^{12}, 4.0×10^{17} sec^{-1} for Miike coal, Akabira coal and Taiheiyo coal respectively, are used. Figure 7 shows the distribution of the activation energy of each coal.

$$E=(RT)\ln[A(V^*-V)/(dV/dT)] \quad (3)$$

These figures show that activation energies for the experiments at atmospheric pressure and under vacuum are almost identical up to the approximately 0.6 conversion for each coal. On the other hand, activation energies for conversions greater than 0.6 are different at atmospheric pressure and under vacuum conditions. It suggests that the reaction at atmospheric pressure is controlled by mass transfer of the remaining heavy materials produced at conversion below approximately 0.6. It is essential to understand the chemistry of remaining materials in the coals in the experiments at atmospheric pressure.

REFERENCES

1. Gavalas, G.R., P.H.-K. Cheng, and R. Jain: Ind. Eng. Chem. Fundam., 20, 113-112 (1981).
2. Gavalas, G.R., R. Jan, and P.H,.-K Chen: ibid., 20, 122-132 (1981).
3. Anthony, D.B. and J.B. Howard: AIChE J., 22, 625-656 (1976).
4. Howard, J.B.: "Chemistry of Coal Utilization", 2nd Suppl. p. 729 (1981).
5. Serio, M.A., D.G. Hamblem, and P.R. Solomon: Energy & Fuels, 1, 138-152 (1987).
6. Solomon, P.R., D.G. Hamblem, R.M. Carangelo, M.A. Serio, and G.V. Deshpande: ibid. 2, 405-422 (1988).
7. Fletcher, T.H., A.R. Kerstein, R.J. Pugmire, and D.M. Grant: Energy & Fuels, 4, 54-60 (1990).
8. Grant, D.M., R.J. Pugmire, T.H. Fletcher, and A.R. Kerstein: ibid., 3, 175-186 (1989).
9. Niksa, S and A.R. Kerstein: ibid., 5, 647-665 (1991).
10. Niksa, S.: ibid., 5, 665-673 (1991).
11. Niksa, S.: ibid., 5, 673-683 (1991).
12. Niksa, S. And C.-W. Law: Combustion and Flame, 94, 293-297 (1993).

Table 1. Analyses of Coals Used

	Ultimate Analysis (daf st%)				Proximate Analysis (dry wt%)			
Coal	C	H	N	S+O(diff.)	V.M.	F.C.	Ash	Water
Taikeiyo	74.87	6.55	0.89	17.69	45.87	43.71	10.42	1.24
Akabira	83.32	6.36	1.40	8.92	40.18	52.92	6.90	0.61
Miike	83.78	6.75	1.01	8.46	44.06	47.23	8.71	0.27

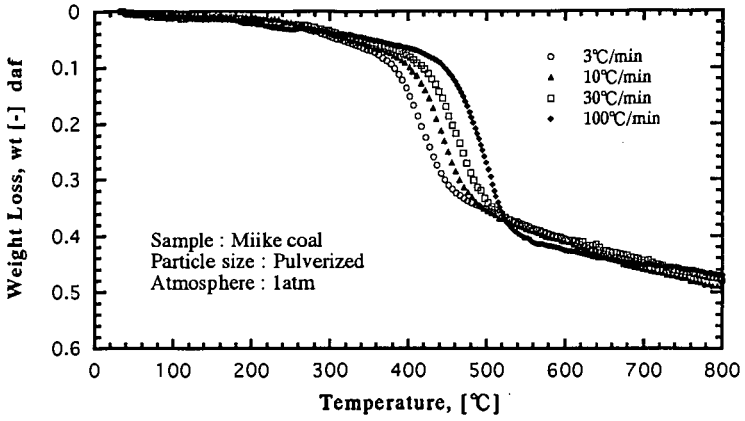

Fig.1 Weight loss curve of Miike coal at atmospheric pressure

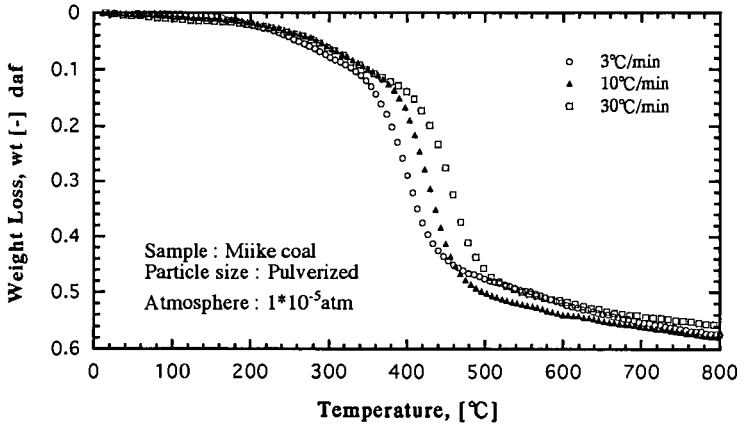

Fig.2 Weight loss curve of Miike coal under vacuum

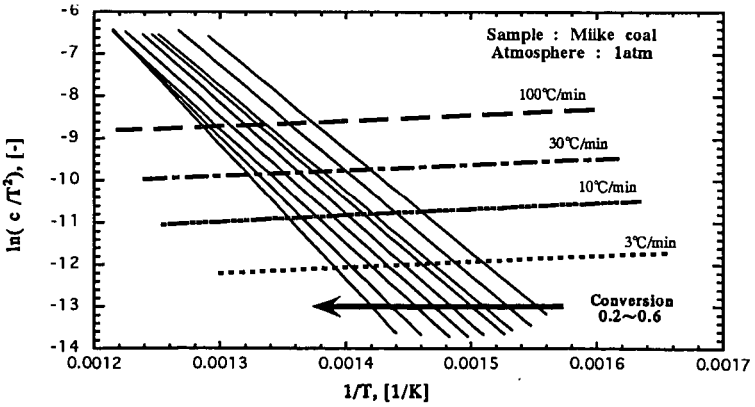

Fig.3 $\ln(c/T^2)$ vs. (1/T) of Miike coal for conversions between 0.2 and 0.6 at atmospheric pressurs

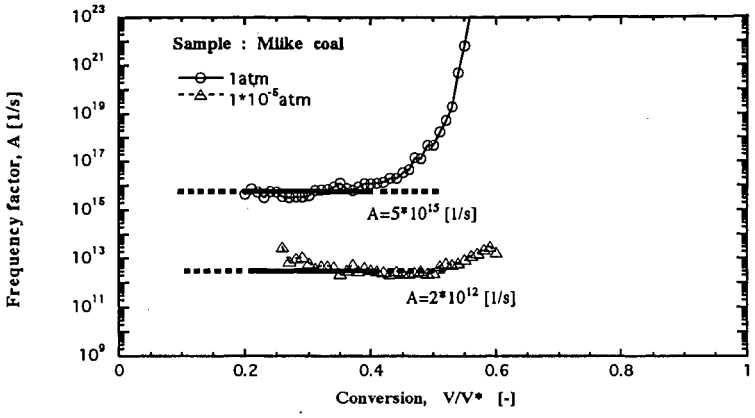

Fig.4 Frequency factor of Miike coal at 0.2-0.6 of the conversion

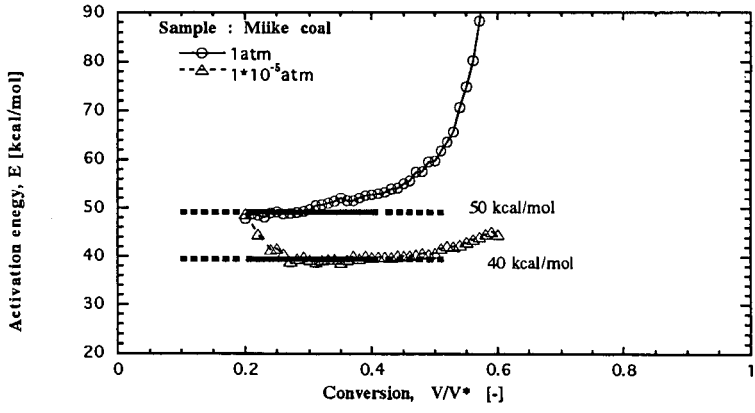

Fig.5 Activation energy of Miike coal at 0.2-0.6 of the conversion

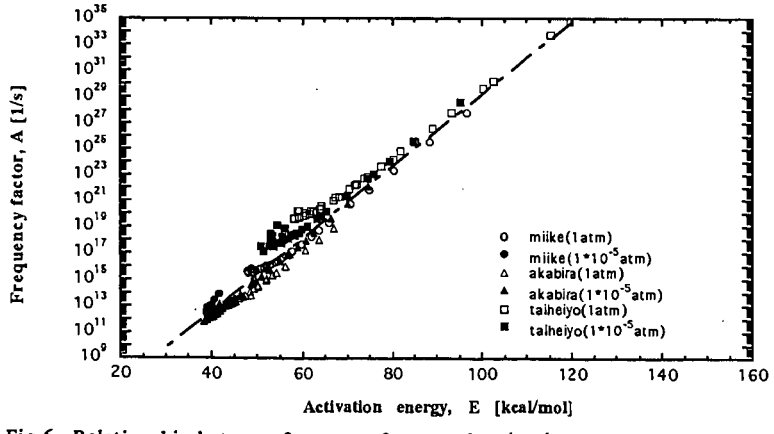

Fig.6 Relationship between frequency factor and activation energy

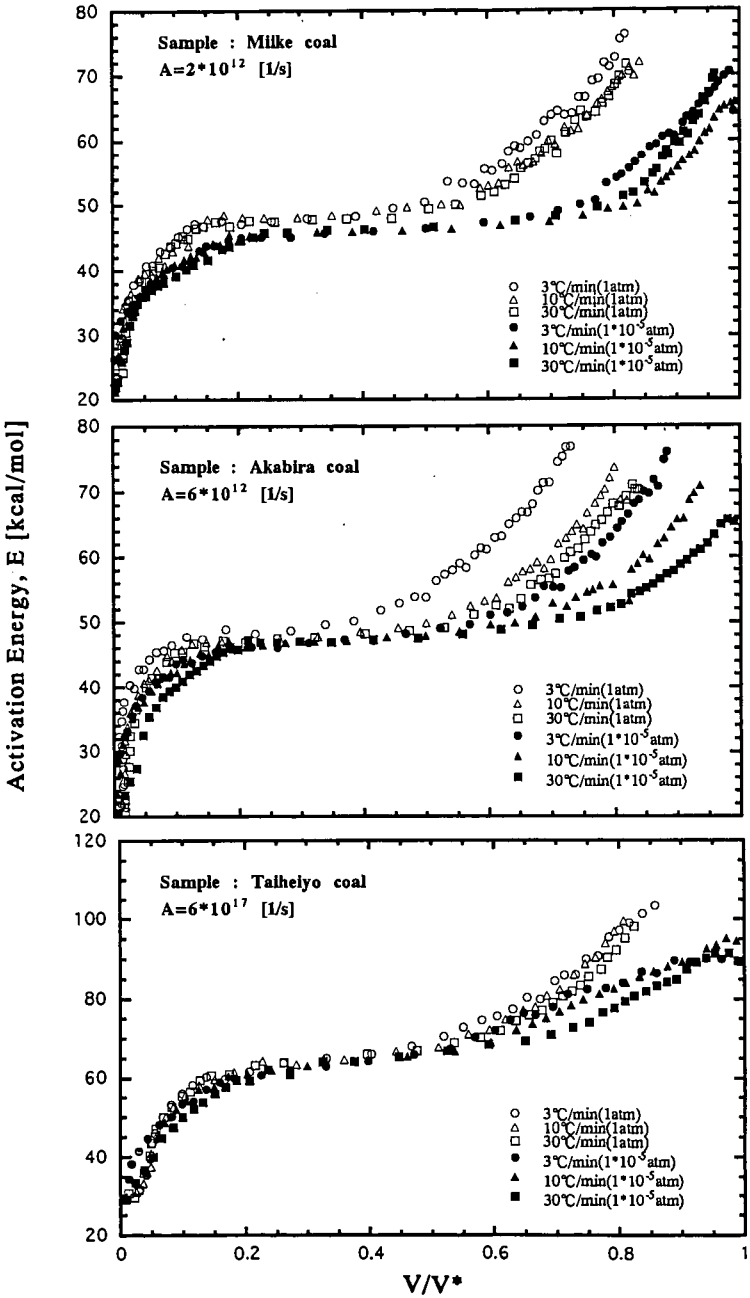

Fig.7 The distribution of activation energy for each coal using a constant frequency factor

CURRENT PRACTICES FOR MODIFICATION OF PAVING ASPHALTS

Hussain U. Bahia and Dario Perdomo
The Asphalt Institute, Research Park Dr., PO Box 14052, Lexington, KY, 40512.

Keywords: Modified Asphalts, Superpave, Asphalt Additives

Introduction

The Superpave binder specification, AASHTO MP1 (1), has introduced new concepts for selecting paving asphalt binders. The specification , in addition to using rheological and failure measurements that are more related to performance, is based on the idea that the criteria to maintain a satisfactory contribution of asphalt binders to the resistance of pavement failures remains the same but have to be satisfied at critical application temperatures. The test procedures require that the material be characterized within certain ranges of strains or stresses to ensure that material and geometric non-linearities are not confounded in the measurements.

These new specification concepts have resulted in re-evaluation of asphalt modification by the majority of modified asphalt suppliers. The philosophy of asphalt modification is expected to change, following these new concepts, from a general improvement of quality to more focus on using modifiers based on the most critical need as defined by two factors:

- The application temperature domain
- The type of distress to be remedied

The new specification requirements should result in a more effective use of modifiers as the amount and type of modifier will be directly related to the application environment and the engineering requirements.

Modification to meet the Superpave Binder Specifications

The Superpave binder specification parameters have been selected such that one or more material properties are used to evaluate the potential contribution of asphalt binders to resistance of critical pavement distress types (2,3):

Workability: Rotational viscosity is used as the indicator of workability. This is a requirement that is not related to climatic conditions, but is necessary to ensure that binders are workable enough so that mineral aggregates can be properly coated and asphalt mixtures can be compacted efficiently to reach the required density.

This requirement is critical for many modifiers currently used because they tend to increase in consistency and thus result in less workability. To achieve required workability, temperatures for mixing and compaction are usually increased. This can result in increased production cost, more volatile loss, increased oxidative aging, and possible degradation of certain modifiers.

Permanent Deformation: Complex shear modulus (G^*) is used as the indicator of total resistance to deformation (rigidity) under cyclic loading . Sine of the phase angle ($\sin \delta$) is used as the indicator of relative elasticity of the binder under cyclic loading. Both parameters are combined in the parameter ($G^*/\sin \delta$) to ensure that the binder will have acceptable contribution to resistance of permanent deformation.

This requirement indicates that modification of asphalts, to resist permanent deformation, can be done either by increasing rigidity, elasticity, or both. Rigidity is a material characteristic that is much easier to alter because of the nature of the asphalt. Rigidity can be increased by oxidation in the refinery process, by using low cost additives that will work as inert fillers, or by using stiffeners that will react with asphalt and change its consistency. Elasticity, on the other hand, requires creating an elastic structure using certain types of clastomeric materials. These materials, mostly polymeric in nature, should exhibit compatibility with the asphalt and be resistant to changes due to oxidation, phase separation, and unstable reaction. Elasticity has been identified as an important property needed to improve pavement performance. This concept is based mostly on few pavement tests sections and accelerated failure tests in the laboratory. How much elasticity is needed, and what is the elastic structure's contribution to the resistance to permanent deformation, is difficult to quantify.
In the Superpave specification the parameter $\sin \delta$ was selected based on the concept of dissipated energy. It is derived with the consideration that asphalts are compared within the linear visco-elastic region. This has important ramifications for some modifiers because their elastic response is different at different strain or stress levels. Strain dependency is discussed in a following section.

Fatigue Cracking: Same parameters (G^* and $\sin \delta$) are used as the indicators of resistance to fatigue cracking. An important distinction is that the specification targeted only strain controlled fatigue as the main fatigue distress. The whole Superpave system (binder and mixture) does not focus on stress controlled fatigue. Using the same energy concepts, the parameter $G^*\sin\delta$ is used to indicate that resistance to strain-controlled fatigue can be achieved by decreasing rigidity (G^*) and/or increasing elasticity (lower $\sin\delta$).

From a modification perspective, decreasing rigidity (measured by G*) is simpler than increasing elasticity. Rigidity can be decreased in the refining process, by using fluxing agents, or with other low cost hydrocarbons that are compatible with asphalts. Increasing elasticity requires the same basic modifications discussed earlier in relation to permanent deformation. It is, however, more complex at intermediate temperatures because most asphalts show a significant amount of elasticity at intermediate temperatures. To add more elasticity, a highly elastic structure created by an elastomer is needed. The same complications discussed in regard to the strain dependency apply at intermediate temperatures. Unmodified asphalts have a narrow range of linear visco-elastic behavior at intermediate temperatures. In the nonlinear range unmodified asphalts show tendency to lose their elastic behavior (increase in δ) differently than asphalts modified with elastomeric materials. This difference can result in dissimilar performance of modified asphalts in the non-linear range.

Low Temperature Thermal Cracking: Because of the important role of the binder in thermal cracking, the Superpave specification includes three parameters that are combined in any one parameter. Creep stiffness, S(@60sec), is used as an indicator of the amount of thermal stresses that can be built in the asphalt due to a given thermal gradient induced strain induced by temperature change. Logarithmic creep rate, m(@60sec), is an indicator of the relative elasticity; higher m (60) values indicate less elasticity and more ability to relax stresses by viscous flow. Failure strain, ε_f, is used as an indicator of brittleness or the ability to stretch without cracking (strain tolerance).

Modification of low temperature properties can be achieved by changing one or more of these parameters. In most cases it is difficult to use modifiers that will change one of these indicators while keeping the others constant. Unlike fatigue, thermal cracking indicators favor modification that results in less elastic binders. This should be easier to achieve since refining processes and additives that result in softer binders either reduce or do not affect the elasticity (higher δ and higher m values). Strain tolerance can be increased by many several mechanisms. Elastomeric polymers can improve strain tolerance. Plastomers and certain fillers can work as crack arresters and increase strain tolerance. Certain hydrocarbons, because of their low glass transition temperature, can significantly improve strain tolerance.

Types and Amounts of Modified Asphalts

There is a large number of modifiers used in paving applications at the present time. In a survey published in 1993 (4), there were a total of 48 commercial brands of asphalt modifiers. These modifiers were classified in 5 classes including 10 fillers/extenders, 16 thermoplastic polymers, 3 thermosets polymers, 1 liquid polymer, 4 aging inhibitors, and 10 adhesion promoters. During the Strategic Highway Research Program (5, 6) 82 asphalt modifiers or modified asphalts were obtained, documented and stored at the Material Reference Library. These 82 sources of modifiers were classified in 8 classes including 39 thermoplastics, 27 anti-stripping agents, 5 anti-oxidants, 2 fibers, 2 extenders, 1 recycling agent, and 1 oxidant. In an internal report by the Engineering Staff of the Asphalt Institute (7), 48 types of modifiers were identified. They were classified into 13 polymers, 10 hydrocarbons, 6 mineral fillers, 6 antioxidants, 6 antistripping additives, 4 fibers, 2 extenders, and 1 oxidant.

The classification of asphalt modifiers can be done based on the composition and physical nature of the modifier, based on the mechanism by which it alters asphalt properties, or based on the target asphalt property that needs to be modified. Table 1 is generated, based on a review of literature (4, 5, 6, 7), to summarize the generic types of asphalt modifiers classified according to the nature of the modifier. The target distress shown in the table is the main distress or property that the additive is expected, or claimed, to affect favorably. The information is based on interpretation of the published information for brands of modifiers that belong to the modifier classes shown. It many cases the reported effects are based on limited data , which means that the effects cannot be generalized to all asphalt and/or aggregate sources.

Typical Effects of Modification On Superpave Binder Parameters

A sample of effect of modification on the Superpave Binder parameters is shown in figures 1 to 4. In all these figures the relative changes (modified/unmodified) in the performance indicators are shown. The base asphalts vary among the modifiers but not for a modifier. Figure 1 shows the effects of some elastomeric polymers (SB and SBR). The ratios are calculated using values measured at temperatures for which the base asphalt meets the respective requirements for each of the parameters. As depicted in Figure 1, the elastomeric polymers show favorable effects on all performance related parameters. G*/sin δ increases, G*sin δ and S(60) decrease, and m(60) and strain at failure increase. The relative changes are however higher for the G*/sin δ and failure strain than the other parameters.

Figure 2 depicts the changes for another asphalt modified with 3 different plastomeric additives at 4% by weight of asphalt. These vary in their molecular weight but all are polyethylene based. The only significant change is seen at high temperatures for the parameter G*/sin δ. It appears that these plastomers are not effective with this particular asphalt at intermediate or low temperatures.

Figure 3 depicts the effects of three different types of crumb rubbers. These are all mixed at 15% by weight of asphalt. The effect on the values of G*/sin δ are more pronounced than the

plastomeric modifiers but the effects on the other parameters are not very significant. These rubbers are not reacted and no extender oils were used in preparation of their mixtures with the asphalt.

Figure 4 depicts the effects of two mincral fillers (C: Calcite and Q: quartz) mixed at 50 % volume concentration. As depicted, these fillers significantly increase G*/sin δ, which is a favorable effect. They, however, also increase G*sinδ, S(60) and they decrease m(60). These effects are not favorable and may contribute to significant increase in fatigue and thermal cracking.

The data presented in Figures 1 to 4 are samples of data collected for specific asphalts. They cannot be generalized for all asphalts. Several of these modifiers/additives react with asphalts and their effects are therefore asphalt specific. They are presented here to give an overview of the general trends of effects. The data clearly shows that the most significant effect is seen at high temperatures in the parameter G*/sinδ. This is expected since asphalts exhibit the least stiffness at higher temperatures. If the effects on G* and sin δ for these modifiers are considered separately, it is clear that the most significant effect is on the value of G*. Even for the elastomeric modifiers, the phase angle did not drop by more than 25 degrees. For an asphalt with a phase angle of 80 degrees, this change will only result in a 15% reduction of sin δ . This finding substantiates the concept that it is more difficult to induce elasticity at high temperatures than to enhance rigidity with most of the modification techniques used currently.

Characteristics not Considered by the Superpave Binder Specifications and Test Protocols

The Superpave binder specification is based on important assumptions that are justified for unmodified asphalts. Several of these assumptions may not be valid for some modified asphalts. Following are some of the critical assumptions or characteristics that are not considered and which are currently being discussed by asphalt researchers.

Dependency of viscosity on shear rate: The rotational viscosity is measured at 135 C at a recommended rate of 20 rpm. This shear rate was selected because most unmodified asphalts show Newtonian behavior (viscosity is independent of shear rate) at this rate. It was also selected to simulate shear rates during pumping and handling in refineries and asphalt plants. Many modified asphalts are highly shear dependent at and above the value of 20 rpm. Modified asphalts can also exhibit elasticity at these high temperatures, which cannot be measured with a viscometer. The current rotational viscosity protocol for Superpave does not include a procedure to measure shear rate dependency and the criteria for workability do not address this characteristic of modified asphalts. In the mixture design requirements of Superpave, it is required to mix at a viscosity of approximately 0.17 Pa-s and compact at 0.28 Pa-s. These low viscosities cannot be achieved for many modified asphalts unless they are heated to extremely high temperatures.

Strain dependency of rheological response under cyclic loading: The rheological properties in the Superpave specification are measured at selected strain levels. These strain levels are selected to be within the linear viscoelastic range for unmodified asphalts. The basis for the selection was the relation between limit of linear behavior and the value of G*. For modified asphalts it is known that this relation may not hold true. Figures 5 to 7 depict strain dependency of selected modified asphalts. Figure 5 is for an asphalt modified with two polymeric modifiers, including both an elastomeric and a plastomeric modifier. Figure 6 is for an asphalt modified with crumb rubber, and Figure 7 is for an asphalt modified with a rigid filler. In all cases it is apparent that there is a shear thinning effect. The G* decreases with strain while the δ increases. Unmodified asphalts also show a shear thinning effect; the linearity limit on the strain scale decreases as the temperature decreases. The Superpave specification does not allow for consideration of strain dependency nor does it refer to a range of strains that are typically encountered in the field.

The concept in the Superpave specification is to select asphalts based on their performance within the small strain (linear) range because pavements should not be designed to encounter large strains. In other words asphalts should be compared within the (safe) pre-failure region within which they do not undergo high deformation or stresses. It should be mentioned however that it is very difficult to estimate the true strain distribution in an asphalt-aggregate mixture under loading. It is difficult because of the irregular shape of aggregates and the random distribution of voids and binder between aggregates. For the specification to be applicable for materials that do not show a wide linear region, a range of strains should be defined and used in testing. Strain dependency should not be considered as an inferior property. Strain dependent materials (nonlinear materials) can perform well if their strain/stress dependency is taken into account.

Thixotropy and effect of mechanical working: Effect of repeated loading at constant rates on G* and δ is another behavior that is not considered in the Superpave specifications. Certain additives can result in a thixotropic network structure that can be destroyed or altered by repeated shearing. Such structure can be destroyed permanently by mechanical working or can be affected temporarily and regained when material is left to rest. Not many asphalt modifiers that are currently used are known to show such a behavior. Figure 8 depicts a typical example of a time sweep for an asphalt before and after modification with polymeric additives. The figure shows that neither the G* nor the δ are changing in this experiment where the asphalts are being sheared at 10 rad/s every 6 seconds for more approximately 66 seconds. Some asphalts modified with Tall oil and some gel-like compounds can show significant changes due to

mechanical working. Similar to strain dependency, thixotropy should not be considered as an inferior material property. If thixotropy is considered properly in testing and evaluation, thixotropic materials can outperform non-thixotropic materials.

Loading rate dependency: The testing in the specification is conducted at selected loading rates that are assumed to be typical under traffic on open highways. It is well recognized that traffic does not move at one speed. It is also known that thermal cooling cycles vary significantly in their cooling and warming rates. Dependency on loading rates is material specific, not only for modified binders but also for unmodified asphalts. The testing rate of 10 rad/s used for cyclic testing, and the loading time of 60 seconds used for the creep testing, are based on simplifications of asphalt behavior. Modification may result in nullifying the assumptions used in these simplifications. The effect of modification on loading rate dependency should be considered in selecting modifiers and a more comprehensive procedure should be included in the specification to evaluate this property.

Time-Temperature Equivalency: Testing for low temperature creep is done at 10 °C higher than the lowest pavement design temperatures. Also in the guidelines for considering slow moving traffic and traffic amount, it is recommended to shift temperature of testing rather than loading frequency. These requirements and guidelines are based on the assumption that the time-temperature equivalency factors are similar for most asphalts. Although there are similarities in time-temperature equivalency factors for asphalts (8), the equivalency factors can vary for asphalts with different glass transition behavior and asphalts that are heavily modified. One of the common modification techniques is to use softer asphalts with good low temperature properties, and use additives to improve high temperature properties. Such a modified asphalt may have a glass transition region that is significantly lower than an unmodified asphalt with equivalent high temperature properties. These two asphalts can show significantly different time-temperature shift factors due to the difference in transition temperature range. The glass transition region and time-temperature equivalency of asphalts are important properties that are not fully considered in the specifications.

Concluding Remarks

The Superpave binder specification introduces a new system that can more accurately evaluate the effect of modifiers on performance related properties of asphalt binders. There is a variety of additives that are used as asphalt modifiers in paving applications. These can be classified based on their composition and/or effects as polymers (elastomeric and plastomeric), fillers, fibers, hydrocarbons, anti-stripping agents, oxidants, antioxidants, crumb rubber, and extenders. A sample of polymers, fillers, and crumb rubber modifiers was evaluated using the Superpave binder tests. The results indicate that they can impart significant changes on the properties measured in the Superpave specification. The main changes they can impart reflect on the rigidity of the binder (G^*) at the intermediate to high pavement temperatures encountered in the field

The testing protocols included in the Superpave specification are not inclusive of certain important characteristics that are typical of modified binders. Among these characteristics are strain dependency, thixotropy, loading rate dependency, and time-temperature equivalency. These characteristics are modifier specific and ignoring them in selecting modifiers may lead to underestimating or overestimating the effect of the modifier on pavement performance. Typical results for strain dependency and mechanical working were presented for a group of selected modifiers. The Superpave specifications should include provisions to measure these characteristics, and guidelines to assess their effects on pavement performance.

References

1. "Standard Specification for Performance Graded Asphalt Binder", AASHTO Designation MP1-93, AASHTO, Gaithersburg, Md., September, 1993.
2. Anderson. D.A., and T.W. Kennedy, "Development of SHRP Binder Specification", Journal of the Association of Asphalt Paving Technologists, Vol. 62 , 1993, P. 481
3. Bahia. H.U, and Anderson, D.A. "The New Proposed Rheological Properties: Why are They Required and How They Compare to Conventional Properties," Transportation Research Board record 1488, Washington, DC, 1995, pp. 32-39.
4. Kristin Peterson, "Specifier's Guide to Asphalt Modifiers", Roads and Bridges Magazine, May 1993, pp. 42-46.
5. M. Mortazavi, and J.S. Moulthrop, "The SHRP Materials Reference Library," SHRP-A-646 report, National Research Council, Washington, D.C. 1993.
6. Rowlett, R.D. et al.," Performance of Asphalt Modifiers: Classification of Modifiers and Literature Review," Center for Construction Materials Technology, SWL, Houston, Texas, April 1990.
7. McGennis, R.B., "Asphalt Modifiers are here to Stay", Asphalt Contractor, April 1995, pp. 38-41.
8. Anderson, D.A., Christensen, D.W., Bahia, H.U., Dongre, R., Sharma, M.G., Button, J. J. "Binder Characterization and Evaluation, Volume 3: Physical Characterization," Report No. SHRP-A-369, The Strategic Highway Research Program, National Research Council, Washington, DC 1994.

Table 1. Generic types of asphalt modifiers currently used for paving applications.

The classification of **CLASS**		EFFECT ON DISTRESS				
		PD[1]	FC[2]	LTC[3]	MD[4]	AGN[5]
1. Mineral Fillers	Carbon black	x				x
	Hydrated lime	x				x
	Fly ash	x				
	Portland cement	x				
	Silica fume	x				
	Baghouse fines	x				
2. Extenders	Sulphur	x	x	x		
	Some fillers (baghouse dust)					
3a. Polymers Elastomers	***Styrene block copolymers***	x	x	x		
	Styrene butadiene diblock (SB)	x		x	x	
	Styrene butadiene triblock/radial block (SBS)	x	x	x		
	Styrene Isoprene (SIS)	x				
	Styrene ethylbutylene (SEBS)					
	Styrene butadiene rubber latex (SBR)	x		x		
3b. Polymers Plastomers	Polychloroprene latex	x	x			
	Polyisoprene (natural and synthetic)	x				
	Ethylene Propylene diene monomer (EDPM)	x				
	Polyisobutylene	x				
	Ethylene vinyl acetate (EVA)	x	x			
	Ethylene methacrylates (EMA)					
	Polyethylene (low density and high density)	x		x		
	Polypropylene	x				
	Polyolefin	x				
4. Crumb rubber	Different sizes, treatments, and processes	x	x	x		
5. Oxidants	Manganese compounds	x				
6. Hydrocarbons	Aromatics			x		
	Napthenics					
	Paraffinics/wax			x		
	Vacuum gas oil			x		
	ROSE process resins	x				
	Asphaltenes	x				
	Tall oil	x	x			
	Natural asphalts	x				
7. Antistrips	Fatty amidoamines				x	
	Imidazolines				x	
	Polyamines				x	
	Hydrated lime				x	
	Organo-metallics				x	
	Acids				x	
8. Fibers	Polypropylene	x	x	x		
	Polyester	x		x		
	Cellulose	x				
	Mineral	x				
	Reinforcement	x	x	x		
9. Antioxidants	Carbamates					
	Lead			x		x
	Zinc			x		x
	Carbon black	x				x
	Hydrated lime				x	x
	Phenols					x
	Ethyoxylated amine				x	x

1: PD: Permanent Deformation
2. FC: Fatigue Cracking
3. LTC: Low Temperature Cracking
4. MD: Moisture Damage
5. AGN: Oxidative Aging

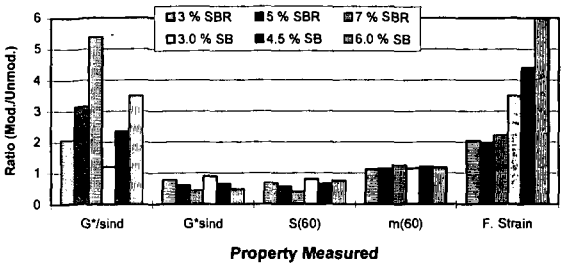

Figure 1. Relative Change in Superpave binder properties after modification with SBR and SB-based modifiers

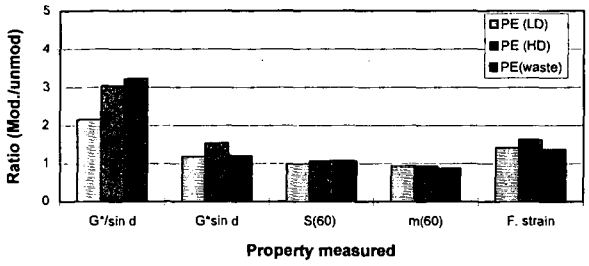

Figure 2. Relative Change in Superpave binder properties after addition of Plastomers

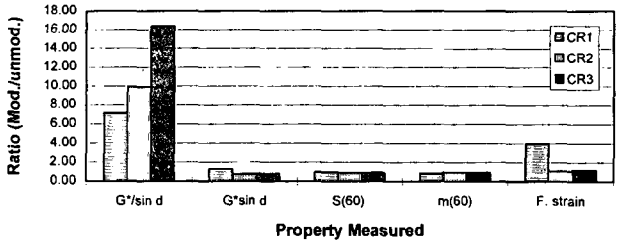

***Figure 3.* Relative change in Superpave binder properties after modification with 3 types of crumb rubber**

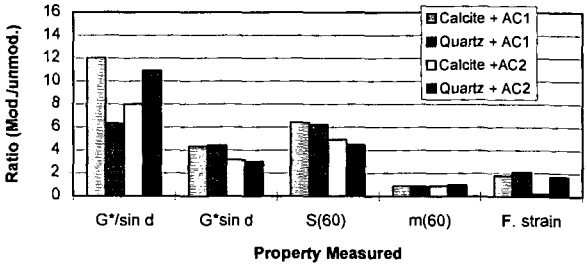

Figure 4. Relative change in Superpave binder properties after addition of mineral fillers

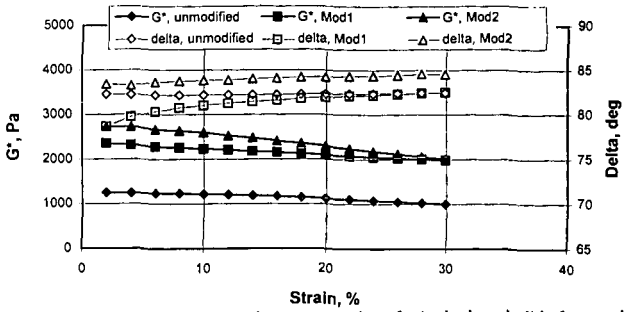

Figure 5. Effect of testing strain on properties of a typical asphalt before and after modification with polymers

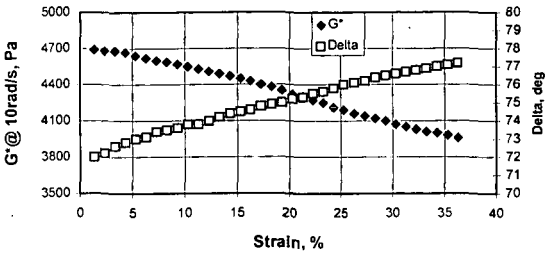

Figure 6. Effect of testing strain on properties of a typical asphalt modified with crumb rubber

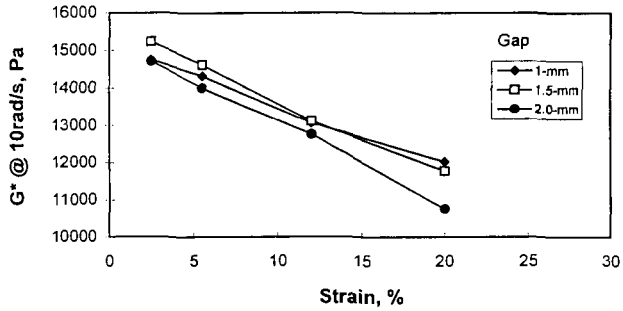

Figure 7. Strain dependency of asphalt filled with rigid filler (Ottawa sand < 0.25 mm) Filler/Asphalt ratio= 0.5 by volume

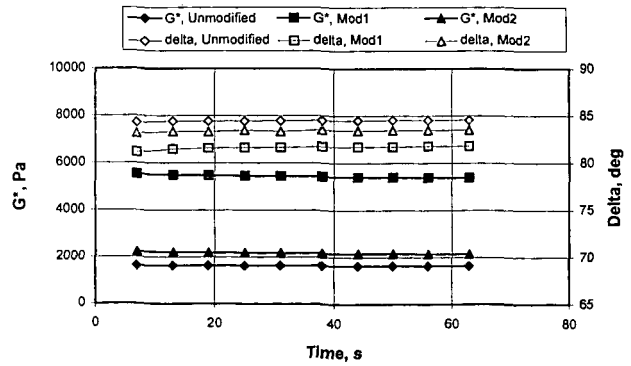

Figure 8. Effect of mechanical working on asphalt properties before and after modification with polymers

FURFURAL MODIFIED ASPHALT OBTAINED BY USING A LEWIS ACID AS A CATALYST

G. Mohammed Memon, FHWA/ EBA Engineering Inc.
Brian H. Chollar, FHWA
6300 Georgetown Pike
McLean, VA 22101

INTRODUCTION

Asphalt is solid or semi-solid at room temperature, becomes soft and starts flowing upon heating, and becomes hard and brittle at very low temperatures.

States have been facing problems such as cracking, rutting, and asphalt adhesion to aggregates in their asphaltic pavements for years. Many polymer additives have been used in asphalt to reduce these problems, but little work has been done using chemically modified products of asphalt to attempt to solve these serious problems of asphalt pavements[1-3]. The above mentioned problems decrease the life of the pavements, resulting in an increase of maintenance and/or replacement costs. There are two types of cracking which can occur in asphalt pavement; one related to load, and the other related to thermal stress. The load-related cracking is known as fatigue cracking and is defined as fracture under repeated or cyclic stress having a maximum value of less than the tensile strength of the material. The thermal cracking occurs due to pavement shrinkage at low temperatures causing the shrinkage stresses to exceed the tensile strength.

FHWA researchers have found furfural to be a suitable candidate for functional group modification of asphalt. The modified product shows improved performance as well as improved rheological properties.[4] The furan ring in the product was found to be the principal component responsible for the product high temperature stiffness, whereas the furan ring (with or without an aldehyde group) was also important in improving the product low temperature properties[2]. The nature of this reaction was determined by FHWA laboratories using different analytical instruments. Phenolic moieties present in asphalt were found to be reacting with furfural (in the presence of an acid as a catalyst) forming a polymeric material[3]. However, mix testing showed corrosive fumes (due to HCl) escaping from the furfural modified asphalt[5].

Thus, a chemically modified asphalt is needed which: has low creep stiffness, has less temperature susceptibility, can resist thermal stress to alleviate thermal cracking, can maintain a high stiffness at high temperatures to resist rutting, and is an environmentally accepted modified product. The major objective of this study was to obtain a furfural modified asphalt with the above properties using a non-polluting Lewis acid, para-toluene sulfonic acid (PTSA), as a catalyst for the reaction.

EXPERIMENTAL METHOD

Materials used: The asphalts[AAD-1(California Coast), AAV-1(North Alaskan Slope), and AAM-1(West Texas Intermediate)] used in this study were obtained from the Strategic Highway Research Program (SHRP) Material Reference Library (MRL), Reno, Nevada. The aggregate used was traprock screenings(#10 diabase) from Vulcan Materials Co. All reagents were of analytical grade from Baxter Scientific Products unless otherwise specified.

Furfural Reaction: 200 g of asphalt was placed in a 500-ml three-necked round-bottomed flask equipped with a mechanical stirrer and a thermometer. The asphalt was heated to 93°C, followed by the addition of PTSA (0.07-0.12 milimoles/gram of asphalt) and then furfural (0.15-0.20 milimoles/gram of asphalt) drop wise with continuous stirring. The contents of the flask were then

heated for 1.5 hours at the same temperature.

Test Methods: Standard tests used to measure the properties of asphalts are given below:

Freeze-Thaw Pedestal Test:[6] The wet environment has an impact on the asphalt-aggregate bond. This bond can be weakened or destroyed if water penetrates into the pavement.

This test measures the water susceptibility of the adhesion of virgin and modified asphalt to the aggregate. The briquettes of the asphalt-aggregate mixture were made according to the Wyoming pedestal test developed by Plancher et al[6]. The samples in jars filled over the top of the briquette level with water were stored in a freezer at -10 to -12°C for 24 hours, cooled to the room temperature, stored in an oven at 60°C for 24 hours, and then examined for surface cracks or breakage. This cycle was continued until the failure of the briquets occurred due to repeated freeze-thaw cycling.

Test Methods:

1. Rolling Thin Film Oven Test (RTFOT), ASTM-D1754-87.
2. Standard Practice for Accelerated Aging of Asphalt Binder Using a Pressurized Aging Vessel(PAV), AASHTO PP1-93 (1A).
3. Test Method for Determining the Flexural Creep Stiffness of Asphalt Binder Using the Bending Beam Rheometer (BBR),AASHTO TP1-93.
4. Test Method for Determining the Rheological Properties of Asphalt Binder Using a Dynamic Shear Rheometer (DSR), AASHTO TP5-93.
5. Corbett Seperation Analysis, ASTM D-4124-86.
6. Thin Layer Chromatography (TLC)[3].
7. Fourier Transform Infrared (FTIR), & Stokes Data Analysis Method[3].

RESULTS AND DISCUSSION:

TLC results of the model polymer made by the interaction of phenol and furfural, using PTSA as a catalyst, shows more polarity in the model polymer than in phenol or furfural. The IR spectrum (figure I) shows that the modified asphalt has more mono and poly substitution on the benzene ring as compared to the corresponding virgin asphalt.

Rheological Properties: Chemical modification of an asphalt with furfural was conducted using a method developed at the Federal-Highway Administration[4]. Figure II shows the continuous SHRP PG grading for virgin and Furfural-Modified asphalts using HCl as a catalyst. The rheological properties of the asphalts used (AAD-1, AAV, & AAM-1)[7], Fu-Modified using HCl and Fu-Modified asphalt using PTSA, are illustrated in figures II, III, IV, and V, respectively. Virgin asphalt AAV passes the criteria for stiffness at 57°C, and the modified binder passes at 63°C. The low temperature rheological data for both virgin and the modified binder pass the SHRP specification at -28°C. The useful temperature range (the sum of the high and low PG grades) for virgin binder AAV is 85°C; that for the modified binder is 91°C. The temperature difference of 6°C is equal to 1 PG grading and is a significant change. From an economic point of view, 1 PG grading will result in a significant cost savings, but the corrosivity of HCl is a major problem. To solve that problem, a new catalyst (p-toluene sulfonic acid, PTSA) was used. The use of PTSA (figure III) provided a modified asphalt product of AAV which showed PG 63-31 continuous PG grading and 94°C as the useful temperature range. The temperature difference between the virgin and the modified product of 9°C is equal to 1.5 PG grading and is slightly better than that of the HCl modified product. Figure IV demonstrates the rheological behavior of virgin AAM-1 and its Fu-modified binder. The continuous high temperature grading for the virgin binder and for the modified binder is at 67 and 78°C respectively. The low temperature grading for both virgin and the Fu-modified binders were found to be -23°C and -

30°C respectively. The useful temperature range for the virgin binder is 90°C; that for Fu-modified binder is 108°C. The difference in the useful temperature range is 18°C (or 3 PG grades), which is extremely significant. Figure V depicts the rheological continous grading for the third asphalt used in this study, binder AAD-1. The virgin binder passes the high temperature stiffness specification at 62°C; the modified binder passes it at 71°C. The creep stiffness and slope for both the virgin and the modified binders pass the specification at -31° and -34°C respectively. The useful temperature range is 90° and 105°C for virgin and modified binder respectively, a 12°C range or 2 PG grades. Thus, these modifications are improving the PG grading simultaneously at both high and low temperatures, but the degree of improvement is asphalt source-dependent.
Moisture susceptibility was checked through the Wyoming freeze thaw pedestal tests and is shown in figure VI. The virgin asphalt AAV-1 failed after 4 freeze-thaw cycles, whereas Fu-modified by HCl and Fu-modifed by PTSA failed after 16 and 18 freeze-thaw cycles, respectively. This indicates that the modified binder is significantly (four times) less moisture susceptible than its corresponding virgin binder.

CONCLUSION: The use of furfural for asphalt modification in presence of a Lewis acid (catalyst) produces a product which is:

- Environmentally acceptable
- Easy to prepare.
- Economical.
- Less temperature and moisture susceptible.
- Improves both the high and low temperature rheological properties simultaneously.
- Asphalt source-dependent in terms of performance.
- Shows potential for higher fatigue and rutting resistance as compared to the corresponding virgin binder.

REFERENCES

1. B. H. Chollar, G. M. Memon, N. Shashidhar, J. G. Boone, and J. A. Zenewitz, "Characteristics of Furfural Modified Asphalt" 73rd TRB Meeting Paper No. 930913, Jan. 1993.
2. G. M. Memon, J. G. Boone, and B. H. Chollar, "Furfural Substitutes for Chemical Modification of Asphalt", ASTM STP 1241, Philadelphia, 1994.
3. G. M. Memon and B. H. Chollar, "Nature of the Chemical Reaction for Furfural Modified Asphalt", 208th ACS National Meeting, Washington, D.C., Aug. 20-25, 1994, 39 # 3, pp870-78.
4. D. Kumari, B. H. Chollar, J. G. Boone, and J. A. Zenewitz,"Chemical Modification of asphalt" FHWA Report No. FHWA/RD-91-193, August, 1992.
5. K. D. Stuart,"Asphalt Mixtures Containing Modified Binders" FHWA Report No.FHWA/RD-92-101, August, 1992.
6. H. Plancher, G. Miyake, R. L. Venable and J. C. Petersen, "A Simple Laboratory Test to Indicate the Susceptibility of Asphalt-Aggregate Mixtures to Moisture Damage During Repeated Freeze-Thaw Cycling," Proceedings of the Canadian Technical Asphalt Association, Vol. 25, pp. 247-262, 1980.
7. G. M. Memon and B. H. Chollar, "Environmentally Benign Asphalt Having Improved Rheological Properties" (Patent applied for), July, 1995.

Figure I

Infrared Spectra of: a) Asphalt AAD-1 and b) Fu-Mod. AAD-1

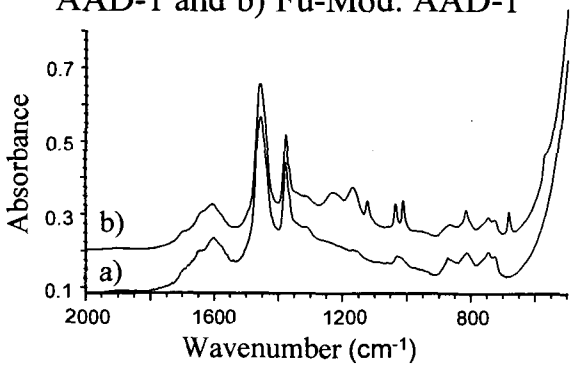

Figure II

PG Grades for Virgin (AAV) and Fu-Mod., Using HCl as the Catalyst

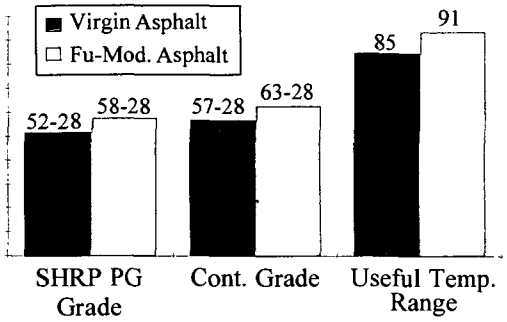

Figure III

PG Grades for Virgin (AAV) and Fu-Mod., Using PTSA as the Catalyst

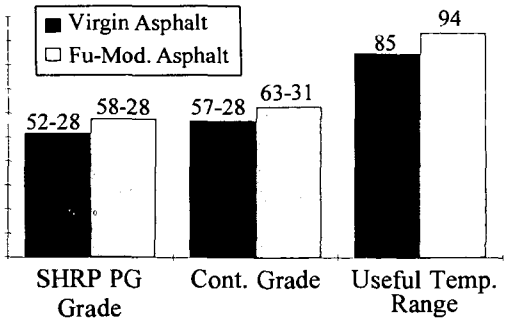

Figure IV

PG Grades for Virgin (AAM-1) and Fu-Mod., Using PTSA as the Catalyst

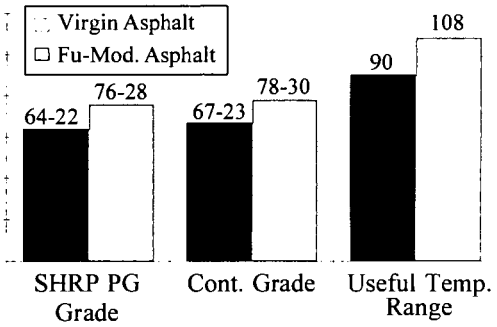

Figure V

PG Grades for Virgin (AAD-1) and Fu-Mod., Using PTSA as the Catalyst

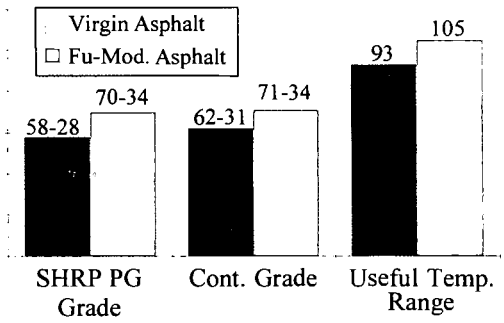

Figure VI

Comparison of Freeze-Thaw Pedestal Tests

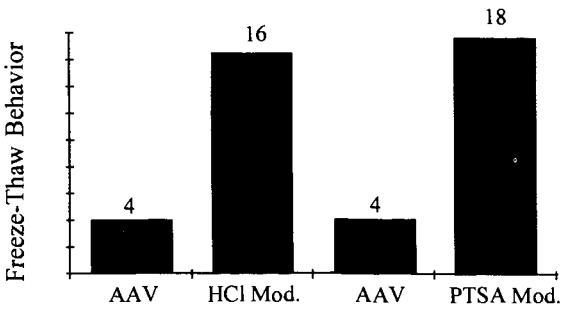

THE UTILITY OF PHENOL-ALDEHYDE CROSS LINKING RESINS IN POLYMER MODIFIED ASPHALT - THE BUTAPHALT(tm) PROCESS

Dennis D. Krivohlavek
Asphalt Technology & Consulting, Inc.
4201 S.W. Hwy. 66
Claremore, Oklahoma 74107

Keywords: Cross Linking, Phenol-Aldehyde Resins, Polymer Modified Asphalt

The use of Phenol-Aldehyde cross linking or vulcanizing resin is well known in the rubber and plastics industry. Previous to our work little (if any) understanding of the utility of these compounds in polymer modified asphalt (or bitumen) was known. This presentation will hopefully enlighten practitioners of the art of asphalt modification on this subject. This art is commercially known as the Butaphalt(tm) Process.

Of initial interest is the mechanism of reaction of Phenol-Aldehyde cross linking resins. As the quantitative analysis of such a mechanism in asphalt would likely need years of effort to resolve, we will look at possible mechanisms in a rubber system. Several publications offer excellent discussions on the art of vulcanization. Science and Technology of Rubber, Second Edition, edited by James E. Mark, et. al., Academic Press, page 366, is such a publication. Therefore, a possible mechanism is illustrated in Figure 1 below.

Figure 1

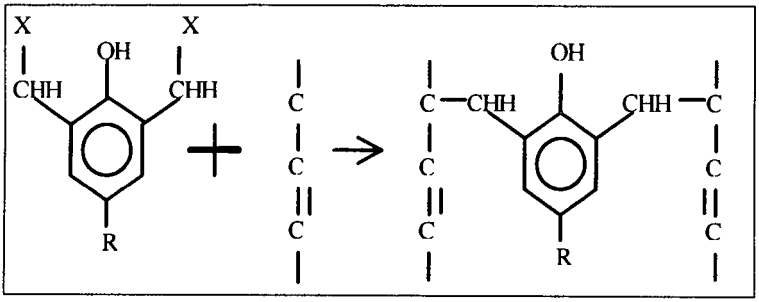

Another possible mechanism for the reactive phenolic resins involves the formation of a quinone across the double bond of the rubber molecule. Again, several sources of information in the literature are available. Science and Technology of Rubber, Second Edition, edited by James E. Mark, et. al., Academic Press, page 368, makes such reference. This mechanism is thought to create a chroman or chromane structure. This chroman(e) structure is illustrated in Figure 2 below.

Figure 2

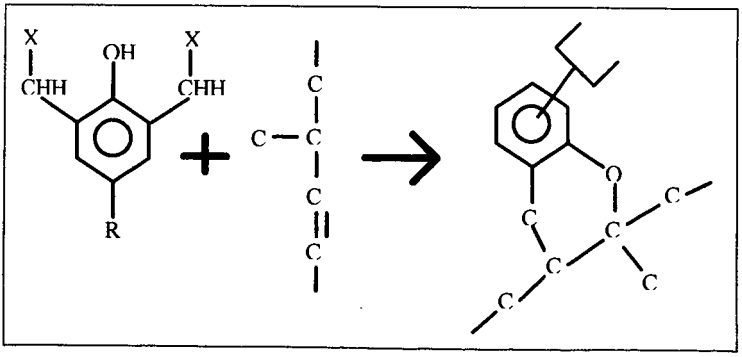

Evidence of some form of a chemical and resulting physical change has taken place in the asphalt can be observed by testing Conventional (abbreviated as Cnvntal in tables below) and Butaphalt(tm) Processing. Such a test program with Lloydminster asphalt was performed. It should be noted that this asphalt is generally considered to be a good to excellent candidate for polymer modification. These select tests and their results are also compared at various concentrations of a commercially available high molecular weight radial styrene butadiene styrene (SBS) polymer. Test results are given in Table 1 below.

Table 1

Tests Results in Celsius	3.50% SBS Cnvntal	3.50% SBS Butaphalt	2.50% SBS Cnvntal	2.50% SBS Butaphalt
Separation @ 162	16.11	-0.14	15.14	-0.14
SoftPt B/4 TFOT	70.00	79.44	54.31	58.33
SoftPt Aft TFOT	50.97	63.89	49.17	56.67
B/4-Aft Soft Pt	-19.03	-15.55	-5.14	-1.66

The Separation Test involved static heated storage for each specimen for 48 hours. Although Lloydminster asphalt is normally considered very good for modification, the Separation value is unacceptable under the Conventional Process. However the Butaphalt(tm) Process corrected this deficiency completely. Notice that these results are independent of the SBS concentrations.

The Softening points are always higher with the Butaphalt Process (tm)for a given polymer level. This is true whether observing these results either before or after the Thin Film Oven Test. The Butaphalt(tm) Process consistently yielded minimum decrease Softening Point differential values through the Thin Film Oven Test. These results would indicate longer storage life at in service storage temperatures. These results should also indicate a better product through the hot mix plant and on the road.

We will next look at an asphalt that is considered to be a "problem" for polymer modification. This asphalt is known to be from a wide variety of combined crude oil feed stocks. Among the possible crude oil selections is Alaskan North Slope. Asphalt made from or containing significant quantities of Alaskan North Slope crude oil have been known to have problems when modified with either SBS or styrene butadiene random polymerized latex (SBR) polymers. This next asphalt was not only reported to have significant Alaskan North Slope crude oil but is also reported to have slightly air blown components used in its manufacturing process. Generally speaking, limited air blowing of a asphalt or its component parts will not be severely detrimental to the final traditional product. But, air blowing a asphalt or its component parts are not desirable for a candidate asphalt for polymer modification. We will again examine the Butaphalt(tm) Process in comparison to a Conventional Process in this asphalt. The same high molecular weight SBS polymer at 2.50% by weight dosage level as previously discussed will be used again. In this study, slightly more of the Butaphalt(tm) compound (commercially known as BLC-720 OR B-720) was used over the previous study given above. We will also look at a different set of physical test results. Selecting different physical tests to examine in this study was purposely done to give the reader a better overall understanding of what Phenol-Aldehyde cross linking resins as used by the Butaphalt(tm) Process offer the asphalt polymer formulation. One such physical test that indicates chemical change in polymer modified asphalt is the Force Ductility test. Figure 3 (on the last page) are the Force Ductility curves generated at 4 Celsius, 5 cm/min pull rate from or by the Butaphalt(tm) Process and the Conventional Process. The solid line represents the Butaphalt(tm) Process with its higher initial peak and higher values throughout its elongation. It is the authors opinion that this over all increased value indicates some form of chemical modification to the asphalt polymer composition. It is further the authors opinion that the binder made by the

Butaphalt(tm) Process with these improved Force Ductility values will yield a final product with better overall service life.

Table 2 below gives test results on Ball and Ring Softening Point. Results are given as before and after the Thin Film Oven Test (TFOT).

Table 2

Test (Celsius)	Cnvntal	Butaphalt
Soft Pt B/4 TFOT	51.11	80.56
Soft Pt Aft TFOT	55.00	65.00
B/4-Aft Soft Pt	+3.89	-15.56

In this case, the Butaphalt(tm) Process had higher overall values both before and after the Thin Film Oven Test. The Conventional Process indicated an increasing softening point value through the TFOT with the Butaphalt(tm) Process indicating the opposite trend.

Table 3 below gives test results on ASTM Kinematic Viscosity. Results are given as before and after the Thin Film Oven Test (TFOT). In this table the Percent Change is calculated as [(B/4 TFOT) - (Aft TFOT) / (B/4 TFOT)] X 100.

Table 3

Kinematic Visc.	Cnvntal	Butaphalt
B/4 TFOT, cStk	495	1500
Aft TFOT, cStk	835	1457
B/4-Aft, cStk	+40	-43
Percent Change	+8.08	-2.87

In this case, the Butaphalt(tm) Process had higher but decreasing values through the TFOT than the Conventional Process. The Butaphalt(tm) Process did have the lowest percent change from the original Kinematic Viscosity.

This same asphalt was also modified with a commercially available SBR latex. The dosage level was 2.50% rubber solids (the same amount as was SBS rubber above) but the amount of Butaphalt(tm) compound BLC-720 was used as with the Lloydminster asphalt of Table 1 above. The process of incorporating the SBR latex into the asphalt is some what proprietary.

The proprietary process of incorporating SBR latex may account for the possibly better than expected Conventional Processing results. This is especially true in Figure 4 (on the last page) illustrating the Force Ductility results. Again, the sample with the Butaphalt(tm) compound BLC-720 (the dashed line) had higher initial peak and overall values. As before, it is the author's opinion that this increased value Butaphalt Process will result in superior binder performance.

As before, we will examine Ring and Ball Softening Point both before and after Thin Film Oven Testing. This work is summarized in Table 4 below.

Table 4

Test (Celsius)	Cnvntal	Butaphalt
Soft Pt B/4 TFOT	51.11	51.11
Soft Pt Aft TFOT	53.33	56.67
B/4-Aft Soft Pt	+2.22	+5.56

Results from this work indicate that this combination of asphalt and SBR latex are equal on initial softening point values. In this case, the Butaphalt(tm) process gave higher values through the TOFT than the Conventional Process. The increase is significant but not to the degree of being detrimental to the product. As a result, the final product in the field may well be very acceptable.

One test parameter that has been historically difficult for SBR latex is Elastic Recovery (ER). In this study, the Elastic

Recovery is improved by the Butaphalt(tm) Process over the Conventional Process. Further, the Elastic Recovery value through the TFOT is still acceptable for the Butaphalt(tm) Process. The ER procedure used a standard ductilometer and to elongate the specimen at 5 cm/min at 10 degrees Celsius to 20cm., relax for 5 minutes, cut about the center and leave undisturbed for sixty (60) minutes. The ends were then brought together and the ductilometer reading recorded. The calculation was as follows: [(initial elongation) - (final reading) / (initial elongation)] X 100 = E R. These results are given in Table 5 below.

Table 5

Elastic Recovery	Cnvntal	Butaphalt
E R B/4 TFOT	53	61
E R Aft TFOT	49	58
B/4-Aft E R	4	3

From this information, one may find that the Butaphalt(tm) Process will allow formulations with improved Elastic Recovery. This improvement could likely mean the difference between acceptable and non acceptable specification product. The change in E R from before TFOT to after TFOT is acceptable for both Conventional and Butaphalt(tm) Processing.

The last area we will discuss deals with the newer test methods as developed by the Strategic Highway Test Program (SHRP). These tests cumulate in a PG grading system. For our purposes, we will look at the PG grading system as a continuous grading system. A continuous grading is determined by the absolute value sum of the high and low PG grading values. In this study, 3.00% by weight of a styrenic block copolymer of a different physical structure and chemical ratio than those previously discussed was processed with a "typical" or "average" asphalt. The PG grading results in a high and a low Celsius temperature service value. These values for the Unmodified or Control asphalt, Conventional and Butaphalt(tm) Processing are given below in Table 6 below.

Table 6

Test Range	Control	Conventional	Butaphalt
High Value	+59	+69	+74
Low Value	-30	-29	-32
Continuous	89	98	106

These results illustrate conclusively that the Butaphalt(tm) process can create superior products in the PG grading system. Improvements are consistent with previous results presented in this discussion. Notice in particular the ability of the Butaphalt(tm) Process to significantly improve both the high and low end of the PG grading. These improvements are a desirable direction over the Control and that provided by the Conventional Process.

In conclusion, the use of Phenol-Aldehyde cross linking resins as reduced to practice in the Butaphalt(tm) Process (Patented) can provide useful tools to improving polymer modified asphalt.

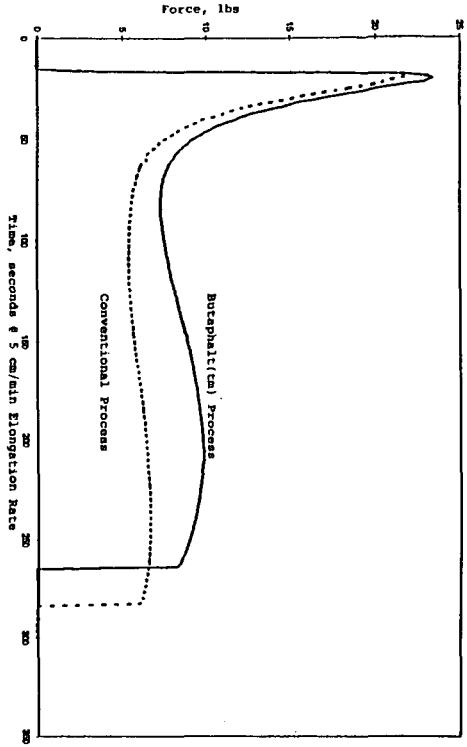

FIGURE 3

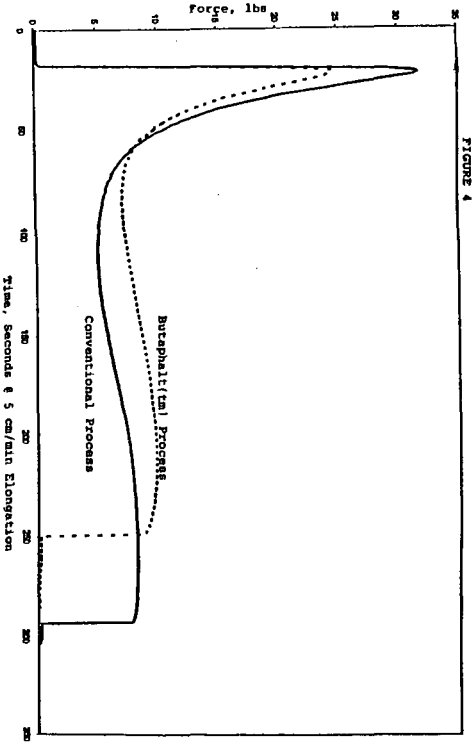

FIGURE 4

COMPATIBILIZER FOR CRUMB RUBBER MODIFIED ASPHALT

M.E.Labib[1], G.M.Memon[2], and B.H.Chollar[2]

[1]Civil and Environmental Engineering Department, New Jersey Institute of Technology, Newark, N.J. 07102

[2]Federal Highway Administration, 6300 Georgetown Pike McLean, Va. 22101

KEY WORDS: Asphalt, Crumb Rubber, Compatibilizer, Epoxy Ring, Crumb Rubber Compatible Asphalt.

INTRODUCTION: The United States of America discards more than 300 million tires each year, and out of that,a large fraction of the tires is dumped into stock piles. This large quantity of tires creates an environmental problem. The use of scrap tires is limited. There is a usage potential in such fields as fuel for combustion and Crumb Rubber-Modified Asphalt binder (CRMA)[1].

The use of crumb rubber in modifying asphalt is not a new technique; it is been used since early 1960 by pavement engineers[2].

Crumb rubber is a composite of different blends of natural and synthetic rubber (natural rubber, processing oils, polybutadiene, polystyrene butadiene, and filler)[3].

Prior research had concluded that the performance of crumb rubber modified asphalt is asphalt dependent. In some cases it improves the rheological properties and in some cases it degrades the properties of modified asphalt[4].

Typical problems encountered in crumb rubber modified asphalt pavement include: raveling of pavement, poor mixing, and inconsistent application in the field.

The major objectives of this research were to achieve proper dispersion of crumb rubber particulates into asphalt and to make crumb rubber compatible modified asphalt with improvement both in high and low temperature properties, which can lead to reduced cracking, rutting, and raveling tendencies of the CRMA pavement. The approach of this study was to join the crumb rubber and asphalt molecules with small bifunctional molecules called compatibilizers.

MATERIALS AND METHODS:

Materials used: Three SHRP core asphalts, a California Coast (AAD-1), a lime treated California Valley (AAG-1), and a solvent treated West Texas intermediate (AAM-1) asphalt, were used in this study. They are representative of many of the asphalts used in the United States. These asphalts cover extended ranges of compositional characteristics such as oxygen concentration, nitrogen concentration, carboxylic acid concentration, amine concentration, asphaltene level, polar aromatic concentration, and others. All of the reagents used were analytical grade from Baxter Scientific Products, McGraw Park, IL, unless otherwise specified. The compatibilizers (polyfunctional epoxides with ethylenic and acrylic backbones) used in this study were made by the DuPont Corporation & Elf Atochem respectively. Crumb rubber (-80 mesh) was supplied by Rouse Rubber Industries Inc.

EXPERIMENTAL METHOD: The crumb rubber compatible asphalt was prepared from 400 g asphalt heated at 163^{0}C in a 600 ml beaker, followed by the addition of the compatibilizer having the epoxy ring with a glycidyl back bone (0.006-0.023 milimoles compatibilizer per g asphalt) to the asphalt with continuous stirring for 15-20 minutes. The crumb rubber (6-15%) was then dispersed into the hot asphalt compatibilizer mixture with continuous stirring and heating for 3 hours.

TEST METHODS: 1. The American Association of State Highway and Transportation Officials (AASHTO) Standard Method, No. PP5-93, was used for the separation test.

2. The AASHTO Standard Test Method, No. TP1-93, was used for determining the flexural creep stiffness of the asphalt binder

[2]To whom correspondence is to be made.

using the Bending Beam Rheometer (BBR).
3. The AASHTO Standard Test Method, No. TP5-93, was used for determining the rheological properties of asphalt binder using a Dynamic Shear Rheometer (DSR).

Rheological Characterization:

High temperature behavior by DSR: A Dynamic Shear Rheometer (Rheometrics DSR II) was used to determine the high temperature rheological properties of the virgin, control, and compatible modified binders by using parallel plate geometry. A time sequence (3 minutes) at three temperatures from 52-76°C, with a torque of 20.66 g.cm at a frequency of 10 rad/s was used. The rheological behavior of the binders was calculated by $G^*/Sin\ \delta$.

Low Temperature Behavior by BBR: A Cannon Bending Beam Rheometer (BBR) was used to determine the low temperature rheological properties of the virgin, control, and compatible modified binders. Samples were run in triplicate at -24, -18, and -12°C to measure the creep stiffness (S value) and the change of stiffness with time (m value).

RESULTS & DISCUSSION: The possible reaction between the asphalt functional groups (carboxylic or amino) and the epoxy groups of the compatibilizer is as follows:

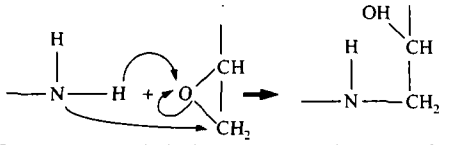

Proposed reaction mechanism between the amine and epoxy groups[5]

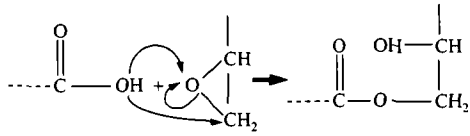

Proposed reaction mechanism between the carboxylic and epoxy groups[5]

This type of mechanism is already reported in literature[5]. In this mechanism, the hydrogen atom of the secondary amine or carboxylic group can open the epoxy ring very easily and bring about the bonding. Physically, formation of clumps was not observed occurring in the compatible modified binder reaction, as it was in the control, an indication of proper dispersion of the crumb rubber into asphalt.

RHEOLOGICAL PROPERTIES:

Rheological properties of the asphalts used (AAD-1, AAG-1, & AAM-1), the control (asphalt mixed with crumb rubber (CRM) under the same reaction conditions), and the crumb rubber compatible modified asphalt are illustrated in figures I through VI. Figures I and II show continuous SHRP performance grading (PG grading) of AAD-1; the virgin asphalt passes the criteria for stiffness at 63°C, the control and modified binder pass at 80°C. Figure I also shows the low temperature rheological data for the virgin, control, and modified binders; the virgin passes the SHRP performance specification at -31°C, the control passes at -28°C, and the modified binder passes at -35°C. Asphalt AAD-1 shows high temperature improvement as compared to the virgin on addition with the CRM (control). The same observation was observed with the modification. However, the low temperature shows a different behavior; the control was degraded as compared to the virgin, but the modified binder shows significant improvement, i.e. by 7°C (more than one PG grading interval). Thus, the addition of crumb rubber to asphalt does not always improve the low temperature properties; asphalt AAD-1 is a case in point. The addition of crumb rubber to asphalt is asphalt dependent. Figure II shows the useful temperature range (the sum of the high and low temperature PG grades) for the virgin, control, and the modified binder of AAD-1. The virgin asphalt shows 94°C as the useful temperature range; whereas, the control and modified binder shows 108°C and

115°C. The product from the addition of crumb rubber and a compatibilizer to asphalt is improved by 2.3 and 3.5 PG-grading intervals (6°C), which, in this economically driven era, is very significant from the refinery point of view. The use of crumb rubber in asphalt is also advantageous in that CRM contains UV resistant additives.

Figure III indicates the rheological properties (continuous PG grading) of asphalt AAG-1, its control, and its modified compatible binder. The addition of crumb rubber to this Californian asphalt shows simultaneous improvement of low and high temperature properties, i.e. from PG 62-19 to PG 66-24. The modified compatible binder shows further improvement for both high and low temperature rheological properties, i.e. PG 72-29. The asphalt, AAG-1, shows low temperature rheological properties that are different from those of asphalt AAD-1. Figure IV shows the useful temperature range for asphalt AAG-1, its control, and its compatible modified binder. The virgin asphalt in this case has a useful temperature range of 81°C, whereas, its control and the modified compatible binder have useful temperature ranges of 90 and 101°C respectively. In this case the addition of crumb rubber and its compatible product shows an increase of 1.5 and 3.3 PG-grading intervals. This is very significant as compared to the virgin material.

Figure V shows the rheological properties of the virgin, control, and modified compatible binder asphalt AAM-1 (Californian valley solvent treated asphalt). The continuous PG-grading for the virgin binder shows PG 66-23°C; whereas, its corresponding control and compatible modified binder shows PG 68-30 and PG 73-32 respectively. The improvement in the PG grading of this asphalt is not as significant as it was for the other two asphalts, but it is still significant. Figure VI shows the useful temperature ranges for the virgin, its control, and its compatible modified binder, as 89, 101, and 105°C respectively. Therefore the addition of crumb rubber shows improvement by 2 and 2.7 PG-grading intervals as compared with the control and the compatible modified binder respectively.

From the above discussion it is clear that the compatible modified binder rheologically performs better than its control or its virgin binder. The process to prepare crumb rubber modified compatible asphalt may be accomplished with some degree of success. In this study the compatible modified binder was not only properly dispersed but reproducible results were also obtained.

CONCLUSION: The use of a compatibilizer can 1) enhance the solubility of crumb rubber into asphalt and 2) improve the rheological properties of crumb rubber modified asphalt. Modified compatible asphalt is advantageous over the virgin and its control by having a wider useful temperature range. The use of modified compatible asphalt has the potential to prevent asphaltic pavement from raveling and may increase the use of scrap tires. The amount of compatibilizer used in asphalt is dependent on the source of asphalt.

REFERENCES:

1. Scrap Tire Management Council, Scrap Tire Use/Disposal Study, Sept. 1990.
2. Charles McDonald, "Sahuaro Concept of Asphalt-Rubber Binders", Proceeding - First Asphalt-Rubber User-Producer Workshop, May 1980.
3. Michael Wm. Rouse, "Production Identification and Application of Crumb Rubber Modifier (CRM) for Asphalt Pavements", presented at the 52nd Annual meeting of the Southeastern Association of State Highway and Transportation Officials, August, 1993.
4. G.M.Memon and B.H.Chollar, "Thermal Characteristics of Crumb Rubber Modified Asphalt", 24th NATAS Conference, San Francisco, CA, Sept. 10-13, 1995, pp 27-32.
5. J.W.Nicholson,"The Chemistry of Polymers", Royal Society of Chemistry, p 73, 1991.

Figure I

Continuous Rheological Grading of Asphalt AAD -1 (Glycidyl)

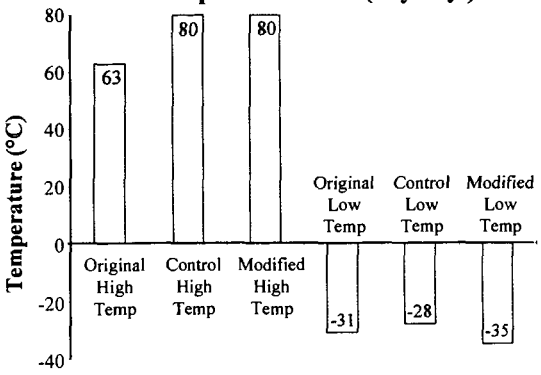

Figure II

Useful Temperature Range for Asphalt AAD-1, Control, and Compatible Modified Binder

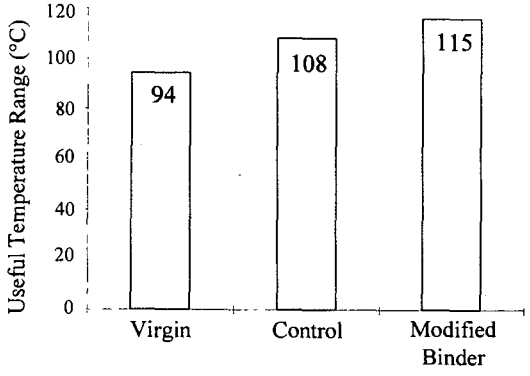

Figure III

Continuous Rheological Grading of Asphalt AAG -1 (Glycidyl)

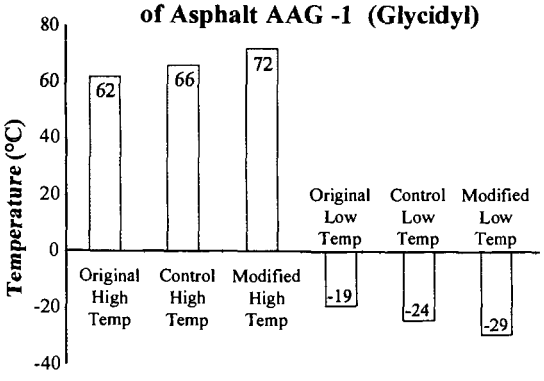

Figure IV

Useful Temperature Range for Asphalt AAG-1, Control, and Compatible Modified Binder

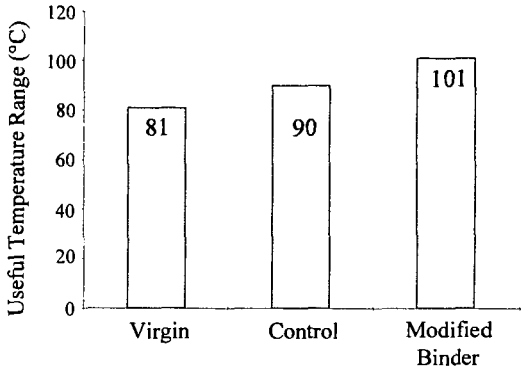

Figure V

Continuous Rheological Grading of Asphalt AAM -1 (Glycidyl)

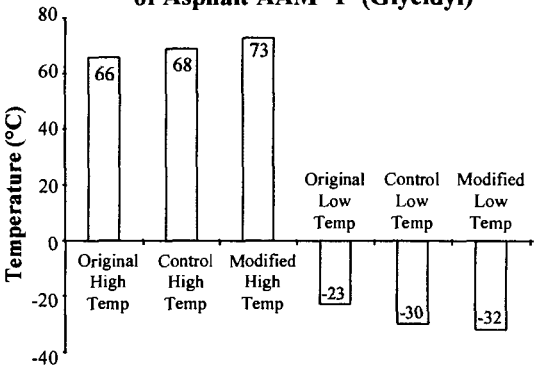

Figure VI

Useful Temperature Range for Asphalt AAM-1, Control, and Compatible Modified Binder

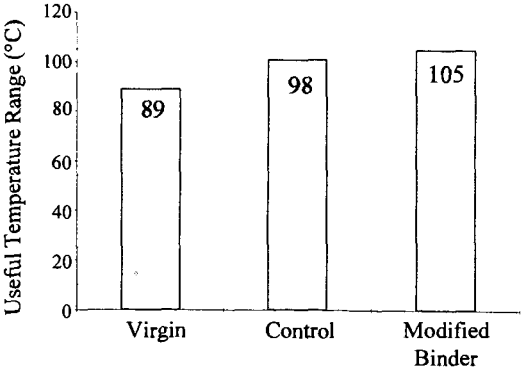

EFFECTS OF CARBOXYLIC ACIDS ON THE RHEOLOGICAL PROPERTIES OF CRUMB RUBBER MODIFIED ASPHALT

Jane E. Tauer and Raymond E. Robertson
Western Research Institute
365 North 9th Street
Laramie, Wyoming 82070

Keywords: Crumb Rubber, Crumb Rubber Modified Asphalt, Asphalt

ABSTRACT

The Federal mandate of 1991-1995 on the use of scrap tires in Federal roadway construction sparked a major interest in gaining a fundamental understanding of the behavior of rubber in asphalt. This study is a systematic elucidation of what chemistry controls the final crumb rubber modified asphalt (CRMA) product quality. We discovered that the type and total acid content in the asphalt are the most influential chemical factors that determine the changes in the important roadway properties of shear modulus (G*) and loss angle (δ) of CRMA. Low acid (<0.005 m/L) asphalts were modified with three types of carboxylic acid and each made into CRMA using typical field mixing conditions of 1 hour at 175°C. Rheological measurements were then made at various storage times up to 192 hours following storage at both 156 and 200°C. We found the changes in CRMA rheological properties correspond to the acid type spiked into the asphalt.

INTRODUCTION

In December 1991 the Intermodal Surface Transportation Efficiency Act (ISTEA) mandated the use of large amounts of rubber from scrap tires in Federally funded roadway construction. In 1995 this mandate was removed but in the time between 1991 and 1995 the mandate sparked much interest in gaining a better understanding of the use of rubber tire material in roadways. Some successful use of tire rubber had been demonstrated for up to twenty years before the mandate in the states of Arizona, California, and Florida. These three states had experimented with the use of finely ground rubber (crumb rubber) mixed with asphalt to make asphalt concrete. Upon examination of their successful uses of this crumb rubber modifier (CRM) to make crumb rubber modified asphalt (CRMA), it became obvious that each state gained a good understanding of the material properties of the CRMA and further employed good engineering design and construction practices in using CRMA to build roads. To a lesser degree, it became obvious that CRMA used in Florida was substantially different from that used in California. This suggested that there were unrecognized differences in materials used by by the two states. An attempt was made to trace the sources of CRM and asphalt crude oil sources used by each state. What became apparent quickly was that both Florida and California used consistent supplies of asphalt in their respective states, but that the asphalt crude sources used in the two states were very different from each other. The California DOT reported the asphalt binder behaved somewhat like a mineral filled asphalt. On the other hand, the Florida DOT reported building with a homogeneous material which suggested that the CRM had dissolved, or digested into the asphalt. The experiences with CRMA related above strongly suggested to us that some unique set of CRMA properties can be expected and can be related back to the crude oil source used to produce each asphalt.

To control the rheological properties of crumb rubber-asphalt mixtures, an understanding of the chemistry involved in the CR-asphalt interaction is necessary. We began our study with a systematic analysis of the variables involved in this interaction, i.e., asphalt type, CR type, mixing time and temperature, and particle size and concentration

BACKGROUND

In previous experiments we found CRMs do not swell significantly in whole asphalt at temperatures of 200°C and times up to 1000 hours, but we found a portion of the crumb rubber (CR) appears to dissolve which leads to changes in the rheology of the CRMA. The rheological changes are different among various asphalts and greater than the effect imparted by Teflon of the same particle size. These changes in rheological properties led to an investigation into what component(s) of the asphalt is (are) interacting with the CR. In order to determine the component(s) involved, asphalts from different crude sources were used in mix experiments. The CRMAs were prepared using standard blending procedures (blended for one hour at 175°C) then tested and stored at 200°C. The CRMAs were checked visually and microscopically each day for changes in the CR. Several of the asphalts had no apparent effect on the CR, however one asphalt had a dramatic effect on CR appearance. After five days at 200°C this mixture had the appearance of a neat asphalt (i.e., very smooth and shiny). We repeated the experiment with this particular asphalt, Strategic Highway Research Program (SHRP) asphalt ABD-1, with the same results. This asphalt has a lime treated counterpart (SHRP AAG-1) which had been tested earlier with no apparent interaction with the CR. Lime is added to this asphalt

to neutralize it's high carboxylic acid content. It then seemed logical that carboxylic acid had something to do with the dissolution of the CR. The experiment was repeated with another high acid asphalt, SHRP AAK-2, with the same results (i.e., the CR dissolved). We then removed the acid fraction from the ABD-1, using ion exchange chromatography, and added it to a low acid asphalt, SHRP AAM-1. Asphalt AAM-1 had also been used in the earlier experiment with no dissolution. Crumb rubber was mixed with both samples and stored for several days at 200°C. After several days the acid free ABD-1-CR mixture showed no signs of interaction, crumb particles were still visible in the mixture. However the acid modified AAM-1-CR mixture had the appearance of a neat asphalt. We now had enough evidence of the involvement of carboxylic acid as the active component or a marker of the active component to begin a series of controlled acid doping experiments.

EXPERIMENTAL

The experimental procedure involves the doping of two low acid asphalts, AAB-1 and AAM-1 with various carboxylic acids (9-anthracene carboxylic acid, stearic acid and cholic acid) at 0.01, 0.02 and 0.03 weight percent. The acid was mixed with asphalt by mechanical stirring at 175°C. The acid-doped asphalts were then mixed using a low shear mixer for one hour at 175°C with U.S. Standard #40 mesh (420μm) CRM and U.S. Standard #40 mesh natural tire rubber (NR). Rheological measurements were taken immediately after mixing. Suitable control samples were prepared and rheological measurements were taken for comparison to the CRMA. The remainder of the CRMAs and control samples were then split. Half of the samples were stored at 156°C for up to 192 hours and the other half at 200°C for up to 192 hours. This experiment is still in progress, but the work to date is presented here. All samples were analyzed using an Rheometrics RDA II rheometer, operated in strain control mode.

RESULTS

Figures 1 through 10 show the results of the acid doping experiments for asphalt AAB-1. The time sequence for all of the data points in the figures, except for figures 3 and 4, are not shown; the data are plotted versus the loss angle or G'. Figures 1 and 5 show the shear modulus and the loss angle data taken at 60° and 25°C for samples stored at 156°C. Figures 2 and 6 show the storage and loss moduli data taken at 60° and 25°C for samples stored at 156°C. Figures 3 and 4 show the storage and loss moduli for CR4-9-anthracene carboxylic acid doped AAB-1 and CR4-AAB-1, and CR4-stearic acid doped AAB-1 and CR4-AAB-1 stored at 156°C and measured at 60°C, respectively. In these figures the storage times of the data points are noted. Figures 7 and 9 show the shear modulus and the loss angle data taken at 60° and 25°C for samples stored at 200°C. Figures 8 and 10 show the storage and loss moduli data taken at 60° and 25°C for samples stored at 200°C.

DISCUSSION

Asphalts are viscoelastic fluids and are evaluated using dynamic mechanical analyzers (DMA). When analyzing asphalts the DMA is run in an oscillatory mode which supplies a periodic deformation at a given frequency, ω. The DMA can calculate several material constants including the magnitude of complex shear modulus, loss angle, storage modulus, and loss modulus. The complex shear modulus, G*(ω), is a complex function of frequency, as shown in equation (1),

$$G^*(\omega)=\frac{\sigma_0}{\epsilon_0}e^{i\delta}= G'+iG'' \tag{1}$$

where δ is the loss angle at a given frequency, σ_0 is the stress amplitude at a given frequency, and ϵ_0 is the strain amplitude at a given frequency. The loss or phase angle, δ, is a function of the internal friction of the material. For a viscous material the loss angle would be 90° and for an elastic material the loss angle would be 0°. The magnitude of G*(ω) is found using equation (2).

$$|G^*(\omega)| = G^* = \sqrt{G'^2 + G''^2} \tag{2}$$

The storage modulus, G', is the real part of the complex shear modulus and is associated with the storage and loss of energy during the periodic deformation (recoverable deformation). The loss modulus, G", represents the imaginary part of the complex shear modulus and is associated with the dissipation of energy and its transformation into heat (permanent deformation). G'and G" can be found using equations (3) and (4).

$$G' = G^* \cos\delta \tag{3}$$

$$G'' = G^* \sin\delta \tag{4}$$

It is obvious from the figures that not only are the acids involved in the interaction of asphalt with CRM, but the type of acid is very important in the interaction. Figure 1 shows G* and δ for AAB-1, acid doped AAB-1, CR4-AAB-1 and CR4-acid doped AAB-1 The samples were stored at 156°C and measurements were taken at 60°C. The data here represent all storage times up to and including the 192 hour. Neat asphalt AAB-1 and acid doped AAB-1 are grouped together in the lower right corner

of the figure. This indicates that the acid doping of AAB-1 has not changed G* and δ (at 60°C) by any significant amount. The next group of data points are found higher up on the right side of the figure. Each of the data points in this set represents a CR4 mixture, measured immediately after the one hour mix time. A significant increase in G* due to the addition of the CR4 is observed. The loss angle has gone from ~89° to ~86° for CR4-AAB-1 (CR4) and to ~85° for the CR4-9-anthracene carboxylic acid doped AAB-1 (A) , but G* has increased from 128 Pa to 702 Pa and 1150 Pa, respectively. From Equation (2) it can seen that this increase in G* must be accompanied by an increase in G′ and/or G″. Figure 2 shows G′ and G″ for these samples. Again the AAB-1 and acid doped AAB-1 are grouped together in the lower left corner. The one hour CR4 mixtures data start in the lower right of the figure and are above the majority of points running from left to right. The CR4-9-anthracene carboxylic acid doped AAB-1 (A) has the largest increase in both G′ and G″, compared to the other CR4 mixtures. The CR4-stearic acid AAB-1 (S) shows the least change in rheological properties, while the CR4-cholic acid AAB-1 (C) is very close to the CR4-AAB-1 (CR4). The data points for the longer storage times run from ~82° loss angle to ~74° loss angle in figure 1 and from G″ of 300 Pa to ~1700 Pa in figure 2. This main stream of data points include the 24 hour to 192 hour storage times. It is important to note that the rheology undergoes the greatest change between the one and 24 hour time period for all CR mixtures. Figure 1 shows that the 24 hour through the 192 hour samples group according to acid type. The CR4-9-anthracene carboxylic acid data is found in the upper left hand side of the figure, the CR4-AAB-1 and CR4-cholic acid AAB-1 are in the next group and finally the CR4- stearic acid AAB-1. Figures 3 and 4 show selected data from figure 2 and the storage times are noted on the data points. In figure 3 we see the data for CR4-9-anthracene carboxylic acid doped AAB-1 and CR4-AAB-1. The CR4-9-anthracene carboxylic acid doped AAB-1 has substantially higher G's and G"s. The addition of 9-anthracene carboxylic acid to AAB-1 has improved the rheological properties in terms of high (60°C) temperature flow. It is believed that somehow the 9-anthracene carboxylic acid is preventing or favorably controlling the dissolution of the CR. The mechanism involved in this process is not yet understood. Stearic acid, however (figure 4) has the opposite effect. It appears to increase the dissolution of the CR, leading to a degradation of high temperature properties when compared to CR4-AAB-1. Stearic acid is used in rubber production as a processing aid and an accelerant and may accelerate the dissolution of rubber in asphalt. Also, it is important to note that the improvement in properties is time dependent. Each reaches a maximum value of G′ and G″ at a different storage time. The CR4-AAB-1 reaches the maximum G′ and G″ at 24 hours and then begins to decline. CR4-9-anthracene carboxylic acid doped AAB-1 reaches its maximum at 96 hours, while the CR4-stearic acid doped AAB-1 reaches its maximum values at 24 hours.

The data pattern in figures 5 and 6 are similar to that in figures 1 and 2, though the AAB-1 and acid doped AAB-1 data points show a slight change rheological properties (figure 6). The effect of the acid type is quite apparent from the data in all of the figures. In figure 1, CR4-stearic acid doped AAB-1 samples show less of a change in G* and δ than the CR4-AAB-1 samples for all storage times. Figures 7 through 10 show comparable data for samples stored at 200°C with the addition of natural rubber AAB-1 mixtures (NR). In these figures the contrast between the one hour sample (G*'s ~480 Pa to 1150 Pa) and the 24 through 192 hour samples (G*'s under 400 Pa) is quite dramatic. Also the loss angles in figure 5 are higher than those in figure 1. After 24 hours at 200°C, the increase in G′ and G″ due to the addition of CR4 has been negated by the increased dissolution of the CR4. The G″ has decreased from 1150 Pa for CR4-9-athracene carboxylic acid doped AAB-1 to 189 Pa, and G′ from 105 Pa to 19 Pa. Figures 7 and 8 show the data for the samples stored at 200°C and measures at 25°C. The data show that NR-AAB-1 has properties similar to the acid doped AAB-1, and the effect of the rubber is minor after 24 hours. In previous studies it was found that the natural rubber dissolved in all asphalts tested within a few hours of mixing. The data points at a loss angle of 70+° are those for the long storage time.

CONCLUSIONS

The addition of carboxylic acids to asphalt AAB-1 produces varying amounts of rheological change in the crumb rubber mix. The interaction is acid type and temperature dependant. The rheological changes occur at a fairly low temperatures in asphalts (typically mixed at 165° to 175°C) in a relatively short time. This is similar to the mixing conditions commonly employed at a CRMA road construction site. At higher temperatures, the interaction proceeds more rapidly. The effect of carboxylic acid type is fairly pronounced. The improvement in high temperature properties for the CR4-9-anthracene carboxylic acid doped AAB-1 is striking, while the CR4 stearic acid doped AAB-1 exhibits a decrease in rheologic properties. The cholic acid added to AAB-1 appears to have almost no effect on the rheology of the CRMA. Each asphalt contains varying types and amounts of naturally occurring carboxylic acids; therefore each crumb rubber mixture will have different properties based on the asphalt composition. The most important aspect for CRMA in roadways may be the fact that the CRMA undergoes a dramatic change in rheologic properties within 24 hours of mixing the CRM and asphalt. It is during this time period that the CRMA is combined with aggregate and the pavement is laid. If the CRMA is graded immediately after mixing, then by the time it is

mixed with aggregate the properties will have changed. It is not until 48, or in some cases 72 hours, after mix that the rheological properties appear to stabilize (figures 1 through 4).

The addition of crumb rubber to asphalt poses many challenges to the paving industry. Only by understanding the chemistry of these systems will we be able to predict the rheological properties of the CRMA.

ACKNOWLEDGMENTS

The authors gratefully acknowledge the Federal Highway Administration for financial support of this work under Contract No. DTFH61-92C-00170. The authors express thanks to Mr. Jack Van Kirk, California DOT, and Mr. Gale Page, Florida DOT, for many helpful discussions. Thanks are also expressed to WRI personnel. Bruce Thomas acquired most of the rheological data. Jan Hart and Paul Holper prepared all of the samples.

DISCLAIMER

REFERENCES

Findley, William N., James S. Lai and Kasif Onaran, Creep and Relaxation of Nonlinear Viscoelastic Materials, Dover Publications, Mineola, N.Y., 1989.

Tschoegl, Nicholas W., The Phenomenological Theory of Linear Viscoelastic Behavior, An Introduction, Springer-Verlag, New York, 1989.

Hofman, Werner, Rubber Technology Handbook, Hanser Publishers, Oxford University Press, New York, 1988.

Key for figures: Neat→AAB-1, A→9-anthracene carboxylic acid moidified AAB-1, S→stearic acid modified AAB-1, C→cholic acid modified AAB-1, CR4→ AAB-1 and CR4, A-CR4→9-anthracene carboxylic acid modified AAB-1 and CR4, S-CR4→strearic acid modified AAB-1 and CR4, C-CR4→cholic acid modified AAB-1 and CR4 and NR→AAB-1 and natural rubber.

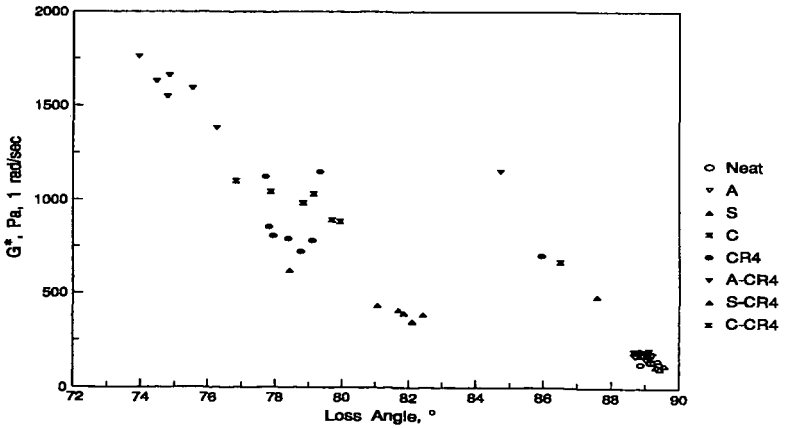

Figure 1. Shear modulus and loss angle of asphalt AAB-1, acid doped AAB-1, and CR mixtures at 60°C and storage temperature of 156°C.

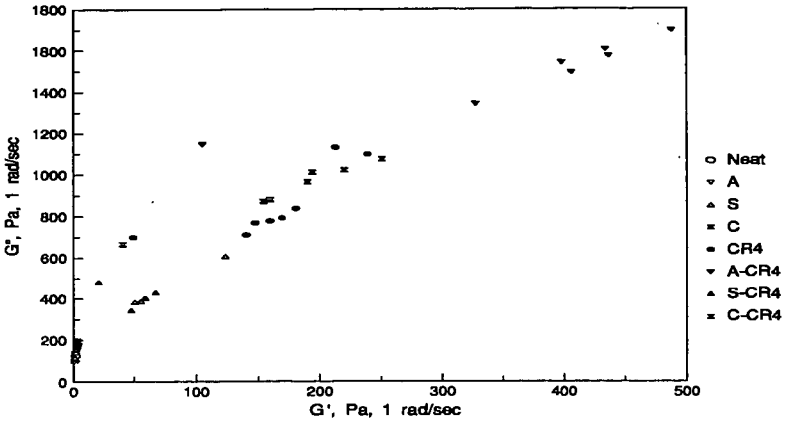

Figure 2. Storage and loss moduli of asphalt AAB-1, acid doped AAB-1 and CR mixtures at 60°C and storage temperature of 156°C.

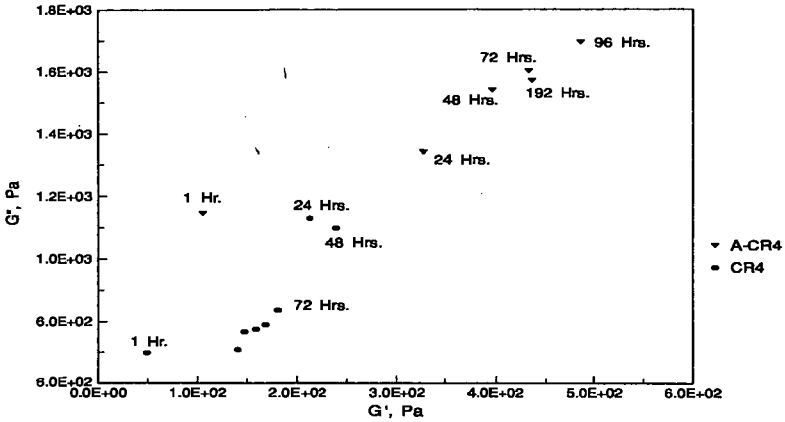

Figure 3. Storage and loss moduli for CR4 9-anthracene carboxylic acid doped AAB-1 and CR4 AAB-1 at 60°C and storage temperature of 156°C.

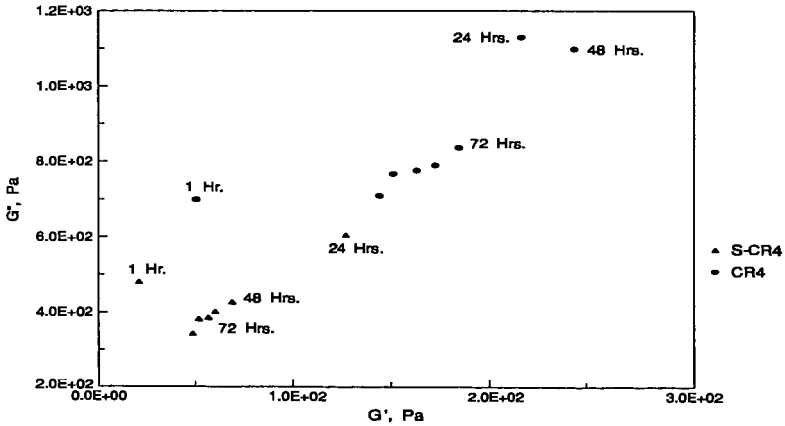

Figure 4. Storage and loss moduli for CR4 stearic acid doped AAB-1 and CR4 AAB-1 at 60°C and storage of 156°C.

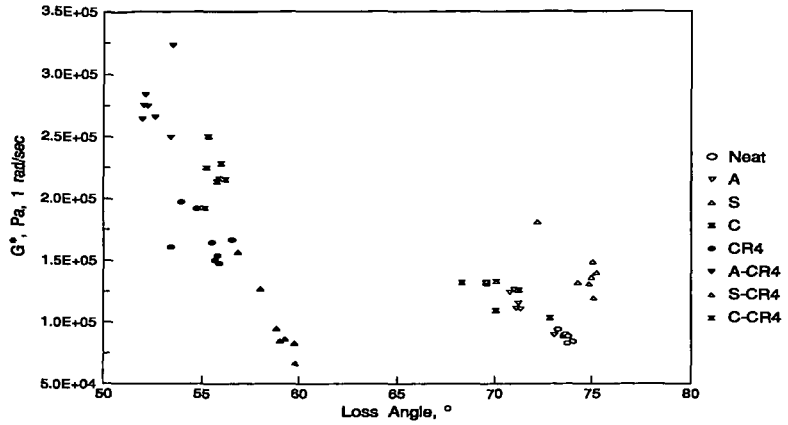

Figure 5. Shear modulus and loss angle of asphalt AAB-1, acid doped AAB-1 and CR mixtures at 25°C and storage temperature of 156°C

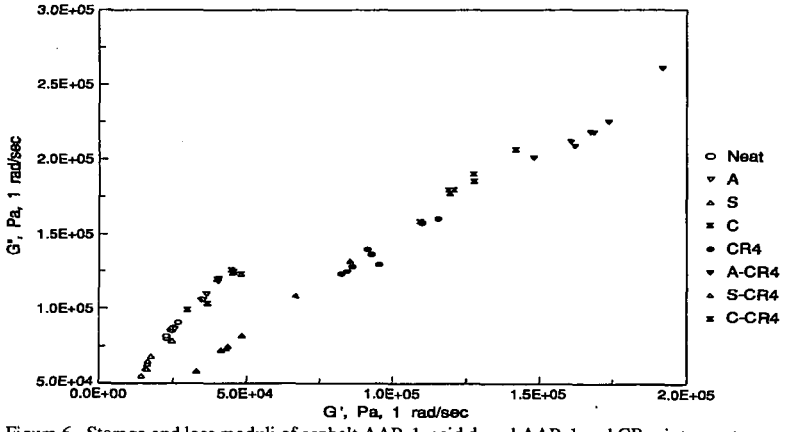

Figure 6. Storage and loss moduli of asphalt AAB-1, acid doped AAB-1 and CR mixtures at 25°C and storage temperature of 156°C.

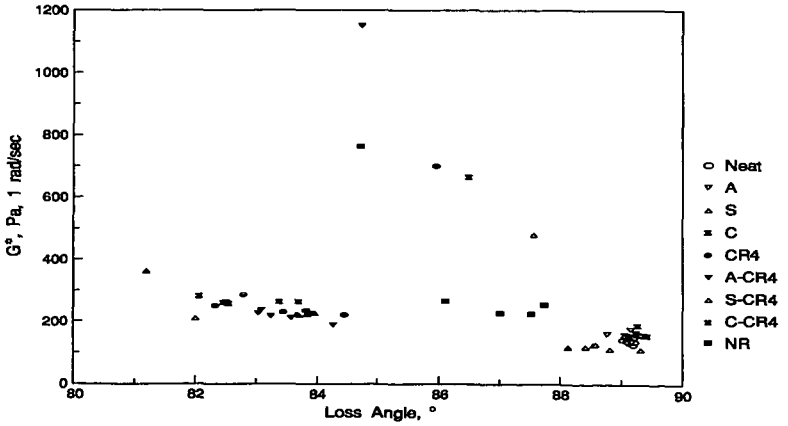

Figure 7. Shear modulus and loss angle of asphalt AAB-1, acid doped AAB-1 and CR mixtures at 60°C and storage temperature of 200°C.

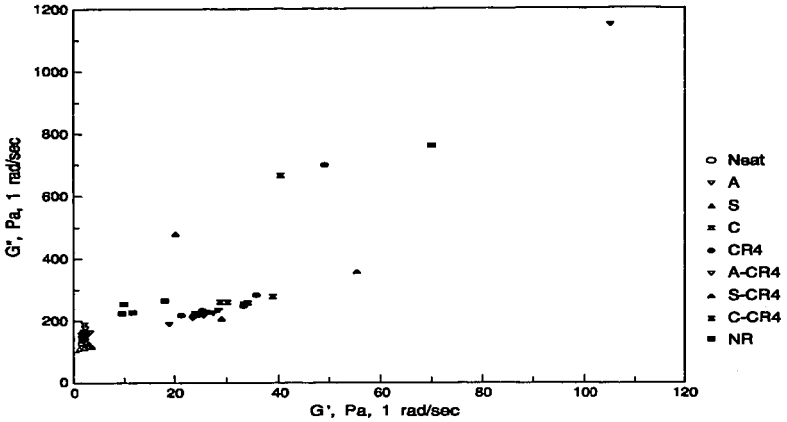

Figure 8. Storage and loss moduli of asphalt AAB-1, acid doped AAB-1 and CR mixtures at 60°C and storage temperature of 200°C.

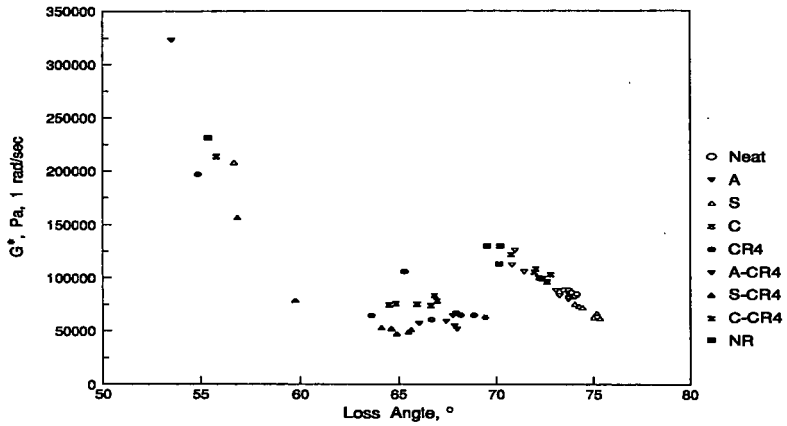

Figure 9. Shear modulus and loss angle of asphalt AAB-1, acid doped AAB-1 and CR mixtures at 25°C and storage temperature of 200°C.

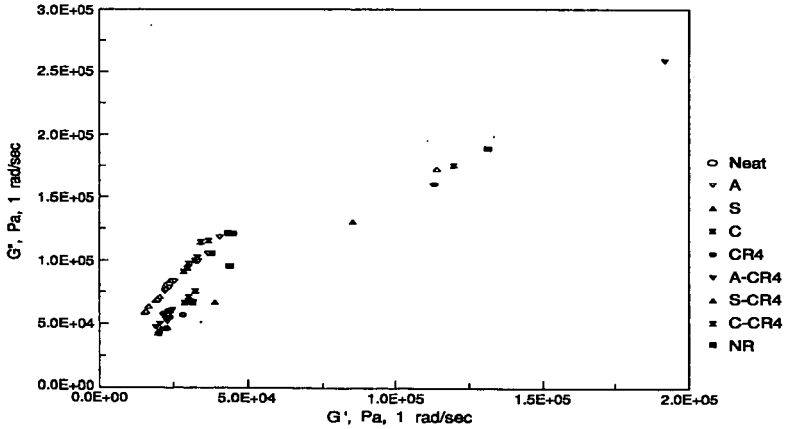

Figure 10. Storage and loss moduli of asphalt AAB-1, acid doped AAB-1 and CR mixtures at 25°C and storage temperature of 200°C.

INVESTIGATION OF THE CURING VARIABLES OF ASPHALT-RUBBER BINDER

T.C. Billiter, J.S. Chun, R.R. Davison, C.J. Glover, and J.A. Bullin
Department of Chemical Engineering
Texas A&M University
College Station, Texas 77843-3122

Keywords: Asphalt-Rubber, Asphalt, Rubber Dissolution

INTRODUCTION

Currently, the paving industry utilizes a curing time of 1 hour at 177°C (350°F) for producing asphalt-rubber binder (1). Billiter et al. (2) showed that at these curing conditions, 1 hour at 177°C (350°F), adding rubber to asphalt was beneficial, with the rubber improving the low-temperature creep stiffness at (-15°C (5°F)), the temperature susceptibility in the 0°C-90°C (32°F-194°F) temperature region, increasing G^* and η^* at 60°C (140°F) and 1.0 rad/sec, and decreasing δ at 60°C (140°F) and 1.0 rad/sec. On the other hand, Billiter et al. (2) showed that the addition of rubber was also detrimental, in that the viscosity increased significantly in the compaction temperature region of 149°C-193°C (300°F-380°F). This increased viscosity can cause compaction problems, with Allison (3) reporting that engineers blamed the compaction problems of asphalt-rubber on undissolved crumb rubber, which they believed had no beneficial effect. Additionally, the engineers reported that improper compaction led to early road failure. High compaction viscosities also led to high air void content for dense-graded mixes (4), which is detrimental since Linden et al. (5) reported a correlation between air voids and performance.

Engineers could solve these problems by producing an asphalt-rubber binder with a non-detrimental compaction viscosity. If Allison (3) is correct, then eliminating undissolved rubber from asphalt-rubber binder would help produce such a binder. Apparently, eliminating undissolved rubber is possible, since Billiter et al. (2), Franta (6), and Zanzotto and Kennepohl (7) have reported that rubber devulcanizes and depolymerizes during the application of high shear and high temperature in the presence of asphalt. Obviously, the production of such an asphalt-rubber binder will require a study of the variables of curing time, curing temperature, and the type and amount of mechanical energy. This work investigates these variables in an attempt to produce such an asphalt-rubber binder.

MATERIALS

Three asphalts were used in this study. Asphalt #1, an AC-10, and Asphalt #2, an AC-5, were acquired from refineries in Texas. Asphalt #3, an AC-10, was produced in the laboratory by blending a commercially available asphalt and a commercially available recycling agent. The asphalt comprised 78% by weight of Asphalt #3 and had a viscosity of 40,710 poise at 60°C (140°F). The recycling agent comprised 22% by weight of Asphalt #3 and had a viscosity of 5.5 poise at 60°C (140°F). Asphalt #3 was produced to study the effect of adding a light aromatic fraction to an asphalt.

Minus 10 and minus 40 mesh rubber were acquired from Granular Products, also known as Tire Gator (TG), located in Mexia, Texas. Additionally, minus 10, 40, and 80 mesh rubber were acquired from Rouse (RS) Rubber located in Vicksburg, Mississippi.

EXPERIMENTAL METHODS

The bending beam rheometer, dynamic shear rheometer, Brookfield rotational viscometer, Fourier transform infrared spectrometer, and size exclusion chromatograph that were in this study are described in Billiter et al. (2).

Mixing Apparatus

To produce the asphalt-rubber binders, asphalts and rubbers were 'cured' or mixed at high temperatures (177, 191, or 204°C (350, 375, or 400°F)). Curing is the application of heat and mixing to an asphalt and crumb rubber mixture in which the rubber may be swelled, disintegrated, dissolved, and/or reduced in molecular size. The curing process, as carried out in this laboratory, involved mixing at high temperatures with a 5.1 cm (2") diameter blade driven at 500 rpm or 1550 rpm by a variable speed motor. The blends were cured in 1 gallon paint cans under a nitrogen blanket to prevent the binder from oxidizing.

Rubber Dissolution Test

The extent to which the rubber had dissolved into the asphalt was determined with the following gravimetric procedure. The analysis was performed using a pre-weighed 0.45 μm syringe filter. A 0.2 gram asphalt-rubber sample was dissolved in 10 ml of THF. The asphalt-rubber/THF solution was sonicated for 30 minutes. The solution was then strained through the syringe filter. The filter was heated in a vacuum oven at 100°C (212°F) for 3 hours, removed from the oven and placed at ambient conditions for 24 hours, and finally weighed. The difference between the final filter weight and the initial filter weight is the weight of the rubber that did not dissolve into the asphalt. This weight, the initial sample size weight, and percent rubber content of the initial sample were used to determine the amount of rubber that dissolved into the asphalt.

EXPERIMENTAL DESIGN

Table 1 shows combinations of temperature, mixer speed, weight percent rubber, rubber mesh size, rubber source, and asphalt used in these sets of experiments. The total curing time was 48 hours for the blends cured at 500 rpm, with samples being taken at 3, 6, 12, 24, 36, and 48 hours. For the 1550 rpm blends, the total curing time was 3 hours, with samples being taken at 1, 2, and 3 hours. Experimental Plan (EP) #1, EP #2, and EP #3 were done to study the variable of curing time. EP #3 was done to study the variable of curing temperature and EP #2 was done to study the variable of mixing power, the authors assuming power is approximately proportional to the square of the blending speed. The asphalt rubber products were evaluated in terms of high-temperature viscosities (>121°C (>250°F)), intermediate-temperature rheological properties (0°C - 90°C, (32°F - 194°F)), low-temperature creep stiffness at -15°C (5°F), rubber dissolution, molecular weight distribution, and Fourier Transform Infrared Spectrometer (FTIR).

RESULTS AND DISCUSSION

As discussed in the introduction, previous results in the literature suggest that the dissolution of rubber during the curing process should lead to better binder properties. Consequently, the primary objective of this research was to study the effect of various curing variables on the dissolution of rubber. Specifically, the curing variables of curing time, curing temperature, and rate of mixing are of greatest interest, with the results of the variables of asphalt type, rubber content, rubber mesh size, and rubber source also being presented.

Each figure focuses on a particular variable. If a graph is referenced, at least one example of the comparison being made will be presented.

Experimental Plan #1

Percent Rubber and Mesh Size

For the asphalts studied, the addition of rubber was positive for the low- and intermediate-temperature properties of a binder; the higher the rubber content, within the range studied, the better the results. For a given mesh size, the 10% rubber level lowered the creep stiffness, and therefore improved the elasticity, more than the 5% rubber level, Figure 1. Obviously, the benefits of the elastic additive were more pronounced at the higher concentration levels, thus producing a more flexible binder. Furthermore, the smaller rubber particles were slightly better at improving low-temperature properties, Figure 1. It is theorized that the smaller rubber particles are better able to interact because of their greater surface area per unit mass. The 60°C complex viscosities were higher for the 10% blends and for the larger rubber particles, Figure 2, thereby producing a binder more resistant to rutting. The increase in complex viscosity is probably more of a particle effect than a surface area effect, thus explaining the larger particles' enhanced performance. In the intermediate temperature region, the temperature susceptibility was lower, and therefore better, for the 10% blends and for the smaller rubber particles, Figure 3. In this work the temperature susceptibility is defined in terms of the Andrade equation (8), $\ln(\eta) = \text{Constant} - E_v/RT$, in which E_v is a viscosity activation energy and is a measure of temperature susceptibility. Adding rubber was detrimental to the high-temperature viscosity of an asphalt. The high-temperature viscosity was higher for the 10% blends and the larger particles, Figure 4.

All binder properties were a function of curing time. Although creep stiffness did not improve substantially with curing time, there was always a slight improvement in creep stiffness with curing time, Figure 1. The 60°C complex viscosity increased with curing time, Figure 2. The high-temperature viscosity decreased with curing time, which is desirable, Figure 4. This phenomenon can be explained qualitatively by imaging the rubber particles as rigid spheres and applying an equation derived by Einstein for the viscosity of a dilute suspension of rigid spheres: $\eta = \eta_s(1+2.5\phi)$, where η is the viscosity of the solution, η_s is the viscosity of the solvent, and ϕ the volume fraction of spheres (9). Obviously, the higher the percent rubber the higher the effective ϕ and thus, the higher the viscosity. Furthermore, the significant decrease in high-temperature viscosity with curing time has to be caused by the rubber particles being reduced in size, thus lowering the effective ϕ, because the viscosity of the asphalt, η_s, is definitely increasing as the particles are devulcanized and depolymerized into the asphalt phase of the solution.

The improvements with curing time in the low- and intermediate-temperature properties, as well as the reduction of high-temperature viscosity, are most certainly explained by the rubber devulcanizing and depolymerizing during the curing process. As noted earlier, the devulcanizing and depolymerizing of rubber during the curing process has been discussed by Billiter et al. (2) and Zanzotto and Kennepohl (7), with support from Franta (6). This phenomenon is represented in Figure 5, a GPC chromatograph of the data of an Asphalt #1 blend as measured by an intrinsic viscosity detector. Figure 5 shows that with curing time there is mass transfer into the asphalt phase. The growth of the peak in the 20 to 25 minute retention time region represents the flux of devulcanized and depolymerized rubber into the asphalt phase of the binder. The molecular weight distribution in this region varies from approximately 190,000 at a retention time of 20.63 minutes to 5,970 at a retention time of 24.37 minutes. Please note that the dissolved rubber molecules represented by the data in Figure 5 are smaller than 0.45 µm (0.45 microns, 4500Å), since each sample was prepared for GPC injection with a filter that had a pore membrane size of 0.45 µm. In fact they are generally smaller than 1000Å, the pore size of the largest GPC column, as the

chromatograms show little indication of exclusion. The particles are most certainly being devulcanized and depolymerized since they are being reduced from a size of 400-2000 microns to smaller than 1000Å during the curing process.

Comparison of Asphalt Type

The interaction of the rubber and the base asphalt was very much dependent upon the asphalt composition. Asphalt #3, produced by combining a highly asphaltenic 40,000 poise asphalt with a lower molecular weight 5.5 poise recycling agent, intially interacted with the rubber much better than the other asphalts. This interaction is most certainly explained by the presence of the lower molecular weight recycling agent, which could have just as easily been called a rubber extending oil since such oils are used in the rubber processing industry. Asphalt #3 was able to dissolve much more rubber with curing time, Figure 6. Apparently, the light aromatics of Asphalt #3 are able to interact with the rubber at a much faster rate than the other asphalts, and thus improve the binder properties faster. Similarly, the increase in the 60°C complex viscosity, Figure 2, and the initial improvement in temperature susceptibility, Figure 3, were much greater for Asphalt #3. Although the temperature susceptibility of Asphalt #3 did not continue to improve with time as fast as the other asphalts, the initial improvement offsets this.

The low-temperature performance of Asphalt #3 without rubber, which had a creep stiffness of 377 MPa, was much worse than either Asphalt #1, 208 MPa, or Asphalt #2, 101 MPa. Apparently, not enough of the light aromatics are present to sufficiently peptize the substantial amount of larger molecular weight material present in Asphalt #3. However, with the addition of rubber, the low-temperature properties of Asphalt #3 improved more than the other asphalts, Figure 1. Once again, the other asphalts improve with curing time at a faster rate than Asphalt #3, but the initial decrease in creep stiffness more than offsets this.

At the other end of the temperature scale, the high-temperature viscosity was also very dependent on both asphalt type and curing time. The high-temperature viscosity of Asphalt #1 blends was the most dependent on curing time, Figure 4.

Comparison of Tire Gator and Rouse

Ground rubbers from two sources were used in this curing study. Rouse rubber was perhaps slightly better at improving the creep stiffness, Figure 1, and 60°C complex viscosity, Figure 2, of Asphalt #1. Sieve analysis showed that for a given mesh size, the size gradation of Rouse rubber was finer than Tire Gator rubber, and thus with more surface area per unit mass, reacted more rapidly, Figure 6. Please note that initially the Rouse -10 mesh particles dissolved faster than even the Tire Gator -40 mesh particles. At high-temperatures the Rouse rubber particles were less detrimental to the viscosity of Asphalt #1, Figure 4. Once again, the Rouse -10 mesh particles are initially better for the binder property than even the Tire Gator -40 particles.

The relative performance of Tire Gator and Rouse rubber was somewhat asphalt dependent. Like Asphalt #1, Asphalt #2 was better able to dissolve the Rouse Rubber, Figure 6. As expected, the creep stiffness, Figure 1, and the temperature susceptibility were better for the Rouse blends. On the other hand, the Rouse rubber was not better for the high-temperature viscosity and the Tire Gator blends actually have a higher 60°C complex viscosity than the Rouse blends, Figure 2. This oddity can most likely be explained by the mesh size, but one of the crumb rubbers may contain more natural than synthetic rubber and be better able to interact with an asphalt of a certain composition.

Experimental Plan #2

Utilizing a higher shear rate significantly increased the interaction of the rubber and the asphalt. Figure 6 shows that as much crumb rubber dissolves in 2-3 hours utilizing a mixing speed of 1550 rpm as dissolves in 48 hours utilizing a mixing speed of 500 rpm. This strongly indicates that the devulcanization and depolymerization of crumb rubber during the curing process is a mass transfer limited process, with the increased dispersion of the higher mixing speed allowing improved swelling of the rubber and therefore, increased interaction between the asphalt and rubber. As with previous results, the flux of rubber into the asphalt phase improved the low-, intermediate, and high-temperature rheological properties of a binder. Thus, curing at a higher shear rate for a shorter period of time produced similar binder properties as curing the same binder at lower shear for a much longer period of time. In fact, corresponding roughly to the power input it is estimated that increasing the mixing speed three fold, decreases the required curing time nine fold.

Experimental Plan #3

Increasing the curing temperature significantly increased the interaction between the crumb rubber and the asphalt. Figure 6 shows that the higher the curing temperature the higher the amount of rubber dissolving. Some of the increased interaction can be explained by the lower asphalt viscosity at the higher temperatures causing increased mass transfer between the asphalt and rubber. However, the majority of the increased interaction is probably due to the rubber-asphalt reaction, like any chemical reaction, being very dependent upon temperature. The rubber-asphalt reaction is one of devulcanization and depolymerization in which breaking of the cross-linking network and shortening of the main chains takes place (6). As before, all rheological properties improved with increased rubber dissolution.

CONCLUSIONS

These results are a powerful indicator that the 1 hour curing time at 177°C (350°F) and relatively low shear, used in the field, are not optimal. On the other hand, the extended curing times utilized in this study would not be agreeable with field personal. However, the results of this study strongly imply that increasing curing temperature and shear rate can reduce the required curing time to an acceptable level. In fact, by utilizing high temperature and high shear, along with extended curing time, the rubber particles can be devulcanized and depolymerized into the asphalt to produce an asphalt-rubber binder that is both homogeneous and truly elastic. This can be done with no trade off in binder properties, in fact binder performance may be enhanced

ACKNOWLEDGMENTS

Support for this work by the U.S. Department of Energy (DOE), Assistant Secretary for Energy Efficiency and Renewable Energy, Office of Industrial Technologies, under DOE Albuquerque Operations Office Cooperative Agreement DE-FC04-94AL94AL99567, the Texas Department of Transportation (TxDot), in cooperation with the Federal Highway Administration (FHWA), and the U.S. Department of Transportation, is gratefully acknowledged. The technical contributions of Mrs. Ann Ferry are greatly appreciated.

DISCLAIMER

The contents of this report reflect the views of the authors who are responsible for the facts and the accuracy of the data presented herein. The contents do not necessarily reflect the official views or policies of the TxDOT, the DOE, or the FHWA. This report does not constitute a standard, specification, or regulation.

REFERENCES

(1) Takallou, H.B., and Takallou, M.B., Elastromerics, 123(7), 19 (1991).
(2) Billiter, T.C., Davison, R.R., Glover, C.J., and Bullin, J.A., Fuel Sci. And Tech. Int'l. (in press).
(3) Allison, K., Rubber World, March and April, 47 and 91 respectively (1967).
(4) Jimenez, R.A., Trans. Res. Rec., 843, 4 (1982).
(5) Linden, R.N., Mahoney, J.P., and Jackson, N.C., Preprint No. 880178 presented at Trans. Res. Board's 68th Annual Meeting, (1989).
(6) Franta, I., Elastomers and Rubber Compounding Materials, Elsevier, New York, N.Y., 302-315 (1989).
(7) Zanzotto, L., and Kennepohl, G.J., Preprint No. 960241 present at Trans. Res. Board's 75th Annual Meeting, (1996).
(8) Andrade, E.N. da C., Nature, 125(3148), 309 (1930).
(9) Rosen, S.L., Fundamental Principles of Polymeric Materials, John Wiley and Sons, 2nd ed., New York, N.Y., 95 (1993).

Table 1. Experimental Plans (EPs)

EP	Asphalt	Rubber Source	Mesh Size	Weight Percent	Mixer Speed	Temperature (°C)
#1	#1	Rouse	-10	10	500	191
		Tire Gator	-10, -40	5, 10		
	#2	Rouse	-10, -40, -80	5, 10		
		Tire Gator	-10, -40	10		
	#3	Rouse	-40, -80	5, 10		
		Tire Gator	-10	5, 10		
#2	#1	Rouse	-10	10	500, 1550	191
	#2	Tire Gator	-40	10		
#3	#1	Tire Gator	-40	10	500	177, 191, 204

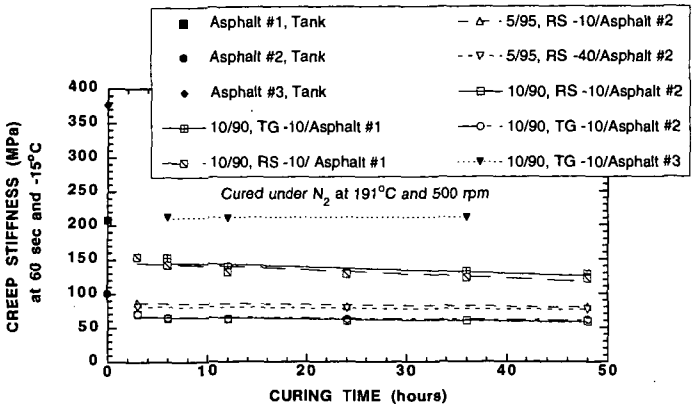

Figure 1. Low-Temperature Data

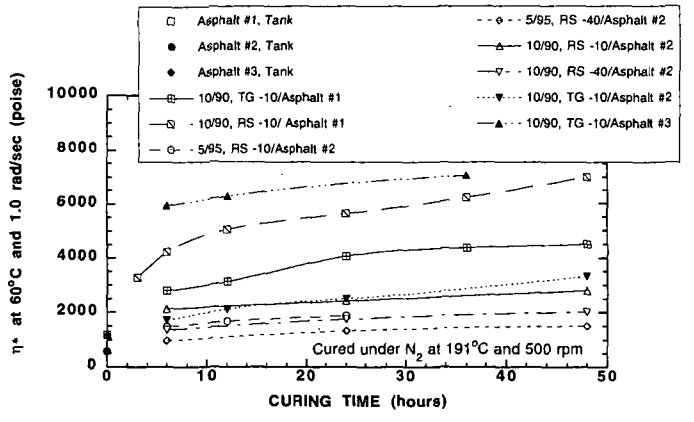

Figure 2. Intermediate-Temperature Data, Complex Viscosity

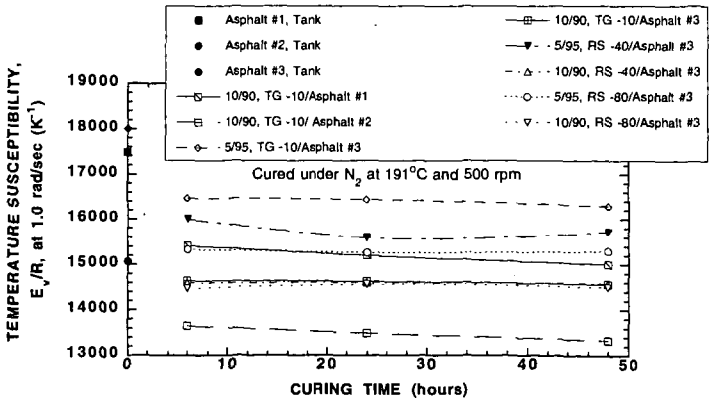

Figure 3. Intermediate-Temperature Data, Temperature Susceptibility

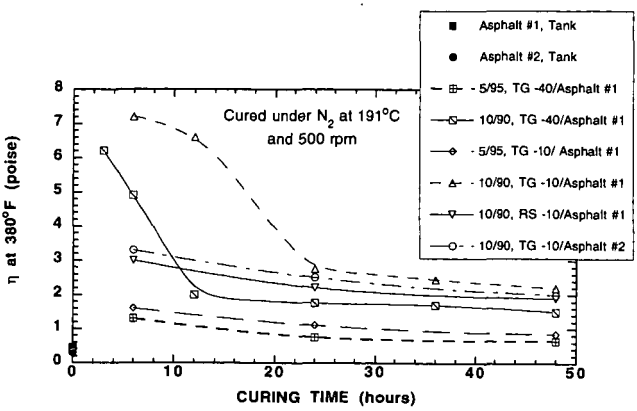

Figure 4. High-Temperature Data

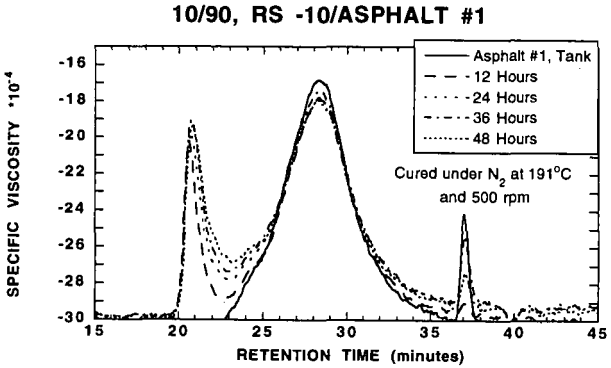

Figure 5. GPC Data for Asphalt #1

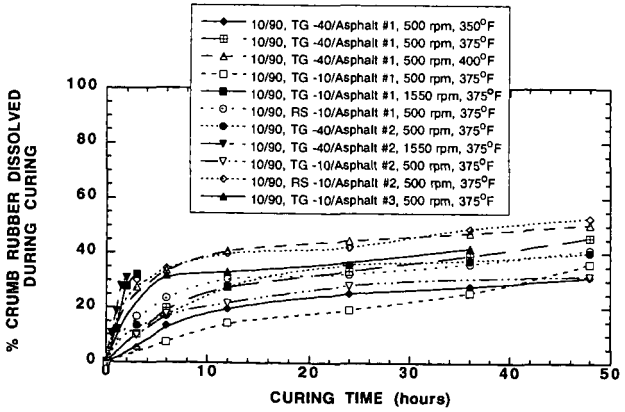

Figure 6. Rubber Dissolution Data

EVALUATION OF THE EFFECTS OF CRUMB RUBBER AND SBR ON RUTTING RESISTANCE OF ASPHALT CONCRETE

Chuang-Tsair Shih, Mang Tia & Byron E. Ruth
Department of Civil Engineering
University of Florida
Gainesville, FL 32611

Keywords: Crumb rubber, SBR, rutting resistance.

ABSTRACT

This paper presents the results of a study to evaluate the effects of addition of crumb rubber (CR) and styrene-butadiene rubber (SBR) on the rutting resistance of asphalt concrete. These two additives were blended with an AC-20 and an AC-30 grade asphalt cements at different levels of concentrations. These modified and unmodified asphalt blends were tested at intermediate and high temperatures to evaluate their rutting resistance characteristics. They were also used to make Florida type S-I structural surface mixtures. These mixtures were made into Marshall-size specimens by using Gyratory Testing Machine (GTM) equipped with air-roller to compact and densify to three compaction levels which simulate three different conditions in the pavement. The FDOT's (Florida Department of Transportation) Loaded Wheel Tester was also used to evaluate the rutting resistance of these asphalt mixtures. The test results indicate that the modified asphalt mixtures show relatively better rutting resistance and shear resistance as compared with the unmodified asphalt mixtures.

INTRODUCTION

With the increasing load and pressure of vehicles tires which are applied to our highway pavements today, one of the major distresses seen on our highway pavements is rutting. One of the promising options to lessen this problem is the use of polymers to modify the asphalt binders. The addition of polymers usually has the effect of increasing the stiffness of the binders at high service temperatures without increasing the stiffness at low service temperatures. This modification of binder properties means that the asphalt mixture could be more rut resistant at high service temperatures while its cracking resistance at low temperatures would not be lessened. Crumb rubber (CR) and styrene-butadiene rubber (SBR) are two of the commonly used asphalt additives for this purpose. The purpose of this study was to conduct a laboratory evaluation of the effects of the addition of crumb rubber and SBR on the rutting resistance of typical asphalt paving mixtures used in Florida.

MATERIALS AND TESTING PROGRAM

Binders Used

Two asphalts, namely an AC-20 and an AC-30 grade asphalts, which are commonly used in Florida, were used as the reference asphalt cements. The additives used were (1) a crumb rubber with a nominal size of #80 mesh (0.177 mm), which has been used in several paving projects in Florida, and (2) a SBR, which was a copolymer of styrene and butadiene. The crumb rubber was blended with the asphalt cements in the laboratory at a temperature of 190 °C. The blending of SBR with the asphalt was done by the company that supplied these modifiers. The asphalts and modified asphalts which were used in this testing program include the following:

(1) AC-20
(2) AC-20 + 15% CR
(3) AC-20 + 3% SBR
(4) AC-30
(5) AC-30 + 10% CR
(6) AC-30 + 3% SBR

Table 1 displays the medium- and high-temperature properties of these six binders. These properties include the (1) penetration at 25°C (ASTM D5) [ASTM, 1995], (2) Brookfield viscosity at 60°C (ASTM D4402) and (3) $G^*/\sin\delta$ values as determined by the dynamic shear rheometer test (AASHTO Designation TP5) [AASHTO, 1993] at 60°C of these six binders at their original state and after the standard Thin Film Oven Test process (ASTM D1754), which simulates the short-term aging effect that occurs in the hot-mixing process.

It can be seen that at 60 °C, which represents a typical high pavement service temperature, both the CR-modified and SBR-modified asphalts are substantially stiffer than their corresponding base asphalts. However, at 25 °C, the CR-modified asphalts are only slightly harder than the base asphalts, while the SBR-modified asphalts are softer than the base asphalts, as seen from the penetration values.

Preparation of Asphalt Mixtures

Each of these six binders was mixed with a limestone aggregate blend at a binder content of 6.5% to produce mixtures which meet the requirements for a Florida DOT S-1 structural mix. Table 2 shows the specific gravities and the gradation of the aggregate blend used, along with the gradation limits for a FDOT S-1 mix.

Compaction and Testing of Asphalt Mixtures in the GTM

The Gyratory Testing Machine (GTM) (ASTM D3387) was used to compact and test these different types of asphalt mixtures. The GTM settings selected were based on the results of a previous study on simulation of traffic compaction [Ruth et al, 1994]. Nine Marshall-size specimens for each of these six different asphalt mixtures were tested. Three of the specimens were compacted to a level that simulates the initial field condition. This was achieved by applying 18 GTM revolutions at 135-149 °C (275-300 °F) using a gyratory angle of 3 degrees, 690 kPa (100 psi) of ram pressure and 62 kPa (9 psi) of air roller pressure. Another three specimens were compacted to a level that simulates the condition after two to three years of traffic. This was achieved by applying an additional 50 GTM revolutions at 60 °C at the same settings after the initial compaction. Three other specimens were compacted to a level that simulates the ultimate condition in the pavement. This was achieved by applying an additional 300 GTM revolutions at 60 °C after the initial compaction.

The gyratory shear, which is an indicator of the shear strength of the materials tested, was also measured during the GTM compaction process.

Preparation of Asphalt Mixture Specimens for Loaded Wheel Tests

The asphalt mixtures were heated to 149 °C (300 °F), mixed and then returned to the oven prior to compaction to 7.6 cm (width) X 3.8 cm (thickness) X 38.1 cm (3" X 1.5" X 15") beam specimens for the FDOT Loaded Wheel Tests. Compaction was achieved by applying a load of 60,000 lbs across the top of the beam and then releasing it, for four cycles. Then, the load of 60,000 lbs was applied for the fifth time, and held for six minutes. The compacted beams were demolded the next day, and allowed to cure at room temperature for seven days. Each beam was preheated in the test chamber at 40.5 °C (105 °F) for 24 hours before testing in the Loaded Wheel Tester.

Loaded Wheel Tests

The Loaded Wheel Tester was intended to simulate the repeated applications of moving wheel loads on the asphalt mixtures tested. A stiff pressurized hose mounted along the top of the beam acted as a tire to transfer the load from the wheel of the moving chassis to the beam. The hose pressure was set at 690 kPa (100 psi) and the moving chassis was loaded with 543 N (122 lb) of steel plates centered above the wheel. The test temperature was set at 40.5 °C (105 °F) and monitored with a thermometer embedded in a dummy specimen placed inside the Loaded Wheel Tester. One loading cycle consisted of a forward and return pass of the loaded chassis. Rut depth measurements were made with a dial gauge at seven different locations on the top of the beam at an interval of 5.1 cm (2 inches), each at 0, 1000, 4000, and 8000 cycles.

The average of three rut measurements at the center was used. This was found to be more consistent in comparison with the average of all seven measurements. The measurements at the ends of the beams tended to be exaggerated due to the combined effects of abrasion by the hose, slower moving loads at the ends and the change in pitch of the chassis.

RESULTS OF GTM TESTS

Tables 3 through 5 display the gyratory shear and the volumetric properties of the mixtures as measured by the GTM at the initial, medium and ultimate compaction, respectively. It can be seen that at the same compactive efforts, the CR-modified mixtures had lower air voids than the unmodified mixtures and the SBR-modified mixtures had the lowest air voids. It is speculated that the lower air voids of the modified mixtures were possibly due to a higher compaction temperature used for these mixtures. However, in spite of their lower air voids, the modified mixtures generally showed a higher gyratory shear strength than the unmodified mixtures, and the difference increased as the compactive effort increased.

RESULTS OF LOADED WHEEL TESTS

The results of the Loaded Wheel tests are displayed in Table 6. It can be seen that the SBR-modified asphalt mixtures show the highest reduction in rut depth as compared with the unmodified reference mixtures (up to 38% at 8000 cycles). The CR-modified mixtures showed a reduction in rut depth of 17 to 21% as compared with the unmodified mixtures. The standard deviations of rut measurements ranged between 0.03 and 0.05 inch. Results of a statistical Duncan's grouping indicate that the SBR-modified asphalt mixtures (AC-20+3%SBR and AC-30+3%SBR) had the least rut depths while the unmodified asphalt mixtures (AC-20 and AC-30) had the highest rut depths among all six types of asphalt mixtures tested.

SUMMARY AND CONCLUSION

The results of this laboratory study show that the addition of crumb rubber and SBR could increase the rutting resistance of asphalt paving mixtures. The CR-modified and SBR-modified asphalts had higher stiffness at 60 °C than the unmodified base asphalts. The modified asphalt mixtures had higher gyratory shear strengths than the unmodified mixtures. The modified mixtures exhibited substantially lower rut depths in the Loaded Wheel tests than the unmodified mixtures. It is also interesting to note, from the results of the GTM tests, that having a low air voids at ultimate compaction condition does not necessarily result in a mixture with lower shear strength.

REFERENCES

American Association of State Highway and Transportation Officials 1993. *AASHTO Provisional Standards*, AASHTO, Washington, D.C.

American Society for Testing and Materials 1995. *Annual Book of ASTM Standard*, ASTM, Philadelphia, Pennsylvania.

Ruth, B.E., Tia, M., Shen, X. and Wang, L.H. 1994. Improvement of Asphalt Mix Design to Prevent Rutting, Technical Report, Department of Civil Engineering, University of Florida, Gainesville, Florida.

Table 1 Medium- and high-temperature properties of the binders used

Asphalt Binder	Penetration at 25°C, 5sec, 100g, (dmm)		Brookfield Viscosity at 60°C at Shear Rate=1/s (poise)		G*/sinδ at 60°C at 10 rad/s (Pa)	
	Original	TFOT Residue	Original	TFOT Residue	Original	TFOT Residue
AC-20	72.5	42.2	2526	5936	3542	7383
AC-20+15%CR	51.7	38.8	20605	25352	13115	22672
AC-20+3.0%SBR	58.5	58.5	10709	14341	9304	11771
AC-30	55.0	35.8	3785	8251	4687	9330
AC-30+10%CR	47.3	34.3	9779	20424	11020	18493
AC-30+3%SBR	57.0	47.0	17407	16426	6593	12917

Table 2 Bulk specific gravities and gradation of the aggregate blend used

Sieve Size	Bulk Specific Gravity of Aggregates Retained	Gradation (% Passing)	FDOT S-I Specification (% Passing)
3/4"	---	100	100
½"	2.375	99	88 - 100
3/8"	2.379	90	75 - 93
No.4	2.345	63	47 - 75
No.10	2.298	47	31 - 53
No.40	2.333	35	19 - 35
No.80	2.655	13	7 - 21
No.200	2.784	4	2 - 6

Table 3 Mix Properties as Measured by the Gyratory Testing Machine at Initial Compaction

Mix Type	Gyratory Shear (psi)	Bulk Density (pcf)	Air Void (%)	VMA (%)
AC-20	61.00	137.2	5.90	16.04
AC-20+15%CR	63.23	137.5	5.30	15.83
AC-20+3%SBR	60.19	140.5	2.20	13.98
AC-30	59.37	137.4	4.93	15.90
AC-30+10%CR	63.38	137.7	5.20	15.75
AC-30+3%SBR	61.25	139.9	2.68	14.40

Table 4 Mix Properties as Measured by the Gyratory Testing Machine at Medium Compaction

Mix Type	Gyratory Shear (psi)	Bulk Density (pcf)	Air Void (%)	VMA (%)
AC-20	63.54	139.4	4.37	14.68
AC-20+15%CR	66.60	141.1	2.84	13.64
AC-20+3%SBR	66.76	142.1	1.10	13.01
AC-30	55.98	139.8	3.27	14.43
AC-30+10%CR	70.28	141.5	2.58	13.41
AC-30+3%SBR	67.41	142.4	0.94	12.87

Table 5 Mix Properties as Measured by the Gyratory Testing Machine at Ultimate Compaction

Mix Type	Gyratory Shear (psi)	Bulk Density (pcf)	Air Void (%)	VMA (%)
AC-20	61.55	141.4	3.02	13.47
AC-20+15%CR	66.09	142.0	2.17	13.05
AC-20+3%SBR	52.33	143.0	0.47	12.45
AC-30	61.93	141.1	3.99	14.62
AC-30+10%CR	63.41	142.4	1.93	12.84
AC-30+3%SBR	73.60	142.8	0.63	12.59

Table 6 Results of Loaded Wheel Test

	Average Rut Depth (inch)			Reduction in Rut Depth as compared with Base AC
	At 1000 Cycles	At 4000 Cycles	At 8000 Cycles	
AC-20	0.146	0.210	0.276	--
AC-20+15%CR	0.136	0.188	0.228	17%
AC-20+3%SBR	0.093	0.144	0.177	36%
AC-30	0.109	0.176	0.262	--
AC-30+10%CR	0.118	0.176	0.207	21%
AC-30+3%SBR	0.092	0.135	0.162	38%

FACTORS AFFECTING THE KINETICS AND MECHANISMS OF ASPHALT OXIDATION AND THE RELATIVE EFFECTS OF OXIDATION PRODUCTS ON AGE HARDENING

J. Claine Petersen
Western Research Institute (retired)
1316 Jennifer Court, Loveland, CO 80537

P. Michael Harnsberger and Raymond E. Robertson
Western Research Institute
365 North 9th Street, Laramie, WY 82070

Keywords: Oxidation kinetics, Oxidation mechanisms, Oxidation products-viscosity relationships

ABSTRACT

The ketones and sulfoxides formed in asphalts are the major determinants of viscosity increase on oxidation. Asphalts initially exhibit a high reactivity with oxygen causing a rapid spurt in the formation of both oxidation products and viscosity increase. This spurt is followed by a slower rate of oxidation and hardening. Different oxidation mechanisms appear operative during these two periods. During the spurt, sulfoxides are the major oxidation product and determinant of viscosity increase, particularly at lower temperatures. Following the spurt, ketones are usually the major product and determinant of viscosity increase. Molecular moieties that are converted to ketones and sulfoxides compete for the reactive oxidant. The ratio of ketones to sulfoxides formed was found dependent on oxygen concentration (pressure), temperature and sulfur content. The relative amounts of sulfoxides and ketones formed under different internal and external environments, and their differing effects on viscosity, are rationalized by the microstructural model of asphalt.

INTRODUCTION

Asphalt oxidation is important because it is the major cause of asphalt hardening, resulting in the deterioration of many desirable asphalt performance properties. In asphalt concrete pavements, oxidative hardening contributes to pavement embrittlement and excessive pavement cracking. Factors affecting the rate of oxidative hardening and the mechanisms of asphalt oxidation are the subjects of this paper.

Oxidation produces polar functional groups in asphalt molecules; ketones (1) and sulfoxides (2) are the major oxidation products; only minor amounts of dicarboxylic anhydrides (3) and carboxylic acids (4) are formed during the advanced stages of oxidation. Methods for their quantification have been developed (5). Viscosity increase accompanies the introduction of the polar functional groups; however, the relative sensitivity to viscosity increase is highly asphalt source (composition) dependent and is related to the component compatibility of the asphalts (6). The more compatible asphalts show lower sensitivity to viscosity increase from oxidation (6-8). Component compatibility is defined as the relative amount of molecular aggregation of the polar asphalt components to form miceller structuring, often referred to as microstructure. The use of the term miceller with reference to asphalt does not imply well defined or spherical components as is common in aqueous systems. In fact, just the opposite is probably true in which irregular shaped molecular agglomerates with poorly defined boundaries and gradual polarity gradients exist within the asphalt matrix.

On oxidation, all asphalts exhibit a hyperbolic-like kinetic curve when log viscosity is plotted versus oxidation time, showing an initial rapid rate of viscosity increase (referred to in this paper as the spurt) followed by a slower, nearly linear rate of viscosity increase (8). Following the viscosity spurt, viscosity increase correlates directly with ketone formation (8-11), with each asphalt having its unique ketone-viscosity relationship. The formation of polar asphaltene components on oxidation also correlates with viscosity increase (12); thus, it follows that the rate of asphaltene formation should correlate with the rate of ketone formation, which relationship has been demonstrated (13,14).

The shape of the kinetic plot, and the effect of asphalt component compatibility on

oxidative aging are shown in Figure 1 for two asphalts studied in the Strategic Highway Research Program (SHRP). Asphalt AAG-1 is a highly compatible asphalt with well dispersed microstructure, while asphalt AAD-1 is at the other end of the compatibility spectrum. The time scales have been time-temperature shifted to offset the effect of temperature on the increase in oxidation rate so that changes in kinetics as a function of temperature can be visually compared. This procedure will be used throughout this paper. Data in Figure 1 are presented to illustrate the effects of component compatibility on oxidation kinetics. The data show that for the highly compatible asphalt AAG-1, there were no significant changes in microstructure on oxidation between 60°C and 80°C that affected the oxidation kinetics, presumably because the oxidation products were solubilized in the asphalt dispersed phase ("solvent" component) precluding their interaction to form significantly larger molecular agglomerates. Thus, the asphalt behaved more like a true solution. However, for the less compatible, more highly associated asphalt AAD-1, lowering the oxidation temperature from 80°C to 60°C significantly reduced the rate of oxidative hardening following the spurt. This lowering is believed the result of molecular immobilization from the formation of microstructure, reducing the reactivity of precursor molecules that form ketones. These effects are discussed in detail elsewhere (8).

In the present paper, the chemical and physicochemical factors that control the phenomena cited above are identified and their effects interpreted and rationalized by the microstructural model of asphalt. A new model for the chemical mechanisms of asphalt oxidation is also presented. Because of the large number of variables affecting asphalt oxidation kinetics, only selected examples can be presented within the scope of this paper. A sequence of papers are planned for future publication in which the subjects presented are discussed in more detail and on larger sets of asphalts.

RESULTS AND DISCUSSION

Oxidation Kinetics and Oxidation Products-Viscosity Relationships. As stated in the Introduction, ketones and sulfoxides are the major identifiable functional groups formed in asphalt on oxidation. Recent data of Liu, et al. (10) relating carbonyl formation with oxygen uptake for SHRP asphalts AAA-1 and AAG-1 were compared by us with total ketones plus sulfoxides formed in these same two asphalts oxidized at Western Research Institute (WRI) using the same oxidation method. Analysis of Liu's data showed that the ratio of oxygen uptake for AAA-1/AAG-1 was 1.32; the corresponding ratio of total ketones plus sulfoxides calculated from the WRI data was 1.31, confirming that ketones and sulfoxides account for essentially all of the oxygen that reacted with these asphalts. It therefore follows, that except for variable volatile loss in asphalt pavement mix plants, nonreversible age hardening of asphalts in pavements is a direct result of ketone and sulfoxide formation.

The rates (kinetics) of chemical oxidation and viscosity increase of asphalts are influenced by asphalt composition, oxidation products formed, temperature, oxygen partial pressure (concentration and/or diffusion rate) and physicochemical effects. These factors are demonstrated for selected asphalts in Figures 2-6. It has been shown (15, 16) that asphalts exposed to 100% oxygen or air at 300 psi (2.07×10^6 Pa) pressure are saturated with oxygen, thus eliminating the need to consider oxygen concentration (diffusion) as a variable in the oxidation kinetics. Elimination of this complicating factor greatly simplifies the study of the kinetics of the oxidation chemistry.

In Figures 2-4, the oxidation and age hardening kinetics of three selected SHRP asphalts having different sulfur contents are considered. The asphalts were aged at 60°C and 100°C using the SHRP TFO-PAV method {300 psi (2.07×10^6 Pa, air)}. Data for AAF-1 (3.4% sulfur) are shown in Figure 2. Kinetic data are shown at the left of the figure and oxidation functional group-viscosity relationships at the right. The time scales are time-temperature shifted as explained for Figure I. Note that during the initial oxidation spurt that sulfoxides are formed at a much faster rate than ketones. This has been found true for all asphalts studied. Further, the relative amounts of ketones and sulfoxides formed and viscosity increase during the spurt are nearly independent of temperature in the absence of oxygen diffusion effects. This was found to hold for all eight SHRP core study asphalts. Following the spurt, the rate of formation of ketones at 60°C is lower than at 100°C, resulting in a corresponding reduction in viscosity increase. These results are interpreted as follows based on the microstructural model

of asphalt (6-8).

First, it is proposed that the mechanisms of oxidation during and after the spurt are different. This is discussed later in the paper. The present discussion relates to oxidation following the spurt. Asphalt AAF-1 is of intermediate compatibility; therefore, as temperatures are decreased, polar, more aromatic components (related to the polar aromatics and asphaltenes generic fractions) associate into agglomerates, thus reducing their molecular mobility and reactivity with oxygen from physicochemical effects (7, 8). That is, the effective concentrations of mobile reactants are reduced by being buried in the microstructure. This is somewhat analogous to what has been observed in micelle catalysis where reaction sites on whole molecules can be buried in the micelle (17). Because the reactive components that form ketones {benzylic carbons, (1, 6)} are highly concentrated in the polar, more aromatic fractions (6), ketone formation is inhibited in the less compatible asphalt AAF-1 at at lower temperatures. Lin, et al. (14) recently showed that the new asphaltenes which form on oxidation are produced primarily from the maltenes fraction. Based on the known composition of the precursors to ketone formation, the new asphaltenes are probably formed primarily from the polar aromatics fraction. The new asphaltenes are reported (14) to have the same effect of viscosity as original asphaltenes, although chemically quite different.

Next, consider the relative effects of ketones and sulfoxides on viscosity increase from data at the right in Figure 2. Note that the ketones formed correlate with viscosity increase as previously mentioned. During the oxidation spurt, for which limited data points are available, it is difficult to assess the relative contribution of sulfoxides and ketones to viscosity increase. However, the linear ketone-viscosity plot and major change in the slope of the sulfoxide-viscosity plot at the point corresponding to the end of the spurt indicate that the ketones are the major determinants of viscosity increase in asphalt AAF-1 oxidized between 60°C and 100°C. The lower concentration of sulfoxides at 60°C following the change in direction of the sulfoxide plot at the point corresponding to the end of the spurt in the kinetic plots could result from either greater thermal instability of the sulfoxides at 100°C and/or the depletion of highly reactive sulfides which form sulfoxides. Obviously, there is no additional contribution to viscosity increase by the sulfoxides formed during 100°C oxidation past the change in slope of the curve represented by about 0.25 mol/L sulfoxides, since the concentration of sulfoxides remains constant. Note also that the slope of the ketone plot is steeper (viscosity increase more sensitive to ketone formation) for 100°C oxidation than for 60°C oxidation, even in the absence of sulfoxide formation. This is evidence that at the higher temperature, ketones are formed deeper in the microstructure because their precursors are liberated for reaction by thermal dissociation of the microstructure.

Before discussing the remaining figures, the following hypothesis based on the microstructural model is presented to explain how ketones and sulfoxides produce viscosity increase. Sulfoxides and ketones are both polar, containing an electronegative oxygen producing a dipole that can interact or associate with other dipoles or induced dipoles. From a polarity standpoint, the sulfoxide functional group is probably as polar or more polar than the ketone. Yet, the ketones formed beyond the oxidation spurt show the major effect on viscosity increase. Thus, it is concluded that the polar nature of the ketones and/or sulfoxides alone is not the fundamental factor responsible for the significant effects on viscosity increase. It is proposed that the size of the associated molecular agglomerates on which these function groups are formed is the primary reason for their profound effects on viscosity. It is well known that the viscosity of polymers is directly related to molecular weight. The ketones are formed predominantly on molecules of the polar, aromatic components where the benzylic carbons are concentrated (6). These ketone precursors are also the molecules believed to be associated in molecular agglomerates in asphalt. As previously mentioned, the maltenes (which contain the polar aromatics) have been shown (14) to be involved in asphaltene formation and viscosity increase. Thus, it logically follows that the ketones, which are most likely formed on already associated molecular species, cause much larger molecular agglomerates to form through their association with other large associated species. As a result, the formation of a single ketone moiety could cause the formation of a much larger agglomerate with significantly greater effective molecular weight, and thus a significant effect on viscosity increase.

On the other hand, the sulfides which are precursors of sulfoxides should be found in

relative abundance in the weakly associated dispersing phase of asphalt, thus sulfoxides formed following the spurt could be concentrated in the dispersing phase. Also, if the sulfide moieties are located in the physical vicinity of the associated phase, the molecules of which they are a part may not have sufficient polarity or aromaticity to cause them to be strongly associated with larger agglomerates. Once sulfoxides are formed, they may then interact with polar constituents present in either the weakly or strongly associated components. However, in either case, they would have limited effect on effective molecular weight increase, and thus viscosity increase, for the following reasons. If the association of sulfoxides occurred in the dissociated (solvent) phase, the association of the sulfoxide with otherwise weakly associated molecules would only about double the effective molecular weight. For typical asphalt molecules, this might be a molecular weight increase from 1000 to 2000 Daltons. If a sulfoxide-containing molecule with no additional highly polar molecular components were to associate with a large agglomerate in the dispersed phase, for example and agglomerate with an effective molecular weight of 30,000 Daltons, this would only increase the effective molecular weight to 31,000 Daltons --- as rather insignificant relative increase. Thus, oxidation of sulfides to form sulfoxides under the conditions just described should have a relatively small effect on viscosity increase. Of course, another reason for the reduced effect of sulfoxides on viscosity following the spurt in some asphalts might be that the concentration of reactive sulfides in the vicinity of the ketone-forming precursors for which they compete to form sulfoxides might simply be depleted.

With the theory presented, consider the data for asphalt AAM-1 and AAA-1 in Figures 3 and 4, respectively. Asphalt AAM-1 (Figure 3) is a compatible asphalt with low sulfur content (1.2%). Because the polar components of this compatible asphalt are well dispersed, the lowering of the oxidation temperature from 100°C to 60°C does not significantly change the state of dispersion (immobilization of the aromatic molecules containing the ketone-forming benzylic carbons) of the asphalt. As a result, no significant physicochemical effect is seen in the kinetic plot at the left in Figure 3 for AAM-1 between 60°C and 100°C, as was seen for the more incompatible asphalt AAF-1 (Figure 2). The similarities of the ketone kinetics at both the high and low temperatures is also reflected in the viscosity plots, again confirming the relationship between ketone formation and viscosity increase. The decrease in sulfoxides with time following the oxidation spurt is unique for asphalt AAM-1 among the asphalt studied to date and is as yet unexplained.

The relatively large increase in viscosity with ketone formation as seen for AAM-1 is not typical for compatible asphalts {compare with the much-studied compatible asphalt AAG-1 (Figure 2)}. Asphalt AAM-1 has a very low heptane asphaltenes content and its molecules are inherently much larger than those of most other asphalts (16). Recent solid state NMR measurements at WRI (18) indicate that asphalt AAM-1 has much larger condensed aromatic ring structures than the other SHRP asphalts. The authors propose that these large polarizable condensed ring structures provide for increased molecular association in this asphalt, and thus its high sensitivity to viscosity increase with ketone formation.

A change in slope of the ketone-viscosity plot at the right in the figure corresponding to the end of the spurt is evident. The combined effect of ketones and sulfoxides on viscosity during the spurt (below 0.15 mol/L ketones) is less than that of the ketones alone following the spurt. This is believed to result from the different oxidation mechanisms operating during the spurt, with the initial major oxidation product being sulfoxides. Further, the spurt oxidation mechanism proposed later on would dictate that during the spurt, oxidation products may be formed on molecules having a different state of dispersion than molecules on which they are formed after the spurt, thus having differing effects on viscosity increase.

Data on the high sulfur (5.5%) asphalt AAA-1 are shown in Figure 4. It is apparent when one compares the relative amounts of ketones and sulfoxides formed in the low sulfur asphalt AAM-1 (Figure 3) with those formed in asphalt AAA-1 (Figure 4), that a much higher ratio of ketones to sulfoxides are formed in the high sulfur asphalt. Note also, except for a slight lowering of the rate of ketone formation at 60°C from physicochemical effects, that the relative amounts of ketones to sulfoxides are almost the same at both high and low temperatures. This has been found to be true for the eight SHRP core asphalts during PAV oxidation, again confirming that the kinetics and

mechanisms of oxidation are similar at all temperatures studied and are not dependent on oxygen concentration, as previously mentioned.

Examination of the data in the kinetic plot at the left in Figure 4 suggests that the relatively small increase in the rate of ketone formation between the 60°C and 100°C may not be sufficient to account for the larger rate of viscosity increase between the two temperatures. These results suggest that the sulfoxides have a greater effect on viscosity increase at the higher temperature in this higher sulfur, less compatible asphalt than in the two asphalts previously considered. An explanation for this is found in the microstructural model. A relatively greater proportion of the reactive sulfides that are precursors to sulfoxides should also be found in more associated species in this less compatible asphalt. Therefore, their formation on more associated molecular agglomerates should have a greater effect of viscosity. Also, since sulfoxides compete with ketones for hydroperoxide precursors to form sulfoxides, the molecular dissociation occurring at the higher temperature would make sulfoxides "deeper" in the associated phase more available for reaction. Therefore, if the sulfoxides were formed deeper in the associated phase at 100°C than at 60°C, then when the viscosity of the 100°C sample is measured at 60°C, sulfoxides would be buried deeper in the associated phase and have a greater effect on viscosity increase. The greater sensitivity of viscosity increase to ketone formation at 100°C than at 60°C (right side of figure) could also be explained using the same argument for ketones as was just presented for sulfoxides, in that at higher temperatures ketones are formed deeper in the microstructure, thus having a greater relative effect on viscosity. Probably physicochemical effects involving both sulfoxides and ketones are responsible for the larger increase in viscosity sensitivity during oxidation at the higher temperature.

Effects of Oxidation at Atmospheric Pressure on Oxidation Kinetics. As previously discussed, high pressure oxidation (PAV procedure) produced sulfoxides and ketones at nearly the same ratios, independent of temperature. However, in a diffusion controlled system at atmospheric pressure in which oxygen concentration within the asphalt is low, the ratio of sulfoxides to ketones produced following the spurt are highly dependent on oxidation temperature. This temperature sensitivity can be seen by comparing the data in Figure 5 for asphalt AAF-1 with the PAV aging data for the same asphalt shown in Figure 2. Aging data for AAF-1 in Figure 5 were obtained using the Thin Film Accelerated Aging Test (TFAAT) in which the asphalt was oxidized as a 160 micrometer film at ambient air pressure. In general, as the oxidation temperature is lowered, the ratio of sulfoxides to ketones increases. Space do not permit comparison of the data for the other seven SHRP core asphalts, but a comparison is planned in a future publication.

The sensitivity to temperature of the ratio of sulfoxides to ketones appears to be related to the degree of molecular association at a given temperature. This is evidenced by the fact that those asphalts which exhibited a reduction of ketone formation and viscosity increase from the physicochemical effects of molecular association at the lower 60°C temperature in the PAV oxidations, as discussed earlier, are more sensitive to an increase in the sulfoxide-to-ketone ratio as temperature is lowered. The effect is pronounced during TFAAT oxidation at 85°C, but almost disappears above 113°C where molecular dissociation is high as indicated by similar ratios (not shown) for a given asphalt at both 113°C and 130°C oxidations. It was also found, and also not shown, that 65°C TFAAT oxidation data obtained on SHRP asphalts AAD-1 (6.9% sulfur) and AAG-1 (1.3% sulfur) oxidation kinetics were quite similar to those for 85°C TFAAT oxidation. Thus, the large change in the TFAAT oxidation kinetics attributed to physicochemical effects occurs between 85°C and 113°C. This is in contrast with results from PAV oxidation where the change occurs between 60°C and 80°C. Although not shown in graphical form, ketone and sulfoxide concentrations at 400 hours of TFAAT oxidation at 85°C for the highly compatible asphalt AAG-1 are 0.15 and 0.21 mol/L, respectively. Corresponding data for ketone and sulfoxide concentrations after a comparable oxidation of 120 hours at 113°C are 0.33 and 0.14 mol/L, respectively. Thus, at higher temperatures and low oxygen concentrations, ketones seem to be formed to some extent at the expense of sulfoxides; however, the total ketone plus sulfoxide concentration is higher at 113°C (0.47 mol/L) than at 85°C (0.36 mol/L). The known thermal instability of sulfoxides at higher temperatures and the dissociation of

more reactive ketone precursors, thus increasing their concentration in the dissociated phase, are possible contributors to this difference.

At the right in Figure 5, note also the large difference between the slopes of the ketone-viscosity plots for oxidation at 85°C and 113°C. As previously discussed, this is again evidence that at higher temperatures ketone precursors dissociate deeper in the asphalt microstructure, and when oxidized to ketones, have a relatively greater influence on viscosity increase. Comparison of Figures 2 and 5 show that this effect is greatly amplified at atmospheric pressure oxidation compared with PAV oxidation.

While theorizing on the mechanism is difficult, the fact remains that the large change in the ratio of sulfoxides to ketones as a function of temperature is primarily influenced by a change in the oxygen pressure (concentration) in the asphalt. Since oxidation in pavements is diffusion controlled at ambient pressures, and oxidative aging characteristics of asphalts may be evaluated using the SHRP procedure at high pressures in which the asphalt is saturated with oxygen, the correspondence between aging at low and high oxygen pressures needs to be rationalized.

Related to the above discussion, Liu and coworkers (10) found a significantly lower level of carbonyl absorption (CA) versus time in asphalts oxidized at 0.2 atmospheres oxygen pressure than at 20 atmospheres pressure at the same temperature for asphalt AAF-1. Linear extrapolation of the CA versus time plot to zero oxidation time (roughly corresponding to the oxidation level at the end of the spurt) shows significantly lower levels of CA (ketones) in the low pressure oxidation. Since CA correlates directly with log viscosity for a given asphalt, there is some question, as Lin, et al. also point out, that aging characteristics predicted from PAV aging may not always correspond well with aging predicted from aging tests run at lower pressures. Our results regarding the effects of temperature on the aging kinetics using high and low pressure aging, particularly for less compatible asphalts, seem particularly germane.

Effects of Oxidation at Low Temperatures and at Atmospheric Pressure. Several years ago the principle author and coworkers (G. Miyake, H. Plancher, and P.M. Harnsberger) at WRI oxidized a series of asphalts as thin films (5 wt%) in Ottawa sand briquettes. These asphalts were the unmodified control samples prepared in connection with a kinetic study to evaluate an oxidation accelerator in asphalt. Oxidations were performed at 45°C. The data obtained on extracted samples for one of these asphalts are shown in Figure 6. Since this oxidation was performed at a relatively low temperature, reaction rates were slow and oxidation during the spurt could be looked at in more detail because a number of data points were obtained during the spurt. When comparing these data with data in the previous figures, it should be noted that very little oxidation occurred following the spurt at the 45°C temperature during the 100 day aging period. Ketone levels never exceeded about 0.025 mol/L. This level is below ketone levels reached at the first data point near the end of the spurt during oxidation at the higher temperatures. It should be noted that although the oxidation temperature was low, the viscosity measurements were made at the same temperature (60°C) as was used for the kinetic studies at the higher temperatures, making these data comparable for interpretation with the higher temperature data.

Important information regarding oxidation during the spurt is apparent in Figure 6. First, the formation of sulfoxides is extremely rapid, even at 45°C, with the virtual exclusion of ketone formation. This is in agreement with the work of Huh and Robertson (19) in which it was shown that the slope of the Arrhenius plot for sulfoxide formation was smaller than that for ketone formation, thus indicating that the activation energy for sulfoxide formation is less sensitive to temperature change than is the activation energy for ketone formation. In the absence of ketone formation, one can conclude that the initial oxidation mechanism during the spurt under near ambient conditions is not a typical hydrocarbon free radical chain reaction which always produces ketones and more free radicals. This result is consistent with the observation of van Gooswillen, et al. (20) who oxidized asphalt in solution and measured the reaction rate by oxygen uptake. They noted no induction period in the oxidation kinetics which is characteristic of classical hydrocarbon chain reactions; they concluded that asphalt oxidation was not of the classical hydrocarbon type.

What is most revealing in Figure 6 is that the viscosity increase corresponds with the

formation of sulfoxides with virtually no ketones being formed. This shows that under the conditions of this experiment, that viscosity increase during the spurt is largely controlled by the formation of sulfoxides, suggesting that the sulfoxides are being formed on associating molecules deep in the polar, highly associated components during the spurt and not in the dispersing phase as may occur for sulfoxide formation following the spurt. In times past at WRI, samples taken from the surface of asphalt stored for and extended periods in sample cans at ambient temperatures have been observed to have sulfoxide concentrations of over 0.3 mol/L with no ketones having been formed.

A Proposed Two-Stage Mechanism for Asphalt Oxidation. As discussed above, sulfoxides were the primary oxidation product formed during the spurt with the virtual exclusion of ketones. The reaction of sulfides to form sulfoxides was also very rapid, yet sulfides in an inert solvent do not react with atmospheric oxygen under these conditions. A highly reactive precursor inherent in the the asphalt that reacts with oxygen to form a hydroperoxide intermediate which then reacts with the asphalt sulfide to form sulfoxides (16) is proposed. Sulfides are well recognized to be very reactive hydroperoxide scavengers and react with hydroperoxides to form sulfoxides with no free radical products. Sulfides are used commercially in hydrocarbon plastics such as polypropylene as hydroperoxide scavengers to prevent the further reaction of hydroperoxides in promoting further hydrocarbon chain reactions. It has recently been proposed by Mill (21) that oxygen initially reacts with a highly reactive hydrocarbon in asphalt such as a hydroaromatic. This type of moiety can be exemplified by saturated, nonaromatic bridgehead carbons fused between aromatic ring structures to form a strained ring between the aromatic rings. Because of the steric strain imposed on the saturated carbon atoms, the hydrogens on these carbons are highly reactive toward abstraction by the oxygen to form hydrogen peroxide and/or hydroperoxides (as proposed by Mill), resulting in aromatization of the nonaromatic ring component. Thus, hydroperoxides are generated which then react with the asphalt sulfides with little or no production of ketones, consistent with the observed asphalt oxidation during the initial stages of the spurt. Then, as the oxidation continues toward the end of the spurt, initiation of a hydrocarbon chain reaction begins with abstraction of a hydrogen from a benzylic carbon, which is a precursor to ketones, forming benzyl free radicals. These radicals can then compete with the sulfides for the available hydroperoxides. These radicals can also begin to react with oxygen to form peroxy radicals, and then continue on to form hydroperoxides with the generation of more benzylic carbon free radicals. Thus, in the latter case, a free radical hydrocarbon chain reaction has begun. Many reaction paths are possible; however, one route is for the hydroperoxide to decompose to form ketones or react with sulfides to form sulfoxides. Once the supply of the highly reactive hydrocarbon precursors previously described is exhausted, the spurt is over, explaining the rapid reduction in the oxidation rate and viscosity increase following the oxidation spurt. After the spurt, ketones form at a much slower, but nearly constant rate via typical hydrocarbon free radical chain reactions. Such chain reactions have previously been proposed (6). Reactive sulfides, as long as available, compete with the hydroperoxide ketone precursors to form sulfoxides.

Figure 7 shows the ketone and sulfoxide concentrations in the eight SHRP core asphalts at the end of the spurt during PAV oxidation at 100°C. Except for the low sulfur asphalts, the concentrations of ketones plus sulfoxides are nearly constant, indicating that these asphalts all have about the same concentration of reactive hydrocarbon precursors. Asphalt AAM-1, which is low in aromatics, might be expected to have a smaller concentration of the highly reactive hydrocarbon precursor, thus explaining its low level of oxidation during the spurt.

As previously mentioned in the discussion of Figure 6, the sulfoxides formed during the spurt appeared to control the viscosity increase during this stage of oxidation. This is explained as follows. If the reactive hydrocarbon precursors are indeed hydroaromatics, as suggested by Mill, then they would be expected to be present in the highly associated molecular agglomerates in which the more aromatic components are found. The formation of a polar sulfoxide group in the microstructure should cause the association of relatively large molecular agglomerates, thus significantly increasing effective molecular weight, and thus viscosity. Sulfoxides formed after the spurt would have less effect on viscosity if they were formed in the weakly associated dispersing phase or on rather nonpolar molecules as previously explained.

The relative abundance of ketones and sulfoxides following the spurt should be a

function of sulfide (related to sulfur) content of the asphalt. Higher sulfide concentrations provide more competition for the hydroperoxide at the expense of ketone formation. This is illustrated by the data in Figure 8 for sulfoxide and ketone formation in asphalts following the spurt. Note the ketone and sulfoxide data in the figure for the high sulfur asphalts AAK-1 and AAD-1. They cease to follow the trend as a function of sulfur content. More ketones begin to be formed at the expense of sulfoxides. Data for 80°C are shown as solid data points to provide evidence that this change in product ratios occurs somewhere between 80°C and 100°C.

As confirming evidence for a dual, two-stage oxidation mechanism for asphalts, the data in Figure 9 are submitted. These unpublished data were obtained several years ago at WRI by H. Plancher in scouting experiments on potential antioxidants in asphalts. In this experiment, a Boscan asphalt was oxidized as a thin film at 130°C with and without 2% of a potential antioxidant, triphenyltin hydroxide (TPTH). It is apparent that the TPTH had no effect on sulfoxide formation during the spurt; however, following the spurt, ketone and sulfoxide formation rate were both significantly reduced, indicating that the reaction mechanism during and after the spurt were not the same.

The Pragmatic Benefit of Sulfur in Asphalts. It has been reported (22) that asphalt sulfur content correlates with asphalt component compatibility as defined by relative viscosity measurements. In general, the less compatible asphalts are more sensitive to oxidative age hardening. Further, it has been shown in this paper that the ratio of sulfoxides to ketones formed on oxidation increases with increasing sulfur content, with sulfoxides being formed at the expense of ketone formation. This is illustrated in Figure 8 for PAV oxidation. The increasing sulfoxide to ketone ratios with increasing sulfur content is further intensified in atmospheric, diffusion controlled oxidation, particularly as the temperature is lowered. This phenomenon was explained in connection with Figure 5, but is characteristic of the SHRP core asphalts. It has also been pointed out that oxidizable asphalt sulfides are potent hydroperoxide scavengers, and thus interfere with the production of free radicals in the hydrocarbon chain reaction following the oxidation spurt. Finally, it has been shown that following the spurt, ketones have a much greater effect on viscosity increase than sulfoxides.

The pragmatic conclusion to all this is that sulfides in asphalts are effective antioxidants and reduce the effect of oxidation on age hardening. Since sulfides compete with ketone precursors, increased sulfide content in the asphalt means that more sulfoxides and less ketones are formed, a favorable situation for reduction in the rate of viscosity increase. This increased sulfoxide content and reduced ketone content tends to offset the increased sensitivity to age hardening of the less compatible asphalts, particularly at low aging temperatures. The effect of temperature on this phenomenon is illustrated in Figure 1 for the low sulfur (1.3%), highly compatible asphalt AAG-1 and the high sulfur (6.9%), rather incompatible asphalt AAD-1. The above arguments could explain why asphalts made from some high sulfur crudes harden and become brittle so rapidly in hot climates, but perform quite well in more moderate climates. With regard to age hardening, it is our belief that the maximum pavement temperature reached during hot days is more critical to eventual age hardening than are the average temperatures. Careful analysis of the data from the extensive California simulated field study of Kemp and Prodoehl (23) seem to confirm this conclusion.

SUMMARY AND CONCLUSIONS

The oxidative hardening of asphalts is a direct result of the formation of ketones and sulfoxides. The relative amount of amount of hardening that they produce depends upon the state of dispersion of the molecules on which they are formed. When formed on a molecule in a highly associated molecular agglomerate, they produce, through association with other associated agglomerates, a much larger molecular weight entity, thus significantly increasing effective molecular weight. When formed on weakly associated molecules, as in highly compatible asphalts or on molecules in the dispersing phase, their association has minimal effect on molecular weight, and thus viscosity increase. The hyperbolic-like plot of property change versus time observed for asphalt oxidation kinetics is the result of two sequential and different oxidation mechanisms. The rapid increase at the onset of the kinetic plot is attributed to reaction of highly reactive hydrocarbon precursors of limited concentration which react with oxygen to form hydroperoxides. The hydroperoxides then react primarily with asphalt sulfides to form sulfoxides with the virtual exclusion of ketone formation during the

initial stages of the spurt. Sulfoxides are the major contributor to viscosity increase during the initial stages of the spurt, at least below 45°C at atmospheric pressure. Towards the end of the spurt, a classical free radical hydrocarbon chain reaction begins to take over. When all of the highly reactive hydrocarbon precursors are exhausted, the spurt is over, after which ketones are formed at a nearly constant rate and are the major determinants of viscosity increase. As asphalt sulfur content increases, the sulfoxide contribution to viscosity increases. Following the spurt, sulfides compete for the hydroperoxide ketone precursors. Thus, less compatible, high sulfur asphalts produce more sulfoxides and less less ketones than highly compatible, low sulfur asphalts. Because asphalt viscosity increase is more sensitive to ketone than sulfoxide formation, the production of more sulfoxides and less ketones in high sulfur asphalts tends to offset their increased sensitivity to age hardening, particularly at low temperatures. Sulfides in asphalt are effective antioxidants. The ratios of sulfoxides to ketones produced at high oxygen concentrations, as during PAV aging, were found independent of oxidation temperature, indicating that the mechanism of oxidation does not change with temperature. The ratio of sulfoxides to ketones, however, increased as sulfur content increased. At lower temperatures, physicochemical effects inhibit ketone formation and thus viscosity increase. During atmospheric pressure oxidation (low oxygen concentrations), the ratio of sulfoxides to ketones is not independent of temperature, but increases as oxidation temperature is lowered. The effect is intensified as the asphalt sulfur content increases and could have pragmatic implications when PAV aging is used to predict pavement aging under atmospheric, diffusion controlled condition.

ACKNOWLEDGMENTS

The authors express thanks and appreciation to the Federal Highway Administration (FHWA) for financial support of this work under FHWA Contract No. DTFH61-92-C-00170. Acknowledgement and thanks are also extended to Western Research and the Strategic Highway Research Program (SHRP) for much past data used in this paper. Janet Wolf is much appreciated for her major contributions to the laboratory work. Dr. Jan Branthaver provided many helpful discussions.

DISCLAIMER

REFERENCES

1 Dorrence, S.M., F.A. Barbour and J.C. Petersen. Direct Evidence of Ketones in Oxidized Asphalts, Anal. Chem., 46, 2242-2244 (1974).

2. Petersen, J.C., S.M. Dorrence, M. Nazir, H. Plancher and F.A. Barbour. Oxidation of Sulfur Compounds in Petroleum Residues: Reactivity-Structural Relationships, Preprints, Div. Petrol. Chem., ACS, 26(4), 898-906 (1981).

3. Petersen, J.C., F.A. Barbour and S.M. Dorrence. Identification of Dicarboxylic Anhydrides in Oxidized Asphalts, Anal. Chem., 47, 107-111 (1975).

4. Petersen, J.C. and H. Plancher. Quantitative Determination of Carboxylic Acids and Their Salts and Anhydrides in Asphalts by Selective Chemical Reactions and Differential Infrared Spectroscopy, Anal. Chem., 53, 786-789 (1981).

5. Petersen, J.C. Quantitative Functional Group Analysis of Asphalts Using Differential Infrared Spectrometry and Selective Chemical Reactions --- Theory and Practice, Transportation Research Record No. 1091, 1-11 (1986).

6. Petersen, J.C. Chemical Composition of Asphalt as Related to Asphalt Durability: State of the Art, Transportation Research Record No. 999, 13-30 (1984).

7. Petersen, J.C. Asphalt Oxidation --- An overview Including a New Model for Oxidation Proposing That Physicochemical Factors Dominate in Oxidation Kinetics, Fuel Science and Technol., Int'l., 11(1), 57-87 (1993).

8. Petersen, J.C., J.F. Branthaver, R.E. Robertson, P. M. Harnsberger, J.J. Duvall and E.K. Ensley. Effects of Physicochemical Factors on Asphalt Oxidation Kinetics, Transportation Research Record No. 1391, 1-10 (1993).

9. Lau, C.K., K.M. Lundsford, C.J. Glover, R.R. Davidson and J.A. Bullin. Reaction Rates and Hardening Susceptibilities as Determined from Pressure Oxygen Vessel Aging of Asphalts, Transportation Research Record No. 1342, 50-57 (1992).

10. Liu, M., K.M. Lundsford, R.R. Davidson, C.J. Glover and J.A. Bullin. The Kinetics of Carbonyl Formation in Asphalts, AIChE Journal, 42(4), 1069-1076 (1996).

11. Martin, K.L., R.R. Davidson, C.J. Glover and J.A. Bullin. Asphalt Aging in Texas Roads and Test Sections, Transportation Research Record No. 1269, 9-19 (1990).

12. Plancher, H., E.L. Green and J.C. Petersen. Reduction of Oxidative Hardening of Asphalts by Treatment with Hydrated Lime --- A Mechanistic Study, Proc., Assn. Asphalt Paving Technol., 45, 1-24 (1976).

13. Lee, D.Y. and R.J. Huang. Weathering of Asphalts as Characterized by Infrared Multiple Reflectance Spectra, Applied Spectroscopy, 27, 435 (1973).

14. Lin, M.S., K.M. Lundsford, C.J. Glover, R.R. Davidson and J.A. Bullin. The Effects of Asphaltenes on the Chemical and Physical Properties of Asphalts, Asphaltenes, Fundamentals and Applications, E.Y. Sheu and O.C. Mullins, ed., Plenum Press, N.Y. (1995) pp. 155-176.

15. Lee, D.Y., Development of a Durability Test for Asphalts, Highway Research Record No. 231, 34-49 (1968).

16. Branthaver, J.F., J.C. Petersen, R.E. Robertson, J.J. Duvall, S.S. Kim, P.M. Harnsberger, T. Mill, F.A. Barbour and J.F. Shabron. Binder Characterization and Evaluation, Volume 2: Chemistry, Strategic Highway Research Program, Final Report No. SHRP-A-368 (1993) p. 204.

17. Jaeger, D.A., J.R. Wyatt and R.E. Robertson. Monochlorination of n-Alkyl Phenyl Ethers in Miceller Sodium Dodecyl Sulfate, J. Org. Chem., 50(9), 1467-1470 (1985).

18. Netzel, D.A., Western Research Institute, Laramie, Wyoming, private communication.

19. Huh, J.D. and R.E. Robertson. Modeling of Oxidative Aging Behavior of Asphalts from Short Term, High Temperature Data as a Step Toward Prediction of Pavement Aging, Paper No. 961112, Presented at the Annual Transportation Research Board Meeting, January, 1996, Washington, D.C., Transportation Research Record (in press).

20. van Gooswillen, G., H. Berger and F. Th. de Bats. Oxidation of Bitumens in Various Tests, Proceedings, European Bitumen Conference, 1985, pp. 95-101.

21. Mill, T. Oxidation Pathways in Asphalts, Presentation at the Thirty-Second Annual Petersen Asphalt Research Conference, Laramie, Wyoming, July 10-12, 1995.

22. Branthaver, J.F., J.C. Petersen, J.J. Duvall and P.M. Harnsberger. Compatibilities of Strategic Highway Research Program Asphalts, Highway Research Record No. 1323, 22-31 (1991).

23. Kemp, G.R. and Prodoehl. A Comparison of Field and Laboratory Environments on Asphalt Durability, Proc., Assn. Asphalt Paving Technol., 50, 492-537 (1981).

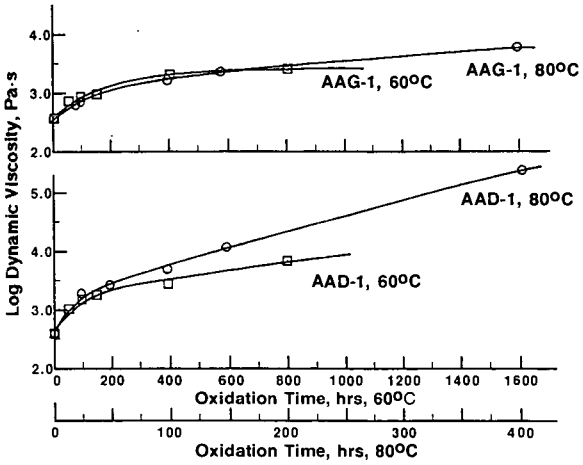

Figure 1. Effects of Temperature and Compatability on Aging Characteristics

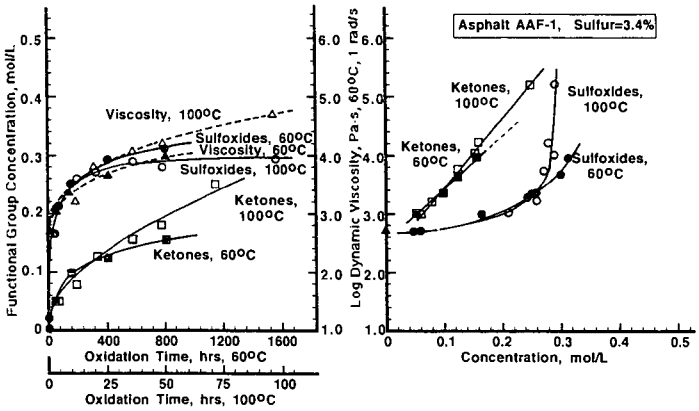

Figure 2. Kinetics and Viscosity-Functional Group Relationsships, PAV Oxidation of Asphalt AAF-1

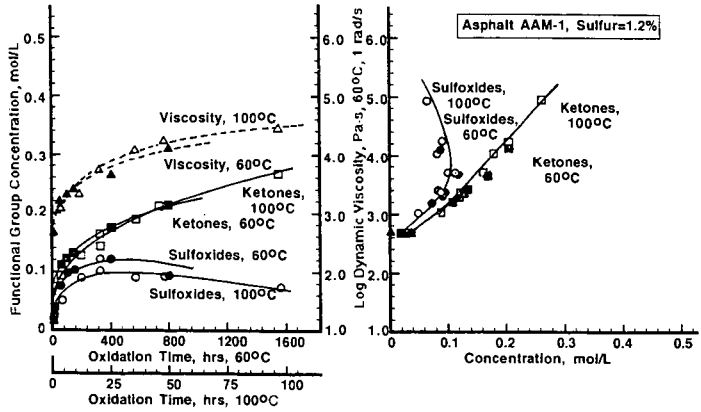

Figure 3. Kinetics and Viscosity-Functional Group Relationships, PAV Oxidation of Asphalt AAM-1

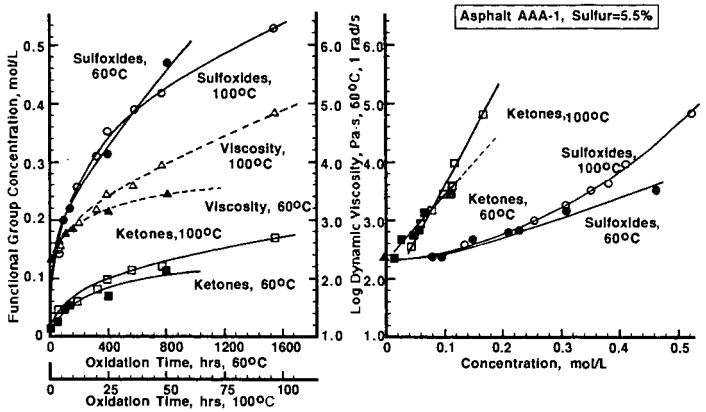

Figure 4. Kinetics and Viscosity-Functional Group Relationships, PAV Oxidation of Asphalt AAA-1

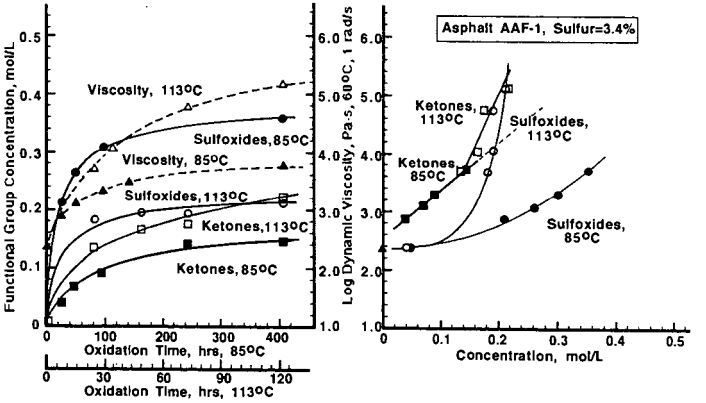

Figure 5. Kinetics and Viscosity-Functional Group Relationships,TFAAT Oxidation of Asphalt AAF-1

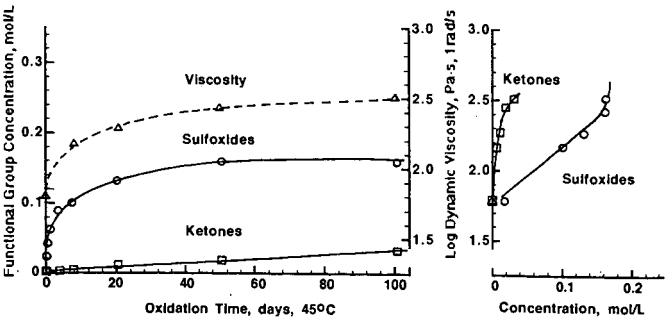

Figure 6. Kinetic Data and Viscosity-Functional Group Relationships for Shell Wood River Asphalt Oxidized at Atmospheric Pressure as a Thin Film on Ottawa Sand at 45°C

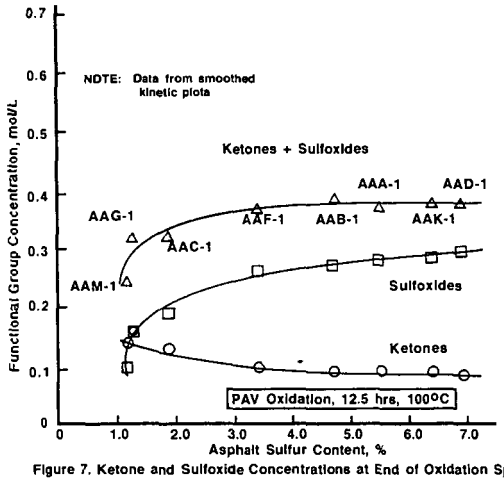

Figure 7. Ketone and Sulfoxide Concentrations at End of Oxidation Spurt

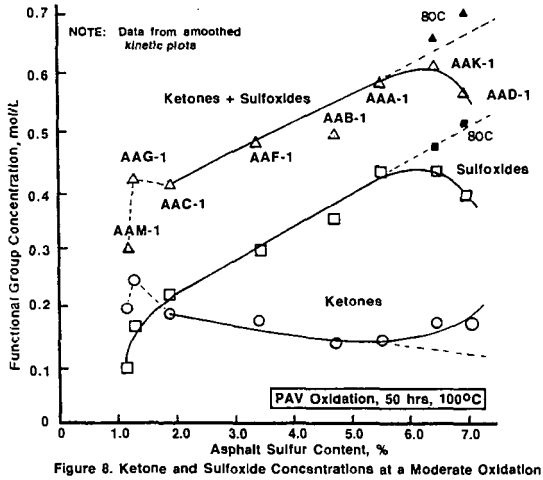

Figure 8. Ketone and Sulfoxide Concentrations at a Moderate Oxidation Level

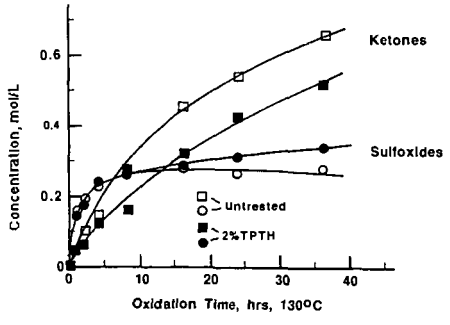

Figure 9. Effect of the Potential Antioxidant Triphenyltin Hyroxide on Oxidation Kinetics of a Boscan Asphalt

THE ROLE OF HYDROAROMATICS IN OXIDATIVE AGING IN ASPHALT

Theodore Mill
Chemistry and Chemical Engineering Laboratory
Stanford Research Institute
Menlo Park, CA 94025

Keywords: Hydroaromatics, Oxidation, Thermochemical kinetics

INTRODUCTION

The pavement engineering community recognized fifty years ago that age hardening and embrittlement of asphalt during service is a primary cause of road failure [Welborn, 1984] and that oxidation of asphalt is the major cause of age hardening [Nicholson, 1937; Traxler, 1961]. Oxidative aging is characterized by oxygen uptake, the formation of sulfoxide and carbonyl groups (as shown by IR spectra), and marked increases in dynamic viscosity and other rheological properties. [Petersen, 1975, 1981 and 1986]. Different asphalts show markedly different rheological changes for similar amounts of oxidation, although elemental analyses indicate a similarity in CHO ratios as well as in molecular weights, with variability only in the heteroatoms, functional groups, and trace metal compositions [Branthaver et al., 1993].

In a SHRP-supported research program, we developed a new hypothesis to account for the oxidation of asphalt, in which hydroaromatic groups in asphalt react with oxygen to form peroxides which are the proximate cause of chemical and physical changes induced by oxidative aging. The purpose of this paper is to examine how oxidation of hydroaromatic groups might proceed and whether hydroaromatics in asphalt fulfill the requirements in asphalt oxidation.

OXIDATION PATHWAYS AND AN OXIDATION MODEL

Triplet oxygen reacts with most organic compounds through free radical pathways, initiated with peroxides and metals [Mill and Hendry, 1980; Mill et al., 1995]. The unusual reactivity oxygen exhibits toward asphalt at temperatures below 100°C must be associated with some highly reactive structural features, such as polycyclic hydroaromatics. Reactions (1) and (2) illustrate the proposed reaction sequence during oxidation of asphalt.

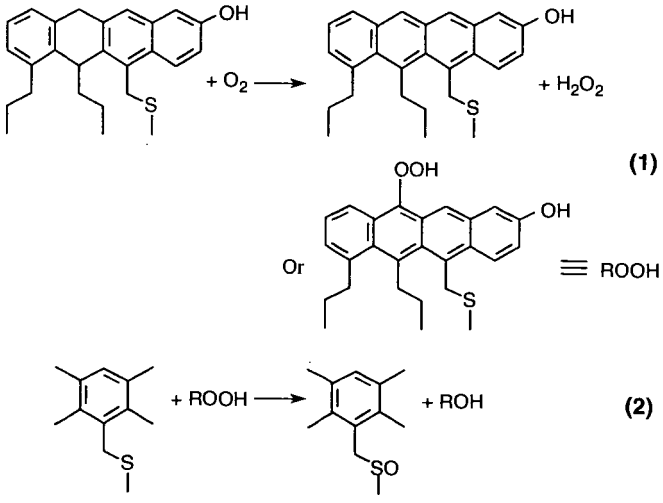

A model for dihydroaromatic reaction with oxygen is found in the smooth reaction of dihydroanthracene ((DHA) with air or oxygen at 100°C in benzene to form hydrogen peroxide and anthracene [Mill et al., 1992]. Figure 1 shows the loss of DHA and the formation of anthracene at 100°C. Added dibutyl sulfide ((DBS), unoxidized by itself at 100°C with air, oxidizes rapidly in the presence of DHA and air at 100°C at rates that correspond to oxidation of DHA to form the peroxide. This induced oxidation is very similar to the induced oxidation of DBS by asphalt heated in air. Although asphalt contains no DHA, we believe that DHA-like hydroaromatics may be present in amounts sufficient to account for the greater part of the direct reaction with oxygen.

KINETICS OF HYDROAROMATIC-OXYGEN REACTIONS

Thermochemical kinetic estimates of the rates of reaction of oxygen and hydroaromatics start with the simple H-atom transfer from the hydroaromatic to oxygen to form the radical pair shown in Reaction (3).

$$HRH + O_2 \longrightarrow HR\bullet + HO_2\bullet \qquad (3)$$

Using heats of formation of these four species, Reaction (1) has a heat of reaction ranging from 130 kJ/mole for DHA and dihydronaphthalene-like hydroaromatics to 159 kJ//mole for tetralin and tetraphenylethane-like hydroaromatics [Benson, 1968; McMillen et al., 1987]. These values correspond to the activation energies of the forward reactions, which, when combined with reasonable estimates for entropy changes, have kinetic parameters corresponding to

$$k_3 = 10^{8.5}\exp(-130{,}000/RT) \text{ to } 10^{8.5}\exp(-159{,}000/RT) \quad (4)$$

For DHA and tetralin, $k_3 = 2 \times 10^{-10}$ M^{-1} s^{-1} and 1.7×10^{-14} M^{-1} s^{-1}, respectively at 100°C. The rate constant for DHA corresponds to a half life for DHA in the presence of 25 atm of oxygen (~1 M) of about 100 years, and for tetralin, a million years! Clearly, this simple scheme fails by a wide margin to predict the experimental half life of 30-40 hours found for DHA in benzene at 100°C with 1 atm of air (see Figure 1).

An alternative model for oxidation of DHA and hydroaromatic analogs involves prior formation of the hydroaromatic (DHA) radical from the molecule assisted homolysis of the hydroaromatic (DHA) by the corresponding aromatic (anthracene) [Bilmers et al., 1986]. The resultant radicals then react with oxygen.

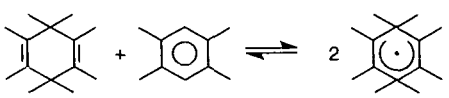

(5)

NM-320525-12

For DHA, Bilmers et al [1986] estimate this process to have an activation energy and log A-factor close to 151 kJ/mol and 8.5, respectively, giving a rate constant at 100°C similar to the value for the tetralin-oxygen reaction and much too slow to be important, even if equimolar amounts of anthracene and DHA were initially present.

Concerted transfer of two hydroaromatic H-atoms to oxygen (Reaction (1)) is exothermic by 63 and 84 kJ/mol with DHA and dihydrophenanthrene,

respectively, and might account for the observed oxidation of DHA, although we do not know what the intrinsic activation energy is for the process. The fast radical-chain oxidation of DHA examined by Bickel and Kooyman [1956] and by Mahoney [1966] to give the corresponding hydroperoxide is difficult to reconcile with the non-initiated oxidation we observed for DHA in benzene. Moreover, radical chain oxidation of hydroaromatics in asphalt is unlikely owing to the presence of effective radical scavenging phenols [Branthaver et al., 1993]; the oxidation would proceed, but much more slowly with a chain length of one. We should point out that a related oxidation of anthrahydroquinone to anthraquinone is the basis for commercial production of hydrogen peroxide from oxygen [Kirchner, 1981]. Asphalts, however, have low concentrations of isolated phenols and probably much lower concentrations of hydroquinones [Branthaver et al., 1993], but we cannot rule out some contribution from this reaction.

HYDROAROMATIC CONTENT OF ASPHALTS

An additional test of the validity of the hydroaromatic model for oxidation of asphalts is the extent to which oxygen uptake is related to the known hydroaromatic content of asphalts. Oxygen uptake data for several SHRP standard asphalts including AAD-1 show that up to one mole of oxygen/kg is taken up over about 100 hrs at 100°C [Branthaver et al., 1993], a significant amount of oxygen, but a small fraction of the aromatic or aliphatic units in typical asphalts with molecular weights ranging from 700 to 1300 Daltons.

Although large numbers of studies of the hydroaromatic content of coals have been published in connection with liquefaction of coal and the role of H-atom donors in the process (Bilmers et al., 1986), few estimates of the hydroaromatic content of asphalts appear to be available. In one recent study, Farcasiu and Rubin [1987] determined the formation of polycyclic aromatic compounds on dehydrogenation of vacuum residues, using uv spectra and mass spectrometry. They found that some fractions of the resid were easily dehydrogenated to give polycyclic aromatic compounds; in one case an average of 13 saturated ring carbons were readily converted to aromatic carbons, indicating that a fairly abundant supply of reactive hydroaromatics are available in some asphalts for the proposed oxidation scheme.

REFERENCES

Bateman, L. and K. R. Hargrave, 1954a, Oxidation of Organic Sulfides I, J. Chem. Soc. 389-398.

Bateman, L., and K. R. Hargrave, 1954b, Oxidation of Organic Sulfides II., J. Chem. Soc., 399-411.

Benson, S. W., 1968, Thermochemical Kinetics, John Wiley and Sons, New York.

Bickel, A. F. and E. C. Kooyman, 1956, Inhibition of the Oxidation of Dihydroanthracene by Alkyl Phenols, J. Chem. Soc. 2215-2226.

Bilmers, R., Griffith, L. L. and Stein, S. E., 1986, Hydrogen Transfer between Anthracene Structures, J. Phys. Chem., 90: 517-523.

Branthaver , J. F., J. C. Petersen, R. E. Robertson, J. J. Duvall, S. S. Kim, P. M. Harnsberger, T. Mill, E. K. Ensley, F. A. Barbour, and J. F. Schabron, 1993, Binder Characterization and Evaluation, SHRP Report SHRP-A-368, Vol. 2, Chemistry.

Farcasiu, M. and Rubin, B. R., 1987. Aliphatic Structures in Petroleum Resids, Energy Fuels 5: 381-386.

Kirchner, J. R., 1981, Hydrogen Peroxide in Kirk-Othmer Encyclopedia of Chemical Technology, M. Grayson, Ed., John Wiley and Sons, New York, Vol. 13, pp. 12-38.

Mahoney, L. R., 1965, Reactions of Peroxy Radicals with Polynuclear Aromatic Compounds II, Anthracene in Chlorobenzene, J. Amer. Chem. Soc. 87: 1089-1095.

Mahoney, L. R., 1966, Inhibition of Free Radical Reactions. II. Kinetic Study of the Reaction of Peroxy Radicals with Hydroquinones and Hindered Phenols, J. Amer. Chem. Soc. 88: 3035-3041.

McMillen, D. F., Malhotra, R., Chang, S.-J., Nigenda, S. E., Fleming, R. H., 1987, Mechanisms of hydrogen transfer and bond scission of strongly bonded coal structures in donor-solvent systems, Fuel, 66: 166611-1620.

Mill, T. and Hendry, D. G., 1980, Kinetics and Mechanism of Free Radical Oxidation of Alkanes and Olefins in the Liquid Phase, in Comprehensive Chemical Kinetics, Vol. 16., C. H. Bamford and C.F.H. Tipper, Ed., Elsevier, Amsterdam, pp. 1-83.

Mill, T., D. S. Tse, B. Loo, C. C. D. Yao, and E. Canavesi, 1992, Oxidation Pathways in Asphalt, 204th Meeting of the ACS, Washington DC, ACS Div. Fuel Chem. Preprints 37: 1367-1375

Mill, T., Jayaweera, I., and Ross, D. S., 1995, Hydrothermal Oxidation of Phenol, in Physical Chemistry of Aqueous Solutions, H. J. White, J. V. Sengers, and J. C. Bellows, Eds., Begell House, New York, pp. 589-592.

Nicholson, V., 1937, A Laboratory Oxidation Test for Bitumens, Proc. A.A.P.T. 9: 208-213.

Petersen, J. C., 1975, Quantitative Methods Using Differential IR for Determining Compound Types Absorbing in the Carbonyl Region in Asphalts, Anal. Chem. 47:112.

Petersen, J. C., 1986, Quantitative Differential Group Analysis of Asphalts Using Differential Infrared Spectrometry and Selective Chemical Reactions-Theor. and Applications, Preprint, 65th Ann. Tran. Res. Board Meeting, Washington, D.C., Jan. 13-17.

Petersen, J. C., S. M. Dorrence, M. Nazir, H. Plancher, and F. A. Barbour, 1981, Oxidation of Sulfur Compounds in Petroleum Residues: Reactivity-Structural Relationships, Div. Petrol. Chem., 181st Meeting of the ACS, New York, NY.

Traxler, R. N., 1961, Relation Between Asphalt Composition and Hardening by Volatilization and Oxidation. Proc. Assoc. Asphalt Paving Technologists 30: 359-373.

Walling, C., 1963, Free Radicals in Solution. John Wiley and Sons, New York.

Welborn, J. Y., 1984, Physical Properties as Related to Asphalt Durability: State of the Art. Trans. Res. Record 999: 31-37.

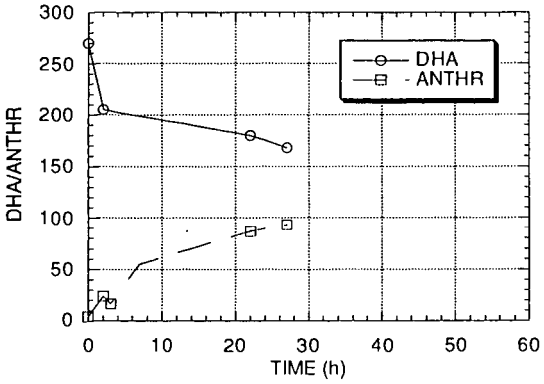

Figure 1. Conversion of 250 μM DHA to A in benzene in air at 100°C

Symposium on Modified Asphalts
Orlando, Florida, August 25-30, 1996

POLYPROPYLENE - ASPHALT MIXTURES FOR WATERPROOFING MEMBRANES

Paolo Italia, Ernesto Brandolese
Production process and modified asphalt project leaders
EURON S.p.A. (Research Company of AGIPPETROLI - ENI Group)
Via F. Maritano 26 - 20097 S. Donato Milanese (MI)
Italy

Keywords: polypropylene-asphalt mixtures, waterproofing membranes, Colloidal Instabiliy Index

Abstract
In any field of polymer-asphalt mixtures application is estremely important to achieve a very good compatibility between the components in order to improve as much as possible the performances due to the polymer content.
In the case of waterproofing membranes application this compatibility reduce, moreover, the amount of polymer required to obtain the best performances.
Using the Colloidal Instability Index Ic, as measured by the Iatroscan device, we propose a correlation between asphalt's chemical characteristics and the polymer minimum amount sufficient to disperse in a stable way the asphalt itself in the polymeric matrix.
As a result, through the proposed correlation, with a simple asphalt composition analysis it is possible to predict its performance when mixed with polypropilene.
In the paper, beside the description of the Iatroscan analytical technique, we also present a method for determining phase inversion based on optical fluorescence microscopy performed on about 30 different samples of asphalt.
We also present the experimental correlation laws between the polymer amount at phase inversion and the asphalt single components content.

1 - Introduction

As a waterproofing material, the asphalt can be used in the industrial field in many different ways: it can be found in finished products such as waterproofing membranes, paints, pastes, mastics and oxidated asphalts.
In Europe, the waterproofing membranes are the most important market; according to the modern manifacture processes these membranes consist of a rigid support (for instance, polyester) impregnated with a mixture of asphalt, polymer and mineral filler.
Each company has its products and its processes and tries to minimize the polymer content (the most expensive material), maintaining at the same time some essential requirements as cold flexibility, thermal stability, and resistance to degradation caused by the atmospheric agents.
It is therefore very important the research for asphalts with good characteristics of compatibility with the polymers in use (mostly atactic polypropylene, a refuse of the isotactic polypropylene, or similar products); compatibility is the capability of the asphalt to combine homogeneously with the polymer, in order to achieve a morphologic structure in which the polymer prevails.
As a matter of fact, even if the mixture consists mostly of asphalt, the so-called reverse phase of the mixture can be achieved with the right quantity of polymer: in fact, the polymer incorporates the particles of asphalt. Only when the polymer prevails the characteristics of elasticity and resistance reach their maximum.

2 - Preparation and valutation of the asphalt/polymer mixtures

In the polymer-asphalt tests carried out in the Asphalt Laboratory of EURON, research company of AGIPPETROLI for energy sector, was used a propylene-base product, having the following characteristics:

melt viscosity at 190°C	mPas	100.000
softening point R. and B.	°C	>150
needle penetration	dmm	20
density at 23°C	g/cm3	0,9
viscosity number "J"	cm3/g	100
molecular weight	Mv	85.000
intrinsic viscosity	g/100ml	1,0
glass transition temperature	°C	<-30

The additivation was carried out according to the following procedure, starting with 200g of mixture at 10% of polymer and adding 2g of polymer each time:

- preheat the asphalt in a nitrogen flow at a maximum temperature of 120°C, in order to transfer 180g in a 250g can. Heat in a thermostated bath at 185°C with air and mix for 15 minutes with a slanted-pallet stirrer, at a speed of 600 rpm;
- add 20g of polymer (10% in the mixture) in small doses, stirring it for 60 minutes, at a constant temperature of 185°C;
- take two drops of the mixture with a glass rod and place them on a slide; these drops must be at once cooled in distilled water, and then dried with a compressed air flow;
- observe then with a fluorescence microscope: observe at least three areas in order to remark possible cases of dishomogeneity (take a small part of the second drop in order to verify the reverse phase even in the sample). Two characteristics must be found in order to ascertain the reverse phase: the continuous polymer phase (white field) with small black drops representing the discontinuous asphalt phase, and the homogeneous scattering of the small drops (see the following pictures);
- if there is no reverse phase, add 2g more of polymer (about 1% more than the previous mixture), and, after stirring for 30 minutes at the constant temperature of 185°C, observe with the fluorescence microscope according to the previous procedure. The test continues according to the procedure until the reverse phase is determined.

In the following pictures it's possible observe no reverse phase (13% of polymer) and reverse phase (16% of polymer) for sample number 9.

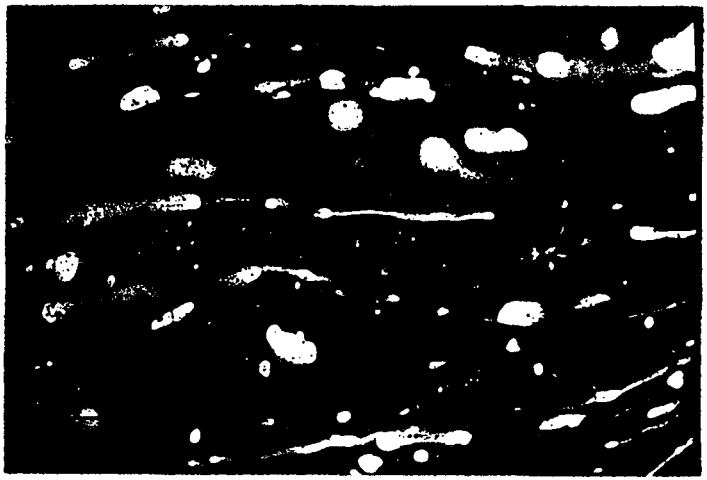

Sample number 9, 13% of polymer: no reverse phase

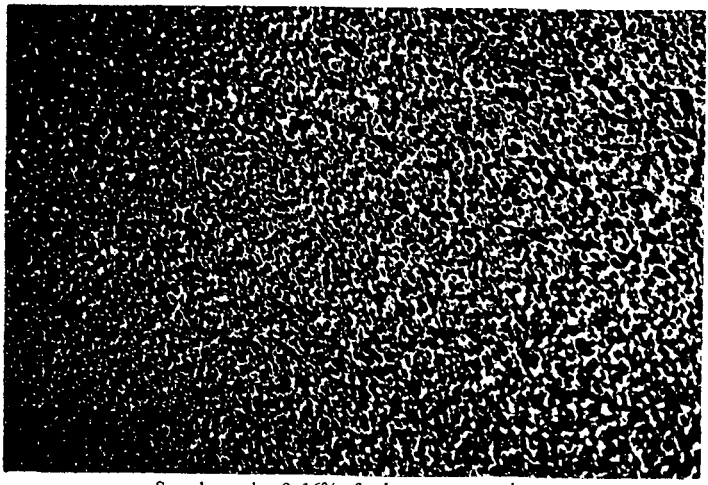

Sample number 9, 16% of polymer: reverse phase

3 - Asphalts characteristics

For each asphalt used in the previous mixtures (27 samples), was determined the usual characteristics and the Colloidal Instability Index with the thin layer chromatographer Iatroscan. The index is the ratio between asphaltenes + saturated and resins + aromatic compounds.

The Iatroscan analysis (mod. MK-5) is a thin layer chromatography (TLC) connected to a patented Flame Ionization Detector, similar to the FID used in gaschromatography. The main difference between the usual TLC and the Iatroscan analysis is that the plate is substituted by a frame consisting of ten small quartz bars, covered by a thin layer of silicon dioxide or sintered alumina, applied with a special technique.

At the end of each bar place with a microsyringe a microliter of the solution at 1% of asphalt in dichloromethane; after completing the frame, put it under elution with solvents in a series of three spot resolution chambers for TLC. After each resolution, eliminate the eluent through stove evaporation. Using the stationary phase of the silicon dioxide and the action of the mobile phase, it is possible to separate the substances according to the degree of polarity and similarity to the solvent. For the asphalts, start with the normal-hexane in order to separate the satured compounds, then use a mixture toluene/normal-hexane for the aromatic compounds, and finish with a mixture of dichloromethane/methanol for the resins which have strong polar characteristics. All that remains on the glass rod is asphaltene.

At the end of the resolution phases, the frame must be placed in an appropriate part of the instrument; here the small bars keep on passing between the two poles of the detector for all its length at constant speed; the process is fully automatic. The organic substances which have been separated on the thin layer are therefore ionizated by the flame and their quantity can be measured. The instrument software makes also possible the data elaboration and the calculation of the per cent composition of the mixture using the method of the normalization of the peak area.

In the following tables the characteristics of the asphalts used in this experimentation are reported together with the chemical composition, the Colloidal Instability Index and the polymer amount necessary to achieve the reverse phase according to the previously described procedure.

sample number		1	2	3	4	5	6	7	8	9
penetration	dmm	257	254	190	194	182	193	185	217	190
softening point R. B.	°C	40.5	41	42.5	39	42	38.5	38.5	39	43
asphaltenes	%wt.	27.4	25.4	20.7	24.1	28.4	23.7	24.5	25.4	25.0
satured	%wt.	8.8	8.9	3.6	2.4	4.2	6.6	3.4	4.2	5.3
resins	%wt.	25.8	27.8	18.7	24.5	21.9	28.3	33.1	30.8	34.3
aromatics	%wt.	38.0	37.9	57.0	49.0	45.5	41.4	39.0	39.6	35.4
index Ic	-	0.57	0.52	0.32	0.36	0.48	0.43	0.39	0.42	0.43
polymer	%wt.	11	13	20	18	14	16	17	16	16

sample number		10	11	12	13	14	15	16	17	18
penetration	dmm	175	172	167	190	165	206	174	155	134
softening point R. B.	°C	40.5	42	45	39	43	39	42	45	43
asphaltenes	%wt.	21.1	25.2	25.5	24.7	23.8	14.8	25.0	28.3	21.6
satured	%wt.	4.1	4.4	2.2	3.6	4.8	4.0	4.7	5.3	3.8
resins	%wt.	37.2	40.1	23.6	33.5	22.2	23.3	18.8	24.1	22.8
aromatics	%wt.	37.6	30.3	48.7	38.2	49.2	57.9	51.5	42.3	51.8
index Ic	-	0.34	0.42	0.38	0.39	0.40	0.23	0.42	0.51	0.34
polymer	%wt.	18	16	18	16	16	24	16	14	22

sample number		19	20	21	22	23	24	25	26	27
penetration	dmm	165	245	168	190	205	155	163	199	190
softening point R. B.	°C	45.5	36	40,5	39	37,5	45	42,5	41	42
asphaltenes	%wt.	28.0	23.2	19.8	19.0	24.9	19.4	21.7	31.9	17.8
satured	%wt.	7.3	4.7	3.6	7.1	3.7	5.3	4.7	6.3	2.7
resins	%wt.	26.2	19.9	23.2	18.6	21.1	24.5	24.2	22.3	16.8
aromatics	%wt.	38.5	52.2	53.4	55.3	50.3	50.8	49.4	39.5	62.7
index Ic	-	0.55	0.39	0.31	0.35	0.40	0.33	0.36	0.62	0.26
polymer	%wt.	13	17	21	18	16	19	18	10	22

4 - Conclusions

Averaging the previously reported data, for each polymer amount at the reverse phase used in the present work, an optimum distribution of the four main asphalt's components has been calculated and related to the Colloidal Instability Index Ic.

content of polymer		10%	11%	13%	14%	16%	17%
asphaltenes	%wt.	31.9	27.4	26.7	28.3	24.6	23.2
satured	%wt.	6.3	8.8	8.1	4.8	4.8	4.7
resins	%wt.	22.3	25.8	27.0	23.0	28.0	19.9
aromatics	%wt.	39.5	38.0	38.2	43.9	42.6	52.2
index Ic	-	0.62	0.57	0.53	0.49	0.42	0.39

content of polymer		18%	19%	20%	21%	22%	24%
asphaltenes	%wt.	22.9	19.4	20.7	19.8	19.7	14.8
satured	%wt.	3.2	5.3	3.6	3.6	3.2	3.9
resins	%wt.	23.9	24.5	18.8	23.2	19.8	23.4
aromatics	%wt.	50.0	50.8	56.9	53.4	57.3	57.9
index Ic	-	0.35	0.33	0.32	0.31	0.30	0.23

From figures of the previous table, it could be concluded that:

1) A poor compatibility is mainly related to an high aromatic and low saturated and asphaltenes content.
   In fact, in the interval of polymer content at the phase inversion from 10 to 24%, we observe a 50% of aromatic increment and a 50% of saturated compounds and asphaltenes decrement, while resins change only about 10%.
2) Only asphalts having an Ic > 0.5 (more then 1/3 of asphaltenes + saturated compounds and less then 2/3 of resins + aromatic compounds) give high polimer compatibility, with reverse phase from 10 to 13% of polymer.

In the next figures it is possible to obtain the trend of the polymer content at the reverse phase as a function of colloidal instability index Ic and as a function of asphaltenes, saturated components, resins and aromatics.
According to the values reported in the Figure 1, it is possible to define the following law of correlation between the polymer amount at the reverse phase and the colloidal instability index:

$$\% \text{ polymer} = 33.9 - 41.7 \times Ic$$

Using this correlation is further possible to calculate the polymer amount at reverse phase for each asphalt type avoiding to prepare and evaluate various experimental mixture.

Figure 1

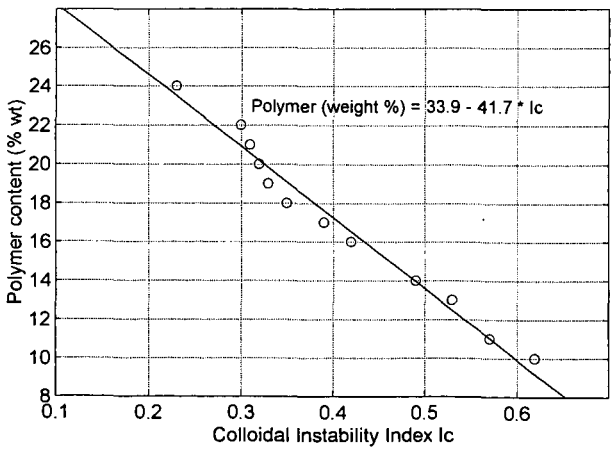

Figure 2

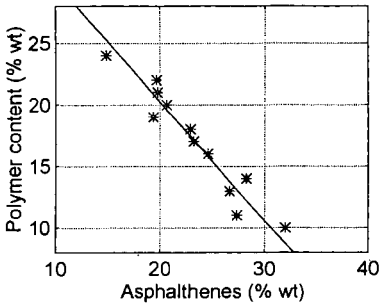

Figure 3

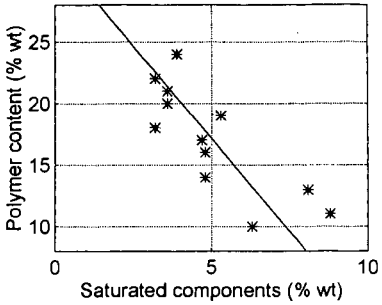

Figure 4

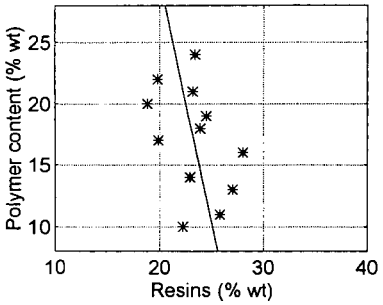

Figure 5

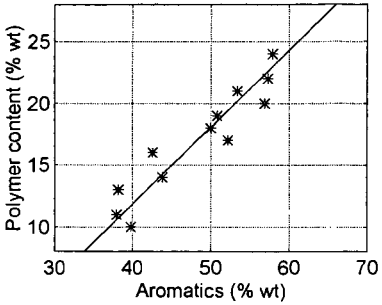

SLOW MECHANICAL RELAXATION IN ASPHALT

J. Stastna and L. Zanzotto
Department of Civil Engineering, The University of Calgary
Calgary, Alberta, Canada T2N 1N4

Key words: asphalt, stretched exponential, dynamic functions

INTRODUCTION

Asphalt (or bitumen) is one of the earliest construction materials used by mankind. However, despite the long history of its use and the important role it plays at the present time, in the construction of pavements, the composition and especially the structure of asphalt is still not fully understood. It is generally believed that asphalt is a multiphase system in which the large and polar molecules called asphaltenes, or their agglomerates are dispersed in the medium consisting of the smaller molecules with low or no polarity. Opinions on how the asphalt structure is arranged vary (1, 2, 3). The study of asphalt structure is made extremely difficult by the nature of this material. Non-invasive methods such as dynamic mechanical or electric testing, which investigate the asphalt in its original state may greatly contribute to our knowledge of the asphalt internal structure.

STRETCHED EXPONENTIAL RELAXATION

Around 1835, in Gottingen, Wilhelm Weber made the first systematic investigation of elastic "after-effect" in silk and glass threads (4). He noted that a weight suspended from such fibres generates an instantaneous elongation followed by an additional time dependent strain which recovered when the load was removed. For the dependence of displacement x on time t, Weber used a power law. The problem of after effect (creep in modern terminology) has been further studied by Rudolf Kohlrausch. He noticed the analogy with time dependent electric displacements, q, in charged capacitors and proposed for this effect the stretched exponential law: $q(t) = q_0 + \exp(-(t/\lambda)^{\alpha})$. In 1863 Frederick Kohlrausch (5) (the son of Rudolf) used the stretched exponential as an empirical fit for creep and relaxation data in silk and glass fibres and in rubber. The stretched exponential law has been revived after more than one hundred years in the study of dielectric relaxation. Usually the analysis of dielectric relaxation in polymers is focused on the complex dielectric "constant" $\varepsilon^*(\omega)$ and its deviation from the form derived from a single relaxation time (6). A change of interest from frequency to time, i.e. from ε^* to the relaxation function $\phi(t)$ has been generated by the work of G. Williams and D. Watts (7). They found that the stretched exponential can fit data for many glassy and polymeric materials. In the past decade this form has been used to fit a wide variety of experimental data, dielectric, enthalpic, dynamic light scattering, magnetic relaxation, reaction kinetics, etc. (8). The possibility to use the stretched exponential in regular and polymer modified asphalts is discussed in the next paragraph.

STRETCHED EXPONENTIAL AND DYNAMIC MATERIAL FUNCTIONS

As usually we assume that for small deformations, the general linear viscoelastic constitutive equation is valid, i.e.

$$\underset{\sim}{\tau}(t) = \int_{-\infty}^{t} -M(t-t')\,\underset{\sim}{\gamma}(t,t')dt' = \int_{-\infty}^{t} G(t-t')\,\dot{\underset{\sim}{\gamma}}(t,t')dt' \qquad 1)$$

Here, $M(t-t') = M(s) = -dG(s)/ds$; M represents the fluid memory, and G is the relaxation modulus (relaxation function). Extra stress tensor $\underset{\sim}{\tau}$ is related to the strain tensor $\underset{\sim}{\gamma}$, or to the rate of strain tensor $\dot{\underset{\sim}{\gamma}}$ via 1). In the case of small amplitude oscillatory shear motion the complex modulus $G^*(\omega)$ is given as (9)

$$G^*(\omega) = i\omega \int_0^{\infty} G(s)\exp(-i\omega s)ds \qquad 2)$$

Assume that the relaxation function, G(s) has the form of stretch exponential,

$$G(s) = C\exp(-(s/\lambda)^{\beta}) \qquad 3)$$

where C, λ, and β are constants.

Using the series representation of exponential function, and the definition of gamma function, the complex modulus $G^*(\omega)$ corresponding to the stretched exponential relaxation can be formally written as

$$G^*(\omega) = C\sum_{k=0}^{\infty} \frac{\Gamma(\beta k+)}{k!}\cos\left(\frac{\pi}{2}(2-\beta)k\right)\left(\frac{1}{\omega\lambda}\right)^{\beta k} + iC\sum_{k=0}^{\infty} \frac{\Gamma(\beta k+1)}{k!}\sin\left(\frac{\pi}{2}(2-\beta)k\right)\left(\frac{1}{\omega\lambda}\right)^{\beta k} \quad 4)$$

Introducing

$$\lambda^{-\beta} \equiv \alpha \quad 5)$$

the storage and the loss moduli generated by the stretched exponential relaxation function 3) are given as follows:

$$G'=(\omega) = C\sum_{k-0}^{\infty} \frac{\Gamma(\beta k+1)}{k!}\left(\frac{\alpha}{\omega\beta}\right)^{k} \cos\left(\frac{\pi}{2}(2-\beta)k\right) \quad 6)$$

$$G''(\omega) = C\sum_{k=0}^{\infty} \frac{\Gamma(\beta k+1)}{k!}\left(\frac{\alpha}{\omega\beta}\right)^{k} \sin\left(\frac{\pi}{2}(2-\beta)k\right) \quad 7)$$

It is clear that these series representations of the components of the complex modulus do not converge for all $\omega\in(0, \infty)$. However, by choosing a finite frequency subinterval $\omega\in(a, b)$ one can always find the values of parameters λ, β, and C in such a way that the series in 6) and 7) will approximate, with the prescribed precision, G′ and G″ on (a, b). This idea is applied in the next paragraph to one regular and one polymer modified asphalt.

REGULAR ASPHALT MODIFIED BY SBS POLYMER

Dynamic material functions of a regular asphalt 200/300 Pen grade have been dynamically tested at different temperatures and the master curves of G′ and G″ (ref. T=0 °C) prepared by the time temperature shifting. The mentioned regular asphalt has been modified by SBS copolymer. It is known (10) that SBS copolymer exhibits a rheological transition from Newtonian to non-Newtonian behavior at a region of higher temperature. In the low temperatures the SBS system is plastic with a yield stress. It is believed (10) that such a transition is generated by a transition of the structure from microphase-separated state to the homogeneous state.

Again the dynamic material functions of this PMA (polymer modified asphalt) have been measured and the master curves of G′ and G″ prepared. The shift factor a_T for these master curves was fitted to Arrhenius and WLF forms.

The domain of experimental master curves G′ and G″ for the regular 200/300 Pen grade asphalt, is log $\omega\in$[-5. 6, 7] and we have found that the series representations 6) and 7) can be used for this sample if the domain is subdivided into three subdomains. These subdomains are: A = {log $\omega\in$[-5.6, 1]}, B = {log $\omega\in$[-1, 2.5]}, *C* = {log $\omega\in$[2.5, 7]}. The given subdomains represent a minimum number of subintervals covering the domain of the master curve for regular asphalt 200/300 Pen grade, in the sense that minimally three stretched exponential; relaxation functions 3) are necessary for the description of the whole master curves G′ and G″. The parameters of the stretched exponentials in all three subdomains are: in A, α = 7.479, β = 0.0857, C = 4.075e+09; in B, α = 6.1826, β = 0.1346, C = 9.4056e+08; in *C*, α = 10.0824, β = 0.237, C = 4.231e+08

The storage, G′, and the loss, G″, moduli were calculated according to Equations 6) and 7). In these calculations the sums of series were terminated when the absolute value of the next term was less than 10^{-9}, thus strictly speaking the calculated values of G′ and G″ are approximations. The compositions of calculated G′ and G″ are compared with the experimental data (master curves at reference T = 0 °C) in Figs. 1, 2. The high frequency (low temperature) behavior is better seen in Fig. 2. The graph of G″ clearly shows the maximum of G″. The high frequency behavior of G′ is probably overestimated by the series approximation in the subdomain C. However, it is also possible that the last three experimental points of Fig. 1 represent the region which is difficult to access experimentally - these points are measured at T = -30 °C, i.e. roughly around the glass transition temperature (T_g ≈ -27 °C).

The domain of experimental master curves G′ and G″, for the PMA is log $\omega\in$[-8, 7.4]. The minimum number of subdomains, covering this domain in the sense of data fit to the least number of stretched exponentials, is four. The subdomains are: $\overline{A}$ = {log $\omega\in$[-8, -2.8]}; $\overline{B}$ = {log $\omega\in$[-2.8, 3.5]}, $\overline{C}$ = {log $\omega\in$[3.5, 5.4]}; $\overline{D}$ = {log ω>5.4}. The last subdomain, $\overline{D}$, covers the interval of low temperatures (again around the T_g of the base asphalt 200/300) Pen grade, and the caution is in place in considering the experimental data in this region. Experimental data were

again fitted to the stretched exponential relaxation, i.e. the series representation 6) and 7) were used in each subdomain. Parameters of the stretched exponentials in these subdomains are: in $\overline{A}$, $\alpha = 4.369$, $\beta = 0.0792$, $C = 3.76e{+}07$; in $\overline{B}$, $\alpha = 7.931$, $\beta = 0.081$, $C = 4.186e{+}09$; in $\overline{C}$, $\alpha = 11.112$, $\beta = 0.2174$, $C = 3.92e{+}08$; in $\overline{D}$, $\alpha = 27.03$, $\beta = 0.3034$, $C = 3.02e{+}08$. The compositions of calculated G', and G" are compared with the experimental data (master curves) in Figs. 3, 4. It is clear that at highest frequencies (lowest temperatures) the fit is not as good as in frequencies $\log \omega \leq 6$. Again one has to stress the experimental difficulties in this region of temperatures.

DISCUSSION

The stretched exponential relaxation function seems to be able to generate reasonably accurate storage and loss moduli for both regular and polymer modified asphalts. The series representation 6) and 7) can be used for the estimates of $G'(\omega)$ and $G''(\omega)$ on any finite subinterval of frequencies. It is clear from the results obtained in the previous paragraph that the parameters of the stretched exponential relaxation function depend on the temperature. Not surprisingly the "relaxation" time λ is very low (order 10^{-11} for regular asphalt, and order 10^{-9} for PMA) at the lowest reduced frequencies (highest temperatures) where asphalts have a Newtonian behavior. On the other hand, at high reduced frequencies (temperatures around T_g in the studied case) the value of λ, in both neat and modified asphalts is of order 10^{-5}.

There are now several mechanisms proposed for the stretched exponential (6), one of the most interesting is the defect diffusion model (7). According to this model, mobile defects move randomly through the medium and generate local conformal abnormalities in the system. On leaving the site of such a local disturbance the defect will cause a disturbance at some other site of the medium. After some time, the neighbourhood of the disturbed "particle" will relax, as the system returns to equilibrium. Thus the migration of defects may cause a mechanical relaxation. If there is a finite concentration (c) of defects, the probability that the "particle" will be reached at time by one of the N defects in a volume N/c is given as (12).

$$\phi(t) = \exp(-cI(t)) \qquad 8)$$

Here I(t) is the number of distinct "particles" attacked by a defect at time t. If each defect undergoes a random walk with the pausing-time distribution $\psi(t)$ there are two important classes of $\psi(t)$. In the first case the form of ψ is exponential

$$\psi(t) \sim \exp(-\lambda t), \quad \lambda = \text{const.} \qquad 9)$$

After some time this becomes a classical diffusion which leads to Debye's result (6), $\phi(t) = \exp(-t/\lambda)$, in three-dimensional case. The second case are distributions with an inverse-power tail

$$\psi(t) \sim t^{-(1+\alpha)}, \quad 0 < \alpha < 1 \qquad 10)$$

In this case

$$I(t) \sim \begin{cases} t^{\alpha} & \text{in 3 dimensions} \\ t^{\alpha/2} & \text{in 1 dimension} \end{cases} \qquad 11)$$

Substituting 11) into 8) one obtains the stretched exponential form. The defect diffusion model is based on the movement of defects. However, the nature of defects is not known, and many possibilities have been suggested. For example, it has been suggested that a mobile carbonate (CO_3) bond is the "defect" in some high-impact resins, (13). In the case of studied asphalts one can see that the exponent β is of order 10^{-2} at higher temperatures and almost four times larger at low temperatures (around T_g of the base asphalt). Thus the "defect" seems to move in a quasi-one-dimensional motion at higher temperatures and perform a three-dimensional walk at temperatures close to T_g.

In conclusion, it appears that the stretched exponential is important not only in theoretical analysis of complex systems, but can also be successfully used in direct modelling of the stress relaxation in such systems. Such modelling in crack sealants will be discussed elsewhere.

ACKNOWLEDGMENT
The authors would like to express their gratitude to Husky Oil Ltd. and to the Natural Sciences and Engineering Research Council of Canada for their financial support of this project.

LITERATURE CITED
(1) Yen, T.F., Advances in Chemistry Ser., Ed. M.J. Comstock, ACS, 195, 139 (1981).
(2) Speight, J.G., Moschopedis, S.E., Advances in Chemistry Ser., Ed. M.J. Comstock, ACS, 195, 1 (1981).
(3) Neuman, H.J., Rahimian, J., Bitumen, 35, 1 (1973).
(4) Mandelbrot, B.B., "The Fractal Geometry of Nature", Freeman, NY, (1982).
(5) Kohlrausch, F., Pogg. Ann. Phys., 119, 352 (1863).
(6) Debye, P., "Polar Molecules", Lancaster Press, Lancaster, Pa., (1929).
(7) Williams, G., Watts, D.C., Trans. Fasad. Soc., 66, 80 (1970).
(8) Kakalios, J., "Hopping and Related Phenomena", World Scientific, Singapore, (1990).
(9) Stastna, J., Zanzotto, L., Ho, K., Rheol. Acta, 33, 344 (1994).
(10)Watanbae, H., Kawahara, S., Kotaka, T., J. Rheol., 28, 393 (1984).
(11)Palmer , R.G., Stein, D., Abrahams, E.S., Anderson, P.W., Phys. Rev. Lett., 53, 958 (1984).
(12)Shlesinger, M.F., Montroll, E.W., Proc. Natl. Acad. Sci. USA, 81, 1280 (1984).
Bendler, J.T., Ann. N.Y. Acad. Sci., 371, 299 (1981).

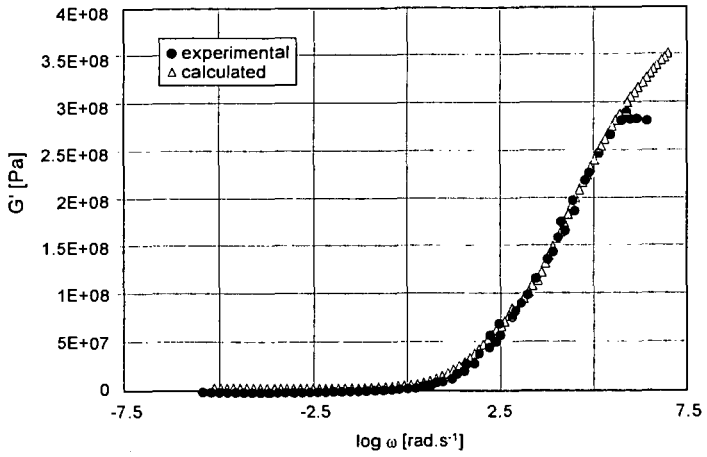

Figure 1. Regular asphalt, G'.

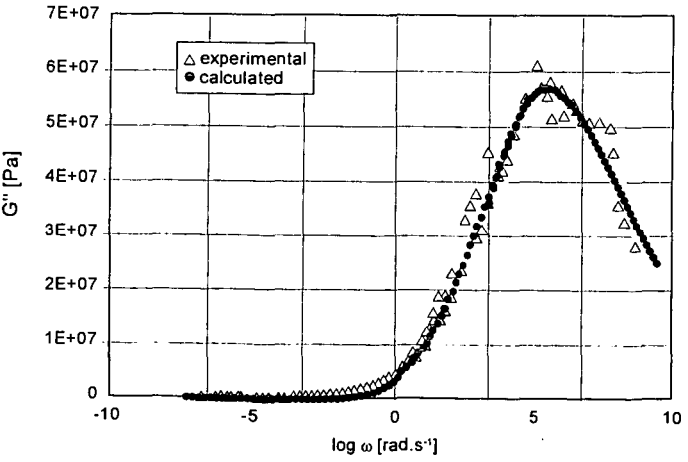

Figure 2. Regular asphalt, G".

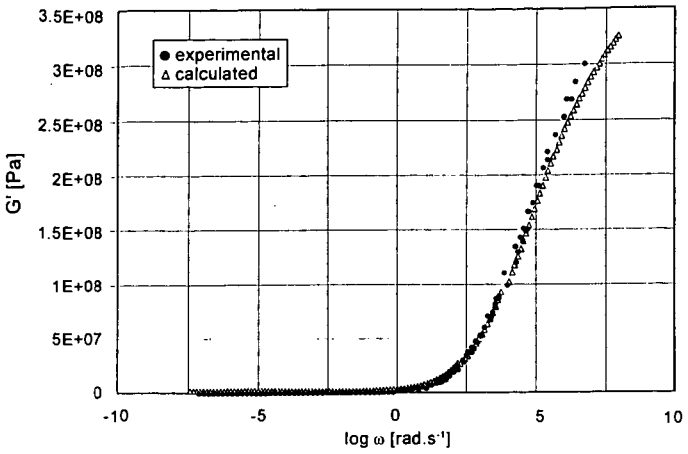

Figure 3. Polymer modified asphalt, G′.

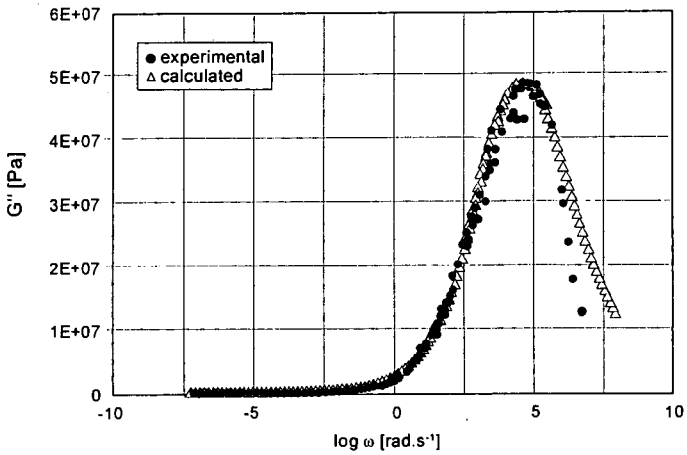

Figure 4. Polymer modified asphalt, G″.

MOLECULAR DYNAMICS AND THE STRUCTURE OF ASPHALTS AND MODIFIED ASPHALTS AT LOW TEMPERATURES

Daniel A. Netzel, Thomas F. Turner, and Francis P. Miknis
Western Research Institute
365 North 9th Street
Laramie, WY 82070

Jeni Soule and Arland E. Taylor
Chemical and Petroleum Engineering Dept.
University of Wyoming
Laramie, WY 82071

Keywords: Asphalts, NMR, Molecular Dynamics

INTRODUCTION

One important fundamental molecular property of an asphalt, which dictates its temperature dependent performance, is the nature of molecular motions associated with the asphalt molecular components. At any given temperature, the extent of molecular motions depends on the intramolecular configuration of the various asphalt components and the manner in which they interact by intermolecular association. Molecular association tends to restrict molecular motions. Changes in structure and composition brought about by chemical reaction with oxygen as a result of aging also strongly affect overall molecular motion in asphalts through enhanced molecular association, which, in turn, affects the overall long term road performance behavior of asphalts.

On a macro scale the performance behavior of asphalts is manifested in changes in the viscoelastic nature of asphalts, that is, changes in their rheological properties. Thus, an understanding of the molecular dynamics should be helpful in the understanding of the viscoelastic nature of asphalts and in predicting the asphalt composition which optimize binder performance. The molecular mobility can be altered through modification of the asphalt chemically, by the physical blending of two or more asphalts, or the introduction of polymeric materials or other additives to asphalts.

The type and extent of molecular motions can be obtained from hydrogen-1 and carbon-13 nuclear magnetic resonance (NMR) relaxation time measurements. These measurements can provide quantitative information on the molecular structure and degree of molecular motions associated with the hydrogen and carbon types and/or groups in asphalts. Because asphalts are solid-like materials, the molecular motions of interest are low frequency, on the order of 1-50 kHz. The motions of most interest for components of asphalt are methyl rotation, segmental motions (full and/or partial rotation of segments) of the long-chain aliphatic hydrocarbons, and phenyl twisting (torsional oscillation). Figure 1 illustrates the different kinds of motions in a complex asphaltic-like molecule. The structure shown in Figure 1 is a simplification of the "average" structure of the molecules found in asphalt as determined from liquid-state NMR parameters. The structure in Figure 1 consists of polycondensed aromatic carbons with methyl and long-chain hydrocarbon group substituents. The complete "average" structure consists of several methyls and long-chain hydrocarbon groups attached to the aromatic carbon cluster. Generally, there are ~ 30% aromatic carbons and ~ 70% aliphatic carbons in an average "asphaltic" molecule. Not shown in the figure are the heteroatoms which are also of major importance to asphalt chemistry.

EXPERIMENTAL

Solid-state ^{13}C NMR measurements were made using a Chemagnetics 100/200 solids NMR spectrometer operating at a carbon frequency of 25 MHz. Variable contact times experiments were conducted using a 7.5 mm rotor spinning at a rate of 4.5 kHz. Other parameters included a pulse width of 5 μs, pulse delay of 1 s, a sweep width of 16 kHz, 1024 data acquisition points, and between 3000 and 7200 transients. Dipolar dephasing spectra were obtained at a contact time of 1 ms. Low temperatures were obtained using a FTS systems XR Series Air-Jet Sample Cooler. The asphalts were selected from the Strategic Highway Research Program (SHRP) Materials Reference Library.

RESULTS AND DISCUSSION

A stack plot of the dipolar dephasing NMR spectra for asphalt AAM-1 at -45°C is shown in Figure 2. These spectra illustrate the chemical shift position of the different carbon types and clearly show the different relaxation rates at -45°C for the different carbon types. The aromatic carbon region (110-150 ppm) is resolved into quaternary (C, ~ 130-150 ppm) and tertiary (CH, 110-130 ppm) carbon types. The tertiary carbon signals decay much faster than the quaternary carbons. At a dephasing time of 160 μs, the only remaining aromatic carbons are the quaternary carbons which span

the region from 110-150 ppm. Thus, it appears that about 50% of total aromatic quaternary carbons are hidden under the tertiary carbon peak at a dephasing time of 1 μs which approximates a standard cross-polarization experiment. The amount of quaternary carbons dictates the size of the aromatic cluster. Thus, a simple integration of the aromatic region will underestimate the total aromatic quaternary carbons.

The rate of change of the aliphatic carbon types is quite dramatic. Almost all of the methine (CH) and methylene carbons (CH_2) (30-50 ppm) have decayed after a dephasing time of 80 μs. In addition, the sharp methylene peak at 32 ppm decays much faster than the methylene shoulder at 30 ppm. The decays of the methyl carbons (15-30 ppm) are much slower than the other carbon types.

The methyl (CH_3) carbons attached to aromatic rings and branched to a linear main-chain hydrocarbon have resonance peaks in the region of 20-30 ppm. These methyl carbons decay faster than the terminal methyl carbons (15 ppm) of a long chain hydrocarbon. The longer relaxation rates for the two methyl carbon types relative to the methylene and methine carbons are due to the faster rotation motions of the methyl carbons compared to the much slower segmental motions of the methylene and methine carbons. It should be noted that the branched methyl carbons decay faster than the terminal methyl carbons indicating that the branched methyl carbons are rotating slower because of hindrance to rotation than the terminal methyl carbons.

$T_{1\rho}{}^H$ of Asphalts and Modified Asphalts

The hydrogen rotating-frame spin-lattice relaxation time constants ($T_{1\rho}{}^H$) have been used as a probe to study the structure of polymer blends.[1,2] The $T_{1\rho}{}^H$ values are determined by the rate of hydrogen spin-diffusion throughout the sample, which in turn depends upon the homogeneity of the blends and extent of molecular motion.

Figure 3 shows the NMR variable contact time CP/MAS data for Conoco Denver Asphalt and the asphalt modified with 2% Elvaloy® AM (an ethylene acrylate copolymer). The $T_{1\rho}{}^H$ values are derived from the slope of the lines between contact times of 0.5 and 6 ms. The $T_{1\rho}{}^H$ for the Conoco asphalt at 23°C was found to be 1.34 ms and for the 2% Elvaloy AM® modified asphalt the $T_{1\rho}{}^H$ value was found to be 0.92 ms. The smaller relaxation time for the modified asphalt suggests that the correlation time for molecular motion is faster. That is, the overall molecular motions within the asphalt were increased at 23°C. With the limited data, it appears that the modified asphalt is a homogeneous blend based on the fact that only one $T_{1\rho}{}^H$ value represents the data.

Figure 4 shows the variable contact time CP/MAS data for Cenex asphalt (a Wyoming AC-20 asphalt) and the asphalt modified with 3% Butonal® NS175 polymer (a cold polymerized anionic styrene-butadiene dispersion). The $T_{1\rho}{}^H$ values for the asphalt and modified asphalts were found to be 1.41 and 1.09 ms, respectively. Based on the smaller relaxation time for the modified asphalts, the molecular motions were enhanced at 23°C. There is evidence that a second $T_{1\rho}{}^H$ could be fitted to the data suggesting therefore that two domains exist in the asphalts. Additional data will be needed to confirm the observation.

The conclusion of enhanced molecular motions (as suggested from the $T_{1\rho}{}^H$ measurements) for the modified asphalts was limited to one temperature (23°C). To fully understand the dynamic behavior of the polymer modified asphalts, measurements must be made over a range of temperatures. The next section describes the methodology used to quantify the extent of molecular motion in asphalts over a temperature range from +20 to -45°C.

Molecular Mobility in Asphalts at Low Temperature

An important feature in the NMR spectra of any material is the increase in the signal-to-noise ratio as the temperature is decreased. The increase in the signal is due to the difference in the population of nuclear spins in the ground state relative to a higher energy state. That is, as the temperature is lowered, the number of spins increases in the ground state increasing the spin differences between the energy states resulting in an increase in the intensity of the NMR signal. The increase in signal can be predicted from the Boltzmann distribution equation and nuclear spin theory. The total spin magnetization, M_o, at any given temperature is given by equation 1.[3]

$$M_o = N\gamma^2\hbar^2H_o/4kT \qquad (1)$$

where:

N = The number of spins in the sample
γ = gyromagnetic ratio of carbon
$\hbar$ = Planck's constant divided by 2π
Ho = Static magnetic field
k = Boltzmann constant
T = Temperature

Because the carbon-13 magnetization is proportional to the NMR spectral integrated area of the carbon moiety of interest ($M_o \propto A$), the relative increase in carbon magnetization (integrated signal area) can be obtained from the ratio of the two temperatures at which the NMR spectra were obtained (Eq. 2).

$$A_2/A_1 = T_2^{-1}/T_1^{-1} \quad (2)$$

Sullivan and Maciel[4] used equation 2 to show that the increase in the NMR signals for Powhatan #5 coal at temperatures below 21°C is due only to the Boltzmann factor (ratio of the absolute temperature). Coal is a very rigid solid without any apparent or significant molecular motion in the range of 10 to 50 kHz throughout the low temperature range. Because of the lack of molecular motion in coal, the dipolar interaction of the carbons and hydrogens in a cross-polarization experiment is very efficient, whereby, most of the carbons are observed at all temperatures and the increase in signal intensity in coal with decreasing temperature is due only to the Boltzmann factor. Figure 5 shows the change in the CP/MAS spectra of asphalt AAA-1 obtained at temperatures of 20 and -45°C. For the same set of conditions, the signal-to-noise ratio in the NMR spectrum at -45 is considerably better than for the spectrum taken at 20°C. Note also that the signal of the methylene carbons (32 ppm) at -45°C is greatly enhanced relative to the signal at 20°C. The signal enhancement is greater than that predicted by the Boltzmann Factor.

Table I lists the relative signal enhancement, A_{max} (t) / A_{max} (20°C), normalized to 20°C data, for the aliphatic carbons in asphalts AAA-1, AAB-1, and AAM-1 at 20, 0, -10, -20, -30, and -45°C. Also given in the table is the theoretical signal enhancement (T^{-1}/T^{-1}_{293}) expected based upon the ratio of temperatures relative to 20°C (293K). The maximum signal for aliphatic carbons was obtained at a contact time of 0.22 ms (independent of temperature). Figure 6 shows the NMR molecular-mobility/temperature profile plots of the aliphatic area ratios as a function of temperature for the three asphalts. Also shown in Figure 6 is the plot of the theoretical relative signal enhancement as a function of temperature based upon the Boltzmann spin population distribution relative to 20°C.

The ratio of the integrated areas for the aliphatic carbons of the three asphalts differ significantly from coal and from the theoretical signal enhancement due to the Boltzmann factor. These differences are the result of extensive molecular motions in asphalts which prevents effective cross-polarization of the carbon and hydrogen spins. However, as the temperature decreases, the molecular motion decreases, the molecular structure of asphalt becomes more rigid-like, the cross-polarization mechanism becomes more effective and, thus, more carbons are observed resulting in an increase in the integrated area ratio with decreasing temperature. Thus, the area ratio can be defined as a molecular rigidity parameter. That is, as the temperature decreases, the molecular structure becomes more rigid-like.

Asphalt AAA-1 shows a greater enhancement of the aliphatic carbon NMR signal over the temperature range from +20 to -45°C than asphalt AAB-1 which, in turn, shows a greater enhancement than asphalt AAM-1. The greater the relative enhancement at any given temperature the more molecular motion involved for the asphalts. Thus, the extent of segmental and rotational motions of the aliphatic carbons in the asphalts can be ranked as follows: AAA-1 > AAB-1 > AAM-1. This ranking is in the same relative order as the glass-transition temperature, viscosities, and various other rheological properties. As shown in Figure 6, for asphalt AAA-1, the relative signal intensity continues to increase after -45°C. A part of this increase is due to the increase in the Boltzmann factor for the rigid-like carbons. In addition, the signal is expected to increase until the motions due to the presence of a significant amount of methyl rotation and some residual main-chain segmental motions of the aliphatic carbons are stopped. Much lower temperatures will be needed to stop most of these molecular motions. The data for asphalt AAM-1 shows a decrease in signal after -30°C. It has not yet been established whether or not the signal will continue to decrease after -45°C (due to temperature effects on other relaxation mechanisms which can affect the cross-polarization rate) or continue rising at a rate dictated by the Boltzmann factor.

The distinction among asphalts based upon the extent of molecular motions over the temperature range of 65°C for the aliphatic carbons suggest that asphalts modified with small percent of rubber or polymers may be amenable to this NMR technique. In addition, the NMR mobility/temperature profile methodology may be useful to study the rate of oxidation as it affects the motions of the aromatic and/or aliphatic carbons.

The NMR molecular-mobility/temperature profile plots of the asphalts follow qualitatively, but inversely, their DSC thermograms throughout the glass-transition region. The NMR plots describe the change in molecular mobility (molecular dynamics) with changing temperature, whereas, the DSC thermograms measure the changes in the thermal energy (molecular energetics) associated with molecular transitions with changing temperature. Both NMR and DSC data can be expressed using

a cumulative-Gaussian equation. A modified form of the equation was used to fit the NMR data shown in Figure 6 (see equation 3):

$$\rho = A_t/A_{20°C} = 0.5\rho_o\ (1 + erf\ [(t - T_{NMR})/(2^{0.5}\sigma)]) + 293.15/(273.15 + t) \quad (3)$$

where:

ρ	=	relative signal enhancement (A_t / $A_{20°C}$)
ρ_o	=	maximum change in relative signal enhancement
t	=	temperature, °C
T_{NMR}	=	Inflection point temperature, °C
σ	=	standard deviation of the distribution
erf	=	error function

The term, 293.15/(273.15 + t), applies the Boltzmann factor to the fit of the data. The coefficients (ρ_o, T_{NMR} and σ) in equation 3 for the aliphatic and aromatic carbons in the three asphalts are given in Table II. Also given are the onset temperatures for molecular motion for the carbon types in each asphalt. The onset temperature was obtained using equation 4.

$$T_{os}^{NMR} = T_{NMR} + (-2\sigma) \quad (4)$$

The standard deviation of the mean (2σ) encompasses 95% of the observed changes in molecular motion.

The NMR inflection point temperatures and the onset temperatures for significant molecular motions of the aromatic carbons are several degrees higher than the aliphatic carbons. That is, upon cooling the motions of the carbon atoms in the polycondensed aromatic rings are slowed down significantly while the long-chain aliphatic carbons and methyl carbons continue to have considerable segmental and rotational motions. In addition, the NMR inflection point temperature and the onset temperatures were found to be higher than the glass-transition temperature and onset temperature measured using DSC. The NMR inflection point temperatures were found to match more closely the defining temperatures of the asphalts.

The increase in the NMR inflection point temperatures and the onset temperatures going from asphalt AAA-1 to AAM-1 is in agreement with their known rheological and performance predictive properties. Asphalt AAA-1 is the softest (considerable amount of molecular motion) of the three asphalts and asphalt AAM-1 the hardest (the least amount of molecular motions). Thus, the softer the asphalt, the lower the temperature needs to be to stop most of the molecular motion.

CONCLUSIONS

Preliminary $T_{1\rho}^{H}$ data on asphalts and polymer modified asphalts suggest that this NMR relaxation technique can be used to measure the extent of the compatibility of the asphalts and polymer on the overall molecular motions of the asphalts. It is the extent of molecular motion which governs many of the rheological properties of the asphalts. NMR molecular-mobility/temperature profile plots of asphalts were found to follow qualitatively their DSC thermograms. Both the NMR inflection point temperature and the onset temperature for molecular motion were found to be higher than the glass transition temperature and the DSC onset temperatures. Because of the high degree of distinction for the different asphalts, the NMR profile plots should be useful in studying the molecular dynamics in modified asphalts.

REFERENCES

1. Natansohn, A., 1992, Polymer Engineering and Science, 32(22), 1711.

2. Simmons, A., and A. Natansohn, 1992, Macromolecules, 25, 1272.

3. Harris, R. K., 1983, "Nuclear Magnetic Resonance Spectroscopy," Pitman Publishing Inc., Marshfield, MA, p. 9.

4. Sullivan, M. J., and G. E. Maciel, 1982. Spin Dynamics in the Carbon-13 Nuclear Magnetic Resonance Spectrometric Analysis of Coal by Cross Polarization and Magic-Angle Spinning, Anal. Chem., 54, 1615-1623.

ACKNOWLEDGMENT

The authors express their appreciation to the Federal Highway Administration for their support of this program under FHWA Contract No. DTFH61-92C-00170. The authors express their thanks to Dr. Robert Statz and Dr. Richard Liu for supplying the polymer modified asphalts. Elvaloy® AM is a tradename of Dupont Company and Butonal® NS 175 is a tradename of BASF Corporation.

Table I. Carbon-13 NMR Aliphatic Carbon Area Ratios for SHRP Core Asphalts AAA-1, AAB-1 and AAM-1 from Variable Temperature Cross-Polarization Experiments

Temperature (t), °C (K)	Temperature Ratio, T^{-1}/T^{-1}_{293}	AAA-1		AAB-1		AAM-1	
		Integrated Area,[a] $A^{Al}_{max}(t)$	Area Ratio, $A^{Al}_{max}(t)/A^{Al}_{max}(20°)$	Integrated Area, $A^{Al}_{max}(t)$	Area Ratio, $A^{Al}_{max}(t)/A^{Al}_{max}(20°)$	Integrated Area, $A^{Al}_{max}(t)$	Area Ratio, $A^{Al}_{max}(t)/A^{Al}_{max}(20°)$
20 (293)	1.00	14.54	1.00	19.19	1.00	26.13	1.00
0 (273)	1.07	24.51	1.69	30.05	1.57	39.33	1.51
-10 (263)	1.11	28.75	1.98	34.99	1.82	46.36	1.77
-20 (253	1.16	35.48	2.44	43.00	2.24	53.67	2.05
-30 (243)	1.20	39.44	2.71	46.67	2.45	57.59	2.20
-45 (228)	1.29	44.75	3.08	52.06	2.71	56.75	2.17

[a] From maximum signal intensity for aliphatic carbons (ct = 0.22 ms)

Table II. NMR Parameters from the Molecular-Mobility/Temperature Profile Plots for the Aliphatic and Aromatic Carbons in Asphalts AAA-1, AAB-1, and AAM-1

Asphalt	Maximum Change in Signal Enhancement, ρ		Inflection Point Temperature, T_{NMR}, °C		Mean Standard Deviation, 2σ, °C		Onset Temperature for Molecular Motion,[a] T_{os}^{NMR}, °C	
	Aliphatic	Aromatic	Aliphatic	Aromatic	Aliphatic	Aromatic	Aliphatic	Aromatic
AAA-1	1.83	1.42	-10.6	-9.5	±38.5	±32.7	-49.1	-42.2
AAB-1	1.44	0.86	-9.1	-7.7	±35.4	±25.9	-44.5	-33.6
AAM-1	0.94	0.61	-2.2	+1.6	±23.9	±19.2	-26.1	-17.6

[a] Based on 2σ (95%) and excluding CH_3 rotation below -50°C.

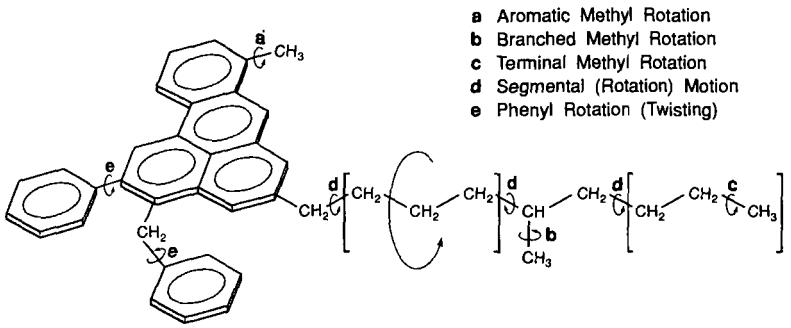

Figure 1. A Simplified "Average" Molecular Structure of Asphalt

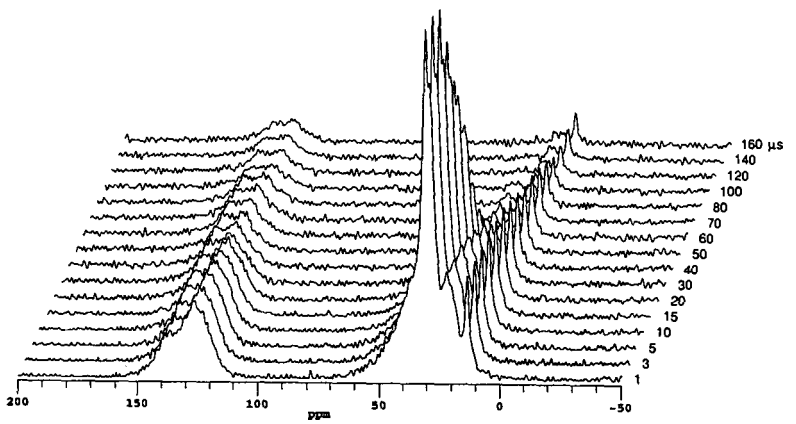

Figure 2. Stack Plot of the ^{13}C Dipolar-Dephasing NMR Spectra for Asphalt AAM-1 at -45°C

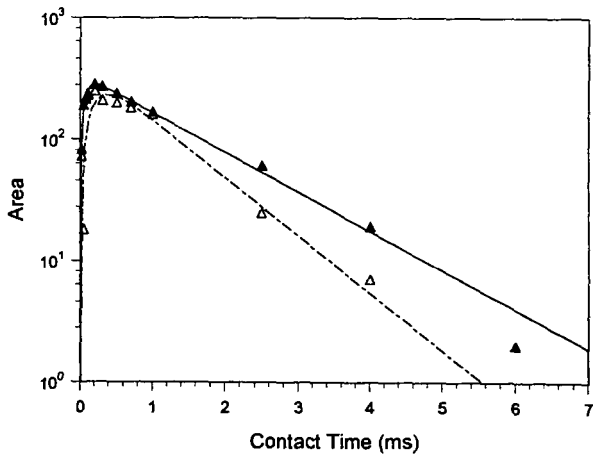

Figure 3. Carbon-13 NMR CP/MAS Variable Contact Time Data at 23°C for Aliphatic Carbons in (▲) Conoco Denver Asphalt, and (△) Asphalt Modified with 2% Elvaloy® AM

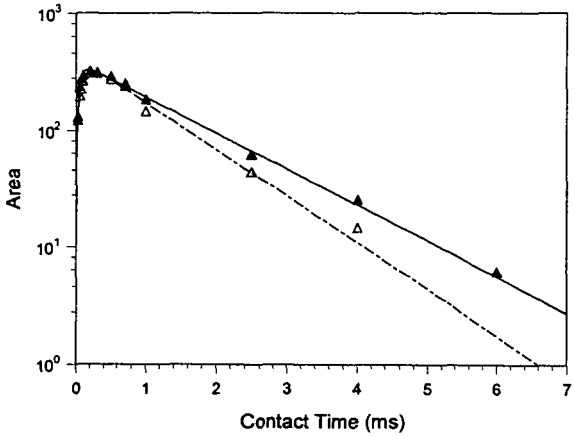

Figure 4. Carbon-13 NMR CP/MAS Variable Contact Time Data at 23°C for Aliphatic Carbons in (▲) Cenex Asphalt and (△) Asphalt Modified with 3% Butanol® NS 175

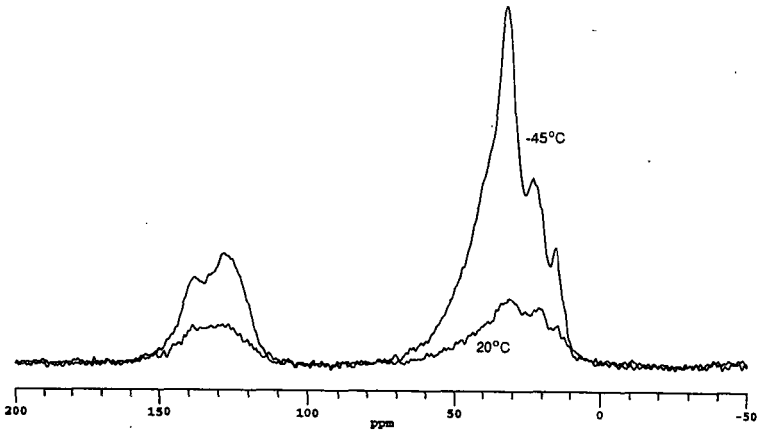

Figure 5. Carbon-13 CP/MAS Spectra of Asphalt AAA-1 at 20 and -45°C

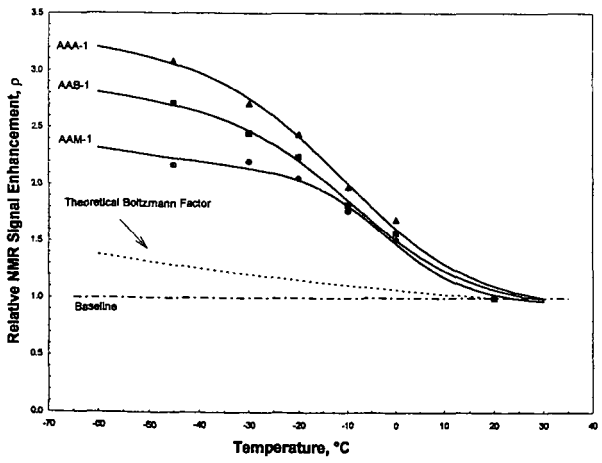

Figure 6. NMR Molecular-Mobility/Temperature Profile Plot for Aliphatic Carbons in Asphalts AAA-1, AAB-1, and AAM-1

SIZE EXCLUSION CHROMATOGRAPHY OF AGED AND CRUMB RUBBER MODIFIED ASPHALTS

John J. Duvall
Western Research Institute
365 North Ninth
Laramie, WY 82070

Keywords: SEC of asphalts, SEC of aged asphalts, SEC of crumb rubber modified asphalts

INTRODUCTION

Preparative size exclusion chromatography (SEC) has been used for several years in our laboratory to provide samples for further analysis and for use in other testing procedures (1). Asphalts have been separated into a first fraction (F-I) that contains nonfluorescing (at 350 nm) materials, and the rest of the asphalt, which is collected in one or more fractions (F-II or F-IIa, F-IIb, etc). The nonfluorescing materials have been shown (1) to contain strongly associating molecules, while the fluorescing materials consist of weakly associating individual and smaller molecules. The fractionation data from these analyses have been related to the rheological property tan delta, and thereby, to rutting and premature pavement cracking. We have developed a high performance liquid chromatography (HPLC) technique that yields these analytical data more rapidly and efficiently than preparative SEC and yet gives chromatograms similar to those derived from preparative SEC. The HPLC procedure described here uses toluene as the carrier as does the preparative procedure.

SEC is a chromatography technique in which separation depends specifically on molecular size and where molecular polarity is a factor only if it promotes molecular association or if the material is of a type to bind to the chromatographic substrate. The column packing has pores of varying sizes that molecules can or cannot enter depending on their size. As a result, the largest molecules, which cannot enter the pores, emerge first from the column(s) and the smallest molecules in the sample, which do enter the pores of the packing and are, therefore, slowed in their passage through the column, emerge last. Some polar molecules may form associated species of varying strengths and if these associations persist under the column conditions they will behave as though they were true molecules with a size similar to the associated species.

A number of other workers have used HPLC/SEC, also known as HPLC-GPC (gel permeation chromatography), to analyze asphalts, among them Jennings et al. (2), who attempted to quantify the data they obtained using a UV/visible diode array detector (DAD). They used tetrahydrofuran (THF) as the carrier and also related their results to highway performance. They also grouped asphalts into four groups according to the asphalts' MSD (molecular size distribution) profiles. Glover et al. (3), used both THF and toluene in their investigations of the HPLC/SEC of asphalts. Brûlé and coworkers published several papers (4) on the HPLC/SEC of unaged and aged asphalts. Bishara et al. (5) have related molecular size data, obtained using an HPLC with a gravimetric finish, to PVN (penetration-viscosity-number), viscosity at 135° C, and other physical properties. Garrick (6) developed a mathematical model from GPC data that predicts GPC profiles from physical properties of asphalts and suggests that the a strong relationship exists between GPC profiles and these physical properties, especially rheological properties. Different combinations of columns with different sized pores have been used in the various investigations.

EXPERIMENTAL

The HPLC equipment consists of a Hewlett Packard Series II 1090 liquid chromatograph with its associated computer hardware and software. There are a DAD, a differential refractive index detector (DRID), a fluorescence detector (FLD), and a fraction collector in place with the HPLC. However, because the sample concentrations used in this work are so large (the DAD, except at high wavelengths, and the FD are swamped), only data from the DRID and gravimetric data are reported here. Fractions are collected using the fraction collector, divested of solvent, and weighed on a balance to provide quantitative data not available from the other detectors.

The column combination in use consists of 2 - 500 Å and 1 - 100 Å 7.8 by 300 mm columns in series. The columns are packed with Phenomenex Phenogel with a 5µ particle size. Toluene is used as the carrier at a flow rate of 1.00 mL/min and the columns are maintained at 40° C. Sample size is around 24 mg of asphalt dissolved in about 220 µL of toluene. The sample is eluted in an hour. However, there is some tailing, so three hours are allowed between sample injections.

Because the samples are quite concentrated, back pressure, probably caused by adsorption of asphalt components in the frits at the ends of the columns, tends to build up after about 75 to 100 runs.

Cleaning is accomplished by backflushing the columns with 25 mL of a 3% methanol in toluene solution at 80° C followed by about 400 mL of toluene. Several samples of an asphalt then are run using normal conditions to condition the columns.

The column combination was calibrated by determination of retention times of several polystyrene standards with known peak molecular weights. Several other compounds of known molecular weight were also examined.

Samples of both unaged, at different concentrations, and asphalts aged to three levels (100°C (212°F) for 12, 20, or 36 hours at 2.07 MPa (300 psi)) were analyzed. Aging was accomplished using the thin film oven/pressure aging vessel technique described earlier (7). Samples of Strategic Highway Research Program (SHRP) asphalts AAB-1 and AAF-1 containing an AC 2.5 Amoco/Wilmington asphalt as a recycling agent were weighed out and then dissolved in toluene. Crumb rubber/asphalt mixtures were prepared by heating a weighed amount of asphalt (SHRP asphalts AAB-1, AAM-1, AAK-2, ABD-1, and ABL-3 were used) at 200°C (392°F) until liquid and then adding a weighed amount of crumb rubber followed by thorough mixing. The crumb rubbers used are both prepared from used tires and include one containing natural rubber designated NR (80 mesh) and one containing both natural and synthetic rubbers designated CR#4 (40 mesh). A sample was then taken which was labeled the zero hour sample. The rest of the CRM was heated under argon at 200°C (392°F) with samples removed at the desired time intervals. As a control, a sample of neat asphalt was heated and sampled under the same conditions as the CRM's. The CRM samples were then treated with toluene in about a 10:1 ratio of toluene to mixture. The partially dissolved samples then were centrifuged for an hour followed by filtration through a 0.22 μ filter using vacuum. The materials left in the centrifuge tube were rinsed further with toluene, centrifuged again, and filtered through the same filter as previously. The rinsing step was repeated and the combined filtrates were divested of solvent, weighed, and the requisite amount of solvent added to give the desired concentration. For all of the asphalts except AAM-1, strings of rubber were seen in the zero and one hour at 156°C (223°F) samples, rubber and carbon black were seen in the samples heated for 24 and 48 hrs, and samples that were heated for longer times seemed not to contain any rubber particles but an increased amount of finely divided carbon black was apparent. For asphalt AAM-1, carbon black first appeared in the 24 hour sample, for the NR mixtures, and increased through the 192 hour sample, while for the CR#4 mixtures, carbon black did not begin to appear until the 168 hour sample and a larger amount was seen in the 192 hour sample.

RESULTS AND DISCUSSION

A calibration curve for the column combination used is shown in Figure 1. The curve shows that the main area of separation for this system lies in the molecular weight range of around 1200 to 14000 Daltons. This is the range seen for SEC fractions F-I through F-IIb for the SHRP core asphalts as reported previously (1).

Early in this work it was necessary to determine the effect of sample size on the chromatogram. Figure 2 shows the results of this study in which it was found that a quite concentrated sample solution was necessary to achieve the desired result, i.e., emulate preparative SEC results. Apparently molecular associations were broken up in the more dilute solutions of asphalt in toluene that occurred when smaller samples were run.

It was necessary to demonstrate the effectiveness of the technique on unaged and aged asphalts so the SHRP core asphalts, both unaged and aged, were all analyzed. Examples of chromatograms of the unaged asphalts AAD-1 and AAF-1 both from the preparative SEC procedure and the HPLC/SEC procedure are shown in Figures 3 and 4 respectively. These figures show the similarity of the chromatograms produced for asphalts for both methods for two quite different asphalts.

Figure 5 shows the overlaid chromatograms of asphalt AAF-1 unaged and aged to three levels as an example of the results for aged asphalts from the technique described here. The chromatograms are drawn so that the largest peak for all four chromatograms is at the same level so that the change in the first part of the chromatogram is readily apparent. The amount of nonfluorescing associating material increases with increased aging. This is in agreement with earlier reports (1, 2, 5).

It was thought desirable to see if this technique could easily differentiate between an untreated asphalt and an asphalt treated with a recycling agent such as a lower viscosity asphalt. Figure 6 shows the overlaid chromatograms of the recycling agent and unaged asphalt AAF-1. As is evident, the recycling agent has as wide an MSD as does the higher viscosity asphalt. The major difference is in the highest molecular size material where the lower viscosity asphalt predominates. Therefore, addition of the recycling agent to the higher viscosity asphalt should show a difference in that region of the chromatogram. However, in Figure 7, where mixtures (5, 10, 25, and 50% AC 2.5) of the

recycling agent and AAF-1 are shown, no difference is apparent until the mixture reaches 25% recycling agent. Differences at the 50% level are easily seen in the figure.

Figure 8 shows data from the mixtures of the two grades of asphalt described above for the first five of nine SEC fractions. These curves show that SEC F-I does indeed grow with the addition of increasing concentrations of recycling agent while fractions F-IIa and F-IIb decrease somewhat but, again, the differences are only apparent at concentrations of 25% and above.. This suggests that this particular column combination would not be useful to analyze mixtures of recycling agents with broad MSD's, such as low viscosity asphalts, and another asphalt except at high concentrations. It appears that only recycling agents that have a narrow MSD might be usefully analyzed by this system.

Mixtures of asphalts modified by addition of various crumb rubbers (CRM's) are being studied extensively in our laboratory and it was suggested that HPLC/SEC might be appropriate to determine the fate of the rubber in the CRM's, i.e., where in the MSD does the dissolved rubber appear? Figures 9 through 12 show chromatograms from the study of the separation of mixtures of crumb rubber (CRM's) and asphalt ABD-1. For example, Figure 9 shows overlaid chromatograms for the neat asphalt and the two CRM's before they had been heated except that necessary for mixing. It can be seen that the chromatogram of the mixture containing NR shows a small increase in the chromatogram in the area of large molecular size indicating that some high molecular size material had been incorporated into the asphalt. The other two chromatograms are essentially the same showing no addition of soluble CR#4 to the asphalt prior to further heating. This suggests that the difference in the crumb rubbers is demonstrated very early in the heating regimen, i.e., that NR is solubilized more easily with asphalt ABD-1 than CR#4. Figure 10 shows the effect of heating on the chromatograms of the neat ABD-1. A very small change in the area of large molecular size is seen for the neat ABD-1 on heating from 0 to 96 to 192 hours. Figure 11 shows chromatograms for the mixture of ABD-1 and NR. As can be seen, changes occur in the large molecular size region of the chromatograms. Heating this mixture for as little as an hour has made a significant change in the very large molecular size region of the chromatogram, that is, a peak is seen at the front edge of the chromatogram. Further heating of the sample gradually fills in the area between that peak and the rest of the chromatogram.. This suggests that the rubber particles break down to a initially yield relatively large molecular size material followed by further breakdown to smaller molecular size material. Figure 12 shows chromatograms for the mixture of ABD-1 and CR#4. In this case, the 0 and 1 hour chromatograms are virtually identical, while the leading edge peak of the 24 hour chromatogram and those for higher levels of oxidation show that CR#4 does not begin to break down as early in the heating regimen with ABD-1 as does NR.

Figures 13 and 14 show chromatograms for both neat asphalt AAB-1 and a mixture of AAB-1 and NR respectively. Figure 13 shows chromatograms how the neat asphalt reacted to different periods of heating at 200°C (392°F). Interestingly, the amount of large molecular size materials formed on heating AAB-1 for 48 hours gradually diminished on further heating suggesting these materials broke down to lower molecular weight materials on sustained heating or became materials that are incapable of forming intermolecular associations. Of the asphalts studied so far, this result is peculiar only to AAB-1 and may be a result of the aging occurring in an argon atmosphere. The chromatograms in Figure 14 show that heating the AAB-1/NR mixture leads to an increase in large molecular size materials with increased heating time. Chromatograms are shown for a heating period of up to only 48 hours because further heating showed no further changes in the chromatograms. This lack of further change suggests that further breakdown of the rubber did not occur after 48 hours of heating with asphalt AAB-1 at 200°C (392°F). Similar chromatograms are obtained for the AAB-I/CR#4 mixture.

Chromatograms similar to those shown for asphalt AAB-1 could be shown for neat SHRP asphalts AAK-2 and ABL-3. Asphalt ABL-3 was supposed to be a replacement for SHRP asphalt AAK-2 but SEC chromatograms show significant differences. At any rate, the chromatograms for both the neat asphalts and the CRM's show a steady increase in the large molecular size region with increased heating time with the mixtures showing the larger increase.

Figures 15 and 16 show chromatograms for asphalt AAM-1 and asphalt AAM-1 with NR respectively. Figure 15 shows the chromatograms for the neat asphalt as a function of heating time and demonstrate that heating neat AAM-1 for 72 hours at 200°C (392°F) causes little change but, additional heating to a total of 96 hours caused a significant increase in the area of large molecular size material. On the other hand, heating the AAM-1/NR mixture showed small but significant changes in the large molecular size region through 24 hours of heating at 200°C (392°F) and, after 48 total hours of heating, a very large change. The chromatograms for the neat asphalt after 96 hours of heating and for the asphalt with NR after 48 hours of heating are similar, but very different from those for the other asphalts. This suggests that the source for the for the additional large molecular size material is the asphalt, not the rubber, and that large molecular size materials from the rubber

seen in the chromatograms from the other asphalts are "buried" under the curve for the materials from the asphalt. However, because the material appears at a shorter heating time for the CRM than for the neat asphalt, it seems possible that something in the rubber catalyzes the formation of large molecular size materials from the asphalt. This could possibly be explained by the presence of finely divided carbon black in the rubber that begins to make its appearance as the rubber breaks down. Perhaps the carbon black particles supply a focal point for potential SEC F-I materials to associate as dust particles do in crystallization. These associations must be stable in toluene in order to be detected by the DRID.

CONCLUSIONS

The HPLC/SEC technique described, i.e., the column combination, column temperature, solvent, and flow rate, has demonstrated the ability to emulate preparative SEC for unaged asphalts and also give chromatograms for aged asphalts that show an increase of large molecular size material is produced on aging in the TFO/PAV. Calibration of the column combination with materials of known molecular weight shows the major separation occurs in the large molecular size material area of the MSD. In addition, analysis of the CRM's has shown that the breakdown products from the heating of the rubbers of the CRM's at 200°C (392°F) appear in the large molecular size region of the MSD. The response of the two crumb rubbers to heating with the asphalts varies in that NR seems to solubilize sooner than does CR#4 for the same asphalt In addition, the two crumb rubbers respond differently to being heated with different asphalts, i.e., solubilizing more rapidly in one asphalt than in another. This HPLC/SEC system has easily shown these differences.

REFERENCES

1. J.F. Branthaver, J.C. Petersen, R.E. Robertson, J.J. Duvall, S.S. Kim, P.M. Harnsberger, T. Mill, E K. Ensley, F.A. Barbour, and J.F. Schabron, "Binder Characterization and Development. Volume 2: Chemistry. SHRP-A-368. Strategic Highway Research Program, National Research Council, Washington, DC, 39-76 (1993).

2. P.W. Jennings, J.A. Pribanic, M.F. Raub, J.A. Smith, and T.M. Mendes, "Advanced High Performance Gel Permeation Chromatography Methodology", SHRP AIIR-14 Final Report (1991).

3. G.R. Donaldson, M.W. Hlavinka, J.A. Bullin, C.J. Glover, and R.R. Davison, J. Liquid Chrom., 11, 749 (1988).

4. B. Brûlé, G. Raymond, and C. Such, "Relationships among Composition, Structure, and Properties of Road Asphalts", in "Asphaltenes and Asphalts, 1. Developments in Petroleum Science, 40" (T.F. Yen and G.V. Chilingarian, Ed.), Elsevier Science B.V. (1994).

5. S.W. Bishara, R.L. McReynolds, and E.R. Lewis, "Interrelationships between Performance-Related Properties of Asphalt Cement and Their Correlation with Molecular Size Distribution", Transport. Res. Rec., 1323 (1991)

6. N.W. Garrick, J. Mat. Civ. Eng., 6, 376 (1994).

7. AASHTO Designation PP1, Edition 1A, September 1993, "Standard Practice for Accelerated Aging of Asphalt Binder Using a Pressurized Aging Vessel (PAV).

DISCLAIMER

ACKNOWLEDGEMENTS

The author thanks the Federal Highway Administration for financial support under Contract No. DTFH61-92C-00170. The author also thanks J.C. Petersen, coworkers J.F. Branthaver and R.E. Robertson for encouragement and helpful suggestions in the preparation of this report, J. Greaser for help in preparation of the manuscript, and Anthony Munari for help in preparation of the figures.

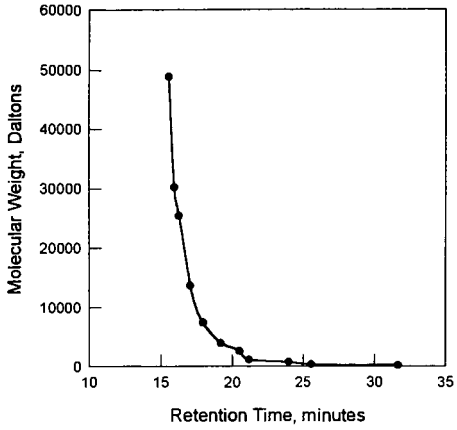

Figure 1. Calibration for column configuration of 2-500 Å and 1-100 Å Phenogel (5μ) columns in series at 40°C (104°F) with 1.0 mL/min toluene carrier

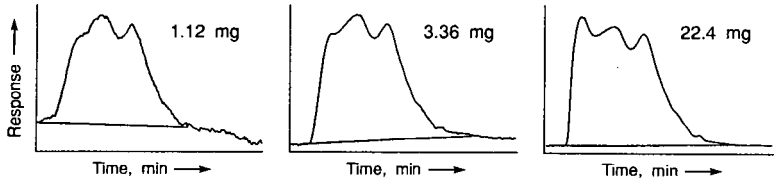

Figure 2. HPLC/SEC chromatograms of asphalt AAD-1 at three sample sizes

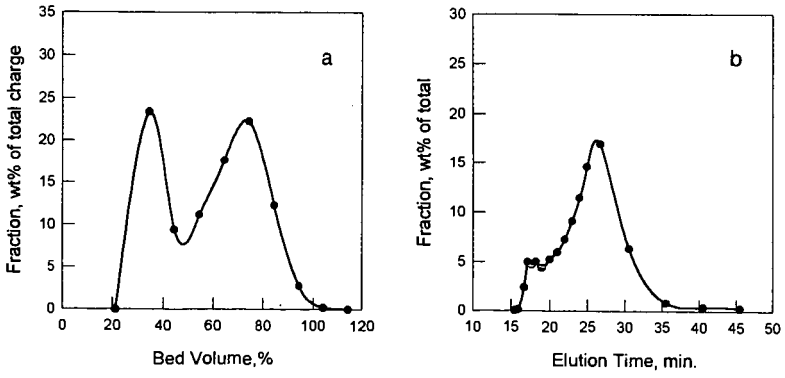

Figure 3. Chromatograms for asphalt AAD-1 from (a) preparative SEC and (b) HPLC/SEC

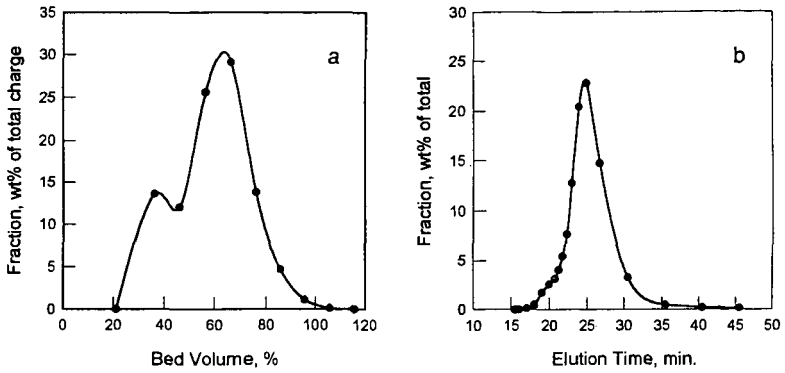

Figure 4. Chromatograms for asphalt AAC-1 from (a) preparative SEC and (b) HPLC/SEC

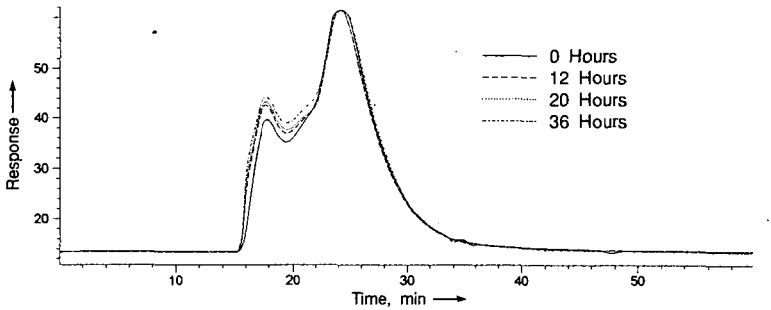

Figure 5. HPLC/SEC chromatograms for asphalt AAC-1 TFO/PAV aged at 100° C (212°F) for different times

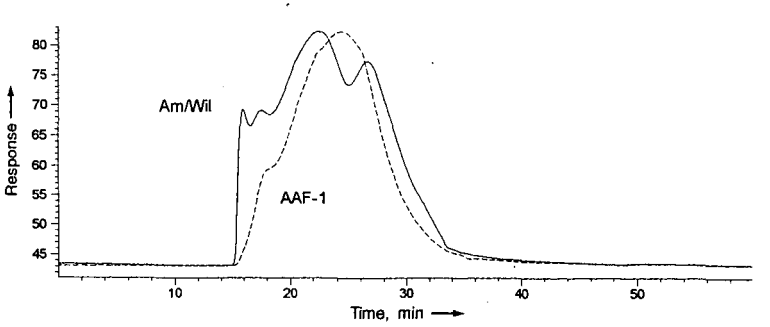

Figure 6. HPLC/SEC chromatograms for asphalt AAF-1 and Amoco/Wilmington AC 2.5

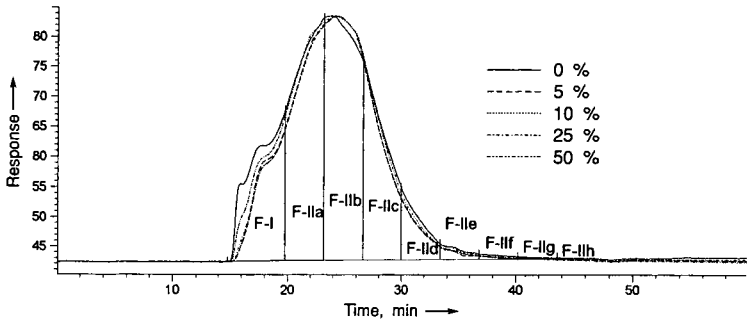

Figure 7. HPLC/SEC chromatograms for asphalt AAF-1 and various percentages of Amoco/Wilmington AC 2.5, showing fraction cutpoints

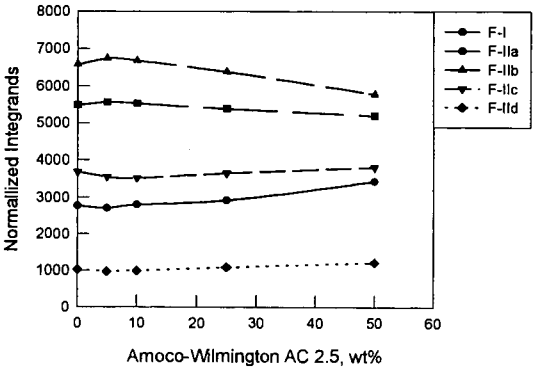

Figure 8. Normalized integrands versus wt% Amoco/Wilmington AC 2.5 in asphalt AAF-1 for various HPLC/SEC fractions

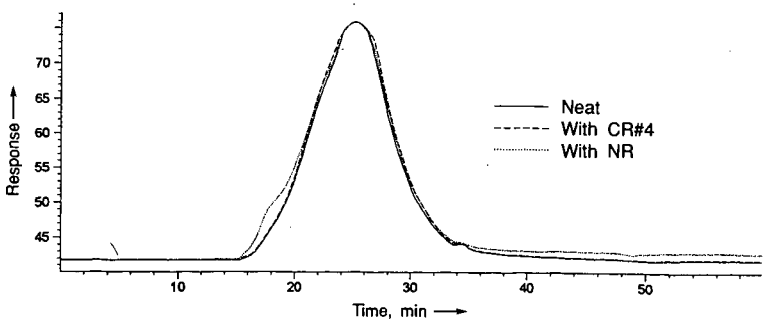

Figure 9. HPLC/SEC chromatograms for asphalt ABD-1 neat and with 12% crumb rubber NR or CR#4 mixed but with no additional heating

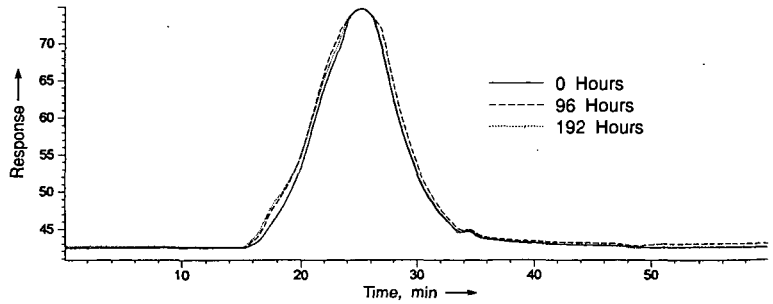

Figure 10. HPLC/SEC chromatograms for neat asphalt ABD-1 heated at 200°C (392°F) for various times

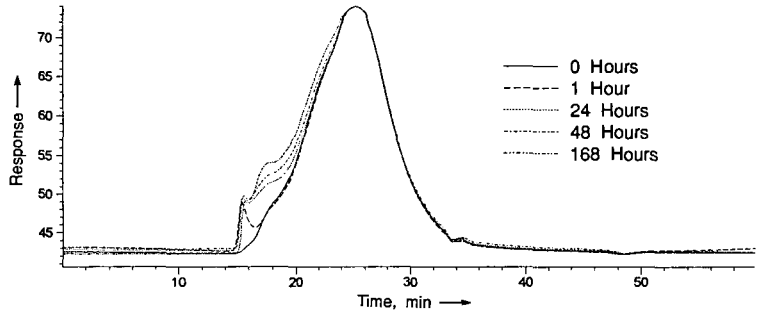

Figure 11. HPLC/SEC chromatograms for asphalt ABD-1 with 12% crumb rubber NR, heated at 200°C (392°F) for various times

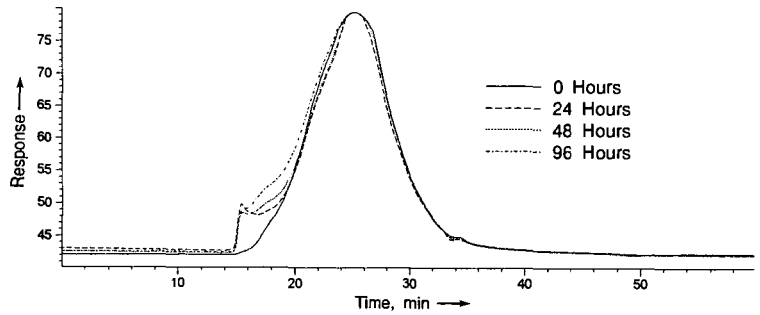

Figure 12. HPLC/SEC chromatograms for asphalt ABD-1 with 12% crumb rubber CR#4, heated at 200°C (392°F) for various times

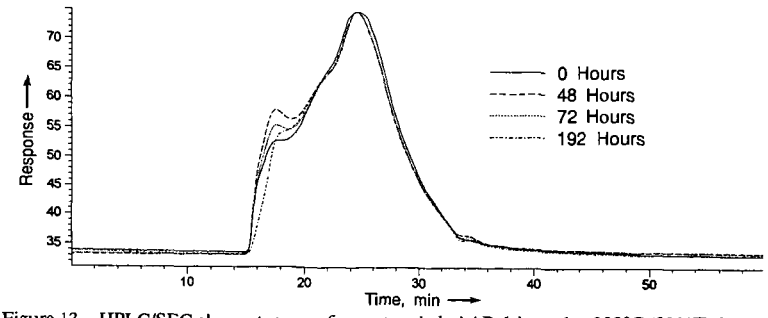

Figure 13. HPLC/SEC chromatograms for neat asphalt AAB-1 heated at 200°C (392°F) for various times

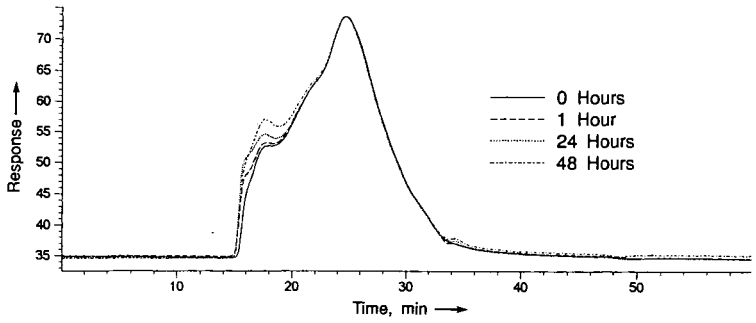

Figure 14. HPLC/SEC chromatograms for asphalt AAB-1 with 12% crumb rubber NR, heated at 200°C (392°F) for various times

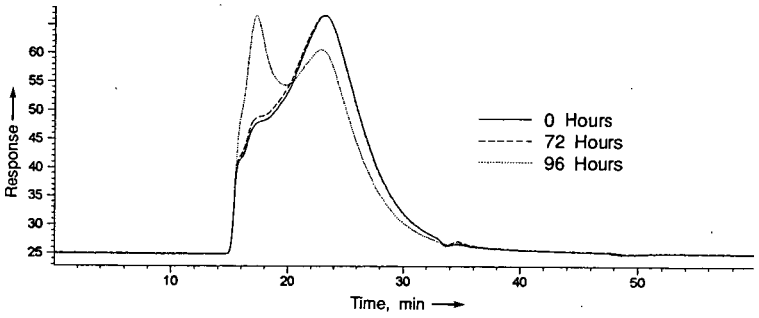

Figure 15. HPLC/SEC chromatograms for neat asphalt AAM-1 heated at 200°C (392°F) for various times

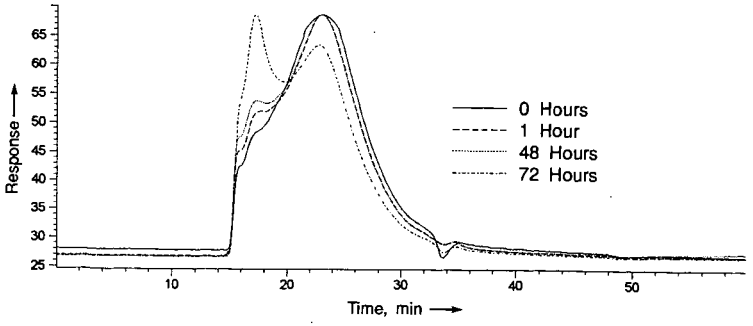

Figure 16. HPLC/SEC chromatograms for asphalt AAM-1 with 12% crumb rubber NR, heated at 200°C (392°F) for various times

ASPHALT COMPATIBILITY TESTING USING THE AUTOMATED HEITHAUS TITRATION TEST

Adam T. Pauli
Western Research Institute
365 North 9th Street, Laramie, WY 82070-3380

Key words: asphalt compatibility, peptization, flocculation

ABSTRACT

The Heithaus titration test or variations of the test have been used for over 35 years to predict compatibilities of blends of asphalts from different crude sources. Asphalt compatibility is determined from three calculated parameters that measure the state of peptization of an asphalt or asphalt blend. The parameter p_a is a measure of the peptizability of the asphaltenes. The parameter p_o is a measure of the peptizing power of the maltenes, and the parameter P, derived from p_a and p_o values, is a measure of the overall state of peptization of the asphalt or asphalt blend. In Heithaus' original procedure, samples of asphalt were dissolved in toluene and titrated with n-heptane in order to initiate flocculation. The onset of flocculation was detected either by photography or by spotting a filter paper with a small amount of the titrated solution. Recently, an "automated" procedure, after Hotier and Robin,[1] has been developed for use with asphalt. In the automated method UV-visible spectrophotometric detection measures the onset of flocculation as a peak with the percent transmittance plotted as a function of the volume of titrating solvent added to a solution of asphalt. The automated procedure has proven to be less operator dependent and much faster than the original Heithaus procedure. Results from the automated procedure show the data to be consistent with results from the original, "classical" Heithaus procedure.

INTRODUCTION

Historically, asphalts have been classified into gel-type asphalts and sol-type asphalts.[2] Gel-type asphalts usually are characterized by non-Newtonian rheological behavior, relatively low variation of viscosity with temperature, and low ductility. Sol-type asphalts exhibit more Newtonian rheological behavior, are highly temperature susceptible, and are more ductile. The two classifications represent extremes, and most asphalts are of intermediate nature. Sol-type asphalts have been designated as compatible asphalts, while gel-type asphalts have been designated as incompatible asphalts.

The terms "compatible" and "incompatible" (or sol-gel) arose from what became known as the colloidal model of asphalt structure. This model considers asphalts to be dispersions of what are termed "micelles," consisting of polar, aromatic molecules in viscous oils. The degree to which the so-called "micelles" form extended gel structures, unstable to heat and shear, will determine the relative degree of incompatibility. In a compatible asphalt, the dispersed materials are well peptized by the oils (maltenes), either because the dispersed materials are small in amount and/or tend not to form strong associations, and/or because the solvent effectively disperses the "micelles." In an incompatible asphalt, associations are more extensive and are not so efficiently peptized by the solvent.

The colloidal model has been subjected to much criticism in recent years. The principal objection is that there is no direct evidence for "micellar" structures, either classical or inverse, in asphalts. The term "micelle," which implies existence of a separate phase with distinct boundaries, may be inappropriate when applied to asphalts. Recently, a microstructural model of asphalt structure has been proposed.[3] In this model, associations of polar molecules of varying sizes are considered to be dispersed in a polar moiety composed of less polar, relatively small molecules. No distinct phase boundaries are believed present. Nevertheless, the concept of compatibility as a measure of mutual miscibility of different chemical components of asphalts is useful. Compatible asphalts do differ from incompatible asphalts in their physical properties and in pavement performance. Highly compatible asphalts are not necessarily good to achieve all important performance related properties and likewise for low compatible asphalts. This makes compromises in compatibility necessary for optimum overall pavement performance.

Asphaltenes are solid materials which precipitate when asphalts are treated with solvents such as n-pentane, n-hexane, n-heptane, etc. Maltenes are the components of asphalts not precipitated by n-alkane solvents. Asphaltenes are more aromatic than maltenes and contain more heteroatoms. Thus intermolecular interactions are more extensive in asphaltenes than in maltenes. This is reflected in the greater molecular weights of asphaltenes compared with maltenes.[4] In the colloidal model of

asphalt structure, asphaltenes are believed to correspond to the dispersed materials and maltenes to the solvent. Therefore, asphaltenes will be mainly responsible for the internal structure of asphalts and will dominate many physical properties.[5] Thus the amount of asphaltenes in an asphalt is a rough measure of compatibility. Compatible asphalts generally have smaller amounts of asphaltenes than incompatible asphalts. Oxidative aging of an asphalt will decrease compatibility by formation of polar molecules, which cause increasing associations and result in more asphaltenes. The ease with which asphaltenes are dispersed is highly dependent on the dispersing power of maltenes, which are also a contributing factor to asphalt compatibility. The best known measurement of compatibility of asphalts that takes all the above factors into account is the Heithaus[6,7] test. In this test, flocculation behavior of asphaltenes is measured. The method is tedious and does not work with waxy asphalts, so a study of asphaltene flocculation behavior to develop an improved compatibility test was implemented.

EXPERIMENTAL

What has been termed the classical Heithaus titration procedure is described below. Four 1.0 g samples of a test asphalt are placed into four 125 mL Erlenmeyer flasks. To the four flasks are added amounts of 1.0, 2.0, 4.0, and 6.0 mL toluene, respectively. After dissolution of the asphalt is completed, the flasks are immersed in a water bath maintained at 25°C (77°F) for 30 minutes. The flasks are titrated with 1.0 mL aliquots of n-heptane. After each addition of n-heptane, the contents of the flask are stirred for several minutes, and then inspected to observe if flocculation has taken place. Flocculation is detected by transferring a drop of the solution to a filter paper with a glass rod. The development of two rings on the filter paper signifies the onset of flocculation. Heithaus parameters p_a, p_o and P are calculated from the flocculation ratio and the concentration, respectively. The flocculation ratio (FR) and concentration (C) are calculated as:

$$FR = \frac{V_S}{V_S + V_T} \tag{1}$$

$$C = \frac{W_a}{V_S + V_T} \tag{2}$$

where V_S is the volume of solvent, V_T is the volume of titrant required to initiate flocculation and W_A is the weight of the asphalt. In the classical Heithaus procedure, FR values are calculated for solutions of asphalt at various concentrations, and concentration values are plotted versus flocculation ratio values. The x and y intercept values FR_{max} and C^{-1}_{min} extrapolated from the FR vs. C line are used to calculate Heithaus parameters p_a, the peptizability of asphaltenes; p_o, the peptizing power of maltenes; and P, the state of peptization of the asphalt, as follows:

$$p_a = 1 - FR_{max} \tag{3}$$

$$p_o = FR_{max}(C^{-1}_{min} + 1) \tag{4}$$

$$P = \frac{p_o}{1 - p_a} \tag{5}$$

The automated Heithaus procedure differs somewhat from the classical procedure. In the automated procedure three to five samples of a test asphalt are weighed into 30 mL vials with Teflon sealed caps. Contrasting with the classical procedure, in which the weight of asphalt is held constant and the volume of solvent is varied, the automated procedure uses different weights of asphalt from sample to sample, and the volume of solvent is held constant. To the vials are added 0.5000 g to 1.0000 g ± 0.0005 g of asphalt in 0.1 to 0.2 gram increments, respectively. Toluene (LC-grade) is added to each vial in 1.000 mL ± 0.005 mL aliquots and the vials are capped and the asphalt sample is allowed to dissolve. Figure 1 depicts the apparatus that has been assembled to preform the automated procedure. The vials containing asphalt solutions are loaded into a reaction vessel maintained at 25°C (77°F) with a temperature controlled water bath and stirred for ten minutes. The temperature controlled solutions are circulated through a 0.1 mm flow cell housed within a UV-visible spectrophotometer using 0.16 cm (1/16") ID viton tubing and a metering pump. The titrant, either iso-octane (LC-grade) or n-heptane (LC-grade) which is also maintained at a constant temperature of 25°C ± 0.1°C (77°F) is introduced into the vial through 0.055 cm (0.022") ID viton tubing with a second metering pump set at a fixed flow rate in the range of 0.300 mL/min to 0.500 mL/min. The change in the percent transmittance at an absorbance wavelength of 740 nm is plotted as a function of titrant flow rate and chart speed on a strip chart recorder. Figure 2 shows a typical

series of titration curves for asphalt AAD-1, one of the Strategic Highway Research Project (SHRP) core asphalts. The volume of titrant added is related to the distance from the start of a curve, when titrant is first introduced, to the apex of the peak (the onset of flocculation), L_p. Heithaus parameters are calculated using values of V_T that are calculated as:

$$V_T = \left(\frac{L_p}{v_c}\right) v_T \qquad (6)$$

where L_p is the distance to the apex of the peak measured in centimeters, v_c is the chart recorder speed in cm/min and v_T is the titrant flow rate in mL/min.

Crossblend mixtures were prepared by mixing an arbitrary amount of maltenes from either asphalt with a specified amount of asphaltenes at the natural abundance level of the asphaltenes in either asphalt, resulting in eight different mixtures. Four of the mixtures have either AAF-1 or AAG-1 asphaltenes, four have either AAF-1 or AAG-1 maltenes, and four are mixed at either the AAF-1 or AAG-1 natural abundance level. Sample mixtures were labeled in terms of maltene type (M), asphaltene type (A), and asphaltene natural abundance level (L). Asphaltene and maltene fractions were mixed in round bottom flasks along with dichloromethane, used to dissolve and disperse the materials. Crossblend mixtures were dried using heat and vacuum distillation.

RESULTS AND DISCUSSION

Repeatability in the automated method is influenced by several variables. These are as follows: Sample concentrations: It was observed that with concentrations less than 0.50 g/mL, that plots of flocculation ratio (FR) versus concentration (C) deviated from linearity. This is assumed to be related to the pathlength of the flow cell; 0.10 mm used in this work. And when solutions greater in concentration than 1.1 g/mL are tested, several hours are required for complete sample dissolution, increasing the likelihood for sample oxidation due to prolonged exposure to the aerated solvent. This left only a narrow range of solution concentrations with which to work with, thus placing a greater emphasis on accuracy in other variables relevant to the procedure, such as accurate sample weights, consistency in titrant flow rate, and consistency in circulation flow rate. Temperature: It was found to be necessary to control both solution temperature and the titrant temperature as well to within 0.1°C. Fluctuations in lab temperature were also found to affect repeatability in data, making recording lab temperature standard practice. Titrant flow rate and flow rate consistency: It was found that in order to achieve an accuracy of approximately 0.05 in the value of P that the flow rate had to be steady to within 0.005 mL/min over a 20 minute period or longer, and that the flow rate had to be below 0.500 mL/min with the sample sizes that were being used. Circulation flow rate: It is necessary to control flow rate because solution viscosities increase with increasing concentrations. It was found that the circulation flow rate needs to be as fast as possible, at minimum the circulation flow rate needed to run at a rate of 10 mL/min and to vary no less than 0.5 mL/min when more concentrated solutions were tested. Stirring rate, for mixture homogeneity and temperature control: The stirring rate needed to be fast enough to adequately mix the solution, but not so fast as to heat the solution. Titrating solvent (iso-octane in place of n-heptane): It was found that certain waxy asphalts (AAC-1 and AAM-1 for example) were difficult or impossible to test using n-heptane as the titrating solvent. When iso-octane, which has a lower solubility parameter ($\delta = 6.90$) than n-heptane ($\delta = 7.46$), was used in place of n-heptane, all SHRP core asphalts could be tested. For non-waxy asphalts, n-heptane is a suitable titrant.

It was determined from a statistical analysis that poor repeatability in the classical procedure was due to systematic error. Figure 3 shows that a correlation, $R^2 = 0.94$ may be drawn between the weight percent of n-heptane asphaltenes for six SHRP core asphalts when plotted versus sample standard deviations in P parameters obtained using the classical procedure. It was surmised that removal of sample from solution for the purpose of performing the spot test to detect the onset of flocculation was the source of operator error in the classical procedure. With more compatible asphalts this error would be more pronounced because, for compatible asphalts (relatively low levels of asphaltenes) more titrant is required to promote the onset of flocculation and the spot testing is preformed more often throughout the titration.

Table 1 shows Heithaus parameter and sample standard deviation data collected by three different operators using the automated procedure titrated with iso-octane, and sample standard deviation data collected by a single operator using the classical procedure, titrated with n-heptane for SHRP core asphalt AAD-1. It is seen from Table 1 that data gathered on this asphalt by three different operators using the automated procedure is almost as repeatable as data gathered by a single operator using the classical procedure. It has been found that compatibility data gathered for asphalts having

higher concentrations of asphaltenes (incompatible) generally give repeatable results using the classical procedure.

The problem that arises in the classical procedure lies in gathering repeatable data for asphalts having lower concentrations of asphaltenes (compatible). Thus, Table 1 shows a notable improvement in data gathered for a compatible SHRP core asphalt; AAM-1, in terms of sample standard deviation values of Heithaus compatibility parameters using both procedures.

Figure 4 depicts P-values for seven SHRP core asphalts using the classical procedure and titrated with n-heptane, plotted versus P-values using the automated procedure and titrated with iso-octane as being consistent with one another. It is not to be expected that the Heithaus parameters obtained by either method will be identical when different titrants are used. Similar plots using p_a and p_o values for the same seven SHRP core asphalts were not in as good agreement. According to Branthaver et al.[8] asphaltenes precipitated from asphalts using iso-octane were found to have different physical properties than asphaltenes precipitated using n-heptane. This raised the question of what p_a and p_o values actually measure. Two hypotheses were formulated. First, p_a and p_o values are representative of the types of asphaltenes and maltenes, respectively found in a particular asphalt; or alternatively, p_a and p_o values are representative of the amount of asphaltenes present in an asphalt.

To verify which hypothesis was correct, asphaltene/maltene crossblend mixtures were prepared from asphaltene and maltene fractions separated from a compatible asphalt (AAG-1) and a somewhat less compatible asphalt (AAF-1). Table 2 shows compatibility data collected on eight AAG-1/AAF-1crossblend mixtures that were titrated with n-heptane using the automated procedure. Results in Table 2 show p_a-values being more closely related to natural asphaltene abundance levels (L) and P-values also somewhat related to natural asphaltene abundance levels. Table 2 also shows p_o values being weakly related to asphaltene type (A), but not asphaltene concentration (C).

CONCLUSION

The application of an automated procedure to test asphalt compatibility appears feasible. Results show the automated procedure to be less operator dependent and more rapid than the classical procedure. Several variables relating to the repeatability of the automated procedure have been isolated, among them; sample concentrations, temperature, circulation, stirring and titrant flow rates, and titrating solvent. Heithaus P parameters measured for seven SHRP core asphalts using both automated and classical procedures show the data to be consistent from one procedure to the other. Asphaltene/maltene crossblend mixtures prepared using SHRP core asphalts AAG-1 and AAF-1were tested using the automated procedure. Results for crossblend mixtures show that measured values of p_a relate more closely to an asphalt's asphaltene concentration, where as, p_o values appear to be influence by asphaltene type.

DISCLAIMER

ACKNOWLEDGMENTS

The author gratefully acknowledges the Federal Highway Administration for its financial support of this work as part of contract No. DTFH61-92-C-00170 at Western Research Institute, Laramie, Wyoming. Automated Heithaus titrations were preformed by A.T. Pauli, P. Holper, J. Hart, S. Salmans, and C. Wright. Classical Heithaus titrations were preformed by D. Colgin, and M.W. Catalfomo. Asphaltene/maltene crossblend mixtures were prepared by J.F. Branthaver and S. Salmans. The manuscript was prepared by A.T. Pauli and J. Greaser. Figures and tables were prepared by T. Munari and A. T. Pauli. The author gratefully acknowledges C. Petersen, R.E. Robertson and J.F. Branthaver for a thoughtful review.

REFERENCES

1. Hoiter, G., and M. Robin. Action De Divers Diluants Sur les Produits Petroliers Lourds: Mesure, Interpretation et Prevision de la Floculation des Asphaltenes. Revue de L' Institut Francais du Petrole, 38, 1983, pp. 101-120.
2. Traxler, R. N. Asphalt: Its Composition, Properties and Uses. Reinhold, New York, 1961.
3. SHRP A-367, Binder Characterization and Evaluation, Volume 1. Strategic Highway Research Program, National Research Council, Washington D.C., 1994, pp. 9-25.
4. Koots, J. A. and J. G. Speight (1975), Relationship of Petroleum Resins to Asphaltenes. Fuel, 54, pp. 179-184.
5. Boduszynski, M. M. Asphaltene in Petroleum Asphalts: Composition and Formation. In "Advances in Chemistry Series: Chemistry of Asphalts," J. W. Bunger and N. C. Li, eds., Am. Chem. Soc., Washington, D.C., 195, 1981, pp. 119-135.
6. Heithaus, J. J. (1960), Measurement and Significance of Asphaltene Peptization. Am. Chem. Soc., Div. Petrol. Chem. Prepr., 5, pp. A23-A37.
7. Heithaus, J. J. (1962), Measurement and Significance of Asphaltene Peptization. J. Inst. Petrol., 48, pp. 45-53.
8. Branthaver, J. F., J. C. Petersen, J. J. Duvall, and P. M. Harnsberger. Compatibilities of Strategic Highway Research Program Asphalts. Transportation Research Record 1323. TRB, National Research Council, Washington D.C., 1991, pp. 22-31.

Table 1. Comparison of the repeatibility in data obtained using either the automated or classical procedure.

Asphalt, procedure, operator:		Heithaus parameters		
		p_a	p_o	P
AAD-1, automated:	Operator-1	0.688	0.682	2.18
	Operator-2	0.686	0.731	2.32
	Operator-3	0.701	0.637	2.13
	Average	0.691	0.683	2.21
	Std. Dev.	0.008	0.047	0.10
AAD-1, classical, single operator:	Average	0.61	1.33	3.43
	Std. Dev.	0.01	0.02	0.04
AAM-1, automated, single operator:	Average	0.907	0.66	7.08
	Std. Dev.	0.006	0.10	0.59
AAM-1, classical, single operator:	Average	0.89	1.26	12.19
	Std. Dev.	0.03	0.04	2.59

Table 2. Heithaus parameters of AAG-1/AAF-1 asphaltene-maltene crossblend mixtures.

Crossblend Mixture Design M A L*	Heithaus parameters		
	p_a	p_o	P
G F F	0.67	1.11	3.35
F F F	0.67	1.03	3.09
G F G	0.76	1.07	4.48
F F G	0.64	2.72	7.59
G G G	0.77	1.37	6.02
F G F	0.66	1.45	4.28
G G F	0.68	1.43	4.41
F G G	0.77	1.04	4.46

*M: maltene type, A: asphaltene type, L: natural abundance level of asphaltenes in asphalt listed.

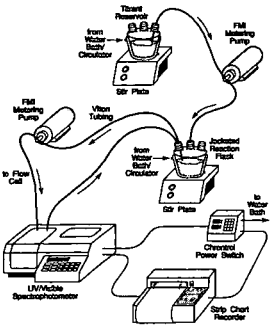

Figure 1. Apparatus used in automated Heithaus procedure.

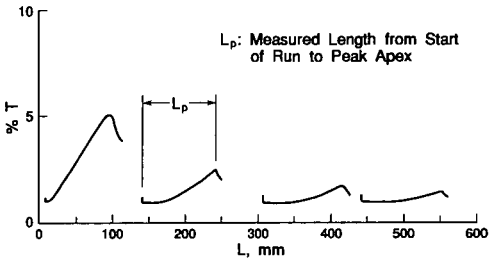

Figure 2. Flocculation peaks of one SHRP core asphalt; AAD-1.

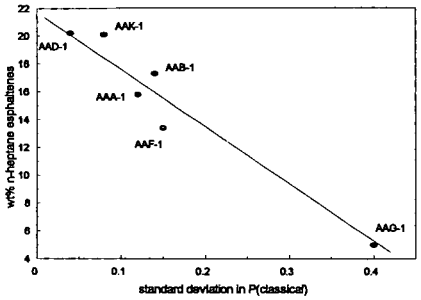

Figure 3. The relationship between asphaltene concentration and sample standard deviations in average values of the parameter.

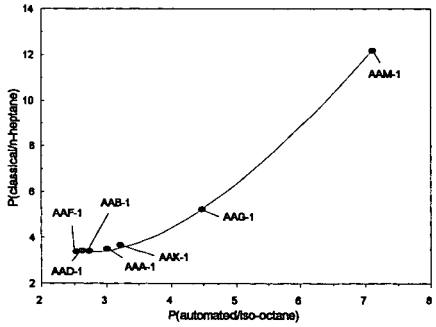

Figure 4. Relationship between Heithaus P parameters obtained using the automated procedure and the classical procedure.

RHEOLOGICAL PROPERTIES OF ASPHALT CROSSBLENDS

Jan F. Branthaver and Stephen L. Salmans
Western Research Institute,
365 North 9th Street, Laramie, WY 82070-3380

Key words: asphalt compatibility, size exclusion chromatography, rheology

ABSTRACT

Properties of blends of asphalts from different sources can not necessarily be predicted by averaging properties of the components. Asphalts may be considered to be combinations of a dispersed and a solvent moiety, the nature and amounts of which vary among asphalts. Asphalt properties will be determined by the manner in which the two moieties interact. In this work, dispersed and solvent moieties were generated from eight asphalts by size exclusion chromatography. Crossblended mixtures of dispersed and solvent moieties from different asphalts were prepared and their rheological properties measured. The influence of the relative amounts and nature of the two moieties on rheological properties were determined. It was found that rheological properties of the crossblended mixtures were greatly affected by the relative amounts of the two moieties. The nature of the two moieties also was influential in determining rheological properties, as the solvent components of some asphalts were found to be compatible with the dispersed moieties of some asphalts but incompatible with others.

INTRODUCTION

The compatibility of asphalt systems long has been of interest to researchers. Traxler[1] discusses the difference in properties among what are designated as compatible (sol-type) and non-compatible (gel-type) asphalts. According to Traxler, well-dispersed, compatible asphalts exhibit high temperature susceptibility of viscosity, high ductility, low elasticity, and low rates of oxidative age hardening. Non-compatible asphalts, which are poorly dispersed, are characterized by low temperature susceptibility, low ductility, pronounced elasticity, and high aging rates. These and other physical properties serve to categorize asphalts according to compatibility. The two fundamental types of asphalts will, of course, vary markedly in pavement performance.

Asphalt compatibility also is related to chemical composition. Non-compatible asphalts tend to be high in asphaltene and sulfur content compared with compatible systems. Heithaus[2] published a laboratory method that assigns numerical values to asphalts and asphalt blends according to compatibility. Heithaus considered asphalts to be dispersions of asphaltenes in a maltene solvent, and asphalt and asphalt blend properties therefore should be determined by the relative amounts of the two materials and the effectiveness by which maltenes disperse asphaltenes. The properties of asphalt blends thus are not necessarily computed additively from properties of their parent asphalts.

Properties of blends of various fractions of different asphalts have been studied. Altgelt and Harle[3] measured rheological properties of various asphaltene-maltene combinations. Traxler[4] studied mixtures prepared using solvent-derived fractions. During the Strategic Highway Research Program (SHRP)[5], mixtures of asphalt fractions prepared by size exclusion chromatography (SEC) were studied. Very large differences in rheological properties of crossblended mixtures of asphalt SEC fractions from different sources were observed. The SEC fractions were chosen because the separation method fractionates solutions of asphalts according to molecular size. If asphalts consist of a dispersed and a dispersing component, the dispersed component should consist of the more polar, aromatic constituents of asphalts, which should be of higher apparent molecular weight than the dispersing, or solvent, component.[6] The two components thus should be to some degree separable by SEC. A large number of asphalts have been separated into two SEC fractions that are believed to approximate asphalt dispersed and solvent components. The properties of the two components have been measured for these asphalts and vary according to source.[5] Relative amounts of the two fractions also vary considerably among asphalts, and this relative abundance of the two SEC fractions in an asphalt is termed the natural abundance ratio. The two fractions are designated SEC Fraction-I and SEC Fraction-II, which correspond to the dispersed and solvent components of asphalts respectively. The relative amounts of the two SEC fractions in an asphalt do not correspond to asphaltene and maltene yields.

Rheological properties of asphalts depend on relative amounts of dispersed and solvent components. The solvent component is much less viscous and less elastic than the dispersed component, which contains the viscosity-building constituents. Presumably, the nature of the two components and the manner of their interaction also affect rheological properties. Another physical property, the glass transition temperature, is determined by the relative amount of the two components and the source

of the solvent component, but not the source of the dispersed component.[7] Other properties conceivably might depend more on the source of the dispersed component than the solvent. It is the goal of this study to quantify the influence of these three factors, source of solvent component, source of dispersed component, and relative amounts of the two, on asphalt rheological properties.

EXPERIMENTAL

The separation of asphalts into two fractions by SEC has been described previously.[8] The SEC Fraction-I materials are friable solids, and the SEC Fraction-II materials are viscous liquids. Crossblended mixtures were prepared by dissolving weighted fractions of each of two different SEC fractions in dichloromethane and combining the two solutions in a round-bottom flask. The flask was attached to a rotary evaporator and was immersed in a water bath. Most solvent was removed by heating the flask to 90°C (194°F) for one hour under vacuum. Residual solvent was removed by replacing the water bath with an oil bath and heating the flask to 130°C (266°F) under vacuum for one hour. The flask and contents were flooded with an inert gas and stoppered. Rheological measurements on the crossblended mixtures were obtained at 25°C (77°F) using a Rheometrics mechanical spectrometer. Usually, 8 mm plates were used, and strain rates of 3-15% were employed, depending on sample stiffness. Phase angles and dynamic shear modulus values were obtained over a wide range of shear rates to generate the Black plots in Figures 1-7. Each sample was annealed before rheological analysis.[8] If this step is not performed, erratic viscosity determinations are observed.

DISCUSSION

As stated above, the purpose of this work is to evaluate the compatibilities of crossblended mixtures of SEC fractions of asphalts and evaluate the influence of three factors on crossblend rheology. The three factors are the source of SEC Fraction-II (solvent), the source of SEC Fraction-I (dispersed component), and relative amount of each fraction in the crossblended mixture.

Eight asphalts studied in SHRP were separated into SEC Fractions I and II by SEC. These eight asphalts, called core asphalts, were intensively studied. They are coded as listed in Table 1, which also lists amounts of each of the two SEC fractions in each asphalt. These amounts are the natural abundance levels, and they vary considerably.

Seven sets of crossblended mixtures were prepared. Each set consists of eight members. In each set, the SEC Fraction-II component is the same. The SEC Fraction-I component is varied among members of the set. The ratio of components for each set is that of the parent asphalt of the SEC Fraction-II component. No set of crossblends was prepared from the SEC Fraction-II of asphalt AAM-1, because of the high natural abundance of SEC Fraction-I in this asphalt. Crossblends involving the SEC Fraction-II of AAM-1 have very high viscosities.[5]

Table 2 lists absolute viscosities of seven sets of crossblended mixtures at 25°C (77°F) and 1.0 rad/s. Each column in Table 2 corresponds to one of the seven sets of crossblends, in which the relative abundance of the two SEC fractions and the nature of the SEC Fraction-II are constant. In each column of data, only the source of the SEC Fraction-I changes from entry to entry down a column. Each row in Table 2 lists viscosities of crossblends in which the SEC Fraction-I source is constant. The SEC Fraction-II source and the relative abundance of the two fractions change from entry to entry along a row.

The entries in Table 2 in which both the SEC fractions are derived from the same source correspond to reconstituted parent asphalts. The viscosities of these mixtures are observed to be two to three times larger than the original asphalts. This is because light ends are lost in the workup process, resulting in somewhat enhanced viscosities in the reconstituted mixtures.

Figures 1-7 are Black plots of rheological data collected on the mechanical spectrometer for the seven sets of crossblends. Dynamic moduli (G*) values at 25°C (77°F) were measured for each mixture at numerous rates of shear, and the value of the phase angle (δ) at each rate of shear was plotted against the G* value. Low δ values indicate substantial elastic components in an asphalt, and vice versa. Asphalts whose Black plots exhibit large δ changes for a given range of G* are shear susceptible. All crossblended mixtures whose Black plots are illustrated in Figure 1 contain 78.3 mass % of SEC Fraction-II of AAA-1. The Black plots of the eight different mixtures vary greatly. The mixture containing SEC Fraction-I of AAD-1 is very distinct from the other seven in that δ values in the Black plot are lower for a given G* value and do not range over wide values of δ. This means that the mixture containing SEC Fraction-I of AAD-1 contains the largest elastic component and is least shear susceptible. On the right side of Figure 1, the mixture containing SEC Fraction-I of AAM-1 is characterized by much larger δ values and lower G* values. The Black plot of this mixture

indicates that its rheological properties will be very different from those of the mixture containing SEC Fraction-I of AAD-1. Due to the composition of the mixtures, the difference must be caused by the nature of the SEC Fraction-I materials. In Figure 1, the curve corresponding to the mixture containing SEC Fraction-I of AAG-1 also is somewhat distinctive. This curve ranges over a wide δ range, indicating that the mixture is highly shear susceptible. The curves corresponding to mixtures containing SEC Fraction-I of AAA-1, AAB-1, AAC-1, and AAF-1 are virtually superimposable. The curve corresponding to the mixture containing SEC Fraction-I of AAK-1 shows that this mixture is not as shear susceptible as most of the other mixtures.

The Black plots of the other six sets of mixtures exhibit similar trends to those observed in Figure 1 (Figures 2-7). Curves representing rheological data for mixtures containing SEC Fraction-I of AAD-1 lie at the lowest values of δ for a given range of G* values, and curves representing rheological data for mixtures containing SEC Fraction-I of AAM-1 exhibit contrary characteristics. In Figure 6, the differences are not very pronounced. This is because the concentration of SEC Fraction-I materials in asphalt AAG-1 is low. The mixtures containing SEC Fraction-I of AAG-1 are most shear susceptible, based on inspection of the Black plots. Again, the lines in Figure 6 are not sufficiently differentiated to demonstrate this tendency. Curves representing rheological data for mixtures containing SEC Fraction-I of the other five asphalts are more or less similar and are intermediate between the other three curves. In Figures 1, 2, 4, and 8, the Black plots of mixtures containing SEC Fraction-I of AAK-1 indicate that these mixtures are relatively less shear susceptible.

The Black plots of the mixtures, and correspondingly their rheological properties, become more distinct as the concentration of SEC Fraction-I in the mixture increases, and vice versa.

Reduced specific viscosities of all the crossblended mixtures have been calculated and are listed in Table 3. In order to do this, relative viscosities of the mixtures first were calculated. The relative viscosity of a mixture is the ratio of the viscosity of the solution divided by the viscosity of the solvent, both measured at the same temperature and rate of shear. For the crossblended mixtures, it is assumed that the SEC Fraction-II component is the solvent, and so relative viscosities may be calculated by dividing each entry in Table 2 by the appropriate entry in Table 1. The viscosities of the SEC Fraction-II materials vary considerably and affect the absolute viscosities of the mixtures. Specific viscosities then are calculated from relative viscosities by subtracting unity (one) from the relative viscosities. Reduced specific viscosities are calculated by dividing specific viscosities by the mass fraction of SEC Fraction-I, the solute, in a mixture. For example, the mass fraction of SEC Fraction-I in the eight mixtures listed in column 1 of Table 3 is 0.217.

Reduced specific viscosities are measures of compatibility of a system. Inspection of Table 3 reveals that the values range from 10, indicating a highly compatible system, to over 1,600, indicating a highly non-compatible system. Four of the sets of eight crossblends (columns 1, 2, 4, and 7 in Table 3) contain ~ 0.21 - 0.25 mass fraction of SEC Fraction-I, so that the concentrations of the dispersed components in these mixtures are more or less equivalent. The other three sets of crossblends (columns 3, 5, and 6 in Table 3) have lower concentrations of SEC Fraction-I (0.11 - 0.14). In most cases, the entries in columns 1, 2, 4, and 7 in Table 3 are much higher than the entries in columns 3, 5, and 6. The exceptions are the last entries in the columns, corresponding to mixtures in which the SEC Fraction-I component is derived from asphalt AAM-1. Therefore the concentration of SEC Fraction-I in a mixture usually strongly influences compatibility of the mixture. The AAM-1 SEC Fraction-I obviously is an unusual material. In columns 1, 2, 4, and 7, Table 3, even if the AAM-1 entries are discounted, reduced specific viscosity values vary greatly. Those mixtures in which SEC Fraction-I is derived from AAG-1 usually have relatively low reduced specific viscosities. Those mixtures in which the SEC Fraction-I is derived from AAD-1 have high reduced specific viscosities. The same trends are observed in the entries in columns 3, 5, and 6, Table 3. In the discussion on Black Plots above, it was emphasized that mixtures containing SEC Fraction-I components of AAD-1, AAG-1, and AAM-1 are unique, but in different ways. Reduced specific viscosities of mixtures containing SEC Fraction-I of the other five asphalts do not appear to vary as systematically. This indicates that specific interactions of these SEC Fraction-I materials with SEC Fraction-II materials influence compatibilities of mixtures. Inspection of columns 1, 2, 4, and 7 shows that the reduced specific viscosity values in column 1 tend to be somewhat higher than those in the other three columns. Therefore the SEC Fraction-II of AAA-1 is the least effective solvent of the four SEC Fraction-II materials. Similar considerations lead to the conclusion that SEC Fraction-II of AAF-1 is a better solvent than that of AAC-1. Concentrations of SEC Fraction-I in the two sets of crossblends are almost identical, and reduced specific viscosities in column 3 are much lower than those in column 5.

If the values in Table 3 are read across in rows instead of columns, it is evident that the nature of the SEC Fraction-II component of a particular mixture does not influence reduced specific viscosities as much as does the nature of the SEC Fraction-I component or the relative amounts of the two

components. Nevertheless there is some influence of the SEC Fraction-II source. The data in Table 3 indicate that certain combinations of materials lead to unexpectedly large incompatibilities or the reverse.

CONCLUSIONS

Crossblended mixtures of asphalts have been prepared from two size exclusion chromatography fractions derived from eight different asphalts. The rheological properties of the mixtures were determined and it was found that, with one exception, the nature of the fraction assumed to correspond to the asphalt dispersed component and its relative abundance strongly influences rheological properties. These materials, which are the initial size exclusion chromatography eluates, are known to contain most of the polar, aromatic viscosity-building components of asphalts. The nature of the fraction corresponding to asphalt solvent components has a lesser influence on measured rheological properties of most crossblended mixtures, again with the exception of one set of mixtures.

REFERENCES

1. Traxler, R. N. Asphalt, Its Composition, Properties, and Uses, Reinhold, New York, 1961. Chapter 5.
2. Heithaus, J. J. (1962), J. Inst. Petrol., 48, pp. 45-53.
3. Altgelt, K. H., and O. L. Harle (1975), Ind. Eng. Chem., Prod. Res. Dev., 14, pp. 240-246.
4. Traxler, R. N. (1960), Preprints, Div. Petrol. Chem., Am. Chem. Soc., 5, pp. A71-A77.
5. SHRP-A-368, Binder Characterization and Evaluation, Volume 2: Chemistry. Strategic Highway Research Program, National Research Council, Washington, D.C., 1993.
6. SHRP-A-367, Binder Characterization and Evaluation, Volume 1. Strategic Highway Research Program, National Research Council, Washington, D.C., 1994, pp. 9-25.
7. Turner, T. F., S. S. Kim, J. F. Branthaver, and J. F. McKay, Symposium on Chemistry and Technology of Asphalt-Containing Materials, 210th Meeting of the Am. Chem. Soc., Chicago, IL, Aug. 22, 1995.
8. SHRP-A-370, Binder Characterization and Evaluation, Volume 4: Test Methods. Strategic Highway Research Program, National Research Council, Washington, D.C., 1994.

DISCLAIMER

ACKNOWLEDGMENTS

The authors thank the Federal Highway Administration for supporting this work under Contract No. DTFH61-92C-00170. Rheological measurements were performed by P. M. Harnsberger and F. A. Reid. J. Greaser prepared the manuscript. Figures were prepared by S. S. Kim.

Table 1. Yields of SEC Fractions of Eight SHRP Asphalts and Viscosities of SEC Fraction-II

Asphalt	Natural Abundance of SEC Fraction, Mass %		Viscosity (25°C; 1.0 rad/s) of SEC Fraction-II, Pa·s
	SEC Fraction-I	SEC Fraction-II	
AAA-1	21.7	78.3	506
AAB-1	20.8	79.2	1,367
AAC-1	13.6	86.4	8,602
AAD-1	21.2	78.8	336
AAF-1	13.3	86.7	53,350
AAG-1	11.2	88.8	62,380
AAK-1	24.8	75.2	1,124
AAM-1	31.8	68.2	26,350

Table 2. Viscosities (Pa·s) of Crossblended Mixtures of SEC Fractions of Asphalts, 25°C, 1.0 rad/s

Parent asphalt of SEC Fraction-I component of mixture	Parent asphalt of SEC Fraction-II component of mixture						
	AAA-1	AAB-1	AAC-1	AAD-1	AAF-1	AAG-1	AAK-1
AAA-1	65,200	179,600	230,100	36,100	642,400	204,400	155,100
AAB-1	90,500	148,400	220,800	36,800	384,900	403,600	198,600
AAC-1	95,900	148,000	156,100	43,300	571,900	362,950	251,300
AAD-1	177,300	223,100	225,400	59,200	884,300	764,800	240,700
AAF-1	101,400	185,400	225,900	50,000	507,000	466,300	217,400
AAG-1	36,700	97,300	138,600	26,600	502,400	405,500	164,750
AAK-1	95,800	145,100	185,700	31,300	344,600	332,250	165,450
AAM-1	3,500	10,200	26,500	3,000	114,900	125,900	10,600

Table 3. Reduced Specific Viscosity Values of Crossblended Mixtures of SEC Fractions of Asphalts, 25°C, 1.0 rad/s.

Parent asphalt of SEC Fraction-I component of mixture	Parent asphalt of SEC Fraction-II component of mixture						
	AAA-1	AAB-1	AAC-1	AAD-1	AAF-1	AAG-1	AAK-1
AAA-1	590	630	190	500	80	20	550
AAB-1	820	520	180	510	50	50	710
AAC-1	870	520	130	600	70	40	900
AAD-1	1,610	780	185	830	120	100	860
AAF-1	920	650	185	700	60	60	770
AAG-1	330	340	110	370	60	50	590
AAK-1	870	510	150	430	40	40	590
AAM-1	30	30	15	40	10	10	30

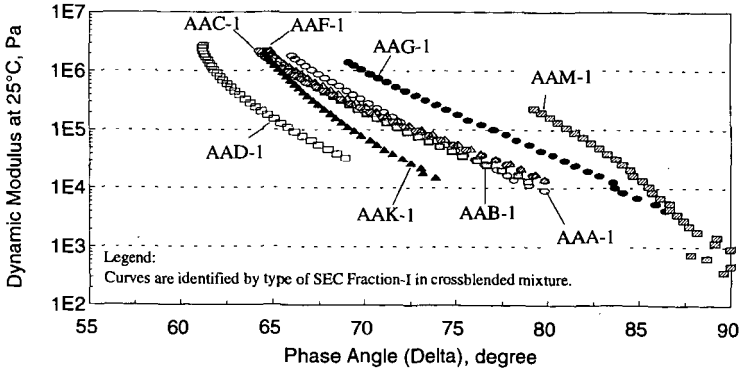

Figure 1. G* vs. phase angle for mixtures of SEC Fraction-II of AAA-1 (78.3%) with SEC Fraction-I (21.7%) of eight different asphalts.

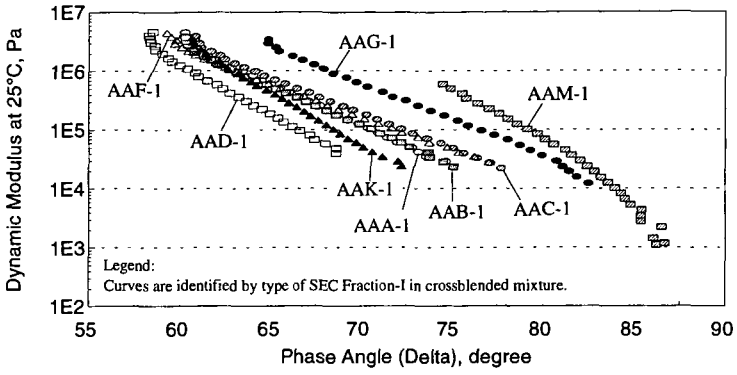

Figure 2. G* vs. phase angle for mixtures of SEC Fraction-II of AAB-1 (79.2%) with SEC Fraction-I (20.8%) of eight different asphalts.

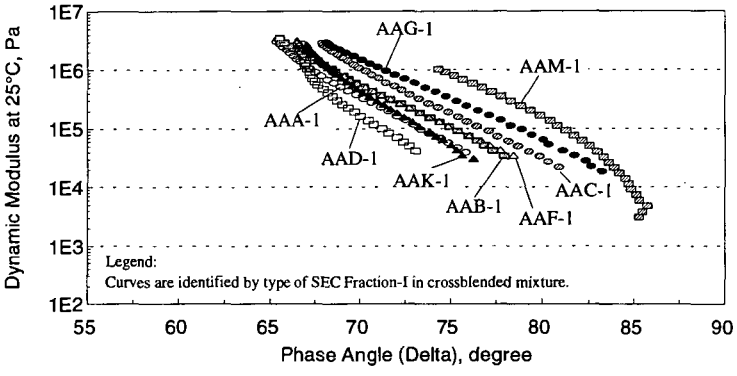

Figure 3. G* vs. phase angle at 25°C for mixtures of SEC Fraction-II of AAC-1 (86.4%) with SEC Fraction-I (13.6%) of eight different asphalts.

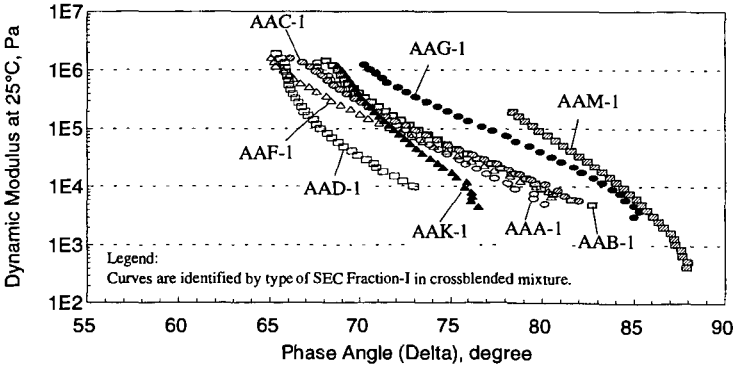

Figure 4. G* vs. phase angle for mixtures of SEC Fraction-II of AAD-1 (78.8%) with SEC Fraction-I (21.2%) of eight different asphalts.

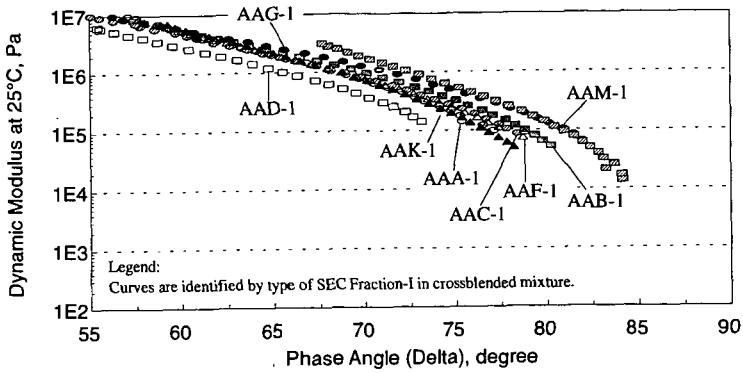

Figure 5. G* vs. phase angle for mixtures of SEC Fraction-II of AAF-1 (86.7%) with SEC Fraction-I (13.3%) of eight different asphalts.

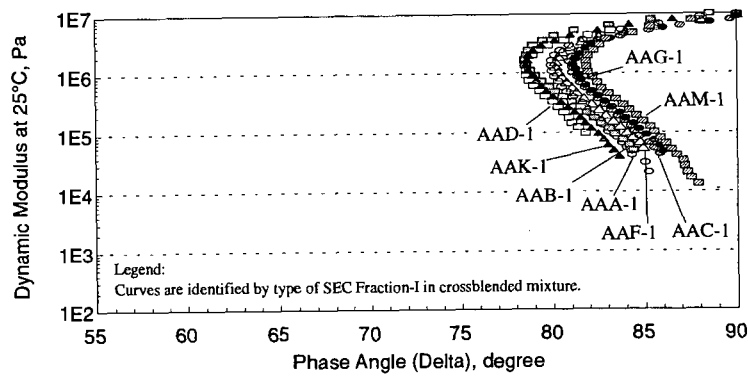

Figure 6. G* vs. phase angle for mixtures of SEC Fraction-II of AAG-1 (88.8%) with SEC Fraction-I (11.2%) of eight different asphalts.

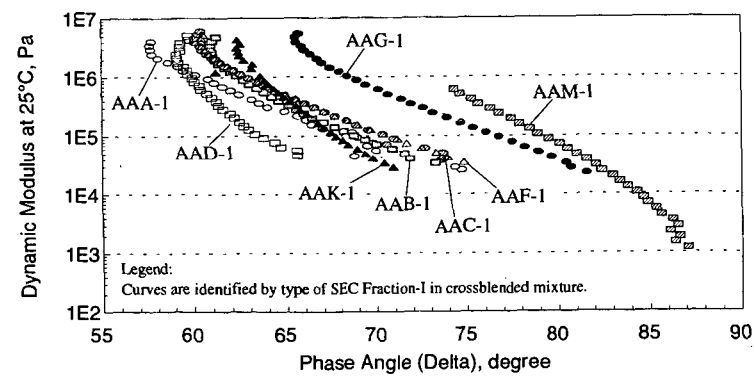

Figure 7. G* vs. phase angle for mixtures of SC Fraction-II of AAK-1 (75.2%) with SEC Fraction-I (24.8%) of eight different asphalts.

CHARACTERIZATION OF RHEOLOGICAL AND THERMAL BEHAVIOR OF ASPHALT CEMENTS MODIFIED BY ETHYLENE COPOLYMERS

Dr Bernard Brulé, Engineer — Entreprise Jean Lefebvre, 11 Boulevard Jean Mermoz, 92200 Neuilly sur Seine, France

Dr Sabine Gazeau, Engineer — Entreprise Jean Lefebvre, Laboratoire Central, Dourdan, France

Keywords: Polymer modified bitumens, differential scanning calorimetry (DSC), rheological behaviour, ethylene copolymers.

1. INTRODUCTION

The rheological properties of bituminous binders govern the subsequent performance of special hot mixtures in pavements. In the case of road pavements, the constraints engendered by moving vehicles are of dynamic origin, and dynamic rheology can be used to analyze the visco-elastic behaviour of the materials subject to loadings whose frequencies are close to those to which the road is subjected.

Differential scanning calorimetry (DSC) can be used to analyze the thermal behaviour of ethylene-copolymer-modified bitumens, and reveals there to be a good match between the melting range of the copolymer and the zone of transition between visco-elastic behaviour and purely viscous behaviour of the material [1].

As a result of SHRP work, dynamic rheology can be used to determine an isomodulus temperature that can be proposed for monitoring performance at high temperatures.

The results given in this paper concern ethylene copolymer/bitumen blends whose melting (and crystallization) ranges and visco-elastic behaviour depend on the type of ethylene copolymer, among other things.

2. ETHYLENE-COPOLYMER-MODIFIED BITUMENS STUDIED

Binders made with a pure straight run bitumen (70/100) and different ethylene copolymers were studied.

The ethylene copolymers used have the following characteristics:

Copolymer A: ethylene and methyl acrylate copolymer (EMA) with high crystallinity and molecular weight.

Copolymer B: ethylene and vinyl acetate copolymer (EVA) with moderate crystallinity and molecular weight.

Copolymer C: ethylene and vinyl acetate copolymer (EVA) with low crystallinity and molecular weight.

These bitumens modified with 10% ethylene copolymers have a continuous polymer matrix within which are dispersed bitumen globules of different sizes (see Figure 1).

3. DIFFERENTIAL SCANNING CALORIMETRY

Ethylene copolymers are semi-crystalline copolymers. They are made of polyethylene crystallites separated from each other by amorphous regions caused by the co-monomer. The peak of ethylene copolymer melting is at lower temperatures than that of the polyethylene, for the co-monomer results in a reduction in the length of crystallizable sequences. The amorphous region is characterized by a glass transition temperature. All these characteristics can be determined by differential scanning calorimetry (DSC).

3.1. Test method

The thermal behaviour of ethylene-copolymer-modified bitumens is characterized by differential scanning calorimetry (DSC) using a Mettler DSC 30 analyzer.

This technique can determine the enthalpy of changes in the physical state of the copolymer such as:

melting: first-order transition characterized by an endothermic signal,

crystallization: first-order transition characterized by an exothermic signal.

The glass transition temperature (Tg), which is an important characteristic of amorphous materials, is a second-order transition. The glass transition temperature of ethylene copolymers is between -20 and -40°C, depending on the ethylene copolymer. This paper will deal only with first-order transitions.

In the experiments the ethylene-copolymer-modified bitumens are softened by heating them, and are placed in a sealed aluminum crucible. They have to be left to stand 24 hours before the sample can be analyzed (time for the structure to stabilize).

All the tests are carried out with a cooling rate of 5°C.min^{-1} to -80°C. The sample is then heated to 120°C at a rate of 5°C.min^{-1}, then cooled to -20°C at a cooling rate of 5°C.min^{-1}.

3.2 Thermograms of ethylene-copolymer-modified bitumens

The thermograms in Figure 2 show the melting ranges of the three ethylene copolymers solvated with a maltenic fraction of the bitumen.

From the thermograms of Figure 2 it would appear that the temperature range defining the melting ranges varies appreciably, depending on the type of ethylene copolymer:

Melting range of ethylene copolymer A: 63-99° ➡ Melting peak : 86°C

Melting range of ethylene copolymer B: 35-81° ➡ Melting peak : 53°C

Melting range of ethylene copolymer C: 27-62° ➡ Melting peak : 48°C

Like the melting ranges, the crystallization ranges depend on the type of ethylene copolymer, as can be seen from the thermograms in Figure 3.

The kinetics of ethylene copolymer crystallization are slow because of copolymer dispersion in the bitumen, which explains the shift between the melting ranges and crystallization.

4. DYNAMIC RHEOLOGICAL TESTS

Pure bitumens and polymers are visco-elastic materials, i.e. their behaviour is between that of an elastic solid and that of a viscous liquid.

Dynamic rheology is an oscillation technique that can be used to study the structure of materials in accordance with frequency (isotherms) and/or temperature (isochrones). It involves submitting the sample to a sinusoidal stress or deformation and measuring the material's response to this loading.

4.1. Test method

Measurements are taken with a Bohlin rheometer which uses plane-plane geometry. The temperature of the sample (immersed in water) is controlled by a thermoregulator. The sinusoidal deformation is chosen after a stress scan in order to locate it within the range of linear visco-elasticity. The results are given in the form of a modulus, G*, for which the imaginary part is the loss modulus, G" (viscous component of the modulus), and the real part is the storage modulus, G' (elastic component of the modulus). The delta phase angle, δ, represents the lag between the stress and deformation.

4.2. Interpretation of results

Examination of the isochrones of the modulus (G*) at 1.5 Hz, under the conditions proposed by the SHRP [2], and by means of analysis of the gradient of variation of modulus G* with temperature, provides an assessment of the temperature susceptibility of bituminous binders [3].

Examination of the isochrones of the delta phase angle, δ determines the temperature range between the visco-elastic region and the flow region of the ethylene-copolymer-modified bitumen.

In addition, examination of G* and δ isochrones allows for assessment of a temperature at which $G^*/\sin\delta = 1$ kPa, the figure the SHRP specifications propose for the verification of binder performance at high temperatures [2].

5. DSC/DYNAMIC RHEOLOGY RELATIONSHIP

The isochrones of the modulus and of the phase angle of bitumen mixes with ethylene copolymers A, B, and C are shown in Figures 4 and 5.

Visco-elastic range

The temperature at which the test begins (15°C) is within the visco-elastic range of the materials.

The rheological behaviour of the pure bitumen is different to that of the highly modified bitumens: its modulus decreases rapidly with the temperature, and it proves to be highly temperature-susceptible. The isochrone of the phase angle does not have a rubbery plateau, contrary to ethylene-copolymer-modified bitumens: its structure collapses gradually as the temperature rises. Its phase angle increases parabolically up to the asymptotic value of 90°. At as little as 18°C, more than 90% of the modulus of the pure bitumen is accounted for by the viscous component (phase angle greater than 65°).

From the isochrones of the modulus, G*, of highly modified bitumens (Figure 4), it can be seen that the reduction of the modulus in accordance with temperature is much lower than that seen with pure bitumens, which is a reflection of the improvement in thermal susceptibility brought about by addition of ethylene copolymer. Additionally, the degree of this variation depends on the type of ethylene copolymer A.

Thus, examination of the isochrones of the modulus allows for classification of binders in decreasing order of temperature susceptibility [4]: pure 70/100 bitumen, bitumen with copolymer C, bitumen with copolymer B, bitumen with copolymer A.

The isochrones of the phase angle in the modified binders (Figure 5) show that these binders are substantially more elastic than pure bitumen (lower phase angles across the whole range of temperatures studied). However, the contribution of the elastic component of the modulus is specific to each ethylene copolymer. It becomes negligible when the phase angle exceeds 65°.

Thus, the bitumen blend with copolymer A is the most elastic of the three modified bitumens studied. This is true for the entire temperature range. The bitumen mix with copolymer B is more elastic than that with copolymer C.

The significant increase in the phase angle of the modified bitumen is observed above 53°C for copolymer B, and above 43°C for copolymer C. This increase is linked to the melting of the ethylene copolymer, as detected by DSC analysis.

Flow region

The flow region corresponds to melting of the ethylene copolymer.

From the thermograms of Figure 2 and the phase-angle isochrones of Figure 5, it can be seen that the increase in the phase angle of the bitumens with copolymers B and C is close to the melting peak (Pf) determined by DSC analysis (53° C and 43°C respectively). The increase in the phase angle induces a decrease in elastic effects and a rise in viscous phenomena. This is because more than 90% of the modulus is attributable to its viscous C component when the phase angle is higher than 65°C [4].

The temperature corresponding to a phase angle of 65° is close to 68°C for bitumen modified with copolymer B and 53°C for bitumen modified with copolymer C.

As for the bitumen modified with copolymer A, its melting range is at higher temperatures (melting peak at 86°C). This is why the phase angle is low (major elastic effects) in the temperature range studied (10-70°C), for the copolymer does not melt.

Copolymer melting therefore results in a major modification in the rheological behaviour of the binders. It shows the temperature range between the visco-elastic field and the flow field. The less temperature-susceptible the ethylene copolymer is, the later flow will start.

It thus appears to be possible to guide the choice of the ethylene copolymer in accordance with the climatic conditions of the site (maximum temperature of the pavement).

6. PROCEDURE FOR DYNAMIC RHEOLOGICAL TESTING

Knowledge of the melting and crystallization ranges of ethylene-copolymer-modified bitumens allows for informed discussion of the effect the procedure for dynamic rheological testing (Bohlin) has on results. This comment particularly concerns modified binders with high copolymer contents, i.e. with a continuous polymer matrix, for binders with a continuous bitumen matrix behave in much the same way as the bitumen itself.

If a sample is placed on the rheometer at a temperature either in the melting range or in the crystallization range, the modulus measured will depend on the temperature history of the material (overmelting phenomenon).

The usual procedure for studying rheological behaviour involves placing the sample at a temperature of around 30°C.

To study the effect of the temperature history on rheological behaviour, isochrones were determined for 15 to 95°C for the bitumen modified with copolymer A, and for 15 to 70°C for the bitumen modified with copolymer C. The sample was then cooled to 15°C and a second isochrone was determined.

Ethylene copolymer A had a melting peak at around 86°C, and its crystallization range is from around 73 to 53°C (Figure 3).

The two isochrones of the modulus were identical, as can be seen in Figure 6.

Ethylene copolymer B has a melting peak around 53°C, and its crystallization range is from around 81 to 35°C (Figure 3). The two isochrones of the modulus are identical, just as for copolymer A.

As for copolymer C, its melting peak is around 43°C, and it starts to crystallize at around 12°C, as is shown in Figures 2 and 3. When the second isochrone starts at 15°C, the crystallization of copolymer C has not yet started. The copolymer overmelts, resulting in a significant reduction of the modulus (Figure 7). The moduli become identical as they enter the flow region.

Knowledge of the thermal behaviour of the ethylene copolymers is therefore very important for proper interpretation of their rheological behaviours (thermal and rheological) depending on the characteristics of the copolymer.

7. SHRP HIGH SERVICE TEMPERATURES

The new SHRP specifications [2] propose that at the mean maximum weekly temperature of the pavement, the value of $G^*/\sin\delta$ of the binder as is should be 1 kPa at a frequency of 1.6 Hz. This value ($G^*/\sin\delta = 1$ kPa) expresses a minimum rigidity, as shown by the following expressions [5]:

$$G^* = 1/J^*$$
$$G^*/\sin\delta = 1/J^*\sin$$

where J^* is the complex compliance (1/Pa).

Associated with an SHRP performance criteria, this temperature can replace the ring and ball (R & B) softening point test in the case of polymer-modified bitumens for which it has been largely demonstrated that the test was not appropriate.

Through interpretation of their isochrones, the rheological behaviour characterization tests presented above allow for easy evaluation of the temperature for which $G^*/\sin\delta = 1$ kPa, and for identification of δ and G^* for that temperature (Table 1).

From Table 1 it can be seen that at temperatures where $G^*/\sin\delta = 1$ kPa, the difference between $G^*/\sin\delta$ and G^* is negligible. The phase angles are sufficiently great to allow the following simplification:

$$\sin\delta \rightarrow 1$$
$$G^*/\sin\delta \rightarrow G^*$$
$$G^*/\sin\delta \rightarrow 1/J^*$$

The isomodulus temperatures are considerably higher than the ring and ball softening points [4]. It is clear that the ring and ball temperatures for ethylene-copolymer-modified bitumens are not isomodulus temperatures.

8. CONCLUSION

Differential scanning calorimetry (DSC) is seen to be a promising technique for characterizing and understanding the behaviour of ethylene-copolymer-modified bitumens.

Dynamic rheology provides an appreciation of the temperature susceptibility of bituminous binders, on the basis of modulus isochrones.

In the case of highly modified ethylene-copolymer-modified bitumens (continuous polymer matrix), the melting ranges of the copolymers and the isochrones of the phase angle are used to determine the temperature range between the visco-elastic region and the flow region. Melting of the copolymer engenders an increase in the phase angle, which is reflected by a gradual decrease in elastic effects and an increase in viscous phenomena. The greater the

crystallinity and the molecular weight of the copolymer, the higher the temperature of the flow area will be.

In addition, knowledge of the thermal behaviour of ethylene copolymers in bitumen makes it possible to discuss the effect of the test procedure on the rheological behaviour analysis of modified binders and the interpretation of results.

The temperature for which $G^*/\sin\delta = 1$ kPa, which is the value proposed in SHRP specifications for checking high-temperature performance, also depends on the characteristics of the copolymer.

BIBLIOGRAPHY

[1] R. SHUTT, C. TURMEL, "Analyse Thermique Différentielle et Propriétés Rhéologiques de Bitumes Modifiés parles Polymères Semi-cristallins", 5th Eurobitume Symposium, Stockholm, Abstracts and Reports, June 1993, pp. 76-80.

[2] D.A. ANDERSON, "Programme SHRP: Méthodes d'essai et spécification des liants", Revue Générale des Routes et Aérodromes, No. 714, January 1994, p. 48.

[3] G. RAMOND, M. PASTOR, C. SUCH, "Recherche des performances d'un liant à partir de son module complexe", 5th Eurobitume Symposium, Stockholm, Abstracts and Reports, June 1993, p. 81.

[4] B. BRULE, M. MAZE, "Les bitumes polymères pour enrobés spéciaux: élastomères ou plastomères?", Revue Générale des Routes et Aérodromes, No. 726, 1995, p. 42.

[5] C. SUCH, G. RAMOND, "Les spécifications SHRP en termes plus usuels - Tentative de décryptage", LCPC, Communication presented to the SHRP Seminar in Lille, Sept 1994.

	R&B (°C)	G* at R&B temp. (Pa)	Phase angle at R&B temp.	T(G*/sin δ) = 1kPa (°C)	G* (Pa) at isomodulus temp.	Phase angle at isomodulus temp.
Bitumen	**45**	9.65E + 03	83	**62**	998	83
Bitumen with copolymer A	**86**	1.85E + 03	63	**96**	974	75
Bitumen with copolymer B	**68**	3.63E + 03	69	**79**	996	79
Bitumen with copolymer C	**56**	2.67E + 03	70	**70**	998	80

Table 1: Conventional and SHRP characteristics at high service temperatures

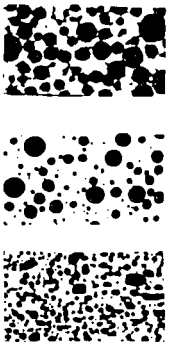

Ethylene copolymer A-bitumen

Ethylene copolymer B-bitumen

Ethylene copolymer C-bitumen

Figure 1: Microstructure of ethylene-copolymer-modified bitumens (10% blends)

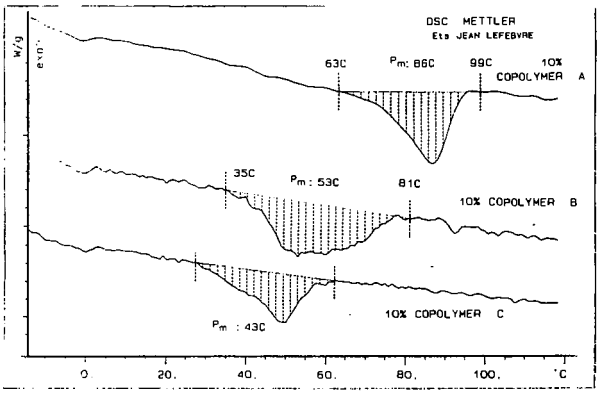

Figure 2: Thermograms of bitumen blends with ethylene copolymer A, B, and C Melting ranges

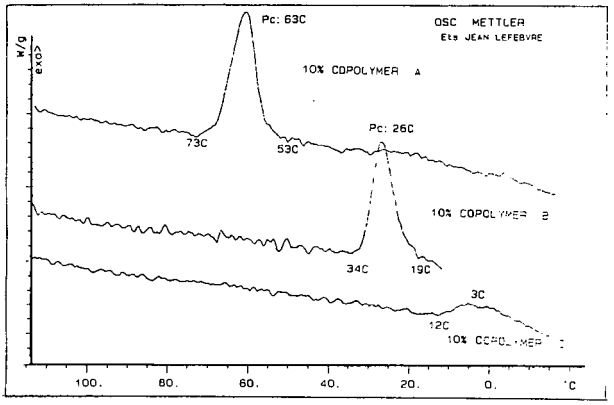

Figure 3: Thermograms of bitumen blends with ethylene copolymer A, B, and C Crystallization ranges

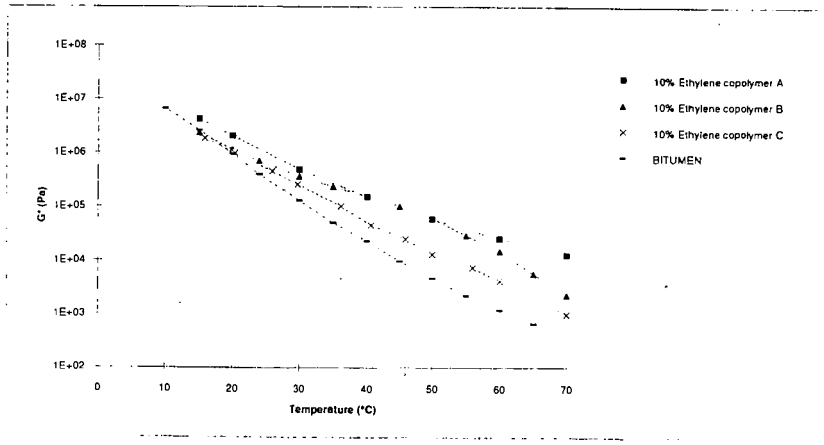

Figure 4: G* isochrones (1.5 Hz) for bitumen blends with ethylene copolymers A, B, and C

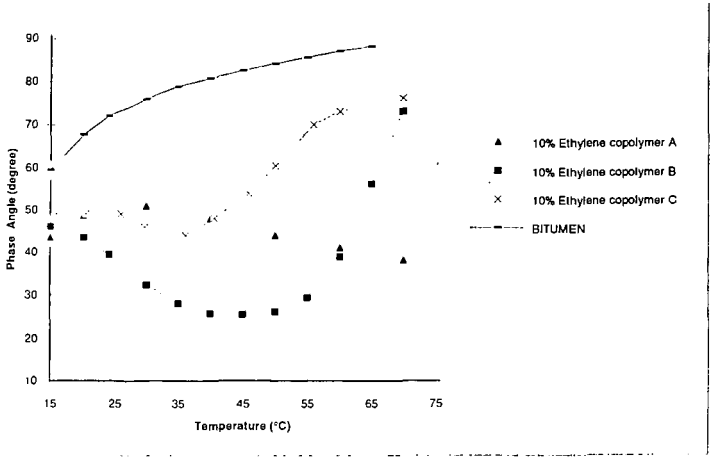

Figure 5: δ isochrones (1.5 Hz) for bitumen blends with ethylene copolymers A, B, and C

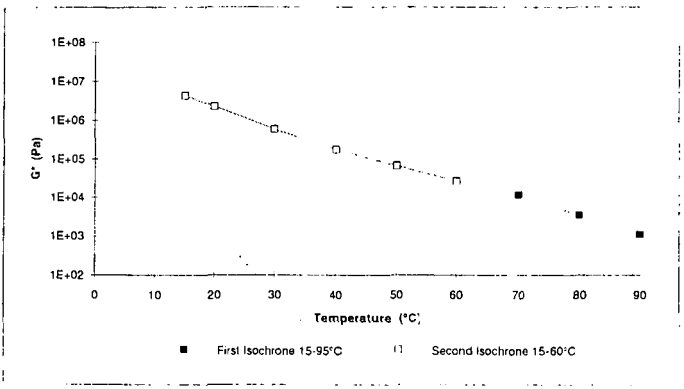

Figure 6: G* isochrones for bitumen modified with 10% of copolymer A

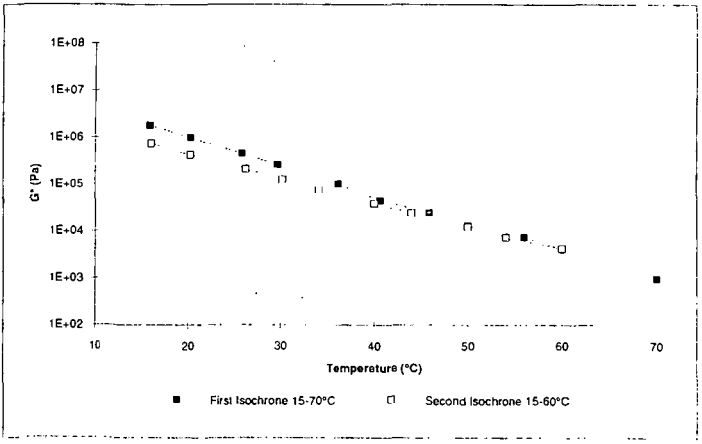

Figure 7: G* isochrones for bitumen modified with 10% of copolymer C

HP-GPC CHARACTERIZATION OF ASPHALT AND MODIFIED ASPHALTS FROM GULF COUNTRIES AND THEIR RELATION TO PERFORMANCE BASED PROPERTIES

H. I. Abdul Wahhab, Mohammad F. Ali,
I. M. Asi, and I. A. Dubabe
King Fahd University of Petroleum and Minerals
Dhahran 31261, Saudi Arabia

Keywords: Modified Asphalts, HP-GPC Characterization, Gulf Countries Asphalts

INTRODUCTION

Asphalt producing refineries in the Gulf countries include Ras Tanura and Riyadh (Saudi Arabia), Al-Ahmadi (Kuwait), and BAPCO (Bahrain). Riyadh and Ras Tanura refineries are located in the central and eastern Saudi Arabia respectively. Arabian light crude oil is used to produce 2000 to 3000 tons of asphalt per day using vacuum distillation, air blowing and grade blending techniques to produce 60/70 penetration grade asphalts in each of these two Saudi refineries. All of the asphalt cement used in Saudi Arabia, Qatar and parts of the United Arab Emirates is supplied by Riyadh and Ras Tanura refineries.

Al-Ahmadi refinery supplies all of the asphalt cement needed for construction in the state of Kuwait. Ratwi-Burgan crude oil mix is used to produce 750 to 1000 tons of asphalt per day using vacuum distillation and air blowing processes.

BAPCO refinery, Bahrain, utilizes crude oils produced from Saudi oil fields and supplies asphalt cement needed for construction in Bahrain, Oman and parts of United Arab Emirates.

The roadway network in Gulf countries has developed more rapidly than in many industrialized countries. The entire roadway network is built using flexible pavements due to the availability of relatively low cost asphalt binders. The asphalt binder plays a significant role in pavement ability to withstand thermal and fatigue cracking and contribute to permanent deformation behavior. Fatani et al [1] in a study about permanent deformation in Saudi Arabia have concluded that the asphalt cement is responsible for a major part of rutting in the region, and that extreme weather conditions of the Gulf countries has promoted an inferior performance of asphalt concrete mixes in the field.

Asphalt binders are thermo-visco-elastic materials where temperature and rate of load application has a great influence on their behavior. Asphalt consistency and hence ability to sustain and hold their fundamental cementing mechanism changes depending on temperature. The pure asphalt lack the proper balance of viscous fluid-elastic sponge properties which usually occur due to an effective elastic network created by molecular association. In recent years various studies have shown that polymer modification can be successful in forming this viscous fluid-elastic sponge balance by creating molecular entanglement in an asphalt.

This study was initiated to evaluate different locally available polymer materials in order to identify potential polymers to modify asphalts to satisfy the performance requirements in the Gulf countries' environmental conditions. The storage stability of the asphalt-polymer blends and the life cycle cost analysis of the polymer modification were also studied.

EXPERIMENTAL

1. Temperature data collection and temperature zoning: Metrology and Environmental Protection Agencies, Directorate of Climatology and other similar agencies in the Gulf countries were approached to provide the research team with the available historical annual environmental data covering the Gulf countries (GC). These data were analyzed and used to build temperature data base and to develop suitable temperature zoning for the GC.

2. Asphalt samples collection: Asphalt binder samples were collected from all asphalt cement producing refineries in the Gulf which include Ras Tanura and Riyadh (Saudi Arabia), Al-Ahmadi (Kuwait), and BAPCO (Bahrain) and an additional sample was collected from Awazel private company which modifies asphalt produced by Riyadh refinery.

3. Asphalt testing: Collected asphalt samples were subjected to comprehensive testing to determine their physical and chemical properties. Testing included:

a. Consistency testing; viscosity at 25°C (ASTM D 3570), 60°C (ASTM T-202-80) and 135°C (AASHTO T-201-80), penetration at 25°C and 4°C (AASHTO T-49-80), softening point (AASHTO T-53-81) and ductility (AASHTO T-51-81). Testing was carried out on fresh and rolling thin film oven (RTFO) residue (AASHTO T-240-78).

b. Performance based testing which was performed on original binder, RTFO residue and pressure aging vessel (PAV) residue [2]. Tests included flash point, rotational viscosity, dynamic shear, mass loss after RTFO, flexural creep stiffness and direct tension failure strain [2].

c. Chemistry, chemical composition of collected samples were determined using Corbett's method, ion exchange chromatography and high pressure gel permeation chromatography (HP-GPC).
The HP-GPC procedure for this study utilized four μ-styragel columns connected in the following order according to size: 10,000, 1000, 500 and 100 Å. Two kinds of detectors, a differential refractometer and a UV absorbance detector (230 nm and 340 nm) were used. HPLC grade tetrahydrofuran (THF) was used as a solvent mobile phase at ambient temperature (24°C) at a flow rate of 1.0 ml/min. the data were accumulated by a millennium 2010 chromatography manager.

4. Asphalt Modification: Asphalt cement which has a performance grade that does not satisfy the binder specification as determined by temperature zoning was modified to improve its quality. Modified binders were subjected to the same set of tests as virgin asphalts.

RESULTS AND DISCUSSION

Asphalt Testing: The complete test results for the collected asphalt samples, temperature data and contour map were published in Al-Abdul Wahhab et al [3].

Results indicate that asphalt cement produced in the Gulf satisfies the low temperature requirement but can only satisfy one zone of 64°C average seven day consecutive maximum temperature. Awazel air blown asphalt met the requirement of PG 70-10 while PG 58-10 and PG 76-10 zones have not been met. This indicates the necessity of modifying locally produced asphalts to meet the performance requirements of these temperature zones.

ASPHALT MODIFICATION

The asphalt modification work was carried out in two phases. The first phase focused on identifying potential polymers while the second focused on the optimization of modification process for the following selected polymers:

LLDPEX - Linear low density polyethylene grade 1182
PP500C - Polypropylene grade 500V
SBS - Styrene - butadiene - styrene

A fourth polymer, crumb rubber from truck tires (CRT) was also included for this study. The polymer modified samples were subjected to physical tests.
Results showed that addition of the polymer material significantly improves the physical and rheological properties of Arab asphalt binders for all sources and all polymer types.

HP-GPC Analysis

A typical HP-GPC profile is shown in Fig. 1. The variable on the x-axis is the time required of a particular size to emerge from the system. The reading on the y-axis is the detector response, which is an indicator of the concentration of asphalt molecules in solution. In order to distinguish HP-GPC profiles, the area under the curve is divided into different sections. Most frequently this is divided into three sections and the area under each section in determined. These three areas are referred to as large-molecular size (LMS), medium-molecular size (MMS), and small-molecular size (SMS) material. However, other researchers felt that these three parameters could not adequately model the subtle differences between the HP-GPC profiles of the asphalts used. Accordingly, for this study a procedure was used in which the area under the curve was divided into eight sections (see Fig. 1). This number was selected as the optimum needed to provide an accurate quantitative model of the HP-GPC profiles.

The cut-off points were selected to have equal elution times. The eight sections are numbered from left to right. Consequently, apparent molecular size decreases progressively from Section 1 to Section 8.

Fig. 1 also compares GPC profiles for fresh, RTFO and PAV aged asphalts. There are clear differences in each of the curves, with the PAV aged and RTFO aged samples showing significant

growth in the large-molecular size (LMS) region (material eluted between 24 and 30 minutes) for this sample. GPC profile Fig. 1 also shows the growth in LMS is accompanied by a gradual decrease in MMS and SMS regions. Profiles of parent asphalts, polymer modified asphalts, and RTFO/PAV asphalts are shown in Figs. 2, 3 and 4.

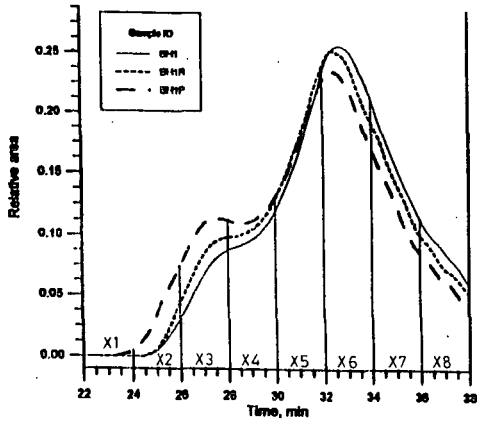

Fig. 1: HP-GPC profiles for original and oxidized asphalts

From the HP-GPC analysis it can be seen that all of the polymer modified asphalts have a larger percentage of fractions # 1, 2, 3 and 4 and a smaller percentage of fractions 5 and 6 than the parent AC-20. It is also apparent from the GPC profile that the fractions # 1, 2 and 3 have considerably increased for RTFO and PAV aged samples (Fig. 4) than modified non-aged asphalt.

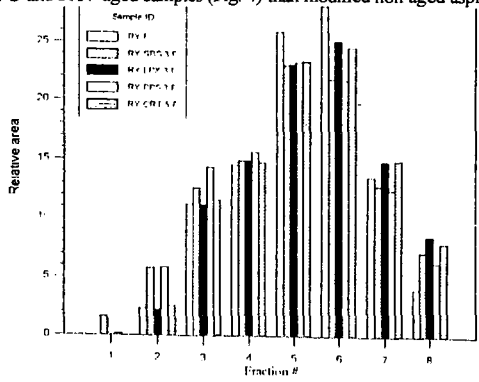

Fig. 2: HP-GPC partitions into Eights of parent AC-20 and polymer modified asphalts

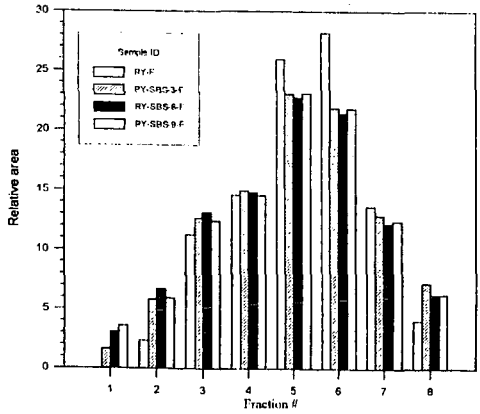

Fig. 3: HP-GPC partitioned into Eights of parent AC-20 and SBS-modified asphalts

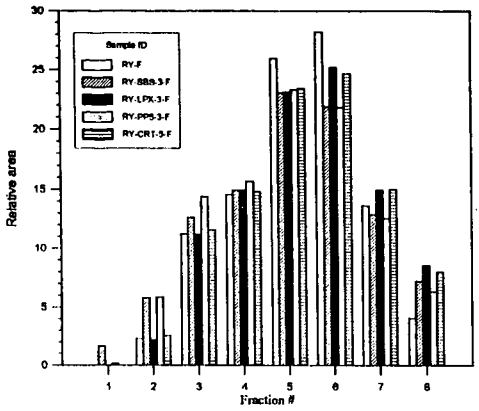

Fig. 4: HP-GPC partitioned into Eights of parent AC-20 and SBS-modified and their RTFO and PAV aged asphalts

Correlation Studies of Asphalt Composition with Its Performance-Related Characteristics :

This sub-task aims at finding the mathematical relation - if it exists - between the physical properties of the asphalt and its chemical composition. The physical properties which are included in this sub-task are shown in Table 1. The chemical composition is represented by the eight fractions (X_1 to X_8) into which the HP-GPC chromatograms were divided. X_1 was dropped from the analysis to get rid of interdependency between the eight fractions of the chromatograms, i.e. if X_1 is kept in the analysis, the sum of X's is always 100.

Table 1: Included physical properties

Used Symbol	Property
SG	Specific Gravity
PEN25	Penetration at 25°C
RPEN25	Retained Penetration at 25°C
PEN4	Penetration at 4°C
RPEN 4	Retained Penetration at 4°
SP	Softening Point
FP	Flash Point
DUC	Ductility
VIS25	Sliding Plate Viscosity at 25°C
VISR25	Viscosity Ratio at 25°C
VIS60	Absolute Viscosity at 60°C
VISR60	Viscosity Ratio at 60°C
RVIS135	Rotational Viscosity at 135°C
VIS135	Kinematic Viscosity at 135°C
VISR135	Viscosity Ratio at 135°C
PI	Penetration Index
PTS	Penetration Temperature Susceptibility
PR	Penetration Ratio
PVN	Penetration Viscosity Number
PVNI	Penetration Viscosity Number for VTS calculation
VTS	Viscosity Temperature Susceptibility
ω_c	Cross Over Frequency
R	Rheological Index
T_d	Defining Temperature
G*	Complex Dynamic Modulus, KPa
S	Flexural Creep Stiffness, MPa
m	Flexural Creep Slope

The purpose of the analysis is to help select from the 7 candidate variables X_2, X_3, ..., X_8 a smaller subset that will adequately explain the response. A number of variable selection procedures are available in the statistical literature. The most commonly used ones are the search over all possible subsets, the forward selection procedure and the stepwise selection procedure. The corresponding SAS PROC RSQUARE, SAS PROC FORWARD and SAS PROC STEPWISE were used and their results are noted. It is generally accepted that all stepwise procedure is vastly superior to the others and thus it is the one relied upon in this analysis.

Table 2 presents models for the different variables, together with their R^2 value and P-value for fresh and polymer modified samples.

Table 2: Regression analysis for fresh samples

Variable	Modification	Model	R^2	P-value
SG	No	$1.09 - 0.003X_3 - 0.002X_6$	0.53	0.0011
PEN25	No	$74.04 + 1.02X_1 - 1.67X_6$ P-value for testing significance of X_1 is 0.12	0.32	0.0297
RPEN25	No	$1.99 + 0.04X_1 - 0.08X_4 - 0.01X_7$ P-value for testing significance of X_7 is 0.10	0.85	0.0001
PEN4	No	$44.1 + 1.43X_3 - 0.9X_6$	0.71	0.0001
RPEN4	No	$0.14 + 0.03X_1 + 0.02X_6$	0.32	0.0316
SP	No	$-44.23 + 2.95X_1 + 0.47X_4 + 1.96X_5 + 1.55X_6$ P-value for testing significance of $X_4 = 0.11$	0.76	0.0001
FP	No	$971.44 - 2.05X_4 - 14.14X_5 - 33.45X_6 - 11.8X_7 + 8.06X_8$	0.97	0.0001
DUC	No	$205.67 - 7.96X_3 - 2.46X_7$	0.68	0.0001
VIS25	No	NO MODEL		
VISR25	No	NO MODEL		
VIS60	No	$(-48.722 + 1.758X_3 + 0.969X_6 + 0.958X_8) \times 10^3$	0.67	0.0002
VISR60	No	$2.66 - 0.04X_7$ P-value for testing significance of $X_1 = 0.10$	0.13	0.0001
RVIS135	No	$560 - 38.22X_3 + 49.68X_5 - 21.5X_8$	0.80	0.0001
VIS135	No	$-443.62 + 49.03X_4 + 16.39X_7$	0.55	0.0008
VISR135	No	$1.02 + 0.03X_6$	0.28	0.0126
PI	No	$-6.35 + 0.31X_3 + 0.13X_7$	0.74	0.0001
PTS	No	$0.05 - 0.001X_1 - 0.0006X_7$	0.77	0.0001
PR	No	$218.18 - 4.74X_3 - 4.14X_7$	0.63	0.0001
PVN	No	$-3.67 + 0.18X_4 + 0.038X_7$	0.63	0.0001
PVNI	No	$1.18 - 0.06X_6$	0.57	0.0001
VTS	No	$4.38 + 0.048X_1 - 0.1X_6$	0.43	0.0063
R	No	$2.132 + 0.17\ X_3$	0.76	0.0001
η_o	No	$8.32 \times 10^{-9} \cdot 1.64 \times 10^{-9} X_8$	0.41	0.0025
T_g	No	No Model		
PEN25	Yes	$87.15 - 5.22\ X_5$	0.63	0.0021
SP	Yes	No Model		
G*@76	Yes	$31776 - 3300\ X_6$	0.44	0.0107
G*@80	Yes	$20516 - 2089\ X_6$	0.38	0.0344
S@-18	Yes	$-1207.3 + 66.6\ X_1 + 85.5\ X_6$	0.77	0.0006
S@-12	Yes	$-678.6 + 44.22\ X_1 + 40.04\ X_4$	0.70	0.0018
m@-18	Yes	$0.391 - 0.0114\ X_1$	0.46	0.0077
m@-12	Yes	$0.489 - 0.0158\ X_1$	0.52	0.0082

It is worth noting that the R^2 value for any model can be increased on the expense of entering variables that are correlated with ones already in the model or that are not significant, and this is one problem the stepwise procedure tries to avoid. For those variables with a very low R^2, for example VISR60 (an R^2-value of 0.13 for fresh samples and in fact no fitted model for aged samples), an explanation would be that either a linear model does not provide a good fit for the data or that there is really no relationship between the dependent variable, in this case viscosity ratio at 60°, and the independent variables, the molecular size distribution. The latter may well be the case, because in that regard a logarithmic transformation was done on the data for all the variables and different statistical procedures were run and the results are a lot like those from a linear model. As a matter of fact, for some there was a slight decrease in the R^2 value. On the other hand, a high value of R^2, for example 0.97 for the variable FP for fresh samples, may not necessarily mean that the given model represents the true relationship if there is no physical evidence to indicate that. This may just be a purely mathematical result with no physical evidence but may warrant further study. An important point that is worth noting is the non-uniformity in the models found for fresh and aged samples. By that, we mean for any variable the model fitted for fresh samples may differ in the number and the nature of the independent variables entered and thus in the magnitude of the regression coefficients and in the R^2 value. That may be attributed to the fact that aged samples are inherently different from fresh ones and thus molecular size distribution is different.

It should be noted that the physical properties of asphalts are measured on whole homogenized sample, whereas the R^2 values reported in Tables 5 and 6 are based on the regression analysis of randomly picked GPC fractions. We conclude by noting that although some of those models may look good, they should be examined carefully and interpreted in accordance with physical results.

CONCLUSION

Addition of polymers significantly improve the physical and rheological properties of Arab asphalts. HP-GPC characterization can be used to predict physical properties of asphalts and modified asphalts.

ACKNOWLEDGMENT

The authors would like to thank King Abdulaziz City for Science and Technology (KACST) for providing support for this research and to the King Fahd University of Petroleum and Minerals for providing the laboratory space and facility.

REFERENCES

(1) Fatani,M.N., Al-Abdul Wahhab,H.I., Balghunaim,F.A., Bubshait, A., Al-Dubabe ,I. and Noureldin, A. S., "Evaluation of Permanent Deformation of Asphalt Concrete Pavement in Saudi Arabia". Final Report, National Res. Proj., KACST, Saudi Arabia, 1992.

(2) Strategic Highway Res. Prog., "The Superpave Mix Design System Manual of Specification, Test Methods and Practices", Report No. SHRP-A-379, Washington, D.C. 1994.

(3) Al-Abdul Wahhab,H.I., Ali, M. F., Asi, I.M., and Al-Dubabe,I. A., "Adaptation of SHRP performance based asphalt specification to the Gulf countries". Progres Report No. 4,AR-14-60, King Abdul Aziz City for Science And Technology, Saudi Arabia, 1995.

EVALUATION OF VALIDITY OF CONVENTIONAL TEST METHODS IN CASE OF POLYMER-BITUMENS

Dr Dariusz SYBILSKI
Road and Bridge Research Institute, Warsaw, Poland

Key-words: polymer-bitumens, non-linear behavior, conventional tests

INTRODUCTION

When testing polymer-bitumens, non-linear behavior of material is observed in test conditions at behavior of conventional, plain bitumens is linear. Polymer-bitumen systems show non-Newtonian behavior in a wider range of temperature and shear than plain bitumens. Paper presents results of testing of polymer-bitumens with discussion of validity of conventional test methods when applied for polymer-bitumen systems. Several polymer-bitumen systems were tested including bitumens modified with SBS elastomers (elastomer-bitumens) and polyolephinic plastomer PO (plastomer-bitumens). Test program contained: penetration at 5, 10, 15, 25, 40, 50°C and at 25°C under load 50, 100, 200g, Softening Point R&B, Fraass Breaking Point, viscosity at 60°C, ductility at 5, 15, 25°C. Viscosity was measured in rotational viscometer at various shear rates. Zero-shear viscosity was calculated from viscosity-shear rate relationship according to simplified Cross Equation [1]:

$$\eta = \frac{\eta_0}{1 + (K \cdot d\gamma / dt)^m}$$

where: η - apparent viscosity, mPas, η_0 - zero-shear viscosity, mPas, $d\gamma/dt$ - shear rate, 1/s, K - constant, s, m - constant.

Wheel-tracking test was conducted on asphalt concrete with polymer-bitumens and plain bitumens in LCPC apparatus at 45°C, load 0.5 kN, contact pressure 0.6 MPa. Rutting resistance was expressed as a number of wheel passes to rut depth 10mm, N_{10}, calculated according to Equation:

$$h = a \cdot \ln^b N$$

where: h - rut depth, mm, N - number of wheel passes, a,b - constants. N_{10} was related to binder properties.

PENETRATION

Elastomer-bitumens show non-linear relationship of log(penetration) vs temperature above 25°C (Fig. 1). Penetration is lower than expected. Bitumen and plastomer-bitumen show linear relationship in temperature range from 5 to 50°C. The same conclusion comes out from penetration test under various load (Fig. 2). In case of elastomer-bitumens relationship of penetration vs load deviates from linear when increasing load. This is not observed in case of bitumen or plastomer-bitumen. Penetration tests showed that elastomer-bitumens are less temperature and load susceptible than bitumen or plastomer-bitumen.

Zero-shear viscosity at 60°C shows a very weak relationship with penetration at 25°C (Fig. 3). Two separate group of polymer-bitumens may be easily recognized depending on consistency of base bitumen used for modification. A great variety in viscosity is observed among polymer-bitumens of equal penetration. In a group of binders of penetration at 25°C from 40 to 70x0.1mm, viscosity at 60°C varies from 4×10^5 mPas to 1.5×10^7 mPas, i.e. the highest value is 38 times of the lowest!

SOFTENING POINT

There is a doubtful relationship between R&B Softening Point and Penetration at 25°C (Fig. 4). The same Softening Point may be obtained by elastomer-bitumens of significantly different penetration. Soft base bitumen highly modified with elastomer (i.e. 6-7% by mass) results in a binder of very high Softening Point, above 70°C, comparative with that obtained by harder base bitumen low modified (i.e. 3-4%).

Relationship of Plasticity Range and Penetration Index in case of some elastomer-bitumens deviates significantly from linear observed in case of plain bitumens and plastomer-bitumens (Fig. 5) as a result of devation of Softening Point and Fraass Breaking Point as well as Penetration from relationships found for bitumens by Heukelom [2].

When relating Softening Point to Zero-shear viscosity at 60°C an interesting shape of relationship was found as linear but with a break point at 68.2°C (with respective Zero-shear viscosity 7380000 mPas) - Fig. 6. The relationship is much stronger than for penetration. A sharp change in slope is

observed at this point which means that below this point increase in Softening Point reflects increase in viscosity of binder while above this point increase in Softening Point does not bring increase in viscosity. This observation may explain doubts in significance of Softening Point in case of some soft highly modified elastomer-bitumens. For a polymer-bitumen of Softening Point 60°C its zero-shear viscosity at this temperature would be 2164000 mPas which is much above 1300000 mPas as determined by Heukelom for plain bitumens.

LOW-TEMPERATURE PROPERTIES

Vonk et al. [3] analysed validity of Fraass Breaking Point for evaluation of low-temperature behavior of elastomer-bitumens. Fraass Breaking Point temperature was compared with accoustic emmision test results, showing that the first did not reflect low-temperature behavior in some cases. Fraass Breaking Point reflects a certain stiffness of binder not its ability to combat tensile strain. Fig. 7 presents results of tests of ductility at various temperatures related to penetration measured at the same temperature. A group of results obtained for penetration below 20x0.1mm has been chosen which represent hard binders tested at 15 or 25°C or soft binders tested at 5°C. Significant difference may be noted when comparing materials of the same penetration from two groups. Plain bitumens and plastomer-bitumens are grouped in the first while elastomer-bitumens in the second. At the same penetration elastomer-bitumen shows higher ductility than plain bitumen or plastomer-bitumen. In average, at penetration of 10x0.1mm bitumen or plastomer-bitumen shows ductility of 5.0cm while elastomer-bitumen of 28.2cm. When considering that ductility test was conducted on hard bitumen, these results may be regarded as reflecting low temperature behavior of binders. No relationship of ductility at low temperature and Fraass Breaking Point was found. Conclusion is similar to that which came out from SHRP: low-temperature properties of bituminous binder shall be characterized by stiffness but also tensile strain.

RUTTING RESISTANCE OF ASPHALT CONCRETE VS BINDER PROPERTIES

Comparison of rutting resistance of asphalt concrete with Softening Point of bituminous binder showed a weak relationship (Fig. 8). Much higher regression coefficient was achieved in case of zero-shear viscosity at 60°C (Fig. 9). However in both cases the same phenomenon may be noted: elastomer-bitumens from soft base bitumen highly modified may be overestimated in terms of rutting resistance when evaluating on base of Softening Point or zero-shear viscosity. In case of the latter the potential reason lies in equipement possibilities which do not allow to approach sufficiently low shear rates [1]. In case of Softening Point a break point may be noted at a point of about 70°C which is the value of break point of realtionship of Softening Point and zero-shear viscosity at 60°C. The best rutting resistance was obtained with harder grade elastomer-bitumen with a lower modification or with highly modified plastomer-bitumen based on hard bitumen.

CONCLUSIONS

Non-linear non-Newtonian behavior of polymer-bitumens may be found in conventional tests depending on temperature and load conditions. All conventional test methods as penetration, R&B Softening Point, Fraass Breaking Point have validity limited to relatively low modified polymer-systems, esecially in case of elastomer-bitumens. In case of Softening Point, the limiting value was found as 68.2°C. Zero-shear viscosity calculated from viscosity-shear rate relationship reflects susceptibility of binder to permanent deformation. The test method is limited with equipement potentials to aproach zero shear conditions in case of highly modified polymer-bitumen systems.

REFERENCES

1. **Sybilski D.**: *Zero-Shear Viscosity of Bituminous Binder and its Relation to Bituminous Mixtures Rutting Resistance.* 75th TRB Annual Meeting, 1996

2. **Heukelom W.**: *An Improved Method of Characterizing Asphaltic Bitumens with Aid of their Mechanical Properties.* Proc. AAPT, Vol. 42 (1973)

3. **Vonk W.C., Robertus C., Jongeneel D.J., Korenstra J.**: *Accoustic emmision: a new tool for assessing the relative performance of binders and asphlats at low temperatures.* The East-West European Road Conference, Warsaw, 22-24 Sept. 1993

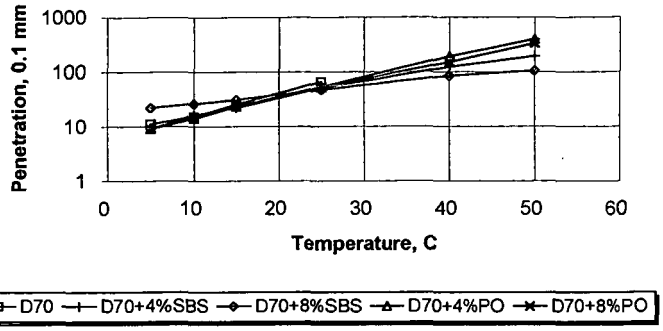

Fig. 1. Penetration vs Temperature of plain bitumen and polymer-bitumens

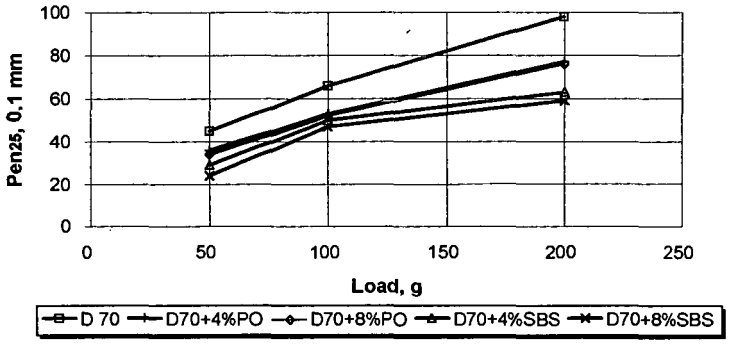

Fig. 2. Penetration vs Load of plain bitumen and polymer-bitumens

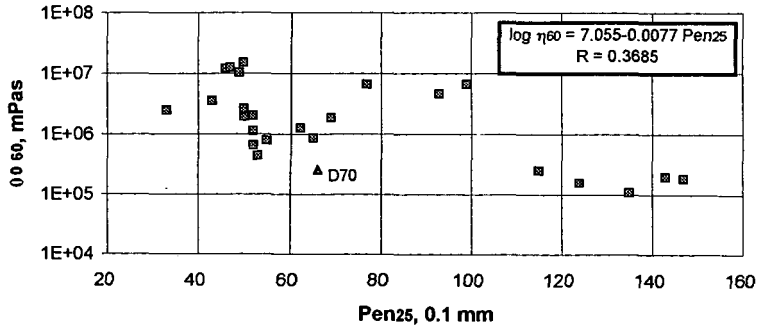

Fig. 3. Zero-shear viscosity at 60°C vs Penetration at 25°C

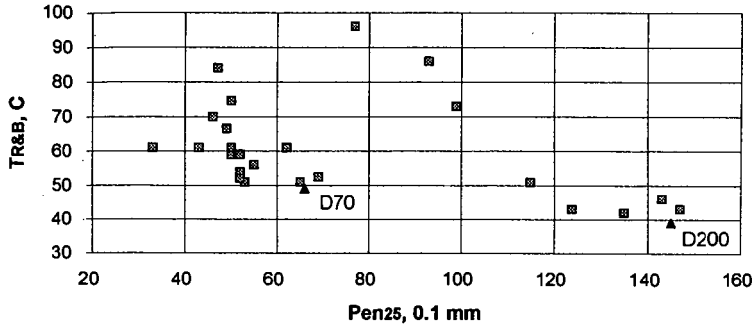

Fig. 4. R&B Softening Point vs Penetration at 25°C

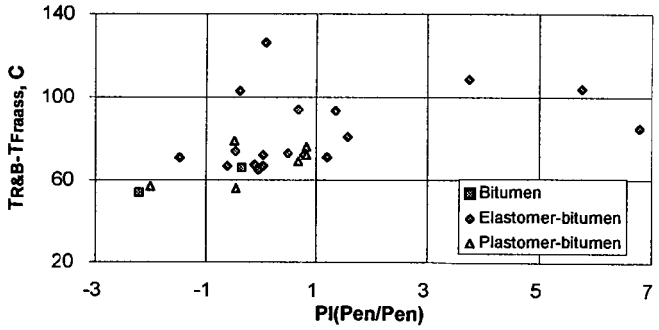

Fig. 5. Plasticity Range ($T_{R\&B}$-T_{Fraass}) vs Penetration Index

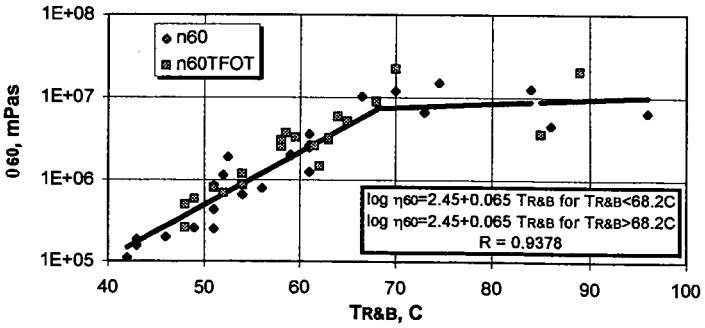

Fig. 6. Zero-shear viscosity at 60°C vs R&B Softening Point

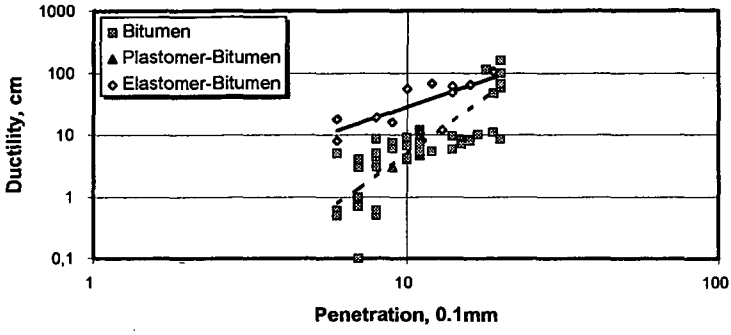

Fig. 7. Ductility vs Penetration at the same temperature (Penetration below 20x0.1mm)

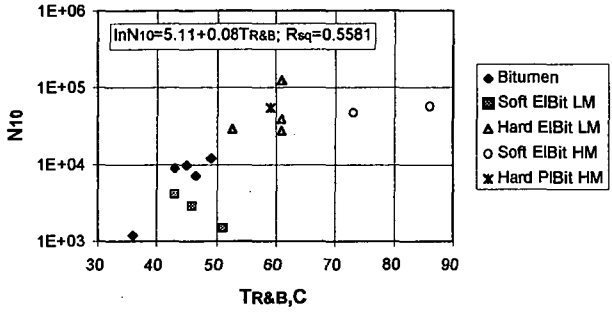

Fig. 8. Rutting Resistance of Asphalt Concrete vs R&B Softening Point of Binder

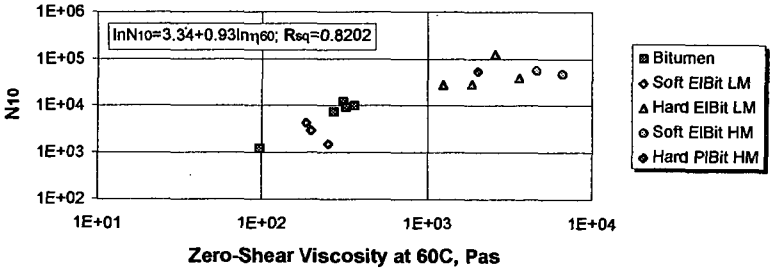

Fig. 9. Rutting Resistance of Asphalt Concrete vs Zero-Shear Viscosity at 60°C of Binder

RHEOLOGICAL PROPERTIES OF ASPHALTS WITH PARTICULATE ADDITIVES

N. Shashidhar
EBA Engineering
5800 Metro Drive
Baltimore MD 21215

Brian H. Chollar
Federal Highway Administration, HNR-20
6300 Georgetown Pike
McLean VA 22101

Keywords: Mastic, particulate composite, rheological properties

INTRODUCTION

The Superpave asphalt binder specifications are performance-based specifications for purchasing asphalt binders for the construction of roads. This means that the asphalt is characterized by fundamental material (rheological) properties that relate to the distress modes of the pavements. The distress modes addressed are primarily rutting, fatigue cracking and low temperature cracking. For example, $G^*/\sin(\delta)$ is designed to predict the rutting potential of pavements, where G^* is the magnitude of the complex shear modulus and δ is the phase angle. The binder for a road that is situated in a certain climatic zone requires the binder to have a minimum $G^*/\sin(\delta)$ of 2200 Pa at the highest consecutive 7-day average pavement temperature the road had experienced. Implicit in such a performance based specification is that the fundamental property, $G^*/\sin(\delta)$, of the binder correlates with rutting potential of the pavement regardless of the nature of the binder. In other words, the specification is transparent to the fact that the binder can simply be an asphalt, or an asphalt modified by polymers, particulates and other materials that can form a two-phase mixture.

There has been limited amount of research to validate the correlation of the Superpave binder parameters with laboratory mix tests and fewer still with pavement performance. The use of modified binders in such validation studies is further limited. Rarer still are studies that use particulate modifiers. Anderson and Kennedy[1] presented the basis for Superpave binder specification and validated these with mix tests. They did not specifically use modified systems, except when talking about low temperature cracking specifications. King et. al.[2] showed a good correlation between the low-temperature cracking predictors, namely, the temperature at which the failure strain is 1% and the temperature when creep stiffness is 200 MPa, to the thermal stress restrained specimen test (TSRST) for various asphalts and polymer modified binders. Hicks et. al.[3] validated the binder specifications with laboratory mixture testing using only unmodified binders. Bouldin et. al.[4] show excellent correlation between $G^*/\sin(\delta)$ and wheel tracking tests, but limit the asphalts to unmodified and styrene butadiene-styrene (SBS) copolymer. In conclusion, the Superpave binder specifications were developed considering primarily unmodified asphalts. Though some validation studies (with laboratory mix tests) consider polymer modified asphalts, they are limited to binders containing modifiers that form a macroscopically homogenous system with the asphalt.

When the Intermodal Surface Transportation Efficiency Act of 1991 was passed, some testing of asphalt modified with ground tire rubber or crumb rubber modifiers (CRM) were reported[5,6]. In these papers the Superpave binder testing was simply applied to testing binder with fairly large (up to -10 mesh = 2 mm) particulates. It was not shown in these papers that the Superpave binder test methods can be used to predict the performance of such binders.

AASHTO provisional procedure PP5[7] deals with the separation of modifiers from asphalt on storing either by formation of the film on the surface or a sludge on the bottom. The practice further ensures that the base asphalt that is used to make modified binder is over 99% soluble. This implies that after passing this test any modifier (including a particulate modifier) can be used provided the modifier does not separate when left standing at 163°C for 48 hours. In a move to limit the kinds of modifiers that could be used, the FHWA Superpave Binder Expert Task Group (ETG)[8] decided "*that the material being evaluated using the Superpave binder specifications must be tested to satisfy the ASTM D5546 solubility criteria. If the material fails this test, it is up to the purchasing agency to accept or reject the material.*" Although such specifications on the use of particulates do impose some restrictions, they do not absolutely disallow the use of particulates. This perhaps should not be done since it will stifle any innovation. However, a basic understanding of the behavior of particulates in asphalt will allow for a more objective evaluation on the benefits (or lack thereof) of particulates in pavements.

Given that the development and validation of Superpave binder tests did not rigorously consider binders with particulate additives, several questions must be answered before the adoption of the Superpave binder specification nationally. These questions broadly fall into three categories:

(1) When particulates are added to asphalt there are issues relating to segregation of the particulates due

to settling or other phenomena. There is the issue of maximum particle size below which the accuracy of measurements with the Superpave testing equipment will not be affected. There may also be other unknown issues that could affect the results. These issues can be summarized by the questions "Can the present Superpave testing procedures be used to test binders with particulate additives? Under what limitations can such modified binders be tested?"

(2) How does modification of binders with particulate additives affect the Superpave grading of these binders? Can the changes in grading be predicted with the knowledge of parameters that completely characterize the rheology of particulate-binder system?

(3) Will a binder whose PG (performance grade) grading is achieved by adding particulate modifiers perform the same as another binder of the same PG grade that is unmodified? In other words, will the changes in binder specification due to particulate modifiers truly reflect on the performance of mixes containing such modified binders in laboratory mixture tests and on the pavement performance?

Obviously, these are loaded questions and require extensive research. The third question above, is the most significant, for, if adding particulates to binders changes a property such as $G^*/\sin(\delta)$ but does not really change the pavement performance, then the binder will have an inflated grade that will not be reflected in the performance. On the contrary, if the addition of certain particulates does enhance the performance of the roads, but this is not truly reflected in the current specifications, then methods must be developed to capture this enhanced performance.

An understanding of the asphalt-particulate system is fundamental to answering any of the above questions. This is the subject of this paper.

Evaluation of particulates in asphalt in the form of fines and mineral dust is not new, nor is the evaluation of particulate composites in polymers and other materials. There are hundreds of research papers that deal with this topic in the materials science literature. In asphalt literature, several investigators have tried to evaluate the effect of fines in asphalt concrete and have attempted ways to predict the stiffening power of fillers in asphalt. Tunnicliff[9] has reviewed the literature for mineral filler-asphalt systems prior to 1962. Another noteworthy paper is the report by Anderson[10] who gives insight into the role of mineral filler in asphalt. In the field of polymers, two recent reviews[11,12] and a book[13] summarize the developments in polymer-melt systems, highly filled systems and general treatment, respectively. The above is not meant to be a complete literature survey, but just a reference to key review papers.

Description of asphalt with particulate additives

The description of the behavior of filled systems in polymer matrises has traditionally been approached from two directions—Einstein's equation[14] and its modifications for polymer liquid and melt systems, and the Kerner's equation[15] and Hashin and Shtrikman's equation[16] and their variations for polymer solid systems. These two approaches were brought together with the expression

$$\left(\frac{\eta}{\eta_1}-1\right) = \frac{2.50(8-10\nu_1)}{15(1-\nu_1)}\left(\frac{G}{G_1}-1\right) \qquad (1)$$

for the relation between viscosity and shear modulus[17]. Here, η is the viscosity, G the shear modulus, v is the poisson's ratio. When the Poisson's ratio is 0.5, then

$$\frac{\eta}{\eta_1} = \frac{G}{G_1} \qquad (2)$$

Thus, the equations developed for η/η_1 should be applicable to G/G_1, and vice-versa. The convention used above will be that used in equations henceforth—subscript 1 denotes the maxtrix, 2 denotes the particulates, and the unsubscripted variables denote the binders with particulates (a composite property).

After an evaluation of many equations in the literature including the Einstein[14], Mooney[18], Roscoe[19], Eilers-van Dijck[20] etc. (which will not be described in this paper) equations, the generalized Nielsen's equation[13,21] was selected for further analysis of asphalts. Nielsen's equation is a modification of Kerner's equation for elastic materials. However, this equation has been applied to many viscoelastic polymers successfully[13]. The Nielsen's equation describes the stiffness dependence on the volume fraction of particulates in terms to two fundamental properties of the system. It further provides a way to account for differences in the stiffness of fillers themselves, the particle-matrix interface energy, and other materials parameters. Such knowledge will help isolate the the various causes for stiffening of binders when particulates are added.

Nielsen's equation describes the modulus ratio between the filled and unfilled system as follows:

$$\frac{M}{M_1} = \frac{1+AB\phi_2}{1-B\psi\phi_2} \tag{3}$$

where M is any modulus and ϕ_2 is the volume fraction of the filler. The constant A takes into account such factors as geometry of the filler phase and poisson's ratio of the matrix, the constant B takes into account the relative moduli of the matrix and filler phases; its value is 1.0 for very large M_2/M_1 ratios.

$$B = \frac{M_2/M_1 - 1}{M_2/M_1 + A} \tag{4}$$

The factor ψ depends on the maximum packing fraction, ϕ_m, of the filler. An empirical equation that satisfactorily describes the relation between ψ and ϕ_m is

$$\psi \doteq 1 + \frac{1-\phi_m}{\phi_m^2}\phi_2 \tag{5}$$

The constant A is related to the generalized Einstein Coefficient K_E by

$$A = K_E - 1 \tag{6}$$

In the case of mineral fillers in asphalt, since the modulus of the filler is much higher than the asphalt, the value of B is unity. Substituting B=1 and equation 5 in equation 3 will yield

$$\frac{M}{M_1} = \frac{1+A\phi_2}{1-(1+C\phi_2)\phi_2} \tag{7}$$

where

$$C = \frac{1-\phi_m}{\phi_m^2} \tag{8}$$

By curve-fitting equation 7 to the data, the constants A and C can be estimated. From these parameters, the generalized Einstein coefficient K_E and the maximum packing fraction, ϕ_m, can be calculated.

Thus, if Nielsen's equation, obtained for filled polymer systems, can be used for asphalts, it is then possible to characterize an asphalt-particulate system using two fundamental properties, K_E and ϕ_m. A knowledge of the variation of K_E and ϕ_m for different asphalt-modifier systems as a function of properties of interest then lead to the selection of appropriate powders for better such properties. Although, this paper restricts the analysis to mineral fillers, this approach can be used for all modifiers used for asphalts as long as they do not completely dissolve in asphalt, but form a discrete, but dispersed phase.

EXPERIMENTAL

Thirteen fillers that were used in a prior study[22] were used with an AC-20 from Venezuela's Lagoven base stock supplied by Koch Material's company, Pennsauken, NJ. Some of the properties of these fillers are listed in Table 1. The particle size distributions for all these fines are reported in a prior study[23]

The asphalt was used in its unaged state for all the experiments. Fines were added to asphalt to make 10 g batches of 4, 8, 12, 16, 20 and 24 volume percent particulates. Care was taken not to form agglomerates during the mixing process. The mastic was continuously stirred as it cooled down to prevent any settling. When the mastic thickened due to cooling, it was then transferred to silicone rubber molds to make pellets for testing with the dynamic shear rheometer (DSR).

Testing of the mastic was done with a Rheometrics RDA II dynamic shear rheometer (DSR) with a FTS torque transducer. The transducer was used in its most sensitive range (200 g-cm full scale). Strain

Table 1. Particulates used in this study†

Code	Sp. Gr.	Rigden Voids	Material
SWE2	2.84	36.5	Granite
SWE3	2.74	38.2	Granite
SWE5	2.91	37.3	Granite
SWE6	2.84	40.0	Granite
SWE7	2.74	33.1	Limestone
CHE1	2.76	38.5	Sandstone
CHE2	2.76	32.8	Limestone
GER1	2.74	35.2	Pure Limestone
GER2	2.87	34.8	Dolomitic Limestone
GER3	2.74	34.5	V. Pure Limestone
GER4	2.76	45.7	Granite
GER7	3.18	69.2	Fly Ash
GER9	2.74	38.2	Limestone

† Data from Reference 19

sweeps were measured at 25°C and 10 rad/s frequency with 8 mm parallel plate geometry and 2 mm gap and at 70°C with a 25 mm parallel plate and 1 mm gap. There has been discussion as to the maximum size particulates that can be used between parallel plates with 1mm gap. In these experiments we have avoided this issue by choosing fine particulates that have over 90 wt% below 75 μm. The issue of maximum particle size will be addressed in later research.

Table 2. The curve-fit parameters for Nielsen Equation at 25°C and 70°C and the calculated ϕ_m and K_E for all powders

	25°C		70°C		25°C		70°C	
	A	C	A	C	K_E	ϕ_m	K_E	ϕ_m
CHE1	2.2	3.1	2.6	4.5	3.2	0.43	3.6	0.37
CHE2	4.2	1.8	4.7	3.7	5.2	0.52	5.7	0.40
GER1	2.5	2.7	3.0	3.4	3.5	0.45	4.0	0.41
GER2	4.0	3.2	3.3	3.5	5.0	0.43	4.3	0.41
GER3	1.6	3.8	2.0	4.2	2.6	0.40	3.0	0.38
GER4	2.5	5.1	2.6	5.3	3.5	0.36	3.6	0.35
GER7	10.5	6.8	12.8	8.5	11.5	0.32	13.8	0.29
GER9	3.0	2.7	2.2	3.8	4.0	0.45	3.2	0.40
SWE2	1.9	5.5	1.6	5.9	2.9	0.35	2.6	0.33
SWE3	2.5	2.7	2.3	3.9	3.5	0.45	3.3	0.39
SWE5	1.0	6.7	2.6	2.8	2.0	0.32	3.6	0.45
SWE6	1.7	4.1	3.4	3.6	2.7	0.39	4.4	0.41
SWE7	1.8	5.3	2.9	4.4	2.8	0.35	3.9	0.37

RESULTS

The strain sweeps obtained for asphalt with varying amount of fines are shown in Figures 1 (25°C) and 2 (70°C). This is a representative of data obtained for all the fines. The data was linear to over 1% strain at 25°C and to over 10% strain at 70°C. For further analysis, values at 0.1 % strain for 25°C and 1% strain at 70°C were considered.

When the ratio of G^* to G_1^* was plotted as a function of volume fraction of particulates (ϕ_2), behaviors such as illustrated in Figures 3 and 4 were observed. These figures also illustrate the curve-fit according to equation 7 And the 95% confidence limits for these curves. The curve-fit parameters are listed in Tables 2 and 3 for measured parameter G^* and G', respectively. It must be noted that for the fines studied, the constant A varied from 1.2 to 6.6 with the exception of GER7 which had A values between 10.5 and 15.2. The constant C varied from 1.0 and 4.7 not including GER7.

The generalized Einstein coefficient K_E and the maximum packing fraction ϕ_m calculated from the curve-fit parameters are listed in Table 2. The variation in constant A is reflected in variation of K_E. The ϕ_m varied from 0.32 to 0.52 for all the powders. It is also interesting that ϕ_m varied as little as 0.04 and as much as 0.12 between measurements at the two temperatures for a given particulate and asphalt. The key to using this approach is in the success in the interpretation of K_E and ϕ_m.

Figure 5 shows the phase angle as a function of ϕ_2 at both 25°C and 70°C. This curve is typical of those of the thirteen mastic mixes in that there is no systematic variation in the phase angle with ϕ_2. Also, the magnitude of variation is ±1°. We can therefore conclude that the phase angle is not effected by the addition of mineral particulates up to 25 volume percent fines.

DISCUSSION

When a powder fills a container, a fraction of the volume of the container is occupied by the powder particles while the rest are voids. The fraction of the volume of the container actually occupied by the powder is defined as the packing fraction, ϕ_2. If the powder packs efficiently, then the volume fraction of

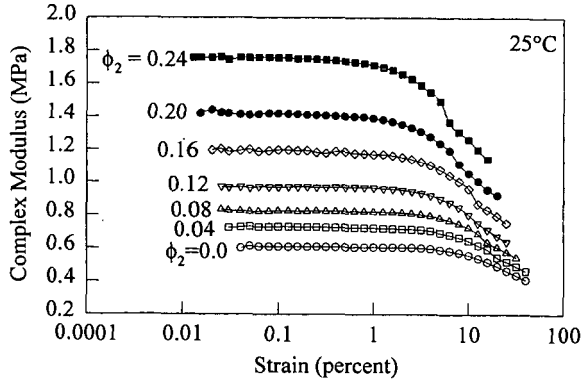

Figure 1. Strain Sweeps at 25°C for asphalt with different amounts of GER9. This is representative of all the powders.

powder in the container, and, hence, the packing fraction, ϕ_m increases. The maximum packing fraction, ϕ_m, is the highest value ϕ_2 can have, and is a function of the average particle size and particle size distribution. Anderson described two refined techniques for measuring ϕ_m , namely, the dry compaction method and the kerosene method[10]. Since ϕ_m is a fundamental property, ϕ_m measured by an independent technique (such as Anderson's) should compare with the value from Nielsen's equation.

Figures 6 and 7 plots the correlation between the ϕ_m from the dry compaction method of Anderson and the ϕ_m obtained as described in this paper. This figure shows there is a poor correlation between the two techniques. The ϕ_m from Equation 6 is consistently lower than the measured value.

In another example, we fit viscosity (25°C) measurements from Traxler[24] to Nielsen's equation and estimated the ϕ_m. The correlation between the estimated ϕ_m and the value measured experimentally[24] (by dry compaction in a glass graduate technique) is plotted in Figure 8. This, in contrast to the data in Figures 6 and 7, shows very good correlation.

Apparently, the success of Equation 7 in estimating ϕ_m in Figure 8 indicates that the equation works in some situations. The problem is to identify when the equation works and how to best use it to gain an insight into the mastic.

A likely reason for disparity between the measured and calculated values of ϕ_m is the fact that the ϕ_m calculated from Nielsen's equation measures the true state of packing for particulates in asphalt, while the

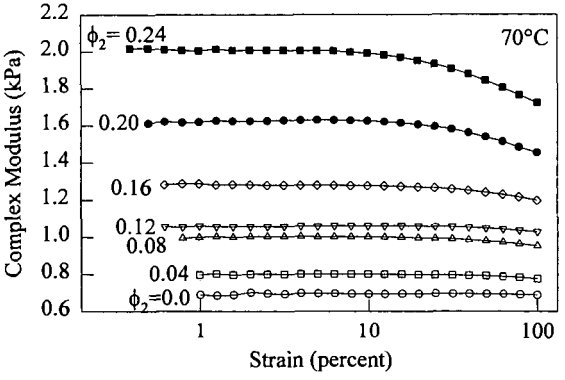

Figure 2. Strain sweeps at 70°C for asphalt with different amounts of GER9. This is representative of the behavior of all the particulates.

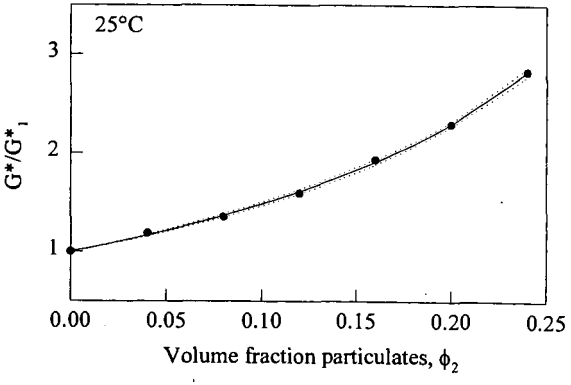

Figure 3. The change in G* ratio as a function of ϕ_2 at 25°C. The solid line is a fit with the Nielsen's equation and the dotted lines are 95% confidence limits for the curve-fit.

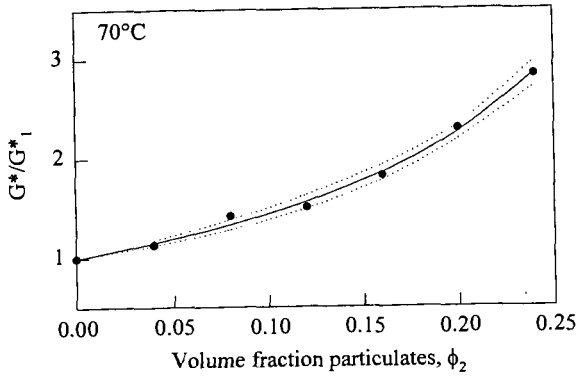

Figure 4. The change in G* ratio as a function of ϕ_2 at 70°C. The solid line is a fit with the Nielsen's equation and the dotted lines are 95% confidence limits for the curve-fit.

dry compaction technique of Anderson measures an ideal case, a state that is unnatural for asphalt systems. The following factors would effect the packing of particulates in asphalt and, hence, the estimates of K_E and ϕ_m[13]:

1. Any particle-particle interaction causing networks (structuring) among particles or formation of agglomerates would decrease the packing of particulates (decreasing ϕ_m). Such interactions will also reflect on higher estimates of K_E.
2. The aggregate shape and aspect will also effect the packing of powders. Higher aspect ratio of particles would increase the K_E and decrease the packing efficiency (decreasing ϕ_m).

On the other hand, the K_E measured for all the powders are close to the theoretical value of 2.5 derived for very dilute spheres[14]. This indicates that the approach is fairly successful in describing the mastic, and there are differences between the powders in terms of shape of particles, their interaction with the asphalt, etc.

Although there are several issues to be resolved, the use of Nielsen's equation allows for a fundamental approach to analyzing particulates and fillers in asphalts. In the asphalt literature, it has been reported that the Rigden voids (which is equivalent to $1-\phi_m$) correlate most with the stiffening power of asphalts[10,22]. The approach presented in this paper indicate that a factor other than Rigden voids (and its equivalent ϕ_m), namely, the generalized Einstein coefficient K_E, also is an important property that predicts the stiffening power of the fines. In fact, both these parameters are equally important in predicting the stiffening power of particulates. These two parameters are a function of the asphalt-particulate system and characterize the system completely. The effect of both these parameters on the stiffening of asphalts will be discussed next in this paper.

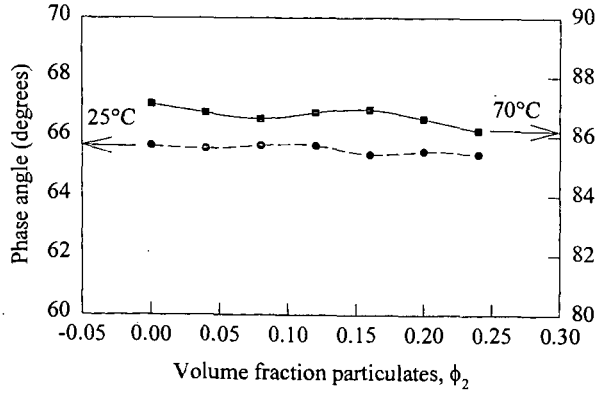

Figure 5. The change in phase angle as a function of ϕ_2 at 25°C and 70°C.

Effect on PG grading

It has been shown that the increase in G* with addition of particulates can be described if we know ϕ_m and K_E. It was shown that for most of the mineral powders used in this study, ϕ_m varied between 0.32 and 0.52 and K_E varied between 2 and 5. By analyzing how G* varies for a range of ϕ_m and K_E, one can predict to what extent the addition of mineral fillers are likely to effect the PG grading if the ϕ_m and K_E are known.

In Figure 5, it was shown that the phase angle did not change with addition of particulates. This indicates that by the addition of particulates the master curve for the asphalt merely shifts towards higher G* without undergoing any change in time dependence. Such a behavior is assumed for low temperature region as well. Since the *m*-value is equivalent to the phase angle, the independence of phase angle to the addition of particulates can be reasonably expected to reflect the independence of *m*-value also. This assumption has to be tested with actual experimental data. This is planned for future work.

The procedure described below was used to evaluate the effect of the addition of mineral fillers on the PG grade of asphalt:

1. The $G^*/sin(\delta)$ was plotted as a function of temperature and fit with a quadratic equation of the form $\log(G^*/\sin(\delta))=\alpha+\beta T+\chi T^2$. From this equation the fractional grading (the temperature when $G^*/\sin(\delta) = 2200$ Pa) for the binder was determined.
2. For $G^*/\sin(\delta)$ at each temperature (52, 58, 64 and 70°C), the $G^*/\sin(\delta)$ for binder with particulates were calculated for given values of ϕ_m and K_E using Nielsen's equation.
3. We now have the estimated $G^*/\sin(\delta)$ vs. temperature data for asphalt with different amount of particulates. For each ϕ_2, a quadratic equation was fit as before to calculate the continuous grade of the mastic. It was found that only the constant α varied with ϕ_2, the constants β and χ being invariant. The fraction grading thus estimated is plotted as a function of ϕ_m and K_E in Figures 9 and 10, respectively.
4. A similar procedure was carried out for creep stiffness at 60 s. The change in fractional grade with the addition of particulates as a function of ϕ_m and K_E are plotted in Figures 11 and 12, respectively.

The invariance of constants B and C with ϕ_2 is the result of assuming that ϕ_m and K_E does not change with temperature. This assumption is consistent with our earlier reasoning that the addition of particulates merely shifts the master curve to higher stiffness. It can however be seen from Table 2 that ϕ_m and K_E do not seem to be different at 70°C than it is at 25°C, which leads us to give credence to this assumption.

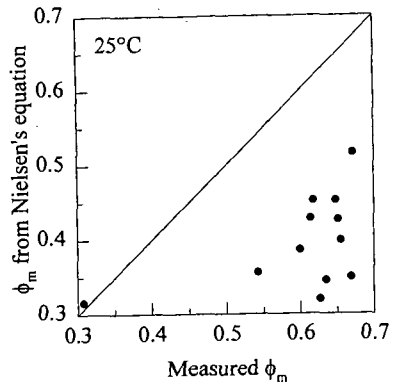

Figure 6. A comparison of ϕ_m estimates from Nielsen's equation (25°C data) and measured by dry-compaction method.

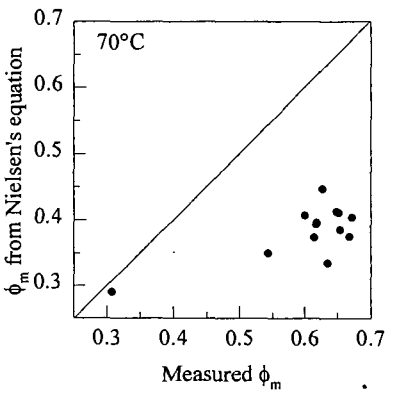

Figure 7. A comparison of ϕ_m estimates from Nielsen's equation (70°C data) and measured by dry-compaction method.

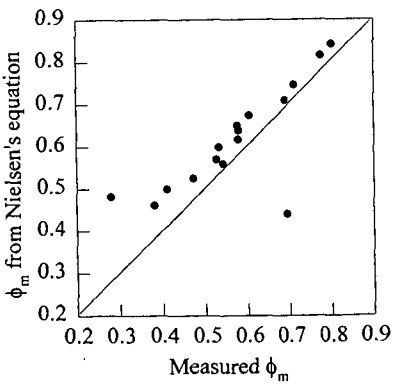

Figure 8. A comparison of ϕ_m estimates from Nielsen's equation (25°C data) and measured by a different dry-compaction method. (Data from Ref. 22)

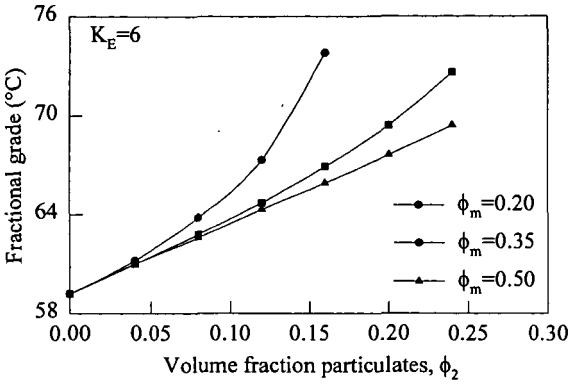

Figure 9. The effect of increasing ϕ_m on the high temperature grade for RTFOT aged asphalts.

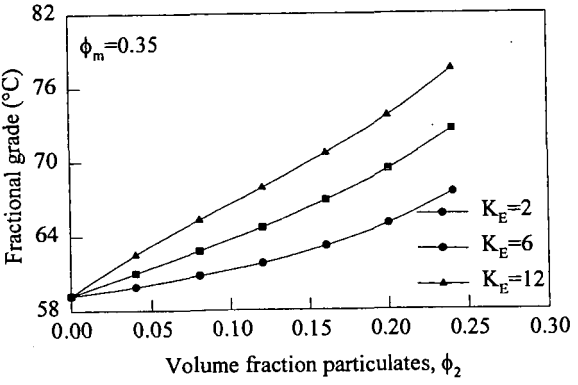

Figure 10. The effect of increasing K_E on the high temperature fractional grade on RTFOT aged asphalts.

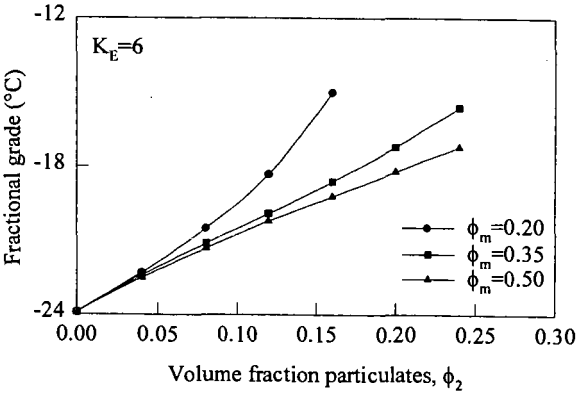

Figure 11. The effect of increasing ϕ_m on the low-temperature fractional grading based on S.

The range of ϕ_m and K_E selected for our study should represent many non-agglomerating mineral fillers. Close packing of particulates can yield a value of ϕ_m higher than 0.5. Very poor packing caused by the hygroscopic nature of the particulates or existence of agglomerates can cause ϕ_m to be less than 0.2. If the particulates are extremely fine, then the ϕ_m and K_E can be very different.

From Figure 9 it can be seen that as fines are added to the asphalt, the high temperature grade increases

by six degrees (one grade) with the addition of 13% particulates when ϕ_m is 0.35 and another grade with additional 10% fines. When the ϕ_m is 0.5, it requires 16% for the first grade and additional 10% for the next grade. On the other hand, if ϕ_m is closer to 0.2, it takes just 8% to increase G*/sin(δ) by a grade and additional 5% for the next grade. Thus as ϕ_m is reduced, G*/sin(δ) becomes more sensitive to the addition of particulates.

Similarly, when K_E=2.0 (Figure 10) it takes as much as 22% particulates to increase G*/sin(δ) by one grade, 13% when K_E is 6, and only 9% when K_E is 12. Since most of the powders studied had K_E between 2 and 6, it can be stated that between 13 and 22% particulates change the high temperature grade by 6°C. Higher the K_E, the more sensitive is the grade to the addition of fillers (stiffening effect).

At the lower end, a similar behavior can be observed. However, it is much subdued at this end for it takes 18% particulates to increase S by one grade at ϕ_m of 0.35 and K_E of 6. It is not known if these parameters ϕ_m and KE, will remain the same as the temperature is lowered. If this behavior can be controlled then it is possible to tailor the fines to effect the high temperature grade while not causing a change in the low temperature properties.

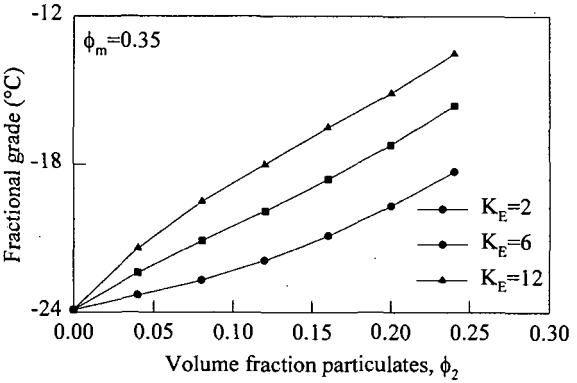

Figure 12. The effect of increasing K_E on the low-temperature grade of binders based on S.

CONCLUSIONS

The following conclusions were made from this study:

1. Nielsen's equation was shown to fit the dependence of stiffness on volume fraction particulates, ϕ2, for thirteen fillers. The parameters in the equation estimates the maximum packing fraction ϕ_m and generalized Einstein coefficient, K_E. Thus the dependence of stiffness on volume fraction can be predicted by knowing these two fundamental parameters.
2. The phase angle did not vary systematically with ϕ_2. The overall change in the phase angle with the addition of up to 25 volume percent particulates was less than 2 degrees.
3. The ϕ_m estimated from Nielsen's equation did not correlate with the ϕ_m measured by compaction technique for the measured data. However, when such a comparison was made for data from literature very good correlation was observed. Thus, more study is required to completely understand the Nielsen's equation for asphalt mastics.
4. For the powders used in our study ϕ_m had values of 0.29 to 0.52, and K_E had values 2.04 to 13.8.
5. The high temperature and low temperature continuous grade increased with addition of fillers. This increase was more sensitive as ϕ_m decreased and as K_E increased. In other words, if ϕ_m is reduced or K_E is increased, the continuous grade increased more rapidly with the addition of particulates.
6. The continuous grade which is synonymous with stiffening power is affected by not just ϕ_m (which is equivalent to Rigden voids) but also to K_E, another independent parameter.

REFERENCES

1. D. A. Anderson and Thomas W. Kennedy, "Development of SHRP binder specifications," *J. Assoc. Asphalt Paving Technol.*, **62**, 481-555, (1993).

2. G. N. King, H. W. King, O. Harders, W. Arand and P. P. Planche, "Influence of asphalt grade and Polymer Concentration on the Low Temperature Properties of Polymer Modified Asphalt," *J. Assoc. Asphalt Paving Technol.*, **62**, 1-22, (1993).

3. R. G.Hicks, F. N. Finn, C. L. Monismith and R. B. Leahy, "Validation of SHRP binder Specification through mix testing," *J. Assoc. Asphalt Paving Technol.*, **62**, 565-614, (1993).

4. M. G. Bouldin, G. M. Rowe, J. B. Sousa and M. J. Sharrock, "Mix Rheology— A Tool for Predicting the High Temperature Performance of Hot Mix Asphalt," *J. Assoc. Asphalt Paving Technol.*, **63**, 182-223, (1994).

5. H. U. Bahia and R. Davies, "Effect of Crumb Rubber Modifiers (CRM) on Performance-related Properties of Asphalt Binders," J. Assoc. Asphalt Paving Technol., 63 414-49, 1994.

6. H. U. Bahia and R. Davies, "Factors Controlling the Effect of Crumb Rubber on the Critical Properties of Asphalt Binders," *J. Assoc. Asphalt Paving Technol.*, **64** 130-162, (1995).

7. AASHTO provisional Specification PP5-93, "Standard Practice for the Laboratory Evaluation of Modified Asphalt Systems," American Association of State Highway and Transportation Officals, March (1995).

8. Minutes of Superpave Binder Expert Task Group meeting, December (1994).

9. D. G. Tunnicliff, A review of Mineral Filler," The Proceedings of the Assoc. Asphalt Paving Technologists," **31**, 118-50, (1962).

10. D. A. Anderson, "Guidelines on the Use of Baghouse Fines" National Asphalt Pavement Association. Information Series 101-11/87. Lanham, Maryland, (1987).

11. Yu. G. Yanovsky and G. E. Zaikov, "Rheological Properties of Filler Polymers," Encyclopedia of Fluid Mechanics. Volume 9: Polymer Flow Engineering, Gulf Publishing Company, Houston, 243-76, (1990).

12. A. V. Shenoy, "Rheology of Highly filled Polymer Melt Systems," Encyclopedia of Fluid Mechanics. Volume 7: Rheology of Non-Newtonian Flows, Ed. N. P. Cheremisinoff, Gulf Publishing Company, Houston, 667-701, (1988)

13. L. E. Nielsen and R. F. Landel, "Mechanical Properties of Polymers and Composites" Chapter 7: Particulate-Filled Polymers, 377-459 Marcel Dekker, Inc. New York (1992).

14. A. Einstein, Ann. Phys., **17**, 549 (1905); **19**, 289, (1906); **34**, 591, (1911)

15. E. H. Kerner, Proc. Phys. Soc., **B69**, 808 (1956)

16. Z. Hashin and S. Shtrikman, J. Mech. Phys. Solids, **11**, 127 (1963)

17. L. E. Nielsen, "The Relation Between Viscosity and Moduli of Filled Systems," *J. Composite Mater.* **2**, [1] 120-23, (1968).

18. M. Mooney, *J. Colloid Sci.*, **6**, 162 (1951)

19. R. Roscoe, *Brit., J. Appl. Phys.*, **3**, 267 (1952)

20. H. Eilers, "Viscosity of Emulsions of a Highly Viscous Substance as a Function of Concentration," *Kolloid Z.*, **97**, 313 (1941).

21. L. E. Nielsen, "Generalized Equation for the Elastic Modulii of Composite Materials," J. Appl. Phys., **41** [11] 4646-7, (1970).

22. B. M. Harris and K. D. Stuart, "Analysis of Filler Materials and Mastics Used in Stone Matrix Asphalt, *J. Assoc. Asphalt Paving Technol.*, **64** 54-95, (1995).

23. B. H. Harris, "Analysis of Minus 150 μm Aggregates for Stone Matrix Asphalt," Internal Report (1994).

24. R. N. Traxler, "Evaluation of Mineral Fillers in Terms of Practical Pavement Performance," *Assoc. Asphalt Paving Technologists Proc.* **8**, 60-77 (1937).

FRACTURE ENERGY SPECIFICATIONS FOR MODIFIED ASPHALTS

Joseph E. Ponniah*
Ministry of Transportation, Ontario
1201 Wilson Avenue, Downsview, ON. M3M 1J8

Ralph A. Cullen and Simon A. Hesp*
Department of Chemistry, Queen's University
Kingston, ON. K7L 3N6

Keywords: fracture, modified asphalts

INTRODUCTION

Low temperature cracking of asphalt pavements is a major performance problem in North America. In the past, extensive research has been done in this area to mitigate this problem. Recent findings by the Strategic Highway Research Program (SHRP) show that asphalt binder properties are by far the dominant factor controlling thermal cracking. Thus, the determination of these binder properties that affect thermal cracking is the key to the successful development of performance-based specifications for asphalt binders.

Traditionally, thermal cracking in asphalt pavements is controlled by using soft grades of asphalt cement based on penetration and viscosity measurements. Although, this approach has met with some success, it did not solve the problem completely. Besides, the emergence of modified asphalts has created a need for developing a suitable testing method for the characterization of binders containing additives. In general, asphalt pavement layers have built-in flaws (construction cracks). In addition, micro-cracks develop at the asphalt-aggregate interface due to differential thermal contraction of asphalt and mineral aggregates [1]. Micro-cracks can cause a localized stress concentration near discontinuities within the binder under thermally induced tensile loads. These stresses often reach a limiting value which leads to premature failures. Current binder specification limits do not consider the material resistance to these failure modes due to localized stress concentration. As a result, the actual performance often varies significantly from that anticipated by the design. What is required is a rational approach by which asphalt binders can be properly evaluated for their effectiveness to resist locally induced premature cracking.

There is some concern that the binder tests developed by SHRP may not be adequate to accurately predict the low temperature performance of modified asphalts. SHRP binder tests are mainly focussed on determining the creep stiffness or failure strains of asphalt binders at selected temperatures. Although these properties are necessary to globally characterize the low temperature behaviour of asphalt binders, they alone are not sufficient to reliably measure the resistance of asphalt binders to premature cracking. A complete knowledge of the damage process both at the micro and macro levels, is required to address the problem of premature fatigue cracking due to localized stress concentration, particularly in modified asphalts.

A review of the literature shows that fracture mechanics principles can be effectively used to control the fracture of materials which occur prematurely due to built-in flaws or cracks. The main objectives of this study are: a) to apply the fracture mechanics principles to characterize the low temperature fracture behaviour of asphalt binders; b) to develop a rational routine testing method using the fracture mechanics principles suitable for evaluating neat and modified asphalt binders with respect to low temperature cracking; (c) to analyze the correlation between the fracture properties and the low temperature performance.

SCOPE

The scope of the work includes: a) determination of binder properties and performance grade (PG) temperatures for the different asphalt binders using conventional and SHRP test methods; b) measurement of fracture properties (fracture toughness, fracture energy) of the asphalt binders selected in (a), using the newly developed fracture test method; c) determination of fracture temperatures of asphaltic concrete specimens containing the same binders as in (a) and (b), using the Thermal Stress Restrained Specimen Test (TSRST); and d) establishment of a correlation among the binder properties (determined from SHRP tests and the fracture test method) and the mix fracture temperature.

* To whom the correspondence may be addressed

APPLICATION OF FRACTURE MECHANICS PRINCIPLES

Fracture mechanics is a technique which identifies the cause of premature failure of materials due to built-in flaws, such as micro-cracks, under a load much smaller than the design load. If the material is homogeneous and behaves in a linear elastic manner, the effect of stress concentration around a micro-crack can be measured in terms of a parameter, called stress intensity factor (K_I). K_I increases with an increase in the external load and when it reaches a critical value, K_{Ic}, unstable fracture occurs. The parameter, K_{Ic}, called the fracture toughness, decreases with an increase in specimen thickness reaching a constant minimum value when plane-strain conditions are reached. This lower level of K_{Ic} is reproducible and can be used as a material property to evaluate the brittle fracture of materials in the same manner as the yield strength is used for structural analyses. This means that the fracture toughness can also be used to study the brittle fracture behaviour of asphalt binders at low temperatures. However, when polymers are added to the asphalt, the modified binder exhibits different failure behaviour at low temperatures, ranging from brittle fracture to plastic deformation or excessive elongation. This is because the modified asphalts usually contain finely dispersed secondary phases within the polymer matrix which contribute to shear yielding mechanisms and thereby prevent brittle failure. Fracture mechanics suggests that, when a material undergoes yielding (creep), it is the rate of energy dissipation (fracture energy) which controls the failure mode from crack initiation to full depth crack propagation. As explained later, fracture energy can be calculated once the fracture toughness and the stiffness modulus values are obtained. Thus, it appears that fracture energy will give valuable and consistent information on the effectiveness of modifiers in increasing the fracture resistance of asphalt binders. The question still remains how effective the fracture energy specification is as compared to the SHRP binder specification with respect to low temperature cracking. An experimental investigation was carried out to compare the correlation between the low temperature performance and the binder properties determined from the fracture test and those from SHRP tests. As well, trial sections were installed in Northern Ontario to compare the findings of the laboratory investigation with the long term low temperature performance of the modified asphalts in the field.

EXPERIMENTAL INVESTIGATION

Materials

Two types of conventional asphalts (85-100 pen and 150-200 pen) and five different modified asphalts were used in the experimental program. These modified asphalts were specifically selected or designed in such a way to give a wide range of performance levels. For this purpose, different modifiers and various grades of base asphalts, ranging from hard (85-100 pen) to soft (300-400 pen) asphalts were used in this study. As such, the performance of different modifiers will not be addressed. The suppliers who participated in this study include: Petro Canada, Huskey Oil, Bitumar, Polyphalt, and McAsphalt.

TESTING PROCEDURES

Thermal Stress Restrained Specimen Test (TSRST)

The Thermal Stress Restrained Specimen test is intended to simulate conditions that a mix would experience in the field. The test specimens of approximately 100x35x35 mm size were made from asphaltic concrete briquettes prepared using the plant mix from the trial sections. Each specimen was glued to the end plates of a test frame located within a temperature controlled chamber. The specimen was restrained by the end plates while the temperature in the chamber was gradually reduced at -10°C/ hour until the specimen failed due to thermally induced stresses. However, the potential change in specimen length due to the thermal shrinkage was compensated by the computer software system which was linked to two linear variable displacement transducers (LVDT) placed in between the end plates. The software uses the signals from the transducers to maintain a constant specimen length during testing. The output gives the temperature and the stress within the material at failure. The measured specimen failure temperature due to low temperature shrinkage is a good performance indicator of different binders used in the specimens.

Table 1: TSRST Results

Binder	Failure Stress (MPa)	Failure Temp (C)
Control 150-200	not tested	not tested
Control 85-100	2.24	-25.7±5.7
A	2.83	-45.4±2.5
B	2.65	-42.8±2.5
C	2.15	-42.9±4.9
D	8.31	-34.4±7.5
E	1.92	-29.5±8.1

A summary of the results together with 90% confidence intervals is presented in Table 1. The results indicate that binder A, with an average failure temperature of -45.4° C, will perform better than the rest, closely followed by binders C and B. The binder which has the lowest resistance to low temperature cracking, as expected, is the 85-100 pen asphalt. This test is time consuming and cannot be used on a routine basis; but it is a valuable research tool for investigating the low temperature performance of asphalt pavements

FRACTURE ENERGY TEST

Fracture energy testing was carried out by using a three point bending beam method (Figure 1) based on ASTM E 399-90 procedures [2]. The neat and modified binder beam samples were prepared using 25 mm wide by 12.5 mm deep by 175 mm long silicone rubber molds which have 90° starter notches, 5 mm deep, at the centre of the bottom surface. The molds were filled with asphalt binders and kept in a freezer at -20 °C for about two hours until they became solidified. The binder samples were then removed from the molds and were kept at the testing temperature for 18 hours. The starter notch in each sample was sharpened with a razor blade prior to testing. The notched beam is then placed on a three point bending apparatus of span 100 mm within an environmentally controlled chamber (Figure 1). The beam was then loaded until failure. From the output, the fracture toughness was computed according to Equation (1).

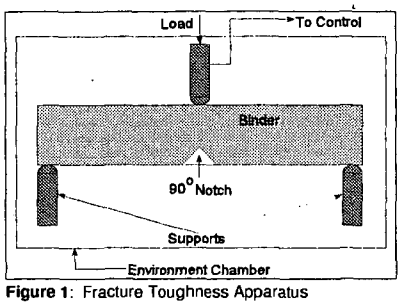

Figure 1: Fracture Toughness Apparatus

$$K_{IC}=\frac{P_f S}{BW^{3/2}}\left[\frac{3\left(\frac{a}{W}\right)^{1/2}\left[1.99-\frac{a}{W}\left(1-\frac{a}{W}\right)\left(2.15-3.93\frac{a}{W}+2.7\frac{a^2}{W^2}\right)\right]}{2\left(1+2\frac{a}{W}\right)\left(1-\frac{a}{W}\right)^{3/2}}\right] \quad (1)$$

Where: K_{IC} is the fracture toughness; P is the failure load; S is the span; B is the specimen depth; W is the specimen width; a, is the crack length .

The fracture energy can then be derived from:

$$G_{IC}=\frac{K_{IC}^2(1-\nu^2)}{E} \quad (2)$$

Where: G_{IC} is the fracture energy (Jm^{-2}); ν is Poisson's ratio; E is Young's Modulus. As Poisson's ratio for asphalt cement at low temperature is very small, it is neglected in the computation of G_{IC} using Equation 2. A couple of tests were carried out to ensure plane-strain conditions as discussed previously so that the fracture toughness values remain constant and reproducible. Secondly, the linear-elastic behaviour of the specimens was achieved by selecting the appropriate low test temperatures. For modified samples, the test temperature was -30 °C and the results are given in Table 2. Fracture toughness values in this table provide information on the type and amount of polymers used while the modulus gives information on the type of base asphalts used. Fracture energy measures the resistance of the binder to fracture. The results show that binder A has a higher resistance to thermal cracking than the rest, followed by binders C and B. The results also show that binder D, which used a harder base asphalt (85-100 pen), gives lower fracture energy while the binders A, B, and C used a softer base asphalt (150-200 pen) to give higher energy values. This supports the common believe that modified binder with a soft base asphalt is most suitable for preventing low temperature cracking.

Table 2. Fracture Energy Test Results at -30°C

Binder	Fracture Toughness ($kNm^{-3/2}$)	Modulus (Mpa)	Fracture Energy (Jm^{-2})
150/200 pen	*	*	*
85/100 pen	*	*	*
A	63.4	0.79	5.1
B	57.0	0.78	4.2
C	57.3	0.73	4.5
D	70.1	1.66	3.0
E	48.4	0.83	2.8

* Samples were too brittle and failed immediately

Figure 2 shows an obvious link between fracture energy and the low temperature TSRST performance. The regression analysis gives a strong correlation coefficient R^2 of 0.933. The good correlation implies that fracture energy can be used to develop a low temperature performance-based specification.

SHRP BINDER TESTS

SHRP binder tests were carried out using the control and modified samples. Table 3 provides the SHRP performance grades (PG) of the conventional asphalts and those of binders A, B, C, D, and E. Figure 3 shows the weak correlation between the PG grade values and the fracture temperatures with an R^2 value of 0.672. Alternatively, the relationship between the binder creep stiffness and fracture temperature was also investigated as shown in Figure 4. There is some improvement in the R^2 value but the correlation is still not as good as for that of G_{IC}. When the results of the SHRP direct tension test were compared with the fracture temperature it gave a very poor correlation (R^2 value = 0.004) as shown in Figure 5.

Table 3: SHRP low temperature performance grade results

Binder	Performance Grade (°C)
Control 150-200	-24
Control 85-100	-20
A	-32
B	-28
C	-26
D	-21
E	-26

PENETRATION TEST

Penetration tests were performed at 25° C after aging the binder using the Rolling Thin Film Oven Test method. Figure 5 shows that the correlation between the penetration values and the fracture temperatures is even better than that observed for the SHRP binder test results. This seems to indicate that SHRP binder testing system has not improved the existing characterization system with regards to modified binders

4.0 CONCLUSIONS

- Fracture energy shows the best correlation (R^2 =0.933) with TSRST failure temperatures .
- Because of the high correlation and the fact that it is a fundamental material property, fracture energy seems to offer promise for use in the development of a low temperature performance-based specification for modified binders.
- The SHRP approach to establish a low temperature performance grade for asphalts based on binder creep stiffness, m-value, and failure strain gives a poor correlation with the TSRST failure temperatures
- The correlation between the penetration test results and the performance is comparable to that observed for the SHRP binder tests. However, the results are not conclusive because of the limited data.

Table 4: Penetration Test Results

Binder	Aged Pen 25° C
Control 150-200	85
Control 85-100	47
A	87
B	65
C	66
D	41
E	39

5.0 RECOMMENDATIONS

- Expand the study so that the effects of aging on fracture toughness / fracture energy properties can be determined
- Establish a set of critical fracture energies so that low temperature Performance Grades can be established using fracture energy testing.
- Relate the experimental data to the field observation from the Hwy 118 test sections in Northern Ontario. This should be done to verify if experimental predictions can be related to actual field performance.

6.0 REFERENCES

1. El Hussein H. Mohamed, Kwang W. Kim, and Joseph Ponniah, "Assessment of Localized Damage Associated with Exposure to Extreme Low Temperatures", Transportation Research Board, Washington, D. C., January, 1996.
2. ASTM Method E 399-90 (1984) Standard Test Method for Plane-Strain Fracture Toughness of Metallic Materials. Philadelphia: ASTM.

ACKNOWLEDGEMENT

Special thanks to Imperial Oil for their assistance in this research work.

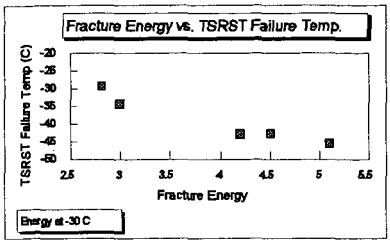

R^2= 0.933

Figure 2: Fracture Energy vs TSRST Failure Temperature

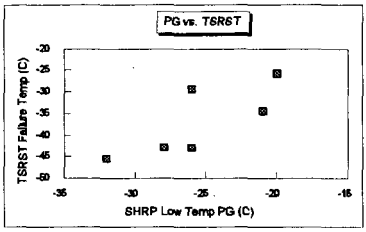

R^2= 0.617

Figure 3: *Performance Grade vs TSRST Failure Temperature*

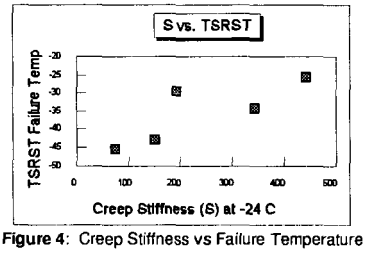

R^2= 0.672

Figure 4: Creep Stiffness vs Failure Temperature

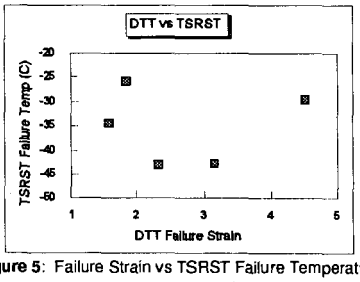

R^2= 0.0004

Figure 5: Failure Strain vs TSRST Failure Temperature

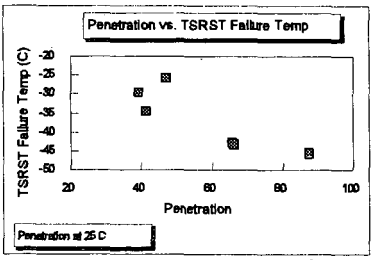

R^2= 0.702

Figure 6: Correlation for Aged Binder at 25°C

HIGH TEMPERATURE PERFORMANCE OF SCRAP TIRE RUBBER MODIFIED ASPHALT CONCRETE

A.(Coom) Coomarasamy*, Research & Development Branch,
Ministry of Transportation, Downsview, Ontario, M3M 1J8, Canada,
Steven Manolis and Simon Hesp*, Department of Chemistry,
Queen's University, Kingston, Ontario, K7L 3N6, Canada.

ABSTRACT

Wheel track rutting tests on mixes modified with 30 mesh, 80 mesh, and very fine colloidal crumb rubber particles show that a very significant improvement in performance occurs with a reduction in the rubber particle size. The SHRP binder test for rutting, which was originally developed for homogeneous systems only, does not predict the performance improvement for smaller rubber particles. If these new scrap rubber binder systems are to be used in pavements then rutting tests on the asphalt-aggregate mixture should be conducted in order to accurately predict high temperature performance.

Keywords: crumb rubber modifier, particle size, rutting

1. INTRODUCTION

Excessive permanent deformation in the form of rutting associated with high temperature service and thermal cracking associated with low temperature service are two major problems affecting the performance of asphalt concrete pavements (1). Widespread adoption of radial tires, with pressures of 138 to 173 psi higher than their bias-ply predecessors and increased traffic volumes have accentuated these problems, especially rutting at high service temperatures. Without rutting, motorists would benefit from better steering control and less danger from hydroplaning in rain or skidding in icy conditions (2).

The demand for asphalt binders with a reduced temperature susceptibility is increasing, as user agencies are insisting on improved performance (3). Modification of the asphalt binder with high molecular weight polymers is one of the methods commonly employed for improving the thermal susceptibility of paving asphalts. Polyethylene, styrene-butadiene, and ethylene vinyl acetate copolymers have all been used successfully to improve upon the performance of asphalt binders (4). For the last three decades discarded rubber tires have also found end-use applications in asphalt binders in order to improve upon both the low- and high-temperature performance of the road surface. However, actual field trials have so far been inconclusive in their assessment of the performance/cost benefits of these materials (5). Use of reclaimed tire rubber for paving applications is also desirable from a solid waste management point of view.

2. BACKGROUND

Experimenting with scrap rubber for asphalt modification started in the 1920's (6). However, development of rubber modified asphalt binders, as they are now most often used throughout North America and in many other countries started in the 1960's, with the introduction of the McDonald process by the Roads Department of the City of Phoenix, Arizona (7). Since the developments in the late 1960's by McDonald and co-workers, various proprietary and generic technologies have evolved for the use of recycled rubber from scrap tires in asphalt binders and rubber modified asphalt concrete.

The dry process which was developed in the late 1960's in Sweden under the trade name Rubit was patented for use in the United States in 1978 under the trade name PlusRide (8). It differs from the wet process in that the crumb rubber is used as a portion of the aggregate and is directly mixed with the aggregate. This process uses crumbs of larger sizes (1/16-1/4 in; ~1.58-6.35 mm) at a loading of 3-4 wt% of the aggregate.This process also requires 1.5-3% more liquid asphalt than a conventional hot-mix. The increased asphalt content is needed to achieve a voids content below 3% in order to prevent premature ravelling of the pavement (9,10). The PlusRide technology has been proven effective in reducing the harmful effects of ice formation on roads (11,12). Other dry process techniques include those developed by the Army Corps of Engineers at the Cold Regions Research Laboratory (CRREL) and the Generic dry technology (13).

---

* *To whom correspondence may be addressed.*

In the wet process, when asphalt cement and crumb rubber are blended together, there is an interaction between these materials. This asphalt-rubber reaction is influenced by the blending/reaction temperature, the length of time the temperature remains elevated, the type and amount of mechanical mixing, the size and the texture of the crumb rubber modifier, and the aromatic component of the asphalt cement. Crumb rubber being a three dimensional network of natural and synthetic rubbers, reinforced with carbon black absorb the light oils from the asphalt cement during the "reaction" which results in swelling and softening of the crumbs. This in turn increases the viscosity of the modified binder (14). The wet process requires the use of at least 20% more liquid asphalt than is used in a conventional hot-mix pavement. In some cases 40-60% more asphalt is used, accounting for most of the increase in both cost and performance. The high initial cost combined with the uncertainty regarding future benefits is probably a factor which has hindered the large scale acceptance of asphalt-rubber technology. It is a fact that the cost of rubber modified pavements, in general, is currently anywhere from 60-150% above the cost of a conventional pavement (16). However, if modest amounts of fine crumb are applied to an asphalt binder, a pavement could be constructed with normal binder contents and aggregate gradations which would result in only a slight overall increase in cost. This approach has already been taken in recent years. Paving trials in Florida (17) and Ontario (18) have used asphalt binders which contain only 7-9% fine crumb rubber (80 mesh) directly blended into the asphalt cement. Initial laboratory and field results are quite promising but it is too early to draw any firm conclusions.

Crumb rubber being a cross-linked product, it has long been thought that devulcanization, partial devulcanization, or depolymerization would provide additional benefits in terms of storage stability and performance improvements. Epps (19) has found in an informal survey that there have been fewer pavements constructed with devulcanized rubber binder systems. The patent literature contains numerous claims on processes for devulcanizing waste tire matter: In 1971, Nikolinski and Dobreva (20) used various process oils to produce devulcanized rubber from waste SBR, nitrile rubber, butyl rubber and 1,4 cis polybutadiene. This is one of the earlier patents which clearly describes the use of aromatic oils in the process. Patents of C.H. McDonald (21), Nielsen and Bagley (22), Sergeeva et al. (23), and Ulicke and Cerner (24) all describe the use of aromatic oil for effecting devulcanization of scrap tire rubber in an asphalt medium. The main drawback with regards to the use of aromatic oils for devulcanization of waste rubber comes from the health hazard associated with these oils. The use of process oil or hydrocarbon liquid under high temperature and shear to render vulcanized rubber into a fluid form is described by Wakefield et al. in 1975 (25). Applications of shearing energy with addition of an aromatic oil to produce bitumen-asphalt compositions is described by van Bochove (26). According to this patent, better control over the material properties were made possible through the application of shearing forces. In 1992 and in 1994, Liang and Woodhams (27,28) described a process for devulcanization of scrap tire rubber in asphalt with the aid of aromatic oils and high shear and subsequently further stabilizing the devulcanized or disintegrated rubber particles by reacting the product with liquid polybutadiene and sulphur. The devulcanized system is mixed with a sterically-stabilized, polyethylene-modified asphalt binder as described in earlier patents by Hesp et al. (29,30). A recent paper by Zanzotto and Kennepohl (2) describes a high temperature, high shear process for devulcanizing scrap tire rubber in liquid asphalt. The authors report that the modified asphalt materials are being tested for their performance in paving mixes. It is apparent that morphology in the asphalt-rubber composition plays a crucial role in determining the properties of the crumb rubber modified binder systems and in the performance of crumb rubber modified asphaltic concrete. The work described here is concerned with achieving improved high temperature performance of asphaltic concrete mixes, taking into consideration the particle size of the asphalt rubber composition. Another paper by the same authors describes the work done on low temperature performance of the asphalt rubber mixes developed for this study (31).

3. EXPERIMENTAL

3.1 Materials

The asphalts used in this study were a 150-200 and an 85-100 penetration grade both obtained from the Lake Ontario refinery of Petro-Canada in Clarkson, Ontario made with crude from the Bow River area in Alberta, Canada.

The 30 mesh, cryogenically ground, passenger car tire rubber sample was obtained from Recovery Technologies of Mississauga, Ontario and the 80 mesh, ambiently ground, tire rubber sample was obtained from Rouse Rubber Industries of Vicksburg, Mississippi.

A dense-graded mix design meeting the Ontario HL-3 specification (32) for surface course mixtures, was used to prepare the asphalt rubber concrete samples for the evaluation of rutting resistance. Limestone coarse aggregate, limestone screenings and natural sand used for sample preparation were supplied by Dibblee Construction of Westbrook, Ontario.

3.2 Procedures

3.2.1 Sample Preparation

Two types of crumb rubber modified binders were prepared by slowly adding 10% by weight of crumb rubber (30 mesh and 80 mesh) to the 150-200 penetration grade asphalt at 170° ±10°C with moderate shearing. The third sample was prepared starting with 10% by weight of a 30 mesh crumb rubber in a 150-200 penetration grade asphalt. Particle size reduction was obtained with a thermo-mechanical process.

The asphalt concrete beams used, consisted of two lifts, each 38 mm from selected mix designs. The bottom lift of each beam was manufactured using a high stability (13600 N) Durham HL-4 mix. The top lift was manufactured using HL-3 mixes containing crumb rubber modified asphalt binder and the unmodified 150-200 and 85-100 penetration grade reference binders. The beams were prepared using a California Kneading compactor.

3.2.2 Dynamic Mechanical Testing

A Rheometrics Dynamic Analyzer RDA II was used for rheological testing. Hot asphalt samples were poured into a combined melts and solids (CMS) test fixture and allowed to cool to room temperature prior to testing. The CMS fixture consists of a 42 mm diameter cup and a bilevel plate which has an 8 mm diameter serrated surface concentric with and projecting from a 25 mm diameter plate. A temperature sweep was used to measure G^*, G', G'' and $\tan\delta$ at four temperatures between 52 and 70°C in intervals of 6°C. A frequency of 10 rad/s was used. Samples were conditioned for at least 11 minutes at each test temperature. A soak time of 180 s, during which time the temperature did not vary by more than 0.1°C, was used prior to each measurement.

3.2.3 Rutting Evaluation

Rutting tests were carried out using a wheel tracking machine purchased from Petro-Canada Ltd. It consists of three parts; a constant temperature reservoir, a wheel carriage assembly and a drive linkage assembly. All of these parts work in unison to produce a back and forth movement of a tire along the lengths of the beam sample (2).

The prepared beam samples were conditioned at 70°C for 6 hours and tested at 60°C after allowing the sample to equilibrate in the constant temperature reservoir. Samples were subjected to 8000 passes (4000 cycles) using a treaded tire (pressurized at 550 kPa) at 60° C to induce rutting. Profilometers were used to obtain the rutting profiles.

4. RESULTS AND DISCUSSION

4.1 Effect of Crumb Rubber Modifier on Rutting Performance

The rut depth results obtained for individual HL-3 asphalt concrete beams and the average values for each mix are presented in Table 1. The mean particle size of the crumb rubber modifier in these systems are also given.

The results show that the resistance to rutting for crumb rubber modified binders is significantly better than that of the reference sample. Improvements over the control sample were about 37%, 51%, and 60% for modified binders containing 30 mesh, 80 mesh and 0.4 μm crumb rubber respectively. It is to be noted that the variation in rut depths between the duplicate samples are reasonable (except for the mix prepared with an 85-100 pen asphalt), considering the fact that the preparation of the concrete beams for these tests involves a series of steps which have to be carefully performed.

Table 1 also gives the rut depth values obtained for an 85-100 pen grade asphalt which is commonly used in high temperature service conditions such as in Southern Ontario. These preliminary results also indicate that, by crumb rubber modification of a softer grade (150-200 pen) asphalt, it may be possible to obtain high temperature rutting resistance comparable to that of an 85-100 pen grade asphalt.

The mean particle size for the thermo-mechanically processed sample was found to be 0.4 microns with a standard deviation of 0.4 microns. This represents a decrease of 1500 times compared to the 30 mesh (590 microns) crumb rubber used for modification. In terms of rutting performance, only about a 25% decrease in rut depth was obtained for a particle size reduction from 30 mesh (590 microns) to 0.4 microns.

4.2 Effects of Crumb Rubber Modifier in Dynamic Shear Measurements

A comparison was made between normalized average rut depths and normalized peformance grades of all the three crumb rubber modified binders and the reference binder as shown in Figure 1. But this comparison does not seem to reveal any trend correlating the PG of a binder with the rutting performance.

The work of Hanson & Duncan (34) on crumb rubber binders also indicates that although the stiffness increases with concentration, there is little variation in $G^*/\sin\delta$ for different gradations of rubber. The gradations of rubber used in their work were GF 16, 40, 80 and 120 mesh sizes, as provided by Rouse Rubber Industries (33).

5. CONCLUSIONS

A thermo-mechanical process employed to incorporate larger 30 mesh size crumb rubber seems to be an effective method for the preparation of crumb rubber modified binder with significantly improved high temperature properties. A limited number of rutting experiments conducted on modified mixes, suggests that the resistance to rutting improves with a reduction in the particle size of the crumb rubber modifier. The SHRP binder test for rutting resistance, which was originally developed for homogeneous systems only, does not predict the performance improvement for crumb rubber modified systems containing smaller rubber particles. Rutting tests on a wheel tracking machine are found to be better for predicting rutting performance of crumb rubber modified systems.

6. ACKNOWLEDGEMENTS

Thanks are due to Albert Chang, Bonnie Wong and Steven Goodman all Co-op students from the University of Waterloo, for their assistance in the preparation of specimens, and to the staff of the Bituminous Section, of MTO, for their assistance in conducting rutting experiments. Financial assistance provided by Ontario Ministry of Environment & Energy to conduct part of this work is gratefully acknowledged.

7. References

1. Epps, J., Petersen, J. C., Kennedy T.W., Anderson, D. and Haas, R. (1986), TRR 1096, Washington, D.C.
2. Yacyshyn, R., Tam, K.K., and Lynch, D.F. (1990) Report EM-93 Engineering Material Office, Ministry of Transportation Ontario, Downsview, Ontario.
3. Sawatzky, H., Temperature Dependence & Complexation Process in Asphalt and Possible Influence on Temperature Susceptibility Conference on HydroCarbon Residue and Wastes Commission Utilization, Edmonton, Alberta, Sept. 4-5, 1991.
4. Wardlaw, K.R. and Shuler, S., Eds (1992) Polymer-Modified Asphalt Binders. ASTM Special Technical Publication 1108, Philadelphia: ASTM.
5. Flynn, L., Roads & Bridges, 12 (1992) 42.
6. Zanzotto, L., and Kennepohl, G. (1996). Presented at the 75th Annual Meeting of the Transportation Board, Washington, D.C.
7. Morrison, G.R., and Hesp., S.A.M. (1995) Journal of Material Science 30, 2584-2590.
8. Bjorklund, A. (1979) in Proceedings of the VII World Road Conference, Vienna.
9. Takallon, H.B. and Hicks, R.G., TRR 1171, TRB, National Research Council, Washington, D.C. (1988) pp. 113-20.
10. McQuillen, J.L., Member, J.F., Takallon, H.B., Hicks, R.G. and Esch, D., Transp. Eng. 114 (1988) 259.
11. Narusch, F.P. Alaska Department of Transportation and Public Facilities, Div. of Design and Construction, Central Region, Juneau, Alaska.
12. Esch, D., TRR 860, TRB, NRC, Washington, D.C. (1992) p. 5-13.
13. Epps, J.A. (1994), NCHRP Synthesis 198, TRB, NRC, Washington, D.C.
14. Heitzman, M., 71st Annual Meeting 12-16 January 1992, Washington, D.C. Preprint 920549.
15. Moore, W., Construction Equipment, February 1991.
16. Tarricone, P., Civil Eng., April 1993, 46.
17. Page, C.G., Ruth, B.E. and West, R.C., 71st Annual Meeting, 12-16 January 1992, Washington, D.C., Preprint 920452.

18. Joseph, P.E., and Kennepohl, G., Report PAV-91-03, Ministry of Transportation Ontario, Downsview, Ontario June 1991.

19. Epps, J., Ontario Ministry of Transportation Meeting on the Use of Crumb Rubber-Modified Asphalt Binders, April 10, MTO, Downsview.

20. Nikolinski, P., and Dobreva, R., Polim. Simp. 1971 (Pub. 1972) vol. 3, pp. 254-9.

21. McDonald (1974), US Patent 4,085,078, Filed on Dec. 1, 1970.

22. Nielsen, D.L. and Bagley, J.R. (1978), US Patent 4,068,023, Filed on May 20, 1976.

23. Sergeeva, M., Zhailovich, I.L., Tumashchik, P.I., and Oreklov, I.A. (1987), USSR Patent SU1289872 A1. Issued on Feb. 15, 1987.

24. *Chemical Abstracts, Vol. 116(8) AN 61360c.*

25. Wakefield, L.B., Crane, G., and Kay, E.L. (1975), US Patent 3,896,059, Filed Feb. 5, 1974.

26. Van. Bochove (1991), European Patent 0439232 A1, Filed Jan. 22, 1991.

27. Liang, Z.Z., and Woodham, R.T. (1992) GB Patent Application. Filed on December 29, 1992.

28. Liang, Z.Z., and Woodhams, R.I. (1994), World Patent Application 94/14896, Priority date: December 29, 1992 - GB 92 27035.4.

29. Hesp, S.A.M., Liang, Z.Z., and Woodhams, R.T. (1993). World Patent Application 93/07219 Priority date: September 30, 1991 - US 863,734.

30. Hesp, S.A.M., Liang, Z.Z. and Woodhams, R.T. (1994), US Patent 5,280,064, Filed on September 30, 1991.

31. Coomarasamy, A. and Hesp, S.A.M., Paving in Cold Areas, October 1996, Niigata, Japan (Paper to be presented).

32. Ministry of Transportation Ontario Laboratory Series, LS Manual.

33. Rouse Rubber Industries Inc. (1992) Company Product Literature, Vicksburg Mississippi.

34. Hanson, D., and Duncan, G.M. (1995), TRR 1488, TRB, Washington, D.C.

TABLE 1

Effect of Crumb Rubber Modified Binder on Rutting of HL-3 Mixes at 60°C after 8000 Passes of a Wheel Tracking machine

Binder System	Run 1 Rut Depth (cm)	Run 2 Rut Depth (cm)	Average* Rut Depth (cm)	Crumb Rubber Particle Size (Microns)
150 - 200	0.84	0.71	0.77	N/A
10% 30 mesh	0.45	0.53	0.49	590 †
10% 80 mesh	0.41	0.35	0.38	177 †
10% 0.4 µm	0.34	0.27	0.31	0.41 ‡
85 - 100	0.15	0.33	0.24	N/A

* *Average of Run 1 & Run 2* † *Sieve size reported by Rouse Rubber Industries*
‡ *Mean particle size as determined by optical image analysis*

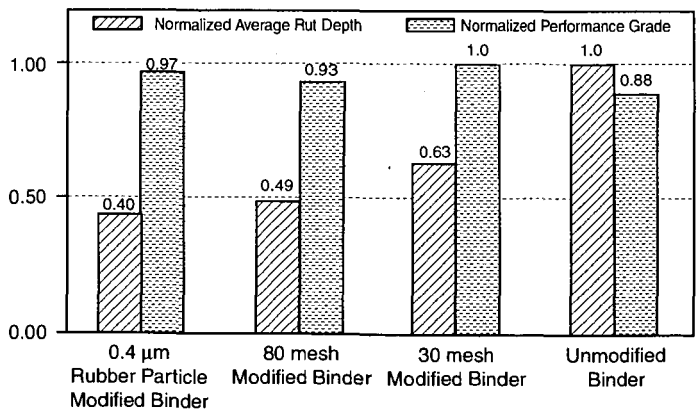

FIGURE 1. Comparison of normalized average rut depth with normalized performance grade

USE OF NUCLEAR MAGNETIC RESONANCE IMAGING TO STUDY ASPHALT

Francis P. Miknis and Daniel A. Netzel
Western Research Institute
365 North 9th Street
Laramie, WY 82070

Keywords: magnetic resonance imaging, asphalt, natural rubber, asphaltenes

INTRODUCTION

Magnetic resonance imaging (MRI) combines the basic principles of magnetic resonance with spatial encoding to obtain images of the distribution of fluids in samples. Because of the sensitivity of the hydrogen nucleus in NMR and because of its favorable relaxation times, water is the fluid most often imaged. This favorable aspect suggests that MRI might be used to obtain valuable information about water susceptibility and moisture damage mechanisms in asphalt. However, it has only been fairly recently that nonmedical applications of MRI have been increasing partly because of improvements in instrumentation and speed of data acquisition. MRI has been used to measure the distribution of fluids in porous rocks [1], ceramics [2], wood [3], other plant materials [4], synthetic polymers [5], solvent diffusion in polymers [6], coals [7,8], and bonding of adhesives [9].

In favorable circumstances, NMR imaging methods can be employed for imaging solid materials such as elastomers. NMR imaging has been used to study the morphology and defects in tire composites and the dispersion of carbon black in sections of tire tread [10] and to detect voids, gaps, and foreign particles in elastomers [11]. NMR imaging has also been used to study aging and phase separation in elastomers and to obtain the kinetics of the aging reaction [12]. In addition, inhomogeneities in natural rubber have been detected and characterized. Komorowski [13] has written a recent review of nonmedical applications of MRI. Little work has been done on the use of MRI in asphalt research.

EXPERIMENTAL

MRI measurements were made using spin echo (SE) or 3 dimensional (3D) imaging techniques. For nonviscous materials, such as water and organic solvents, the spin echo technique provided the best images because the relaxation times of nonviscous liquids were generally long and therefore more favorable for spin echo imaging. For elastomeric and viscous materials, the relaxation times of the protons were generally too short for spin echo imaging. Consequently, the 3D technique was used for these materials.

Magnetic resonance imaging experiments were carried out at a nominal proton resonance frequency of 200 MHz using a Chemagnetics/Otsuka Electronics microimaging probe. Samples for NMR imaging experiments were placed in 23 mm (OD) glass vials, which were then placed in 25 mm(OD) glass tubes. The tubes were inserted into the MRI probe and were positioned in the probe using O rings such that the cross sections to be imaged were contained in the experimental field of views (FOV).

Typical instrument parameters using the spin echo technique were echo times of 10-40 ms, a pulse delay of 1 s, a free induction decay size of 256 data points, 256 phase encodes, and a gradient strength of 34 G/cm. Eight slices, 1 mm thick and separated by 1 mm were obtained. The measuring time was ~ 1 hr. Images using the 3D method were made using an echo time of 2 ms, a pulse delay of 1 s, a free induction decay size of 256 data points, 128 phase encodes, 50 acquisitions and a gradient strength of 69 G/cm. Eight slices were usually obtained. The measuring time was 14.2 hrs for these experiments.

RESULTS AND DISCUSSION

MRI Measurements on Asphalts. MRI measurements cannot be obtained on asphalts at room temperature because the lack of molecular mobility (high viscosity), causes the NMR signal to decay away before any spin echoes can be formed. However,

there are some techniques that can be employed to decrease the viscosity and to increase the relaxation time, T_2, so that images of asphalt are obtained. One approach is to acquire images at elevated temperatures where the asphalt viscosity is reduced and the relaxation times are lengthened. Cursory MRI experiments of this nature have been performed using a heat gun to melt asphalt and to acquire images as soon as possible while the sample is cooling. Images of asphalt have been obtained in this fashion but are not shown here. The experiments demonstrated that temperature can be used as an aid in imaging asphalts.

The use of solvents to dissolve asphalts is another approach to imaging asphalts. However, this approach poses some problems because the solvent and dissolved asphalt both contain protons so that the respective contributions from each set of protons to the NMR image is not evident. Chemical shift imaging is a possible solution in this situation, albeit a remote one given the present state-of-the-art of NMR imaging. The use of deuterated solvents is another way to circumvent this problem.

For certain applications, signals from the solvent may not present problems as illustrated by the images in Figure 1. This is a set of images for an asphalt dissolved in an equal volume of toluene and titrated with isooctane to the point at which flocculation occurs and asphaltenes begin to precipitate. After a period of time the asphaltenes settle out to form a layer, the height of which depends on the amount of isooctane used to precipitate the asphaltenes.

Figure 1 is also an example of how the experimental parameters can be chosen to enhance the signal contrast between different components of the system. In Figure 1, the spin echo time was varied from 10 to 40 ms. For the shorter echo time (10 ms), the image shows little contrast because for this echo time the NMR signals from all the components are strong. As the echo time gets longer, the contrast between the asphaltenes and solvent improves. For an echo time of 40 ms, the NMR signal from the asphaltenes has decayed considerably and appears as a dark gray band at the bottom of the vial. The NMR signals from the asphalt/toluene/isooctane components are still strong for this echo time and appear as the bright areas in the figure. If the layer of asphaltenes is of interest, the solvent and dissolved asphalt do not present a problem so long as long echo times are used to form the images. This procedure is referred to as T_2 weighting.

There is a thin black layer between the solvent and asphaltenes which is very noticeable in the images taken at a 40 ms echo time (Figure 1). To obtain some idea of the nature of the black layer, a spatula was inserted to the bottom of the vial and an "X" pattern was scribed to disrupt the asphaltene/solvent interface (Figure 2). The images of the asphaltenes show that the surface was apparently rigid as indicated by the pieces of the black layer that were broken and scattered throughout the asphaltene layer. The nature of this layer is not known at present. This layer could be a part of the asphaltene layer that is becoming more rigid with time at the asphaltene/solvent interface. A more rigid system would have shorter relaxation times and would appear darker in the NMR images. The layer could also be due to oxidation of the maltenes, which are then attracted to the highly polar surface of the asphaltenes and form a distinct layer at the interface. Other possibilities also exist and investigations are continuing to characterize this layer.

Natural Rubber in Asphalt. Although the federal mandate on the use of crumb rubber in paving applications has been removed, there still is sufficient interest to more fully understand the compatibility and physicochemical interactions of asphalt and crumb rubber materials. Preliminary MRI measurements were conducted on the feasibility of observing the presence of natural rubber in asphalt and the possibility of natural rubber dissolution in asphalt after heat treatment. A conical piece of natural rubber was submerged in an asphalt and heated to a temperature of 160 °C for 16 hrs. The asphalt had a high carboxylic acid content and carboxylic acids have been shown to dissolve different rubber materials when heated to 200 °C for extended periods of time (Tauer and Robertson, this symposium)[14]. Images of the asphalt/natural rubber system were acquired before and after heating using the 3D technique (Figure 3). Only the protons in the rubber are imaged using the 3D imaging sequence. Images of the asphalt are not obtained because the proton relaxation times of asphalt are too short. The image of the heated sample (Figure 3b) is not as clear as

that of the unheated sample (Figure 3a). The current interpretation is that the less sharp image of the heated sample is a result of reactions that have taken place at the surface of the natural rubber cone. Reactions between the natural rubber and components in the asphalt could cause the relaxation times of the protons in both materials to be slightly different at the surface than that of the bulk natural rubber leading to less sharp images. Further experiments along these lines are in progress.

Asphalt/Water/Aggregate Systems. Moisture damage in pavements generally leads to stripping, raveling and late rutting. One probable mechanism responsible for these failures is loss of adhesion of the asphalt at the aggregate interface. Water is suspected to play a major role in this damage mechanism. Direct observation of this failure mode has been difficult because of the lack of suitable instrumental techniques. Magnetic resonance imaging (MRI) methods may offer an approach to study this mechanism because of the favorable response of water in MRI experiments. However, little research has been done on the use of MRI to study asphalt/aggregate/water interactions in order to validate whether MRI methods can provide insight into moisture damage mechanisms.

MRI measurements were made on pieces of aggregates that were embedded in asphalt and covered with a layer of water. A spin echo pulse sequence was used to image the cross-sections of the asphalt/aggregate/water system in the XZ plane, before and after freeze thaw cycling, to determine whether water had any effect on the asphalt/aggregate interface. Three asphalts of differing stiffness and three different aggregate systems were studied. However, preliminary MRI measurements indicated that a limestone aggregate would be the easiest to observe changes as a result of the freeze thaw cycling. The other aggregates had varying amounts of magnetic components and therefore could not be imaged.

Of the three asphalts studied, only one showed displacement of asphalt from the aggregate after freeze thaws. This is shown in Figure 4. Comparison of the boundary at the water/aggregate/asphalt interface in the lower left center of each panel, before and after freeze thawing, shows an increase in the amount of water extending downward into the asphalt along the aggregate. The penetration began after 4 freeze thaws and increased slightly with successive freeze thaws, although there was not much difference after 6 freeze thaws.

SUMMARY

Applications of magnetic resonance imaging to study various aspects of asphalts are in their infancy. Consequently, a number of imaging methods and instrumental parameters need to be investigated to determine the feasibility of MRI to study asphalts. In this study, exploratory MRI measurements were made on the precipitation of asphaltenes from asphalt, observation of natural rubber in asphalt, and the possible interaction of water with asphalt at an aggregate interface. The MRI experiments showed that image contrast between asphaltenes and the precipitating solvent can be improved by varying the echo time used to form the images. Natural rubber in the presence of asphalt can be observed using 3D imaging methods, leading to the possibility of studying solvent swelling and possible dissolution of crumb rubber by components of the asphalt. MRI measurements of asphalt/water/aggregate systems showed evidence of water penetration at the aggregate interface. In all cases, the results were sufficiently encouraging to warrant additional investigations.

DISCLAIMER

ACKNOWLEDGMENTS

The authors gratefully acknowledge support of this work by the Federal Highway Administration under Contract No. DTFH61-92-C-00170. Technical discussion with Dr. Joseph Ford of Chemagnetics/Otsuka Electronics was also appreciated.

REFERENCES

1. Sarkar S.N., E.W. Wooten, and R.A. Komoroski, Appl. Spec., 1991, 45, 619.
2. Ackerman J.L., L. Garido, J.E. Moore, and W.A. Ellingson, Polymer Prepr., 1990, 31, 145.
3. Chang S.J., J.R. Olsen, and P.C. Wang, For. Prod. J., 1989, 39, 43.
4. Cofer G.P., J.M. Brown and G.A. Johnson, J. Magn. Reson.,1989, 83, 608.
5. Rothwell, W.P.; Holocek, D.R.; Kershaw, J.A.
6. Weisenberger L.A., and J.L. Koenig, NMR Investigations of Case II Diffusion in Polymers, in Solid State NMR of Polymers, L.J. Mathias, ed., Plenum Press, New York, 1991, 377-386.
7. Webb A.G., K. Motsegood, and R.B. Clarkson, Fuel, 1993, 72, 1235.
8. Hou L.; Cody, G.D.;French, D.C.; Botto, R.E.; Hatcher, P.G. Energy Fuels, 1995, 9, 84.
9. Koenig J.L., Application of NMR Imaging to Polymers, in Solid State NMR of Polymers, L.J. Mathias, ed., Plenum Press, New York, 1991, 61-79.
10. Sarkar S.N. and Komoroski R.A., Macromolecules, 1992, 25, 1420.
11. Chang C. and Komoroski R.A., Macromolecules, 1989, 22, 600.
12. Blumler P. and B. Blumich, Macromolecules, 1991, 24, 2183.
13. Komoroski R.A., Anal. Chem.,1993, 65, 1068A.
14. Tauer, J.E.; Robertson, R.E. Prepr. Pap.-Am. Chem. Soc., Div. Fuel Chem., 1996, 41, Symp. on Modified Asphalts.

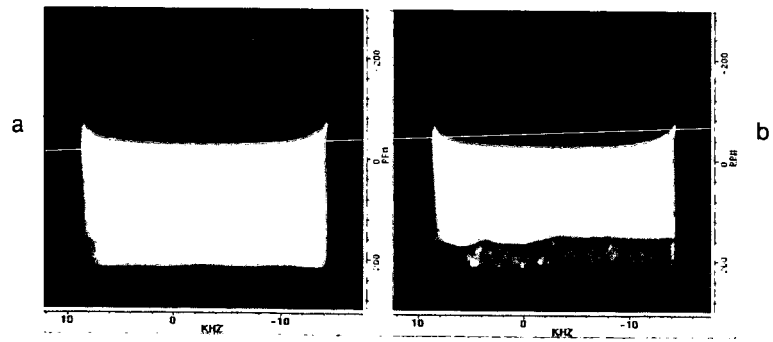

Figure 1. Spin echo images of asphaltene settling illustrating T_2 weighting to enhance image contrast: (a) 10, and (b) 40 ms echo time.

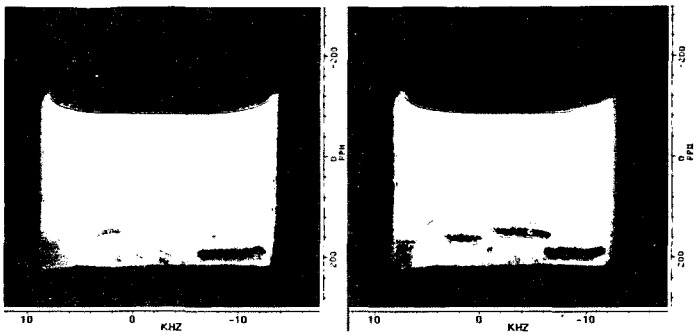

Figure 2. Spin echo images of asphaltene layer after stirring.

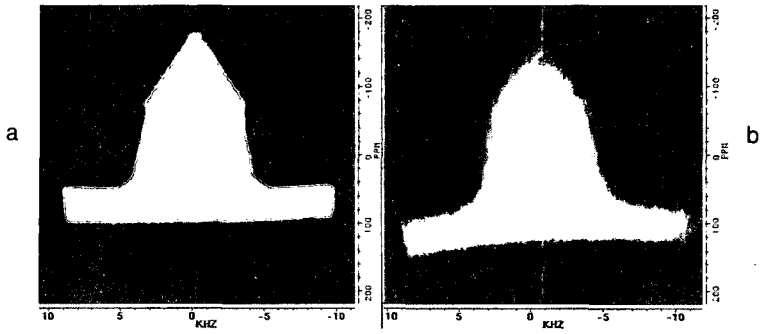

Figure 3. 3D images of natural rubber submerged in asphalt: (a) unheated, (b) heated for 16 hrs at 160 °C.

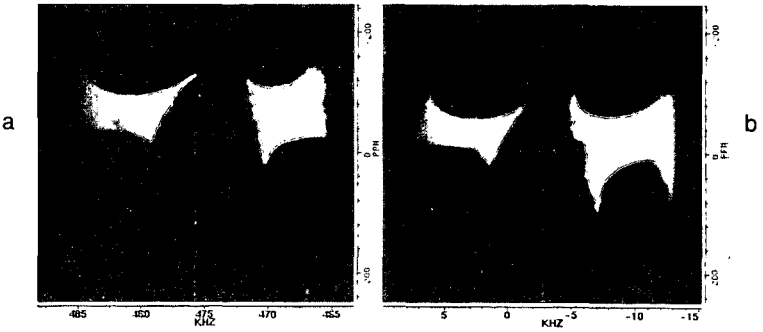

Figure 4. Spin echo images of SHRP asphalt AAM-1 and MRL aggregate RE in water after: (a) 0, and (b) 6 freeze thaws.

CARBON DIOXIDE REMOVAL FROM NATURAL GAS USING AMINE SURFACE BONDED ADSORBENTS

Orlando Leal,* Carmelo Bolivar,* Cesar Ovalles,† Argelia Urbina,† Javier Revette† and Juan Jose Garcia†, *Escuela de Quimica, Universidad Central de Venezuela and †INTEVEP, S. A., Apdo. Postal 76343, Caracas 1070A, Venezuela.

Keywords: Carbon dioxide removal, surface-bonded, adsorbents

INTRODUCTION

The results of research on the greenhouse effect have shown, among other things, that the concentration of trace gases occurring in the atmosphere such as carbon dioxide, methane, nitrous oxide, ozone and halocarbons have grown significantly since the ore-industrial times. During this period, the CO_2 level has risen 30% to nearly 360 ppm from a pre-industrial era level of 280 ppm [1]. On the basis of a variety of evidence a consensus is emerging among researchers that humans beings, primarily through their burning of fossil fuels, are already perturbing Earth's elimate [2]. All specialists agree that without drastic steps to curb greenhouse gas emissions, the average global temperature will increase 1 to 3.5 °C during the next century because effective level of carbon dioxide are expected to double sometime between the years 2050 to 2100 [3]. It may be that human-generated emissions of carbon dioxide will have to be reduced by as much as 50-80% to avoid major climate changes. Such a reduction in the CO_2 emissions rate probably cannot be accomplished without a massive switch to non-fossil energy sources. However, it has been proposed that emissions from fossil fuels can be moderated by three strategies: exploiting the fuels more efficiently, replacing coal by natural gas and by recovering and sequestering CO_2 emissions [4]. A rough analysis, based on the use of currently accepted values, shows that natural gas is preferable to other fossil fuels in consideration of the greenhouse effect [5] and improvements can be obtained if natural gas is upgrading by scrubbing the carbon dioxide out of it.

Removal of carbon dioxide from gaseous streams have been a current procedure in the chemical industry. The presence of tiny amounts of CO_2 can act as poison in catalytic processes such as ethylene polymerization or ammonia synthesis [6]. Therefore, several procedures have been devised to eliminate carbon dioxide from ammonia plants as well as natural gas and fuel gas power plants. Three different approaches have been used: absorption on liquid amines [7], adsorption on solid materials [8], and membrane technology [9]. The former makes extensively use of alkanolamines in plants operating at low temperatures and high pressures. In this case inhibitors should be used to prevent the corrosion problem arising from the formation of highly reactive carbamates. A process commercially known as Selexol, uses a mixtures of polypropyleneglycoldimethyl ethers and CO_2 removal is based on physical adsorption in much heavier molecules [10].

The use of membranes top remove carbon dioxide and other acid gases was assessed by Bhide and Stein [9]. Aromatic polyimide separation membranes are particularly useful for CO_2 enrichment [11], because they are able to achieve high flow rates with good selectivity and relatively low temperatures. This procedure proved effective to removed carbon dioxide in concentration ranging between 5 and 40 mol %. However, membrane saturation might produce gas losses [11].

The removal of CO_2 from closed ambients, such as submarines, by solid adsorbents has been described elsewhere [12]. A solid matrix, usually an inorganic oxide, was chemically modified to obtain a material which reversibly adsorbed carbon dioxide from atmospheres containing about 1 % by volume of CO_2. The adsorbent, which had a clay component as agglomerant, showed approximately a capacity of 20 l of wet carbon dioxide per kg of adsorbent. When silica gel was used as a solid, the modification of its surface could be accomplished by reaction with aminoalkoxysilanes such as 3-aminopropyltriethoxysilane, though condensation to the hydroxyl groups present on the silica gel surface. This process might involve the reaction of one, two or three hydroxyl groups at the surface per molecule of alkoxysilane. Therefore, the nature of the bonded species will depend upon the number and distribution of the hydroxyl groups at the surface of the silica gel. Previous studies indicated that annealed and rehydroxylated silica gel has a surface hydroxyl concentration of 4.6 -OH groups per square nanometer[13], of which 1.4 hydroxyl groups/nm^2 are interacting non-hydrogen bonded species and the remaining 3.2 hydroxyl/nm^2 are interacting groups arranged in pairs. All these groups can be involved in the reaction of the surface of the silica with polyalkoxysilanes. From C, N, H microanalysis studies, Burwell [14] concluded that this reaction gives a product with an average composition corresponding to the detachment of the silane to the surface, according to reaction (1).

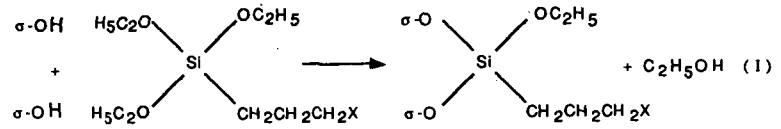

Where σ = silicon atom at the surface of silica and
X = NH_2 for 3-aminopropyltriethoxysilane

Recent NIR and ^{29}Si CP/MAS NMR studies have shed light on the nature of the surface species of the resulting material [5]. These results are consistent with the occurrence of a surface reaction between the aminoalkoxysilane and the OH groups of the silica gel, which act as anchorage points to the solid surface as was previously proposed in reaction (1). The adsorption of CO_2 was found to take place by formation of a carbamate species (I) on the modified surface of the material, where two amino groups are involved per carbon dioxide molecule adsorbed as indicated in eq.(2).

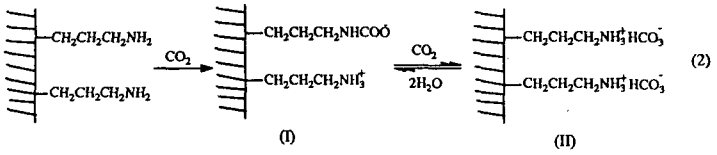

In the presence of water, the capacity of CO_2 adsorption is duplicated due to a surface chemical transformation of the carbamate (I) into two adsorbed bicarbonate (II) molecules. This adsorption of carbon dioxide is reversed when the adsorbent is heated at 100 °C.
In this article, we described the effects of gas pressures (1.4 to 20 atm), space velocity (from 6 to 36 h^{-1}), water content and modification of the inorganic matrix on the adsorption process and removal of carbon dioxide from natural gas (ca. 8 % by volume) using surface chemically modified adsorbents.

EXPERIMENTAL

Surface Modification

Adsorbents were prepared as described elsewhere [12]. In the preparation, different silica gels were used as solid matrixes but in all cases the procedure involves azeotropic drying with an organic solvent, surface modification by reaction with an alkoxysilane solution, washing and drying of the resulting materials. Activation of adsorbents was carried out by heating at 100°C under nitrogen or natural gas stream prior to use. A typical preparation resulted in a material having coverages of about 2.8 molecules of aminopropyl groups/nm^2 (1.27 mmol of nitrogen/g), determined by C, H and N microanalysis.

Apparatus

Solid adsorption capacity tests of carbon dioxide were carried out on a continuos flow experimental system (see Fig. 1) built out of stainless steel tubing equipped with temperature, pressure and mass flow controllers. The adsorbents were confined in two parallel cylinders which allow its activation and use in an alternate fashion. Each cylinder is loaded with 250 g of adsorbent. A Varian 3400 gas chromatograph equipped with a 6 feet stainless steel column of 10% carbowax 20M on chromosorb W-HP 80/100 mesh was used to monitor the samples.
Natural gas having a composition of 83.1% of methane, 7.6% of ethane, 0.7% propane, 0.2% butanes, 0.1% pentanes and 8.3% carbon dioxide was used in the scrubbing tests which were carried out at pressures ranging between 1.4 to 20 atm a flow rates of 28 and 170 cubic feet per hour (1000-6000 liter/h). Natural gas had a maximum content of water of 130 ppm.

RESULTS AND DISCUSSIONS

Activation of the adsorbent was done by heating in a gas stream to eliminate any water or carbon dioxide which has been adsorbed from the atmosphere prior the experiments. This activation was carried out either in flowing nitrogen or the same natural gas being stripped, and results showed

that it is effective in either gas. A lower capacity was found when natural gas was used due to the residual carbon dioxide contained in it which remained in the reactor as the temperature was lowered from activation to room temperature. However this decrease is limited to less than 5%. Experiments performed at different space velocities showed that the adsorbed carbon dioxide started to be liberated by temperature programmed desorption (TPD) above 40ºC and the process of release was maintained until above 100ºC [12, 15]. The center of the peak is shifted to lower temperatures as the space velocity increases. At a space velocity of 2.4 h^{-1} (1.2 l/h) the adsorption band is centered at 10ºC and desorption is completed at 110ºC whereas at a space velocity of 0.6 h^{-1} (0.3 l/h) the desorption band is centered at 90ºC and desorption is completed at 120ºC. On the other hand if the desorption temperature was held at 140ºC the adsorbent is regenerated in 2 h.

The influence of space velocity on the adsorption of carbon dioxide is shown in Fig. 2 where 100% corresponds to complete stripping of CO_2 from a natural gas containing 8.3% CO_2 and activation was undertaken under nitrogen as carrier. It is clear form this that as space velocity increases from 6 to 36 h^{-1} (28 to 170 scf/h) the breakthrough time is reduced from 14 to 2.5 h, however the elution front remains clear-cut confirming the chemical nature of the surface adduct. The process also quantitatively subtracts carbon dioxide from the natural gas stream.

The influence of the pressure on the adsorption process is shown in Fig. 3. The capacity of the adsorbent before immediate breakthrough, when the system is operated at atmospheric pressure, is 14.0±0.7 liters of dry carbon dioxide per kilogram of adsorbent. At a pressure of 4 atm the obtained capacity is 13±2 l of CO_2/Kg taken as average value at the different space velocities tested. Whereas at a pressure of 20 atm (300 psi) the adsorptive capacity has dropped to 8.3±0.2 l of CO_2/Kg before immediate breakthrough. However a marked effect of the pressure is noticed here as the carbon dioxide seems to interact stronger with the adsorbent.

When carbon dioxide is saturated with water an increase of the capacity is observed, from 8.1 to 13.1 l of CO_2/Kg at a space velocity of 170 scf/h (Fig. 4). Carbon dioxide scrubbing by the adsorbent leads to an enrichment of the natural gas as it is presented on Table 1.

The adsorbent used in all the above experiments was a modified silica/clay aggregate described before (Adsorbent I) [12]. Two new adsorbents were obtained: a) using an extrudated silica gel as matrix (Adsorbent II), b) using a silica gel Davison 923 with a surface area of 700 m^2/g (Adsorbent III). The rest of the preparation procedure remained the same.

Adsorbent II showed a lower performance than adsorbent I and only at pressures higher than atmospheric carbon dioxide was adsorbed at room temperature. Adsorbent III resulted a better scrubber for carbon dioxide and there was an enhancement of the adsorptive capacity to a maximum of 28.5 liters of wet CO_2 per Kg of adsorbent at a pressure of 60 psi (4 atm).

When these materials are exposed to water vapor after being saturated their surface with carbon dioxide, production of small amounts of a substance with odor evoking an aldehyde compound is noticed. MS analysis revealed the presence of 2-methyl benzaldehyde. On the other hand, meta-xylene was detected on the solid NMR analysis as a residue from the preparation procedure. Thus, a reaction as the one shown below (eq. 3) conceivably had occurred:

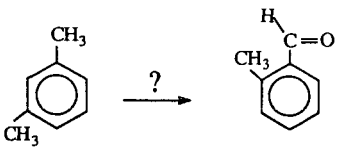

(3)

This reaction and its mechanism is under investigation.

In summary, we have prepared an adsorbent which can be used to remove carbon dioxide from natural gas at pressures higher than atmospheric pressure. This removal is selective and reversible, and carbon dioxide is released by heating the adsorbent at about 110ºC using nitrogen or the same natural gas as carrier. Improvements on the capacity of the adsorbents could be done by changing the solid matrix.

REFERENCES
1. Report, United Nations Intergovernmantal panel on Climate Changes, Dec 1995.
2. C. D. Keeling, T. P. Whorf, M. Wahlen and J. Van der Plicht, Nature, 375, 666 (1995).
3. B. Hileman, Chem. & Eng. News, nov. 27, 18 (1995).
4. W. Fulkerson, R. Judkins and M. Sanghyi, Sci. Amer., 83 (1990).
5. H. Rodhe, Science, 248, 1217 (1990).
6. M. Buckthorp, Nitrogen, 113, 34 (1978).
7. K. Volkamer and U. Wagner, Fertilizer, 139 (1983).
8. D. A. Boyta, U. S. Patent No. 3,847,837 (1974).
9. B. D. Bhide and S. A. Stern, J. Membr. Sci., 81, 209 (1993).
10. V. A. Shah, Energy Prog., 8, 67 (1988).
11. M. Weinberg, U. S. Patent No. 5,234,471 (1993).
12. O. Leal, C. Bolivar, G. sepulveda, G. Molleja, G. Martinez and L. Esparragoza, U. S. Patent No. 5,087,597 (1992).
13. J. H. Boer, M. E. Hermans and J. M. Vleeskins, K. Ned. Akad, Wet, B60, 44 (1957).
14. R. L. Burwell, Jr., Chem. Technol, 370 (1974).
15. O. Leal, C. Bolivar, C. Ovalles, J. J. Garcia and Y. Espidel, Inorg. Chim. Acta, in press (1996).

Table 1. Enrichment fo Natural Gas by removal of carbon dioxide.

Component[a]	Initial concentration molar %[b]	After removal molar %
CH_4	82.9	89.1
CO_2	7.0	-
C_2H_6	9.8	10.5
C_3H_8	0.24	0.26
C_4	0.03	0.03
C_5^+	0.02	0.02

[a]Experiment run at space velocity = 36 h^{-1} and activation of adsorbent done under nitrogen.
[b]Molar composition determined by GC using internal standard.

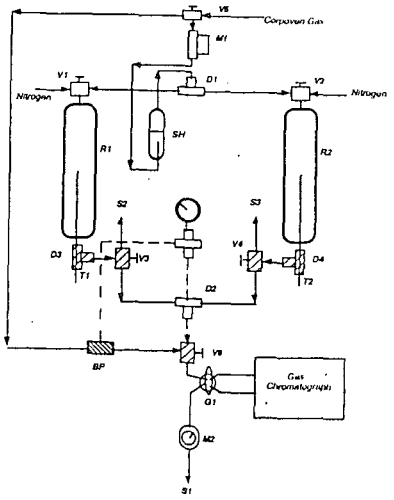

Fig. 1. Schematic diagram of flow system. D = flow splitters, R = reactors, S = gas aoutlet, T = thermocouple, V = three way valves, SH = water saturator, BP = back pressure valve, M1 = mass flow controller, M2 = flowmeter, M3 = manometer.

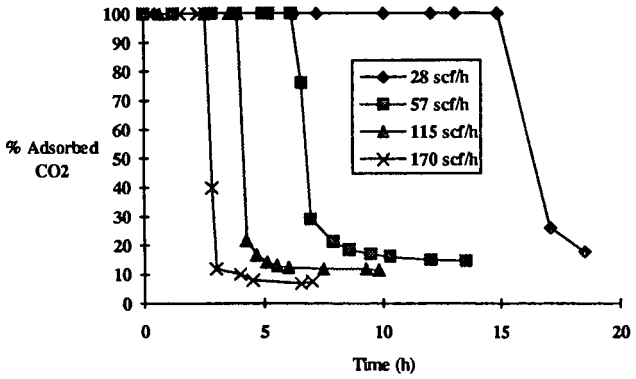

Fig. 2. Effect of space velocity on adsortion of CO_2 on adsorbent I from natural gas.

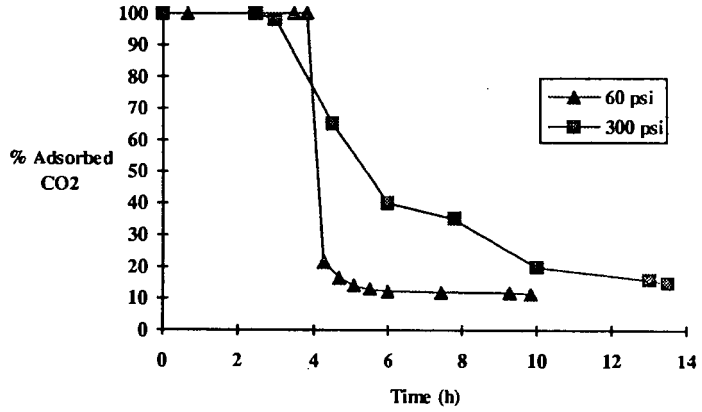

Fig. 3. Effect of pressure of operation on the removal of CO_2 on adsorbent I from natural gas.

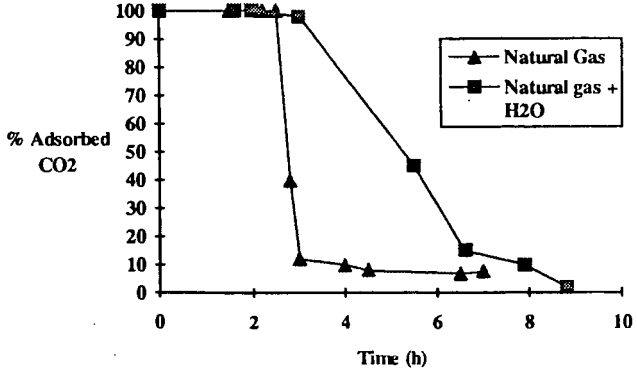

Fig. 4. Influence of water on the removal of CO_2 on adsorbent I from natural gas.

Comparison of CO_2-Sources for Fuel Synthesis

T. WEIMER, K. SCHABER

Institut fuer Technische Thermodynamik und Kaeltetechnik University of Karlsruhe, Germany;

M. SPECHT, A. BANDI

Center for Solar Energy and Hydrogen Research, Stuttgart, Germany

Keywords: CO_2 **recovery, Climate neutral fuel synthesis,** CO_2 **sources**

1 Strategies for the Substitution of Fossil Fuels

As it has been estimated in several publications, e.g. [3], the combustion of fossil fuels contribute with about 50 % to the global warming due to the increasing concentration of atmospheric CO_2. Short term strategies for the reduction of the CO_2-emissions are energy saving and efficient utilization. But as a successful long term strategy to stabilize the atmospheric CO_2-content only the substitution of fossil fuels by renewable energy sources can be accepted. The potential of renewable energy sources is by several magnitudes higher than any estimated future world energy demand, [7]. Unfortunately, large renewable energy sources are almost located far away of the main energy consumption areas, e. g. in desert regions, mountains or over the oceans. If there is no realistic possibility to join an electric grid, renewable energy must be transported by energy carriers. For the intercontinental transport of energy as well as for energy storage, the generation of chemical energy carriers is the best alternative. Possible alternatives are hydrogen or liquid carbonaceous energy carriers.

On the other hand, mobile applications of carbonaceous fuels have the most dynamic growth of all energy consumption sectors. Here chemical energy carriers are again the best alternative for the storage of energy on board. Both, hydrogen and methanol generated from renewable energy sources can be applied as energy carrier in automobiles. In opposite to fossil fuels, they open the possibility to use high efficient fuel cells in transport applications. Even automobiles with high efficient combustion engines consume about the double amount of energy per mileage then fuel cell equipped cars. Therefore in mobile applications as well as for electricity the renewable generated energy carrier can substitute about the double of fossil primary energy. The most likely choice for the large scale substitution of fossil energy carriers is the generation of electricity from renewable energy or fuels for mobile applications with remote renewable energy sources.

2 Renewable Fuels for Mobile Applications

For the generation of a climate neutral fuel using renewable energy, a closed loop process without net emissions is necessary. The generation of hydrogen from water achieves the monoxide shift reaction is shown in figure 1. With the CO_2 recovery and compression to 60 bar a reduction of the energetic efficiency of the power station to 38,1 % from 43,6 % without CO_2 recovery was estimated. 88 % of the CO_2 emissions are recovered For simplifying the further discussion pure Carbon with a heating value of 393 kJ/Mol is assumed as energy source. In the basic case without CO_2 recovery we achieve an electric output of 171 kJ(el)/Mol Carbon leading to a specific CO_2 emission of 5,85 Mol CO_2/MJ(el). To achieve this electrical output of 171 kJ(el) in the process including a CO_2 recovery unit, 1,14 Mol of Carbon have to be fired at the new efficiency of 38,1 %. CO_2 recovery of 88 % leads to 1,14*0,88=1 Mol CO_2/171 kJ(el) and CO_2 emissions of 0,14 Mol CO_2/171 kJ(el) equivalent to 0,82 Mol CO_2/MJ(el). The additional fossil energy demand E_{Carbon} for the recovery of the 1 Mol CO_2 is 0,14 Mol carbon with a heating value of 393 kJ/Mol, leading to:

$$E_{Carbon} = 55 kJ/Mol\, CO_2 . \quad (1)$$

A compression of CO_2 to 60 bar is included in the energy demand. The energy demand for drying and liquefaction of the compressed CO_2 is neglected.

Power plants fired with Natural Gas have lower specific emissions of CO_2. A power plant fired with Natural Gas can achieve specific CO_2 emissions of only 2,3 Mol CO_2/MJ(el) without any CO_2 recovery process. Because of the lower partial pressure of CO_2 in the flue gas compared to the resulting partial pressure of coal gasification a chemical absorption process with MEA Solutions leads to the lowest specific energy demand for CO_2 recovery

in natural gas fired power plants. This process was investigated by Suda et. al., [5]. Suda achieved in a pilot plant a steam demand of about 170 kJ/Mol CO_2 and an electric energy demand of 2,6 kJ/Mol CO_2. Unfortunately, the power plant efficiency without CO_2 recovery was not published by Suda et. al. The fossil energy demand for the CO_2 recovery should be in the range of 180 kJ/Mol CO_2 assuming high efficiencies for steam and electricity generation. For the utilization in a distant located fuel synthesis, the CO_2 has to be dried, compressed and liquefied for transportation. Taking the estimated energy demand of Hendriks [1] for compression, additional 10 kJ(el)/Mol CO_2 are required, leading to a total fossil energy demand E_{NG} of

$$E_{NG} = 200kJ/MolCO_2\,. \tag{2}$$

The drying and liquefaction are again neglected in the estimated energy demand. The CO_2 recovery process reduces the specific CO_2 emissions to the very low value of 0,3 Mol CO_2/MJ(el).

In existing facilities of the lime and cement industry the carbon dioxide content in the flue gas is about 60 % at atmospheric pressure. A promising alternative for CO_2 recovery is flue gas compression before a physical absorption process to avoid thermal regeneration of the scrubbing liquid. The compression of the flue gas from atmospheric pressure up to 10 bar at a temperature of 330 K and of the recovered CO_2 up to 60 bar from atmospheric pressure lead to a resulting electric energy demand of about 25 kJ/Mol CO_2. With an energetic efficiency in the range between 40 and 50 % for the generation of electricity the fossil energy demand for CO_2 recovery in the lime and cement industry is in the same range (50-60 kJ/Mol CO_2) as for the CO_2 recovery process in coal fired power plants.

The utilization of CO_2 from concentrated emissions for fuel synthesis at remote renewable energy sources leads independent of the kind of source to a long distant transport of the recovered CO_2. For this purpose CO_2 has to be liquefied and transported. The CO_2 must be dried before liquefaction, for example by absorption with triethylene-glycol, and cooling water at temperatures below 293 K is required for the liquefaction. At least special transport facilities are necessary.

3.2 Enrichment of CO_2 from Atmosphere

A process for the recovery of CO_2 from the atmosphere can be located anywhere. Two process designs, based on absorption of CO_2 in caustic solutions, have been estimated, [7]. Taking solar energy as energy input, a process with precipitation of limestone from the scrubbing solution is more attractive than a regeneration of the scrubbing solution by electrodialysis, which is an interesting alternative if wind or hydro power are the energy sources. The basic design of the solar energy CO_2 recovery process is shown in figure 2. An electric energy demand of 70 kJ/Mol CO_2 and a heat demand of 250 kJ/Mol CO_2 was estimated, [7]. Investigations show that an electric energy demand of about 40 kJ/Mol CO_2 is achievable for the absorption process. Optimization of the precipitation can minimize the thermal energy demand for limestone decomposition to about 200 kJ/Mol CO_2, similar to the energy demand in the limestone industry for the thermal decomposition process. Solar efficiencies of 0,2 for the generation of electricity and 0,7 for heat generation lead to a solar energy demand E_{Solar} of

$$E_{Solar} = 500kJ/Mol \quad CO_2\,. \tag{3}$$

The recovered CO_2 can be processed directly without transportation or storage. Drying is not necessary. Additionally, because the CO_2 is produced at temperatures of about 1200 K, solar high temperature processes like a conversion to carbon monoxide with hydrogen can be attached to the recovery process. A disadvantage is the need for absorption columns with huge diameters to process the air with a low CO_2 content of 0,035 %. As the required packing height is only three to five meters and low cost concrete can be used for the column, the investment costs should be moderate. Nevertheless, additional investigations for secure uniform fluid flows in the absorption column at energy optimized conditions with low pressure drop are necessary.

3.3 Comparison of Renewable and Fossil Energy Demand

A direct comparison of the fossil energy demands (1), (2) with the renewable energy demand (3) shows a much greater energy demand for the CO_2 recovery from the atmosphere compared to concentrated emissions. But the fossil energy demand for CO_2 recovery is consumed at locations with a high energy demand and could be directly used in different

alternative manners. The renewable energy source, if used for CO_2 enrichment and fuel synthesis instead of electricity generation will be located remote.

The only alternative utilization of the renewable energy used for the CO_2 enrichment from the atmosphere is supplying the fuel synthesis. A solar efficiency for the generation of methanol (MeOH) using atmospheric CO_2 of 0,136 has been estimated [7]. Neglecting the energy demand for the CO_2 enrichment and all losses during transport of CO_2 and methanol a very high solar efficiency of 0,16 for the generation of methanol can be assumed. With the renewable energy demand (3) of 500 kJ/Mol CO_2 for the enrichment of 1 Mol CO_2 from the atmosphere an alternative synthesis of only 80 kJ MeOH is possible. Assuming application in fuel cell equipped cars, these 80 kJ MeOH can substitute the double amount of gasoline. Instead of the enrichment of 1 Mol CO_2 from the atmosphere with 500 kJ solar energy the substitution of 160 kJ gasoline with the aid of these 500 kJ renewable energy is therefore possible under optimistic assumptions.

The comparison of the possible fossil energy substitution

$$E_{subs} = 160kJ/Mol \quad CO_2 \tag{4}$$

resulting from the solar energy demand (3) with the fossil energy demand (1), (2) leads to a more realistic energetic estimation for a decision between the different CO_2 sources for climate neutral fuel synthesis.

4 Comparison of the CO_2 Sources

The most efficient recovery processes of CO_2 from concentrated emissions achieve an optimistic energy demand of about 50 kJ/Mol CO_2 (1) obtaining gaseous CO_2 at 60 bar pressure. The costs per ton CO_2 recovered are estimated by [1] to 25 DM/t. But here the costs for drying, liquefaction, storage and transportation are not included. For the intercontinental transport tank ships will be employed. Because at ambient temperatures huge high pressure tanks at 60 bar would be required, low temperature transport at temperatures of 200 K at ambient pressure will be preferred because of lower costs. This causes investment for well isolated tank ships with cooling of the CO_2 during transport. An alternative is to cool the CO_2 by evaporation with resulting CO_2 losses.

The CO_2 recovery from the atmosphere will achieve an equivalent fossil energy demand of less than 160 kJ/Mol CO_2 (4). The only investment are for the absorption column and for the solar heated drying and thermal decomposition of limestone. No infrastructure for transport and storage of CO_2 is necessary. A combination of the CO_2 recovery from air with other solar high temperature processes is possible increasing the efficiency for the fuel generation process. This will reduce the energy demand for the methanol synthesis with atmospheric carbon dioxide as basic product. If this process is optimized, an energetic and economic comparison of the whole methanol synthesis process with renewable energy and different CO_2 sources will show the most promising CO_2 source.

Although further investigations and development are still necessary, the CO_2 recovery from air seems to be the better alternative compared to the CO_2 recovery from concentrated emissions even from today's state of investigation. The higher energy demand is supplied by remote located climate neutral energy. But the savings in investment costs compared to the utilization of concentrated CO_2 sources needing a complex infrastructure can be taken for the extension of the renewable energy plant. The more extensive use of renewable energy can supply the energy demand for the CO_2 enrichment from air.

References

[1] C.A. Hendriks, K. Blok, and W.C. Turkenburg. *Energy*, 16:1277, 1991.

[2] IEA. Carbon dioxide capture from power stations. Technical report, International Energy Agency, 1994.

[3] Enquetekomission des dt. Bundestags Schutz der Erdatmosphaere. *Mehr Zukunft fuer die Erde*. Economica Verlag, Bonn, 1995.

[4] M. Steinberg and A.S. Albanese. BNL 50877: Environmental control technology for atmospheric carbon dioxide. Technical report, Brookhaven National Laboratory, Upton NY, 1978.

[5] T. Suda, M. Fujii, and K. Yoshida. *Energy Conv. Mgmt.*, 33:317, 1992.

[6] Various. In *Proceedings of the 2nd International Conference on CO_2 Removal*, Kyoto, 1994.

[7] T. Weimer, K. Schaber, and et al. *Energy Conv. Mgmt.*, 37(6-8):1351–1356, 1996.

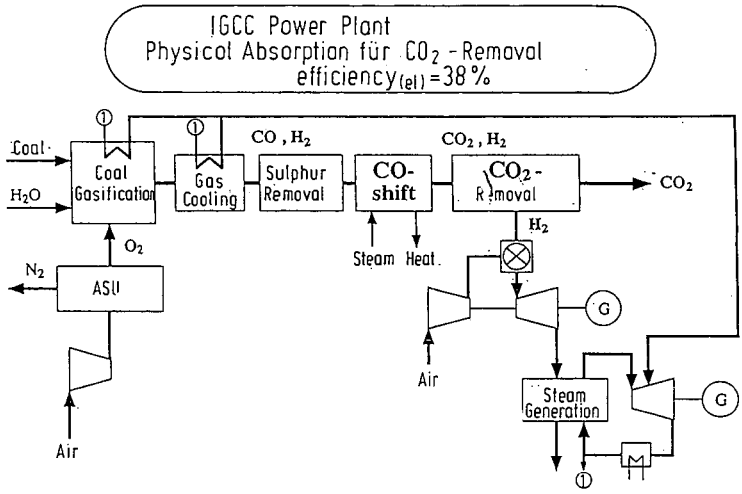

Figure 1: Coal fired Integrated Gasification Combined Cycle (IGCC) process for generation of electricity with CO_2 recovery and compression to 60 bar

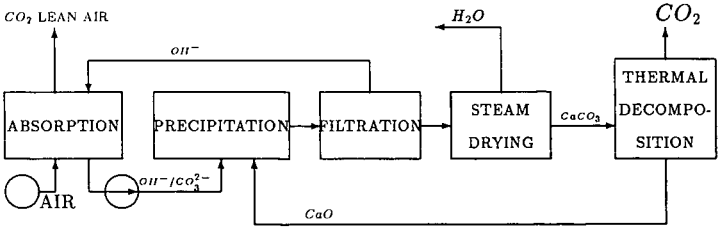

Figure 2: CO_2-Recovery from Air with Precipitation of Limestone

CARBON DIOXIDE UTILISATION IN THE CHEMICAL INDUSTRY.

Michele Aresta, Eugenio Quaranta, Immacolata Tommasi.
Department od Chemistry,
University of Bari,
Bari, 70126 Italy.

Keywords: Carbon dioxide, mitigation, disposal, utilisation.

1. Introduction

Carbon dioxide as a raw material for the Chemical Industry is receiving growing attention because : i) if recovery of CO_2 from flue gases will be implemented, huge amounts of CO_2 will be available; ii) environmental issues urge to develop new processes/products, avoiding toxic materials. Several uses of CO_2 appear to be responding to both (i) and (ii), i.e. use as a solvent (supplanting organic solvents) use as a building blok for carboxylates/carbonates (supplanting phosgene); use as carbon-source in the synthesis of fuels (supplanting CO or coal/hydrocarbons). These options will be evaluated and their potentiality discussed.

2. Energy for human activities.

The amount of carbon based fuels used today all over the world is such to produce every year 19.6 Gt of CO_2, that are equivalent to 5 Gt of C.[1] To this amount must be added the carbon dioxide formed in autocombustion of woods or produced as the effect of deforestation (*ca.* 2 Gt as C) that leads to a total amount of *ca.* 7 Gt of C per year. The forecast is for a rapid increase of anthropogenic carbon dioxide that might reach, alone, the level of 7 Gt as C per year in ten years. To stabilize the CO_2 immission into the atmosphere would mean to "avoid" an amount of carbon dioxide sizeable at *ca.* 2 Gt of carbon per year. This task is not easy to be reached considering the expansion of the use of energy, and demands an integrated approach and a combination of technologies.

3. The carbon dioxide mitigation technologies.

The technologies that may contribute to reduce the carbon dioxide immission into the atmosphere can be categorized as follows.[2]

* *Efficiency technologies: energy production.*
* *Efficiency technologies: energy use.*
* *Fuel shift.*
* *Fixation in biomasses (plants and algae).*
* *Carbon dioxide recovery from concentrated sources.*

The latter approach concerns the recovery from sources that contain carbon dioxide in much higher concentration than the atmosphere.

Carbon dioxide can be recovered from flue gases, using: liquid phases (monoethanolamine, MEA, by far the most used, or organic carbonates or ethers); solid phases (zeolites, oxides); or membranes.

The last approach is the most interesting and promising for coming years, while MEA is the most largely used today.

Research is needed to improve the membrane technology, mainly for ameliorating the separation of carbon dioxide from dinitrogen.

In general, the recovery technology and its cost are quite well established. Pilot and demonstration plants are available. The technology is ready for a large scale application so that in principle, if we consider only the "concentrated and continuous" sources of carbon dioxide (power plants, industrial sources), 60% of the produced carbon dioxide could be recovered.

The question is, thus: what to do with the recovered carbon dioxide?

Two options are open forwards: i) disposal; ii) utilisation and recycle.

4. Disposal of carbon dioxide: a ready technology?

Disposal of carbon dioxide in natural fields is considered with an increasing interest for the amount that could be potentially eliminated. The following options have been considered:

i) elimination in aquifers;
ii) confination in depleted gas or oil wells;
iii) ocean disposal.

Each of these options requires a careful analysis of consequences and demands research in order to exclude possibilities of disasters to ecosystems. Limitations are: high cost, availability of sites, and capacity of available sites. Moreover, they cannot be considered of general application.

5. Utilisation of carbon dioxide.

Another approach to design the fate of recovered carbon dioxide is its utilisation.[3,4] The use of carbon dioxide can be either technological (that does not imply its conversion) or chemical (that means to use CO_2 as a source of carbon in the synthesis of chemicals).

5.1 Technological use.

Presently, the technological use of carbon dioxide has a market of ca. 10 Mt y^{-1}.[5] Carbon dioxide is used as: solvent, additive for beverages, water treatment, fumigant, moulding and soldering agent, propellent in place of CFC, in fire estinguishers.

The utilisation of carbon dioxide as reagent in the chemical industry can take place through the

a) fixation of the entire molecule;
b) reduction to other C1 or Cn molecules.

Today, most of the CO_2 used by the chemical industry is extracted from natural wells. As the extraction price is close to that for recovery from fermentation and other industrial processes, or from power plants, it may be that in the near future carbon dioxide recovered from electric energy production could find a large application in the chemical industry.

5.2 Utilisation of carbon dioxide in synthetic chemistry.

The utilisation of CO_2 as source of carbon for the synthesis of products classified as fine- or bulk-chemicals is considered with increasing interest.[4,5] New synthetic processes using carbon dioxide have been discovered. Some of them may be developed at the industrial level if suitable economic conditions were created.
The introduction of the "carbon tax" could be the "driving force". In fact, the "environmental cost" of some currently operated processes could become a convincing issue for the innovation of industrial processes.
The development of a chemical industry based on CO_2 would have the following positive consequences:

- *avoiding the use of toxic materials in some industrial processes.*
- *Taking a step forward energy and raw materials saving through the adoption of more direct synthetic procedures.*
- *Using less drastic operative conditions.*
- *Substituting CO_2 to fossils (coal, oil, gas) as source of carbon for some industrial applications.*
- *Saving energy by recycling carbon.*
- *Boosting research for the utilisation of solar energy.*
- *Using a safe solvent.*

As the utilisation approach could contribute to solve the problem of the control of atmospheric CO_2 level, it is necessary to synthesize products with a market of several million tons per year (Mt y^{-1}) and requiring a low energy input. Products with a very long life appear quite attractive. In case of short-lived products, a very fast reaction kinetics would be required.

Species which have a market of a few thousand tons (kt) per year, cannot be considered for their contribution to the control of the emission of CO_2. Nevertheless, if they have a high added value and if the synthesis from carbon dioxide implies a simpler procedure compared to the actual synthetic methodology, the innovation could have a remarkable economic interest.
The life of a product is a very important factor. In fact, when we use a carbon based product, this is transformed again into CO_2. For example, fixing carbon dioxide in chemical substances which have a very short life wouldn't, at a glance, give a significant contribution to the problem of the control of CO_2 emission, even if large quantities were fixed. If the kinetics of formation were fast, and the methodology simple and highly effective, the application would be of industrial interest, as it would help to save resources, recycling carbon. This is the case of urea and its derivatives.
Therefore, the correct evaluation of the contribution that a synthetic procedure based on CO_2 can give to the mitigation of CO_2 or to the development of a "green industry", requires a complex analysis based on the criteria listed below.[5,6]
- *Added value of the product.*
- *Market demand of the product.*
- *Demand of energy for the synthesis of the product.*
- *Transformation rate of CO_2 (yield and selectivity towards the product).*
- *Life of the product.*

Actually, we can separate two different approaches to carbon dioxide utilisation:
* *the first related to the opportunity of utilising CO_2 for developing a "green chemistry",*
* *the second relevant to the mitigation of the greenhouse effect.*

These two points of view may appear sometimes diverging.

5.3 Synthesis of fuels, intermediates, and fine chemicals.

CO_2 can be fixed in a chemical substance:
(i) as it is;
(ii) in a reduced form.

The species belonging to *case (i)* are:
carboxylates (RCOOR), carbonates (ROCOOR) and polycarbonates, carbamates (RR'NCOOR'') and polyuretanes, ureas and their derivatives.
Other *C1 molecules (CO, CH_2O, CH_3OH, CH_4)*, or the homologous species Cn and their derivatives belong to *case (ii).*
These two processes can require a different energy input.
A process that could be operated in the near future is the substitution of CO_2 to phosgene, $COCl_2$, a toxic species (LC_{50} 3 mg L^{-1}) currently synthesized from carbon monoxide (obtained from coal) and chlorine. Phosgene has a world market of about 6-8 Mt per year and is used in the synthesis of carbonates, polycarbonates, carbamates, polyuretanes, N-phenylureas, symmetric and asymmetric ureas, etc.
As the phosgene production will not expand (no more plants can be builded), the utilisation of carbon dioxide may become a reality.

The synthesis of methanol from CO_2 also deserves attention. This product can be used as fuel or as a raw material for the synthesis of chemicals. The market might be of hundreds million tons per year.
The conversion of CO_2 into methanol requires dihydrogen. Indeed, this approach can result of great interest if a cheaper and easier conversion of water into hydrogen were found.

6. Economics of adoption of a new synthetic procedure.

It is obvious that the direct use of CO_2 for the synthesis of chemicals is doubly beneficial as it cuts the use of carbonaceous fossils and allows the recycling of CO_2. Processes based on CO_2 have already been developped, but not yet implemented as they are more expensive than conventional ones.

It is worth to note that often current costs of production do not include the **"environmental costs"**: if we should consider them, the use of CO_2 as raw material for the synthesis of chemicals would become economically favourable, in a number of cases.
Considered the time necessary for R&D, it is possible that by the year 2010, more processes converting CO_2 into useful chemicals might be operated, supporting the development of a "green chemical industry".
For sure, such "know-how" will be a tool for market penetration, considering the current attitude to the assessment of the eco-compatibility of products and processes through a quantitative life cycle assessment.

7. Conclusions.

We have seen that the control of the accumulation of CO_2 in the atmosphere can be performed through different technologies based on: efficiency in energy production and use, energy saving, utilisation of alternative energies, recovery of CO_2. The latter technology, and the consequent CO_2 disposal in natural fields or utilisation, require a correct cost-benefit analysis, for assessing the application potentiality in the short-medium-long term.
Carbon based fossil fuels, liquid or gaseous, have the correct energy concentration and most probably will continue to be the main energy source in the short-medium term.
As liquid and gaseous hydrocarbons should be available for next 30 years and modern conversion methodologies and technologies allow an effective conversion of large amounts of coal into liquid fuels, a considerable part of the energy demand could be still covered by carbon based fuels in the next 50 years or so.
However, coal is estimated to be available for next two or three centuries at the proper rate of utilisation. Therefore, the CO_2-mitigation options discussed in this lecture deserve a thorough consideration.
Science and Technology open new horizons and offer solutions for political and economic evaluation.

REFERENCES.

1) M. Aresta, in "*Carbon Dioxide as a Source of Carbon*", M. Aresta and G. Forti eds., Reidel Publ., pp. *1-22*, 1987.

2) IEA-OECD Expert Seminar on "*Energy technologies for reducing emission of greenhouse gases*", Paris, 12-14 April, 1989.

3) M. Aresta, IEA-OECD Expert Seminar on "*Energy technologies for reducing the emission of greenhouse gases*", Paris, 12-14 April 1989, IEA-OECD Publications Vol **1**, p. *599-617*, 1989.

4) M. Aresta and J.V. Schloss eds., "*Enzymatic and Model Reduction and Carboxylation Reactions for Carbon Dioxide Utilization*", Kluwer publ., 1990.

5) M. Aresta, E. Quaranta and I. Tommasi, in "*Energy Conversion Management*" Vol. **33**, pp *495-504*, 1992.

6) M. Aresta, in "*Energy Conversion Management*", Vol. **34**, pp *745-792*, 1993.

BIOMASS REACTIVITY IN GASIFICATION BY THE HYNOL PROCESS

Yuanji Dong
Acurex Environmental Corporation
4915 Prospectus Drive
Durham, NC 27709

Robert H. Borgwardt
U.S. Environmental Protection Agency
National Risk Management Research Laboratory
Air Pollution Prevention and Control Division
Research Triangle Park, NC 27711

Keywords: biomass gasification; gasification kinetics; biomass-to-methanol.

INTRODUCTION

Methanol has many advantages to be considered as an alternative fuel. About 75% of methanol production uses natural gas as feedstock. Use of biomass as feedstock to produce methanol is of current interest because it offers substantial benefits for reduction of greenhouse gas emissions. The research and development of biomass-to-methanol processes, one of which is called Hynol, are now in progress.

The Hynol process was proposed to utilize biomass as a feedstock and natural gas as a cofeedstock to increase methanol yield and reduce costs (Steinberg and Dong, 1994). The process consists of three reaction steps: (1) gasification of biomass with the H_2-rich gas recycled from methanol synthesis, (2) steam reforming of the produced gas with an addition of natural gas feedstock, and (3) methanol synthesis from the H_2 and CO produced by the reformer. A schematic flow diagram of the process is shown in Figure 1. Since the reaction of biomass with the H_2 in the recycle gas to form CH_4 is exothermic, the heat so generated is able to offset the energy required for other endothermic reactions in a Hynol gasifier. As a result, no expensive O_2 plant or external heat source is needed for gasification. The use of natural gas as cofeedstock eases the requirement for a consistent composition of biomass feedstock. The integrated cyclical process configuration helps ensure the completion of overall conversion and increases thermal efficiency. CO shifting is not necessary and the requirement for acid gas removal is reduced, which lowers capital and operating costs.

A theoretical evaluation of the Hynol process conducted by the Air Pollution Prevention and Control Division (APPCD) of the National Risk Management Research Laboratory, U.S.Environmental Protection Agency (EPA), showed that the Hynol process represents a promising technology for maximizing fuel production inexpensively and with minimum greenhouse gas emissions (Borgwardt, 1995). Consequently, the APPCD established a laboratory to further assess the process feasibility. In the first phase of the study, a thermobalance reactor (TBR) was installed and used to evaluate biomass reactivity in gasification at the operating pressure, temperature, and feed gas composition specific for the Hynol process. The experimental work also attempted to improve understanding of the variables affecting Hynol gasification and identify needs for process development. This article summarizes the TBR results.

EXPERIMENTAL

A flow diagram of the TBR system is detailed in Figure 2. The reactor is electrically heated and consists of a 35-mm I.D. stainless steel reactor pipe, a 305-mm O.D. pressure vessel, and a topwork which accommodates a weight transducer for measurement of sample weight during reaction. A pulley assembly is used to raise and lower a sample basket between the topwork and the reaction zone.

To initiate an experimental run, a basket with known weight of biomass sample was placed into the topwork through the removable window. A constant helium flow was introduced to the topwork to protect the wood sample from contact with process gas prior to entry in the reaction zone. Mass flow controllers were used to control the flow rates of H_2, CH_4, CO, and CO_2 from individual gas cylinders to obtain the desired feed gas composition. Steam was added to the feed gas from a steam generator fed with distilled water by a metering pump. The gas mixture was further heated by a superheater and then entered the reactor. The reactor exit gas was cooled in a condenser to remove moisture, and then depressurized through a back-pressure regulator before it was vented to atmosphere. When pressure and temperature in the reactor system were stabilized at the desired levels, the sample basket was lowered into the reaction zone and the change in sample

weight was automatically recorded by the transducer as a function of reaction time. A computer was used to control the TBR system and log experimental data. After gasification, the basket was raised back into the topwork and the reactor was depressurized and cooled. The discharged char was then weighed to determine the final sample weight. Because changes in gas composition across the sample are negligible, the reaction can be considered to take place at constant operating conditions.

In this study, the Hynol feed gas refers to a composition -- H_2 = 65.83%; CH_4 = 11.63%; CO = 8.95%; CO_2 = 2.32% and steam = 11.27% -- which is based on the results of a Hynol process simulation. Poplar wood, which is considered a primary candidate for large scale production as an energy crop for fossil fuel displacement (Wright, 1995), was used as a representative biomass sample. It was grown in North Carolina and cut to desired sizes and dried before its use. Composition is presented in Table 1.

KINETIC MODEL AND DATA TREATMENT

The weight transducer output was recorded as a function of reaction time during a test. The records were converted into the data of variation in sample weight with time. The biomass conversion, X, on an ash-free basis was then calculated by :

$$X = \frac{W_0 - W}{W_0 - W_0 C_A} \tag{1}$$

where W_0 is the initial sample weight, W is the sample weight at any reaction time, C_A is the weight fraction of ash obtained from the ultimate analysis of the original sample, and X is thus also a function of reaction time.

General observation of the reaction behavior revealed that biomass gasification under Hynol conditions involves two types of reactions: a rapid reaction, which may complete in a few seconds, involving devolatilization and pyrolysis reaction of the volatile matter in biomass with H_2 and steam; and a very slow reaction of residual carbon with the process gas which requires hours to finish. To quantitatively describe the rate of gasification, these two reactions are assumed to be first order with respect to the remaining solid reactants. The rate of the rapid reaction can be expressed as:

$$\frac{dX_1}{dt} = k_1 (X_C - X_1) \tag{2}$$

and the rate expression for the slow reaction is:

$$\frac{dX_2}{dt} = k_2 (1 - X_C - X_2) \tag{3}$$

where X_1 and X_2 are the conversions by the rapid and slow reactions at time t, X_C is the maximum attainable conversion by the rapid reaction, and k_1 and k_2 are the reaction rate constants for the rapid reaction and the slow reaction, respectively.

By integrating Equations (2) and (3), the total biomass conversion can be expressed by:

$$X = X_1 + X_2 = 1 - X_C \exp(-k_1 t) - (1 - X_C) \exp(-k_2 t) \tag{4}$$

The model involves three parameters: X_C, k_1, and k_2, which are functions of operating conditions such as biomass properties, reaction temperature, pressure, and feed gas composition. They can be determined by fitting Equation (4) to the experimental conversion data obtained from TBR tests.

RESULTS AND DISCUSSIONS

The above model was used to correlate the experimental data obtained from TBR tests. Figure 3 is a typical example of curve fitting results by the model, showing good agreement between the experimental data and the model regression over the entire reaction period.

Four different sizes of poplar particles were used to investigate the effects on gasification: 7/16-in diameter cylinders, 1/4-in diameter cylinders, 1/8-in cubes, and 20 to 30 mesh sawdust. The

rate of the rapid reaction increased significantly as a result of higher heat transfer and intraparticle diffusion rates when particle size was reduced from 7/16- to 1/8-in. Agglomeration during gasification was observed for the particles larger than 1/8-in, which inhibited gas diffusion within the particles. Sawdust heated up more quickly, and no agglomeration was observed. Experimental results showed that, at 30 atm and 800°C, about 87% of the 1/8-in poplar particles and 90% of the sawdust can be gasified by the Hynol feed gas in 60 min.

The analysis of the charred samples obtained from 7/16-in poplar particles showed that some of the volatile matter remains after gasification. However, for 1/8-in poplar particles or sawdust, nearly all of the H and O were converted into product gas in 20 min.

The agglomerates of residual chars formed in the TBR were fragile. If a fluidized bed gasifier is used, agglomeration is not likely to occur as a result of attrition; therefore, higher reaction rate and conversion than observed in TBR testing are expected in such systems.

The rapid-reaction stage of poplar gasification was found to be essentially completed in less than 0.2 to 0.3 min, contributing most of the biomass conversion. A small additional conversion is contributed by the slow reaction. To achieve high biomass conversion, sufficient gasification time must be provided. Tests showed that biomass conversion increased from 85 to 90% when gasification time extended from 20 to 150 min. The comparison between the compositions of chars after 20 and 150 min gasification indicated that there was virtually no further conversion of H and O in the char after 20 min and that the additional conversion resulted from the reaction of carbon with the process gas.

Experimental results of 60-min gasification with sawdust and 1/8-in poplar particles at different reaction temperatures showed great increase in biomass conversion and gasification rates when temperature increased from 750 to 950°C as shown in Figure 4. The rate constants for the rapid and slow reactions, k_1 and k_2, at different reaction temperatures were determined by fitting the experimental data for gasification of 1/8-in poplar particles. The rate constants thus obtained were plotted against the reciprocal of the absolute temperature, as shown in Figure 5, and expressed as functions of reaction temperature by the Arrhenius equation:

$$k_i = k_{i0} \exp(-\frac{E_i}{RT}) \qquad (5)$$

where subscript i is 1 for the rapid reaction and 2 for the slow reaction. E_i is the activation energy. The results obtained were: $k_{10} = 108.85\ min^{-1}$, $E_1 = 3.78$ kcal/mol, $k_{20} = 22925\ min^{-1}$, and $E_2 = 34.1$ kcal/mol. The maximum attainable conversion by the rapid reaction, X_C, was also correlated as a function of temperature for gasification of 1/8-in poplar particles by:

$$X_C = 0.9611 - 0.000149T \qquad (6)$$

where T is the reaction temperature in °C. With Equations (4), (5), and (6) and the values of k_{10}, E_1, k_{20}, and E_2, the conversions of 1/8-in poplar particles at different temperatures and gasification times were predicted. Figure 6 compares the prediction with the conversion data obtained from the separate experimental tests at different temperatures and gasification times. The comparison covers a temperature range of 750 to 950°C and a gasification time range from 0.2 to 150 min for 1/8-in poplar particles gasified by the Hynol feed gas at 30 atm. The activation energy obtained for the rapid reaction was low, implying that heat transfer dominates the rates of devolatilization and pyrolysis of biomass in the TBR.

The effect of feed gas composition on poplar gasification was investigated by varying the flow rates of individual gas components under constant system pressure. Helium was used as an inert "make-up" gas for this purpose. At 30 atm and 800°C, the final conversion of poplar wood gasified by pure helium after 60 min was about 6% lower than that obtained under pure H_2. If the conversion obtained after 60 min of gasification is plotted against H_2 partial pressure (P_{H2}), a linear relationship, conversion = $0.0017 \times P_{H2}$, was found. When steam partial pressure in the feed gas was varied from 7 atm to zero while the partial pressures of other gas components remained constant, the conversion was proportional to steam partial pressure or $0.003 \times P_{H2O}$. Negligible effects on the gasification conversion and reaction rate of 1/8-in poplar particles were observed as the CH_4 in the feed gas was reduced from the simulated Hynol composition, 11.63%, to zero. Replacing CO and CO_2 in the feed gas with helium did not affect the gasification rate. The conversion and reaction rates of 1/8-in poplar particles gasified by the Hynol feed gas were nearly the same as those observed by the feed gas containing no CO and CO_2.

REFERENCES

Borgwardt, R. (1995): The Hynol Process, Presented at Symposium on Greenhouse Gas Emissions and Mitigation Research, Washington, DC. June 27-29.

Steinberg, M. and Dong, Y. (1994): Process and Apparatus for the Production of Methanol from Condensed Carbonaceous Material, U.S. Patent 5,344,848.

Wright, L. (1995): Demonstration and Commercial Production of Biomass for Energy, Proceedings, Second Biomass Conference of the Americas, NREL/CP-200-8098, National Renewable Energy Laboratory, Golden, CO, pp. 1-10.

TABLE 1. COMPOSITION OF POPLAR WOOD USED

Carbon (wt.%)	51.52	Volatile (wt.%)	91.38
Hydrogen (wt.%)	6.20	Fixed carbon (wt.%)	8.15
Oxygen (wt.%)	41.37		
Ash (wt.%)	0.47	Higher heating value	
Sulfur (wt%)	0.02	(Btu/lb dry wood)	8768.
Nitrogen (wt.%)	0.42		

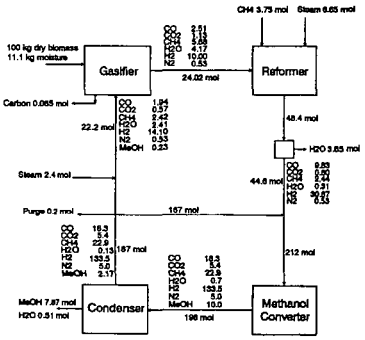

Figure 1. Schematic flow diagram of the Hynol process.

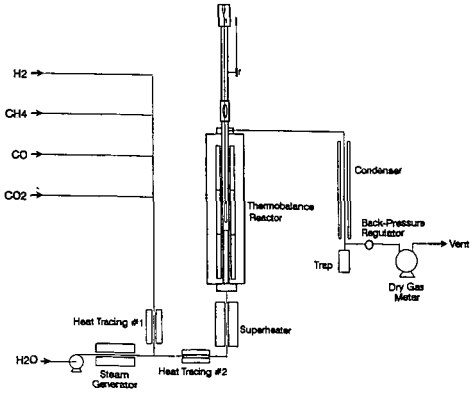

Figure 2. Flow diagram of the TBR system.

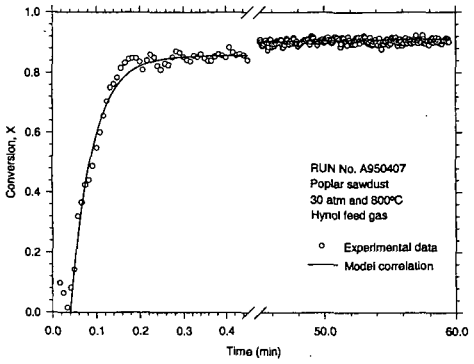

Figure 3. Example of TBR experimental data fitting by the model.

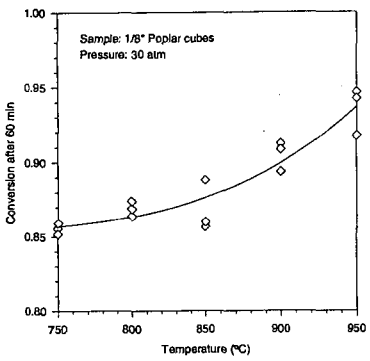

Figure 4. Effect of reaction temperature.

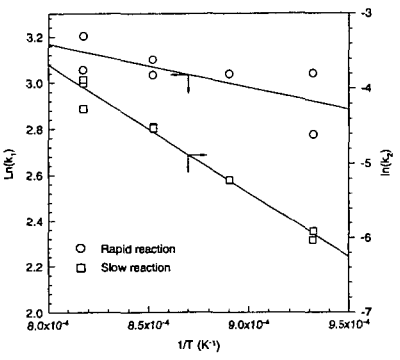

Figure 5. Arrhenius plots of the rate constants.

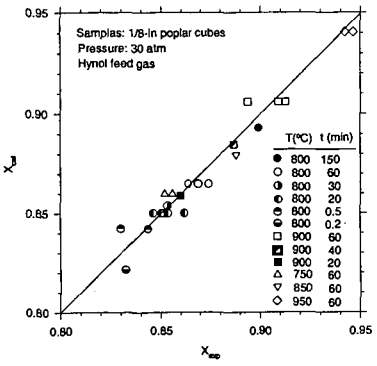

Figure 6. Comparison of the model prediction with experimental conversion data.

New Era will come with New Concept in Refinery

Masaya Kuno
1-7-13 Tsuruma, Machida-shi
Tokyo 194, Japan Member of JPI

Keywards:
Conventional crude distillation system to make crude lighter and white oil is theoretically wrong.

1) Introduction

Since the "day one", crude had been distilled at first stage, nobody except author has found out the defects of system.
Author had appealed HSP, that is, HydroStripping Process world wide since 1981. This concept was presented in Hydrocarbon Processing September1981(1) , that is, treating crude with hydrogen rich gas for the subsequent vapor phase HDS. Recently, many data have been obtained and found out the following points.

(1) Distillate are not final products, which means it is against 2nd law of energy, that is, increasing entropy of the system.

There exists a possibility in saving energy of the system.

(2) Distillate contain S-Compounds which are able to play the important role in cracking of heavier portion in crude under hydrogen rich gas.

Therefore, distillation operation in first stage is wrong, esp., so when refiner aims to produce white oil and lighter too much.

2) What is S-Compound effect ?

S-Compounds in each fraction such Naphtha, Gasoline, Kerocene and Gas Oil must be severely reduced to meet the stringent request of environmental problem. However, such lighter fractions including S-Compounds are dispersed into crude and mixed with heavier portion, which fits the best for heavier portion cracking under hydrogen and hydrogen sulfide at lower temperature without catalyst.

S-Compounds in situ is considered to be a good electron absorber, i.e., hydrogen atom catcher which means hydrogen carrier to cracking portion where S-Compounds promote under hydrogen, radical reaction of heavier portion on the surface of metal. These phenomena is explained from following data.

For example, hydrogen sulfide was used for cracking of polypropylene under hydrogen pressure 3.0 MP at 673 K w/o cat. H_2S was added to this experiment 1.0vol%, where 97% of distillate product composed of Naphtha 53%, Kerocene 23%, Gas Oil 19% with 2% gas portion were obtained after 1hr on auto-clave test while no addition case showed only 35% distillate and 40% heavier oil and solid state 20% with 5% gas portion. From Journal of JPI Young Society.

This catalytic activity of H_2S is explained as wall effect of auto-clave metal surface, composed of 18 Cr-8Ni and Fe oxide, which was discovered by Dr. Nakamura, PhD., Fujimoto's room, Tokyo University.

H_2S is so active that it is used as a detective reagent for in-organic Compounds in chemical analysis. This result may be plausible such as sulfiding operation in HDS where H_2S or CS_2 are used for activation of catalyst surface at start-up.

The importance of this experiment is not only showing the possibility of heavier, asphaltenic and resinic portion reduction
but also proposing new phase for theoretical approach of hydrocracking including actual industrial application.

H_2S may turn to HS^- + H^+ or so in situ, above 403 K on the transit metals., where proton move so fast following thermal and free electron from wall, or HC that it does not always needs surface area too wide for activation.

Under rising temperature, there begin to exist the unbalanced distribution of electron on HC. H^+ is apt to go to radical portion of HC and HS^- goes to aromatic portion, where they are cut to be stabilized, that is, each portion become to be the most stable state., which can be judged from the work of Bergius and Pier before World War II. Fig.1, Fig.2

Heavier portion is apt to stick the metal surface due to higher viscosity and unbalanced distribution of electron or so and ready to crack after absorbing thermal electron and hydrogen
under acidic environment by H_2S or so at lower temperature.

The above can be used for explaining about lighter S-Compound effect because they are apt to proceed the metal surface and turn to hydrogen donar or that carbenium ion such HS-Compounds after heated up under hydrogen, transferred from in and out cluster on the metal surface,which become radical, hydrite rich through protonation (2), while heavier HC is stickey enough to be catched on the metal surface and be enforced to react with them.

H_2S helps accelerate this transformation such as sulfiding on catalyst where Metal-Sulfur bridge is made on the surface .
H^+ approaches to S-molecule to make H-S compounds or so while HS^- goes to aromatic compounds on the transit sulfided metal.

Sulfur own effect on coal liquidification reaction is well known, especially, as bronsted acid, under hydrogen at above 703 K.
Some process need no catalyst on coal liquefaction except sulfur.

3) Operation condition when treated with hydrogen rich gas.

3)-1 Pressure

Too much hydrogen donor is said to stop the radical reaction which also can be explained on the above figures (3).

Hydrogen donor can not transfer electron too much, they cap the cut point and become stabilized by themselves, that is,
only become aromatic compounds, which means no need of high pressure hydrogen for hydrocracking of crude. Hydrogen partial pressure is estimated from crude specification, PONA, C/H ratio and metals contents. 2 or3 MP is enough to keep HS^-, galvanic hydro-sulfide state.

Hydrogen donor is reduced at some rate at Desalter because Fe-Cl compounds have such ability (4). So, Desalter must be installed to reduce Cl, sea water for anti-corrosion and for hydrogen donor.

Radical reaction is also interrupted by cation so that cation should be trapped by anion, esp., Sulfur Compounds .

3)-2 Temperature

The reaction temperature is very sensitive because it depends on products spec., to be produced and on its mechanism of reactions. Hydrogenation is exothermic and thermal cracking is endothermic. Where at lower temperature, the former reaction is forwarded while heavier portion is just to be cracked under hydrogen on sulfided metals to naphtha and S Compound by H^+, HS^- and then at higher temperature, the latter reaction is overlapped. Fig. 3

4) The meaning of mixture of heavier oil and lighter oil is as follows.

4)-1 S-Compounds around the heavier cluster become electron, hydrogen deposits when the condition of reaction reach the some level, they will start cracking reaction as catalytic, reactive points.

4)-2 The reactant are transferred through solvent around cluster. But electron rich radical is transferred to heavier unstable portion and continue cracking the remaining heavier portion at above said deposit points.

4)-3 Electronic equivalence of heavier portion seems zero at glance, is very changeable, unstable , depending on around condition so that even slight lighter portion can make better reaction condition to crack such as solvent effect which disperse heavier portion wider and make it differential parts to separate electronically and help radical approach to right points.

4)-4 Too much condensed state such carbonaccous asphaltene, resin and metals complex should be avoided because they are promoting their familiar components production when making white oil, even burning oil to meet such as CAAA in U.S.A..

4)-5 Recently, soluble metal compounds have been informed to exert much more catalytic activity in coal liquefaction (5).

Therefore, without catalyst, more preferable reactive field may be obtained in lighter crude oil which contents metal compounds.

Because only catalyst is solid and interrupt mixing effect, transfer of heat and etc. while hydrogen partial pressure, sulfur compounds, transit metal's surface and temperature are indispensable factors.

5) Conclusion

From thermodynamic, chemical reactionary and electrical equivalent points of view, existing atmospheric distillation is of problem, not economical when refiner need white oil and light oil too much.

Conventional refinery system is of try and error concerned technology, experimental technique. However, recent developed technology has begun to reveal the intrinsic quality of such intricate complex compounds.

Tubes of heat exchangers and pipe lines have enough surface to be activated by H_2S and S-Compounds with hydrogen, on alloy steel.

This new concept, treating crude with hydrogen rich gas leads to BottomlessRefinery, Jet Fuel and Naphtha Rich Refinery, therefore, Refiner should treat the crude under hydrogen at first stage if refiner want to obtain lighter and white oil too much at the lowest cost.

Under hydrogen treating and HDS combination, thiophene is not produced. Heavier residue Catalytic Cracking Process is not to be used any more, the same as sweating process of lighter HC.

Ironically, S-Compounds are indispensable for hydrocracking, not suitable for burning hydrocarbon, which leads us to contemplate that that mysterious, histrical birth of the Earth. We are now struggling against environmental problem evoked by noble petroleum, sulfur and oxygen, aiming at sustainable economic development.

Reference only,
HS^- may become H_2S at high press H_2 . There needs some state to be maintained for reaction field where HS^- may continue to decompose the heavier hydrocarbon like sharp knife edge with H^+ and electron.

Typical reaction are as follows.

H_2S --- H^+ + HS^- a ------Main Reaction >403K
HS^- + H_2 --- H_2S + H^- b ------HDS Reaction >473K

a + b

H_2 --- H^+ + H^- c

These basically reaction are proceeded through or on the S-M bridge.
Each equation depends mainly on temperature and hydrogen pressure.
Equation c is rarely occurred and has not detected so far.

Literature cited.

(1) Masaya Kuno, Hydrocarbon Processing (1981)
(2) B.W.Wojciechowski, Synposium on Hydrogen Transfer in Hydrocarbon Processing ,ACS (1994)
(3) Junich Kubo H. Higashi, Y Ohmoto and H Arao ditto.
(4) Johr H. Penn and Jinhai Wang ditto.
(5) T. Kondoh, A. Matsumura, K. Okegawa, I Saitoh, Sigen and Kankyo Vo.2, No.5 (1993)

Reference
Dr. Kabe, 1983, treated Taching Crude with hydrogen, CS_2 as activator, toluene as solvent and catalyst Ni-Co-Al O at 673 K.
under hydrogen pressure 100 K/G, reaction time 5 hr using autoclave.
No activator case showed nothing paticular.

The result was residue 40% down, while Naphtha increased 5 times that is, 30 wt% and middle increased a little, 20 to 25 wt%.
Journal of JPI, Vol 26 No3 1983.

Fig.1 shows the typical image

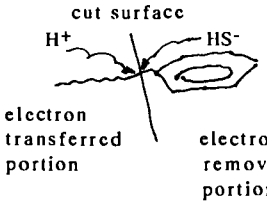

sulfided composition is stabilized

lighter S Compound is made.

lighter portion is produced heavier

where is cut is depends on the solvent spec, around the HC and on other condition such temp or so.

(Hexane soluble and the like) (Benzene soluble or so)

Heat of hydrogenation is enough to cut c-c bond at above 573K.
Produced heat of hydrogenation is transferred around lighter solvent and / or activate another portion to be radical.

Fig.2 shows the typical image on metal surface

on the surface of metal

Thermal electron comes from heated metal surface through Metal-Sulfur bridge

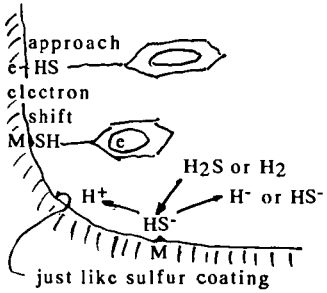

Electron proceed and move to aromatic Compounds which is under lower electron density.

When electron become rich in aromatic Compounds. H^+ can easily approach and cut the C=Cbonds after hydrogenation.

M-S bridge also protect to transfer thermal electron from C=C bonds hydrocracking to metal surface, which cause not to evoke carbon making.

Fig. 3 shows the operational condition

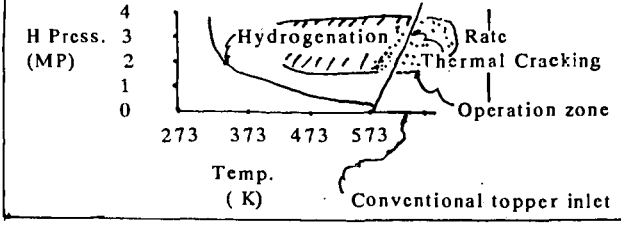

ACID RAIN, PROMOTING THE ACCUMULATION OF CO_2 IN SURFACE WATERS ?!

Shuping Bi
Chemistry Department, Nanjing University, Nanjing, 210093, P.R.China

Keywords: acid rain, elevated concentrations of aluminum, surface waters

ABSTRACT

Acid rain and increase of CO_2 concentration in atmosphere are the important problems to the global changes. In the past, people studied them separately. Someone found that lakes are sources of atmopheric CO_2,but the mechanism is not clear. In this paper, we present our investigation on this question by using chemical equilibrium model. Theoretical calculation indicates that: in the acidic range of pH<5, P_{CO_2} may change from 1×10^{-4} to 0.1 atm without altering pH value of waters due to the buffering actions of Al^{n+} and H^+; Oppositely, the pH is very sensitive to the P_{CO_2} in the neutral (pH> 5) surface waters. Therefore, we come to the conclusion that acidified surface waters may hold much more CO_2 than neutral waters. Acid rain, also promotes the accumulation of CO_2 in surface waters !

INTRODUCTION

There is increased concern over the supersaturation of carbon dioxide in the surface waters of lakes [1,2]. Processes that add and remove CO_2 occur simultaneously in the surface waters of lakes. Data on the partial pressure of carbon dioxide in the surface waters from a large number of lakes (1835) with a worldwide distribution show that only a small proportion of the 4665 samples analyzed (less than 10%) were within $\pm$ 20% of the equilibrium with the atmosphere and that most samples (87%) were supersaturated. Furthermore, lakes showed an enormous range of CO_2 concentrations from 175-fold below to 57-fold above atmospheric equilibrium at the extremes. This indicates that lakes are sources rather than sinks of atmospheric CO_2. The probable reason for this excess CO_2 may be due to the large accumulation of organic matter in the tundra and its respiration in soil or lake waters [3,4]. Thermokarst and fluvial processes cause great erosion of peat and release of dissolved organic carbon (DOC) into lakes and rivers [5-7], and this C may be respired to CO_2 [8,9]. There is also direct evidence that dissolved inorganic C in ground is moving from land to lakes and rivers, movement of CO_2-charged ground waters into the river can easily account for the high P_{CO_2} observed in the river. However, this explanation is not very satisfying, because it does not consider the effect of the pH of surface waters. As we know, acid rain is a very serious problem to the global changes. One of the consequences of the acidic precipitation is that H^+ and aluminum concentrations increased in the surface waters.[10,11] In this paper, we try to link the excess CO_2 with the acid rain by considering the effects of Al^{n+} and H^+ buffering actions in acidifed surface waters. A theoretical model based on the chemical equilibrium equations is developed for evaluating the interactions of P_{CO_2} and pH. Water quality data from the literatures for about 20 sampling stations are analyzed by our model. Interesting conclusion was obtained.

THEORY

We initially make the following assumptions:

(1) the surface water studied is in equilibrium with the natural gibbsite. It is a dilute solution with low ionic strength [12];

(2) in acidic pH range, Al^{n+} and H^+ dominate the buffering system. The chemical speciation of aluminum in acidic surface waters is complicated because Al^{3+} forms complexes with OH^-, SO^{2-}_4, F^- and organic compounds.[13]

(3) $[Al^{3+}]$ can be predicted as a function of pH using an aluminum trihydroxide solubility relation. $Al(OH)_3 + 3H^+ = Al^{3+} + 3H_2O$, $[Al^{3+}]=K_{sp}[H^+]^3$ [14];

(4) concentrations of Fe and Mn are very low, their reactions with ligands (F^-, SO_4^{2-}, OH^-, and organic solute) are insignificant [15];

(5) organic solutes in natural waters are presented as a triprotic acids, while two species of aluminum-organic solutes are depicted [16];

(6) no adsorption of anions was taken into account;

(7) for an open system, the following reactions controlling the CO_2 concentrations take place: (P_{CO_2} is the partial pressure of CO_2)

$$[H_2CO_3^*] = K_H P_{CO_2} \quad (1)$$
$$[HCO_3^-] = K_{C1} K_H P_{CO_2}/[H^+] \quad (2)$$
$$[CO_3^{2-}] = K_{C1} K_{C2} K_H P_{CO_2}/[H^+]^2 \quad (3)$$

By employing the electroneutrality relationship, we can write:

$$E_N = E_{N,Al-OH} + E_{N,Al-F} + E_{N,Al-SO_4} + E_{N,Al-Org} + E_{N,CO_3} + C_B - C_A + [NH_4^+] - [F^-] + [H^+] - [OH^-] \quad (4)$$

E_N is the discrepance in electroneutrality, in which contributions from various compoents $E_{N,i}$ are:

$$E_{N,Al-OH} = 3[Al^{3+}]+2[Al(OH)^{2+}]+[Al(OH)_2^+]-[Al(OH)_4^-] \quad (5)$$
$$E_{N,Al-F} = 2[AlF^{2+}]+[AlF_2^+]-[AlF_4^-]-2[AlF_5^{2-}] \quad (6)$$
$$E_{N,Al-SO_4} = [AlSO_4^+]-[Al(SO_4)_2^-] \quad (7)$$
$$E_{N,Al-Org} = [AlHOrg^+]-3[Org^{3-}]-2[HOrg^{2-}]-[H_2Org^-] \quad (8)$$
$$E_{N,CO_3} = -2[CO_3^{2-}]-[HCO_3^-] \quad (9)$$

C_B is the sum of basic cation equivalence ($2[Ca^{2+}]+2[Mg^{2+}]+[K^+]+[Na^+]$ in eq/L), C_A is the sum of acidic anion equivalence ($2[SO_4^{2-}]+[NO_3^-]+[Cl^-]$ in eq/L).

E_N is a function of $[H^+]$, $E_N = f(H^+)$. By using Newton-Raphson method, $[H^+]$ can be calculated:

$$[H_{i+1}^+]=[H_i^+]- \frac{E_N}{\left(\frac{\partial E_N}{\partial H}\right)} \quad (10)$$

$[H^+]$ is the hydrogen ion concentration at the i th iteration and $[H_{i+1}^+]$ is the hydrogen ion concentration at the i th + 1 iteration. Equations (1-10) express the relationship of P_{CO_2} with pH in surface waters and can be used to evaluate their interactions. With fixed P_{CO_2}, pH can be given; On the other hand, P_{CO_2} can also be calculated at a fixed pH by iteration. The mass balance is:

$$C_F^* = [F^-]+[HF]+[AlF^{2+}]+2[AlF_2^+]+3[AlF_3]+4[AlF_4^-]+5[AlF_5^{2-}] \quad (11)$$
$$C_{SO_4}^* = [SO_4^{2-}]+[AlSO_4^+]+2[Al(SO_4)_2^-] \quad (12)$$
$$C_{Org}^* = [Org^{3-}]+[HOrg^{2-}]+[H_2Org^-]+[H_3Org]+[AlHOrg^+]+[AlOrg] \quad (13)$$

A GW-BASIC computer program was developed to perform the necessary calculation. All chemical reactions equilibrium constants are cited from literatures [12-14].

RESULTS AND DISCUSSION

Atmospheric deposition and processes occuring in the soil are responsible for the observed surface water chemistry in a catchment. [19] CO_2 partial pressure in soil is commonly much higher than atmospheric CO_2 partial pressure ($10^{-3.5}$ atm). When the solution is removed from

contact with the soil matrix and exposed to the atmosphere (that is when water enters the stream channel), two situations may be occuring for the CO_2, depending on the pH value of the surface waters. Figure 1 gives the results of the theoretical calculation of pH values as the function of C_B-C_A under various P_{CO_2} values for surface waters. We can use it to explain the influence of pH on the accumulation of CO_2 concentrations in surface waters.

(1) the surface water is in the acidic range of C_B-C_A < -200 μ eq/L, P_{CO_2} may increase from 1×10^{-4} to 0.1 atm without change of pH. Acidic conditions restrict the dissociation of CO_2 (H_2CO_3) to H^+ and HCO_3^- due to the buffering actions of Al^{n+} and H^+. This means that much more CO_2 concentrations can be accumulated in surface waters under acidic condition;

(2) CO_2 is not easy to accumulate in the surface water which is of C_B-C_A > 0 μ eq/L. Under this condition, the water is poorly buffered and small changes in CO_2 concentration can significantly affect pH. Higher P_{CO_2} needs lower pH. Otherwise, the pH of the solution will increase, causing CO_2 lost to the atmosphere.[20,21] This means that when water enters the neutral stream channel from soil, excess CO_2 concentrations can not be accumulated in surface waters due to the increase of pH.

Figure 2 depicts the " P_{CO_2} *vs.* pH " relationship for analyzing the practical sampling water quality data. The data are cited from the literatures [22-26]. The values of P_{CO_2} are calculated from pH measured. After pH > 5, P_{CO_2} is not more than 20 P_o. Conversely, P_{CO_2} increases rapidly as an exponential function at pH < 5. Lakes are a small but potential important conduit for carbon from terrestrial sources to the atmospheric sink. Acid rain, also promotes the accumulation of carbon dioxide in surface waters!

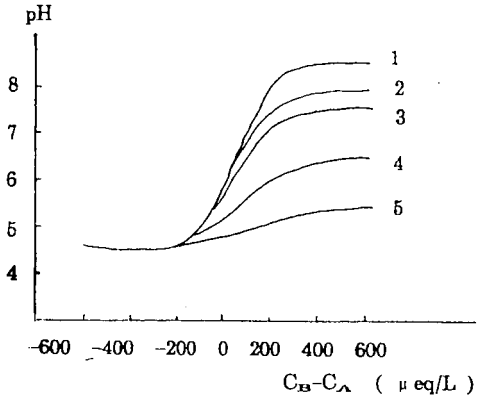

Fig.1 plot of " pH *vs.* C_B-C_A "
P_{CO_2} (atm):
1 — 1×10^{-4}, 2 — 3.16×10^{-4},
3 — 1×10^{-3}, 4 — 1×10^{-2},
5 — 1×10^{-1}

ACKNOWLEDGEMENT

This project is financed by the National Natural Science Foundation of China, Fok Ying Tung Education Foundation of Hong Kong and State Education Committee Foundation of China. The author thanks Prof.Rongshi Cheng, Hongyuang Chen, Ying Wang and Director of Smithsonian Environmental Research Center D.L.Correll for their supports and help.

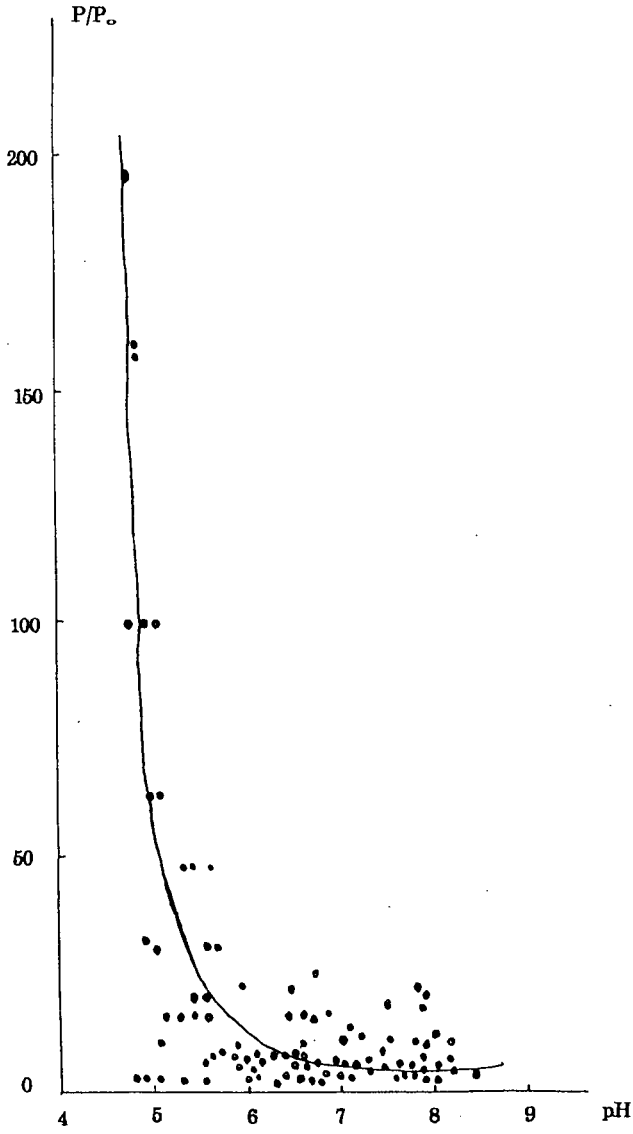

Fig.2 plot of " P_{CO_2} *vs.* pH " ($P_o = 3.16 \times 10^{-4}$ atm)

REFERENCES

1. J.J.Cole, N.F.Caraco, G.W.Kling and T.K.Kratz, Science., 265 (1994) 1568
2. G.W.Kling, G.W.Kipphut and M.C.Miller, Science., 251 (1991) 298
3. G.W.Kling, G.W.Kipphut and M.C.Miller, Hydrobiologia., 240 (1992) 23
4. D.W.Schindler et al, Science., 177 (1972) 1192
5. D.M.Schell, Science., 219 (1983) 1068
6. B.J.Peterson, J.E.Hobbie and T.L.Corliss, Can.J.Fish.Aquat.Sci., 43 (1986) 1259
7. P.I.Coyne and J.J.Kelley, Limnol.Oceanogy., 19 (1974) 928
8. P.V.Sellmann, J.Brown, R. I. Lewellen, H. Mckim and C. Merry, " The classification and geomorphic implications of thaw lakes of the arctic coasta plain,Alaska " (Rep 344, US Army Cold Regions Research and Engineering Lab, Hanover, NH, 1975)
9. P.P.Tans, I.Y.Fung and T.Takahashi, Science., 247 (1990) 1431
10. G.Sposito, The Environmental Chemistry of Aluminum. CRC Press,Inc. Boca Raton, Florida, 1989.
11. W.H.Durum and J.Haffty, Geochim Cosmochim Acta., 27 (1963) 1.
12. W.D.Schecher and C.T.Driscoll, Water Resource Research., 23 (1987) 525.
13. Shuping Bi, analyst., 120 (1995) 2033
14. W.D.Schecher, Ph.D Dissertation. Syracuse University. Syracuse, New York, 1988.
15. E.Tipping, C.Woof and M.A.Hurley, Water Res., 25(1991) 425.
16. C.T.Driscoll and W.D.Schecher, Environ.Biochem.Health., 12 (1990) 28.
17. Shuping Bi, Anal.Chimica.Acta., 314 (1995) 111
18. Shuping Bi and Wei Ying, Analyst., 120 (1995) 2805
19. J.J.Bisogni Jr and S.L.Arroyo, Water Res., 25 (1991) 185
20. B.J.Cosby, G.M.Hornberger, J.N.Galloway and R.F.Wright, Environmental Science and Technology., 19 (1985) 1144
21. W.Stumm and J.J Morgan, Aquatic Chemistry., Wiley-Interscience, New York, 1981
22. L.A.Baker, C.D.Pollman and J.M.Eilers, Water Resources Res., 24 (1988) 1069
23. J.R.Webb, B.J.Cosby, J.N.Galloway and G.M.Hornberger, Water Resources Res., 25 (1989) 1367
24. A.T.Herlihy, P.R.Kaufmann, M.R.Church, P.J.Wigington Jr, J.R.Webb and M.J.Sale, Water Resources Res., 29 (1993) 2687
25. D.R.Dewalle and B.R.Swistock, Water Resources Res., 30 (1994) 1955
26. M.B.David, G.F.Vance and J.S.Kahl, Water Resources Res., 28 (1992) 389
27. K.B.Easthouse,D.E.Spyidakis and E.B.Welch, Water, Air and Soil Pollu., 71 (1993) 377
28. K.E.Webster,P.L.Brezonik and B.J.Holdhusen, Water,Air and Soil Pollu., 67 (1993) 397
29. R.Harriman, B.R.S.Morriam, L.A.Caines, P.Collen and A.W.Watt, Water, Air and Soil Pollu., 32 (1987) 89
30. M.Lachance, D.Brouard and G.Walsh, Water, Air and Soil Pollu., 39 (1988) 311
31. H.B.Xue and J.L.Schnoor, Water, Air and Soil Pollu., 75 (1994) 61
32. S.Ikeda, J.Motonaka, T.Koizumi and T.Ishikawa, Anal Sci., 7 (1991) 1077
33. R.Giovanoli, J.L.Schnoor, L.Sigg, W.Stumm and J.Zobrist, Calys and Caly mine., 36 (1988) 521
34. B.O.Rosseland et al, Environ Pollu., 78 (1992) 3
35. R.F.Wright, Environ.Sci., 22 (1988) 178
36. M.Papineau and J.Haemmerli, Water, Air and Soil Pollu., 61 (1992) 95

THE STABLE HIGH TEMPERATURE CO_2-ACCEPTOR. THERMOANALYTICAL STUDY

August R. Brun-Tcekhovoi[1], Sergei S. Kurdyumov[1], Leonid A. Rudnitsky[2]
[1]Inst. of Petrochem. Synth. 117912, Leninskii pr.29. Moscow, Russia
[2]Inst. of Nitrogen Ind., 109815, Zemljanoi Val, 50, Moscow, Russia

Keywords: CO_2 acceptor, thermoanalytical methods, durability

The studied high temperature CO_2-acceptor intended for the persistent removal of CO_2 from chemical reactors fits special requirements. It is characterized by the high CO_2 capacity and durability; its structure stability is held on the cyclic variation of inner stresses produced by the consequence of carbonation-decarbonation. The acceptor which consists of CaO and MgO (periclase) has been prepared from dolomite. Experimental data demonstrate CaO phase to work as CO_2-acceptor and MgO one to form a rigid framework, which provides the stability to the grains structure. The volume of $CaCO_3$ phase formed exceeds twice the initial volume of CaO phase. However, this effect is eliminated due to the periclase framework: acceptor grains do not demonstrate any expansion on $CaCO_3$ formation.

The CO_2-acceptor was developed with the properties allow using it on new effective technology of the methane steam reforming process (ASMR). The main peculiarity of this technology is continuous CO_2 remove from the reaction zone of ASMR by means of solid acceptor which continuously circulates through this zone.

The acceptor should demonstrate sufficient high activity on interaction with CO_2. Besides the acceptor must have a high attrition resistance (AR). Finally it must be stable enough to both these parameters. The most suitable materials for producing CO_2-acceptor is dolomite $CaCO_3.MgCO_3$.

At temperature ranges of ASMR-process dolomite is decomposed by two stages:

$$CaCO_3.MgCO_3 \text{ ----------} > CaCO_3 + MgO + CO_2$$
$$CaCO_3 + MgO \text{ ----------} > CaO + MgO + CO_2$$

Formed due to stage (1) MgO is inactive because of sintering after formation. An active component of acceptor is CaO, which is formed as a result of reversible reaction (2). The direct using of dolomite as a CO_2-acceptor is impossible mainly because of phase transition which accompanied both indicated reactions.

Disordering of crystal lattice leads to lowering of AR. So the proceeding of the low temperature stage (1) induces the decrease of initial value of AR for dolomite from about 40% to zero. Stage (2) is accompanied by the transition $CaCO_3$ phase to CaO and vice versa.

The dolomite destruction due to phase transition made impossible a realization of prospective technology of coal-gasification known as "CO_2-acceptor process". Simultaneously an ability of dolomite to lose activity due to sintering was also found out. All these data were obtained on semi commercial plant.

According to our purposes the grain of the acceptor must include a stable and chemical inert framework, distributed in all volume of grain. Active component (CaO) is disposed in the space cells of the framework.

MgO was chosen as a matter for creating a framework because of its ability to sintering and formatting inactive and stable periclase. Further it would be expedient to choose dolomite as a MgO-containing material, which includes CaO also.

During our experiments we have developed a method of dolomite treatment which allows producing CO_2-acceptor, not having the lacks typical for dolomite.

The above discussed practical-important properties of studied solids were determined using the next methods: 1) activity A_{CO2} was determined as CO_2 in carbonated samples; 2) the value of AR was determined in the device, simulated the air-lift at a linear velocity equaled 25-30 m/s.

The stability of samples was characterized by changing the values of A_{CO2}.AR and by the specific surface in the long runs with intermittent cycles of decomposition (1100-1200K) and carbonation (by 900-950K). Total duration of the tests was 100h, a number of cycles was near 50.

The fresh acceptor has a high value of AR (80%), which near twice higher that for fresh dolomite. In test the AR value was lowered during 10-30h, then it remained near constant and equaled to that for fresh dolomite. The AR values for carbonated and decomposed samples differed insignificantly. It means that for the acceptor the transition of $CaCO_3$ to CaO does not affect its structure.

The A_{CO2} value was in fact constant changed within 25 to 27 percent. This is in good agreement with the almost constant value of the specific surface, which is equal to 2.3-2.6 m^2/g for decomposed samples and to 0.4-0.8 m^2/g for carbonated samples.

For the study of formation of CO_2-acceptor we have chosen two thermoanalytical methods: thermogravimetry and dilatometry. This permitted us firstly to register the value of mass changing and the rate of this process and secondly to register the grain-framework response to the consequence variation the volume of the active phase.

The work was carried out by microbalance "Sartorius" and dilatometer "Netzsch" adapted by us for the work in different gases flow at the temperatures from ambient to 1000°C. The same programs and conditions of experiments were used for different methods. The data on mass change and elongation are given in dimensionless form $\Delta m/m$ and $\Delta l/l$.

First of all, the behaviors of natural dolomite and acceptor in course of the cyclic $CaCO_3$-CaO transitions were compared. In this series of experiments, the carbonate decomposition in air flow was studied only. Dilatometric curves for heating of samples are given in Fig. 1 as dependencies of temperature coefficient of linear expansion on the temperature. Dilatogram of the first decarbonation of natural dolomite (curve 1) indicates the great extent of contraction in the temperature range higher than 600°C and, especially, higher than 700°C, where decomposition of calcium carbonate takes place. At the second decarbonation (curve 2) the considerable contraction peak in the range of 400-600°C has been observed which corresponds to decomposition of magnesium carbonate. Further in the not large temperature interval (from 600 to 700°C) the grain structure is evidently supposed by calcium carbonate phase, but its decomposition at temperature higher than 700°C induces endless contraction of grain which indicates to the destruction of sample.

Dilatogram of the first decarbonation of acceptor (curve 1a) shows not so significant effect of decreasing temperature coefficient in the temperature range corresponding to decomposition of magnesium carbonate and not so large contraction peak in the temperature range higher than 700°C corresponding to the decomposition of calcium carbonate.

As the cycling proceeds, the first effect disappears really, and the second decreases. On the fourth cycle (curve 2a) we obtain at almost whole temperature range the positive temperature coefficient of thermal expansion decreasing at temperature - higher 800°C only. Thus cycling the accepter (two-phase system) leads to stabilization of the grain framework, but cycling the natural dolomite (one-phase system) induces destabilization of its structure and then destruction of the grain.

Then the comparative study of accepter samples different in intensity of natural dolomite treatment which transforms it to CO_2 accepter was carried out. These intensities are represented below in arbitrary units (a.u.).

In Fig. 2 the thermogravimetric curves for acceptors obtained by mild and by severe treatment of dolomite are compared (5 and 18 of a.u. correspondingly). Previously these samples were decarbonated, after that they were linear heated and cooled in CO_2 flow. The curve for sample 5 is continuous line, the curve for sample 18 is noted by stars. It can be seen that the interaction with CO_2 begins at quite low temperature (from 300 to 400°C), but it proceeds not so quickly and follows up to relatively high temperature. The thermogravimetric curve for sample 18 is displaced to high temperatures essentially (approximately by 200K) as related to the curve for sample 5. This is connected evidently with the fact, that transforming natural dolomite into acceptor is followed by the scaling acceptor structure, - decreasing its porosity and, may be, section of transport pores and other effects inducing decrease of rate of interaction

with CO_2. Thermogravimetric curve for sample 18 exceeds the temperature of thermodynamic equilibrium for calcium carbonate decomposition before ending the carbonation. Nevertheless it can be seen that capacities of both samples are close enough and quite large: the quantity of CO_2 uptake exceeds 30% of mass of the sample containing MgO and $CaCO_3$. Decomposition of carbonate proceeds in both samples with high and close rates. The decrease of temperature returns the samples into the region of carbonate formation. Thermogravimetric curves for cooling testify the high rate of carbonation, but exceed the saturation at more low level than those for heating. This fact is induced, may be, by sintering CaO becoming real at this quite high temperature after CO_2 isolation.

Consider now the response of grain structure to calcium carbonate formation and decomposition. In Fig. 3, one from thermogravimetric curves for heating and cooling the sample 18 in CO_2 flow shown in previous figure and corresponding dilatogram, the scale for ordinate of which is increased approximately hundred times are presented. This permits us to use the common ordinate y for representation dilatogram (dotted line) and thermogravimetric curve and to compare the both curves. At heating dilatogram character corresponds to thermal expansion of the sample. The similar curve in the bottom part of the figure corresponds to thermal contraction at cooling. Thermogravimetric curve for heating demonstrates at 600°C the beginning of calcium carbonate forming. At 750°C - approximately 30% of calcium oxide transforms into carbonate. The total volume of reacting and forming phases increases approximately by 30%, however dilatogram does not indicate any expansion of sample.

On the contrary at 700°C in spite of forming the carbonate with considerable rate deceleration of thermal expansion and then contraction of sample is observed the latter finishes in the temperature region corresponding to decomposition of carbonate and isolation of CO_2.

During the cooling of the sample at temperature about 870°C thermogravimetric curve indicates increasing the sample mass - approximately by 10% (30% of CaO forms carbonate).

There is insignificant splash in dilatogram - this effect corresponds approximately to thermal expansion of the sample at heating by 10-12 K. Thus the carbonate formation does not induce practically any expansion of accepter. This result testifies apparently that there is some functional and space separation of two phases in accepter. Components of these phases (CaO and MgO) constituted previously one-phase structure of dolomite. It may be thought that after segregation of phases magnesium oxide transforms into stable inert form - periclase. The latter forms grains framework keeping its stability and sitting the second phase - calcium oxide which is the accepter really so that volume variations of the latter do not lead to the excess inner framework stresses. Suggested scheme is apparently simplified.

Consider Fig. 4 permitting to coincide thermogravimetric (top figure) and dilatometric (bottom figure) curves for heating in air the accepters 5 and 18 subjected previously to treatment with CO_2 at high pressure, i.e. saturated completely. The dotted lines correspond to the sample 5. It can be seen that sample capacities are very high and close to one another (the calculation with regard to carbonated sample is given). Thermogravimetric curves of carbonate decomposition also coincide practically. It can be seen not large displacement (not more than 1%) in the region where decomposition of magnesium carbonate takes place - about 500°C. Analogous displacement can be observed in dilatogram for sample 18 shown in bottom figure and for some other samples. The fact that quite small quantity of decomposed magnesium carbonate can induce dilatometric effect permits us to suppose that activation of MgO can proceed on interphase boundaries where the reaction of calcium oxide can catalyze the surface layers of periclase. As thermogravimetric curves for decarbonating samples 5 and 18 practically coincide, the corresponding dilatometric effects appear to be different: sample 18 indicates more less contraction than sample 5. Evidently this is connected with larger durability and rigidity of its framework.

While during heat treatment of samples in carbon dioxide flow or in air effects of volume increase are practically absent the contraction of samples is often observed. Evidently contraction of samples in induced by a complex of reasons, which require further investigation.

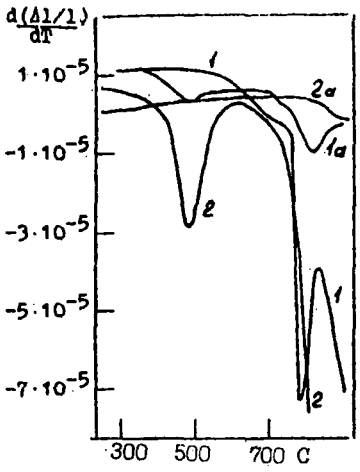

Figure 1. The dependencies of the linear expansion coefficient on temperature for cyclic heating of natural dolomite (1 and 2) and CO_2 acceptor (1a and 2a)

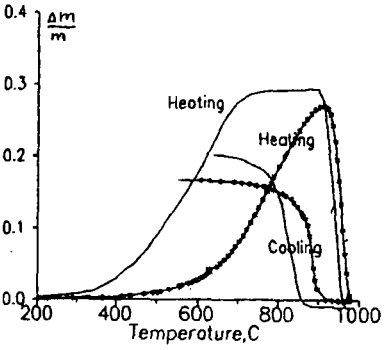

Figure 2. The thermo-weight curves of the heating and cooling in the CO_2 flow for acceptors 5 and 18 (marked with stars).

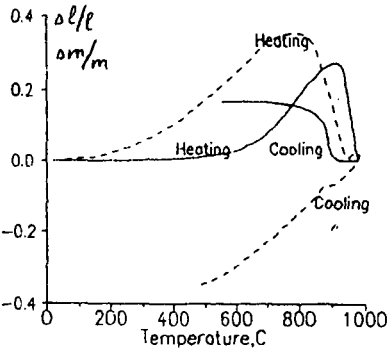

Figure 3. The comparison of the thermogravimetric and dilatometric (dotted line) curves of the heating and cooling in the CO_2 flow for acceptor 18. The y axis scale (elongation) is enlarged about 100 times.

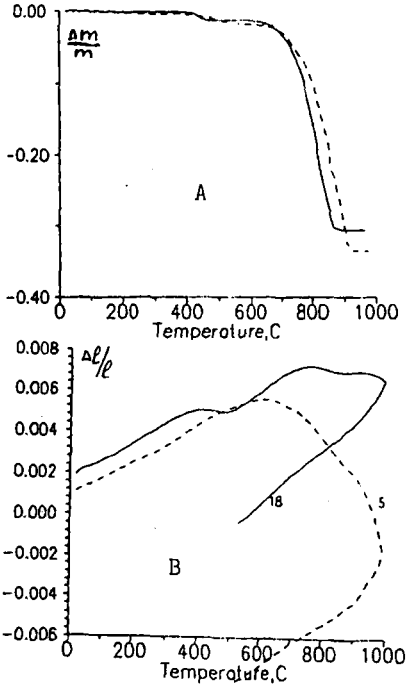

Figure 4. The comparison of the thermo weight (a) and dilatometric (b) curves of the heating and cooling in the air flow for acceptors 5 (dotted line) and 18.

FROM CARBON DIOXIDE TO C_2 ORGANIC MOLECULES

Jin K. Gong,* Chris A. Wright, Matthew Thorn, James W. McGill, Angela Sutterer, Shannon M. Hinze, and Ryan B. Prince
Department of Chemistry
Southeast Missouri State University
Cape Girardeau, MO 63701

Keywords: Nickel Carbon Dioxide, Wittig Reaction, Nickel Ketene Complex

Abstract

Research on the conversion of carbon dioxide into C_2 or higher organic molecules has received much attention in recent years. The key to the success of this research is carbon-carbon coupling. This paper reports the modified synthesis of a nickel carbon dioxide complex, $(Cy_3P)_2NiCO_2$, (Cy = cyclohexane) and the "Wittig Reaction" of this coordinated nickel carbon dioxide complex. The formed nickel ketene complex, $(Cy_3P)_2Ni[\eta^2\text{-}(C,O)\text{-}CH_2{=}C{=}O]$, has an unusual η^2-C,O bonding mode instead of the normal η^2-C,C for the later transition metals. The pathway of this "Witting Reaction" is an unprecedented example for a transition metal carbon dioxide complex.

Carbon dioxide chemistry has been a research topic for many research groups due to its fundamental importance and practical applications. To develop efficient catalytic processes in which carbon dioxide can be used as a carbon source is one of the main objectives of this research area.[1] Carbon-carbon coupling is the key to achieve C_2 or higher organic molecules. We are reporting the first example of "Wittig Reaction" on a coordinated carbon dioxide nickel complex.

Coordination of carbon dioxide to a transition metal is one of the initial steps in the catalytic conversion of carbon dioxide into useful organic molecules. The electronic structure of carbon dioxide is perturbed by bonding to a transition metal center. Different types and degrees of altered reactivities have been observed for different coordination modes of carbon dioxide. Two coordination modes for mononuclear metal carbon dioxide complexes have been reported[8]. They are η^2 side-on coordination and η^1-C coordination.

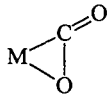

η^2-side-on coordination

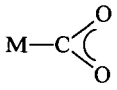

η^1-C coordination

η^1-end-on coordination

The η^2-side-on and η^1-C coordination modes are well established. The η^1 end-on coordination is a proposed mode as a result of calculation and has only been mentioned once as an intermediate in the literature[36]. Theoretical studies of these coordination modes of carbon dioxide have given a better understanding of the factors governing the bonding in carbon dioxide complexes. The η^2 side-on mode is preferred when the metal has a $d\pi$ orbital as the HOMO and the empty $d\sigma$ orbital pointing to the carbon dioxide ligand. One of the examples is Mo(0) in Cp_2MoCO_2, where Cp = cyclopentadiene. The η^1-C mode is most favored when

the HOMO is mainly composed of a dσ orbital and when the metal is in a low oxidation state, as found in the d^8 complexes[17].

The η^2- coordinated nickel carbon dioxide complex, $(Cy_3P)_2NiCO_2$, is favored as a starting complex with the ylide due to the electrophilic carbon of the coordinated CO_2. The complex was first prepared by Michele Aresta in 1974[1a,4]. Based on the literature procedures, the preparation was modified to a one step procedure:

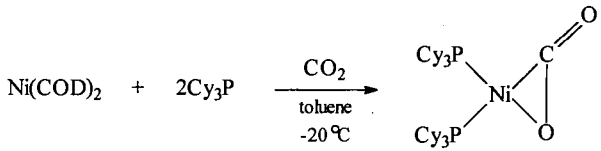

where COD is 1,5-cyclooctadiene. A 50 ml Schlenk reaction flask was charged with $Ni(COD)_2$, two equivalent of tricyclohexylphosphine and a minimum amount of anhydrous toluene in a nitrogen atmosphere dry box. The reaction flask was immediately brought out of the dry box and placed in an ice/salt cooling bath. bubbled the reaction solution with carbon dioxide gas via a syringe needle for about thirty minutes. During the above process, the product was precipitated out as yellow crystalline solid. The product was filtrated and washed with a small amount of ether in the dry box. The yield is around 85%. The spectral data are in agreement with the literature values. The C=O in coordinated CO_2 is characterized by a strong IR band at 1740 cm^{-1}. The $^{31}P\{^1H\}$ NMR of $(Cy_3P)_2NiCO_2$ in C_6D_6 shows a singlet at 37.32 ppm at 298 K. The $^{31}P\{^1H\}$ NMR of $(Cy_3P)_2NiCO_2$ in THF-d_8 at 188K shows two doublets $^2J_{p\text{-}p}$ = 39.6 Hz at 51.7 and 20.2 ppm, respectively[4]. The estimated value for the free activation temperature of the dynamic process at the coalescence temperature (233 K) is 39.3 KJ mol^{-1}.

Trialkyl phosphorus ylides, $R_3P{=}CH_2$, are strong nucleophiles. They react with organic ketenes and aldehydes to form alkenes via a [2+2] cycloaddition mechanism. Such ylides can also react with bridging carbonyls in $[\eta^5\text{-}CpFe(CO)_2]_2$ and $Ni_2(\mu\text{-}CO)(CO)_2(dppm)_2$, dppm = bis(diphenylphosphino) methane, to form μ-alkylidene complexes through the same C-C bondformation mechanism[5]. The carbon of η^2-CO_2 metal complexes has demonstrated some interesting reactivities towards nucleophiles[6]. The reaction between a metal CO_2 complex and an ylide is an unprecedented example in carbon dioxide chemistry. When $(Cy_3P)_2NiCO_2$ is treated with excess of trimethyl phosphorus ylide at room temperature in toluene, a nickel ketene complex is formed[7]:

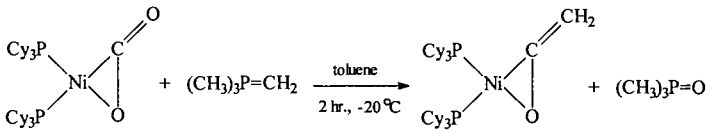

Free organic ketenes are very reactive molecules. They can be stabilized by transition metal complexes. Transition metal ketene complexes are important intermediates in catalysis such as in the Fischer-Tropsch process. The process involves the catalytic CO activation and carbon-carbon coupling chemistry[8]. Ketenes can be bonded to transition metal complexes in a wide variety of ways[8a].

The two common bonding modes for mononuclear ketene complexes are η^2-(C, O) and η^2-(C, C). Traditionally, the η^2-(C, O) mode is considered to be favored by early transition metal complexes due to the electrophilic property of early transition metals. The η^2-(C, C) mode is preferred by late transition metal complexes. Several nickel ketene complexes have been reported and characterized spectroscopically to be the η^2-(C, C) bonding mode[8a]. The nickel ketene complex we obtained in the above reaction is characterized to be η^2-(C, O) bonded. A strong stretch at 1611 cm^{-1} is assigned to the C=C double bond. The first structure of an η^2-(C, O) bonded nickel ketene complex was reported recently by Hofmann's group[9]. The nickel diphenylketene complex, (dtbpm)Ni[η^2-(C, O)-Ph_2C_2O], has a strong band at 1643 cm^{-1} for the C=C double bond, where the chelated ligand, dtbpm, is Bis(di-tert-butylphosphino)methane.

Transition metal ketene complexes have demonstrated much interesting chemistry. The coordinated ketene can be readily converted to various organic molecules such as alcohols, aldehydes, acetones and acids[8]. The preliminary investigation shows that the nickel ketene complex we isolated has its own characteristic reactivity which is different from the η^2-(C, C) species, $(Ph_3P)_2Ni[\eta^2$-(C, C)-CH_2=CO], reported in the literature[10]. Our nickel ketene complex can react with HCl to generate acetaldehyde. Ligand effect studies are underway to understand the bonding modes of η^2-(C, C) and η^2-(C, O) to nickel complexes.

Acknowledgment. We acknowledge Research Corporation for the Cottrell College Science Award (C-3394) and GRFC of Southeast Missouri State Univ. C. A. Wright is grateful to the NASA JOVE scholarship.

References

1. (a) Ayers, W. M. *Catalytic Activation of Carbon Dioxide*; ACS Symposium Series 363, New York, April 13-18, **1986**. (b) Palmer, D. A.; Eldik, R. V. *Chem. Rev.* **1983**, *83*; 651. (c) Darensbourg, D. J.; Kudaroski, R. A. *Adv. Organomet. Chem.* **1983**, *22*, pp 129-168. (d) Braunstein, P.; Matt, D.; Nobel, D. *J. Am. Chem. Soc.***1988**, *110*, 3207-3212. (e) Caballol, R.; Marcos, E. S.; Barthelat, J-C. *J. Phys. Chem.* **1987**, *91*, 1328-1333. (f) Gambarotta, S.; Arena, F.; Floriani, C.; Zanazzi, P. F. *J. Am. Chem. Soc.***1982**, *104*, 5082-5092. (g) Jessop, P. G.; Ikarlya, T.; Noyorl, R. *Nature*, **1994**, *368*, 231-233.

2. (a) Sneeden, R. P. A.; Villeurbanne, C. N. R. S. *Comprehensive Organomet. Chem.*; Wilkinson, G: Perga Press: New York, **1982**; *8*, pp 225-283. (b) Eisenberg, R.; Hendriksen, D. E. *Adv. Catal.* **1979**, *28*, 79. (c) Braunstein, P.; Matt, D.; Nobel, D. *Chem. Rev.* **1988**, *88*, pp 747-764.

3. Aresta, M.; Nobile, C. F.; Sacco, A. *Inorganica Chimica Acta*, **1975**, *12*, 167.

4. (a) Aresta, M.; Nobile, C. F.; Albano, V. G.; Forni, E.; Manassero, M. *J. Chem. Soc. Chem. Comm.* **1975**, 636. (b) Aresta, M.; Gobetto, R.; Quaranta, E.; Tommas, I., *Inorg. Chem.* **1992**, 31, 4286

5. (a) Korswagen, R.; Alt, R.; Ziegler, M. L. *Angew Chem Int. Ed. Engl.* **1981**, *20*, 1049. (b) Gong, J. K.; Kubiak. C. *Ph.D. Thesis*, **1990**, Purdue Univ. W. Lafayette, IN.

6. (a) Aresta, M.; Nobile, C. *J. Chem. Soc., Dalton Trans.*, **1977**, 708. (b) Arce, A. J.; Deeming, A. *J. Chem. Soc., Chem. Commun.*, **1982**, 364.

7. The $^{31}P\{^{1}H\}$ NMR (CD_3CN, 85% H_3PO_4 external) for $(Cy_3P)_2Ni[\eta^2$-(C, O)-CH_2=CO]: singlet at δ 27.15 ppm, The coupled spectrum of the byproduct, Me_3P=O, shows a multiplet of ten peaks centered at δ 37.98 ppm due to the coupling of phosphine to the nine protons in Me_3. FTIR: 1611 (s) cm^{-1} for C=C, ^{1}H NMR for the CH_2 group of the coordinated ketene is at δ 2.45 (br) ppm, The yield is 52%.

8. (a) Geoffroy, G. L.; Bassner, S. L., *Adv. Organomet. Chem.*, **1988**, *28*, 1. (b) Collman, J. P.; Hegedus, L. S.; Norton, J. R.; Finke, R. G. *Principles and Applications of Organotrasition Metal Chemistry*, Univ. Sci. Books, **1987**, p657-659. (c) Wolczanski, P. T.; Bercaw, J. E. *Acc. Chem. Res.* **1980**, *13*, 121. (d) Masters, C. *Adv. Organomet. Chem.* **1979**, *17*, 61. (e) Blyholder, G.; Emmet, P. H. *J. Phys. Chem.* **1960**, *64*, 470. (f) Ichikawa, M.; Sekizawa, K.; Shikakura, K,; Kawai, M. *J. Mol. Catal.* **1981**, *11*, 167. (g) Takeuchi, A.; Kratzer, J. R. *J. Phys. Chem.* **1982**, *86*, 2438. (h) Muetterties, E. L. *J. Chem. Rev.* **1979**, *79*, 479. (i) Bell, A. T. *Catal. Rev.* **1981**, *23*, 203. (j) Herrmann, W. A. *Angew. Chem., Int. Ed. Engl.* **1982**, *21*, 117.

9. Hofmann, P.; Perez-Moya, L.; Steiglmann, O.; Riede, J. O*rganomettallics*, **1992**, *11*, 1167.

10. (a) Miyashita, A.; Shitara, H.; Nohira, H. *J. Chem. Soc., Chem. Commun.* **1985,** 850. (b) Miyashita, A.; Grubbs, R. H. *Tetrahedron Lett.* **1981**, *22*, 1255.

ACETYLENE-MEDIATED ALKYLATION OF MONOALKYL CARBONATES AND CARBAMIC ACIDS WITH *TERT*-AMINE

Yoshiyuki Sasaki
National Institute for Resources and Environment,
16-3 Onogawa, Tsukuba-shi 305, Japan

Keywords: Carbon Dioxide, Dialkyl Carbonate, Acetylene

Carbonic acid diesters and carbamic acid esters are useful organic substances as intermediates for the syntheses of pharmaceutical, agricultural, and the other chemicals. They are currently synthesized in industry using the processes based on phosgene or carbon monoxide. On the other hand, since carbon dioxide is an abundant and cheap carbonyl carbon source, and is much less toxic than those raw materials, substantial efforts have been focused on its fixation into carbonyl compounds including carbonic acid diesters and carbamic acid esters.[1] However, their syntheses based on carbon dioxide reported so far require rather expensive substrates like alkyl halides, and are not competitive with the currently adopted industrial processes.

The author and his co-workers previously reported that carbamic acids derived from CO_2 and *sec*-amines reacts with alkynes to give vinyl *N,N*-dialkylcarbamates in the presence of Ru complexes.[2] However, a similar reaction using alcohols, which would give vinyl alkyl carbonates, failed probably because of the insufficient nucleophilicity of alcohols compared with *sec*-amines,[3] save that acetylenic alcohols react with CO_2 to give cyclic carbonates, 2-oxo-propyl alkyl carbonates, 2-oxo-propyl *N,N*-dialkyl-carbamates, or 4-methyl-2-oxo-1,3-oxazolines in the presence of *tert*-amine, *sec*-amine, or *prim*-amine respectively.[4] During the attempt of reacting monoalkyl carbonates with acetylene in the presence of *tert*-amine and Ru complexes, however, a slight formation of dialkyl carbonates was observed. Further investigation revealed that this product is formed even in the absence of ruthenium or any other transition metal complexes. This means that this reaction is totally different from the ruthenium catalyzed synthesis of vinyl *N,N*-dialkyl carbamates. Moreover, one of the alkyl groups of dialkyl carbonates was found to come from *tert*-amines originally added with the intention of increasing the nucleophilicity of alcohols while the other from alcohols. Thus, either symmetric or unsymmetric carbonic acid diesters are formed as a main product according to the alkyl groups of alcohols and *tert*-amines[eq. (1)].

$$R'OH + CO_2 + R_3N \xrightarrow{HC\equiv CH} R'OCO_2R + R_2NCO_2R \qquad (1)$$

Also formed are alkyl *N, N*-dialkylcarbamates, all the alkyl groups of which are originated from *tert*-amines. Therefore, this reaction may be represented as the alkylation of monoalkyl carbonates and carbamic acids with *tert*-amines; carbamic acids are considered to be formed from CO_2 and *sec*-amines resulting from the dealkylation of *tert*-amines.

In a typical experiment, acetylene(30mmol) is introduced in a 50mL-autoclave containing *tert*-amine(30mmol) and alcohol(200mmol) at -50℃. After CO_2 is pressurized at 5MPa at ambient temperature, the autoclave is heated at a designated temperature for 16h or 40h. The products obtained are identified by spectroscopical comparison with their authentic samples either purchased or synthesized using chloroformic acid esters and analyzed by GLC. Unreacted *tert*-amines and acetylene recovered together with CO_2 through an accumulated gas-flow meter are also analyzed by GLC.

In the reaction with ethanol and triethylamine, diethyl carbonate and ethyl *N, N*-diethylcarbamate are

formed in fair yields at the reaction temperatures higher than 120℃, while practically no product is obtained at 80℃ as shown in Table 1. The conversion of acetylene increases significantly with reaction temperature, while that of triethylamine levels out at about 42% with the result that the total yield of diethyl carbonate and ethyl *N, N*-diethylcarbamate based on triethylamine remains at 40% even at 180℃; but, the selectivity for these products is as high as 95%. Triethylamine is recovered unreacted in the reaction without acetylene even at 160℃. On the other hand, acetylene is mostly consumed and 33% of triethylamine is converted in the reaction without CO_2, but naturally there is no CO_2 containing product formed. This means that the presence of CO_2 rather suppresses the conversion of acetylene to some extent.

The yield of diethyl carbonate and the conversion of triethylamine increase from 32% and 45% to 78% and 83% respectively with decrease in the amount of triethylamine introduced from 30mmol to 5mmol in the reaction at 160℃ for 40h as shown in Table 2. The yield of ethyl *N, N*-diethylcarbamate, on the other hand, reaches its maximum at 13% with 20mmol of triethylamine(entry 2). Neither diethyl carbonate nor ethyl *N, N*-diethylcarbamate is formed without triethylamine(entry 5). When triethylamine is used in smaller amounts, a significant formation of diethylamine is observed in the resulting reaction solution, which accounts for the formation of ethyl *N, N*-diethylcarbamate; *N, N*-diethylcarbamic acid derived from CO_2 and diethylamine formed by the preceeding alkylation of monoalkyl carbonate must be alkylated in place of monoalkyl carbonate with triethylamine. It is also found that diethylamine is partially converted to triethylamine and small amounts of diethyl carbonate and ethyl *N, N*-diethylcarbamate are formed in the reaction using diethylamine instead of triethylamine(entry 6). These results, as well as the fact that the total yield(86%) of the products exceeds the conversion of triethylamine(83%) in the reaction with 5mmol of triethylamine(entry 4), suggest that more than one ethyl group in triethylamine can be used for alkylation but most probably at the expense of higher consumption in acetylene under certain conditions.

The results of the reactions with several alcohols and *tert*-amines are summarized in Table 3. When *n*-propanol is used instead of ethanol, ethyl *n*-propyl carbonate is formed in the yield of 22% together with ethyl *N, N*-diethylcarbamate(7%) and di-*n*-propyl carbonate(1%). This result clearly shows that one of the ethyl group of diethyl carbonate formed in the reaction with ethanol mostly comes from triethylamine. The slight formation of di-*n*-propyl carbonate, however, suggests that the ester exchange reaction of dialkyl carbonate occurs to some extent in excess alcohols. This reaction becomes rather significant when allyl alcohol is used probably because of its high nucleophilicity; 19% of ethyl allyl carbonate is formed together with diallyl carbonate(8%) and ethyl *N, N*-diethylcarbamate(14%). It is not yet clear why the carbamate is obtained in such a high yield in this reaction compared with the other saturated alcohols. Tri-*n*-propylamine can be also used in place of triethylamine for the reactions of these alcohols, although it shows a little lower reactivity; 12-21% yields of the corresponding *n*-propyl carbonates are formed together with small amounts of symmetric carbonates and *n*-propyl *N, N*-di-*n*-propylcarbamate. All the reaction solutions are homogeneous but colored in brown when the reaction has proceeded, while the use of either methanol or trimethylamine results in the formation of polymers probably because of their excessive reactivity toward acetylene.

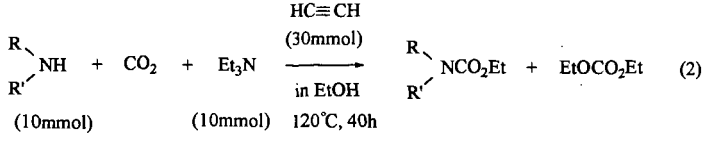

(2)

R=R'=Et;	23%	21%
R=*n*-Pr, R'=H;	34%	14%

The effect of the addition of *sec*- or *prim*-amine is demonstrated in eq. 2. When diethylamine is added to the reaction of ethanol and triethylamine at 120℃ for 40h, ethyl *N, N*-diethylcarbamate is formed in a higher yield(23%) than diethyl carbonate(21%). On the other hand, the addition of *n*-propylamine leads to the formation of ethyl *N*-*n*-propylcarbamate in good yield(34%); also formed are less amounts of diethyl carbonate(14%) and *N, N*-diethylcarbamate(5%).

There are two possible mechanisms for the present reaction as shown in Scheme 1; one includes the nucleophilic attack of monoalkylcarbonate, $ROCO_2^-$, on to one of the three alkyl radicals of hydrotrialkylammonium, R_3NH^+, followed by the addition of the liberated *sec*-amine to acetylene so that the equilibrium should be shifted to the right by giving dialkylvinylamine, $R_2N\text{-}CH{=}CH_2$, and the other includes the attack of monoalkylcarbonate on to trialkylvinylammonium, $R_3N\text{-}CH{=}CH_2^+$, formed by the preliminary addition of hydrotrialkylammonium to acetylene. In either case, although dialkylvinylamine itself has not yet been detected by GLC analysis probably because of its instability under the reaction conditions, its temporal formation seems plausible, because acetylene is substantially consumed during the reactions and converted to some polymeric materials, which can be observed after distillating the reaction solutions. Therefore, it is considered that dialkylvinylamine is partially decomposed to dialkylamine and acetylene polymers, and partially polymerized as such.

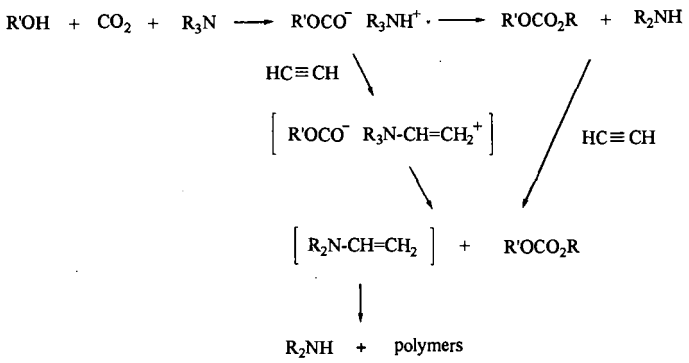

Scheme 1 Estimated reaction mechanism.

The following experiment has been performed in order to obtain a deeper understanding about the reaction mechanism. When the reaction of ethanol, CO_2, tri-*n*-propylamine, and tetraethylammonium bromide is performed under similar conditions as described in Table 1, diethyl carbonate is obtained in the yield of 3.3mmol while only a small amount(0.1mmol) of ethyl *n*-carbonate is formed(eq. 3).

$$\underset{(200\text{mmol})}{EtOH} + \underset{(50\text{MPa})}{CO_2} + \underset{(30\text{mmol})}{n\text{-}Pr_3N} + \underset{(30\text{mmol})}{Et_4N^+Br^-} \xrightarrow[16\text{h}]{160^\circ C} \underset{(3.3\text{mmol})}{EtOCO_2Et} + \underset{(0.1\text{mmol})}{n\text{-}PrOCO_2Et} + \underset{(6.4\text{mmol})}{Et_3N} + n\text{-}Pr_3NH^+Br^- \quad (3)$$

This result indicates that the monoethyl carbonate formed from ethanol and CO_2 does not react with its counter cation, hydro-tri-*n*-propylammonium, but with tetraethylammonium added, thereby suggesting that the latter mechanism including the preliminary formation of trialkylvinylammonium is likely. This process is analogous to the insertion of hydrotrialkylammonium hydroxide[5] or

chloride[6] to acetylene giving trialkylvinylammonium salt, $R_3N\text{-}CH{=}CH_2^+ X^-$. The following step, the attack of monoalkylcarbonate to trialkylvinylammonium giving dialkyl carbonate, is analogous to the esterification of carboxylic acids with large steric hindrances by forming tetramethylammonium salts and their thermal decomposition.[7]

The present reaction not only provides a new synthetic method of carbonic and carbamic acid esters involving only industrially available starting materials, but also shows a new type of CO_2 fixation without catalyst.

References

(1) (a) McGhee, W. D; Riley, D. P.; Christ, M. E.; Christ, K. M. *Organometallics*, **1993**, *12*, 1429. (b)Oi, S.; Kuroda, Y.; Matsuno, S.; Inoue, Y. *Nippon Kagaku Kaishi*, **1993**, 985.

(2) (a)Sasaki, Y.; Dixneuf, P. H. *J. Chem. Soc., Chem. Commun.*, **1986**, 790. (b) Sasaki, Y.; Dixneuf, P. H. *J. Org. Chem.*, **1987**, *52*, 314. (c) Mahé, R.; Sasaki, Y.; Bruneau, C.; Dixneuf, P. H. *J. Org. Chem.*, **1989**, *54*, 1518.

(3) Unpublished result.

(4)(a)Sasaki, Y. *Tetrahedron Lett.*, **1986**, 1573. (b)Sasaki, Y. *Bull. Natl. Res. Inst. Poll. Resour.*, **1987**, *16*(4), 13.(c)Sasaki, Y.; Dixneuf, P. H. *J. Org. Chem.*, **1987**, *52*, 4389.

(5) Gardner, C.; Kerrigan, V.; Rose, J. D.; Weedon, b. C. l. *J. Chem. Soc.*, **1949**, 780.

(6)Reppe, W. et al. *Annalen der Chemie*, **1956**, *601*, 81.

(7) Prelog, V.; Piantanida, M. *Z. Physiol. Chem.*, **1936**, *244*, 56.

Table 1. Effect of the Reaction Temperature[a)]

No.	Temp. (℃)	— Yield(%)[b)] —		— Conv.(%) —	
		$EtOCO_2Et$	Et_2NCO_2Et	Et_3N	$HC{\equiv}CH$
1	180	32	8	42	85
2	160	30	9	41	74
3	140	28	9	39	66
4	120	19	5	28	44
5	100	4	0	10	34
6	80	0	0	6	18
7[c)]	160	0	0	3	-
8[d)]	160	0	0	33	97

[a)] CO_2(5MPa), Et_3N(30mmol), EtOH(200mmol), Acetylene(30mmol), 16h.
[b)] based on triethylamine. [c)] without acetylene. [d)] Ar(5MPa).

Table 2. Effect of the Amount of Et_3N[a)]

No.	Et_3N (mmol)	— Yield(%)[b)] —		— Conv.(%)—	
		$EtOCO_2Et$	Et_2NCO_2Et	Et_3N	$HC\equiv CH$
1	30	32	11	45	96
2	20	42	13	56	86
3	10	65	12	77	80
4	5	78	8	83	83
5	0	-	-	-	21
6[c)]	0	4	1	- 9	81

[a)]CO_2(5MPa), EtOH(200mmol), Acetylene(30mmol), 160℃, 40h.
[b)]based on amine. [c)]Et_2NH(5mmol).

Table 3. Effect of the Alcohols and *tert*-Amines[a)]

R_3N	R'OH	—— yield(%)[b)] ——			— conv.(%) —	
		$R'OCO_2R$	$R'OCO_2R'$	R_2NCO_2R	R_3N	$HC\equiv CH$
Et_3N	EtOH	30	-	9	41	74
Et_3N	*n*-PrOH	22	1	7	35	68
Et_3N	CH_2=$CHCH_2OH$	19	8	14	42	89
n-Pr_3N	EtOH	17	3	2	26	46
n-Pr_3N	*n*-PrOH	12	-	1	16	38
n-Pr_3N	CH_2=$CHCH_2OH$	21	6	4	32	56

[a)]R_3N(*ca.* 30mmol), R'OH(200mmol), acetylene(30mmol), CO_2(5MPa), 160℃, 16h,
[b)]based on amine.

COPOLYMERIZATION OF 1,2-EPOXY CYCLOHEXANE AND CARBON DIOXIDE USING CO_2 AS BOTH REACTANT AND SOLVENT

Michael Super†, Enoch Berluche*, Christine Costello* and Eric Beckman†
†University of Pittsburgh, Chem. Eng. Dept., 1249 Benedum Hall, Pittsburgh, PA 15261
*Exxon Research and Engineering Company, Annandale, NJ

Keywords: Polymerization, Carbon Dioxide, 1,2-Epoxy Cyclohexane (Cyclohexene Oxide)

ABSTRACT

The copolymerization of 1,2-epoxy cyclohexane (cyclohexene oxide; CHO) and carbon dioxide was performed using no other solvent than carbon dioxide itself. A CO_2-soluble, ZnO-based catalyst was synthesized and used to catalyze the polymerization. Polymerizations were conducted at different temperatures, pressures and mole fractions of CHO giving rise to polymer yields as high as 69% with catalyst activities as high as 400 g polymer/g Zn. The best results were obtained at temperatures from 100-110°C and at mole fractions of CHO above $X_{C.O.}$=0.15. This polymer was >90% polycarbonate with weight average molecular weights (M_w) ranging from 50,000-180,000.

INTRODUCTION

Recent advances involving the use of carbon dioxide to replace organic solvents have attracted attention due to environmental concerns and the interesting properties of CO_2 at high pressures. At supercritical conditions the solubility parameter, dielectric constant and density of carbon dioxide are all comparable to that of liquids, while the surface tension and viscosity are comparable to gases. With modifications to equipment (to accommodate pressure) CO_2 can be substituted for some organic solvents while achieving or enhancing end results. This technique has been successfully employed, in such operations as extractions[1] and emulsion/dispersion polymerizations.[2-5] In each of these cases the CO_2 acts as the extracting medium or solvent, it's advantages being high rates of diffusion and easy recovery of products.

In the literature other researchers have shown that CO_2 can be successfully used as a reactant in organic polycarbonate synthesis (**Scheme 1**). Cyclic carbonates and polycarbonates have been formed using CO_2 and a variety of catalyst systems, many of which are zinc-based.[6-30] The nature of these catalysts has required use of an appropriate organic solvent to homogenize the reaction mixture,

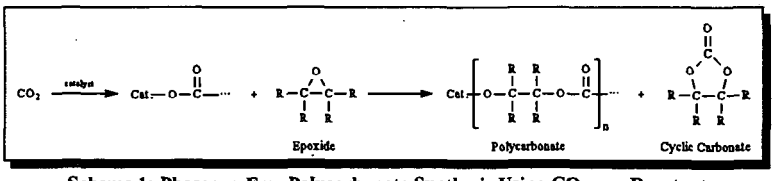

Scheme 1: Phosgene-Free Polycarbonate Synthesis Using CO_2 as a Reactant

but a few examples can be found in the literature where reactions were performed in the absence of any solvent.[23-25,30] The literature contains data on a large number of catalyst systems, where the yields of copolymer were as high as 70%. Unfortunately, the catalyst activities were usually low (5-40 g polymer/g Zn) with the exception of Darensbourg's catalyst[30] (which gave ~366 g polymer/g catalyst for the CHO/CO_2 copolymerization). The catalysts Darensbourg developed include (2,6-diphenylphenoxide)$_2$Zn(diethyl ether)$_2$, (2,6-diphenylphenoxide) Zn(THF) and (2,4,6-tri-*tert*-butylphenoxide)$_2$Zn(diethyl ether)$_n$, n<2[30]. These catalysts employ mononuclear Zn(II) phenoxide derivatives with bulky substituents to enhance the activity of the Zn(II) complexes. This work describes the use of a new catalyst based on the methylene-chloride soluble catalysts developed by ARCO[26], but which has been modified to allow solubilization in supercritical carbon dioxide. Other researchers have shown that molecules constructed of fluoroether, fluoroalkyl or silicones are soluble to varying extents in carbon dioxide.[1-5,31] Therefore, the procedure for synthesizing the catalysts consists of taking the half-ester of maleic anhydride and attaching a CO_2-soluble tail, by way of a hydrocarbon spacer. Allowing the synthesized molecule to complex with ZnO creates the active catalyst. The catalyst structure can not be specifically determined, due to the catalyst's inability to crystallize, but a representative drawing of the catalyst's molecular formula is shown in **Figure 1**.

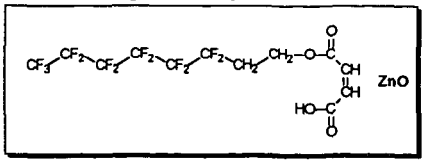

Figure 1: Fluorinated Half-Ester Complexed with ZnO (8.44% Zn by weight)

This work will explore the copolymerization of CO_2 and cyclohexene oxide (CHO) to synthesize polycyclohexene carbonate (PCHC), without using organic solvents. The reaction studied (**Scheme 2**) forms a copolymer which includes a small amount of ether repeat units and the 1:1 adduct, 1,2-

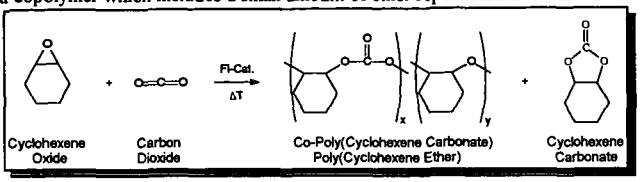

Scheme 2: Polycyclohexene Carbonate from CO_2 and Cyclohexene Oxide

cyclohexene carbonate (CHC). The effects of running this reaction at various pressures, temperatures, and mole fractions of the epoxide on the yield and nature of the polycyclohexene carbonate formed will be discussed.

EXPERIMENTAL

Materials: Cyclohexene Oxide (Aldrich Chemicals, Milwaukee, WI) was distilled under reduced pressure over CaH_2. The purified CHO monomer was then transferred under N_2 to flasks equipped with stopcocks, and stored under N_2 until used. Methylene chloride (99.9% assay) and anhydrous methyl alcohol (99.9% assay) were used to separate and precipitate the reactor products (Mallinckrodt Specialty Chemicals Co.; Paris, KY)

Research Grade CO_2 (Airco Special Gases; Riverton, NJ) and Supercritical Grade CO_2 (Liquid Carbonic; Chicago, IL) were used after passing through a series 62, high pressure purifier, which removes oil and water from gas and liquid systems (Liquid Carbonic). Nitrogen with 99.99% purity (Liquid Carbonic) was passed through the high-pressure purifier and then into the reactor without further purification.

Synthesis of Zn-perfluoroalkyl Catalyst: A flask was charged with 8.56 g (87.3 mmoles) of maleic anhydride, then flushed with N_2. The maleic anhydride was heated at 55°C and melted. Tridecafluoroctanol, 31.8 g (87.3 mmoles), was flushed with N_2 and transferred via a Teflon needle to the melted maleic anhydride. A solution of 0.73 ml (5.24 mmoles) of triethyl amine in 15 ml of toluene was next transferred to the mixture. *[Note: both the amine and toluene were distilled from calcium hydride.]* The mixture was stirred and heated at 55°C overnight. Upon cooling, the perfluoroalkyl monoester that formed was isolated by vacuum filtration and vacuum dried at 50°C overnight to recover 34 g (84% yield). The perfluoroalkyl monoester was purified by recrystallizing it 5 times in hexane or 2 times in benzene. Purified perflouroalkyl monoester, 12 g (27.26 mmoles) and zinc oxide, 2.22 g (27.26 mmoles) was added to a 250 ml three necked flask, equipped with condenser, mechanical stirrer and N_2 inert gas. Both solids were flushed with N_2, then 100 ml anhydrous 1,1,2-trichlorotrifluoroethane was transferred over the solids. The mixture was refluxed at 50°C for 24 hours. The synthesized Zn-perfluroalkyl catalyst was recovered by filtration with a pressure funnel. The filtrate was stripped to dryness and vacuum dried at room temperature overnight. The Zn-perfluroalkyl catalyst collected was 13.4 g (90.6% yield).

Polymerization of Polycyclohexene Carbonate: All reactions were performed in 50 ml heated reactors (Pressure Products Industries; Warminster, PA) capable of 6000 psig maximum working pressure at 340°C, and equipped with magnetically driven mixers. An air driven, gas booster compressor (Haskel Inc; Burbank, CA) was used to generate CO_2 pressure.

In a typical polymerization, the catalyst was weighed and placed into the reactor body under a natural atmosphere. The reactor was then sealed and flushed with flowing nitrogen at an inlet pressure of 100 psig and atmospheric outlet pressure for ½ - 2 hours. During this time, a measured amount of CHO was added to an addition piping under N_2 atmosphere using a graduated, glass syringe. The addition piping was then attached vertically to the reactor inlet. CO_2 at its' vapor pressure (≈850 psi at 25°C), was then used to 'push' the CHO into the reactor. After the injection of monomer, the reactor was isolated and heated to the reaction temperature. Once the reaction temperature was reached, pressurized CO_2 was added slowly (~200 psi increase in reactor pressure, letting temperature reach within 1°C of the reaction temperature each time) until the destination pressure and temperature were reached, a process which lasted 30-45 minutes. After the reaction was completed, the reactor was cooled to below 30°C and the gaseous reactor contents slowly bubbled through methylene chloride. The liquid and solid reactor contents were collected using methylene chloride to dissolve them from the reactor body and head. The reactor body and head were again rinsed with methylene chloride and this rinse was combined with the products obtained from the first reactor wash to make-up the total reaction products.

Purification of Products: The reactor rinse, the solvent used for collecting gaseous reactor contents, and reactor wash were combined and filtered. The solvent was removed under vacuum and the solid or viscous liquid reactor products were then dried in vacuo and weighed to determine the "Crude" yield. A concentrated solution was then made by dissolving the dried reactor products in a small amount of methylene chloride; this solution was then added to a large volume of methanol

from which a white, solid product precipitates. The precipitate was filtered and both the solid precipitate and the filtered solution were retained. The solid was re-dissolved in methylene chloride, concentrated and re-precipitated in fresh methanol two additional times. The solid was dried under vacuum at ~50°C, and then weighed to determine the methanol-insoluble fraction of the product. The three methanol solutions collected from the precipitations were combined and the methanol removed under vacuum at 50-70°C. Residual solids were dried under vacuum at ~50 C to recover the methanol-soluble fraction of the product.

Characterization of Polymers: Polymer molecular weights were measured using gel permeation chromatography (GPC, Waters 150CV) and polystyrene standards. The fraction of polycarbonate repeat units was determined using a Bruker MSL 300 NMR.

RESULTS AND DISCUSSION

Polycyclohexene carbonate was synthesized at different polymerization temperatures, while keeping the pressure constant, to determine the effects on the polymer product. Each reaction was run for 24 hours and the catalyst to monomer ratio of {moles of Zn} to {moles of cyclohexene oxide (C.O.)} was also kept constant. The reactor volume is unchanging, though, and the same volume of C.O. and weight of catalyst were used throughout this series. Therefore, the number of moles of CO_2 that are loaded into the reactor at constant pressure decreases as the temperature is increased throughout the temperature series. Another way to say this is that the mole fraction of C.O. increases as the temperature increases. This relationship is shown by following the mole fraction of C.O. on **Table 1**.

Table 1 also shows other results of the varying temperature reaction series. In **Table 1** the polymer yield is presented in another form, g Polymer/g Zn, to indicate the catalysts' activity at different conditions. For comparison purposes, previous Zinc-based catalysts for the formation of polycarbonate from epoxides generally give 10-40 g Polymer/g Zinc. At higher temperatures the catalyst selectivity towards polymer decreases favoring the formation of MeOH-soluble products.

Changing the reaction pressure also has an effect on the reaction products. In a separate series of reactions the pressure was changed while the temperature remained constant at 109-110°C and the polymerization was allowed to react for 24 hours. And while the catalyst to monomer ratio of {moles of Zinc} to {moles of C.O.} was kept the same as the other series, this set of experiments was done with half of the reactants as the variable temperature experiments. This means that there was more CO_2 present in the reaction mixture or that the reactions were run at lower mole fractions of C.O.. Again the same volume of C.O. and weight of catalyst were used over the entire range of pressures, therefore more CO_2 was present as the reaction pressure increased. This relationship is represented by a decrease in the mole fraction of C.O. with increasing pressures as shown in **Table 2.** The effect of this variation is not clear, but it seems that at these mole fractions the percentage of by-products formed is independent of pressure.

Table 2 also shows the yield results as a function of the changing pressure. The depression in yields at 4000 psig can not be attributed to the phase behavior in this set of experiments. Although, the yield depression shown at 4000 psig though can not be explained from what we know about the phase behavior of this system, the general trend of decreasing yields for the experiments run at 3000, 4000 and 5000 psig can be partially explained by the fact that the product yields decrease as the mole fraction of C.O. decreases. In the changing pressure experiments, the number of moles of CO_2 introduced at constant temperature increase as the pressure is increased. Therefore, the mole fraction of C.O. decreases and this results in decreasing yields.

A series of five reactions were run at varying mole fractions of C.O. to study the effect on the reaction products. These reactions were run for 24 hours at a constant pressure of 2000 psig and a constant temperature of 109-110°C. The catalyst to monomer ratio of {moles of Zinc} to {moles of C.O.} was again kept constant. **Table 3** shows the characterization results of the polymer product from this series. In this series of reactions, only the mole fraction of C.O. was varied.

The product yields show a decreasing trend at lower mole fractions of C.O. This could be attributed to lower solvating properties at low mole fractions of C.O. The CO_2-C.O. system could require certain co-solvent properties (a large enough solvating power for reactants and products) in order for good yields to be achieved. When the required co-solvent properties are not met, due to a large excess of CO_2, the reaction system might prefer to produce MeOH-soluble products rather than the desired polycarbonate polymer.

CONCLUSIONS

A system for synthesizing polycarbonate from epoxides, which uses a CO_2-soluble catalyst and CO_2 as a reactant and the only solvent can produce high polymer at high turnover rates. Polycarbonates containing >90% polycarbonate linkages with weight average molecular weights of 50,000-150,000 are obtained. Although the effects of pressure seem to point to 2000 psig and 110°C as the best conditions for this polymerization, further studies operating in other regimes of the phase diagram might prove enlightening. The Zinc-based, CO_2-soluble catalyst system shows an order of magnitude higher turnovers than previously reported and the catalyst has high selectivity towards polymer under certain conditions. More work needs to be done to fully understand this system,

especially in the area of phase behavior. In a system where CO_2 is both reactant and solvent the phase behavior of the system can influence the results, and this influence needs to be completely understood to determine to best operating conditions for this synthesis.

ACKNOWLEDGMENTS

We are especially grateful to Bayer, DOE and Exxon for supporting this work financially. Special thanks goes to Brett Hyndman and Tonya Slavic for assistance with the lab work and to Exxon's Joe Sissano for help during the initial stages of this work.

REFERENCES

1. M. McHugh, V. Krukonis, Supercritical Fluid Extraction, Principles and Practice, Butterworths: Boston. (1986)
2. T.A. Hoefling, R. M. Enick, E.J. Beckman, *J. Phys. Chem.*, **95**, 7127. (1991)
3. J.M. DeSimone, Z. Guan, C.S. Elsbernd, *Science*, **257**, 945. (1992)
4. T.A. Hoefling, R.R. Beitle, R. M. Enick, E.J. Beckman, *Fluid Phase Equilibria*, **83**, 203. (1993)
5. D.A. Newman, T.A. Hoefling, R.R. Beitle, E.J. Beckman, R.M. Enick, *J. Supercrit. Fluids*, **6**, 205-210. (1993)
6. S. Inoue, H. Koinuma and T. Tsuruta, *Polymer Letters*, 7, 287-292. (1969)
7. S. Inoue, H. Koinuma and T. Tsuruta, *Polymer Journal*, **2**, No. 2, 220-224. (1971)
8. S. Inoue, H. Koinuma, Y. Yokoo and T. Tsuruta, *Die Makromolekulare Chemie*, **143**, 97-104. (1971)
9. S. Inoue, M. Kobayashi, H. Koinuma and T. Tsurata, *Die Makromolekulare Chemie*, **155**, 61-73. (1972)
10. M. Kobayashi, S. Inoue and T. Tsurata, *Journal of Polymer Science: Polymer Chemistry Edition*, **11**, 2383-2385. (1973)
11. R.J. De Pasquale, *J.C.S. Chem. Commun.*, 157-158. (1973)
12. S. Inoue, T. Tsurata, T. Takada, N. Miyazaki, M. Kambe and T. Takaoka, *Applied Polymer Symposium*, **26**, 257-267. (1975)
13. S. Inoue, *CHEMTECH*, **Sept.**, 588-594. (1976)
14. T. Tsuda, Y. Chujo and T. Saegusa, *Chem. Commun.*, 415-416. (1976)
15. W. Kuran, S. Pasynkiewicz, J. Skupińska and A. Rokicki, *Die Makromolekulare Chemie*, 177, 11-20. (1976)
16. W. Kuran, S. Pasynkiewicz and J. Skupińska, *Makromol. Chem.*, 177, 1283-1292. (1976)
17. T. Hirano, S. Inoue and T. Tsuruta, *Makromol. Chem.*, 177, 3245-3253. (1976)
18. W. Kuran, S. Pasynkiewicz and J. Skupińska, *Makromol. Chem*, **178**, 47-54. (1977)
19. K. Soga, K. Uenishi, S. Hosoda and S. Ikeda, *Makromol. Chem.*, **178**, 893-897. (1977)
20. W. Kuran, S. Pasynkiewicz and J. Skupińska, *Makromol. Chem.*, **178**, 2149-2158. (1977)
21. K. Soga, K. Hyakkoku, K. Izumi and S. Ikeda, *Journal of Polymer Science: Polymer Chemistry Edition*, **16**, 2383-2392. (1978)
22. K. Soga, K. Hyakkoku and S. Ikeda, *Makromol. Chem.*, **179**, 2837-2843. (1978)
23. K. Soga, K. Uenishi and S. Ikeda, *Journal of Polymer Science: Polymer Chemistry Edition*, **17**, 415-423. (1979)
24. K. Soga, etal., *Polymer J.*, **13**(4), 407-410. (1981)
25. G. Rokicki, W. Kuran and B. Pogorzelska-Marciniak, *Monatshefte für Chemie*, **115**, 205-214. (1984)
26. U.S. Pat 4,783,445, H.-N. Sun (to Arco Chemical Co.). (Nov. 8, 1988)
27. U.S. Pat. 5,026,676, S. Motika, T. Pickering, A. Rokicki, K. Stein (to Air Products and Chemicals, Inc., Arco Chemical Co., Mitsui Petrochemical Industries Ltd.). (June 25, 1991)
28. L.-B. Chen, *Macromol. Chem., Macromol. Symp.*, **59**, 75-82. (1992)
29. W. Kuran and T. Listoś, *Macromol. Chem. Phys.*, **195**, 977-984. (1994)
30. (a) D.J. Darensbourg, *Abstract and presentation from the "Third International Conference on Carbon Dioxide Utilization (ICCDU III)"*, U. of Oklahoma, April 30-May 4, 1995. (b) D.J. Darensbourg and M.W. Holtcamp, *Macromolecules*, **28**, 7577-7579, 1995.
31. F. A. Adamsky, E.J. Beckman, *Macromolecules*, **27**, 312. (1994)

TABLE 1: EFFECT OF TEMP. ON POLYCYCLOHEXENE CARBONATE FORMATION
Conditions: P=2000 psig, *t=24 hours*, $N_{Zn}/N_{C.O.}=3.3x10^3$

T (°C)	CONV.	SEL.	% CAR. (NMR)	$X_{c.o.}$	g POLY / g Zn	M_w ($x 10^{-3}$)	M_w/M_n
60	5.7%	0.2%	58%	0.11	1.30	—	—
70	11%	6.3%	92%	0.12	41.1	120	27
80	28%	22%	81%	0.15	146	232	11
80	30%	17%	89%	0.13	116	109	5.8
90	-----	9.1%	87%	0.15	61.5	114	6.6
90	11%	0.08%	80%	0.16	0.53	104	5.0
100	57%	30%	95%	0.16	203	174	14
100	79%	68%	93%	0.16	457	109	6.4
110	65%	50%	97%	0.18	328	195	12
110	84%	69%	96%	0.16	440	68.1	4.2
120	75%	61%	94%	0.20	406	56.2	3.6
130	60%	45%	87%	0.21	307	43.4	3.0
172	50%	2.4%	29%	0.24	15.8	9.8	2.4

TABLE 2: EFFECT OF PRES. ON POLYCYCLOHEXENE CARBONATE FORMATION
Conditions: *t=24 hours*; T=110°C; $N_{Zn}/N_{C.O.} = 3.3x10^{-3}$

P (psig)	CONV.	SEL.	% CAR. (NMR)	$X_{c.o.}$	g POLY / g Zn	M_w ($x10^{-3}$)	M_w/M_n
1000	70%	50%	86%	0.20	329	59.1	3.7
2000	75%	57%	91%	0.10	408	60.4	5.4
3000	63%	45%	83%	0.061	297	74.1	4.4
3000	57%	37%	92%	0.062	254	66.2	4.9
4000	32%	17%	89%	0.049	114	89.6	5.6
4000	28%	14%	96%	0.050	115	60.8	4.1
5000	49%	32%	87%	0.047	229	55.8	3.0
5000	30%	7%		0.040	40.2	38.5	2.7

TABLE 3: EFFECT OF $X_{c.o.}$ ON POLYCYCLOHEXENE CARBONATE FORMATION
Conditions: 2000 psig, *t=24 hours*; T=110°C; $N_{Zn}/N_{C.O.} = 3.3x10^{-3}$

$X_{c.o.}$	CONV.	SEL.	% CARB. (NMR)	M_w ($x10^{-3}$)	M_w/M_n	g POLY / g Zn
0.28	82%	65%	96%	106	3.3	421
0.18	65%	50%	97%	195	12	328
0.16	84%	69%	96%	68.1	4.2	440
0.10	75%	57%	91%	68.7	5.1	408
0.023	59%	4.8%	65%	23.8	1.8	35.0

PHOTOELECTROCHEMICAL REDUCTION OF CO_2 USING SILICATE ROCK POWDER SUSPENDED IN WATER

Kiyohisa Ohta, Youko Ohguchi, Satoshi Kaneco, and Takayuki Mizuno
Dept.of Chem. for Materials, Fac.of Eng.,
Mie Univ., Mie, Tsu, 514, JAPAN

Keywords: Photoelectrochemical reduction of CO_2, andesite powder, methanol and formic acid.

INTRODUCTION

Until now, numerous investigators have reported chemical fixation of carbon dioxide, such as electrochemical, photochemical and photoelectrochemical reductions (1-5). In these methods, relatively, a few studies on the photoelectrochemical conversion of CO_2 have been reported.

We have recently presented a photochemical reduction of carbon dioxide and hydrogen formation by using andesite sands as a photocatalyst under sunlight irradiation (6). At ambient temperature and atmospheric pressure, 6.5×10^{-2} ml g^{-1} methane and 7.0×10^{-2} ml g^{-1} of hydrogen were formed from carbon dioxide and water on the andesite.

This report presents the photoelectrochemical reduction of CO_2 using silicate rock (andesite) powder suspended in water.

EXPERIMENTAL

For photoelectrochemical reduction of CO_2, a home-made cell (Figure 1) with a platinum anode (30 mm x 10 mm i.d., 99.95% purity) and a copper cathode (30 mm x 10 mm i.d., 99.95% purity) was used. The cathode compartment was separated from the anode compartment with a Nafion 115 membrane. 0.1 M $KHCO_3$ solution as an electrolyte was placed in the cell. After andesite rock powder was added to the catholyte, carbon dioxide was bubbled into the catholyte for 5 min at a rate of 40 ml min^{-1}. Carbon dioxide in the cell was reduced at a constant potential, which was controlled by a potentio-galvanostats (Model HA-501, Hokuto Denko, Japan), as irradiating light. During the reduction, andesite rock powder was dispersed by stirring. A Xe lamp (Ushio Tech. Xebex Xe-ARC 160, 1kW) was used for the illumination. The electrochemical reduction of CO_2 was investigated at -1.0 to -2.5 V vs.SCE and at 0 to 60°C. The Faradaic efficiency of products was calculated from 50 C charge-passed at each potential. Products were analyzed by gas and liquid chromatography.

Andesite rocks was shattered in an iron mortar and then the powder was sieved by stainless sieves to get 31.8-24.5 mm size. After washing with 1M-nitric acid and distilled-deionized water, the rock powder was dried by heating at 150 °C for 8 h in an oven. Trace contaminants (hydrocarbon, carbon monoxide, hydrogen, etc.) in carbon dioxide gas used in this study were checked.

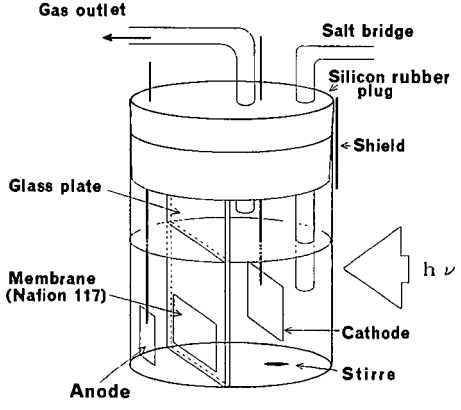

Figure 1. Cell for photoelectrochemical reduction.

RESULTS AND DISCUSSION

In previous study (6), it was found that under sunlight irradiation methane and hydrogen were formed from carbon dioxide and water on andesite sands at ambient temperature and atmospheric pressure. However, it needed the time of >10 h to obtain these products by the photochemical reduction. It was too long to obtain an adequate quantity of the products. Therefore, a photo-electrochemical reduction of CO_2 using andesite powder suspended in water was performed. First, the cyclic voltammograms in the electrolyte suspended andesite powder were measured with and without the irradiation. From the voltammograms, it was found that the electrochemical reduction of CO_2 occurred at -1.0 to -2.5 V vs.SCE and by the irradiation the current density increased about 1.5 times that obtained under no illumination.

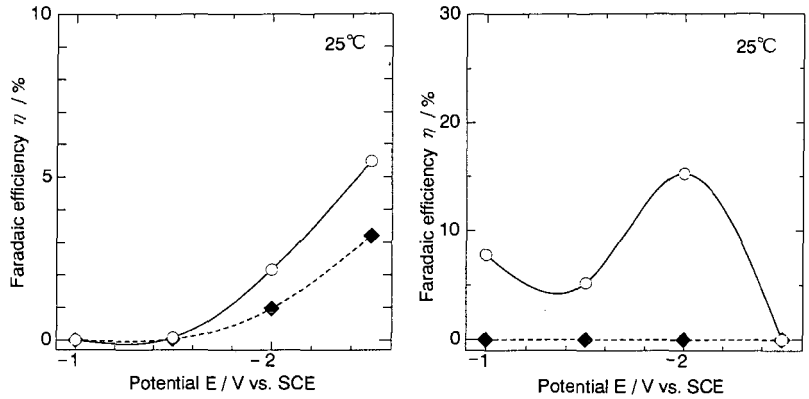

Figure 2. Faradaic effiencies of CH_2 formation at Cu electrode saturated with CO_2 in 0.1 M $KHCO_3$. ○ : Andesite suspension and illumination, ◆: No andesite
Figure 3. Faradaic effiencies of CH_3OH formation at Cu electrode saturated with CO_2 in 0.1 M $KHCO_3$. ○ : Andesite suspension and illumination, ◆: No andesite

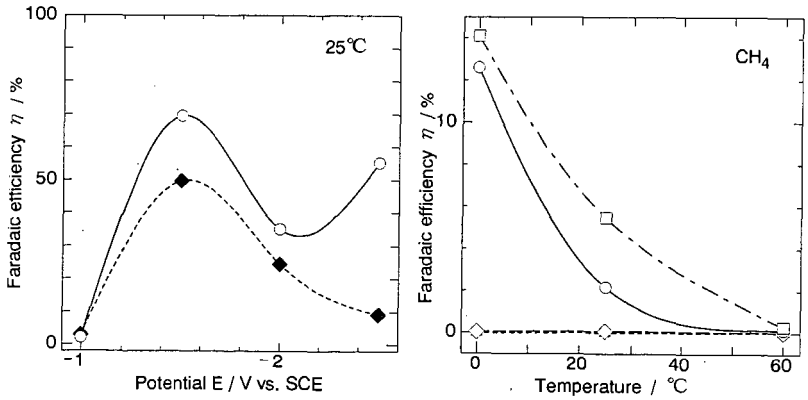

Figure 4. Faradaic effiencies of H_2 formation at Cu electrode saturated with CO_2 in 0.1 M $KHCO_3$. ○ : Andesite suspension and illumination, ◆ : No andesite
Figure 5. Effect of temperature on the effiency at Cu electrode saturated with CO_2 in 0.1 M $KHCO_3$ (Andesite suspension and illumination).
△ : −1.0 V, ◇ : −1.5 V, ○ : −2.0 V, □ : −2.5 V,

Effects of illumination and potential

The effects of illumination and potential on Faradaic efficiency of products were investigated at 25°C. The products were

hydrogen, methane, methanol, ethylene, carbon monoxide and formic acid. By illumination, the amounts of methane, methanol and hydrogen formed were larger than those of these products obtained without andesite, as shown in Figure 2-4. Furthermore, the Faradaic efficiencies for these products under irradiation were large, compared with the efficiencies obtained in the case of andesite addition and no illumination. These facts prove the large effect of andesite addition and illumination.
However, by the addition of andesite and the illumination the formations of ethylene, carbon monoxide and formic acid decreased. The Faradaic efficiency of methane increased as the potential became negative. The outstanding effect of andesite and illumination was observed in the case of methanol formation. The maximum was obtained at -2.0 V. The maximum hydrogen generated at -1.5 V.
At 0°C, the illumination and andesite affected on the formations of hydrogen, carbon monoxide and formic acid. Especially, the effect was outstanding for the formation of formic acid at -2.0 V. At 60°C, the effect by the addition of andesite and the illumination was not observed the formation of those products except for hydrogen formation.

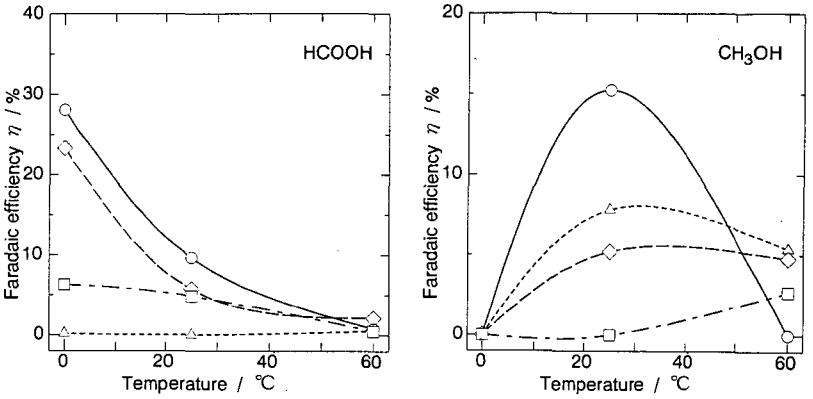

Figure 6. Effect of temperature on the effiency at Cu electrode saturated with CO_2 in 0.1 M $KHCO_3$ (Andesite suspension and illumination).
△ : -1.0 V, ◇ : -1.5 V, ○ : -2.0 V, □ : -2.5 V,
Figure 7. Effect of temperature on the effiency at Cu electrode saturated with CO_2 in 0.1 M $KHCO_3$ (Andesite suspension and illumination).
△ : -1.0 V, ◇ : -1.5 V, ○ : -2.0 V, □ : -2.5 V,

Effects of temperature
The effect of temperature on Faradaic efficiency of products was investigated at -1.0, -1.5, -2.0 and -2.5 V. The results for methane, methanol, and formic acid are shown in Figure 5-7. The Faradaic efficiencies of methane, ethylene and formic acid decreased with temperature. The maximum formation of methanol was obtained at 25°C. In the case of monoxide formation, the maximum efficiency was observed at 0°C and -2.0 V and the formation was almost independent of temperature. Hydrogen formation increased with temperature. The efficiency of hydrogen formation was beyond 100 % at 60°C.
Under optimal experimental conditions, the Faradaic efficiencies of hydrogen, methane, methanol, ethylene, carbon monoxide, and formic acid were 120 % at -2.5 V and 60°C, 14 % at -2.5 V and 0°C, 15 % at -2.0 V and 25°C, 2.7 % at -2.5 V and 0°C, 0.88 % at -2.0 V and 0°C, and 28 % at -2.0 V and 0°C, respectively.

In described above, the effects of light irradiation and the addition of andesite are evident. Accordingly, X-ray diffraction signal of the andesite was measured for getting a key of the mechanism. The components of the andesite were multiple oxides consisting of SiO_2, TiO_2, Al_2O_3, Fe_2O_3, FeO, MnO, MgO, CaO, Na_2O, K_2O, H_2O, P_2O_5, etc. Therefore, the reducing power may be due to an active site such as TiO_2 on the andesite and the semiconductivity. Something like free electron generated on

andesite probably gives desirable electrochemical reduction of CO_2. However, the detail mechanism could not be made clear.

Consequently, it was found that this method with andesite had effect on formic acid and methanol formation and hydrogen formation by the catalyzed photoelectric dissociation of water. Since silicate rock catalyst such as andesite is easy and cheep to get, the carbon dioxide reduction system developed may be able to have the economic feasibility in large scale hydrogen, methane, formic acid and methanol productions.

ACKNOWLEDGMENTS: This work was supported financially by the Ministry of Education of Japan and the Research Foundation for the Electrotechnology of Chubu.

REFERENCES

(1) Collin,J.P.;Sauvage,J.P. *Coordination chem.rev.* **1989**, 93, 245.
(2) Ayers,W.M.,Editor, *Catalytic activation of carbon dioxide, ACS Sym.ser.*, 363, pp.1-204, ACS, Washington,DC, 1988: Rethwisch,D.G.;Dumesic,J.A. *ibid.*, Chap.8.
(3) Inoue,T.;Fujishima,A.;Konishi,S.;Honda,K. *Nature*, **1979**, 227, 637.
(4) Taniguchi,I. *in Modern aspects of electrochemistry*, Plenum: New York, 1989; Vol 20, pp. 327-400.
(5) (a) Halmann,M. In "Energy resources through photochemistry and catalysis"; Gratzel,M., Ed.; Academic Press: New York, 1983; Chap.15. (b) Halmann,M.;Aurian-Blajeni,B. *Proc.of the 2nd European Commun.Photovolt.Sol.Energ.Conf.*, **1979**, 682.
(6) Ohta,K.;Kawamura,T.;Kuroda,S;Mizuno,T. *Proc.Electrochem.Soc.* **1994**, 93-18, 85.

CO_2 UTILIZATION BY GAS DISCHARGES

Kamel H. Fotouh and Changjun Liu
Department of Chemical Engineering, Prairie View A&M University
Texas A&M University System, Prairie View, TX 77446

Keywords: CO_2 Utilization Gas Discharge Methane Conversion

INTRODUCTION

Carbon dioxide is the end product to complete combustion of all fossil fuels. The generation of carbon dioxide is the primary cause for the greenhouse effect. However, carbon dioxide is a potential carbon source. To utilize such a plentiful carbon source, it has been considered carbon dioxide as a feedstock for organic synthesis of carbonyl- and carboxyl-containing compounds or as an oxidant for oxidative synthesis of more valuable organics (Krylov and Mamedov, 1995; Xu and Moulijn, 1996). The heterogeneous catalysis has been extensively thought to be the desirable technique for CO_2 utilization. Especially, for the oxidative synthesis, the radical reactions have been demonstrated (Nishiyama and Aika, 1990). But, a difficulty faced in the regular catalytic conversion of carbon dioxide to usable chemicals is the industrial CO_2 emissions containing "poisonous" gases, e.g., SO_x. Although gas "scrubbing" is usually conducted first to eliminate the poisonous gases from flue gases, trace SO_x can still remain in the gases. Regarding this, some alternative technology should be investigated. The previous researches on the oxidative conversion of methane have indicated that the plasma radical reactions are quite similar to the heterogeneous catalytic radical reactions (Oumghar *et al.*, 1995), but the plasma way has a higher efficiency in initiating radicals. Reduction of CO_2 from flue gases using a corona discharge at the same time with reduction of SO_x and NO_x has also been performed by Higashi *et al.* (1985) and Xie *et al.*(1991). Maezono and Chang (1990) tried to produce the commercial CO by reduction of CO_2 from combustion gases using dc corona torches. The plasma promoted catalytic reduction of CO_2 from flue gases has also been reported (Jogan *et al.*, 1993). The oxidative synthesis of aldehydes from methane and carbon dioxide by gas discharges has been reported as early as 1930s (Finlayson, 1935). A gas mixture containing 58% methane and about 33.3% carbon dioxide was used for such a synthesis in the temperature range of 25°C to 500°C. No further mechanism analysis was reported. Exactly, carbon dioxide can contribute one of its two oxygen atoms for oxidative synthesis by electronic dissociative attachment reactions:

$$e + CO_2 \rightarrow CO + O^- \quad (1)$$

or

$$e + CO_2 \rightarrow CO + O + e \quad (2)$$

The O^- and some metastable states of O have been well-known as active oxygen species for oxidative synthesis of organics (Oumghar, et al., 1995). Gas discharge (glow, corona, arc and silence discharges) is an abundant resource of free radicals. The potential to develop a technique, in which oxidative synthesize of high-valued hydrocarbons together with removal of CO_2, NO_x and SO_x is very economically attractive. The by-product of such a technique is carbon monoxide, which can be also applied for organic synthesis, e.g., F-T synthesis. In this paper, the results of oxidative methane conversion to ethane and ethylene using CO_2 as an oxidant by streamer corona discharge is reported.

EXPERIMENTAL APPARATUS AND PROCEDURE

The quartz tube reactor (with an I.D. of 6 mm and a tube length of 600 mm) for the streamer corona discharge synthesis consists of two electrodes. The top wire electrode and the lower cylindrical hollow electrode with a diameter 1 mm less than the inner diameter of the quartz tube is shown in figure 1. The gap between the two stainless steel electrodes is 12 mm. The feed gas flow enters the upstream wire electrode and exits at the downstream one. The streamer corona discharge is generated between these two electrodes by an AC generator, with which a high voltage transformer is applied. The AC voltage provides an easy way to generate the streamer discharges, which takes place only when the voltage reaches a sufficiently high level during each half cycle, as shown in figure 2. In the discharge volume, the interaction between accelerated charged particles (i.e., electrons and ions) and other chemical species (i.e., molecules and radicals) takes place. This interaction leads to the formation of new chemical species, like ethane, ethylene and carbon monoxide.

(Figures 1 and 2)

The feed gases CO_2 ,CH_4 and the dilution gas Helium are adjusted by controlling the flow rate. The effluent product gases run through a condenser to eliminate the moisture from the gas mixture. This gas mixture from condenser is then analyzed by an on line gas chromatography (HP5890) using a TCD detector. The gas pressure inside the reactor is slightly above the atmospheric pressure. All the experiments are initiated at room temperature (around 25°C). No attempt has been made to heat or cool the reactor externally. The gases from the gas cylinders

are mixed and then fed into the quartz reactor where a streamer corona discharge is generated. The input power to the high-voltage transformer is measured by recording the current and voltage.

With such an experimental device, the methane and carbon dioxide conversions are defined as:

Methane conversion = (moles of methane consumed/moles of methane introduced) * 100%

CO_2 conversion = (moles of CO_2 consumed/moles of CO_2 introduced) * 100%

The yield of C_2 hydrocarbons is as following:

Yield of ethane = 2 * (moles of ethane formed)/(moles of methane consumed) * 100%

Yield of ethylene = 2 * (moles of ethylene formed)/(moles of methane consumed) * 100%

RESULTS

All the corona discharge reactions are started at room temperature. The gas temperature reaches 200°C to 500°C depending on the different reaction conditions. The reaction temperature is measured by an insulated copper-constantant thermal couple situated upstream or downstream of reaction zone. The detail of such temperature measurements with plasma or electric field has been discussed elsewhere (Kingston and Jassie, 1988; Oumghar *et al.*, 1994).

The experimental results are shown in figure 3 to 6. Figure 3 shows the effect of applied voltage. When the applied voltage reaches 3.75kV, the gas discharge is initiated. The discharge reactions lead to the change in compositions. From figure 3, the reaction rate of methane and carbon dioxide have significant variations above 4.4 kV of the applied voltage. The composition of ethane increases with increasing in the applied voltage at the very beginning and then decreases, while the composition of ethylene increases slightly with increasing in the applied voltage. Figure 3 shows a significant increase in the composition of carbon monoxide. This suggests that part of C_2 products are destroyed to form CO by the increasing voltage. According to figure 3, it is not suggested that high voltage should be applied if the favorable C_2 products can not be moved out of the discharge reactor quickly.

(Figures 3, 4, 5 and 6)

The effect of CO_2 /CH_4 ratio is shown in figure 4. From reactions (1) and (2), more CO_2 in the feed will generate more active oxygen species for methane conversion. This has been demonstrated in figure 4. The conversion of CO_2 and CH_4 monotonically increase with increasing amount of carbon dioxide when the partial pressure of methane is kept constant. The yield of ethane decreases with increasing CO_2 / CH_4 ratio. This means ethane has been converted to form some different species. The yield of ethylene shows a maximum when the CO_2 / CH_4 ratio is equal to 2. The decrease in yield of ethylene suggests that an increase in the amount of the oxidant, CO_2 , leads to the complete oxidation of hydrocarbons.

Figure 5 shows the effect of flowrate on the discharge reactions. The high flowrate results into a short residence time. The experimental results demonstrate that a higher yield of ethylene occurs at the lower flowrate or longer residence time. The conversion of CO_2 and CH_4 and the yield of ethylene decrease with the increase in the flowrate, but the yield of ethane increases. This suggests that ethane is a primary product and ethylene is the secondary product, which is formed by the oxidative of dehydrogenation of ethane. The same conclusion has also been drawn from figures 3 and 4, and can be further confirmed by the effect of frequency.

The streamer corona discharge generated by AC electric field is characterized with the temporary DC corona discharge, established within each half-cycle, as shown in figure 2. The effect of frequency is thought to be on the duration of each temporary DC corona discharge. Experimental results shown in figure 6 shows that the long duration (low frequency) is disfavorable for the yield of ethane and ethylene. The yield of ethane decreases with decreasing the frequency, but the yield of ethylene shows a maximum at frequency of 70Hz. This suggests that ethane is converted to ethylene at the lower frequencies, while at too low frequencies (less than 70 Hz) ethylene is also converted and complete oxidation occurs. The largest change in conversion of CO_2 and CH_4 is observed at the frequency of 70 Hz.

DISCUSSION

Here, we have experimentally confirmed that the streamer corona discharge oxidative coupling of methane using CO_2 as an oxidant is much more effective than the heterogeneous way, by which the yield of C_2 hydrocarbons was limited to less than 9% because of the difficulty in activation of catalysts (Nishiyama and Aika, 1990; Xu and Moulijn, 1996). This can be explained from the thermodynamics. The total synthesis reactions (Krylov, 1992):

$$2CH_4 + CO_2 = C_2H_6 + CO + H_2O, \quad \Delta G°_{1073K} = 35 \text{ kJ/mol} \qquad (3)$$

and

$$2CH_4 + CO_2 = C_2H_4 + 2CO + 2H_2O, \quad \Delta G°_{1073K} \sim 0 \text{ kJ/mol} \qquad (4)$$

Both these reactions are a little thermodynamically unfavorable, especially the first one. A high reaction temperature is expected for these two reactions with limited C_2 yield, if the regular catalytic way is employed. Other thermodynamically favorable reactions of CO_2 and CH_4, e.g., syngas (CO + H_2) formation, will compete with these C_2 formation reactions such regular catalytic techniques at sufficiently high temperatures. Considering this, the plasma can be

applied for enhancing the competitiveness of reactions (3) and (4). Also, from the thermodynamic point of view, the plasma will be useful for two classes of systems (Veprek, 1972): systems in which the reaction is allowed thermodynamically but hindered kinetically, and systems with which the reaction does not proceed due to an extreme chemical equilibrium constant in the absence of plasma. Reactions (3) and (4) would be covered by the first system. For this kind of reactions, a weak discharge, e.g., streamer discharge, can promote greatly the reactions. Such weak discharge promoted reactions are characterized themselves with low gaseous temperature and high electronic temperature. And, as the reaction temperature was experimentally measured to be less than 500°C, and according to researches on methane pyrolysis (Holmen *et al.*, 1995), no direct methane conversion was generated under 1000°C, therefore we may exclude the possibility of methane pyrolysis to higher hydrocarbons during our experiments. Basically, in our discharge system, a streamer corona discharge is applied to initiate the reactions. The streamer discharge, as mentioned before, has been known to produce electrons with electron energy of about 6eV (Eliasson and Kogelschatz, 1991), and such a low energy is insufficient to activate the kinetically inert methane molecule which possesses an appearance potentials of ions of around 12eV (Sorensen, 1995) although methane was passed directly through the discharge. The initiation reactions are thought to be the streamer corona-induced plasma decomposition of CO_2 as described in reactions (1) and (2). Such formed oxygen species, O^- or O with some excited state or metastable state is very active for the coupling reactions and can lead to the products observed. The main reactions responsible for ethane, ethylene and carbon monoxide are as follow:

a. Methane Radical Formation:

$$CH_4 + O^- \rightarrow CH_3\bullet + OH^- \quad (5)$$

$$CH_4 + O \rightarrow CH_3\bullet + OH \quad (6)$$

b. Ethane Formation:

$$CH_3\bullet + CH_3\bullet \rightarrow C_2H_6 \quad (7)$$

c. Ethylene Formation:

$$C_2H_6 + e \rightarrow C_2H_5\bullet + H \quad (8)$$

$$C_2H_6 + O^- \rightarrow C_2H_5\bullet + OH^- \quad (9)$$

$$2C_2H_5\bullet \rightarrow C_2H_4 + C_2H_6 \quad (10)$$

$$C_2H_5\bullet + CH_3\bullet \rightarrow C_2H_4 + CH_4 \quad (11)$$

d. H_2O Formation:

$$2H + O \rightarrow H_2O \quad (12)$$

$$2OH \rightarrow O + H_2O \quad (13)$$

$$2OH^- \rightarrow O^{2-} + H_2O \quad (14)$$

e. CO Formation:

$$CH_x\bullet + O \rightarrow HCHO + H \quad (15)$$

$$HCHO + O \rightarrow OH + CHO \quad (16)$$

$$CHO + O \rightarrow OH + CO \quad (17)$$

CONCLUSION

CO_2 formation is a significant cause of greenhouse effect. Methane contributes also to the greenhouse effect. The combination of conversion of methane and carbon dioxide to more useful chemicals has potential industrial applications. Regarding these, we presented a streamer discharge system to oxidatively convert methane to ethylene using CO_2 as an oxidant. The results achieved right now shows the following:

(1) Conversions of methane and carbon dioxide and yield of ethylene increase with increasing input voltage and increasing CO_2 amount in the feed. The increasing CO_2 composition, however, will reduce the yield of C_2 hydrocarbons.

(2) The low flowrate leads to large conversions of methane and carbon dioxide and high yield of ethylene.

(3) The low frequency results in large conversions of methane and carbon dioxide but the maximum yield of ethylene occurs at the frequency of 70 Hz.

(4) All the experiments right now come to an end that ethylene is a second product.

REFERENCES

Eliasson B. and Kogelschatz U. Nonequilibrium volume plasma chemical processing. *IEEE Trans. on Plasma Sci.*, 19, 1063., 1991

Finlayson D. Manufacture of aliphatic aldehydes. US Patent 1,986,885

Higashi M., Sugaya M., Ueki K. and Fujii K. Plasma processing of exhaust gas from a diesel engine vehicle, in *Proc. Int. Conf. on Plasma Chem.*, 2, 366., 1985.

Holmen A., Olsvik O. and Rokstad O.A. Pyrolysis of natural gas: chemistry and process concepts. *Fuel Processing Tech.* 42, 249.,1995Jogan K., Mizuno A., Yamamoto T. and Chang J.-S. The effect of residence time on the CO_2 reduction from combustion flue gases by an AC ferroelectric packed bed reactor. *IEEE Trans. on Industry Applications*, 29(5), 876., 1993.

Kingston H.M. and Jassie L.B. Monitoring and predicting parameters in microwave dissolution. In: *Introduction to Microwave Sample Preparation.* Kingston H.M. and Jassie L.B., ed., ACS, Washington, DC, 1988.
Krylov, O.V. Methods for increasing the efficiency of catalysts for the oxidative condensation of methane, *Russian Chem. Rev.*, 61, 851.,1992.
Krylov O.V. and Mamedov A.Kh. Heterogeneous catalytic reactions of carbon dioxide. *Russian Chemical Reviews*, 64(9), 877., 1995.
Lee J. and Grabowski J.J. Reactions of the atomic oxygen radical anion and the synthesis of organic reactive intermediates. ***Chem. Rev.***, 92, 1611.,1992
Maezono I. and Chang J.-S. Reduction of CO_2 from combustion gases by dc corona torches, *IEEE Trans. on Industry Applications*, 26(4), 651., 1990.
Nishiyama T. and Aika K.-I. Mechanism of the oxidative coupling of methane using CO_2 as an oxidant over PbO-MgO. *J. of Catalysis*, 122, 346., 1990.
Oumghar A., Legrand J.C., Diamy A.M. and Turillon N. Methane conversion by an air microwave plasma. *Plasma Chemistry and Plasma Processing*, 15(1), 87., 1995.
Oumghar A., Legrand J.C., Diamy A.M., Turillon N. and Ben-Aïm R.I. A kinetic study of methane conversion by a dinitrogen microwave plasma. *Plasma Chemistry and Plasma Processing*, 14, 229., 1994.
Sorensen S.L., Karawajczyk A., Stromholm C. and Kirm M. Dissociative Photoexcitation of CH_4 and CD_4. *Chem. Phys. Letter*, 232, 554.,1995
Veprek, S. Chemical Evaporation and Deposition of Solids in a non-Isothermal Plasma. *J. of Crystal Growth*, 17, 101., 1972
Xie Z., Jogan K. and Chang J.S. The effect of residential time on the reduction of CO_2 in combustion flue gases by a corona torch, in *Conf. Rec. of IEEE-IAS Meeting*, 814., 1991.
Xu X.-D. and Moulijn J.A. Mitigation of CO_2 by chemical conversion: Plausible chemical reactions products. *Energy & Fuels*, 10, 305., 1996.

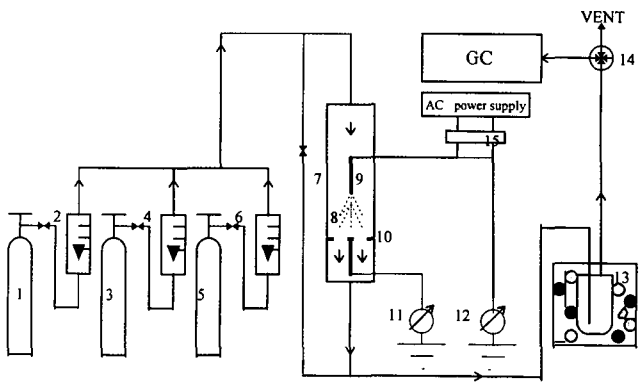

FIGURE 1 SCHEMATIC OF EXPERIMENTAL SETUP

1,3,5 Gas Cylinders	2,4,6 Flow Meter	7 Reactor	8 Streamer Discharge
9 Wire Electrode	10 Cylindrical Electrode	11 Current Meter	12 Voltage Meter
13 Condenser(with dry ice)	14 Multiway Value	15 H.V.Transformer	

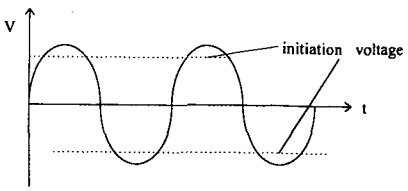

Figure 2 The AC Voltage

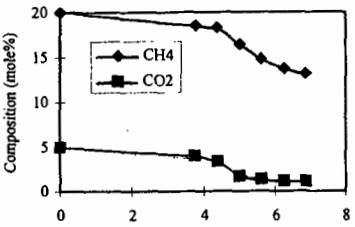

(a) Reactants

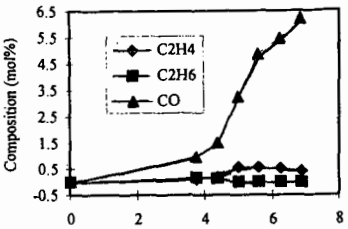

(b) Products

Figure 3 The effect of applied voltage

Flowrate : 100 ml/s Frequency: 60 Hz CO_2/CH_4: 4 (0.2 atm./0.05 atm.) Total Pressure: 1 atm

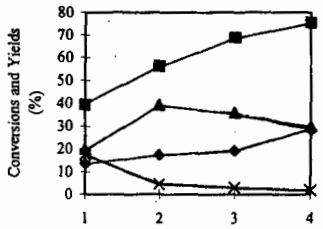

Figure 4 Effect of CO2/CH4

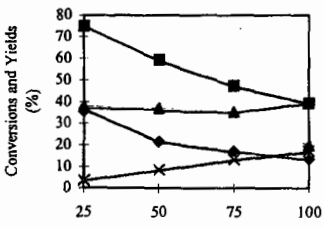

Figure 5 Effect of flowrate

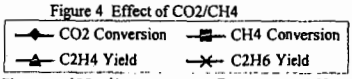

Flowrate : 100 ml/s Frequency: 60 Hz
CH_4 Partial Pressure: 0.05atm Total Pressure: 1 atm
Applied Voltage: 5.6kV

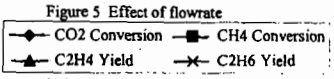

Frequency: 60 Hz Applied Voltage: 5.6kV
CO_2/CH_4: 4 (0.2 atm./0.05 atm.) Total Pressure: 1 atm

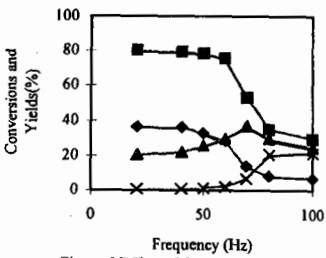

Figure 6 Effect of frequency

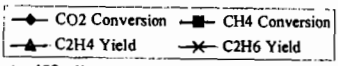

Flowrate : 100 ml/s Applied Voltage: 5.6kV
CO_2/CH_4: 4 (0.2 atm./0.05 atm.) Total Pressure: 1 atm

ACTIVATION OF CARBON DIOXIDE AS AN OXIDANT OVER ZSM-5 ZEOLITE-SUPPORTED METAL OXIDE CATALYSTS

Sang-Eon Park, Jong-San Chang, and Min Seok Park
Industrial Catalysis Research Lab., Korea Research Institute of Chemical Technology (KRICT), P.O.Box 107, Daeduck Danji, Taejeon 305-606 , Korea

Keyword: carbon dioxide as an oxidant, oxygen-deficient spinel oxides, ZSM-5 zeolite support

INTRODUCTION

Chemical fixation of carbon dioxide has been concentrated on the conversion of CO_2 with various kinds of reductants into the usable chemicals in mass(1). These are mainly based on the reduction of CO_2. As a different way, CO_2 can be considered as an oxidant. Bartholomew(2) reported that oxidizability in the gasification of coke was the following order: O_2[105] > H_2O[3] > CO_2[1] > H_2[0.003], which numbers in parenthesis indicated the relative ratios of the gasification with oxidants. CO_2 has been called as nontraditional, unusual or mild oxidant and oxygen transfer agent. In this sense, carbon dioxide could be proposed as an oxidant in the oxidative conversions of hydrocarbons.

There have been some examples of utilization of carbon dioxide as an oxidant(3-5). Krylov and Mamedov(3) have studied on the oxidative conversions of alkanes, alkenes, and alcohols with carbon dioxide over Mn oxide-based catalysts and reported that oxygen generated during CO_2 reduction might participate in both partial oxidation and dehydrogenation. Yoo *et al.*(4) showed that Fe/Mo/borosilicate catalyst could activate CO_2 which could be functioning as a promoter and co-oxidant for the gas-phase oxidation of alkylaromatics with oxygen as well. Sugino et al.(5) reported that considerable increase in the conversion of ethylbenzene was observed with an iron-loaded catalyst in the presence of carbon dioxide, which revealed that the reaction proceeded via an oxidative dehydrogenation mechanism by CO_2.

Even though ZSM-5 zeolite has favorable adsorption property for various gases, micropore structure, high surface area, and highest thermal stability among zeolites, it has been rarely applied for supporting metal oxides. However, recently a few trials for utilizing ZSM-5 zeolite as a support for metal oxides have been appeared(6). In our previous study, it was shown that ZSM-5 zeolite could play an important role as a support for the reduced KNiCa oxide in CO_2 reforming of methane(7).

Ferrite-type oxides are known as materials exhibiting ferri- or ferromagnetism as spinel oxides and oxygen deficiency in structure(8). However, catalytic application of these ferromagnetic oxides are not so much. As an example of catalyst, ferrite was reported to be active for the selective oxidative dehydrogenation of hydrocarbons(9). Recently, it was shown that oxygen-deficient ferrites or magnetite was very reactive in the decomposition of CO_2 to carbon at 300°C(10).

In this study, the oxidative transformation of hydrocarbons such as propane and ethylbenzene was investigated by using CO_2 as an oxidant over zeolite-supported spinel oxide catalysts such as ferrites or magnetite having oxygen deficiency.

EXPERIMENTAL

Zeolite-supported magnetite ($Fe_3O_{4-\delta}$) and metal-containing ferrites ($MFe_2O_{4-\delta}$, M = Ni^{2+}, Mg^{2+}) were prepared by air oxidation of aqueous suspensions of Fe(II) and M(II) mixed hydroxides in slightly alkaline solution(11). These catalysts were dried *in vacuo* at 80°C and calcined under N_2 flow at 400°C for 3h. Zeolites used as supports were NaZSM-5 (Zeocat PZ-2, Si/Al = 980) and NaY (Zeocat Z6-01-01, Si/Al = 2.4). Loading of metal oxide on all the catalysts was 1.5 or 5.0 wt.%. Zeolite-supported KNiCa oxide (0.8 wt.% K-5 wt.% Ni-12 wt.% Ca), prepared by the solid-reaction method(7), was tested in the propane conversion for comparison.

All the catalytic measurements were carried out in a fixed-bed quartz reactor (i.d., 10 mm) at atmospheric pressure. In the case of oxidative dehydrogenation of ethylbenzene with CO_2, the reaction was performed by feeding ethylbenzene into the reactor by passing CO_2 through the ethylbenzene saturator thermostated at 25°C. The condensed effluent was analyzed by FID-GC. And effluent gases were analyzed by on-lined TCD-GC. The propane conversion with CO_2 were carried out at 800°C. The reactant gas mixture consisted of carbon dioxide and propane (CO_2/C_3H_8 = 3) diluted with nitrogen was co-feeded into the reactor. The gaseous compositions of reactants and products were analyzed by on-lined TCD-GC.

RESULTS AND DISCUSSION

Reactions of propane with carbon dioxide

Four types of reactions could be occurring during propane conversion with CO_2. Each of them to a different extent on different catalysis; propane dehydrogenation by CO_2 into propylene, selective decomposition into ethylene, non-selective decomposition into methane, and deep conversion into CO and H_2, so-called reforming. The conversion of propane with carbon dioxide over zeolite-supported metal oxide catalysts was found to be conducted in an oxidative manner by looking at the products such as propylene, ethylene, methane, and CO with H_2 and water (as shown in Table 1). Two-types of activity patterns depending on the catalysts were obtained. One was catalyst system giving the oxidative dehydrogenation activity which produced olefins such as propylene and ethylene. The other was the reforming activity which produced syngas together with methane.

Even though magnetite and ferrites catalysts produced carbon directly from carbon dioxide(8), zeolite-supported catalysts were found to be effective not only for the propane dehydrogenation into olefins, but also for CO_2 activation into CO. These activities were very much dependent on metallic components in spinel oxide as well as thier loadings. For example, 1.5 wt.% $NiFe_2O_{4-\delta}$/ZSM-5 showed higher conversions of propane and CO_2 than those of 1.5 wt.% $Fe_3O_{4-\delta}$/ZSM-5 due to the high activity on the reforming of propane and non-selective CH_4 production instead of the oxidative dehydrogenation activity on ferrite-loaded catalyst. The activities of ZSM-5-supported spinel oxides such as magnetite and ferrite were strong in the formation of olefins comparing with the reduced KNiCa/ZSM-5, which was known as a good catalyst in the formation of syngas(6). This result indicated that active sites for the oxidative conversion into olefins and the reforming seemed to be different. It suggested that an active site of spinel supported catalysts was not metallic Ni, but rather oxygen defects or oxygen deficiency. Higher loading of ferrite oxides resulted in the increased propane conversion with the decreased propylene selectivity and large increase in ethylene selectivity, and attributed to rather decrease in the CO_2 conversion. In propane conversion with CO_2, carbon dioxide was considered to be dissociatively cleavaged on the oxygen-deficient sites into carbon monoxide and surface oxygen species, which could be functioning as an oxidant for the conversion of propane into olefins and syngas in an oxidative manner.

Effect of CO_2 in the dehydrogenation of ethylbenzene

The results of catalytic activities in the dehydrogenation of ethylbenezene with supported ferrite catalysts are shown in Table 2. The catalysts were used after reduction at 500°C for 1h, prior to using in the reaction. Specific activity in Table 2 indicates moles of styrene produced per mole of metal oxide in an hour. The dehydrogenation of ethylbenzene with CO_2 over hydrogen-treated ferrite catalysts produced styrene and hydrogen. Considerable activities for the reaction were observed with zeolite-supported ferrite catalysts. When the reaction was conducted under an excess of CO_2 stream, higher catalytic activity over $NiFe_2O_{4-\delta}$/ZSM-5 was obtained than in the case of a N_2 stream. Moreover, the dehydrogenation reaction over the catalyst using a N_2 stream exhibited considerable carbon deposition on the catalyst as compared to using a CO_2 stream. In addition, small amount of carbon moxide during the reaction in a CO_2 stream was detected together with small amount of water. The zeolite-type as support had also influence on the activity in production of styrene. Comparing with dehydrogenation activity, ZSM-5 zeolite for supported ferrite catalysts appeared to be more suitable to support than Y zeolite. These results showed that zeolite-supported ferrite catalysts were to be active in the dehydrogenation of ethylbenzene to styrene and their activities were enhanced due to the presence of CO_2. This indicated that the dehydrogenation reaction was enhanced by the oxidative manner due to the presence of CO_2.

Evidence of oxygen deficiency by looking at the CO_2 dissociation

The activity of CO_2 decompostion into C over H_2-treated ferrite or magnetite was found to be closely related with their oxygen deficiency(8). In order to confirm the role of oxygen deficiency of the supported spinel catalysts, the CO_2 dissociation into CO after reducing the catalysts with 5% H_2 at 500°C for 1h before putting into CO_2 pulse at 400°C. Supported-ferrite and magnetite catalysts showed significant activity of CO_2 dissociation even at lower temperature of 400°C, as presented in Table 3. In all cases, the amount of CO formed decreased greatly at initial stage and gradually at later stage with increase of the pulse numbers.

It was found that specific activities of CO formation over supported-ferrite or magnetite catalysts was much higher than those of unsupported nickel ferrite and reduced KNiCa/ZSM-5 as a reforming catalyst which was supposed to have a small oxygen deficiency. As above mentioned, the zeolite-type as support had also influence on the activity of CO formation. The activity of $Fe_3O_{4-\delta}$/ZSM-5 was almost two times higher than that of $Fe_3O_{4-\delta}$/Y with same loading of $Fe_3O_{4-\delta}$. Moreover, the lower loadings of metal oxide gave the higher specific activities. It means that dispersion of oxygen deficient sites or oxygen defects was more efficient for the CO_2 dissociation.

It was known that ferrites and magnetite materials treated with H_2 at high temperature produced oxygen deficiency(12). It was considered that their ferromagnetism were partially related with their oxygen deficiency. In this sense, ferromagnetism of zeolite-supported ferrite or magnetite catalysts and CO_2 interaction with their ferromagnetism were examined by EPR (electron paramagnetic resonance) analysis. For example, very intensive FMR (ferromagnetic resonance) signal in EPR spectrum of 5 wt.% $Fe_3O_{4-\delta}$/ZSM-5 catalyst appeared only after evacuation at 500°C for 1h. This FMR signal gave a g value of 1.9 with Δ Hpp = 1140 G (data not shown). After treatment with CO_2 at 600°C for 30 min, FMR intensities were significantly decreased. This supports that oxygen produced from CO_2 dissociation over the catalyst filled up the oxygen defect sites and resulted in the diminution of ferromagnetism.

In summary, not only oxygen from CO_2 molecule could be utilized as an oxidant but also surface design for chemisorptive CO_2 activation would be important in the heterogeneous activation of CO_2 as an oxidant. It was demonstrated that not only oxygen-deficient oxides such as ferrite amd magnetite were active in the simultaneous activation of carbon dioxide and hydrocarbons, but also ZSM-5 zeolite could be suggested as a good support for the high dispersion of these spinels.

ACKNOWLEDGEMENTS

We acknowledge the financial support by the Ministry of Environment and Ministry of Science and Technology.

LITERATURE CITED

(1) Halmann, M.M., Chemical Fixation of Carbon Dioxide, CRC, Boca Raton (1993).
(2) Bartholomew, C.H., Chem. Eng., Nov. 12, 96 (1984).
(3) Krylov, O.V. and Mamedov, A. Kh., Ind. Eng. Chem. Res., 34, 474 (1995).
(4) Yoo, J.S., Lin, P.S. and Elfline, S.D, Appl. Catal., 106, 259 (1993).
(5) Sugino, M., Shimada, H., Turuda, T., Miura, H., Ikenaga, N. and Suzuki, T, Appl. Catal., 121, 125 (1995).
(6) Simard, F., Sedran, Sepulveda, Figoli, N.S. and de Lasa, H.I., Appl. Catal. A: General, 125, 81 (1995).
(7) Chang, J.-S., Park, S.-E, Lee, K.W. and Choi, M.J., Stud. Surf. Sci. Catal. 84, 1587 (1994).; Chang, J.-S., Park, S.-E and Chon, H., Appl. Catal., in press (1996).
(8) Wohlfarth, E.P., Ferromagnetic Materials, Vol. 3, North-Holland Publishing Co., Netherlands (1982).
(9) Stobbe, D.E., van Buren, F.R., Hoogenraad, M.S., van Dillen, A.J. and Geus, J.W., J. Chem. Soc., Faraday Soc., 87(10), 1639 (1991).
(10) Tamaura, Y. and Tabata, M., Nature, 346, 255 (1990).
(11) Kanzaki, T., Nakajima, J., Tamaura, Y. and Katsura, T., Bull. Chem. Soc. Jpn., 54, 135 (1981).
(12) Togawa, T., Wada, Y., Yoshida, T. Tsuji, M. and Tamaura, Y., Mat. Res. Soc. Symp. Proc., 344, 51 (1994).

Table 1. Conversion of Propane with CO_2 over Zeolite-Supported Metal Oxide Catalysts at 800°C[a]

Catalyst	Conversion, %		Yield, %		Olefin Yield, %	Olefin/ CH_4	CO/Olefin
	C_3H_8	CO_2	C_3H_6	C_2H_4			
1.5% $Fe_3O_{4-\delta}$/ZSM-5	66.1	18.5	31.0	15.1	46.1	2.77	1.7
5% $Fe_3O_{4-\delta}$/ZSM-5	97.3	8.7	7.7	41.0	48.7	0.23	0.9
1.5% $NiFe_2O_{4-\delta}$/ZSM-5	98.4	57.8	-	14.0	14.0	0.11	17.3
5% $MgFe_2O_{4-\delta}$/ZSM-5	94.0	21.8	6.0	36.5	42.5	0.30	2.0
KNiCa/ZSM-5[b]	68.2	91.6	4.8	-	4.8	0.05	38.2

[a] Reaction Condition : 800℃, $P(C_3H_8) = 10$ kPa, $CO_2/C_3H_8 = 3$, GHSV = $2 \times 10^4 h^{-1}$.
[b] Same as Condition (a) except $CO_2/C_3H_8 = 2$; used in reaction after reduction 700°C for 1h.

Table 2. Dehydrogenation of Ethylbenzene with CO_2 over Zeolite-Supported Ferrite Catalysts at 600°C[a]

Catalyst	Styrene Yield (%)	Specific Activity[d]
$NiFe_2O_{4-\delta}$/ZSM-5	38.3	100.8
$NiFe_2O_{4-\delta}$/ZSM-5[b]	33.9	89.2
$NiFe_2O_{4-\delta}$/Y[c]	22.2	58.4
$MgFe_2O_{4-\delta}$/Y	19.2	43.3

[a] Loading of ferrites = 1.5 wt.%; W/F = 60 g-cat h/mol; CO_2/EB = 30 : 1 (mol/mol); Catalyst pretreatment: reduction at 500°C for 1h. [b] under N_2 flow without CO_2. [c] reaction at 500°C.
[d] mol of styrene/metal oxide-mol h.

Table 3. The Dissociation of CO_2 over Zeolite-Supported Metal Oxide Catalysts at 400°C[a]

Catalyst	Amount of CO formed[c] (μ mol)	Specific Activity[d]
$NiFe_2O_{4-\delta}$	1.18	2.7
1.5% $NiFe_2O_{4-\delta}$/ZSM-5	0.75	117.2
1.5% $Fe_3O_{4-\delta}$/ZSM-5	0.46	70.9
5% $Fe_3O_{4-\delta}$/ZSM-5	0.62	28.7
5% $MgFe_2O_{4-\delta}$/ZSM-5	0.49	19.6
1.5% $Fe_3O_{4-\delta}$/Y	0.24	37.0
1.5% $NiFe_2O_{4-\delta}$/Y	0.22	34.4
KNiCa/ZSM-5 [b]	1.63	19.1

[a] after reduction at 500 °C for 1h. [b] measured at 600°C after reduction at 700°C for 1h.
[c] One pulse contained 30.2 μ mol of CO_2. [d] mmol of CO/mol of metal oxide.
[e] mmol of CO/ mol of metallic Ni.

EFFECTS OF SIMULATED FLUE GAS ON GROWTH OF MICROALGAE

JOHN T. HAUCK[1], GREGORY J. OLSON[2],
STEPHANIE J. SCIERKA, MILDRED B. PERRY, AND MOHAMMAD M. ATAAI[3]

U.S. Department of Energy
Pittsburgh Energy Technology Center
P.O. Box 10940
Pittsburgh, PA 15236

[1]Carnegie Mellon Research Institute, 4400 Fifth Avenue, Pittsburgh, PA 15213
[2]Little Bear Laboratories, Inc., P.O. Box 1434, Red Lodge, MT 59068
[3]Chemical Engineering Department, University of Pittsburgh, Pittsburgh, PA 15261

Keywords: carbon dioxide, microalgae, fossil fuel combustion, SO_x, NO_x.

INTRODUCTION

Studies have demonstrated that the atmospheric carbon dioxide level is increasing on a global scale due to the emissions from increased combustion of fossil fuels. Current CO_2 emissions due to combustion of fossil fuels are estimated to be 2×10^{10} tons/yr (1). These emissions are implicated as a major contributor to the 1-2 ppm annual increase in atmospheric CO_2 concentration; the present level of atmospheric CO_2 is 360 ppm. Efforts are now under way to develop possible methods to minimize CO_2 emissions.

One method proposed for minimizing the CO_2 emissions from power plants is to grow microalgae in flue gas streams (1-7), converting CO_2 to algal biomass which could then be converted to fuels, chemicals, and foods. Algae can utilize CO_2 efficiently, yielding three to five times more biomass per land area than typical crops and terrestrial plants. Flue gas contains not only CO_2 but also oxides of sulfur and nitrogen that may be toxic to algal growth either by lowering the pH of solutions or by direct inhibition. High levels of CO_2 (10-15%) found in flue gas could also be inhibitory to algal growth.

For this work two strains of microalgae were obtained and cultured to measure their ability to fix CO_2 under realistic flue gas conditions. The selection of Chlorella vulgaris was based on previous work with various Chlorella species of microalgae for removal of CO_2 from flue gas streams (1,3). Cyanidium caldarium was selected because of its ability to thrive in an acidic environment and at slightly elevated temperatures.

Several studies of CO_2 removal using microalgae have been reported in literature (1-4), but the toxicity of the flue gas components has not been well-documented. This study identifies SO_2 as an inhibitory component of flue gas and highlights the inhibition of algal growth in the presence of SO_2 by using cultivation conditions which accelerate the rate of SO_2 absorption in cultures.

MATERIALS AND METHODS

Algal Strains and Culture Conditions

C. vulgaris strain 30581 was obtained from the American Type Culture Collection, Rockville, Maryland. The C. caldarium culture was obtained from an acidic seep in the vicinity of Frying Pan Creek north of the Norris Geyser Basin in Yellowstone National Park, Wyoming.

The C. vulgaris strain was grown on liquid algal proteose medium (8), containing 1.0 g bacto peptone (Difco) and one drop of a 1.0% $FeCl_3$ solution in 940.0 ml deionized water. In addition, the medium contained (g/L): $NaNO_3$ (0.250); $CaCl_2$ $2H_2O$ (0.033); $MgSO_4$ $7H_2O$ (0.075); K_2HPO_4 (0.075); KH_2PO_4 (0.175); NaCl (0.025). Prior to inoculation this solution was autoclaved at 121°C for 30 minutes. The pH of the final medium was adjusted to approximately 7.5 with sterile 1N NaOH.

The C. caldarium strain was grown on Allen's medium (9), which contains (g/L): $(NH_4)_2SO_4$ (1.3); KH_2PO_4 (0.28); $MgSO_4$ $7H_2O$ (0.25); $CaCl_2$ $2H_2O$ (0.07); and $FeCl_3$ $6H_2O$ (0.02). The pH was adjusted to 1.8 with 10N H_2SO_4. To this sterile autoclaved solution was added 1.0 ml of a 0.2 um filter-sterilized trace metals solution. The trace metals solution contained (g/L): Na_2EDTA (1.5); $FeCl_3$ $6H_2O$ (0.194); $MnCl_2$ $4H_2O$ (0.082); $ZnCl_2$ (0.01); $CoCl_2$ (0.004); Na_2MoO_4 (0.008).

Stock cultures of C. vulgaris were grown in 250-ml Erlenmeyer flasks under constant fluorescent illumination and static incubation at 20-25°C. Stock cultures of C. caldarium were grown at 45°C in 250-ml metal-capped baffled shake flasks under constant fluorescent illumination with shaking at 180 rpm.

Growth of the algae was monitored by measurement of change in optical density at 750 nmwith time (Perkin-Elmer Lambda 3B UV/Vis spectrophotometer). The spectrophotometric absorbance measurements of cultures were related to biomass concentration by drying cell samples, collected on preweighed membrane filters, to constant weight at 105°C. A linear

relationship between culture absorbance at 750 nm and dry weight concentration for both C. vulgaris and C. caldarium was observed. For example, an absorbance of 0.3 corresponds to dry weight concentrations of 78 mg/L and 58 mg/L for C. vulgaris and C. caldarium, respectively. Absorbance values greater than approximately 0.3 were diluted appropriately to allow for accurate spectrophotometric measurement. In addition, small samples of the cultures were withdrawn regularly and observed by phase contrast and fluorescence microscopy employing UV (365 nm) illumination to determine cell concentration and viability. Culture pH was also monitored but was not controlled.

Experimental Reactor Setup

Growth of the two strains of microalgae, when aerated with various gases, was conducted in a small bioreactor setup. These growth tests were conducted in a five-gallon aquarium maintained at either 25°C or 45°C, depending on the alga being tested. The 45°C temperature was maintained using a 300 W laboratory immersion heater. The lower temperature was maintained by the room temperature and fluorescent lighting. The water in the aquarium was circulated using a laboratory stirrer to maintain uniform temperature.

Glass bubbler tubes (40-ml, Ace Glass Company, Vineland, NJ) were used as the algal growth vessels. Five separate tubes containing 30 ml of culture solution inoculated with the various microalgae were run in most experiments. A five-port gang valve was used to split the incoming gas from the cylinder so that five bubbler tubes could be used concurrently to determine reproducibility of algal growth in each experiment. The bubbler tubes were suspended in the aquarium and illuminated continuously with fluorescent lights mounted outside two sides of the aquarium. The light intensity was measured with a digital light meter (Model D-2000, Sylvania Light Company, West Seneca, NY) and found to be approximately 6000 lux. This light intensity was not chosen based on optimum light considerations but rather was the resultant intensity achieved using standard fluorescent lights in the reactor setup.

The various gases were bubbled through the inlet tube in each bubbler, which was submerged to the bottom of the cultures. A side-arm exit port on the bubbler tubes allowed the gas to escape. The exit gas was then vented into a hood. The flow rate of the gas mixtures through each bubbler tube was measured with either a soap-film flow tube (Supelco Inc., Bellefonte, PA) or a digital flowmeter (Humonics Optiflow 520, Fairfield, CA). A flow rate of approximately 15 ml/min through each bubbler tube was used in all experiments. Several gas mixtures (Matheson Gas Products, Inc., Secaucus, NJ) were used to evaluate their effects on both algal strains.

RESULTS AND DISCUSSION

Algal Growth in Experimental Reactor Setup

Growth of both algal strains, when aerated with compressed air and a 5% CO_2-in-compressed air mixture, was investigated. The results from the 5% CO_2 exposure are shown in Figure 1. It should be noted that the biomass concentration of C. vulgaris using the 5% CO_2-in-air mixture (0.57 g cells/L) was about threefold higher than that with compressed air (0.20 g cells/L) in each bubbler tube and for C. caldarium the 5% CO_2-in-air mixture the cell concnetration showed a twentyfold increase in biomass to 3.0 g cells/L when compared with that in the presence of ambient air in shake flasks.

To determine the influence of elevated CO_2 levels found in flue gas, growth of the algal strains were monitored when aerated with a gas mixture composed of 15% CO_2, 3% O_2, balance N_2 (Figure 1). This gas composition was selected because it approximates the levels of CO_2 and O_2 in a typical flue gas stream from a coal-fired power plant. Both C. vulgaris and C. caldarium grown in 15% CO_2 exhibited a significant increase in biomass as compared to that with air aeration. The growth rate and cell yields were approximately equivalent to that obtained using the 5% CO_2 gas mixture. The ability for growth of this strain of C. caldarium using elevated CO_2 levels supports previous findings by Brock indicating enhanced growth of this alga in high CO_2 environments (10).

The ability of each alga to grow with aeration from SO_2-containing simulated flue gas mixtures was also examined (Figure 2). In a simulated flue gas consisting of 200 ppm SO_2, 15% CO_2, 3% O_2, balance N_2, the growth of C. vulgaris was completely inhibited as indicated by the steady decrease in culture absorbance from time zero. In addition, microscopic examination of samples of the cultures from the replicate bubbler tubes showed a declining cell concentration. Reduction in the number of viable algal cells was also suggested first by a decrease, and finally an absence, of UV-induced fluorescence. In contrast to C. vulgaris, C. caldarium initially exhibited some growth in the simulated flue gas containing SO_2 (Figure 2). It should be noted that this growth was approximately ca. 130 times less than that observed in an enriched CO_2 atmosphere. The different patterns of inhibition for the two algae depends to some extent on the values of optimum pH for their growth relative to the final culture pH.

The change in pH of five replicate bubbler tubes as a function of gas exposure time in Figure 3. A significant decrease in pH from 7.3 to 2.3 was observed for C. vulgaris. The

effect of the simulated flue gas on the pH was less pronounced for C. caldarium cultures. Upon introduction of the simulated flue gas, the pH was lowered to ca. 1.3 which is within the optimal range for growth of C. caldarium. Thus, the lowering of the pH by the flue gas does not inhibit growth of this alga but rather can provide the acidic environment needed for its growth. The growth inhibition of C. caldarium may have resulted from exposure to the SO_2 or some hydrolysis product.

The drop in pH, caused by the solubility of SO_2 in aqueous solutions, was particularly evident in the initially neutral pH cultures of C. vulgaris. Thus, inhibition of C. vulgaris appears to have resulted from the low pH created relative to the optimal value of about pH 7, since the growth medium was not effectively buffered to prevent acidification. The SO_2 in the simulated flue gas almost certainly had a negative effect on the growth of this alga just as was shown for C. caldarium. However, this was not proven in this study and further experiments using buffered media are needed to determine if the SO_2 itself is toxic to C. vulgaris.

Determination of Possible Growth Inhibitors

FTIR spectrophotometric analysis of the simulated flue gas indicated that no measurable amounts of contaminants, in particular the presence of SO_3 or CO. This indicates that SO_2 or an aqueous reaction product of SO_2 is the toxic agent responsible for inhibition. This is particularly evident with C. caldarium; growth occurs initially, but is inhibited after 20 hours. This pattern would be consistent with the accumulation of dissolved SO_2 or an aqueous oxidation product which occurs due to the high solubility of SO_2 in water (11).

To test this hypothesis one of the replicate bubbler tubes inoculated with C. caldarium was equipped with a "pre-bubbler" tube filled with deionized water. This pre-bubbler served as a scrubber for the flue gas prior to the gas being bubbled through the experimental culture tube. Initially, good growth occurred, similar to that when aerated with the 15% CO_2 gas mixture lacking SO_2, but inhibition prevailed at about two days (Figure 4). Apparently, the SO_2 is accumulated initially in the pre-bubbler solution, decreasing the concentration of SO_2 entering the experimental growth tube. The pre-bubbler tube delayed inhibition of the culture from 20 h to approximately 50 h but could not prevent it.

Figure 4 may also explain results of short-term studies in which operating conditions, such as flow rate (v/v. min), may delay the inhibitory effect of SO_2 containing flue gas (5). Since our experiments were designed for rapid saturation of SO_2 by using high flow rates, the inhibitory effect is clearly noticeable even with short exposure times.

Growth of C. caldarium on a NO_x-only flue gas consisting of approximately 50 ppm NO_x, 15% CO_2, 3% O_2, in balance N_2 was also tested. The growth of C. caldarium did not appear to be significantly inhibited by the NO_x flue gas which was tested only on this alga (Figure 5). This is an important finding since NO_x is a potentially harmful agent to growth of biological systems. Thus, C. caldarium may have considerable advantages for its use as an agent for CO_2 removal from flue gas. The apparent tolerance of this alga to nitrogen oxides and low pH environments make it a logical candidate for further studies of growth in flue gas streams.

CONCLUSIONS

A major problem in the large-scale farming of unicellular algae is the control of competing organisms. C. caldarium has the advantage, although not unique, of having the ability to grow in highly acidic media and at elevated temperature, where competitors are not viable. It has been shown that this alga is capable of growth in an environment with temperatures up to 57°C and as acidic as 1N H_2SO_4 (10). Because of this tolerance to acidity and elevated temperatures that may accompany flue gas streams, further investigation of C. caldarium for the removal of CO_2 from flue gas appears to be warranted. These studies should include assessing the possibility of adaptation of cultures to SO_2-containing flue gas to obtain further insight to the nature of inhibition for development of SO_2-resistant strains.

ACKNOWLEDGEMENTS

One of the authors (J.T.H.) held an appointment as a Graduate Student Research Participant at the Pittsburgh Energy Technology Center. In addition, another author (M.M.A.) held an appointment as a visiting faculty member at the facility. These programs are administered for the U.S. Department of Energy by Oak Ridge Institute for Science and Education, Oak Ridge, Tenn.

DISCLAIMER

Reference in this report to any specific commercial product, process, or service is made to facilitate understanding and does not necessarily imply its endorsement or favoring by the U.S. Department of Energy.

REFERENCES

1. Negoro, M., Shioji, N., Miyamoto, K., Miura, Y. (1991), *Appl. Biochem. Biotech.* **28/29**, 877-886.

2. Brown, L.M., "Biological Capture of CO_2 from Flue Gas," extended abstract presented at the Eighth Annual Coal Preparation, Utilization, and Environmental Control Contractors Conference, Pittsburgh, PA (July 1992). Contact US DOE/PETC Center for Conference Management, P.O. Box 18209, Pgh., PA 15236. 1-800-441-0875 (in PA) or 1-800-441-9927 (outside PA).

3. Watanabe, Y., Ohmura, N., Saiki, H. (1992), *Energy Convers. Mgmt.* **33**, 545-552.

4. Laws, E.A., Berning, J.L. (1992), *Biotech. Bioeng.* **37**, 936-947.

5. Woodward, C.A., MacInnis, J.M., Lewis, S.N., Greenbaum, E. (1992), *Appl. Biochem. Biotech.* **34/35**, 819-826.

6. Nishikawa, N., Hon-Nami, K., Hirano, A., Ikuta, Y., Hukuda, Y., Negoro, M., Kaneko, M., Hada, M. (1992), *Energy Convers. Mgmt.* **33**, 553-560.

7. Laws, E.A., Berning, J.L. (1991), *Bioresource Tech.* **37**, 25-33.

8. Nerad, T.A., ed. (1991), *ATCC Catalogue of Protists*, 17th ed., American Type Culture Collection, Rockville, MD.

9. Allen, M.B. (1959), *Arch. Mikrobiol.* **32**, 270-277.

10. Brock, T.D. (1978), *Thermophilic Microorganisms and Life at High Temperatures*, Springer-Verlag, New York.

11. Meites, L., ed. (1963), *Handbook of Analytical Chemistry*, McGraw-Hill, New York.

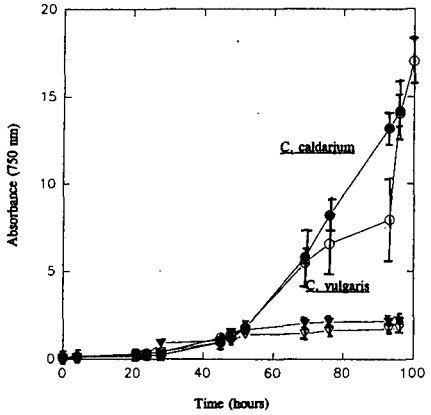

Figure 1. Growth of the strains, C. caldarium and C. vulgaris, exposed to 5% CO_2/air (●,▽) and 15% CO_2, 3% O_2 balance N_2 (○,▼).

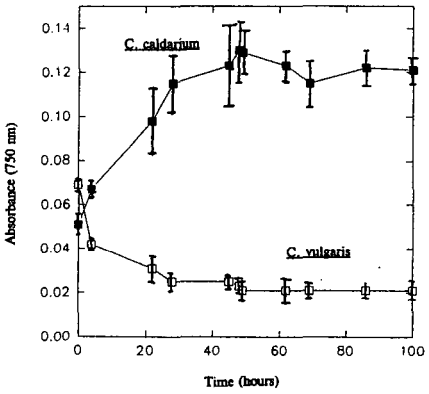

Figure 2. Growth of C. caldarium and C. vulgaris exposed to 200 ppm SO_2, 15% CO_2, 3% O_2 balance N_2.

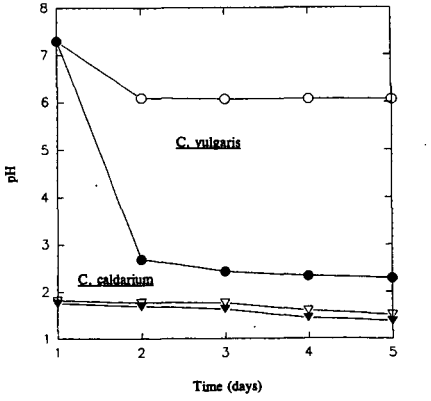

Figure 3. Change in C. caldarium and C. vulgaris culture pH as a function of simulated flue gas exposure. Cultures were aerated with 15% CO_2, 3% O_2 balance N_2 (▽,○) and 200 ppm SO_2, 15% CO_2, 3% O_2 balance N_2 (▼,●).

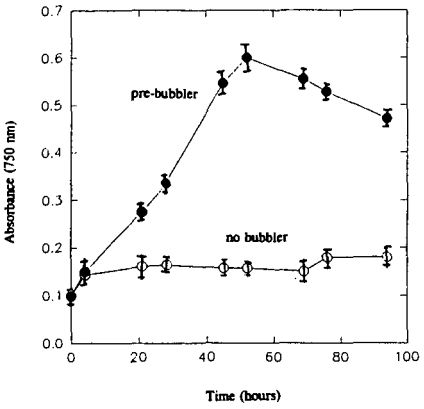

Figure 4. The effect of an SO_2 scrubber (prebubbler) on the growth of C. caldarium exposed to 200 ppm SO_2, 15% CO_2, 3% O_2 balance N_2.

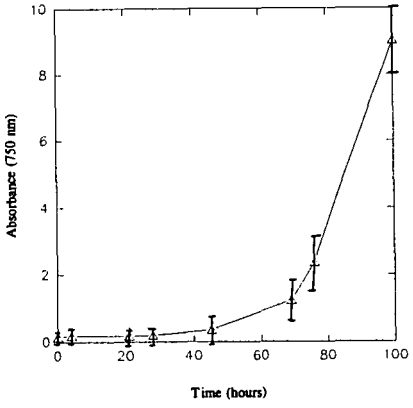

Figure 5. Growth of C. caldarium exposed to NO_x-only flue gas.

CURRENT ASPECTS OF CARBON DIOXIDE FIXATION BY MICROALGAE IN KOREA

J.S. Lee, K.D. Sung, M.S. Kim, S.C. Park and K.W. Lee*
Biomass Team, Alternative Energy Research Dept., KIER
71-2 Jang-dong, Yuseong-ku, Taejeon, Korea
* Catalysis Division, KRICT, 100 Jang-dong, Yuseong-ku, Taejeon, Korea

Key words: CO_2 fixation, flue gas from power plants, CO_2 tolerant microalgae.

ABSTRACT

The carbon dioxide fixation by microalgae has several merits such as the CO_2 recovery and the production of useful chemicals. Since the flue gas from a industry has some unfavorable conditions such as high CO_2 concentration and toxic chemicals like SO_x, NO_x contained in flue gas for the cultivation of most microalgae, it is important to apply a suitable strain of microalgae for the fixation of carbon dioxide emitted from various industrial sources. The current status for carbon dioxide emission from thermal power plants, which are major in Korea, is going to be described. Some research work has been done in KIER to get a suitable microalgae. Among the various microalgae tested in our laboratory, *Chlorella* sp., HA-1 and *Chlorococcum littorale* showed the satisfactory performance. The experimental results for culturing of the two microalgae will be presented.

INTRODUCTION

Global warming due to increased carbon dioxide concentration in the atmosphere is a threat causing widespread concern. CO_2 is a green house gas, as are methane, chlorofluorocarbons and water vapor. The CO_2 concentration in the atmosphere is reported to be risen by about 25% since industrial revolution(1,2). In the same time, the temperature of the northern hemisphere has also increased by 0.5℃. A prudent response is to reduce emissions of greenhouse gases while the science underlying global warming is resolved.

Various physicochemical methods such as wet and dry absorption, adsorption, and membrane separation technologies have been developed and the absorption method has been put into practice for the elimination of carbon dioxide(3) but further disposal of the trapped CO_2 is a costly process.

Biological methods, in particular using microalgal photosynthesis, have several merits such as no requirements for the pretreatment of flue gas and the further disposal of trapped CO_2 and mild conditions for CO_2 fixation. Carbon fixed by microalgae is incorporated into carbohydrates, lipids, so energy , chemicals, or foods can be produced from algal biomass.

The flue gas from power plants and steel mills contain about 10-20% of CO_2. If the CO_2 gas is once condensed by chemical or physical means to remove toxic chemicals, the gas fed for microalgal cultivation may contain higher concentration of CO_2. It has been reported, however, that high concentrations of CO_2 inhibits the rate of algal photosynthesis. Silva and Pirt reported that *Chlorella vulgaris* 211/8k strain, which is tolerant to high CO_2 concentration, showed a maximum growth rate at 7% CO_2 concentration(4). Practical growth studies with high concentrations of CO_2 have been initiated(5,6). Negoro et al. examined several strains of marine microalgae on their tolerance to 5 or 15% CO_2 and reported that some of them could grow without pH adjustment(7). Strains preferring low pH values can cut operation costs considerably by elminating pH control. If the microalgae can be grown at high densities, the size of culturing facilities may be reduced. Desirable properties of microalgae, for the direct biological utilization of CO_2 from flue gas, are summarized in Table 1.

Many works have been carried out to find some microalgae to fit the requirements described above(8-10). Various microalgae, which may be used for CO_2 fixation work, have been obtained from several culture collections and tested in our laboratory for their feasibility for CO_2 fixation in Korea.

At first, in this paper, current aspects for the CO_2 emission in Korea is going to be described, and subsequently some preliminary works for the development of the biological fixation process of CO_2 from flue gas in KIER will be presented.

CURRENT ASPECTS OF CARBON DIOXIDE EMISSION IN KOREA

As Korea is getting developed, the amount of CO_2 emitted has been increased rapidly. Recently global warming by CO_2 have been emerged as a major environmental problem threatening global ecosystem and a concern over it is increasing gradually in Korea like in many other nations. On account of this, Korean government assisted national R&D program for CO_2 by energy conservation and renewable energy utilization, CO_2 fixation by various methods and conversion or utilization of CO_2 for various uses. Among these projects, the biological fixation of CO_2 is considered to be the most environmentally friendly technology, and hence it is started to be investigated in several universities, government institutes such as Korea Research Institute of Chemical Technology(KRICT) as well as Korea Institute of Energy Research(KIER).

Total CO_2 emission in the world was reported to be 5,696 million tons of carbon in 1988(11). Korea is responsible to a 0.88% of the total emission. It corresponds to 49.89 million tons of

carbon. The power generation shares 15.9% of total Korean CO_2 emission. Industry shares 34.1%, transportation 14.9%, others 35.1%. Among the major CO_2 emitters, only the industry and power generation sectors can take the measures to reduce or recover the CO_2 from exhausted gases.

The capacity of fossil-fuel burning power plants in Korea today is about 14,300 megawatts(MW), about 50% of it is driven by heavy oil burning plants. Coal burning power plants shares 31%, LNG buring power plants 18%. As shown in Figure 2, the contirbution of several fuels for eletricity generation and hence for CO_2 emission is predicted to be changed significantly in the future. According to the national plan, the number of coal-burning power plants will be remarkably increased; the capacity of coal-burning power plants is planned to be 67% of total thermal power capacity 2010 (Figure 2).

The flue gas composition is greatly dependent on the type of fuel used as shown in Table 2. The flue gas from coal-burning power plants generally has the highest concentrations of SO_x, NO_x which are toxic compounds against the microalgal growth. Unless some pretreatments to reduce the SO_x, NO_x concentrations is made, the gas can not be directly purged into microalgal culture. On the other hand, flue gas from LNG and diesel oil burning power plants is believed to have acceptable concentrations of SO_x, NO_x concerning literature. Carbon dioxide in the flue gas can be directly fixed by microalgae. The growth rate of microalgae is greatly dependent on the cultivation temperatue and most microalgaes exhibit the maximum growth rate between 25℃ and 35℃. Since CO_2 fixation process by microalgae requires a large area for light absorption, it is believed to be installed outdoors for large scale application. Thus the control of cultivation temperature become normally very difficult.

In case of power plant application of the process, cooling water discharge temperature might determine the cultivation temperature of microalgae. Average temperature of cooling water from typical fossil-fuel burning power plant in Korea is shown in Table 3. The table shows that the minimum temperature recorded in February is 13.4℃. The lowest temperature is apparently too low for the proper cultivation of normal microalgae. However, the problem is believed to be overcome by thermal insulation or solar energy technologies such as a green house in winter.

BIOLOGICAL CARBON DIOXIDE FIXATION WORK IN KIER

Recently several applied studies aimed at the direct biological fixation of CO_2 out of the flue gases from thermal power plants have been carried out(11-13). Although the direct use of discharged gases reduces the cost of pretreatment, it imposes extreme conditions on microalgae such as high concentrations of CO_2 and the presence of toxic chemicals like SO_x, NO_x to microalgae. The best suited microalgal strain for this purpose should be selected in terms of tolerance to environmental stresses.

Materials and methods

Strain

A marine microalga *Chlorococcum littorale* and a fresh-water microalga *Chlorella* sp. HA-1 were used in this work. Each strain was obtained from Marine Biotechnology Institute(Japan) and National Institute of Environmental Studies(Japan), respectively. These strains were selected on the basis of high growth rate at high CO_2 level. The medium used for culturing *C. littorale* has following composition: (in g/l) KNO_3 1.25, KH_2PO_4 1.25, $MgSO_4 \cdot 7H_2O$ 1.25, NaCl 15, 1 ml of Fe solution, and 1 ml of A_5 solution. Fe solution consists of 1l water, $FeSO_4 \cdot 7H_2O$ 2, and 1 ml of concentrated H_2SO_4. MBM media(7) used for culturing of *Chlorella* sp. HA-1 has the following composition: (in mg/l), KNO_3 250, $MgSO_4 \cdot 7H_2O$ 75, K_2HPO_4 75, KH_2PO_4 175, NaCl 25, $CaCl_2 \cdot 2H_2O$ 10, $FeSO_4 \cdot 7H_2O$ 2, H_3BO_3 2.86, $MnSO_4 \cdot 7H_2O$ 2.5, $ZnSO_4 \cdot 7H_2O$ 0.222, $CuSO_4 \cdot 5H_2O$ 0.079, Na_2MoO_4 0.021. The initial pH was 6.

Batch culture

The microalgal culture experiments were conducted to investigate the growth characteristics of the microalgaes under various culture conditions. The culture equipment is shown in Figure 3. The system consists of 1l Erlenmeyer flasks as culture vessel, water bath, fluorescent lamp, CO_2 enriched air supplier. The maximum average light intensity at the surface of the culture vessel was 8 Klux. CO_2 enriched air was prepared by mixing pure CO_2 from a cylinder and air from an air pump, and filter sterilized. The temperature of the culture vessel was maintained in the water vessel equipped with a temperature controller(Jeo Tech Co., Korea). pH was not regulated. Light intensities, CO_2 concentrations, and temperature were varied in accordance with experimental conditions specified.

Assay

Light intensities were measured by a light sensor (Licor Inc, USA). Cell growth was determined either by the optical density at 660 nm using UV-spectrophotometer (HP8452A, Hewlett-Packard Inc., USA) or by dry-cell weight after filtration on cellulose acetate filter(0.45μm, Millipore Co., USA), followed by drying at 105℃ overnight.

Results and discussion

The effects of light intensities and CO_2 concentrations on the cultivation of microalgae were investigated for CO_2 fixation from concentrated sources such as a power plant.. *C. littorale* and *Chlorella* sp. HA-1 were selected for further experiments after screening by their performance.

The effects of 3, 6, 8 Klux light intensities on the growth of *C. littorale* at 25℃ and 10% CO_2 concentration were investigated. As shown in Figure 4, the growth rates of *C. littorale* were almost the same at 6 and 8 Klux with 0.19g cell/day-1 growth. However, the growth rate at 3 Klux was 0.12g cell/day-1. This corresponds to only 60% of the growth rate at sufficient light. Figure 5 shows the growth of *Chlorella* sp. at various light intensities. Higher than 8 Klux light intensities is believed to inhibit the growth and the growth rate at 3 Klux was 0.15g cell/day-1, about 70% of its maximum at 6 Klux.

It is concluded that the light intensities around 6 Klux are sufficient for the proper growth of them, higher light intensities are of no effect with *C. littorale* and even harmful for the case of *Chlorella* sp. HA-1.

The industrial CO_2 sources are of relatively high concentration with concentration range from 10 to 20% CO_2 than natural sources . Therefore, the concentrated CO_2 resistance of the microalgae was experimented with 10, 20, 30% of CO_2 concentrations. The growth of *C. littorale* was not inhibited at 10 and 20% concentrations as shown in Figure 6., hence considering only CO_2 concentration, there might be no problem with the *C. littorale* for the CO_2 fixation application from power plant exhaust gas. However, the growth rate was declined to about half at 30% CO_2 concentration.

Figure 7 shows the CO_2 resistance of fresh water microalga *Chlorella* HA-1. This species exhibits the growth inhibition at the CO_2 concentration higher than 10%. In consequence, the CO_2 resistance of the *Chlorella* HA-1 was believed to be lower than that of marine alga *C. littorale*. Combined cycle power plants located in-land in Korea are burning LNG as fuel, and using fresh water as cooling water. Since these LNG power plants discharge the emissions containing only 9-10% CO_2, the *Chlorella* HA-1 could be applied for the CO_2 fixation in the case of in-land LNG power plants.

The effects of cultivation temperatures on the growth of microalgaes were also considered. The two species showed maximum growth in the temperature range from 26°C to 30°C. The minimum average temperature of cooling water in a typical thermal power plant was 13.4°C in February, however, the problem is believed to be overcome by thermal insulation or solar energy technologies such as green house in winter.

ACKNOWLEDGEMENT
This project was supported by Korean Ministry of Environment and Ministry of Science and Technology.

REFERENCES
(1) Barnola,J.M., Raynaud,D., Korotkevich, and Lorius,C., Nature, 329, 408 (1987).
(2) Neftel,A., Oeschger,H., Schwander,J., Stouffer,B., and Zumbrunn,R., Nature, 295, 220 (1982).
(3) Yokoyama,T., "Japanese R&D on CO_2 Removal", Coal for Development Conference Proceedings, London, UK, 23-26th March (1993).
(4) Silva,H.J. and Pirt,S.J., J.Gen.Microbiol., 130, 2833 (1984).
(5) Pirt,M.W. and Pirt,S.J., J.Gen.Microbiol., 119, 321 (1980).
(6) Lee,Y. and Hing,H.K., Appl.Microb.Biotech., 31, 298 (1989).
(7) Negoro,M., Shioji,N., Miyamoto,K., and Miura,Y., Appl.Biochem.Biotechnol., 28/29, 877 (1991).
(8) Watanabe,Y. Ohmura,N., and Saiki,H., Energy Conv.& Management, 33(5-8), 545 (1992).
(9) Kodama,Y., Ikemoto,H., and Miyachi,S., J.Marine Biotechnol., 1, 21 (1993).
(10) Takeuchi,T., Utsunomiya,K., Kobayashi,K., Owada,M. and Karube,I., J.Biotechnol., 25, 261 (1992).
(11) Saiki,H., "Measures for CO_2 reduction by Japanese electric power industry", 1st CO_2 workshop at KRICT, Taejeon, Korea, 20-21 June (1993)
(12) Laws,E.A., Biores.Technol., 37, 25 (1991).
(13) EPRI Project 2612-11, Electric Power Research Institute, Palo Alto, CA (1990).
(14) Hamasaki,A., Shioji,N., Ikuta,Y., Hukuda,Y., Makita,T., Hirayama,K., Matsuzaki,H., Tsukamoto,T., and Sasaki,S., Appl.Biochem.Biotechnol., 45/46, 799 (1994).

Table 1. Desirable properties of microalgae for CO_2 fixation

High CO_2 tolerance
Low pH tolerance
Stable and high growth rate in the linear phase
Capability of growing at high cell densities
SO_x, NO_x tolerance
Thermotolerance

Table 2. Flue gas composition of thermal power plants using various fuels

Components / Fuel	CO_2, %	SO_x, ppm	NO_x, ppm
Coal			
Anthracite*	15 - 16	860	200
Bituminous**	15 - 16	360	240
LNG	9 - 10	negligible	140
Diesel oil	15 - 16	180	negligible

* : Produced in Korea

** : imported low sulfur coal

Table 3. Temperature (°C) of the cooling water from fossil-fuel burning power plants in Korea.

	Jan.	Feb.	Mar.	Apr.	May	Jun.	Jul.	Aug.	Sep.	Oct.	Nov.	Dec.
Intake water	5.6	4.6	8.4	11.8	17.3	22.2	24.6	25.5	26.2	20.3	15.7	8.0
Cooling water	15.6	13.4	20.2	22.6	28.6	33.0	34.0	33.0	33.3	29.7	26.2	18.5

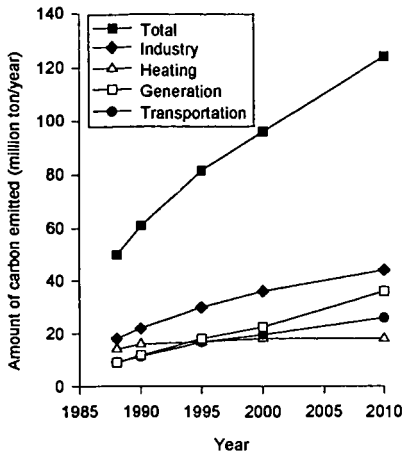

Figure 1. Domestic CO_2 emissions by secter of energy use in Korea.

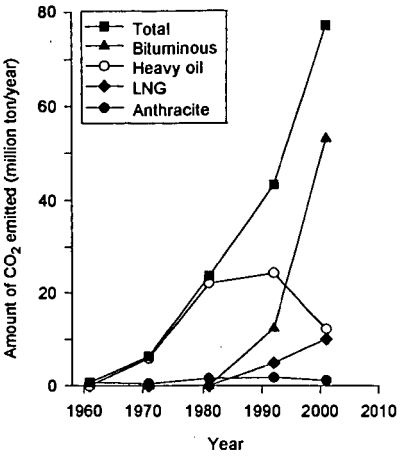

Figure 2. CO_2 emission from fossil-fuel burning power plants in Korea.

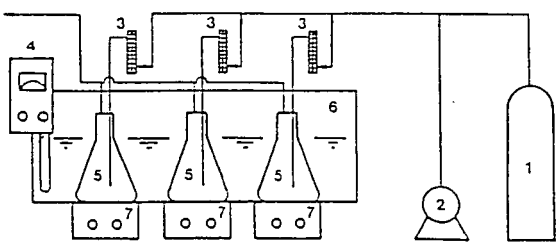

Figure 3. Schematic diagram of microalgal CO_2 fixation equipment.

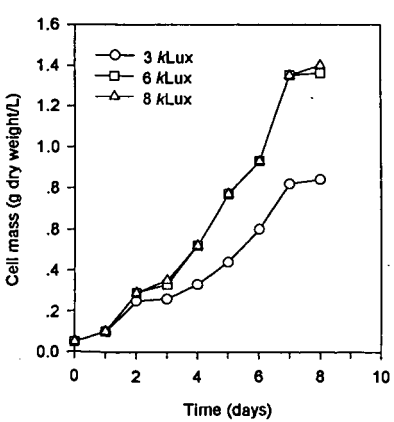

Figure 4. The effect of light intensities on the growth rate of *C.littorale*. The CO_2 concentration and the temperature were 10% and 26°C respectively.

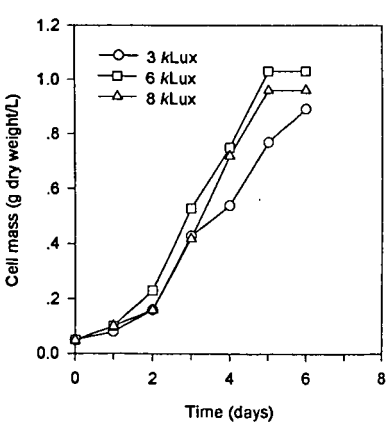

Figure 5. The effect of light intensities on the growth rate of *Chlorella* sp., HA-1. The CO_2 concentration and the temperature were 10% and 26°C respectively.

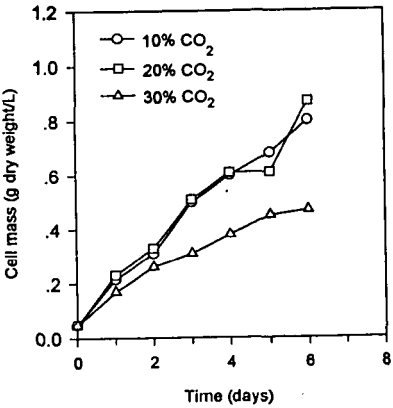

Figure 6. The effect of CO_2 concentrations on the growth rate of *C.littorale*. The experiment was carried out at 30°C and at light intensity of 6kLux.

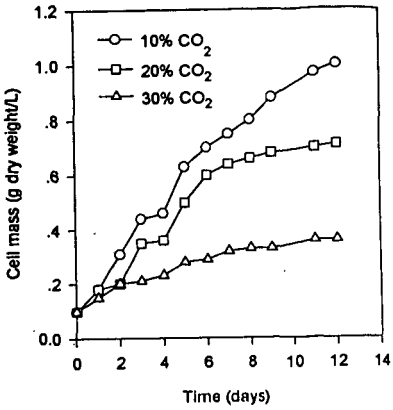

Figure 7. The effect of CO_2 concentrations on the growth rate of *Chlorella* sp., HA-1. The experiment was carried out at 30°C and at a light intensity of 6kLux.

BIOCONVERSION OF CO_2 TO ETHANOL AND OTHER COMPOUNDS

Thomas M. Wahlund, Tyrrell Conway, and F. Robert Tabita
Department of Microbiology, The Ohio State University,
484 West 12th Avenue, Columbus, Ohio 43210-1292

Keywords: Microbial CO_2 fixation, recombinant DNA, ethanol

INTRODUCTION

The light-driven process of CO_2 fixation and its conversion into a myriad of larger organic molecules is a remarkably successful strategy employed by all plants. Likewise, there are numerous types of bacteria that are capable of extremely efficient CO_2 fixation, including those that use light-driven processes, as well as several species that are capable of using the energy obtained from chemical oxidations to fuel CO_2 reduction in the dark. However, nowhere in nature can an organism be found that has coupled CO_2 fixation to significant ethanol production. With the realization that fully one-third of the corn starch used for biological ethanol formation is lost through the production of CO_2 gas, it would be desirable to discover some way to use this CO_2 for the production of value-added chemicals or other products of interest. In this paper, we discuss recent experiments to couple the metabolism of CO_2 to the synthesis of ethanol using recombinant DNA technology. A chimeric bacterium was constructed so that CO_2 may be metabolized to ethanol.

RATIONALE AND EXPERIMENTAL APPROACHES

A logical strategy for genetically engineering microorganisms with the capacity for efficient ethanol production became possible when the genes that encode the key enzymes of ethanol biosynthesis from pyruvate were cloned from the bacterium *Zymomonas mobilis* (Conway *et al.*. 1987a; Conway *et al.*, 1987b). Indeed the *Z. mobilis* pyruvate decarboxylase (*pdc*) and alcohol dehydrogenase (*adh*) genes, when expressed in *Escherichia coli*, were found to enable this host to divert a significant amount of its normal metabolic profile to ethanol synthesis (Ingram and Conway, 1988). Since a common metabolic intermediate of virtually all central metabolic pathways is pyruvate, there is considerable interest to couple pyruvate formation to ethanol synthesis. Many autotrophic bacteria use the reductive pentose phosphate or Calvin-Benson-Bassham (CBB) pathway to convert CO_2 to organic matter. Since pyruvate is a key intermediate here as well, we considered the possibility that some of this pyruvate might be converted to ethanol in a CO_2-fixing chimeric bacterium overexpressing the *Z. mobilis pdc* and *adh* genes.

Much has been learned of the molecular biology and biochemistry of CO_2 fixation in microorganisms (Tabita, 1988; Tabita, 1995) and recently the potential for the regulated expression of foreign genes under autotrophic growth conditions in phototrophic bacteria has become established (Falcone and Tabita, 1991). Although much still needs to be learned about promoter structure and other aspects of gene expression in autotrophic bacteria, it was considered well worth the effort to determine whether it would be feasible to use existing technology to convert CO_2 into ethanol. The basic idea behind this approach is illustrated in Figure 1, where it is envisioned that recombinant *Rhodobacter* species would reduce CO_2 to ethanol under purely autotrophic (organic carbon-free) growth conditions. In this scheme, hydrogen is used as the ultimate reductant in the absence of oxygen under photosynthetic growth conditions and pyruvate (a product of the CBB pathway) is reduced to ethanol through the mediation of plasmid-encoded *pdc* and *adh* genes (Figure 2). Alternatively, one may take advantage of the ability of these organisms to fix CO_2 in the dark in the presence of oxygen, again in the absence of organic carbon. The versatility of these bacteria is further underlined by their ability to also use various organic compounds, instead of hydrogen, as electron donors.

RESULTS

The feasibility of using *Rhodobacter* and related organisms for foreign gene expression was first determined by constructing a promoter-plasmid vector capable of directing the synthesis of an easily assayed indicator enzyme, ß-galactosidase (encoded by the *lacZ* gene of *E. coli*). A variety of growth conditions, known to influence CO_2 fixation-related gene expression, was assessed in both *R. sphaeroides* and the related organism *R. capsulatus*. These conditions included anoxygenic growth under photoautotrophic (PA) conditions in a CO_2/H_2 atmosphere, aerobic chemoautotrophic (CLA) growth conditions in the dark in a $CO_2/H_2/O_2$ atmosphere, anoxygenic photoheterotrophic (PH) growth conditions in the light using organic carbon as an electron donor, and aerobic chemoheterotrophic (CH) growth conditions in the dark in the presence of organic carbon. In *R. sphaeroides*, maximum ß-galactosidase activity was obtained

in PA-grown cells, which reflected the high level of RubisCO (the major CO_2 fixation enzyme of the CBB pathway) associated with these growth conditions in this organism (Tabita, 1988; Tabita, 1995; Falcone and Tabita, 1996). The lowest level of ß-galactosidase was found in PH-grown cells, which also was reflected by the lower levels of RubisCO. Intermediate levels were obtained in CLA-cultured *R. sphaeroides* and to our surprise CH-dependent growth yielded fairly high levels of ß-galactosidase, while the level of RubisCO was at its expected lowest point. In *R. capsulatus*, the same promoter-*lacZ* construct showed a definitive and pronounced enhancement of ß-galactosidase activity under CLA-growth conditions, with much lower activity in PA-grown cells, and basically background levels in PH and CH-cultured *R. capsulatus*.

The results with the promoter-*lacZ* fusion-indicator constructs generally yielded much lower levels of ß-galactosidase than we might have expected based on previous studies with the same promoter directing transcription of foreign RubisCO genes (Falcone and Tabita, 1993). There are several reasons why *lacZ* may not have been as highly expressed as the genes encoding RubisCO with this vector, including factors related to the posttranscriptional processing of the message. Despite these results, we determined if it might be possible to use this vector to express the *pdc* and *adh* genes in *R. sphaeroides* and *R. capsulatus*, under the various growth conditions reported above. Basically, the same pattern of *adh* gene expression was obtained as above, namely the highest levels of alcohol dehydrogenase activity were obtained under PA and CLA growth conditions with *R. sphaeroides* and *R. capsulatus*, respectively. Again, with this vector the level of *adh* expression was not nearly as great as we had hoped based on prior RubisCO gene expression studies. The regulated expression of *adh* (and also *pdc*) did, however, encourage us to examine whether genetically engineered *R. sphaeroides* and *R. capsulatus* were capable of synthesizing ethanol under CO_2-fixation conditions. Both strains produced between 0.07 and 0.08 percent (w/v) ethanol in culture filtrates of photoautotrophic-grown cells. Furthermore, both alcohol dehydrogenase activity and the amount of ethanol synthesized could be significantly enhanced by the addition of xylose to the growth medium under PH growth conditions. Up to 0.023 percent ethanol (w/v) was obtained in *R. sphaeroides* and about 0.014 percent ethanol was produced by *R. capsulatus* cultures, with maximum levels reached at a considerably faster rate for *R. capsulatus*.

Another factor to be considered in any microbial process to produce ethanol is the tolerance of the host organism to ethanol. Each strain of *R. sphaeroides* and *R. capsulatus* employed in our study was sensitive to fairly low concentrations of ethanol. In Figure 3, the specific growth rate and the maximium extent of growth of each organism in a xylose-mineral salts medium under PH growth conditions was determined. As shown in this figure, higher concentrations of ethanol most affected the extent of growth and not the rate of growth. However, the data do show that in terms of the specific growth rate, *R. capsulatus* was considerably more resistant to ethanol. It must be kept in mind, however, that both strains of *R. capsulatus* and *R. sphaeroides* are laboratory strains that have not been otherwise altered. Thus, it may be possibile to modify the existing strains, and select for higher alcohol tolerance, as we have for temperature tolerance (Weaver and Tabita, 1983). Another alternative would be to isolate new strains.

DISCUSSION

These studies conclusively show that CO_2 may be converted to ethanol by two species of *Rhodobacter* under anoxygenic conditions in the light or under dark aerobic growth conditions. A promoter-vector molecule, which had been previously shown to be maximally effective under growth conditions which favored active CO_2 fixation, was adapted for these studies; e.g. in the absence of organic carbon. Although the overall level of *pdc* and *adh* gene expression was not as great as we had expected, the fact remains that CO_2 was converted to ethanol, both in the light and in the dark. Current studies are devoted to optimizing the position of the relevant genes within this vector and to stabilizing the *pdc* and *adh* transcript. In addition, other potential vectors have been developed which might prove even more suitable. Surprisingly, the use of xylose in photoheterophic cultures substantially enhanced ethanol production with our original vector, perhaps precluding the need for hydrogen as an electron donor for metabolism. Since xylose is a major constituent of corn starch, its use to stimulate plasmid-directed ethanol production in an organism with a highly active reductive pentose phosphate pathway may lead to a novel source of biologically synthesized ethanol. In this vein, it will be important to determine the total amount of ethanol derived from CO_2 and/or xylose carbon since these bacteria are known to oxidize organic carbon sources to CO_2 and refix and use this CO_2 as an electron acceptor (Tabita, 1995).

ACKNOWLEDGMENTS

This work was supported by a grant from the Consortium for Plant Biotechnology Research.

REFERENCES

1. Conway, T. Osman, Y.A., Konnan, J.I., Hoffman, E., and Ingram, L.O. (1987a) Promoter and nucleotide sequences of *Zymomonas mobilis* pyruvate decarboxylase. J. Bacteriol. 169, 949-954.
2. Conway, T., Sewall, G.W., Osman, Y.A., and Ingram, L.O. (1987b) Cloning and sequencing of the alcohol dehydrogenase II gene from *Zymomonas mobilis*. J. Bacteriol. 169, 2591-2597.
3. Ingram, L.O., and Conway, T. (1988) Expression of different levels of ethanologenic enzymes from *Zymomonas mobilis* in recombinant strains of *Escherichia coli* . Appl. Env. Microbiol. 54, 397-404.
4. Tabita, F.R. (1988) Molecular and cellular regulation of autotrophic carbon fixation in microorganisms. Microbiol. Rev. 53, 155-189.
5. Tabita, F.R. (1995) The biochemistry and metabolic regulation of carbon metabolism and CO_2 fixation in purple bacteria. *In*, Anoxygenic Photosynthetic Bacteria (R.E. Blankenship, M.T. Madigan, and C.E. Bauer, eds.) pp. 885-914, Kluwer Acad. Publ. The Netherlands.
6. Falcone, D.L., and Tabita, F.R. (1991) Expression of endogenous and foreign ribulose 1,5-bisphosphate caraboxylase/oxygenase (RubisCO) genes in a RubisCO deletion mutant of *Rhodobacter sphaeroides*. J. Bacteriol. 173, 2099-2108.
7. Falcone, D.L., and Tabita, F.R. (1993) Complementation analysis and regulation of CO_2 fixation gene expression in a ribulose 1,5-bisphosphate carboxylase-oxygenase deletion strain of *Rhodospirillum rubrum*. J. Bacteriol. 175, 5066-5077.
8. Weaver, K.E., and Tabita, F.R. (1983) Isolation and partial characterization of *Rhodopseudomonas sphaeroides* mutants defective in the regulation of ribulose bisphosphate carboxylase/oxygenase. J. Bacteriol. 156, 507-515.

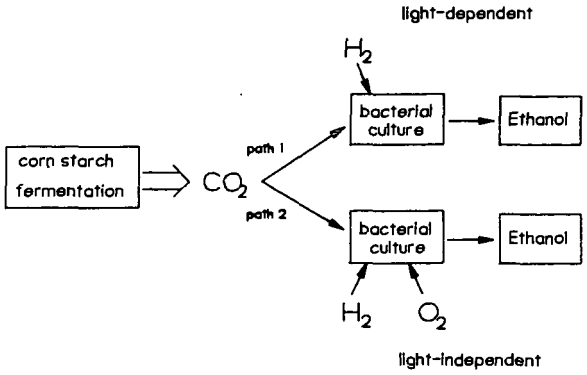

Figure 1. A general scheme to couple light-dependent and light-independent CO_2 fixation to ethanol production.

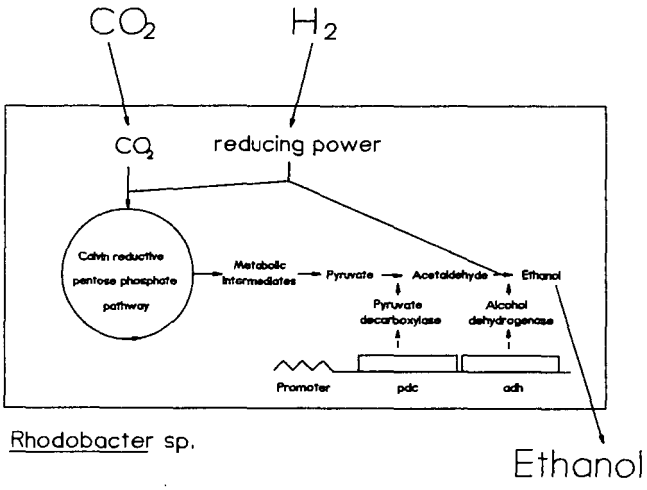

Figure 2. Ethanol synthesis using metabolic intermediates and pyruvate produced through the CBB reductive pentose phosphate pathway of CO_2 fixation.

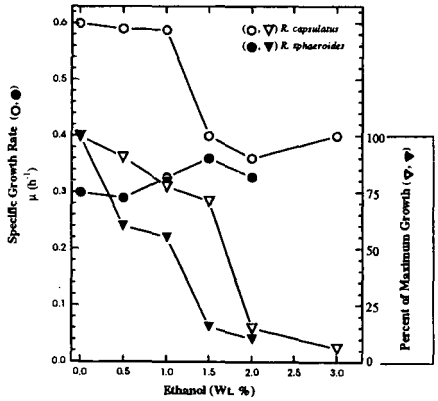

Figure 3. Specific growth rate (μ) and maximum extent (%) of growth in batch cultures of *R. sphaeroides* and *R. capsulatus* grown in a mineral salts-xylose medium containing different initial concentrations of ethanol. Cultures were bubbled with 1.5% CO_2/98.5% H_2 in the light.

METHANOL SYNTHESIS FROM CO_2 AND H_2 OVER Cu/ZnO-BASED MULTICOMPONENT CATALYSTS

Masahiro SAITO[1],*, Masami TAKEUCHI[2], Tadahiro FUJITANI[1], Jamil Toyir[3], Shengcheng Luo[3], Jingang Wu[3], Taiki WATANABE[2] and Yuki KANAI[2]

1) National Institute for Resources and Environment (NIRE), 16-3 Onogawa, Tsukuba-shi, Ibaraki 305, Japan
2) Research Institute for Innovative Technology for the Earth (RITE), 9-2 kizukawadai, kizu-cho, Soraku-gun, Kyoto 619-02, Japan
3) RITE (NEDO Industrial Technology Researcher), 16-3 Onogawa, Tsukuba-shi, Ibaraki 305, Japan

Keywords: CO_2 hydrogenation, methanol synthesis, Cu/ZnO-based multicomponent catalyst

INTRODUCTION

The greenhouse effect of carbon dioxide has been recognized to be one of the most serious problems in the world, and a number of countermeasures have been proposed so far. Catalytic hydrogenation of CO_2 to produce various kinds of chemicals and fuels has received much attention as one of the most promising mitigation options. In particular, methanol synthesis by CO_2 hydrogenation has been considered to play an important role in the transportation of hydrogen energy produced from natural energy such as solar energy, hydropower and so on, as shown in Fig. 1[1]. According to some estimations[2], an electric power of 300 MWh could be obtained from a methanol fired power plant in Japan, if methanol synthesized from CO_2 and H_2 produced by a electrolysis of water using an eletcric power of 1000 MWh is transported to Japan through the system shown in Fig. 1.

A practical methanol synthesis process greatly requires a high performance catalyst, which must be highly active and selective for methanol synthesis and also stable for a long period in a continuous operation. NIRE and RITE have been doing a joint research on methanol synthesis by catalytic hydrogenation of carbon dioxide. The authors have elucidated the role of metal oxides contained in Cu/ZnO-based ternary catalysts, and then developed Cu/ZnO-based multicomponent catalysts containing two or three metal oxides [3]. Furthermore, we have examined the change in the activity of the multicomponent catalysts during a long term methanol synthesis test, and investigated the methanol synthesis over the multicomponent catalysts by using a reactor with a recycling equipment for unreacted gases.

EXPERIMENTAL

All of the Cu/ZnO-based catalysts were prepared by a coprecipitation method, which was described in detail elsewhere [4]. Two kinds of Cu/ZnO-based multicomponent catalysts named MCA ($Cu/ZnO/ZrO_2/Al_2O_3$) and MCB ($Cu/ZnO/ZrO_2/Al_2O_3/Ga_2O_3$) were prepared by selecting metal oxides on the basis of the role of metal oxide. A commercial catalyst ($Cu/ZnO/Al_2O_3$) for methanol synthesis from syngas was used for comparison. A conventional fixed bed flow reactor was used both for short-term methanol synthesis tests and for long-term tests. Furtheremore, a recycle reactor equipped with a compressor for recycling unreacted gases was used for investigating practical methanol synthesis operations. The catalyst fixed in a reactor was reduced in a gas mixture of H_2 (10%) and He (90%) at 523 K with a total pressure 5 MPa. The hydrogenation of CO_2 was then carried out at 523 K with a total pressure of 5 MPa in a fixed bed flow reactor by feeding a gas mixture of H_2 and CO_2 with a mole ratio of $H_2/CO_2=3$. The reaction products were analyzed by means of gas chromatographs directly connected to the reactor. The catalyst activity was measured 2h after supplying the feed gas to the reactor except for a long term methanol synthesis test. The total copper surface area of each catalyst after the reaction (Cu_{total}) was determined by the technique of N_2O reactive frontal chromatography (RFC) after re-reducing the post-reaction catalyst with H_2 at 523 K [5].

RESULTS AND DISCUSSION

The main products of CO_2 hydrogenation over Cu/ZnO-based catalysts were methanol, CO and water. Methane, dimethyl ether and methyl formate were also detected in the reaction products, but the selectivities for the by-products were less than 0.1%.

The methanol synthesis activities which were expressed by mass-time yields of methanol (MTY), Cu_{total} and the specific activities, i.e. MTY/Cu_{total}, of Cu/ZnO-based ternary catalysts ($Cu/ZnO/M_xO_y$) containing various metal oxides were examined. Table 1 shows the activities of a Cu/ZnO catalyst and the ternary catalysts containing the optimum amounts of Ga_2O_3, Al_2O_3, ZrO_2 and Cr_2O_3, which were higher than that of a Cu/ZnO catalyst by factor of 43%, 40%, 30% and 17%, respectively.

Fig. 2 shows the methanol synthesis activity of Cu/ZnO-based ternary catalysts containing Ga_2O_3, Al_2O_3, ZrO_2 and Cr_2O_3 on varying the content from 5 to 40 wt% as a function of total Cu surface area (Cu_{total}). For each metal oxide contained in the Cu/ZnO-based catalysts, a linear relationship between MTY and Cu_{total} was seen, indicating that the specific activity is identical for each metal oxide even if the content of a metal oxide in a Cu/ZnO-based catalyst is varied. The specific activities for the Cu/ZnO-based catalysts containing Ga_2O_3 and Cr_2O_3 were greater than that of a Cu/ZnO catalyst by factor of 40% and 30%, respectively. On the other hand, the specific activity was not altered by the addition of Al_2O_3 or ZrO_2, though these metal oxides play a role in increasing Cu surface area. This indicates that the addition of Al_2O_3 or ZrO_2 improves the dispersion of Cu particles without changing the specific activity of a Cu/ZnO catalyst, while Ga_2O_3 and Cr_2O_3 are not effective for improving the dispersion of Cu, but are effective for increasing the specific activity of a Cu/ZnO catalyst.

Table 2 shows the methanol synthesis activities of the multicomponent catalysts. The activities of the multicomponent catalysts were higher than those of the ternary catalysts, and MCB exhibited the highest activity. The total Cu surface area of MCA was higher than that of $Cu/ZnO/Al_2O_3$, but the specific activity of MCA was the same as that of $Cu/ZnO/Al_2O_3$. On the other hand, the specific activity of MCB was higher than that of $Cu/ZnO/Al_2O_3$, though the total Cu surface area of MCB was a little smaller than that of $Cu/ZnO/Al_2O_3$. These findings indicate that the promoting effect of metal oxides is exerted on the multicomponent catalysts as well as on the ternary catalysts.

Fig. 3 shows the activities of the multicomponent catalysts, $Cu(50)/ZnO(45)/Al_2O_3(5)$ and $Cu(50)/ZnO(50)$ as a function of the temperature on pretreatment in H_2 ranging from 523 K to 723K. The activities of all the catalysts decreased with increasing pretreatment temperature mainly due to the decrease in Cu surface area by the sintering of Cu particles. However, the activities of MCB and MCA decreased only 10% and 15% even in pretreatment at 723 K, respectively. while the activities of the ternary catalyst and the binary catalyst decreased 30% and 85%, respectively. This suggests that the sintering of Cu particles can be suppressed by the addition of Al_2O_3, ZrO_2 and/or Ga_2O_3 to Cu/ZnO.

A methanol synthesis catalyst for a practical process is highly required to have a stable activity for a long period in a continuous operation. A long-term methanol synthesis test was performed at 523 K with a total pressure of 5 MPa by using a gas mixture of CO_2, CO and H_2, because unreacted gases and CO must be recycled to the reactor in a practical process. Fig. 4 shows the change in the activity with time on stream of MCB, which was the best catalyst among all the catalysts tested, including a commercial catalyst used for methanol synthesis from syngas. The activity of MCB decreased only by 17% in 1000 h during the test, but unchanged from 1000 h to 3400h. On the other hand, the activity of the commercial catalyst decreased by 20% in 1000 hr, and still decreased to 75% of the initial activity in 2100hr. These findings clearly indicate that the multicomponent catalyst developed in the present work is very stable for a long period in a continuous methanol synthesis operation.

Practical methanol synthesis must be performed by using a rector with recycling equipments for unreacted gases, because the conversion of CO_2 to methanol at reaction equilibrium is very low under ordinary reaction conditions, for example, 17% at 523 K and 5 MPa. Therefore, methanol synthesis using a recycle reactor was also investigated. The products of CO_2 hydrogenation at 473 K to 548 K with a total pressure of 5 MPa in the recycle reactor were methanol, CO, water, methane, ethane, dimethyl ether, methyl formate, ethanol, propanol and butanol, but the yields of the products other than methanol, CO and water were very small. The selectivity for methanol in the products except CO and water was more than 99.8%. The reaction products were cooled to 270 K in a gas-liquid separator connected to the reactor. Liquid products collected in the gas-liquid separator were taken out of the reactor, and unreacted gases as well as gaseous products such as CO, methane, ethane and dimethyl ether were recycled back to the reactor. The concentrations of methane, ethane and dimethyl ether in a recycled gas mixture remained constant after some initial period in CO_2 hydrogenation without purging unreacted gases. Table 2 shows the composition of liquid products except H_2O taken out of the recycle reactor. The purity of methanol was 99.96 wt%, and higher than that obtained in a commercial methanol synthesis from syngas. This finding suggests that the lower CO concentration in the feed gas should result in the lower yield of by-products and thus the higher methanol purity.

CONCLUSIONS

The role of metal oxides such as Ga_2O_3, Al_2O_3, ZrO_2 and Cr_2O_3 contained in Cu/ZnO-based ternary catalysts for methanol synthesis from CO_2 and H_2 was classified into two categories: to improve the Cu dispersion and to increase the specific activity.

The Cu/ZnO-based multicomponent catalysts developed on the basis of the role of metal oxides were highly active and stable for a long period in a continuous methanol synthesis operation.

The conversion of CO_2 in a make-up gas to methanol at 473 K to 523 Kwith a total pressure of 5 MPa was more than 99.9% during the methanol synthesis over the multicomponent catalyst using a reactor with a recycling equipment for unreacted gases because the yields of by-products were less than 0.1%.

In conclusion, the presented results clearly show that the Cu/ZnO-based multicomponent catalysts developed in the joint research are highly effective for a practical methanol synthesis via CO_2 hydrogenation.

ACKNOWLEDGMENT

The present work was partly supported by New Energy and Industrial Technology Development Organization (NEDO).

REFERENCES

[1] H. Sano, Proc. Int. Symp. on CO_2 Fixation & Efficient Utilization of Energy, Tokyo, Japan, p. 117(1993).
[2] S. Kubo, private communication
[3] M. Saito, T. Fujitani, I. Takahara, T. Watanabe, M. Takeuchi, Y. Kanai, K. Moriya, T. Kakumoto, Energy Convers. Mgmt, **36**, 577 (1995).
[4] T. Fujitani, M. Saito, Y. Kanai, M. Takeuchi, K. Moriya, T. Watanabe, M. Kawai, and T. Kakumoto, Chem, Lett., **1993**, 1079.
[5] G. C. Chinchen, K. C. Waugh, and D. A. Whan, Appl. Catal., **25**, 101(1986).

Table 1 Activities of Cu/ZnO and Cu/ZnO-based ternary catalysts containing the optimum amount of metal oxides

Catalyst	Composition (wt%)	Cu surface area[a] (m^2/g-cat)	Methanol synthesis activity[b] (g-CH_3OH/kg-cat•h)	Specific activity (mg-CH_3OH/m^2•h)
Cu/ZnO	50/50	36.5	516	14.1
Cu/ZnO/Ga_2O_3	50/25/25	37.6	738	19.6
Cu/ZnO/Al_2O_3	50/45/5	47.1	721	15.3
Cu/ZnO/ZrO_2	50/40/10	46.0	665	14.5
Cu/ZnO/Cr_2O_3	50/45/5	32.8	602	18.4

a) Total Cu surface (Cu_{total}) of the catalysts re-reduced at 523 Kafter CO_2 hydrogenation were measured by N_2O reactive frontal chromatography.
b) Reaction conditions : weight of catalyst=1 g, H_2/CO_2 ratio in the feed=3, feed gas rate =300 ml/min, temperature=523 K, total pressure=5 MPa.

Table 2 Activities of Cu/ZnO-based multicomponent catalysts

Catalyst	Cu surface area[a] (m^2/g-cat)	Methanol synthesis activity[b] (g-CH_3OH/kg-cat•h)	Specific activity (mg-CH_3OH/m^2•h)
Cu(50)/ZnO(45)/Al_2O_3(5)	47.1	721	15.3
MCA(Cu/ZnO/ZrO_2/Al_2O_3)	49.9	767	15.3
MCB(Cu/ZnO/ZrO_2/Al_2O_3/Ga_2O_3)	44.5	785	17.6

a) Total Cu surface areas of the catalysts re-reduced at 523 K after CO_2 hydrogenation were measured by N_2O reactive frontal chromatography.
b) Reaction conditions : weight of catalyst=1 g, H_2/CO_2 ratio in the feed=3, feed gas rate =300 ml/min, temperature=523 K, total pressure=5 MPa.

Table 3 The composition of liquid products (except water) from a recycle reactor in this work[a], compared with that from a commercial plant for methanol synthesis from syngas[b]

Compound		Composition	
		This work	A commercial plant
Methanol	**CH_3OH**	**99.96 wt%**	**99.59 wt%**
Methyl formate	$HCOOCH_3$	330 ppm	700 ppm
Higher alcohols (C_2-C_4)	ROH	30 ppm	530 ppm
Hydrocarbons (C_6-C_{10})	C_nH_m	-	50 ppm
Dimethyl ether	$(CH_3)_2O$	-	230 ppm

a) Reaction conditions : catalyst=Cu/ZnO/ZrO_2/Al_2O_3/Ga_2O_3, H_2/CO_2 ratio in the make-up gas=3, temperature=517 K, total pressure=5 MPa.
b) cited from a booklet on ICI methanol synthesis catalysts.

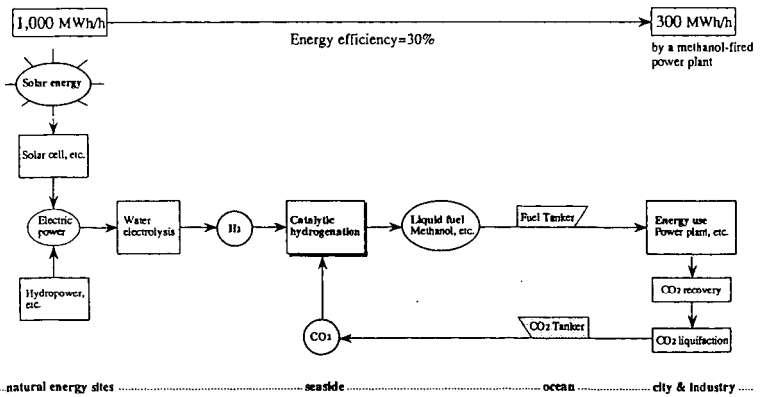

Fig. 1 Global energy network combined with catalytic hydrogenation of CO_2

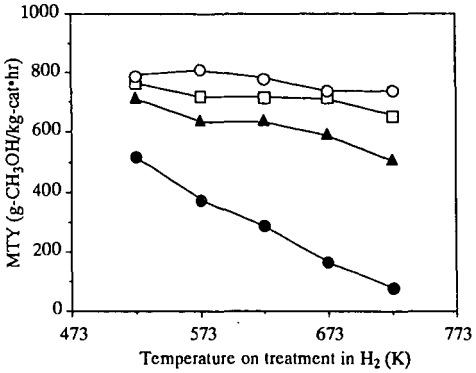

Fig. 3 Activities of various Cu/ZnO-based catalysts as a function of temperature on treatment in a stream of H_2
Reaction conditions were the same as shown in Table 1.
O:MCB(Cu/ZnO/ZrO_2/Al_2O_3/Ga_2O_3), □:MCA(Cu/ZnO/ZrO_2/Al_2O_3), ▲:Cu(50)/ZnO(45)/Al_2O_3(5), ●:Cu(50)/ZnO(50)

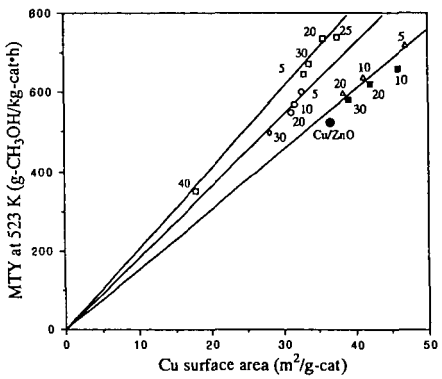

Fig.2 Methanol synthesis activity (MTY) at 523 K as a function of Cu surface area.
Reaction conditions were the same as shown in Table 1.
The contents (wt%) of metal oxides in the Cu/ZnO-based catalysts are indicated in the figure.
Cu content of the catalysts was 50 wt%.
□:Cu/ZnO/Ga_2O_3, O:Cu/ZnO/Cr_2O_3, Δ:Cu/ZnO/Al_2O_3, ■:Cu/ZnO/ZrO_2, ●:Cu/ZnO (50/50).

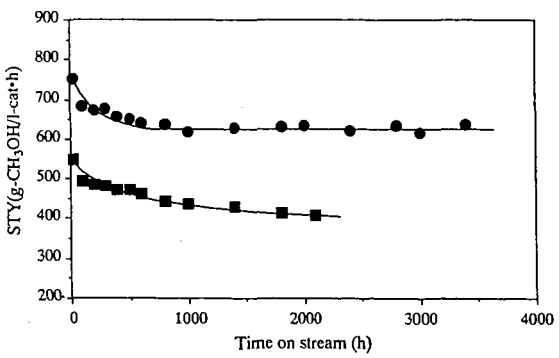

Fig. 4 Change in the activities of a multicomponent catalyst (Cu/ZnO/ZrO_2/Al_2O_3/Ga_2O_3, ●) and a commercial catalyst used for methanol synthesis from syngas (Cu/ZnO/Al_2O_3, ■) during a long-term test of methanol synthesis.
The reaction conditions: temperature=523 K, pressure=5 MPa, SV=10,000, feed gas composition=CO_2(22)/CO(3)/H_2(75).

CATALYTIC HYDROGENATION OF CO_2 INTO HYDROCARBONS: SUPPORT EFFECTS ON Fe AND Fe-K CATALYSTS.

Ki-Won Jun, Soo-Jae Lee, Myuong-Jae Choi and Kyu-Wan Lee
Catalysis Division
Korea Research Institute of Chemical Technology
Taejon 305-600, Korea

Keywords: CO_2 hydrogenation, Hydrocarbons, Support effects

INTRODUCTION

Since accumulation of carbon dioxide in the atmosphere is now regarded as one of the major reasons of the Global Warming, interest in the reutilization of carbon dioxide is on the increase [1-10]. It is desirable for the reutilization of carbon dioxide to develop the technology for the hydrogenation of carbon dioxide to valuable materials such as light olefins or liquid hydrocarbons.

However, relatively little attention has been paid so far to the catalytic hydrogenation of carbon dioxide while carbon monoxide hydrogenation has been extensively investigated with the purpose of utilization of coal as a carbon source. In previous studies [11-16], iron-based catalysts, which are originally used in the Fischer-Tropsch (F-T) reaction, have been applied to the hydrogenation of carbon dioxide to hydrocarbons. According to the results, however, it seems that those catalysts are not satisfactory because they give only small yield of C_{2+} hydrocarbons with the significant production of carbon monoxide and methane. It seems that the different catalytic properties are required for the hydrogenation of carbon dioxide because the chemical properties of carbon dioxide is different from carbon monoxide. Therefore, more systematic work is necessitated in order to develop suitable catalysts for the production of light olefins or liquid hydrocarbons from carbon dioxide hydrogenation.

While varying potassium content in the alumina-supported Fe-K catalysts, we found that the catalysts having high K content (K/Fe atomic ratio = 0.5-1.0) give considerably high conversion and selectivity to C_{2+} hydrocarbons and light olefins [17]. In the present work, we have investigated the support effects on Fe and Fe-K catalysts with the hydrogenation of CO_2.

EXPERIMENTAL

Silica gel, γ-alumina and titania (anatase) were used as the support materials. The BET surface areas, pore volumes and average pore diameters of support materials were determined by N_2 adsorption at -196°C adsorption using a volumetirc apparatus (Micromeritics ASAP 2400). Characteristics of support materials are listed in Table 1.

Supported iron oxide catalysts with an iron loading of 20%(w/w) were prepared by impregnating silica gel, γ-alumina (Strem, 157m^2/g) and titania (anatase) with an aqueous solution of $Fe(NO_3)_3 \cdot 9H_2O$. To prepare supported iron-potassium catalysts with K/Fe molar ratio = 0.5), an adequate amount of K_2CO_3 was added into the aqueous solution of $Fe(NO_3)_3 \cdot 9H_2O$ before impregnation. After the impregnation, the catalyst samples were dried at 383 K for 24 hr and calcined in air at 773 K overnight.

The temperature programmed decarburization was performed with the catalysts reacted with a mixture gas of carbon dioxde and hydrogen at 573 K and 1 atm for 30 min followed by cooling down to room temperature with purging helium. The gas was changed to hydrogen and the temperature of catalyst bed was increased to 923 K with the ramp of 5 K/min. The evolved product was mainly methane and it was analyzed continuously by a flame ionization detector, which gave the temperature programmed decarburization profile.

The catalytic hydrogenation of carbon dioxide was performed in a

continuous fixed bed reactor. The catalyst was reduced in a flow of hydrogen at 723 K for 20~24 hr. After the reduction, the catalyst was brought to the reaction temperature and then the feed changed to the mixture gas of carbon dioxide and hydrogen. Space velocity was 1900 ml/g-cat.·h. The products were analyzed by a gas chromatograph (Chrompack CP 9001) equipped with thermal conductivity and flame ionization detectors. Carbon monoxide, carbon dioxide and water were analyzed on a Porapak Q column and the hydrocarbons on a Poraplot Q capillary column. The experimental data were taken after 24 hr of the reaction.

RESULTS AND DISCUSSION

In the temperature programmed decarburization, the suraface carbides are investigated by the temperature programmed decarburization, which shows the relative amount and stability of surface carbon species formed during the reaction.

Figure 1 shows the decarburization profile of the supported iron catalysts after treatment at the reaction condition for 30 min. The decarburization profile of the Fe/silica catalyst shows a single peak with a maximum peak temperature of 690 K. However, with the γ-alumina supported catalyst, the profile shows two peaks (685 K and 725 K), which indicates the presence of two types of carbides. The peak appearing at higher temperature (725 K) represents that more stabilized carbide is formed during the reaction on Fe/γ-alumina. With the titania (anatase) supported catalyst, the profile shows two peaks also, but high temperature shift. The result of the high temperature shift reveals that supporting on titania (anatase) increases the stability of surface carbides on the catalyst. It seems that interaction between iron and supports exists with $Fe/\gamma\text{-}Al_2O_3$ and Fe/TiO_2, as compared to the silica supported catalyst. It is likely that the enhancement of carbide stabilization is due to the metal-support interaction.

The hydrogenation of carbon dioxide over supported iron catalysts produces both carbon monoxide and hydrocarbons, and the influence of support on the activity and selectivity of the reaction was examined.

Table 2 shows the results of CO_2 hydrogenation on supported Fe catalysts at 573 K and 10 atm. The conversion data reflect that activities for CO_2 hydrogenation decrease in order Fe/TiO_2, $Fe/\gamma\text{-}Al_2O_3$, Fe/SiO_2. This apparently indicates that the catalytic activity is not dependent on the surface area of support material. From the selectivity data, it will be seen that the catalysts Fe/TiO_2 and $Fe/\gamma\text{-}Al_2O_3$ show much higher selectivity for hydrocarbons than Fe/SiO_2. Furthermore, Fe/TiO_2 and $Fe/\gamma\text{-}Al_2O_3$ give higher selectivity for C_{2+} hydrocarbons as compared to the silica supported catayst. Especially, Fe/TiO_2 shows the highest selectivity for C_{2+} hydrocarbons. These results also indicate that the metal-support interaction exists with $Fe/\gamma\text{-}Al_2O_3$ and Fe/TiO_2. The high product selectivity for long-chain hydrocarbons with Fe/TiO_2 might be correlated with the results of decarburization which show that the carbides formed during the reaction are more stabilized by titania (anatase) support. It is reported that iron carbides are responsible for the formation of long-chain hydrocarbons in CO_2 hydrogenation [16].

We found that the promotion of Fe/Al_2O_3 with high K content gives the improvement in the catalytic performance for CO_2 hydrogenation to hydrocarbons [17]. The influence of support on the catalytic performance of Fe-K (K/Fe = 0.5) was examined also. Table 3 shows the results of CO_2 hydrogenation on supported Fe-K catalysts at 573 K and 10 atm. With silica and titania supports the addition of potassium decreases the catalytic activity and selectivity for hydrocarbons. In contrast, with γ-alumina support, the addition of potassium increases the catalytic activity. However, with all catalysts, the addition of potassium increases the selectivity for C_{2+} hydrocarbons and light olefins. It should

be noted that the combination of Fe, K and γ-alumina makes the catalyst bearing considerably high activity and selectivity. It seems that γ-alumina is not only a support but a kind of promotor in Fe-K/γ-Al_2O_3.

SUMMARY
The effects of support on CO_2 hydrogenation into hydrocarbons over Fe and Fe-K catalysts have been investigated. The catalysts were prepared by impregnation using silica gel, γ-alumina and titania (anatase) as supports. The results of temperature programmed decarburization showed that weak interaction between iron and support exists with Fe/γ-Al_2O_3 and strong interaction with Fe/TiO_2. The titania-supported iron catalyst gave much higher coversion and selectivity towards C_{2+} hydrocarbons than silica-supported iron catalysts. It is likely that the high catalytic activity and selectivity of Fe/TiO_2 are due to metal-support intraction. While potassium was being introduced into the catalysts as a promotor, it was found that potassium increased the selectivity for C_{2+} hydrocarbons and olefins on all supports, but increased the catalytic activity on only γ-alumina. The combination of Fe, K and γ-Al_2O_3 makes the catalyst highly active and selective for CO_2 hydrogenation to C_{2+} hydrocarbons and light olefins. It seems that γ-alumina functions as a promotor in Fe-K/γ-Al_2O_3.

ACKNOWLEDGEMENT
This research being one of the National G7 projects is supported by the Ministry of Science and Technology and the Ministry of the Environment in Korea.

REFERENCES
1. B. Delmon, Appl. Catal. B 1 (1992) 139.
2. J.H. Edwards, Catal. Today 23 (1995) 59.
3. G.C. Chinchen, P.J. Denny, D.G. Parker, M.D. Spencer and D.A. Whan, Appl. Catal. 30 (1987) 333.
4. Y. Amenomiya, Appl. Catal, 30 (1987) 57.
5. K.G. Chanchlani, R.R. Hudgins and P.L. Silveston, J. Catal. 136 (1992) 59.
6. R.A. Koeppel, A. Baiker and A. Wokaun, Appl. Catal. A 84 (1992) 77.
7. S.G. Neophytides, A.J. Marchi and G.F. Froment, Appl. Catal. A 86 (1992) 45.
8. K. Fujimoto and T. Shikada, Appl. Catal. 31 (1987) 13.
9. T. Inui, K. Kitagawa, T. Takeguchi, T. Hagiwara and Y. Makino, Appl. Catal. A 94 (1993) 31.
10. M. Fujiwara, R. Kieffer, H. Ando and Y. Souma, Appl. Catal. A 121 (1995) 113.
11. D.J. Dwyer and G.A. Somorjai, J. Catal. 52 (1978) 291.
12. G.D. Weatherbee and C.H. Bartholomew, J. Catal. 87 (1984) 352.
13. T. Suzuki, K. Saeki, Y. Mayama, T. Hirai and S. Hayashi, React. Kinet. Catal.Lett. 44 (1991) 489.
14. M.-D. Lee, J.-F. Lee, C.-S. Chang and T.-Y. Dong, Appl. Catal. 72 (1991) 267.
15. J.-F. Lee, W.-S. Chern, M.-D. Lee and T.-Y. Dong, Can. J. Chem. Eng., 70 (1992) 511.
16. M.-D. Lee, J.-F. Lee and C.-S. Chang, Bull. Chem. Soc. Jpn., 62 (1989) 2756.
17. P.H. Choi, K.-W. Jun, S.-J. Lee, M.-J. Choi and K.-W. Lee, Catal. Lett., accepted.

Table 1. Characteristics of supports

Support material	BET surface area (m^2/g)	Pore volume (cc/g)	Average pore diameter (Å)
SiO_2	462	0.731	63
Al_2O_3	157	0.407	104
TiO_2	10	0.030	118

Table 2. Effects of support on CO_2 hydrogenation performance of Fe catalysts[a]

Catalyst	Conv. (%)	Selectivity (C %)		Distribution of HC (C %)			O/P ratio in C_{2-4}
		CO	HC	C_1	C_{2-4}	C_{5+}	
Fe/SiO_2	22.1	61.6	38.4	59.7	34.2	6.1	0.02
Fe/Al_2O_3	43.9	4.7	95.3	27.1	54.2	18.7	0.01
Fe/TiO_2	51.3	5.2	94.8	25.2	54.3	20.5	0.05

[a]CO_2 hydrogenation at 1900 ml/g/h, 573 K and 10 atm

Table 3. Effects of support on CO_2 hydrogenation performance of Fe-K (K/Fe = 0.5 atom ratio) catalysts[a]

Catalyst	Conv. (%)	Selectivity (C %)		Distribution of HC (C %)			O/P ratio in C_{2-4}
		CO	HC	C_1	C_{2-4}	C_{5+}	
$Fe-K/SiO_2$	14.2	62.6	37.4	14.1	59.0	26.9	3.20
$Fe-K/Al_2O_3$	57.7	12.7	87.4	7.1	48.2	44.7	7.11
$Fe-K/TiO_2$	8.4	58.1	41.9	16.6	54.3	30.4	1.01

[a]CO_2 hydrogenation at 1900 ml/g/h, 573 K and 10 atm

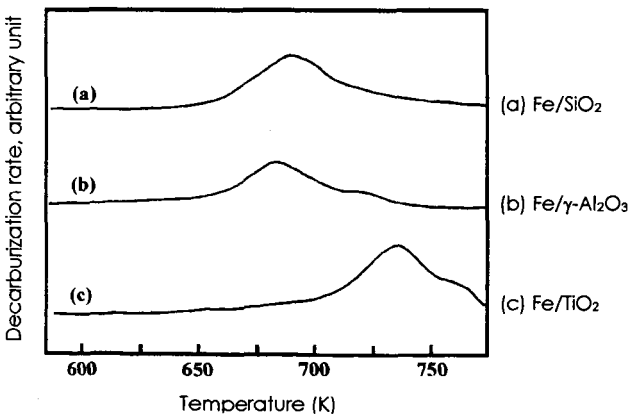

Figure 1. Temperature programmed decarburization of carbides on the catalyst surface.

HYDROGENATION OF CARBON DIOXIDE OVER Fe-ZnO/HY COMPOSITE CATALYST

Masahiro Fujiwara, Roger Kieffer†, Hisanori Ando, Qiang Xu, Yoshie Souma
Osaka National Research Institute, AIST-MITI, 1 Midorigaoka, Ikeda, Osaka 563, Japan
†LERCSI, ECPM Strasbourg, 1, rue Blaise Pascal, 67008 Strasbourg Cedex, France

Keywords: Hydrogenation of carbon dioxide; Composite catalyst; Fe-ZnO catalyst

INTRODUCTION

Fe-based catalysts are often used for various fields of catalytic reactions. F-T (Fischer-Tropsch) reaction is a representative example. It is well known that the Schulz-Anderson-Flory law determines the distribution of hydrocarbons in F-T reaction. To overcome this limitation, the composite catalysts comprised of Fe-based catalyst and zeolite have been examined (1). Although these composite catalysts produced branched hydrocarbons and improved the selectivity of hydrocarbons, the distribution was essentially restricted by the Schulz-Anderson-Flory law in almost cases.

We have already reported (2,3) that hydrocarbons were obtained efficiently from carbon dioxide and hydrogen over another type of the composite catalysts which are prepared by the physical mixing of Cu-based catalysts and zeolite (4). This catalytic system combining methanol synthesis and MTG (Methanol-to-Gasoline) reaction presents a novel method for hydrocarbon synthesis which is free from the Schulz-Anderson-Flory law. We recently found (5) that, in the hydrogenation of carbon dioxide, Fe-ZnO/HY composite catalyst produced hydrocarbons with a similar distribution to the composite catalysts comprised of Cu-Zn-chromate and zeolite (3), while Fe-ZnO catalyst (6) acted as a typical F-T catalyst to afford hydrocarbons with the Schulz-Anderson-Flory distribution. This presentation describes the entire studies of the hydrogenation of carbon dioxide over Fe-ZnO/HY.

EXPERIMENTAL

Fe-based catalysts were prepared by the coprecipitation of the corresponding nitrates using sodium hydroxide. The precipitate was washed five times, dried at 120°C for 6 h and calcined at 350°C for 3 h. The composite catalysts were obtained by the physical mixing of equal amounts of Fe-based catalyst and zeolite. HY [JRC-Z-HY4.8(2)] and NaY (JRC-Z-Y4.8) were provided from the Reference Catalyst of the Catalysis Society of Japan.

The hydrogenation of carbon dioxide was carried out using a pressurized flow-type fixed-bed reactor (2). The two stage reactor reaction was carried out using two separate stainless-steel reactors in series with the same diameter which were heated at the same temperature by the respective furnaces. The carbon monoxide adsorption and dissociation were carried out on a pulse reactor. TPR (Temperature-programmed reduction) measurement was carried out as follows; the catalyst (0.5 g) was heated (temperature increase rate: 10°C/min) in a glass tube reactor under a 10% H_2/He gas flow (31 ml/min). The consumption of the mass number 2 was monitored by an on-line quadrupole mass spectrometer. As the composite catalyst used for the hydrogenation of carbon dioxide was not suitable for this measurement because of carbon remained on the catalyst, Fe-ZnO(4:1)/HY pretreated by pure hydrogen at 350°C for 6 h, calcined at 350°C in air to re-oxidize was employed as a model used composite catalyst.

RESULTS AND DISCUSSION

The drastic differences of the catalytic behaviors of Fe-based catalysts were observed between sole catalysts and the corresponding composite catalysts with HY as shown in Table 1. Especially, the difference between Fe-ZnO(4:1) and Fe-ZnO(4:1)/HY is remarkable. From the hydrocarbon distribution shown in Fig. 1, it seems that Fe-ZnO(4:1) worked as a F-T catalyst and Fe-ZnO(4:1)/HY acted as the composite catalyst which was made of methanol synthesis catalyst and zeolite. The high selectivity of the branched hydrocarbons (For example: iso-C_4/n-C_4=5.5) in the case of this composite catalyst also suggested that these hydrocarbons cannot be produced by F-T reaction and that MTG reaction over zeolite was responsible for this formation. It is also noteworthy that ethylene and propylene were yielded in good selectivities. Most of studies on the composite catalysts for the hydrogenation of carbon oxides were unsatisfactory in the olefin formation so far (1,2). It is also paid attention that the yield of hydrocarbons decreased (from 9.8 to 0.7 C-mol%) over Fe catalyst by the mixing of HY. Fe/HY produced carbon monoxide exclusively, although the decrease of the total conversion of carbon dioxide was not serious (from 18.6 to 15.3%). In other cases such as Fe-Cr_2O_3 and Fe-Al_2O_3, the yields of hydrocarbons were very low. Cobalt catalyst was also studied because it is well known as an active F-T catalyst. In the absence of HY, Co-ZnO (4:1) produced methanol, and hydrocarbons obtained were only methane. Carbon monoxide was formed exclusively over the corresponding composite catalyst. Methanation was decisively inhibited and the hydrocarbon formation by the combination of methanol synthesis and MTG reaction was not observed in this case. Therefore, the noticeable change of the catalytic behaviors of Fe-based catalyst from F-T reaction to methanol synthesis was observed only in Fe-ZnO.

Different composite catalysts such as Fe-ZnO/NaY and Fe-ZnO/SiO_2 were also examined. Although the composite catalyst with NaY produced methanol and dimethylether in high selectivities, the yields of hydrocarbons were poor. The acidity of NaY is not enough to the conversion of methanol into hydrocarbons. However, the formation of dimethylether showed that methanol is obtained in considerable yield and is able to be transformed by acidic mechanism. In the case of Fe-ZnO/SiO_2, hydrocarbons were obtained in the Schulz-Anderson-Flory

distribution, indicating that F-T reaction took place. The acidic HY was required for this change of the catalytic behaviors of Fe-ZnO. In addition, two reactor reaction in series (Fe-ZnO and HY were packed in the first or the second reactor, respectively.) gave methane with high selectivity, and the distribution of hydrocarbons was completely different from the reaction over Fe-ZnO/HY. Therefore, it is evident that the function of Fe-ZnO/HY was not to combine F-T reaction over Fe-ZnO and the reforming reaction of hydrocarbons over zeolite.

Table 1. Hydrogenation of Carbon Dioxide over Fe-Based Catalyst[a)]

Catalyst[b,c)]	Conv. of CO_2 (%)	Convert to (C-mol%) C_1	C_{2+}	Oxy[d)]	CO
Fe	18.6	1.4	8.4	0.0	8.8
Fe/HY	15.3	0.3	0.4	0.0	14.6
Fe-ZnO	17.2	7.6	3.1	0.5	6.0
Fe-ZnO/HY	13.3	0.4	4.5	0.2	8.2
Fe-Cr_2O_3	28.1	0.5	0.1	0.3	27.2
Fe-Cr_2O_3/HY	24.9	1.1	0.6	0.0	23.2
Fe-Al_2O_3	19.5	3.2	1.6	0.5	14.2
Fe-Al_2O_3/HY	15.9	0.3	0.3	0.0	15.3
Fe-ZnO/NaY	6.0	0.1	0.6	3.0	2.3
Fe-ZnO/SiO_2	11.6	3.9	1.1	1.1	5.5
Fe-ZnO+HY[e)]	11.2	2.1	2.0	0.0	7.1
Co-ZnO	7.3	1.0	0.0	2.1	4.2
Co-ZnO/HY	10.2	0.0	0.0	0.0	10.2

a) 350°C, 5 MPa, SV=3000 ml/g-cat./h, H_2/CO_2=3, results after 6 h. b) Fe/Metal=4 (atomic ratio). c) Equal amount of Fe-based catalyst and HY was physically mixed for the composite catalysts. d) MeOH+MeOMe. e) Reaction using two reactors in series; Fe-ZnO in the first reactor and HY in the second reactor, SV=6000 ml/g-cat./h.

The effect of the zinc content on the catalytic behaviors was next examined as shown in Fig. 2. In the case of composite catalysts, Fe/HY and Zn/HY gave hydrocarbons in very poor yields. However, Fe-ZnO/HY with various zinc contents produced hydrocarbons in up to 5% yields, and the selectivities of C_{2+} hydrocarbons in all hydrocarbons were high [Fig. 2.(A)]. Although the zinc content was not a crucial factor in the hydrocarbon synthesis, the best yield of hydrocarbons was observed in Fe-ZnO(4:1)/HY. Fe-ZnO of which zinc content was higher than 33% can be considered as methanol synthesis catalyst, because methanol was obtained in up to 3% yield and the formation of hydrocarbons including methane was very low. It is understandable that hydrocarbons were obtained via MTG reaction in the case of the corresponding composite catalysts. However, the catalytic behaviors of Fe-ZnO(4:1)/HY were not expectable. Fe-ZnO(4:1) was a typical F-T catalyst because of the distribution of hydrocarbons approximately following the Schulz-Anderson-Flory law. On the contrary, in the case of the corresponding composite catalyst, Fe-ZnO acted as a methanol synthesis catalyst rather than a F-T catalyst [Fig. 1.(A)] . It seems that only the solid-solid interaction between Fe-ZnO and HY we noticed before (2) can explain this modification of the catalytic behaviors.

According to XRD measurement, Fe-ZnO with a zinc content lower than 33% prior to the reaction consisted of α-Fe_2O_3 and $ZnFe_2O_4$. In the catalyst used, the diffraction patterns of α-Fe_2O_3 disappeared completely and those of $ZnFe_2O_4$ remained. This suggested that α-Fe_2O_3 transformed to other iron species. As the active species for F-T reaction are generally obtained by the reduction of α-Fe_2O_3 via Fe_3O_4, the iron species derived from α-Fe_2O_3 seem to be the catalytic sites for F-T reaction. On the other hand, the diffraction patterns of ZnO and $ZnFe_2O_4$ were detected in Fe-ZnO with zinc contents higher than 33%. After the reaction, all peaks still remained only to become sharper. The catalytic activity for methanol synthesis of Fe-ZnO(1:2) was higher than that of ZnO as shown in Fig. 2. (A), indicating that not only ZnO (7) but also $ZnFe_2O_4$ are responsible for methanol synthesis. Fe-ZnO(2:1) can be regarded as pure $ZnFe_2O_4$, because its content of zinc and iron is similar to $ZnFe_2O_4$ and only the peaks of $ZnFe_2O_4$ were observed before the reaction by XRD measurement. However, ZnO as well as $ZnFe_2O_4$ were detected in the catalyst used. The spinel structure of $ZnFe_2O_4$ was destroyed during the reaction. Although evaluating the catalytic activity of pure $ZnFe_2O_4$ was unsuccessful, $ZnFe_2O_4$ is thought to be a significant component of Fe-ZnO to produce methanol. Moreover, in the case of the composite catalyst, it seems that some iron species from α-Fe_2O_3, which are deactivated not to be active for F-T reaction, promote this methanol synthesis, because the best yield of C_{2+} hydrocarbons was observed in Fe-ZnO(4:1) which is composed of α-Fe_2O_3 and $ZnFe_2O_4$.

The reaction of carbon monoxide, which is an important intermediate of F-T reaction, is also significant to reveal the influence of zeolite on the catalytic activity of Fe-ZnO. Carbon monoxide adsorption and dissociation experiments also show the change of the catalytic behavior of Fe-ZnO(4:1). The amount of adsorbed carbon monoxide can be related to the number of metallic sites active for F-T reaction. Furthermore, the amount of dissociated carbon monoxide was found to be correlated with the formation of C_{2+} species (8). Especially, this dissociation experiments at 300°C is advantageous so as to know the ability of the catalyst for F-T reaction, because the dissociation of carbon-oxygen bond in carbon monoxide is the first step of hydrocarbon formation in the conventional mechanism of F-T reaction. Table 2 shows the clear differences of the reaction manner of carbon monoxide between on Fe-ZnO and on Fe-ZnO/HY. In the case of Fe-ZnO, the adsorption of carbon monoxide was approximately the same as the reported one of α-Fe_2O_3 (9). The conversion of carbon monoxide at 300°C was very high, whereas only a limited part of carbon monoxide was involved in the Boudouart reaction, and the major part of converted carbon monoxide remained on the catalyst as surface carbon evidenced by carbon analysis. Thus, Fe-ZnO was very active for the dissociation of carbon monoxide to be an effective F-T catalyst. On the contrary, the ability of adsorbing carbon monoxide on Fe-ZnO/HY was extremely low, and the conversion of carbon monoxide at 300°C was lower than Fe-ZnO. From these results, it is obvious that the catalytic activity of Fe-ZnO for F-T reaction was diminished in the composite catalyst by the solid-solid interaction with HY.

Table 2. Adsorption and Reaction of Carbon Monoxide on Catalysts

Catalyst[a]		Fe-ZnO (4:1)	Fe-ZnO (4:1)/HY
CO adsorption (μmol)[b]		15.4	1.2
CO reaction (%)[c]	Total conv. of CO	78 (29)[d]	24 (21)[d]
	Carbon content (wt-%)[e]	2 (<0.1)[f]	<0.1 (3.8)[f]

a) Catalyst was pretreated by 20%H_2/N_2 for 5 h at 370°C. b) Measured by the pulse reaction of carbon monoxide (0.5 ml) at room temperature. Per 1 g of Fe-ZnO. c) Measured by the pulse reaction of carbon monoxide (0.5ml) at 300°C. d) Boudouart reaction determined by the amount of carbon dioxide detected by TCD. e) After the nine pulses of carbon monoxide. f) Catalyst used for the hydrogenation of carbon dioxide.

The solid-solid interaction was confirmed by TPR (Temperature-programmed reduction) measurement as well. The first hydrogen consumption which is thought to be caused by the reduction of α-Fe_2O_3 to Fe_3O_4, was observed at 313°C in Fe-ZnO (4:1) and also in Fe-ZnO(4:1)/HY without pretreatment. However, the temperature of the first hydrogen consumption was detected at 337°C in Fe-ZnO/HY pretreated at 350°C. Furthermore, this temperature was shifted to 376°C in Fe-ZnO/HY pretreated at 400°C. The solid-solid interaction between Fe-ZnO and HY changed the reducibility of the Fe-ZnO. These results also show that zeolite crucially affects the characteristics of Fe-ZnO.

From all results discussed here, it is obvious that hydrocarbons are produced by F-T reaction over Fe-ZnO(4:1), and by the combination of methanol synthesis and MTG reaction over Fe-ZnO(4:1)/HY, respectively. Fe-ZnO(4:1) consists of α-Fe_2O_3 and $ZnFe_2O_4$ in XRD measurement before reaction, and α-Fe_2O_3 produces the active species for F-T reaction by the reduction. F-T reaction works mainly in the presence of carbon monoxide formed by the reversed water-gas-shift reaction or by the decomposition of the methanol. However, in the presence of zeolite, the active sites for F-T reaction are inhibited by the solid-solid interaction with zeolite during the catalytic reaction. This effect was ascertained by the results of the carbon monoxide pulse experiments. The serious deactivation of Fe catalyst for F-T reaction also supports this phenomenon. On the other hand, the methanol formation can be attributed to Fe-promoted $ZnFe_2O_4$ or the related species. It seems that the influence of zeolite on this methanol synthesis is of minor importance. Therefore, hydrocarbons are produced via methanol over Fe-ZnO/HY. In other Fe-based catalysts such as Fe-Cr_2O_3 and Fe-Al_2O_3, no active species for methanol synthesis was included to result in the extremely poor yields of hydrocarbons over the corresponding composite catalysts. Co-ZnO includes no effective sites for methanol synthesis working with zeolite. The active species for F-T reaction was deactivated completely and, consequently, only carbon monoxide was obtained by the reversed water-gas-shift reaction.

The plausible reaction scheme is illustrated in Fig. 3. Fe-ZnO(4:1) has two kinds of reaction sites, that is, 1) metallic iron or other iron species active for F-T reaction derived from α-Fe_2O_3, and 2) Fe-promoted $ZnFe_2O_4$ or the related species for methanol synthesis. In the absence of zeolite, the F-T reaction sites exert their activity to produce hydrocarbons with the Schulz-Anderson-Flory distribution, whereas methanol formed is decomposed into carbon monoxide to promote F-T reaction. In the case of the composite catalyst, the F-T reaction sites are deactivated by zeolite while the catalytic activity for methanol synthesis is mostly maintained. Methanol formed which is not decomposed into carbon monoxide reacts over HY to form hydrocarbons with non-Schulz-Anderson-Flory distribution by MTG reaction. As carbon monoxide yielded

from methanol does not take place F-T reaction, the selectivity of carbon monoxide was very high in the case of the composite catalysts.

CONCLUSIONS

Fe-ZnO/HY composite catalyst is an original system which is able to produce olefins with a particular non-Schulz-Anderson-Flory distribution. The Fe-ZnO shows two kinds of catalytic sites, that is, iron species effective for F-T reaction formed from α-Fe_2O_3, and Fe-promoted $ZnFe_2O_4$ effective for methanol synthesis. In the absence of zeolite, the F-T reaction sites are very active to produce hydrocarbons with the Schulz-Anderson-Flory distribution. On the other hand, the sites for F-T reaction are deactivated and the sites for methanol synthesis promoted by iron species exhibit the catalytic activity in the case of the composite catalyst. Therefore, hydrocarbons were obtained by MTG reaction with a non-Schulz-Anderson-Flory distribution over Fe-ZnO/HY. The mechanism of the deactivation of the active sites for F-T reaction by zeolite is under investigation.

REFERENCES

1. P. D. Caesar, J. A. Brennan, W. E. Garwood and J. Ciric, *J. Catal.*, **1979**, *56*, 274 ; L. A. Bruce, G. J. Hope and J. F. Mathews, *Appl. Catal.*, **1984**, *9*, 351; Y. G. Shul, T. Sugiura, T. Tatsumi and H. Tominaga, *Appl. Catal.*, **1986**, *24*, 131; F. Nozaki, T. Sodesawa, S. Satoh and K. Kimura, *J. Catal.*, **1987**, *104*, 339; R. J. Gormley, V. U. S. Rao, R. R. Anderson, R. R. Schehl and R. D. H. Chi, *J. Catal.*, **1988**, *113*, 193; K. Fujimoto and K. Yokota, *Chem. Lett.*, **1991**, 559; C.-K. Kuei and M.-D. Lee, *Can. J. Chem. Eng.*, **1991**, *69*, 347; F. A. P. Cavalcanti, A. Yu. Stakheev and W. M. H. Sachtler, *J. Catal.*, **1992**, *134*, 226; Y.-M. Huang, X.-B. Meng, Z.-Y. Dang, S.-Z. Weng and C.-N. Zhang, *J. Chem. Soc., Chem. Comun.*, **1995**, 1025.
2. M. Fujiwara and Y. Souma, *J. Chem. Soc., Chem. Commun.*, **1992**. 767; M. Fujiwara, R. Kieffer, H. Ando and Y. Souma, *Appl. Catal. A*, **1995**, *121*, 113.
3. M. Fujiwara, H. Ando M. Tanaka and Y. Souma, *Appl. Catal. A*, **1995**, *130*, 105.
4. C. D. Chang, W. H. Lang and A. J. Silvestri, *J. Catal.*, **1976**, *56*, 268; T. Inui, T. Hagiwara, O. Yamase, K. Kitagawa, H. Yamaguchi and Y. Takegami, *J. Jpn. Pet. Inst.*, **1985**, *28*, 225; K. Fujimoto, H. Saima and H. Tominaga, *J. Catal.*, **1985**, *94*, 16; K. Fujimoto and T. Shikada, *Appl. Catal.*, **1987**, *31*, 13; K. Fujimoto, H. Saima and H. Tominaga, *Ind. Eng. Chem. Res.*, **1988**, *27*, 920; K. Fujimoto, H. Saima and H. Tominaga, *Bull. Chem. Soc. Jpn.*, **1988**, *61*, 2547; T. Inui and T. Takeguchi, *Catal. Today*, **1991**, *10*, 95; T. Inui, T. Takeguchi and K. Kitagawa, *Proc. 10th Intern. Congr. Catal.*, Budapest, 1992, Elsevier, Amsterdam, 1993, p.1453; T. Inui, K. Kitagawa, T. Takeguchi, T. Hagiwara and Y. Makino, *Appl. Catal. A*, **1993**, *94*, 31.
5. M. Fujiwara, H. Ando, M. Matsumoto, Y. Matsumura, M. Tanaka and Y. Souma, *Chem. Lett.*, **1995**, 839; M. Fujiwara, R. Kieffer, H. Ando, Q. Xu and Y. Souma, submitted.
6. S. L. Soled, E. Iglesia, S. Miseo, B. A. DeRites and R. A. Fiato, *Topics in Catal.*, **1995**, *2*, 193.
7. K. Klier, *Adv. Catal.*, **1982**, *31*, 243.
8. P. Chaumette, Ph. Courty, A. Kiennemann and B. Ernst., *Topics in Catal.*, **1995**, *2*, 117.
9. J. P. Reymond, B. Pommier, P. Meriaudeau and S. J. Teichner, *Bull. Soc. Chim. Fr.*, **1981**, 173.

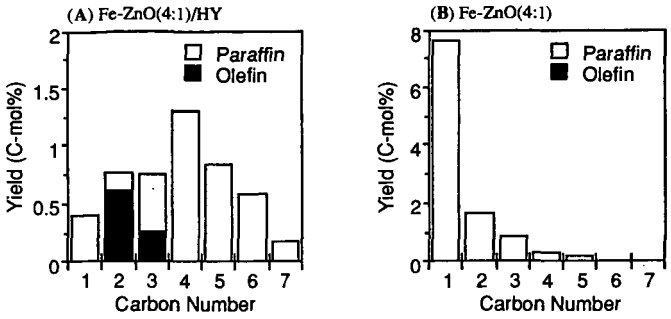

Figure 1. Hydrocarbon Distribution over (A) Fe-ZnO(4:1)/HY and (B) Fe-ZnO(4:1).

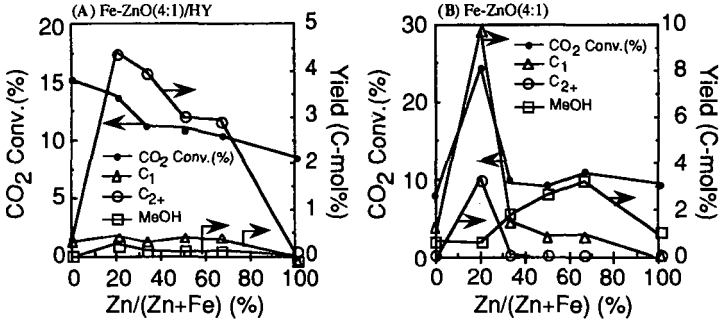

Figure 2. Effect of Zinc Content in (A) Fe-ZnO(4:1)/HY and (B) Fe-ZnO(4:1).

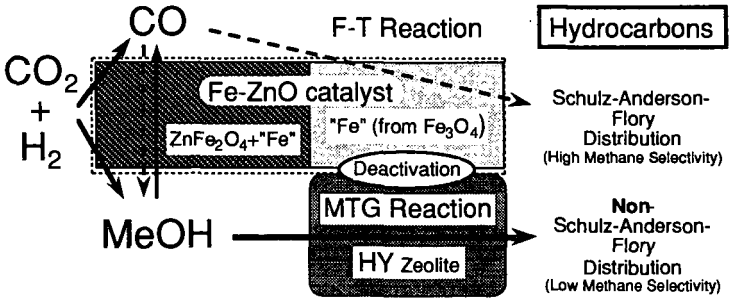

Figure 3. Reaction Scheme of Hydrocarbon Synthesis over Fe-ZnO/HY.

ELECTROREDUCTION OF CARBON DIOXIDE IN AQUEOUS SOLUTIONS AT METAL ELECTRODES

Jan Augustynski, Beat Jermann and Piotr Kedzierzawski
Department of Chemistry, University of Geneva
1211 Geneva 4, Switzerland

Keywords : CO_2 reduction, electrolysis, electrode activation

INTRODUCTION

The quantities of carbon stored in the form of atmospheric carbon dioxide, CO_2 in the hydrosphere and carbonates in the terrestrial environment substantially exceed those of fossil fuels. In spite of this the industrial use of carbon dioxide as a source of chemical carbon is presently limited to preparation of urea and certain carboxylic acids as well as organic carbonates and polycarbonates. However, the situation is expected to change in the future, if effective catalytic systems allowing to activate carbon dioxide will become available. In this connection, the electrochemical reduction of CO_2 , requiring only an additional input of water and electrical energy, appears as an attractive possibility. For more than 100 years formic acid and formates of alkali metals were considered as the only significant products of the electroreduction of carbon dioxide in aqueous solutions. The highest current efficiencies, exceeding 90 %, were obtained either with mercury or with amalgam electrodes [1-5]. The only comprehensive study regarding kinetics of CO_2 reduction in aqueous solution has been performed by Eyring et al. [6,7] using a mercury cathode. The proposed mechanism includes two charge transfer steps, eq. 1 and 3, separated by a rapid chemical reaction, eq. 2 .

$$CO_2 + e^- \rightarrow CO_2^{\cdot-}{}_{(ad)} \qquad (1)$$

$$CO_2^{\cdot-}{}_{(ad)} + H_2O \rightarrow HCO_{2(ad)} + OH^- \qquad (2)$$

$$HCO_{2(ad)} + e^- \rightarrow HCO_2^- \qquad (3)$$

The involvement of the radical anion $CO_2^{\cdot-}$ as the intermediate of the reduction at the mercury electrode has also been confirmed by the photoemission measurements [8]. Small amounts of $CO_2^{\cdot-}$ radical anions have as well been identified at a lead cathode using modulated reflectance spectroscopy [9]. It is important to mention, in this connection, that both these cathodes exibit high overvoltages for the CO_2 reduction (for the mercury electrode, for example, it exceeds 1V at a current density of $1 mA/cm^2$). This is consistent with a strangly negative value of the half-wave potential of the reaction

$$CO_2 + e^- \rightarrow CO_2 \qquad (4)$$

close to -2V versus standard hydrogen electrode (SHE). Other "soft" metal cathodes, particularly indium and tin allow still to obtain formates with high current efficiencies but at lower overvoltages [10,11]. As all these metals (i.e., Hg, Pb. In and Sn) exhibit high overvoltages for the reduction of water (hydrogen evolution), it was believed for the long time that this must be the necessary characteristic of every efficient electrocatalyst of CO_2 reduction. It was the observation by Hori et al. [12,13] that medium hydrogen overvoltage cathodes, gold, silver and copper are able to promote fomation of gaseous products of CO_2 electroreduction which has led to a marked regain of interest in this process. These authors have in fact demonstrated that the electrolysis of slightly alkaline solutions containing alkali metal hydrogen carbonates and CO_2, when conducted at gold and silver leads to the formation of carbon monoxide with faradaic yields attaining 100%. On the other hand, in the case of a copper cathode, the CO_2 reduction continues further to form hydrocarbons-methane and ethylene as well as ethanol. The next paragraphs are devoted to the discussion of the most important features of the CO_2 reduction at these three cathodes (Au, Ag, Cu).

EXPERIMENTAL

All the electrolysis experiments related in the next paragraph were carried out in a two-compartment, tight Teflon® cell. The cathodic compartment contained ca. 30 cm^3 of electrolyte and was separated from the anodic one by a Nafion® membrane The cell was equipped with a cyclic gas flow system. Before each electrolysis run, CO_2 supplied from a gas cylinder was passing through catholyte and gas circuit during 2 h to saturate the solution and to fill the system with CO_2. The total volume of the gas enclosed in the system was 185 cm^3 and its circulation rate 12 cm^3 min^{-1}. High purity metals rods (7 mm in diameter, 99,999%) served as cathodes. Solutions were prepared from reagent grade, chemicals and twice distilled water. In order to eliminate heavy metal contaminants, a constant current preelectrolysis (25 $\mu A/cm^2$) was usually conducted for a least 48 h, under nitrogen atmosphere, between two platinum electrodes separated by a Nafion® membrane. 99.99% CO_2 was further purified by passing through an activated charcoal filter before being introduced to the cathodic compartment of the cell and to the gas flow system. Analyses of the gaseous as well as solution products of the reaction were carried out on a Hewlett Packard 5890 Model gas chromatograph. The gas was sampled periodically with a gas syringe during the electrolysis, but products in the electrolyte were analysed once electrolysis run was completed. The chromatographic column Porapak HayeSepQ was employed to determine hydrocarbons and the reaction products in the solution, whereas analyses of CO were performed with the Carbosieve S-II column.

RESULTS AND DISCUSSION

The common feature of the gold, silver and copper cathodes is the occurrence of poisoning during electroreduction of CO_2 [15-18]. This poisoning is less severe for gold, where it results in a decay of the current (at constant controlled potential) without affecting faradaic efficiency of CO formation [17]. than in the case of silver for which η (CO) tends to decrease as a function of time [16,20]. The heaviest deactivation is observed for the copper electrode, where CO_2 reduction is virtually stopped after 20-40 min of continuous electrolysis being replaced by hydrogen evolution [18,19]. This problem being mentioned only in few among many papers devoted to this subject [19] it renders difficult any systematic comparison of the results obtained by different authors. In fact, in most cases the described experiments were conducted for very short periods of time corresponding to the passage of about 10C/cm^2 of the cathode surface. This is just less than the electrolysis duration after which, for example, a severe deactivation of the copper electrode usually starts. This phenemenon is illustrated by a series of curves in Fig. 1. Importantly, the copper electrode behaved in a similar way whether the electrolyte was pre-electrolysed or not. Moreover, XPS (X-ray induced photo-electron spectroscopic) analysis of the copper samples polarized for 2h at -1.72V in both kinds of 0.5M $KHCO_3/CO_2$ solutions (ie, with and without preelectrolysis) revealed only the presence of Cu, O and C signals. In particular, none of the metal elements present in trace amounts in $KHCO_3$ such as, for example, Fe, Zn, Cr, Pb or Cd was detected. The time associated with the deactivation of the cathode was no more affected by the degree of purity of the copper metal (99.999% vs. 99.9%). It is to be pointed out that the observed poisoning of the Cu electrode affects selectively the CO_2 reduction while, at the same time, the rate of hydrogen evolution tends to increase (cf. variation of the electrolysis current vs. time in Fig. 1. This kind of behaviour can be expected in the case of formation of the elemental carbon [19] or of a layer of organic products [20,21] at the Cu surface. An in situ electrochemical activation method has been demonstrated to act very efficiently against the inhibition of the copper cathode versus the CO_2 reduction. Such a treatment involves a periodic anodic stripping of the nascent poisoning species from the electrode surface by means of a series of 2-3 rapid voltammetric sweeps, repeated each 5-10 min. over the entire electrolysis run. The electrode activation requires less than

1 percent of the total electrolysis time (i.e., 2-3 s each 5 or 10 min.) and consumes a negligible extra amount of electrical charge (Fig. 2). Application of such a potential program allows high faradaic efficiencies of CH_4, C_2H_4 and C_2H_5OH to be maintained over long electrolysis runs. As shown in Fig. 3, no electrode deactivation was observed during a 8-days long continuous electrolysis experiment. While the total rate of hydrocarbon formation remained remarkably constant as electrolyses progressed, an increase of the amount of ethylene accompanied by a decrease of the amount of methane were in general observed. These variations in the product distributions are probably associated with the structural changes occurring at the electrode surface.

REFERENCES

[1] M.E. Royer, *C.R. Acad. Sci. Paris 70* /(1870) 73.

[2] A. Cohen, S. Jahn, *Ber. Dtsch. Chem. Ges. 37* (1904) 2836.

[3] R. Ehrenfeld, *Ber. Dtsch. Chem. Ges. 38* (1905) 4138.

[4] F. Fischer, O. Prziza, *Ber. Dtsch. Chem. Ges. 47* (1914) 256.

[5] M. Rabinovich, A. Mashovets, *Z. Elektrochem. 36* (1930) 846.

[6] W. Paik, T.N. Andersen, H. Eyring, *Electrochim. Acta 14* (1969) 1217.

[7] J. Ryu, T.N. Andersen, H. Eyring, *J. Phys. Chem. 76* (1972) 3278.

[8] D.J. Schiffrin, *Faraday Discuss. Chem. Soc. 56* (1973) 75.

[9] A.-W.B. Aylmer-Kelly, A. Bewick, P.R. Cantril, and A.M. Tuxford, *Faraday Discuss. Chem. Soc. 56* (1974) 96.

[10] K. Ito, T. Murata, S. Ikeda, *Bull. Nagoya Inst. Technol. 27* (1975) 369.

[11] Yu.B. Vassiliev, V.S. Bagotzki, N.V. Osetrova, O.A. Khazova, N.A. Mayorova, J. Electroanal. Chem. 189 (1985) 271.

[12] Y. Hori, K. Kikuchi, and S. Suzuki, *Chem. Lett.* (1985) 1695.

[13] Y. Hori, A. Murata, K. Kikuchi, and S. Suzuki, *J. Chem. Soc. Chem. Commun*, (1987) 728.

[14] Y. Hori, K. Kikuchi, A. Murata, and S. Suzuki, *Chem. Lett.* (1986) 897.

[15] J. Augustynski, A. Carroy, A.S. Feiner, B. Jermann, J. Link, P. Kedzierzawski, and R. Kostecki, Proceedings of the International Conference on Carbon Dioxide Utilisation, pp. 331-338, Bari, 26-30 September 1993.

[16] R. Kostecki and J. Augustynski, *J. Appl. Electrochem. 23* (1993) 567.

[17] P.Kedzierzawski and J. Augustynski, *J. Electrochem. Soc. 141* (1994) 58.

[18] B. Jermann and J. Augustynski, *Electrochim. Acta 39* (1994) 1891

[19] D.W. De Wulf, T. Jin, and A.J. Bard, *J. Electrochem. Soc. 136* (1989) 1686

[20] R. Kostecki and J. Augustynski, *Ber. Bunsenges. Phys. Chem. 98* (1994) 1510.

[21] S. Kapusta and N. Hackerman, *J. Electroanal. Chem. 134* (1982) 197.

[22] Y. Hori, A. Murata, and R. Takahashi, *J. Chem. Soc. Faraday Trans. I 85* (1989) 2309.

Fig. 1 Changes in the current efficiency of methane and ethylene occuring during first 2 hours of the electroreducion of CO_2 in 05.M $KHCO_3$ solution at a copper electrode maintained at a constant potential of -1.72 V (vs. SHE). Temperature 22°C. All copper electrodes etched in a HCl solution [18].

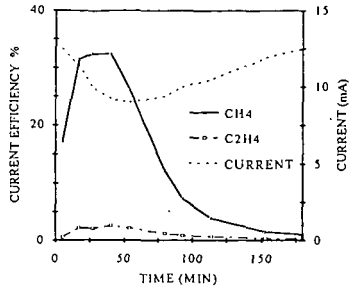

a) 99,9% copper cathode, non-preelectrolyzed $KHCO_3$ solution

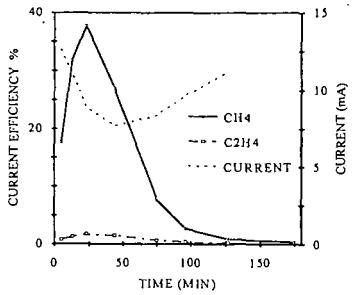

b) 99,999% copper cathode, non preelectrolyzed $KHCO_3$ solution

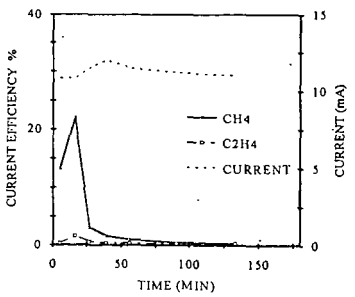

c) 99,9% copper cathode, preelectrolyzed $KHCO_3$ solution

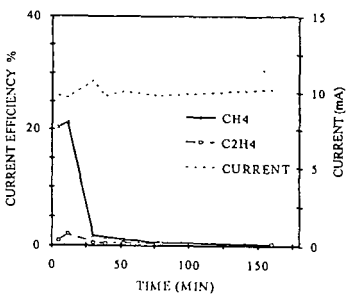

d) 99,999% copper cathode, preelectrolyzed $KHCO_3$ solution

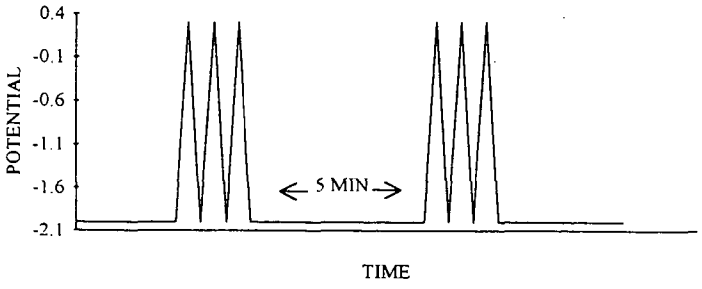

Fig. 2 Schematic representation of the anodic activation treatment (3 successive potential scans at 5 V/s into anodic region) applied to the copper electrode in the course of CO_2 electrolysis.

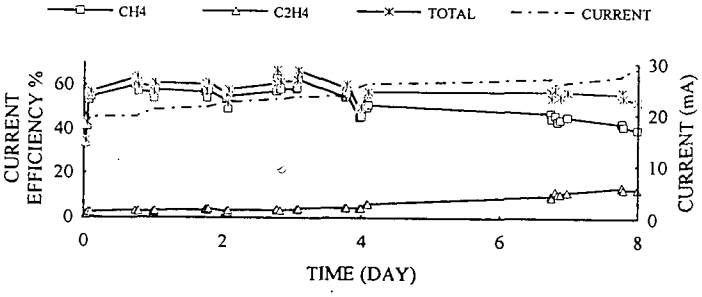

Fig. 3 Results of the 8-days long continuous electrolysis of CO_2 sat. 0.5M K_2SO_4 solution performed at an activated copper electrode (0.28 cm^2) at 22°C. Potential -1.72 V

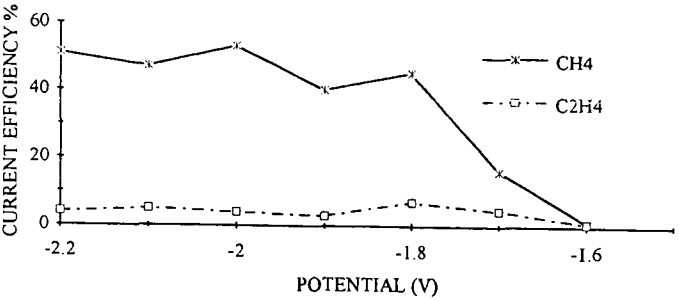

Fig. 4 Steady-state distribution of the CO_2 electrolysis products at the copper electrode as a function of the potential

CO_2 reducton reactions in heterogeneous oxidation and catalytic cracking processes

Ag.Kh .Mamedov ,Institute Petrochemical Processes ,
30 Telnov st., 37OO25 , Baku ,Azerbaijan ,(8922) 66-6I-5O

Abstract - The paper contains the results of heterogeneous catalytic activation of CO_2 by various organic substances, generalizes main scientific aspects of the new direction - "Oxidative Catalysis by Carbon Dioxide " ,and develop the petrochemical oxidative processes using carbon dioxide as an oxidant.

I.INTRODUCTION

Catalytic processes of oxidation of organic substances are realized mainly in the presence of oxygen. Low selectivity is characteristic of them due to partial conversion of crude product into CO_2.

In this connection the elaboration of new classes of oxidative processes, based on the nontraditional oxidant -carbon dioxide, is of great importance both to theory and practice and to environmental protection.

We aim to reduce CO_2 by hydrogen evolved from organic compounds IN SITU reaction,i.e. to realize the reduction of carbon dioxide with simultaneous selective oxidation of organic compounds. The reduction of carbon dioxcide with alkanes, olefins, alcohols and highmolecular parafins were studied as examples of these reactions:

$C_mH_{2n+2} + CO_2$ --------> $C_mH_{2n} + CO + H_2O$ (1)

$2C_2H_4 + CO_2$ --------> $C_4H_6 + CO + H_2O$ (2)

$CH_3OH + CO_2$ --------> $CH_2O + CO + H_2O$ (3)

C_mH_{2n+2} (m>6)+ CO_2 ---> products of catalytic cracking (4)

2.EXPERIMENTAL

Experiments were carried out in a flow vibro-fluidizied catalyst bed reactor atatmosphere pressure.Catalysts were prepared by usual impregnation method on SiO_2 and Al_2O_3 usingappropriate metal salts.As metal salts Mn,Cr,Fe,K,Mo,V,W,Ca and Ni were used.These catalysts were dried at 120°C and calcined at 700-8OO°C for 5 hours.

3.RESULTS AND DISCUSSION

Model example of the specified reactions is the oxidation of methane by carbon dioxide. Investigation of CH_4 interaction with CO_2 showed that the traditional regularities of this reaction,known for nickel catalysts ,are not valid in the case of manganese system ,where there is no formation of carbon even during the reaction of CO_2 in equimolar mixture with CH_4.At 930 °C full conversion of CO_2 and CH_4 was observed,yielding the equimolar mixture of $CO+H_2$ [I].

In the reaction of ethane with CO_2 the regularities of alkane oxidation with CO_2 change a little.The reduction of C-H bond energy in the case of ethane leads to the decrease of CO_2 activation temperature.

Reaction of C_2H_6 takes place at 800-830 °C .For simultaneous activation of CO_2 and dehydrogenation of ethane the catalyst has to combine reduction-oxidation and basic functions.K-Cr-Mn-O/SiO_2 system meets these requirements,in its presence the conversion of CO_2 satisfies to 52,3%,that of ethane was -82,6% with ethylene selectivity of 76,8 % [2].Contents of ethylene and carbon monooxide in the reaction mixture are similar ,thus making it possible to use this mixture without separation for carbonylation of ethylene.

The main tendency of propane oxidation with CO_2 is similarto those observed one in ethane conversion.During oxidation of propane by carbon dioxide the products are C_3H_6,C_2H_4,CO.In the presence of K-Cr-Mn-O/SiO_2 catalyst at 830°C olefins yield was 73% with the olefins selectivity of 78%.[3].

Another regularity is characteristic for isoutane rehydrogenation.The reaction of isobutane with carbon dioxide proceeds mostly by dehydrogenation mechanism followed by hydrogen oxidation. Apparently this is the result of quick decreasing of C-H bond energy in the raw from methane to isobutane.

Stoichiometric equations of isobutane conversion can be represented as follows:

$$i\text{-}C_4H_{10} \longrightarrow i\text{-}C_4H_8 + H_2 \qquad (5)$$

$$H_2 + CO_2 \longrightarrow H_2O + CO \qquad (6)$$

The yield of isobutylene in this reaction amounts to 45%, and its concentration was 20% in gas volume. The ratio of CO to H_2 is close to I with the high isobutylene selektivity (82 %).

Propylene in this case is by -product.The gas composition allows to recommend the new alternative process of isobutane oxidation by carbon dioxide with production of MTBE:

$$i\text{-}C_4H_8 \longrightarrow \text{alkylation} \longrightarrow \text{MTBE}$$

$$i\text{-}C_4H_{10} + CO_2 \longrightarrow C_3H_6 \longrightarrow CO + H_2 \longrightarrow CH_3OH$$

CO

H_2

Combination of endothermic reaction of isobutane dehydrogenation with exothermic one of methanol production from $CO+H_2$ makes it possible to decrease twice energy consumption of the process and carry it out partially by thermoneutral scheme.

One of the new reactions with CO_2 participation is ethylene oxidation,which is characterized by ethylene dehydrodimerization into butadiene.Cleavage of the C-H bond in ethylene with formation and dimerization of vinyl radicals in the presence of mild oxidant - carbon dioxide , unlike molecular oxygen proceeds selectively .Conversion of C2H4 in this process is not yet high,butadiene yield is 8-IO% [4].

During CO_2 reaction with methanol takes place the partial oxidation reaction .On Mo-Mn-O/SiO_2 catalyst high selectivity of CH_2O formation (90%) takes place [5].

Mechanism of CO_2 reduction during oxidation of organic substances have been established and showed ,that the properties and reactivity of surface oxygen ,generated by carbon dioxide is different essentially from the properties of oxygen ,generated from molecular oxygen.

The surface oxygen,generated by carbon dioxide ,is homogeneous,but the content of the oxygen.generated by CO_2 in catalyst, , is 5-6 times lower,than in the case of reoxidation by molecular oxygen.

The study of the conversion of various organic substances under the the condition of stages separation showed that the rate of CO formation during CO_2 reduction in catalyst reoxidation stage is much lower ,than the rate of CO formation under stationary conditions .Besides CO_2 reduction and catalyst reoxidation proceed with high rate only at higher temperatures than 700°C .At the same time under stationary conditions CO2 reduction up to CO occurs mainly from 620°C.In order to elucidate this phenomenon ,we carried out experiments with addition of 1-2% H_2 into CO_2.It has been established ,that the addition of l% H_2 into CO_2 leads to abnormally sharp increase of CO_2 reduction rate to CO.

The observed phenomenon and the initiating effect of H_2 is probably connected with CO_2 reduction proceeding in the presence of hydrogen by new chain mechanism.

This mechanism of CO_2 activation allows to carry out in its presence not only the reactions of reduction-oxidation type,but also of acidic basic ones.Such possibility has been discovered in new reactions of oxidative cracking .Thus,destructive conversion of heptane,which was chosen as a cracking model hydrocarbon in the presence of CO2 proceeds more efficiently than in its absence [6].

REFERENCES

1.Mamedov Ag.Kh., Mirzabekova S.R., Shiryayev P.A., Shashkin D.P., Neftekhimiya.,1 ,30 (1990)

2.Mamedov Ag.Kh., Mirzabekova S.R.,Neftekhimiya.,3,250 (1992)

3.Mamedov Ag.Kh.,Mirzabekova.,Aliev V.S.,Neftekhimiya.,3 ,335 (1991)

4.Mirzabekova S.R., Mamedov Ag.Kh., Aliev V.S., Neftekhimiya.,2 ,114 (1993)

5.Mirzabekova S.R.,Mamedov Ag.Kh.,Neftekhimiya.,I,30 (1993)

6.Mirzabekova S.R.,Mamedov Ag.Kh.,Krylov O.V.,Kinetika i kataliz.,I,184 (1993)

THE SERENDIPITOUS ASSOCIATION OF SEDIMENTARY BASINS AND GREENHOUSE GASES

Brian Hitchon
(Hitchon Geochemical Services Ltd., Box 79088, 1020 Sherwood Drive,
Sherwood Park, Alberta T8A 5S3, Canada)

W.D. Gunter and Thomas Gentzis
(Alberta Research Council, PO Box 8330, Edmonton, Alberta T6H 5X2, Canada)

Keywords: greenhouse gases—aquifer disposal; coalbed methane; carbon dioxide—disposal

INTRODUCTION

Sedimentary basins are the major world repository of fossil fuels—these include petroleum and natural gas, and coal. Industry has grown up over some of the sedimentary basins and in many cases is the source of major greenhouse gas emissions, the most important of which is CO_2. This is a relationship which might be expected. The realization that greenhouse gas emissions may be contributing to global warming has led to research into the mitigation of the effects of these emissions by natural processes, by use in manufacture of chemicals, and by disposal into oceans or sedimentary basins.

One of the more promising avenues of research has been into the disposal of CO_2 into aquifers deep in sedimentary basins. Of the various methods that have been suggested for the disposal of CO_2 in sedimentary basins (in geological structures such as salt domes, in depleted oil and gas reservoirs, in coalbeds, or in aquifers), only that in aquifers involving mineral trapping renders the CO_2 harmless. There is an additional advantage because the volume of pore space available in deep aquifers far exceeds that of salt domes, depleted hydrocarbon reservoirs, or enhanced oil recovery projects. Further, aquifers are widely distributed and, very important, they underlie most point sources of CO_2 emission. Carbon dioxide is an ideal candidate for aquifer disposal because of its high density and high solubility in water at the relatively high pressures that exist in deeper aquifers. This technology is economically viable and is in active development in areas as widely separated as the North Sea and Indonesia. Recently, a suggestion has been made that in addition to disposing of CO_2 into aquifers, it may also be used to remove methane from deep coalbeds. The methane–CO_2 mixture would be separated at the surface and the methane used as fuel, in the normal way. While this would produce more CO_2, the solution to that problem is clear. The CO_2 fraction of the gas that is returned to the surface could be re-used for more methane recovery or disposed of in deep aquifers. This recycling of gases is possible because there is a close association of the fossil fuel resources of sedimentary basins and the greenhouse gas emitting industry that is based on those fuels. We regard this as a serendipitous association.

SEDIMENTARY BASINS AND FOSSIL FUELS

There is a natural association of sedimentary basins (which are accumulations of sedimentary rocks) and fossil fuels through the processes of (1) accumulation of organic matter in the original sediments, (2) its burial to depths where temperatures can change (mature) the character of the organic matter, and (3) in the case of petroleum and natural gas, which are fluids, create structures into which they can migrate and accumulate. These processes result in the development of fossil fuel deposits in the sedimentary basins, and the association is a natural one. Therefore, we should expect a relation between the sedimentary basin, the exploitation of its fossil fuels, and the resulting greenhouse gas emissions.

Despite the wide range of processes that may act on basins, the relation is strong. Any specific basin may be a prolific hydrocarbon producer or not, depending on its geological history. The age of the rocks will also play a part in determining the probability of oil, natural gas, or coal being present. Despite these variables, all sedimentary basins have a common feature in the nature of the fluid that effectively fills all the pore spaces—formation water—for oil and gas are rare fluids in terms of their volume in sedimentary basins, despite their dominant economic importance. The next part of this note deals with the processes that control the movement of formation water in sedimentary basins, because it is this fluid (and the space it occupies), and not oil and gas, that is important for aquifer disposal of CO_2.

HYDROGEOLOGY OF SEDIMENTARY BASINS

It is important to understand that most sedimentary rocks contain pore space between the mineral particles, and the pores are filled with fluid, mostly formation water but occasionally hydrocarbons. Any joints, fractures or faults are also filled with formation water. The original pore space is reduced due to compaction by overlying sediments, but seldom does it disappear altogether even in the most deeply buried rocks. The pore space can also be reduced by the deposition of minerals from the formation water during diagenesis. Conversely, the formation water may be of such a composition as to dissolve minerals from the rock, perhaps even creating more pore space than in the original deposit. There is a chemical balance between the formation water and the rock, through water-rock interaction processes. This balance will be disturbed if CO_2 is injected into the sedimentary rock.

Formation water and other fluids in sedimentary basins are in constant motion, though the rate of movement is generally slow; in the Alberta Basin it is of the order of 1–10 cm/year. Fluids move through the pore spaces of the rocks basically under two forces. In the early history of sedimentary basins the driving mechanism is compaction, with the direction of movement upward and toward the existing shoreline. Once the sedimentary rocks are uplifted, the fluids in the rocks come under the influence of the meteoric water system, and fluid movement in the rocks is controlled by the local topographic elevation. This means that, as

a general rule, major upland areas are regions of recharge and major lowlands are discharge areas. The internal flow system in sedimentary basins is governed by (1) differences in the ability of the different rock types to transmit water, (2) processes due to uplift and erosion that may counter the normal topographically controlled forces, and (3) buoyancy effects due to salinity contrast between formation waters. For our purposes, however, the important thing to remember is that all formation water is in motion, however slow.

Equally important is the fact that different sedimentary rocks transmit water to different degrees. The attribute that describes this ability to transmit water is called permeability. It is unrelated to the absolute porosity (or void space) of the rock, and reflects the degree to which the pores are interconnected; an isolated pore, no matter how large, cannot transmit water. Sedimentary rocks are therefore of three types, with respect to their ability to transmit water—aquifers, aquitards and aquicludes. Aquifers are rocks from which water can be pumped or into which water can be injected; examples include most sandstones and limestones. Aquitards allow movement of water through them over geological periods of time, but pumping and injection are not feasible; examples include shales. Aquicludes are barriers to water movement, and the best example is a salt bed. Note that these definitions are for any rock, so a highly fractured shale or granite can be a good aquifer, depending on the interconnectedness of the fractures. When any fluid is injected into an aquifer it will move out from the injection well under the influence of the imposed pressure. It is important to determine the rate of movement of the injected material and the path that it may be expected to follow. It is the task of the hydrogeologist to determine the natural, undisturbed hydrogeological regime, and then see how the injected material will perturb the natural system. In conjunction with the geochemist, it is possible to predict the effects resulting from the injection of CO_2 into deep aquifers in a sedimentary basin.

AQUIFER DISPOSAL OF CO_2

The most comprehensive evaluation of the aquifer disposal of CO_2 is that carried out by the Alberta Research Council in the Alberta Basin—summarized in Hitchon (1996 and references therein). There are two ways in which CO_2 can be trapped in aquifers: (1) hydrodynamic trapping and (2) mineral trapping. At their most fundamental, these concepts refer to the injection of liquid CO_2 into aquifers, at least 800 m deep, in sedimentary basins, and into situations that either (1) trap the CO_2 into flow systems for geological periods of time (hydrodynamic trapping) or (2) convert the CO_2 to carbonate minerals and thus render it immobile (mineral trapping).

Aquifers suitable for injection of CO_2 must satisfy the following general conditions: (1) the top of the aquifer must be > 800 m deep (at this depth the CO_2 will be in a supercritical state); (2) the aquifer should be capped by a regional aquitard (sealing unit); (3) the aquifer should have enough porosity and adequate permeability; the near-well permeability should be high to allow good injection capability, but the regional permeability should be low so that the residence time of the CO_2 is high; (4) the injection site should be close to the CO_2-emitting source.

The strategy is therefore: (1) to identify the point sources of CO_2 emission; (2) to carry out a detailed, regional-scale hydrogeological analysis of the basin to identify suitable disposal aquifers that satisfy the conditions of depth, capping, permeability and storage capacity; and (3) to carry out detailed hydrogeological, injectivity and geochemical studies for the identified aquifers in the immediate vicinity of the CO_2 sources.

Hydrodynamic Trapping

When CO_2, or any fluid, is injected into an aquifer at an appropiate pressure below the fracture pressure, it moves out from the injection well and flows with the natural flow regime. For the Alberta Basin, simple calculations show that times of the order of millions of years will still find the CO_2 within tens of kilometers of the injection site. This geological time-scale trapping of CO_2 in deep regional aquifers as a result of very low flow velocity is called hydrodynamic trapping because it depends on the hydrodynamic regime of the formation waters. Some CO_2 will dissolve in the formation water and travel as a dissolved phase; this allows the processes of diffusion, dispersion and convection to be brought into play. In the Alberta Basin the main transport mechanisms for dissolved CO_2 are molecular diffusion and dispersion; this means that the dissolved CO_2 will spread laterally over a larger mass of rock than if convection was the main transport mechanism, leading to an increased sweep efficiency.

In contrast with CO_2 injection in depleted oil and gas reservoirs, injection into deep aquifers in sedimentary basins has the advantage that it is not limited by reservoir location, size and properties.Thus there are many aquifers in the Alberta Basin suitable for CO_2 disposal; some thin, isolated aquifers in the Cretaceous and post-Cretaceous sedimentary succession in the southwestern part of the basin have the additional significant property that the flow of formation water is downdip, basin-inward, toward hydraulic sinks created by shale elastic rebound as a result of Tertiary-to-Recent erosion. Thus disposal of CO_2—and of any other liquid wastes—in these aquifers in this area will lead to the permanent capture and retention of CO_2 and other wastes (on a geological time scale).

Mineral Trapping

The chemistry of formation water and rock mineralogy play an important part in determining the potential for CO_2 capture through geochemical reactions. Most important, these reactions sequester the CO_2 in immobile form as carbonate minerals.

The dominant volatile components that affect mineral dissolution/precipitation reactions are CO_2, H_2S, SO_2 and O_2. These gases dissolve in the aqueous phase and alter the pH through reactions coupled to the dissociation of water. Reactions of the following type occur when CO_2 dissolves in water:

$$H_2O + CO_2 = \underset{\text{bicarbonate}}{HCO_3^-} + \underset{\text{proton}}{H^+}$$

So, initially, some of the CO_2 is held in the aqueous phase as bicarbonate. Only minor amounts of bicarbonate ion and the proton will be produced, no matter how high the pressure of CO_2. This is the reason that formation waters alone are not acceptable sinks for CO_2. However, the proton results in acid conditions in the water and, therefore, the possibility of attack on the silicate minerals present in the aquifer. The attack results in free ions of elements such as Ca, Mg, and Fe being released:

$$\underset{\text{anorthite}}{H_2O + CaAl_2Si_2O_8} + \underset{\text{proton}}{2H^+} = \underset{\text{calcium}}{Ca^{2+}} + \underset{\text{kaolinite}}{Al_2Si_2O_5.(OH)_4}$$

One of the fastest geochemical reactions is the precipitation of calcium carbonate, which occurs when free Ca ions exist in the presence of bicarbonate ions. The reaction produces calcite, and it is this reaction that forms the theoretical basis for the sequestering of the CO_2 as the mineral calcite.

$$\underset{\text{calcium}}{Ca^{2+}} + \underset{\text{bicarbonate}}{HCO_3^-} = \underset{\text{calcite}}{CaCO_3} + \underset{\text{proton}}{H^+}$$

The overall result is just the sum of these three reactions:

$$\text{Anorthite} + 2H_2O + CO_2 = \text{Kaolinite} + \text{Calcite}$$

There are similar reactions for the formation of calcium-magnesium carbonate (dolomite) and iron carbonate (siderite). For the more complex minerals commonly found in aquifers, the reaction is of the form:

$$\text{Feldspars} + \text{Clays} + CO_2 = \text{Kaolinite} + \text{Calcite} + \text{Dolomite} + \text{Siderite} + \text{Quartz}$$

where the CO_2 is permanently fixed as the carbonate minerals calcite, dolomite and siderite. Mineral traps of CO_2 are most effective when the aquifer contains minerals that are proton sinks—that is, the basic silicate minerals such as the feldspars and clay minerals. Consequently, mineral trapping of CO_2 is favoured in sandstone aquifers over carbonate aquifers.

In the Glauconitic Sandstone aquifer of the Alberta Basin, the process of mineral trapping was examined using a water-rock reaction computer model, PATHARC.94. Based on aquifer mineralogy and estimated grain size, and using a formation water from the same aquifer, injection of CO_2 into the Glauconitic Sandstone aquifer was modelled under reservoir conditions. The times for reacting out for the various minerals are: kaolinite 80 years; biotite (as an analogue for glauconite) 100 years; albite (Na-feldspar) 540 years; and K-feldspar 820 years. The resulting mineral assemblage will consist of quartz, and significant amounts of muscovite and siderite. Calculations show that there will be complete equilibrium in 820 years, resulting in the trapping of 6.2 moles of CO_2 relative to each kilogram of formation water in the aquifer.

In summary, in the Alberta Basin, suitably located injection sites far from the basin edge and injection at depths > 800 m result in geologically long times before breakout to the surface occurs—if at all. By that time, if mineral trapping has not occured, the pressure of CO_2 will have been reduced to such an extent (from the original injection pressure) due to solution, diffusion and dispersion that the breakout will be a harmless event, occuring over a much longer period than the original injection period.

CARBON DIOXIDE, AQUIFERS AND SEDIMENTARY BASINS

Carbon dioxide disposal into low permeability, deep aquifers in sedimentary basins has been shown to be technically feasible and perhaps offers the largest potential for the landlocked areas of the world. A preliminary economic assessment indicated that significant costs will be incurred due mainly to CO_2 capture, purification and compression, and secondarily due to the field facilities required. Despite these expenses, a recent report on the Sleipner Vest Field in the North Sea indicates that the 9.5% CO_2 will be reduced to 2.5% in the sales gas, with about 1 million tonnes per year of the waste CO_2 being injected into Tertiary sandstones; injection is scheduled to start 1996-10-01. An even larger project is the proposed removal of the 71% CO_2 in the natural gas of the Natuna Field in Indonesia—one of the largest gas fields in the world with reported 1270 billion m^3 of recoverable hydrocarbon reserves. It is proposed to inject the waste gas into two carbonate aquifers near the field; construction of the facilities is scheduled to last eight years.

The work reported for the Alberta Basin has demonstrated the concepts of hydrodynamic and mineral trapping of CO_2 injected into deep aquifers using information based on a real situation. The capacity of the Alberta Basin aquifers for storage of CO_2 exceeds 20 gigatonnes. The procedures and method of conducting a hydrogeological evaluation of a potential injection site can be emulated world-wide, as can the geochemical modelling. The numerical modelling resulted in nomograms specific to the Alberta Basin, but these nomograms are also viable in other world basins where the basin and reservoir data are similar. Not all sedimentary basins are suitable for injection of CO_2—some because their basin architecture is not suitable, others because they are remote with respect to both distance and appropriate point concentrations of CO_2 emissions. Nevertheless, the results can be used in many world sedimentary basins which are in areas with

fossil fuel exploitation. The Sleipner Vest and Natuna examples cited above indicate that injection of CO_2 into aquifers is now a practical process in the petroleum industry and economically viable. The conclusion of the Final Report of the Joule II Project, *The Underground Disposal of Carbon Dioxide*, is that underground disposal is a perfectly feasible method of disposing of very large quantities of CO_2, such as are produced by fossil fuel fired power plants and most other large point sources of CO_2 (Holloway *et al.*, 1996). The same authors conclude that the next major step in implementing CO_2 storage from power plants should be the demonstration of the storage process. The Sleipner Vest and Natuna projects are essentially large-scale demonstrations of the practicality of the underground disposal of CO_2. It is in this context that the Alberta study (Hitchon, 1996) is offered for world-wide application as an example of the methodology developed to prove the concept of hydrodynamic and mineral trapping of CO_2 in aquifers.

COALBED DISPOSAL OF CO_2

Water and gases are generated during the conversion of plant material to coal, and they are either adsorbed onto the coal or are dissolved into the pore spaces. Methane is the dominant gas (about 95%), with the remaining gases including ethane, CO_2, N_2, He and H_2; H_2S is found only in trace amounts, even in high-S coals, a factor that is related to the nature of the S in coals. The amount of methane formed can be related to the maturity of the coal. The methane associated with coalbeds is termed coalbed methane (CBM).

The attraction of disposing of CO_2 in coalbeds is that it can be coupled directly with the production of methane, a fossil fuel (Gunter *et al.*, 1996). Unlike aquifer disposal of CO_2, the status of research on the recovery of methane from coalbeds using CO_2 is at an embryonic stage. It has been known for two decades that CO_2 is very effective in displacing methane from crushed coal under laboratory conditions; initially, this work was mainly aimed at improving the safety of coal mining. In the late 1980s, through a series of patents, Amoco Corporation demonstrated the potential use of CO_2 and other gases to produce methane from deep coalbeds that are considered unmineable for technological or economic reasons. The injected CO_2 is trapped by sorbing to the coal, thereby displacing the methane which flows to the production well. In 1995, Amoco started their first of a series of three nitrogen pilots, with an additional CO_2-pilot to be tested in the field in 1996.

Conventional or primary CBM recovery has been a practical operation in several coal-fields around the world, most notably in the USA. The process effectively involves the depressuring of the coalbed, which releases the adsorbed methane, as well as methane dissolved in the formation water. Although the method is conceptually simple, there are problems with recovering the methane at the imposed reduced pressure. This results in a delay in methane production and there are large amounts of formation water produced—that must be disposed to the subsurface. The disposal of CO_2 in these methane-rich coalbeds partially solves these problems by (1) increasing the drive pressure, (2) sorbing the CO_2 onto the coal and thereby driving off the methane, hence increasing the rate and the amount of methane produced, and (3) decreasing the relative rate of water production. Consequently, it is expected that this new technology will considerably increase the CBM reserves available for exploitation in North America. The fact that the coalbeds retain most of the CO_2 injected is an additional environmental benefit.

The bulk of the CBM in Canada lies in the Alberta Basin. There is CBM production from many different coal basins in the USA, but around 96% comes from just two—the San Juan Basin, located in southwestern Colorado and northwestern New Mexico, and the Black Warrior Basin in Alabama. Estimates of the CBM resource in North America vary greatly, but by all reasonable estimates, a huge amount exists. In the USA, estimates of CBM resources range form 275 to 649 TCF; in Canada there is considerable more uncertainty, and estimates range over an order of magnitude, from 200 to 3000 TCF.

Experimentally, measured adsorption isotherms for binary and ternary mixtures of CO_2, methane and N_2 show that the equilibrium gas and adsorbate phase compositions differ considerably, and that the total amount of gas mixture adsorbed is strongly dependent on composition and system. Carbon dioxide is the most strongly adsorbed gas , then methane, with N_2 being the least adsorbed. The approximate adsorption ratios are 4:2:1; that is, 4 molecules of CO_2 are adsorbed compared to 2 molecules of methane and 1 molecule of N_2, when comparing pure gases at the same temperature and pressure. Using a very conservative estimate of 150 TCF for the methane resource of the Alberta Basin, the total capacity for sorption by the deep coals of the Alberta Basin is approximately 10 gigatonnes of CO_2—very similar to that estimated for the aquifers of the Alberta Basin.

There is no reported field evaluation such as was carried out by the Alberta Research Council for aquifer injection of CO_2 in the Alberta Basin. However, what work has been done suggests that the concept of disposing of CO_2 or flue gas (a mixture of N_2 and CO_2) from the waste stream of power plants into coalbeds has considerable merit. An evaluation similar to that for aquifer CO_2 disposal is currently being carried out for the Alberta Basin.

CONCLUSIONS

Sedimentary basins, fossil fuel resources, and deleterious greenhouse gas emissions are all closely associated. To exploit the fossil fuels is to produce the greenhouse gases. This does not have to be so. The main greenhouse gas produced by the burning of fossil fuels is CO_2. Rather than discharge CO_2 to the atmosphere, it has been suggested that it be either disposed of in deep aquifers in the same sedimentary basins from which the fuel was extracted, or it be injected into deep coalbeds in the same basins to release the adsorbed methane. The former concept has been evaluated by the Alberta Research Council using field data from the Alberta Basin. Similar methodology is proposed for the Sleipner Vest Field in the North Sea,

and for the Natuna Field, Indonesia. Unlike aquifer disposal of CO_2, injection into coalbeds is not as technologically advanced. However, the concept appears viable, and a proof of concept study is being carried out for the Alberta Basin.

This note has been concerned with two of the five methodologies available for the mitigation of CO_2 emissions from the burning of fossil fuels by disposal in sedimentary basins. These two processes have much in common, and it is pertinent to close with a cartoon (Figure 1) that outlines their main features. Compared to the other three technologies, the two discussed at length in this note potentially can trap much larger volumes of CO_2. The association of sedimentary basins, fossil fuel resources and the mitigation of greenhouse gas emissions from the burning of the fuels is indeed serendipitous.

REFERENCES

Gunter W.D., T. Gentzis, B. Rottenfusser and R. Richardson (1996) *Deep Coalbed Methane in Alberta, Canada: A Fossil Fuel Resource with the Potential of Zero Greenhouse Gas Emissions.* Paper to be presented at the Third International Conference on Carbon Dioxide Removal, Massachusetts Institute of Technology, September 9-11, 1996.

Hitchon B. (editor) (1996) *Aquifer Disposal of Carbon Dioxide: hydrodynamic and mineral trapping—proof of concept.* Geoscience Publishing Ltd. (Box 79088, 1020 Sherwood Drive, Sherwood Park, Alberta T8A 5S3, Canada).

Holloway S., J.P. Heederik, L.G.H. van der Meer, I. Czernichowski-Lauriol, R. Harrison, E. Lindeberg, I.R.Summerfield, C. Rochelle, T. Schwarzkopf, O. Kaarstad and B. Berger (1996) Conclusions and recommendations. In *The Underground Disposal of Carbon Dioxide.* Contract No. JOU2 CT92 0031, Final Report. Chapter 9, p. 320–322. British Geological Survey.

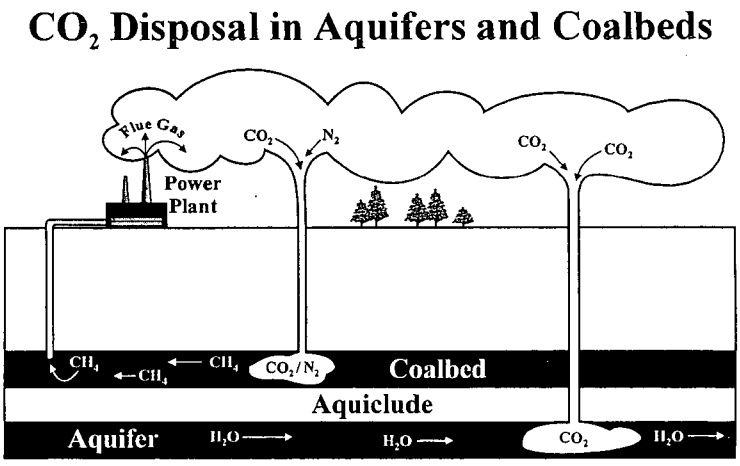

Figure 1. Cartoon showing the relation among sedimentary basins, fossil fuel resources, and the mitigation of CO_2 emissions from the burning of fossil fuels by injection into deep aquifers and the recovery of methane from coalbeds.

IS CO_2 DISPOSAL POSSIBLE?

W.S. Fyfe, R. Léveillé, W. Zang, Y. Chen
Dept. Of Earth Sciences,
University of Western Ontario
London, Ontario, Canada

Keywords: deep CO_2 fixation, deep biosphere

INTRODUCTION

Recently, Moore and Braswell[1] have reviewed the present state of knowledge of the carbon cycle. As they state: "the carbon cycle is still not adequately understood or quantified globally. Using averages for the 1980's, sources of atmospheric CO_2 exceed identified sinks by 1.8 - 1.2 PgC per year". It is interesting to examine their diagram of the global carbon cycle, and to note that there is essentially no attention given to processes deep in the earth's crust. One of the most interesting recent observations on the nature of the biosphere has been the discovery of thriving colonies of microorganisms at depth[2]. While workers on the alteration of seafloor basalts had suggested the actions of deep organisms, problems related to possible deep bio-corrosion of nuclear waste containers have stimulated more careful observations. Pedersen[2] has reviewed the present state of knowledge, and reported the present record of microorganisms at depths of 4.2 km below the surface, at temperatures up to 110°C.

CO_2 AND THE THREAT OF GLOBAL WARMING

Emissions of greenhouse gases, including CO_2, are on the rise. In developing countries, emissions are increasing the fastest and may soon equal those of developed countries. In countries like India and China, coal and other fossil fuels will continue to be a major source of energy for the next few decades. Thus emissions will continue to rise. Although programmes for reductions in greenhouse gas emissions are needed and encouraged, the inadequate actions by governments may soon make it necessary to develop alternative and more direct strategies to reduce the amount of greenhouse gases being emitted to the atmosphere. Currently, research on such strategies revolves primarily around three main ideas: disposal of CO_2 in the oceans, in deep aquifers, and in oil or gas reservoirs (IEA[3]). Another strategy involves the disposal of CO_2 in the form of carbonate minerals (Seifreitz[4]; Dunsmore[5]; Lackner et al.[6]; Fyfe et al.[7]). In nature, such a process occurs on a global scale during the weathering of silicate minerals. Typical of such reactions are:

$$CaAl_2Si_2O_8 + CO_2 + H_2O \rightarrow Al_2Si_2O_5(OH)_4 + CaCO_3$$
Anthorite Kaolinite Calcite/Aragonite

$$2\,Mg_2SiO_4 + CO_2 + 2\,H_2O \rightarrow Mg_3Si_2O_5(OH)_4 + MgCO_3$$
Forsterite Serpentine Magnesite

$$Fe_2SiO_4 + 2\,CO_2 \rightarrow 2\,FeCO_3 + SiO_2$$
Fayalite Siderite Silica

This natural sink of CO_2 accounts for nearly 80% of the sum of all carbon sinks. These reactions are exothermic. It has also been shown that these reactions can be catalyzed by microorganisms, such as cyanobacteria (Ferris et al.[8]; Tazaki et al.[9]). Thus, it is possible to enhance this 'natural' process to remove significant amounts of CO_2 from fossil fuel plants and from the atmosphere? Could CO_2 be pumped underground in suitable rock formations where microbial populations are plentiful? Can we enhance the growth of these microorganisms in situ to make the whole process feasible, a sort of bioremediation of the atmosphere? The exothermic nature of the reactions is an added bonus as geothermal energy could be used to partially 'fuel' the operation, make it more economically feasible, and produce useful warm water.

CO_2 DISPOSAL

Seifritz[4] was one of the first to point out that the natural weathering of silicates resulting in carbonate mineral formation could potentially be enhanced as a way of permanently disposing of

CO_2. Two problems were initially acknowledged: a sufficiently large source of Ca (and Mg-Fe) and the kinetics of the silicate-to-carbonate reaction. Dunsmore[5] suggested the evaporititic salts and brines of the Alberta Sedimentary Basin would provide an ample source of Ca and Mg, which could be transformed into carbonates. The advantage of using this basin is that it is in the heart of the fossil-fuel industry in Canada where existing infrastructures could potentially be modified for CO_2 transport and disposal. Lackner et al[6] equally showed that common silicate minerals like olivine and plagioclase in rocks could also act as sources of Ca and Mg. As for the kinetics of reactions, microorganisms can enhance the rate of silicate weathering by producing organic acids (Hiebert and Bennett)[10] and catalyze carbonate precipitation by acting as nucleation sites form mineral growth (Ferris et al.[7]; Tazaki et al.[9]). Storage of CO_2 in carbonate minerals has also been briefly discussed in relation to aquifer disposal (IEA[3]; Bachu[11]) and ocean dumping (Harrison et al.[12]).

MICROBES, EXTREME ENVIRONMENTS, AND BIOMINERALIZATION

Microorganisms are able to survive in a wide variety of harsh environments, ranging from low to high temperatures, highly acidic to highly alkaline, saline, and dry conditions (Edwards[13]). The upper limit for thermophilic bacteria appears to be ~ 110°C , with some species showing optimum growth at temperatures as high as 105°C (Edwards [13]). However, many workers believe this upper limit could in fact be as high as 150°C, providing that the pressure is sufficiently high to increase the boiling point of water (Edwards 13; Gold[14]). At deep sea hydrothermal vents, barothermophilic bacteria can also withstand immense pressures in addition to the elevated temperatures. Also bacteria can survive in very high concentrations of CO_2 at these vents (Childress et al.[15]).

Bacteria are not only ubiquitous at the Earth's surface and at deep-sea vents, but within the lithosphere as well. Bacterial populations have been found at over 4000 m deep in boreholes drilled into crystalline rocks in Sweden, in deep thermal groundwaters, in oil bearing sedimentary rocks, and over 1000 m deep in a basaltic aquifer (Pedersen[2]; Szewzyk et al.[16]; L'Haridon et al.[17]). In the latter case, the bacteria appear to derive their energy solely from hydrogen produced by geochemical reactions.

Microorganisms are know to influence carbonate mineral formation in a variety of environments from cold waters on lava plains in Iceland (Ferris et al.[7]; Tazaki et al.[9]) to hot springs in Kenya and New Zealand with water temperatures well above 90°C (Jones and Renault[18]). Biomineralization of Fe-Mn oxides and sulphides at high temperatures and pressures has also been reported from deep sea hydrothermal vents (Juniper and Tebo[19]). At these vents, microorganisms are also involved in the transformation and weathering of existing hydrothermal deposits.

WORK IN HAWAII AND ICELAND

In both Hawaii and Iceland, secondary carbonate minerals develop as weathering products from Ca and Mg silicates in fractures, cracks, pores, and in large sea caves of basaltic rock. Carbonate minerals identified by XRD include calcite ($CaCO_3$) (see fig. 1) aragonite ($CaCO_3$), magnesite ($MgCO_3$), hydromagnesite ($Mg_5(CO_3(OH)_2 \cdot 4H_2O$) and dolomite ($(Ca,Mg)CO_3$). Other minerals such as clays and silica were also identified as weathering products.

Carbonate minerals were found in association with extensively fractured basaltic lava rocks in Iceland. These minerals occur in thin crusts on weathered basalt and their formation was shown to be mediated by microorganisms (Ferris et al. [7]). Calcite forming in a not spring microbial mat in Iceland has also been shown to be influenced by microorganisms, in particular cyanobacteria (Tazaki et al.[9]).

In Hawaii, carbonate minerals appear to precipitate from meteoric waters trickling down the interior surfaces of large sea caves. The meteoric waters in the caves are most likely rich in organics as the exterior surface is densely vegetated. The carbonates occur in thin coatings (< ~5 mm) on the interior surface of the caves and in the near-surface pores, cracks and vesicles of the basalt 'host rock'. Our preliminary calculations show that a significant part of the missing carbon dioxide of the carbon cycle could be explained by such processes.

REFERENCES

1. Moore, B.; Braswell, B.H. *Ambio* **1994**, 23, 4-12.
2. Pedersen, K. *Earth Sci. Rev.* **1993**, 34, 243-260.
3. IEA. 1994. Carbon disposal from power stations. International Energy Agency Greenhouse Gas R&D Programme, Gloucesterhire, U.K.
4. Seifritz, W. *Nature*, **19??**, 345, 486.

5. Dunsmore, H.E. *Energy Conversion & Management*, **1992**, 33, 565-572.
6. Lackner, .S.; Wendt, C.H.; Butt, D.P.; Joyce, E.L.Jr.; Sharpt, D.H. *Energy*, **1995**, 20, 1153-1170.
7. Fyfe, W.S.; Zang, W.; Chen, Y.; Léveillé, R. *Chemical and Engineering News*, **1996**, April 8, 5.
8. Ferris, F.G.; Weise, R.G.; Fyfe, W.S. *Geomicrobiology Journal* **1994**, 12, 1-13.
9. Tazaki, K.; Ishida, H.; Fyfe, W.S. Clays controlling the environment. **1995**, 30-37.
10. Hiebert, F.K.; Bennet, P.C. *Science*, **1992**, 258, 278-281.
11. Bachu, S.; Gunter, W.D.; Perkins, E.H. *Energy Conservation and Management*, **1994**, 35, 269-279.
12. Harrison, W.J.; Wendlandt, R.F.; Sloan, E.D. *Applied Geochemistry*, **1995**, 10, 461-475.
13. Edwards, C. Microbiology of extreme environments, Open University Press, **1990**.
14. Gold, T. *Proceedings of the National Academy of Science, USA*, **1992**, 89, 6045-6049.
15. Childress, J.J.; Lee, R.W.; Sanders, N.K.; Felbeck, H.; Oros, D.R.; Toulmond, A.; Desbruyeres, D.; Kennicutt, M.C.; Brooks, J. *Nature*, **1993**, 362, 147-149.
16. Szewzyk, U.; Szewzyk, R.; Stenstrom, T.-A. *Proceedings of the national Academy of Science, USA*, **1994**, 91, 1810-1813.
17. L'Haridon, S.; Reysenbach, A.-C.; Gleinat, P.; Prieur, D.; Jeanthon, C. *Nature*, **1995**, 377, 223-224.
18. Jones, B; Renault, R.W. *Canadian Journal of Earth Sciences*, **1996**, 33, 72-83.
19. Juniper, S.K.; Tebo, B.M. The microbiology of deep-sea hydrothermal vents, CRC Press. **1995**, 219-253.

Figures

Fig. 1. SEM image showing filamentous microorganisms on mineral surfaces of Hawaii basalt. The arrow points to $CaCO_3$ crystals.

A

MODELING THE OCEANIC STORAGE OF FOSSIL FUEL EMISSIONS

Arturo A. Keller, Charles J. Werth
Department of Civil Engineering, Stanford University, Stanford , CA 94305
and
Robert A. Goldstein
Electric Power Research Institute, Palo Alto, CA 94303

KEYWORDS: global carbon cycle, ocean disposal, fossil fuel emissions

ABSTRACT

We use the GLOCO model to analyze the potential for oceanic storage of carbon dioxide emissions from fossil fuel combustion, as well as the effect on atmospheric CO_2 (pCO_2) concentration. From a sensitivity analysis of the global carbon cycle, we find that the rate of transport of carbon to the deepest oceanic layers is rather insensitive to the atmospheric-ocean surface gas exchange coefficient, but to a larger extent on the upwelling velocity. The location of the carbon emissions, whether they are released in the atmosphere or in the middle of the oceanic thermocline, has a significant impact on the maximum pCO_2 subsequently reached, suggesting that oceanic burial of a significant fraction of carbon emissions (e.g. via clathrate hydrides) may be an important management option for limiting pCO_2 buildup. The effectiveness of ocean burial decreases asymptotically below about 1000 m depth, considering a one-dimensional ocean model, i.e. perfect mixing at the various ocean levels where the carbon is injected. With a constant emissions scenario (at 1990 levels), pCO_2 rises to 501 ppmv by the year 2100 if all the emissions go to the atmosphere. With ocean burial of 50% of the fossil fuel emissions at a depth of 1000 m, pCO_2 rises only to 422 ppmv. An alternative scenario looks at stabilizing pCO_2 at 450 ppmv; with no ocean burial of fossil fuel emissions, the rate of emissions has to be cut drastically after the year 2010, whereas oceanic burial of 2 GtC/yr allows for a smoother transition to alternative energy sources.

INTRODUCTION

Capturing carbon dioxide emissions at the smokestack and injecting them into the ocean has been proposed by Marchetti (1977), Hoffert *et al.* (1979), Liro *et al.*(1992), Golomb *et al.*(1992), Kheshgi *et al.*(1994) and others. These previous studies have relied on simple oceanic box models, and have mostly been used to analyze the response of a pulse injection rather than the projected ramp increases in anthropogenic carbon dioxide emissions due to fossil fuel combustion, and neglecting the impact of carbon storage in terrestrial biomes in both the transient and equilibrium carbon cycle response.

For this analysis, we use the GLOCO model (Hudson *et al.*, 1994), a global carbon cycle model with a mechanistic description of physical and biogeochemical processes in the terrestrial biomes and oceans. The model considers eight terrestrial biomes, two oceans (high and low latitude, each broken further into surface and deep layers) and one well-mixed atmosphere. Complete atmospheric mixing is assumed since the model's time step is one year. The model allows the input of different anthropogenic carbon emissions (CO_2 and CH_4), from industrial as well as agricultural and forestry activities (including land-use changes). Temperature of each biome or ocean can be independently modeled as a function of atmospheric CO_2 concentration.

The oceanic carbon cycle model used in GLOCO is based on the HILDA model (Siegenthaler and Joos, 1992), an outcrop-diffusion model. In addition to discerning between high and low latitude oceans, the model has a significant spatial resolution in the vertical direction, with 68 layers of deep low-latitude ocean. Chemical equilibrium controls the final distribution of carbon. GLOCO considers the dissociation of water, carbonic, boric and dissolved organic carbon-based acids, as well as the assimilation of carbon to particulate organic carbon (POC) and dissolved organic carbon (DOC), deposition of calcium carbonate in sediments and remineralization of POC and DOC. Each layer is considered to reach equilibrium rapidly, but due to transport limitations, the system as a whole can take thousands of years to achieve equilibrium once it is perturbed. The non-linear chemical equilibrium is coupled with convection-diffusion processes. Carbon is also transported downward to the deep ocean by the oceanic "biological pump".

The terrestrial biome models are based on a generic biome module describing photosynthesis, respiration and growth by vegetation, and microbial decomposition of plant litter and soil organic matter, with parameter values for each biome: temperate, boreal and tropical forests, grasslands, woodlands, tundra, deserts and agriculture. Carbon and nitrogen are cycled within the biome; these nutrients are allocated to the various plant tissues, and the fluxes of carbon and nitrogen in and out of the biome are considered. The rates of the biological processes are temperature dependent, to incorporate the effect of potential temperature rise in the coming centuries.

We assume that the carbon dioxide from fossil fuel combustion would be injected as a clathrate hydrate, which has been shown (Sakai *et al.*, 1990; Saji *et al.*, 1992) to form a stable phase at the pressure, temperature and salinity of the deep ocean (>500 m). Our analysis has two major assumptions. First, we assume that the injected clathrate dissolves and mixes completely and instantaneously at the depth it is injected in the low-latitude ocean. In fact, the clathrate should sink, due to the higher density of the clathrate hydrate relative to the surrounding water, and the clathrate phase should be even more stable at greater depths. Our second simplification is to neglect calcite dissolution in the bottom waters of the ocean which is expected to result in additional long term storage of carbon (Hoffert *et al.*, 1979; De Baar, 1992). Our simplifications are overall conservative and would tend to understate the additional storage of carbon in the deep ocean. The assumption that mixing at the injection depth is instantaneous may be conservative or not depending on the local water transport, i.e. upwelling or downwelling.

SENSITIVITY OF OCEAN TRANSPORT PARAMETERS

Considering that most of the carbon emitted to the atmosphere will eventually end up in the oceans (Keller and Goldstein, 1994), and that the approach to equilibrium is constrained mostly by oceanic physical transport, we sought to determine how important was the choice of ocean transport parameter values to reaching equilibrium. For example, there are a number of studies on the atmosphere-ocean gas-exchange coefficient (Robertson and Watson, 1992; Broecker and Maier-Reimer, 1992; Stanton, 1991; Volk and Bacastow, 1989), and its spatial and temporal variability (Etcheto *et al.*, 1991; Erickson, 1989). Values of the gas-exchange coefficient vary by more than an order of magnitude. How significant is this in terms of our analysis?

Another important parameter is the upwelling velocity of deep water in lower latitudes. Upwelling brings cold, nutrient rich water to the surface, and thus a larger upwelling velocity may increase the rate of oceanic net primary productivity, increasing the flux of carbon to DOC and sediment pools (Bacastow and Maier-Reimer, 1991; Baes and Killough, 1986) resulting in a larger carbon storage. In addition, from a mass balance on water, a larger upwelling velocity would result in a larger downward water flux at higher latitudes, carrying carbon-enriched surface waters to greater depth.

The parameter values used in the calibration of the GLOCO model correspond to those in the oceanic HILDA model, which has been used to study the distribution of radioactive tracers, matching the measured concentration profiles adequately. Given the variability in the published values of these two transport parameters, we studied the effect of increasing or decreasing them by an order of magnitude, which covers more than the published variability in parameter values. A pulse of 594 Gt C is instantaneously released in the atmosphere, to simulate a doubling of the atmospheric CO_2 (pCO_2) from its preindustrial value, and then the system is allowed to relax to a new equilibrium situation. The effect on pCO_2 is presented in Figure 1. The base case considers the calibration parameter values for GLOCO.

Increasing or decreasing the gas-exchange coefficient by a factor of 10 has very little impact on the rate at which equilibrium is reached. If the gas-exchange rate is increased by a factor of 10, there is virtually no change in the pCO_2 profile, when compared with the base case. Analyzing the profiles of dissolved inorganic carbon (DIC) in the ocean, we observe that only the top ocean layers, above the thermocline, are affected, and only by a small amount. Reducing the resistance of gas transfer to the surface of the ocean does not significantly increase the overall rate of carbon storage in the ocean because it is limited by downward transport. And the additional carbon in the surface waters does not result in additional uptake as DOC or POC, since carbon is not the limiting nutrient. The atmospheric response is slightly larger for the case where the gas-exchange coefficient is reduced by a factor of 10. In this case, the resistance to gas transfer does result in slightly larger atmospheric concentrations, in particular at early times. As expected, the equilibrium atmospheric concentration is the same for all cases.

If our current estimate of the upwelling velocity was off by a factor of 10, the impact on our predictions of future pCO_2 would be important only in the case of much greater upwelling velocities. If the upwelling velocity was $1/10^{th}$ of our current estimate, the effect would be minimal in terms of our pCO_2 predictions. However, an actual upwelling velocity ten times larger than our current estimates would result in significant increase in carbon storage both in DOC and sediments. Given that oceanic carbon storage would increase, the equilibrium would shift and less carbon would then be stored in the terrestrial biomes, as well as in the atmosphere. The net reduction in total carbon stored in the atmosphere is on the order of 35 Gt C. The impact is greatest at larger times (>200 years).

OCEAN BURIAL OF CARBON FROM FOSSIL FUEL COMBUSTION

If the same 594 Gt C pulse is injected into the ocean at a depth of 500 m as DIC, considering the calibration transport parameter values, the global carbon cycle approaches equilibrium relatively fast, redistributing carbon in the ocean, and releasing carbon to the atmosphere (Figure 1). In less than two hundred years, pCO_2 practically reaches its equilibrium value. There is no change in DOC or oceanic carbon sedimentation rates, and the approach to equilibrium is actually only delayed by the terrestrial biome uptake of the incremental atmospheric carbon. In effect, we have "bought" a delay of about 200 years in the maximum pCO_2 by burying the fossil fuel emissions at a depth of 500 m. What is the effect of burying the emissions at different depths? Can we have a bigger impact by injecting at deeper levels? And at what point does this approach become less effective?

Considering the same pulse (a 2x carbon pulse, based on the preindustrial atmospheric concentration), we studied the effect on pCO_2 of injecting at deeper ocean levels (Figure 2). All the atmospheric CO_2 profiles approach the same equilibrium value of around 325 ppmv after 750 years. However, the maximum pCO_2 is reached much later depending on the injection depth. And the maximum pCO_2 is lower as we increase the injection depth (Figure 3). We can continue to inject at lower and lower depths, but this analysis suggests that going deeper than 1500 m is not effective in terms of reducing the maximum pCO_2, since we reach an asymptotic value. In fact, it may be argued that the difference in the maximum pCO_2 between injecting at 1000 m and injecting at 1500 m, of less than 8 ppmv, does not justify the larger expense of injecting the carbon 500 m deeper.

Studying the response of the global carbon cycle to a pulse injection is useful because it is easier to compare among models, without the added complexity of varying scenarios. However, the real perturbation to the global carbon cycle is not an instantaneous pulse but rather a continuous increase in anthropogenic carbon emissions to the atmosphere. Currently the system has already been perturbed significantly from its preindustrial levels, so that if we suddenly stopped all anthropogenic emissions to the atmosphere, the system would relax to a new equilibrium position. We studied three potential carbon emissions scenarios. The first involves achieving the current target of voluntarily limiting carbon emissions to their 1990 levels for all nations. The second carbon emissions scenario is the IPCC 92a scenario (Business as Usual). The third scenario looks at limiting carbon emissions such that pCO_2 stabilizes at 450 ppmv. To achieve the stabilization goal, carbon emissions from fossil fuel combustion and land use changes have to be drastically reduced in the next century. Whether we can make the transition to this lower rate of emissions is not entirely clear. Ocean burial of some of the emissions would make the transition easier, by providing some additional time for all nations to switch to either renewable or non-fossil fuel based energy sources.

In Figure 4 we present the result of the first scenario, i.e. carbon emissions at constant 1990 levels. Even with this lofty goal, pCO_2 rises from 354 ppmv in 1990 to 525 ppmv by the year 2100, or 48%. As we increase the fraction of the emissions that is buried in the ocean at a depth of 1000 m, beginning in the year 2000, the maximum pCO_2 by the year 2100 drops significantly. The technology for ocean burial is not in place to begin capturing, transporting and injecting carbon into the ocean by the year 2000, and significant additional modeling with a three-dimensional ocean model must be done before we know where the injection points may be, but this analysis indicates that there may be considerable reduction in the growth of pCO_2 in the future, by burying a fraction of the emissions directly in the ocean.

What if there is no action to reduce carbon emissions, and they grow as projected by the Business as Usual scenario of the IPCC? GLOCO projects a doubling of pCO_2 by the year 2100, to more than 700 ppmv (Figures 5a, 5b). If we followed the same emissions trajectory, but then decided that we should put an arbitrary cap on the maximum pCO_2 of 450 ppmv, as suggested by the 1994 IPCC modeling exercise (Enting et al., 1994) how long could we continue on the Business as Usual trajectory? And what would have to be the needed reduction in carbon emissions to reach the 450 ppmv cap? In Figure 5a we present the fossil fuel emissions trajectory obtained by inversing the GLOCO model. We could maintain the Business as Usual trajectory until the year 2010, at which time we would have to drastically reduce emissions from 8 GtC/yr to around 1 GtC/yr by 2060. The resulting

pCO_2 profile is shown in Figure 5b. If by the year 2010 we had implemented the technologies needed for burying 2 GtC/yr directly into the ocean at a depth of 1000 m, then we could add this level of fossil fuel emissions (2 GtC/yr) to the drastic carbon emissions trajectory, buying some time for the implementation of other energy sources, and making a wiser use of our fossil fuels (Figure 5a and 5b).

CONCLUSIONS

We have analyzed the sensitivity of the GLOCO model, a global carbon cycle model, to two major oceanic transport parameters. The actual value of the globally averaged gas-exchange coefficient is not well known, but our analysis suggest that in terms of the rate of carbon storage in the ocean, the model is rather insensitive to the value of this parameter, even if our calibration value is off by a factor of 10. The transport of carbon into the deep ocean is not controlled by the air-sea gas exchange.

If the upwelling velocity was much lower than our current estimates, it would also have only a minor effect on the global carbon cycle. However, if the actual value was 10 times larger than the current estimate, then the equilibrium would shift, due to upwelling of nutrients to the surface, resulting in a larger DOC pool and greater rates of sedimentation. The larger carbon storage in the ocean would be offset by a reduction in carbon in both the terrestrial biomes and the atmosphere. This indicates that further research should be directed towards understanding the globally-averaged value of the upwelling velocity.

Using the GLOCO model, we studied the effect of disposing some of the anthropogenic carbon emissions directly into the ocean, possibly as clathrate hydrides. Injection of carbon into the deep ocean becomes less and less effective, in terms of the maximum atmospheric CO_2 observed, suggesting that the optimal depth is somewhere around 1000 m.

If we take no action to reduce fossil fuel emissions (IPCC 92a case), then pCO_2 will more than double by the end of the next century. Even if we constrain emissions to their 1990 levels for the next 110 years, we can expect a rise of around 48% in pCO_2 levels. Burying a fraction of the emissions deep in the ocean would reduce the rate of increase in pCO_2 and thus the potential for an increased greenhouse effect and its implications. Public pressure, as well as political pressure from interested parties (e. g. insurance companies) may result in capping pCO_2 to a fixed level, for example 450 ppmv. This would result in significant reductions in combustion of fossil fuel in a relatively short amount of time. Burying a fraction of the emissions would provide some relief, and would allow for a smoother transition to alternative energies.

REFERENCES

Bacastow, R. and Maier-Reimer, E.: 1991, 'Dissolved Organic Carbon in Modeling Oceanic New Production', *Global Biogeochemical Cycles*, 5: 71-85.

Baes, C. F. and Killough, G. G. : 1986, 'Chemical and Biological Processes in CO2-Ocean Models', in *The Changing Carbon Cycle, A Global Analysis*, ed. J. R. Trabalka and D. E. Reichle, Springer-Verlag, New York.

Broecker, W. S. and Maier-Reimer, E.: 1992, 'The Influence of Air and Sea Exchange on The Carbon Isotope Distribution in the Sea', *Global Biogeochemical Cycles*, 6: 315-320.

De Baar, H. J. W.: 1992: 'Options for Enhancing the Storage of Carbon Dioxide in the Oceans: A Review', *Energy Conversion and Management*, 33(5-8): 635-642

Enting, I. G., T. M. L. Wigley and M. Heimann, 1994, 'Future Emissions and Concentrations of Carbon Dioxide: Key Ocean/Atmosphere /Land Analyses', *CSIRO Technical Paper 31*, CSIRO, Australia

Erickson, D. J.: 1989, 'Variations in the Global Air-Sea Transfer Velocity Field of CO2', *Global Biogeochemical Cycles*, 3: 37-41.

Etcheto, J., Boutin , J. and Merlivat, L.: 1991, 'Seasonal Variation of the CO2 Exchange Coefficient over the Global Ocean using Satellite Wind Speed Measurements', *Tellus*, 43B: 247-255.

Golomb, D. S., Zemba, S. G., Dacey, J. W. H. and Michaels, A. F.: 1992, 'The Fate of CO2 Sequesters in the Deep Ocean', *Energy Conversion and Management*, 33(5-8): 675-683

Hoffert, M. I., Wey, Y. C., Callegari, A. J. and Broecker, W. S.: 1979, 'Atmospheric Response to Deep-Sea Injections of Fossil-Fuel Carbon Dioxide', *Climatic Change*, 2: 53-68.

Hudson, R. J. M., Gherini, S. and Goldstein, R. A.: 1994, 'Modeling the Global Carbon Cycle: Nitrogen Fertilization of the Terrestrial Biosphere and the "Missing" CO2 Sink', *Glob.Biogeochem.Cycles*, 8:3, 307-333

IPCC: 1992, 'Climate Change 1992: The Supplementary Report to the IPCC Scientific Assessment', ed. J. T. Houghton, B. A. Callender and S. K. Varney, Cambridge University Press, UK.

Keller, A. A. and Goldstein, R. A.: 1994, 'The Human Effect on the Global Carbon Cycle: Response Functions to Analyze Management Strategies', *World Resource Review*, 6: 63-87

Kheshgi, H. S., Flannery, B. P., Hoffert, M. I. and Lapenis, A. G.: 1994, 'The Effectiveness of Marine CO2 Disposal', *Energy*, 19(9): 967-974

Liro, C. R., Adams, E. E. and Herzog, H. J.: 1992, 'Modeling the Release of CO2 in the Deep Ocean', *Energy Conversion and Management*, 33(5-8): 667-674

Marchetti, C.: 1977, 'On Geoengineering and the CO2 Problem', *Climatic Change*, 1: 59-68

Robertson, J. E. and Watson, A. J. : 1992, 'Thermal Skin Effect of the Surface Ocean and its Implications for CO2 uptake', *Nature*, 358: 738-740.

Saji, A., Yoshida, H., Sakai, M., Tanii, T., Kamata, T., and Kitamura, H. : 1992, 'Fixation of Carbon Dioxide by Clathrate-Hydrate', *Energy Conversion and Management*, 33(5-8): 643-649.

Sakai, H., Gamo, T., Kim, E. S., Tsutsumi, M., Tanaka, T., Ishibashi, J., Wakita, H., Yamano, M. and Oomori, T.: 1990, 'Venting of carbon dioxide-rich fluid and hydrate formation in mid-Okinawa Trough Backarc Basin', *Science*, 248: 1093-1096.

Siegenthaler, U. and Joos, F. : 1992, 'Use of a Simple Model for Studying Oceanic Tracer Distributions and the Global Carbon Cycle', *Tellus*, 44B: 186-207.

Stanton, B. R.: 1991, 'Ocean Circulation and Ocean-Atmosphere Exchanges', *Climatic Change*, 18: 175-194.

Volk, T. and Bacastow, R.: 1989 'The Changing Patterns of ΔpCO2 between Ocean and Atmosphere', *Global Biogeochemical Cycles*, 3: 179-189.

Figure 1. Time dependent atmospheric carbon response due to an instantaneous pulse of 594 GtC, for various oceanic transport parameter values, compared to the base case (calibration values and pulse in the atmosphere).

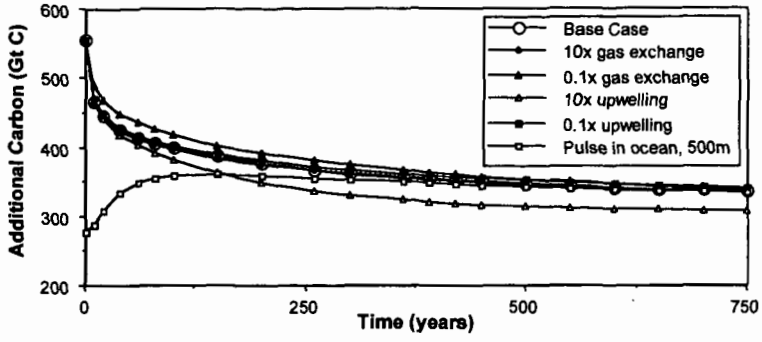

Figure 2. Atmospheric concentration (pCO_2) profiles after the injection of an instantaneous pulse of 594 Gt C directly to the atmosphere (base case) or at various depths in the low-latitude ocean.

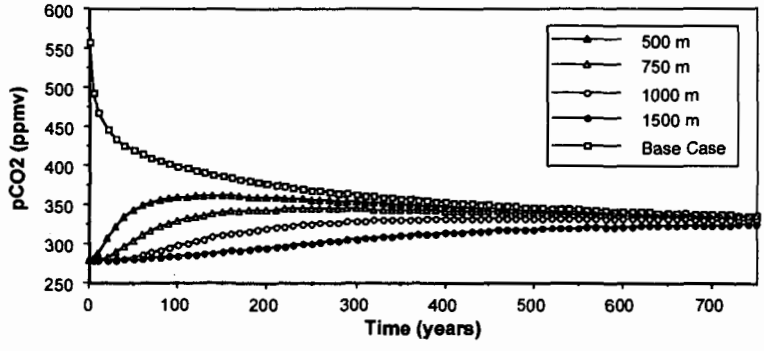

Figure 3. Maximum pCO_2 predicted during the 750 years of simulation as a function of low-latitude ocean burial depth.

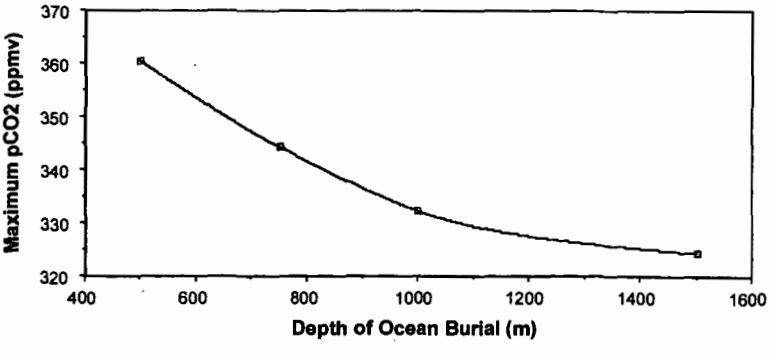

Figure 4. Atmospheric concentration (pCO_2) profiles for a constant emissions scenario at 1990 levels, considering direct emission to the atmosphere or increasing oceanic burial.

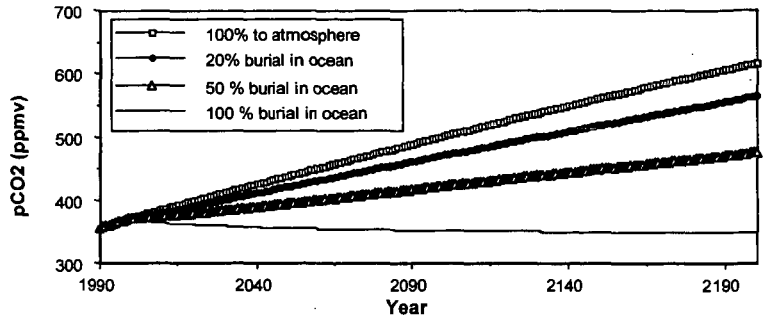

Figure 5a. Carbon emissions from combustion of fossil fuels considering the IPCC 92a Business as Usual scenario and two control scenarios aimed at achieving a stable pCO_2 of 450ppmv with and without ocean burial of emissions.

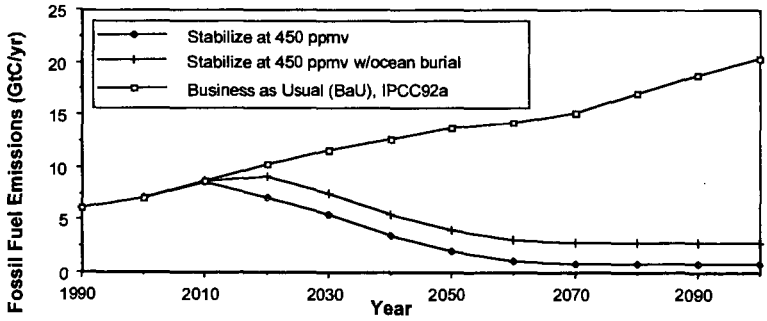

Figure 5b. Atmospheric concentration (pCO_2) profiles for the Business as Usual scenario and the two control scenarios targeting a maximum pCO_2 of 450 ppmv.

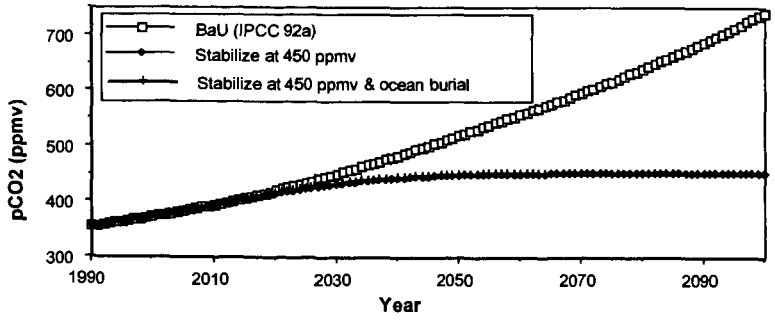

HIGHLY EFFICIENT DISPOSAL OF CO_2 INTO THE OCEAN BY GAS-LIFT METHOD
(BASIC CHARACTERISTICS OF GLAD SYSTEM)

Takayuki Saito
National Institute for Resources and Environment
16-3, Onogawa, Tsukuba, Ibaraki 305, Japan

Takeo Kajishima
Department of Mechanical Engineering, Osaka University
2-1, Yamadaoka, Suita, Osaka 565, Japan

Ryuichi Nagaosa
National Institute for Resources and Environment
16-3, Onogawa, Tsukuba, Ibaraki 305, Japan

Keywords: Carbon dioxide, Gas-lift method, Ocean disposal

INTRODUACTION

7.1 ± 1.1GtC/y of CO_2 was discharged into the atmosphere due to the human activities of energy production and its consumption in 1992 (*1*). Since its discharged rate is quite large in such a matter and CO_2 discharge is continued as long as fossil fuel is consumed, the global warming problem brought by CO_2 is very difficult to solve. Many kind of methods and ideas have been proposed for the problem, however, it is very hard to find out methods to be effective and realized within an early stage.

The mass transfer rate of CO_2 from the atmosphere to the ocean is low (*2*). The ocean has an enough capacity to absorb the whole of CO_2 which is emitted by the consumption of total fossil fuel of 7×10^{12} tonC (*3*). Therefore, CO_2 disposal into the ocean is a reasonable and hopeful option to reduce the global warming. The ocean disposal is not an ultimate technology to avoid the global warming, but emergency measures for the rapid increase of CO_2 concentration in the atmosphere. The ocean disposal is required to be low cost and energy saving as well as possible. The deeper releasing can isolate CO_2 for longer period. Therefore, the deep-sea releasing might be most reliable from a viewpoint of long period isolation of CO_2. However, the liquefaction and transportation of it to the great depth consume a large amount of extra energy and cost (*4*). Thus, we must solve these two contradictory matters; namely reliability and cost.

We propose the GLAD (Gas-Lift Advanced Dissolution) system for CO_2 release into deep-sea as the answer to above-mentioned problems. The GALD system is significantly efficient comparing with previous ideas. In the present paper, the principle of the GLAD system is described and its characteristics is estimated based on recent numerical and experimental results.

SOME PROBLEMS ON PREVIOUS IDEAS FOR CO_2 DISPOSAL

The previous ideas of CO_2 disposal into the ocean are classified into the following categories: the first one is storage of liquid CO_2 on the deep-sea floor deeper than about 3000m. In this case, the surface of the CO_2 pond is expected to be covered by CO_2-hydrate. However, the behavior of CO_2-hydrate in the actual ocean floor is not completely understood (*5*). The second one is direct release of liquid CO_2 into deep water of 1000-3000m in depth (*6*). The released liquid CO_2 should be immediately dissolved and diffused into sea-water to reduce environmental impacts. In these case, the liquefaction of CO_2 and its transportation to great depths consume a large amount of energy and have high cost. Besides, the compressed energy of liquid CO_2 is also disposed in the ocean without work.

The third one is shallow injection of CO_2 gas and gravity current. Haugan and Drange proposed the idea which was direct release of CO_2 gas into the sea-water at the depth of 200-400m and expecting sink of CO_2 enriched solution to deep-sea by the density difference between the solution and ambient sea-water (*7*). Adams et al. improved the CO_2 release system, which was a large vessel fixed on the floor of continental slope at a depth of about 200m (*8*). These ideas are superior to the first and second ones from a viewpoint of energy and cost saving. However, there are uncertain matters from a viewpoint of fluid dynamics in these ideas, such as 1) the upward plume generated by the bubbles, 2) the horizontal turbulence diffusion before the solution reaching at enough depths to be sequestrated for long period and 3) existence of density and/or temperature stratified layer in the ocean (*9*). In addition, considering that biological activities are very high in the area shallower than 200m depth, more deeper release of CO_2 solution without consuming extra energy is quite better. Thus, the uncertainty in the technology and the secondary environmental impact of the previous ideas should be solved simultaneously.

PRINCIPLE OF THE GLAD SYSTEM

The concept of the GLAD system is illustrated in Figure 1 (*9, 10*). The GLAD is an inverse J shape pipeline settled in shallow to deep water. CO_2 gas is injected into the shorter leg (hereafter, called dissolution pipe) of the GLAD at the depth of about 200-400m. Injecting CO_2 bubbles into the dissolution pipe, a gas-liquid bubbly flow is formed and a pumping action is generated by gas-lift effect. The buoyant plume rises in the dissolution pipe, and the bubbles dissolve in sea-water in some ascent. Fresh sew-water flows into the dissolution pipe at its bottom. As a result, the bubble dissolution and the transportation of the CO_2 enriched sea-water to great depth are accelerated by these effects. On the other hand, the longer leg (hereafter, called drain pipe) is used as a transportation and drain pipe for the CO_2 enriched sea-water to the area deeper than 1000m. The density of the solution is larger than that of ambient sea-water. An additional driving force to downward current is promoted by the density difference. Accordingly, the dense solution is released from the end of the drain pipe into deep water very efficiently.

NUMERICAL MODELING AND EXPERIMENTAL APPARATUS

Numerical modeling The numerical models for the gas-liquid two-phase flow in a vertical pipe of inner diameter D were developed (*10*). In the present paper, the outline of the numerical method is described. The basic equations, namely conservation law of mass and momentum, are employed. Defining the density and momentum of the gas-liquid mixture as $\rho=\alpha\rho_G+(1-\alpha)\rho_L$ and $\rho v=\alpha\rho_G v_G+(1-\alpha)\rho_L v_L$ respectively, the equations are as follows:

$$\frac{\partial \rho}{\partial t}+\frac{\partial(\rho v)}{\partial z}=Q_G, \tag{1}$$

$$\frac{\partial(\rho v)}{\partial t}+\frac{\partial\left(\alpha\rho_G v_G^2\right)}{\partial z}+\frac{\partial\left[1-\alpha\right]\rho_L v_L^2}{\partial z}=-\frac{\partial p}{\partial z}-\rho g-\frac{4\tau_w}{D}, \tag{2}$$

where α is the void fraction, ρ the density, v the velocity, and the subscripts G and L denote gas and liquid phase, respectively. The vertical direction is represented by z, Q_G is the gas injection rate, p the static pressure, and τ_w the shear friction at the pipe wall, respectively. The void fraction is evaluated by the mass conservation of gas phase

$$\frac{\partial(\alpha\rho_G)}{\partial t}+\frac{\partial(\alpha\rho_G v_G)}{\partial z}=Q_G+\Gamma_G, \tag{3}$$

where Γ_G denotes the gas dissolution rate. In addition, gas equation is employed. As the temperature is assumed to be constant, the energy equation is not needed. To close these equations, the drift flux model which determines the velocity of each phase is applied. Assuming mass transfer coefficient k is constant, Γ_G is evaluated as

$$\Gamma_G=5.24\rho_G k\left(\alpha^2/D^2\Delta_z\right)^{1/3}, \tag{4}$$

where Δ_z is the length of the computational cell (*10*).

The finite difference method is applied to discretized the basic equations. The implicit time marching scheme for density and pressure is adopted to deal with the high compressibility of the gas phase (*11*). The method was applied to a conventional air-lift pump of 200m long, and the numerical results showed reasonable agreement with the experimental data (*12*).

Experimental apparatus The experimental apparatus for the GLAD system is illustrated in Figure 2. Stainless steel pipes ⑨ and ⑩ (100mm in inner diameter and 8190mm in length) are connected to the GLAD dissolution pipe. They allows us to simulate the pressure conditions from the atmospheric to the 200m depth. The dissolution pipe ① is an acrylic pipe of 25mm in inner diameter and 7690mm in total length. At 840mm from the pipe bottom, CO_2 gas is injected by the gas injector ⑦, which is made of 108 19G needles. This injector can form almost uniform bubble diameter for any flow rate of CO_2 gas within the range of the present work.

4 double-optical-fiber probes ② (*13*) shown in Figure 3 are attached on the dissolution pipe in order to measure both of the bubble chord length and the bubble velocity. Each probes can be placed at any radius in the pipe. The optical signals from the probes are detected by the photo-multipliers, and the outputs from the multipliers are converted and recorded in a personal computer. The probability density function obtained by analyzing the probe signal is different from that of the bubble-water two-phase system (*14*), however there is some relationship between these probability density functions. In order to obtain the probability density function of the two-phase system by means of image analysis, a high-speed video camera (200 flames/sec at 20μsec shutter speed) ④ was employed (*15*).

RESULTS AND DISCUSSIONS ON GLAD SYSTEM

Numerical results The numerical results for the same dimensions as those of the experimental apparatus are shown in Figures 4 and 5. To compare the influence of k, two kinds of values, k=1 $\times 10^{-4}$ m/s, 2×10^{-4} m/s, are provided. The initial diameter of the bubbles was given as $r_0=3.6\times$

10^{-3}m (which is obtained by our experiments). CO_2 injection rate was inputted as q_{in} = 0.0164, 0.0328, 0.0656, 0.1312 and 0.2624g/s. Figure 4 compares the effect of CO_2 injection rate on the void fraction at the top of the dissolution pipe (α_{Exit}) and recirculation water velocity (J_L). In the case of k=2 × 10^{-4}, the bubbles dissolve completely for q_{in} <10^{-1}g/s, and positive J_L indicates a gas-lift effect takes place. The results fulfills the aim of the GLAD system successfully. In another case, they do not dissolve completely, however, mass flow rate of the CO_2 gas at the top of the dissolution pipe is negligible. Figure 5 shows the vertical profile of the void fraction for above-mentioned q_{in}. Near the gas injection point, the bubbles dissolve very rapidly, and in downstream of this region, the dissolution rate decreases for the both case of k.

Experimental results Comparisons of the experimental results with the numerical ones on both of the void fraction and the recirculation water velocity are shown in Figure 6. In the experiment, the void fraction is determine by taking account of bubble shape given by analyzing the video images. Strictly speaking, the definitions of the void fractions are different. Experimental data mean time void fraction, on the other hand, the numerical ones mean spatial void fraction (*16*). We think, however, the agreement between the experimental and the numerical data is reasonable. In addition, the numerical J_L shows good agreement with the experimental one. In conclusion, the accuracy of our numerical method and modeling is confirmed. In this experiment, a longer pipe is needed for CO_2 to dissolve in water completely. The authors reported, for example, the flow control is effective for complete dissolution of CO_2 bubbles (*9*). The feasibility of the GLAD system has been confirmed by the experiments. Considering the agreement between the experimental results and the numerical ones, the numerical simulation method for a scale-up plant of the GALD system is established.

Model plant and cost estimate In this section, a result of cost estimate for the model plant listed in Table 1 is discussed. (See (*17*) for the detail.) In our estimate, it is assumed that the exhausted rate of CO_2 is 100kg/s and 90 units of the GALD system are employed. The construction charge for both of the GLAD systems and the gas transportation system is about US$ 590 million. If the period of durability is more than 15 years, the operation charge per year, which include the electric power rates, labor costs and the maintenance cost, is about US$ 59 million. Note that the cost for CO_2 capture and separation from the exhausted gas is not included. As a result, the approximate cost of CO_2 disposal into deep-sea form a 1000MW fired power plant by the GALD system is US$ *100 million* per year. This corresponds to 1 cent/kWh. The comparison of the cost of the GLAD system with previous ideas is summarized in Table 2.
Still more, the model plant requires only 4% of the generated electricity from the power plant. Note that the cost estimate for CO_2 capture and separation by DOE includes compression to over 100bars. If this compression energy is used effectively for the GLAD system, the cost for it can be rather less than 1 cent/kWh. The GLAD is most competitive to previous methods for deep-sea disposal of CO_2 from a economical point of view.

CONCLUSIONS

The basic characteristics of the GLAD system is examined experimentally. The accuracy of our numerical method is confirmed by the experimental data. Based on these results, the availability of the GLAD system to dispose CO_2 into deep-sea is confirmed from a standpoint of cost and energy. We can conclude the GLAD is the most competitive with previous ideas for CO_2 disposal into the ocean. We are grateful to Dr. Kosugi of Sumitomo Metal Industries, Ltd. for his contribution to the cost estimate and useful discussions.

REFERENCES

1 IPCC, *Climate Change 1994*, Cambridge University Press, (1995).
2 Watanabe, Y., et al., *J. Geophys. Res.*, Vol.99, pp.195-213 (1994).
3 Hoffert, M.I., et al., *Climatic Change*, Vol.2, pp.53-68, (1979).
4 DOE Report, DOE/ER-30194, Vol.I, pp35-37, (1993).
5 Ohsumi, T., *Energy Convers. Mgmt.*, Vol.34, pp.1059-1064, (1993).
6 Liro, C.R., Adams, E.E. and Herzog, H.J., *Energy Convers. Mgmt.*, Vol.33, No.5-8, pp.1059-1064, (1992).
7 Haugan, P. M. and Drange, H., *Nature*, 357, pp.318-320, (1992).
8 Adams, E. E., et al., *Proc. 2nd US/Japan Workshop on Global Change*, Honolulu, (1993).
9 Saito, T., Kajishima, T. and Nagaosa, R., *Proc. Int. Conf. Technol. for Marine Env. Preservation*, Tokyo, pp.875-881, (1995).
10 Kajishima, T, Saito, T., Nagaosa, R. and Hatano, H., *Energy Convers. Mgmt.*, Vol.36, No.6, pp.467-470, (1995).
11 Kajishima, T and Saito, T., to be publish in *Int. J. Japan Soc. Mech. Engs.*, (1996).
12 Saito, T., et al., *Proc. Oceans '89, IEEE*-No.89CH27805-5, pp.48-53, (1989).
13 Hatano, H., Khattab, I.A.H., Nakamura, K. and Ishida, M., *J. Chem. Eng. Japan*, Vol.19, No.5, pp.425-430, (1986).
14 Liu, W. and Clark, N.N., *Int. J. Multiphase Flow*, Vol.21, No.6, pp.1073-1089, (1995).
15 Saito, T., Kajishima, T., Kiyono, F. and Masuyama, T., *ASME, FED*-Vol.209, pp.107-113, (1995).
16 Welle, R., *Int. J. Multiphase Flow*, Vol.11, No.3, pp.317-345, (1985).
17 Kajishima, T, Saito, T., Nagaosa, R. and Kosugi, S., to be published in *Energy, Int. J.*, (1996).

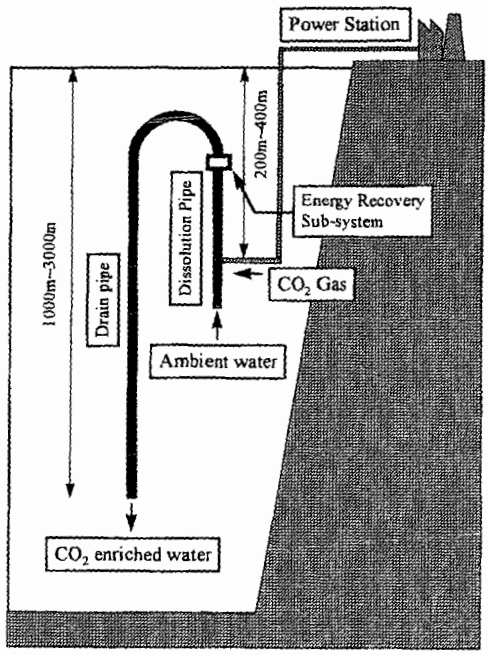

Figure 1. Concept of the GLAD system.

The dissolution and the drain pipes are about 100-200m and about 1000-3000m in length, respectively. CO_2 gas is pumped by a compressor and transported by a pipeline from a fired power plant to the GLAD. In the case that the water recirculation velocity is too high for complete dissolution of the bubbles, a resistance such as a turbine will be equipped near the top of the dissolution pipe. This suggests that excess momentum energy can be recovered. The GLAD system and the disposal method were applied for US and Japanese patent by T. Saito and T. Kajishima (1994, 1995).

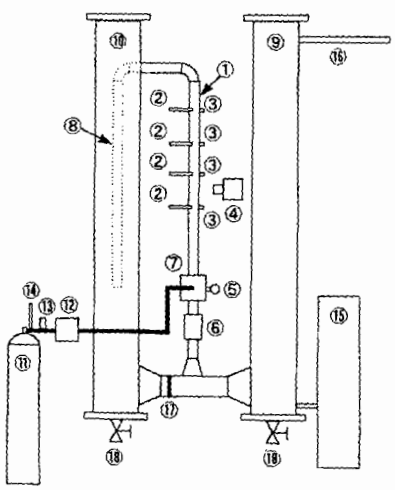

① Dissolution pipe
② Double-optical-fiber Probe
③ Pressure transducer
④ High-speed video camera
⑤ Pressure transducer
⑥ Electromagnetic flow meter
⑦ Gas injector
⑧ Drain pipe
⑨ Suction side pressure vessel
⑩ Drain side pressure vessel
⑪ Gas cylinder
⑫ Gas flow meter
⑬ Pressure transducer
⑭ Thermometer
⑮ Accumulator
⑯ Water and pressure supply line
⑰ Orifice
⑱ Drain valve

Figure 2. Outline of the Experimental Apparatus for the GLAD System

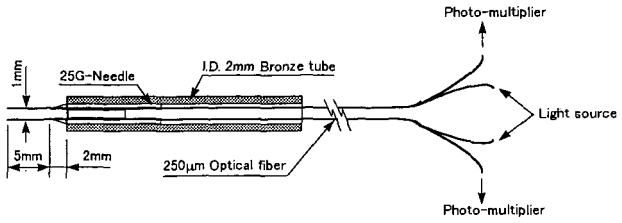

Figure 3. Structure of the double-optical-fiber probe

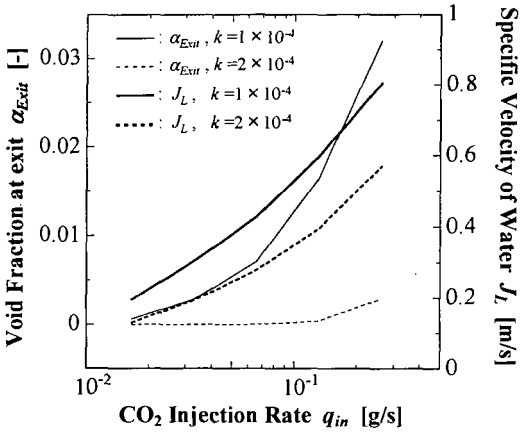

Figure 4. Recirculation velocity of water (J_L) and the Void fraction of CO_2 (α_{Exit}) at the top of the dissolution pipe.

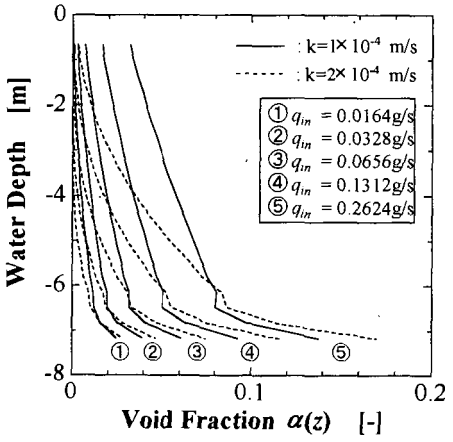

Figure 5. Profile of void fraction of CO_2 gas in the dissolution pipe.

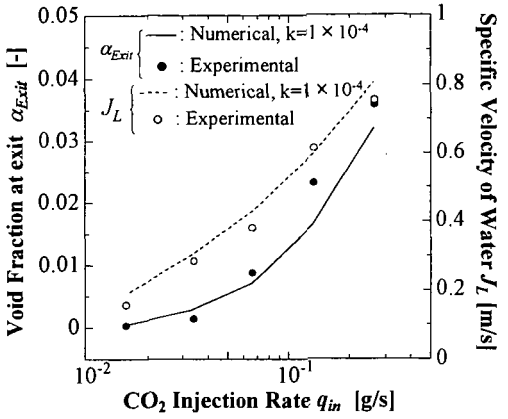

Figure 6. Comparison of the experimental results with the numerical ones.

Table 1. Dimensions of the model plant

GLAD system (fixed by tension-legs)	CO_2 gas transportation system	Power plant (fossil fuel fired)
Steel pipe : I.D.=0.5m, L=300m Inlet depth = 400m Injection depth=390m Drain pipe : I.D.=1.0m, L=10km spirally reinforced FEP	Compressor : 7Mpa, 55m^3/s 412000kW Pipeline : I.D.=0.5m, L=100km	Output power=1000MW CO_2 exhausted rate=100kg/s

Table 2. Comparison of both of previous ideas and the GLAD system

Method	Cost of capture and separation[1),3)] [cent]	Cost of disposal[2)] [cent]
Previous[3)]	1.1 ~ 4.9[3)]	0.6 ~ 6.7[3)]
GLAD	1.1 ~ 4.9[3)]	< 1

1) Includes costs for compression (to over 100bars) and dehydration
2) Includes transportation costs
3) DOE Report, DOE/ER-30194(1993)

THE EFFECT OF HYDRATE FORMATION ON CO_2 JET INSTABILITY

H. Teng[1], S.M. Masutani[2], C.M. Kinoshita[2], and G.C. Nihous[3]
[1]National Institute of Materials and Chemical Research
1-1 Higashi, Tsukuba, Ibaraki 305 JAPAN

[2]University of Hawaii, Hawaii Natural Energy Institute
2540 Dole Street, Holmes 246, Honolulu, Hawaii 96822 USA

[3]Pacific International Center for High Technology Research
2800 Woodlawn Drive, Suite 180, Honolulu, Hawaii 96822 USA

Keywords: hydrate; carbon dioxide; jet instability

Abstract–Disposal of captured CO_2 in the deep ocean or in underground aquifers currently is being considered as a means to control atmospheric levels of this greenhouse gas. Long-term sequestration demands that CO_2 be released at depths where water temperatures and pressures foster the formation of a solid hydrate phase. Previous theoretical and experimental studies have demonstrated that the kinetics of formation of the CO_2 hydrate can proceed rapidly, with characteristic times of the order of a second. Under certain liquid CO_2 jet discharge scenarios, hydrate formation may have important implications related to jet instability. An analysis was performed to assess the nature and magnitude of these effects. It was determined that hydrate formation may pose problems under certain discharge conditions.

1. INTRODUCTION

Efforts to stabilize greenhouse gas emissions are underway in many industrialized nations. Carbon dioxide (CO_2) currently is the most important of these gas species, due to the preponderant quantities being released into the atmosphere by anthropogenic sources–largely through the combustion of fossil fuels. While CO_2 emissions from combustors may be reduced through fuel switching and efficiency improvements, direct control technologies also are being investigated which extract CO_2 from flue gases for reuse or disposal in the deep ocean or underground.

Modeling studies [1] have suggested that captured CO_2 must be discharged at depths greater than 500 m in the ocean in order adequately to forestall return to the atmosphere. Two primary disposal scenarios have been proposed wherein liquefied CO_2 is transported from the surface via a submerged conduit and released either at intermediate depths (typically between 500 and 1,500 m) or in the abyssal zone below 3,000 m. The former scenario acknowledges the current depth limitations of undersea pipeline deployment and maintenance. Disposal in the very deep ocean was conceived as a means to avoid potential problems related to buoyancy of the liquid CO_2 effluent at depths above 3,000 m (i.e., the CO_2 will rise toward the surface as it slowly dissolves).

Since CO_2 is a non-polar substance and water is strongly polar, liquid CO_2 is only slightly soluble in seawater; consequently, CO_2 released from a submerged pipeline (typically as jets issuing through discharge orifices) is hydrodynamically unstable and will break up into a dispersed droplet phase. The dynamics of this instability determine the distribution of droplet sizes which, in turn, can impact subsequent dissolution, coalescence (or agglomeration), and transport phenomena.

Although jet instability has been investigated extensively, earlier studies do not adequately address one important aspect of the liquid CO_2-seawater system: at conditions representative of the proposed marine disposal scenarios (i.e., pressures greater than 44.5 bar and temperatures less than 283 K), a solid hydrate phase will form at the CO_2-seawater interface. The effect of hydrate formation on discharge jet instability is poorly understood. The present theoretical study was undertaken as a response to this deficiency.

Naturally occurring CO_2 hydrates in the ocean were detected in a submersible study of a hydrothermal field in the Okinawa trough [2]. A CO_2 hydrate layer was observed to form rapidly at the interface between CO_2-rich fluid (containing approximately 86% CO_2), secreted from the seafloor at depths of 1,335-1,550 m, and the surrounding 3.8° C seawater. The solid tubes which resulted were fragile and easily fractured by hydrodynamic forces, resulting in a cylindrical pattern of break up. This study demonstrated that hydrate formation can influence jet instability–in some cases precluding droplet formation.

Laboratory investigations [3,4,5] of liquid CO_2 jets in high-pressure and low-temperature water report three patterns of jet break up corresponding to different degrees of influence by the hydrate phase. At very low jet velocity, droplets form at the discharge orifice and are immediately covered with a hydrate film. These droplets easily agglomerate (but do not coalesce) at the orifice if they are not removed quickly. Higher velocities result in a cylindrical jet. Hydrate formation on the surface of this jet may proceed rapidly enough to produce a tube-like solid structure. Further increase in jet velocity leads to normal break up into droplets. These droplets will be encased by a hydrate film that can assume a snow-like quality under certain conditions [3].

Conventional instability theory and related data predict that a liquid jet discharging into another dissimilar liquid will break up into a dispersed droplet phase. Observations made in the ocean and in the laboratory, however, suggest that other break up modes are possible and may be induced by a solid hydrate phase. This study investigates the phenomena of CO_2 jet break up in the deep

ocean and attempts to provide a theoretical basis to identify situations where jet instability may be affected by hydrate formation.

2. LIQUID CO_2 JET BREAK UP IN SEAWATER

When liquid CO_2 effluent is discharged through an orifice into seawater, droplets will form as a result of interfacial instability [6]. This instability arises from interfacial tension and/or differences in the velocities of the two fluids. At low jet velocities, break up always leads to a train of uniformly-sized droplets [4,5,7]. At high jet velocities, break up produces multiple non-uniformly-sized droplets [3,4].

The present study restricts its focus to the laminar instability flow regime [6] that is characterized by jet break up leading to a uniformly-sized droplet train. For these flows, closed form relationships can be derived for important instability parameters. Although turbulent jets are clearly relevant to the marine disposal problem, the associated mathematics are prohibitively complex and will not be pursued directly here.

For laminar flow, Rayleigh's maximum-instability theory [8] applies: break up is induced by the most unstable of numerous waves that can form on the jet surface from an initial disturbance. This "most-unstable wave" is identified by a maximum-growth-rate in amplitude. Jet instability can then can be characterized by a break up time, t_b, which represents the induction period experienced by a quantity of jet fluid between discharge from the orifice and the formation of droplets.

Consider a liquid CO_2 jet in seawater. In the absence of a hydrate phase, jet instability is described by the following characteristic equation [6]:

$$\left[1+\frac{\rho_{seawater}\eta}{2\rho_{CO_2}}\frac{K_0(\eta)}{K_1(\eta)}\right]\beta^2 + 2Z\eta^2\beta = \eta^2(1-\eta^2)+\frac{1}{2}W_e\eta^3\frac{K_0(\eta)}{K_1(\eta)} - N_s\eta^2. \qquad (1)$$

Here, ρ_i is the density of fluid i (i = CO_2 or seawater); $\eta \equiv k\, r_0$ is the dimensionless disturbance wavenumber with k the dimensional disturbance wave number and r_0 the orifice radius; K_0 and K_1 are zeroth- and first-order modified Bessel functions of the second kind; $\beta \equiv \omega\,(2\,\rho_{CO2}\,r_0^3/\sigma)^{1/2}$ is the dimensionless growth rate in disturbance amplitude with ω the dimensional growth rate in the disturbance amplitude and σ the interfacial tension; $Z \equiv (3\mu_{CO2}+\mu_{seawater})/(2\,r_0\,\rho_{CO2}\,\sigma)^{1/2}$ is a modified Ohnesorge number with μ_i the viscosity of fluid i; $W_e \equiv 2\,r_0\,\rho_{seawater}\,U^2/\sigma$ is the Weber number with U the jet velocity; and $N_s \equiv (C_s/\sigma)(d\sigma/dC)$ is an interfacial tension number with C_s and C, respectively, the solubility and concentration of CO_2 in seawater. Based on Rayleigh's maximum-instability theory, a relationship may be derived for the jet break up time [6]:

$$t_b = \left[\ln(r_0/\alpha_0)\right](2\rho_{CO_2}r_0^3/\sigma)^{1/2}/\beta_m, \qquad (2)$$

where α_0 is the amplitude of the initial disturbance and β_m is the dimensionless maximum-growth rate of the disturbance amplitude, which may be determined from equation (1).

Examination of equations (1) and (2) indicates that jet instability is affected by the discharge parameters, U and r_0, and by fluid properties, ρ_i, μ_i, σ, C_s, and C. Over the range of depths being considered for liquid CO_2 disposal, fluid properties do not vary greatly. It is reasonable, therefore, to estimate the magnitude to t_b by adopting representative property values for substitution into (1) and (2) . At a depth of 500 m, seawater temperature at most locations outside of major currents is about 279 K. Corresponding densities of seawater and CO_2 are approximately 1030 and 895 kg/m^3, respectively. The interfacial tension number, N_s may be estimated as

$$N_s = \left(\frac{d\sigma}{dC}\right)\frac{C_s}{\sigma} \cong \frac{\sigma_m-\sigma}{C_s}\frac{C_s}{\sigma},$$

where σ_m and σ are, respectively, values of interfacial tension with and without mass transfer (between the jet and the seawater). Thermodynamic theory can be applied to estimate interfacial tension [6]. At 279 K, σ =71.23 × 10^{-3} N/m and σ_m = 70.09 × 10^{-3} N/m. Hence, N_s = -0.016, indicating that the system is tension-decreasing. For jets discharging from moderately-sized orifices (say, with diameters > 1 mm), the modified Ohnesorge number, Z, is of the order 10^{-3}, which implies that the damping term in (1) (i.e., the second term on the LHS of the equation) may be neglected. With this simplification, and assuming conditions at 500 m, (1) becomes

$$\beta^2 = \eta^2\frac{1.016-\eta^2+0.5W_e\eta K_0(\eta)/K_1(\eta)}{1+0.577\eta K_0(\eta)/K_1(\eta)}. \qquad (3)$$

Equation (3) indicates that $\beta_m = \beta_m(\eta, W_e)$. In general, β_m increases with W_e (and, hence, with increasing jet velocity, U, and orifice size, r_0). From experiments reported in literature [6], it is

estimated that, for the CO_2/seawater system, $\ln(r_0/\alpha_0) = 10.7$. Employing this value in (2), a representative jet break up time is given by $t_b \cong (1.7 \times 10^3)(r_0)^{1.5}/\beta_m$.

The preceding developments are predicated on the assumption that the formation of an interfacial, solid hydrate phase during the induction (i.e., pre-break up) period of the jet exercises a negligible influence on the amplification of surface disturbances. While, in reality, this must not be true under certain flow conditions (otherwise the unconventional break up modes noted in the preceding section could not occur), it is acceptable for the purpose of this study which, as discussed below, seeks to compare characteristic times of (unimpeded) jet break up and hydrate formation to establish regimes where the hydrate effect may be neglected or may be significant.

3. HYDRATE FORMATION AT THE CO_2-SEAWATER INTERFACE

The CO_2 hydrate is a clathrate compound having a body-centered structure formed by linkage of 46 water molecules. The clathrate has two pentagonal-dodecahedral cavities and six tetrakaidecahedral cavities. When all cavities are occupied by CO_2 molecules, the hydrate has a chemical formula of $8CO_2 \bullet 46H_2O$ or $CO_2 \bullet 5.75H_2O$. In reality, all cavities cannot be occupied [9], so the hydrate always contains fewer than the stoichiometric number of CO_2 molecules [10].

Hydrate formation is a physiochemical process. During this process, water molecules form a hydrogen-bonded framework (i.e., the clathrate) and CO_2 molecules enter the cavities of the clathrate as "guests." The hydrate framework is formed with geometric distortions and, therefore, the clathrate is unstable unless a large percentage of the cavities are filled with CO_2 molecules [10]. Hydrate formation at the CO_2-seawater interface can be expressed as

$$CO_2 + nH_2O \Rightarrow CO_2 \bullet nH_2O, \tag{4}$$

where n is the hydrate number (n = 5.75 at stoichiometric conditions). The kinetics of interfacial CO_2 hydrate formation have been investigated in previous modeling studies [11,12]. It was concluded that hydrates would form rapidly at conditions representative of the deep ocean and that the resulting solid layer would be very thin. These predictions agree reasonably well with the limited experimental results reported in the literature.

The CO_2-seawater hydrate kinetics may be characterized by a formation time, t_f, which corresponds to the period required for a solid layer to develop after a liquid CO_2 phase and seawater phase are brought into contact. The theoretical expression for the hydrate formation time is [12]

$$t_f = 6.91\left(\rho_h M_h^{-1}\right)/\left(\kappa C_s\right), \tag{5}$$

where κ is the effective rate constant of the formation reaction and ρ_h and M_h are, respectively, the CO_2 hydrate density and molar mass. It can be argued that, under the near-isothermal conditions of the deep ocean, the parameters in (5) remain essentially constant [6,12]. An estimate of t_f that can be compared with t_b can then be obtained utilizing representative values of these parameters: for $C_s = 0.91$ kmol/m^3 [13], $\kappa = 30$ s^{-1}, $\rho_h = 1.112 \times 10^3$ kg/m^3, and $M_h = 147.5$ kg/kmol [11], the hydrate formation time in the deep ocean is $t_f = 1.91$ s.

4. HYDRATE EFFECTS

Expressions for the characteristic times of jet instability, i.e., break up, and surface hydrate formation were obtained in the preceding sections. It is proposed that the relative magnitudes of these characteristic times can be utilized to indicate whether hydrate formation will exercise an effect on liquid CO_2 jet instability. The physical reasoning is as follows: if t_b is much shorter than t_f, then hydrates will not form in significant quantity on the jet surface prior to break up and, hence, jet instability will be unaffected; if, on the other hand, t_b is much longer than t_f (or of comparable magnitude), then a thin, solid hydrate layer will encase the jet, inhibiting the surface deformation required to induce jet break up. These two regimes are considered below.

4.1 Pre-Jet-Breakup Effects

The structure of the CO_2 jet will be affected when significant quantities of surface hydrates form prior to break up. Since hydrate formation time in the deep ocean is essentially constant, jet break up time becomes the relevant parameter. To be conservative, only maximum predicted values of this parameter, $t_{b,max}$, will be considered here; hence, low jet velocity cases are of interest (i.e., $We \rightarrow 0$). Employing the expression $t_b \cong (1.7 \times 10^3)(r_0)^{1.5}/\beta_m$ and solving (3) to determine β_m when $We \rightarrow 0$ [6], it can be shown that $t_{b,max} \geq t_f = 1.91$ s when $r_0 \geq 6.7$ mm. This implies that the pre-jet-breakup hydrate effects may become non-negligible when discharge orifice size exceeds a critical value, here, about 14 mm diameter.

If $t_f << t_{b,max}$, then rapid hydrate formation will establish a solid layer on the surface of the jet at the early stage of instability. This layer will inhibit surface deformation; thus, the jet remains stable and a solid tube can grow to encase the jet. Since the hydrate tube is very thin and fragile [2], it is easily broken by hydrodynamic forces. The breaking of hydrate tubes results in the cylindrical instability mode observed in the ocean at hydrothermal fields [2].

In reality, jet velocities are finite and, therefore, $t_b < t_{b,max}$. Figure 1 presents a comparison of t_f and t_b calculated for a range of jet velocities and discharge orifice diameters under deep ocean conditions. From this figure, it is observed that jet break up time increases with increasing orifice diameter and decreases with increasing jet velocity. The results imply that, for a given orifice diameter, interference by hydrates can be avoided by appropriate selection of jet velocity. To minimize pre-jet-break up effects, relatively small values of orifice diameter should be selected and/or velocities should be maintained at moderately high values.

4.2 Post-Jet-Breakup Effects

If $t_b \approx t_f$, then hydrate formation effects only are significant during the latter stages of jet instability, i.e., near to the end of the jet. Here, break up produces droplets covered with a hydrate layer. If $t_b << t_f$, then a conventional droplet break up pattern will be observed; however, the rapid kinetics of formation ensure that these droplets also will quickly be encased by a hydrate film.

Although hydrate formation does not significantly affect jet instability when $t_b < t_f$, it can impact the subsequent dissolution and dispersion of the droplet phase. The hydrate layer on the droplet surface is chemically stable [10] and will remain on the droplet (albeit undergoing cycles of collapse and regeneration) as it dissolves and is transported in space by buoyancy, currents, or turbulence [3,12]. Since water molecules at the hydrate surface have broken hydrogen bonds (note that each water molecule can form four hydrogen bonds) arranged toward the seawater phase [10,14], they will rapidly establish a bond when encountering a similar hydrate surface. Hence, CO_2 droplets brought in contact by hydrodynamic forces will easily agglomerate to form a droplet cluster [5,6,7,9,15]. The hydrate interphase, however, prevents the liquid CO_2 of the individual droplets from contacting and, therefore, inhibits coalescence into a single, larger droplet. This agglomeration phenomena has been observed in the laboratory.

5. CONCLUSIONS

A study was conducted to assess the effects of hydrate formation on the stability and break up of jets of CO_2 effluent released in the deep ocean. Within the laminar instability flow regime, a relationship was obtained for a characteristic jet break up time that could be applied for comparison with a hydrate formation time. It was proposed that two regimes exist which are defined by the relative magnitudes of t_b and t_f. When $t_b << t_f$, instability phenomena occur much faster than hydrate formation and jet break up is determined purely by hydrodynamics. When $t_b >> t_f$, a thin hydrate layer forms on the jet surface at the early stage of instability. Since this layer separates the CO_2 and seawater phases, surface deformation of the jet is impeded and, thus, the jet remains stable. The resulting tube-like hydrate structure is fragile and easily fractured by fluid forces, producing the cylindrical mode of jet break up observed near hydrothermal vents in the ocean.

Hydrate formation effects on jet instability are believed not to be significant when $t_b \approx t_f$ or $t_b << t_f$; in this regime, jet break up produces a train of droplets. Rapid formation kinetics ensure that these droplets will quickly be encased by a thin hydrate shell. This hydrate phase is chemically stable and will remain on the droplets, inhibiting dissolution and promoting agglomeration.

Since, over the range of depths proposed for marine CO_2 disposal, t_f is predicted to vary only slightly, the sole determining parameter to assess the importance of hydrate formation on instability is t_b. It was shown that jet break up time depends on fluid properties, jet velocity, and orifice diameter. Large orifices result in long break up times, which increase the probability that hydrate formation will induce non-conventional instability phenomena. Low jet velocities tend to produce the same effect. Although the present results do not consider the important category of turbulent flows, they can be applied to evaluate a range of discharge conditions relevant to the ocean disposal concept.

ACKNOWLEDGMENTS

Partial funding for this study was provided by U.S. Department of Energy Grant No. DE-FG22-95PC95206. This support does not constitute an endorsement by the Department of Energy of the views expressed herein.

REFERENCES

1. Nihous, G.C., Masutani, S.M., Vega, L.A., and Kinoshita, C.M., *Climatic Change* **27**, 225 (1994).
2. Sakai, H., Gamo, T., Kim, E.S., Tsutsumi, M., Tanaka, T., Ishibashi, J., Wakita, H., Yamamoto, M., and Oomori, T., *Science* **248**, 1093 (1990).
3. Aya, I. and Yamane, K., HTD–Vol. 215, 17 (1993).
4. Masutani, S.M., Kinoshita, C.M., Nihous, G.C., Teng, H., and Vega, L.A., *Energy Convers. Mgmt* **34**, 865 (1993).
5. Hirai, S., Okazaki, K., Araki, N., Yoshimoto, K., Ito, H., and Hijikata, K., *Energy Convers. Mgmt* **36**, 471 (1995).
6. H. Teng, Ph.D. Thesis, University of Hawaii at Manoa (1994).
7. Nishikawa, N., Ishibashi, M., Ohta, H., Akutsu, N., Tajika, M., Sugitani, T., Hiraoka, R., Kimuro, H., and Shiota, T., *Energy Convers. Mgmt* **36**, 489 (1995).
8. Rayleigh, Lord, *Theory of Sound*, Dover, N.Y. (1945).
9. Teng, H., to appear in *Int. J. Chem. Kinetics*, **28** (1996).
10. Teng, H., Yamasaki, A., and Shindo, Y., to appear in *Chem. Eng. Sci.*, **81** (1996).

11. Shindo, Y., Lund, P.C., Fujioka, Y., and Komiyama, H., *Int. J. Chem. Kinetics* **23**, 777 (1993).
12. Teng, H., Kinoshita, C.M., and Masutani, S.M., *Chem. Eng. Sci.* **50**, 559 (1995).
13. Liro, C.R., Adams, E.E., and Herzog, H.J., *Energ Convers.Mgmt* **33**, 667 (1992).
14. Teng, H., Yamasaki, A., and Shindo, Y., to appear in *Energy: The International Journal* **21** (1996).
15. Fujioka, Y., personal communication, March 29, 1996.

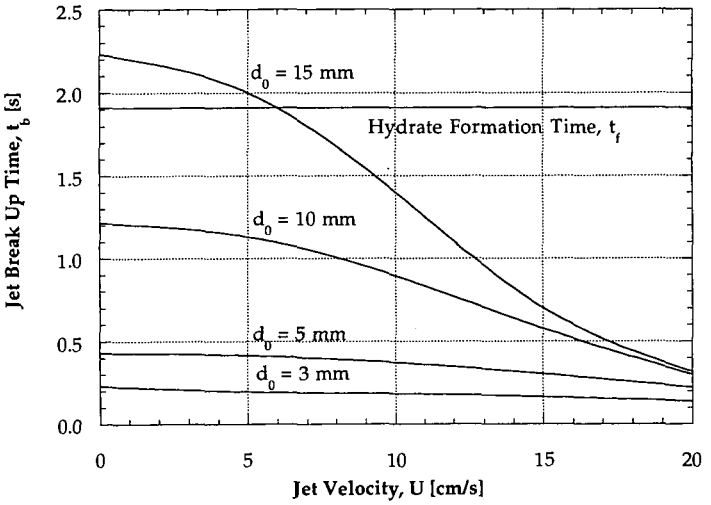

Figure 1. Comparison of hydrate formation times, t_f, and liquid CO_2 jet break up times, t_b, calculated for different discharge orifice diameters, d_0, under deep ocean (500 m) conditions.

FORMATION AND GROWTH OF CO_2 CLATHRATE HYDRATE SHELLS AROUND GAS BUBBLES OR LIQUID DROPS.

Gerald D. Holder[1] and Robert P. Warzinski

U.S. Department of Energy, Pittsburgh Energy Technology Center, Pittsburgh, PA 15236
[1]University of Pittsburgh, School of Engineering, Pittsburgh, PA 15261

Keywords: Carbon dioxide disposal, clathrate hydrates, mathematical model

INTRODUCTION

Deep ocean disposal of CO_2 may be required to mitigate rises in its atmospheric levels if other measures are ineffective and the worst global warming scenarios begin to occur. Work at PETC is directed at evaluating the technical feasibility of this option for long-term disposal.

At the pressures and temperatures associated with the depths required for effective sequestration of CO_2 (>500 m), the crystalline CO_2 clathrate hydrate ($CO_2 \cdot nH_2O$, $6 < n < 8$) can form (1). Clathrate hydrates are a special type of inclusion compound in which small molecules, such as CO_2, are held in cavities formed by hydrogen-bonded H_2O molecules by van der Waals forces (1,2). The formation of the CO_2 clathrate hydrate can either facilitate or complicate the sequestration of CO_2 in the ocean (3). Sequestration would be facilitated if the clathrate hydrates form as solid crystals dense enough to sink and thus increase the residence time of the CO_2 in the ocean. The formation can complicate sequestration if a thin coating of the hydrate forms on the surface of injected bubbles or drops of CO_2. This complication would hinder dissolution of the CO_2 and permit its rise to unacceptably shallower depths and thus its premature return to the atmosphere. Being able to predict the fate of CO_2 hinges on our understanding of these phenomena and their likely occurrence in ocean disposal scenarios.

In this report, experimental and theoretical results concerning the formation of hydrate shells on gas bubbles and liquid drops of CO_2 are presented. The experimental observations show that, in the presence of hydrate crystals, a thin hydrate shell forms from a nucleus at one point on the surface of the bubble or drop and then rapidly spreads out along this surface. A model was developed to estimate both the thickness of the initially formed shell and bounds on the ultimate thicknesses of shells in saturated and unsaturated environments. The model assumes that the ultimate thickness of the shell is governed by the diffusion of the CO_2 through the hydrate shell and diffusion or convection of dissolved CO_2 away from the hydrate-covered particle.

EXPERIMENTAL

All of the experimental observations were made in a high-pressure, variable-volume view cell of 10 to 40 cm^3 capacity. The view cell was enclosed in a chamber where the temperature could be maintained in the region of interest (0 to 10°C). The formation of hydrates was observed by injecting CO_2 (99+ % purity) into water treated by reverse osmosis. More complete descriptions of the view cell and the basic experimental procedures have been published (3,4).

RESULTS AND DISCUSSION

Much of the research on the impact of hydrate formation on ocean disposal of CO_2 has focused on the rates of hydrate formation and growth around a gaseous bubble or liquid drop of CO_2 injected into a large body of water (5,6,7). Teng, et al. have assumed that the CO_2 hydrate shell grows uniformly from 'hydrate clusters' that exist in the water around an initially hydrate-free drop (5). They also assume that the growth of hydrates is limited by the kinetics of the process and that the hydrate clusters can exist in water with local CO_2 concentrations lower than would exist if in equilibrium with hydrates. The values they get for hydrate formation time and thickness depend on the value they use for their rate constant, but there is no rational way of estimating its value.

Experiments have been performed at PETC in a high-pressure, variable-volume view cell in which the formation, dissolution, and relative densities of CO_2 hydrates have been studied (7). In the course of these experiments, several observations have been made of hydrate shells forming on either freshly injected gaseous bubbles or liquid drops of CO_2 in water already containing hydrate crystals. In all such cases, the hydrate shell grew from a nuclei at the point on the surface in contact with crystalline hydrate and then rapidly spread out along the drop or bubble surface. Others have also reported similar phenomenon (8). These observations do not support the view that a hydrate shell forms gradually from a uniform dispersion of nascent hydrate clusters on the surface of the drop. Two specific examples from our experimental work are described below.

In one experiment, four individual drops of liquid CO_2 were sequentially injected into the view cell that contained water and hydrate crystals which had earlier formed in the experiment around the injection port. The fate of each individual drop was monitored before the next drop was introduced. The temperature in the cell was 8.3°C and the pressure in the cell ranged from 16.0 to 18.0 MPa during the injection sequence. The drops were approximately 0.5 to 1.0 cm in diameter. Immediately upon injection, a thin hydrate coating began to form at the point of contact between the drop and the hydrate mass on the injection port. The hydrate shell grew from this point and completely enveloped the drop in 1 to 2 s.

In another experiment, several individual gaseous bubbles of CO_2 formed from a hydrate mass in the view cell when the pressure was decreased below the CO_2 vapor/liquid equilibrium point. The cell was at 5.6°C. The vapor/liquid equilibrium point at this temperature is near 3.5 MPa. The gaseous bubbles were between 0.3 and 0.5 cm in diameter. A hydrate coating immediately began to form, again starting at the point of contact between the bubble and the hydrate mass. The bubbles were completely covered in about 1 s.

Based upon the experimental observations, we propose a model assuming that a hydrate shell rapidly forms around the bubble of gas or drop of liquid CO_2. Instead of depending on the kinetics of the hydrate formation process to determine the thickness of the hydrate shell, we assume that the rate of thickening or thinning of the shell is determined by the diffusion of CO_2 through the shell and diffusion or convection of the dissolved CO_2 away from the hydrate-covered bubble or drop. Based on this assumption, we are able to put bounds on the thickness of the initially formed shell and on the thicknesses of shells in environments saturated and unsaturated with respect to CO_2. The specific case discussed below in presenting the model refers to liquid CO_2 drops in water, although the technique would be applicable to any gaseous or liquid molecule capable of forming hydrates.

Initial Shell Thickness

If a spherical drop of CO_2 is introduced into a large body of water, the CO_2 will dissolve in the water at the interface and diffuse away. Hydrates can only form if the pressure of the drop, P, is greater than the pressure required for hydrate formation at the temperature of the system, P_H. For steady-state diffusion from the drop into an infinite reservoir, the concentration profile is given by

$$C = C_0 * \frac{R_0}{r} \qquad (1)$$

where C_0 is the concentration of the CO_2 at the interface of the drop of radius R_0 and C is the CO_2 concentration at any position $r > R_0$.

Our observations and the observations of others (8) indicate that drops of CO_2 or other molecules capable of forming hydrates can exist in water for long periods of time (hours to days) without the formation of hydrates even though their formation is thermodynamically possible. This delay is thought to be due to the absence of primary nucleation events that must occur prior to crystallization of the hydrate (8). Under such conditions, C_0 can exceed the concentration of CO_2 that would be possible with hydrates present, which is the saturated concentration, C_H, at P_H.

Figure 1 illustrates the basic premise of the model by showing possible concentration profiles around a CO_2 drop both in the absence and presence of a hydrate shell. The saturation concentration at the hydrate equilibrium pressure is 0.01 g/ml. The saturation concentration at the system pressure in the absence of hydrates is 0.02 g/ml. The conditions which lead to these concentrations are not unique, but such concentrations might pertain, for example, if the CO_2 were injected into the ocean at 2000 meters and hydrates were stable at 1000 meters. If no hydrates formed for a period of time, the upper concentration profile would develop. Once hydrates formed, all the CO_2 in excess of 0.01 g/cc could contribute to the formation of the hydrate shell. This excess would all be in the first 0.5 cm of water surrounding the bubble. It is also assumed that none of the gas in the drop can diffuse through the hydrate fast enough to be incorporated into the initial hydrate shell. As soon as a molecularly thick hydrate shell forms, the only CO_2 available for initial hydrate formation is the excess dissolved CO_2.

If the concentration difference is integrated from R_0 to the value of $r=r_H$ (radius where the CO_2 concentration in the absence of hydrates is equal to the CO_2 concentration in the presence of hydrates at the edge of the shell, i.e., 1.0 cm in Figure 1), the amount of CO_2 available for initially forming a hydrate shell can be determined as shown below.

$$\text{Excess hydrate former} = m_{xs} = \int_{R_0}^{r_B} (C_0 - C_H) 4\Pi r^2 dr \qquad (2)$$

$$= 4\Pi R_0^3 C_H [(C_0/C_H)/2 * ((C_0/C_H)^2 - 1) - .333 * ((C_0/C_H)^3 - 1)]$$

The ratio, C_0/C_H, can be approximated by the ratio P/P_H even though solubilities (concentrations at equilibrium) are not necessarily linear with pressure. Using the composition of hydrates (6.15 mol water/mol CO_2) and the specific volume of hydrate (22.4 mL/mol H_2O) allows the thickness of the hydrate shell, Δr, to be calculated as follows (9).

$$\Delta r = \frac{\frac{m_{xs}}{44.01} * 6.15 * 22.4}{4\Pi R_0^2} \qquad (3)$$

Table 1 shows typical shell thicknesses for CO_2 hydrate shells formed at oceanic temperatures for drops of various size at different CO_2 concentrations. The values in the first three columns were selected to illustrate the effects of drop size (R_0), hydrate equilibrium concentration (C_H, which is a function of temperature and pressure), and the amount of excess CO_2 over that required for hydrate formation (C_0/C_H). The fourth column was calculated using Equation 2 and assumes that all of the excess CO_2 (m_{xs}) forms hydrates of uniform thickness. The fifth column represents the maximum hydrate thickness under these scenarios and was calculated using Equation 3. The final column represents the ratio of hydrate shell thickness to the size of the initial hydrate-free drop.

Table 1. Thickness of Initial Hydrate Shells formed from CO_2 Droplets injected into the Ocean at 0-15 C and Depths of 0-3000 meters.

R_0, cm	C_H g/mL	C_0/C_H	Mass of CO_2 in Hydrate, g	Δr, cm	$(\Delta r)/R_0$
0.1	0.01	1.5	0.000018	0.00045	0.0045
0.5	0.01	1.5	0.002291	0.00224	0.0045
1.0	0.01	1.5	0.018326	0.00448	0.0045
1.0	0.02	1.5	0.036652	0.00897	0.0090
1.0	0.03	1.5	0.054978	0.01345	0.0134
1.0	0.03	2.0	0.251327	0.06150	0.0615
1.0	0.02	2.0	0.167551	0.04100	0.0410
0.5	0.06	1.2	0.002011	0.00197	0.0039
0.5	0.06	2.0	0.062832	0.06150	0.1230

Note that in the cases shown in Table 1 the shell is always less than 0.1 cm in thickness. Thicker shells could result if the value of C_0/C_H were higher, but such values are unlikely unless the injection depth was very great (i.e., 3000 meters). In cases where the equilibrium concentrations greatly exceed the hydrate equilibrium concentrations (large C_0/C_H), it is less likely that steady-state, diffusion-controlled concentration profiles would be developed for the liquid CO_2 prior to hydrate formation. The maximum excess CO_2 is dissolved when this steady state is reached, so the formation of the hydrate shell from excess dissolved CO_2, which is less than the maximum, will result in a thinner hydrate shell. Also, in cases where the CO_2 is dispersed more quickly than occurs with steady diffusion, there would be less excess CO_2 and the shell would be thinner than given in these estimates. Thus, this analysis gives an estimate of the upper limit of the initial hydrate shell thickness which would be less than 0.1 cm.

Steady-State Shell Model

Once the hydrate shell forms around a body of CO_2, its thickness can either increase or decrease. If the drop is in a reservoir which is unsaturated with CO_2, then the shell thickness will reach some steady-state value. The shell remains at constant thickness and the CO_2 diffuses through the shell, causing the drop to shrink. For this to occur, the flux away from the drop must equal the flux through the shell. This is expressed in the equation below.

$$D_H \frac{C_0 - C_H}{\Delta r} 4\Pi R_I^2 = -D_W \left(\frac{\partial C}{\partial r}\right)_0 4\Pi R_0^2 \qquad (4)$$

In this equation, D_H and D_W are the diffusivities of CO_2 in the hydrate and water, respectively, C_0 and C_H are the equilibrium concentrations of CO_2 in water at the system pressure and the hydrate equilibrium pressure, respectively, and R_0 and R_I are the outer and inner radius of the shell, respectively. $(\partial C/\partial r)_0$ is the concentration gradient of CO_2 in the water phase at the outside of the hydrate shell. Note that the inside of the hydrate shell is pure CO_2, but C_0 represents the true driving force since at this concentration in water the chemical potential is equal to the chemical potential of the pure CO_2.

The thickness of the hydrate shell, Δr, can be determined using the following equation obtained by rearrangement of Equation 4.

$$\Delta r = \frac{-\frac{D_H}{D_W}(C_0 - C_H)}{(\partial C/\partial r)_0 (R_0^2/R_I^2)} \qquad (5)$$

At pseudo-steady state, the thickness is constant as determined by the above equation. For a thin shell, the ratio of radii will be nearly 1.0 and can be eliminated. The concentration gradient at the surface of the hydrate can be determined by a steady- or unsteady-state diffusion model.

Steady-State Infinite Reservoir

Further approximation can be made by assuming that CO_2 is diffusing away from the drop at steady state into a water phase that is very large in extent. The only mathematical requirement is that diffusion be radially symmetric and that the concentration decreases to zero far from the drop. In this case, the concentration gradient at R_0 is represented by $-C_H/R_0$. Replacing the concentration gradient term in Equation 4 with this latter term and rearranging gives the following equation.

$$\frac{\Delta r}{R_I} = \frac{\frac{D_H}{D_W}\left[\left(\frac{C_0}{C_H}\right) - 1\right]}{\left(\frac{R_0}{R_I}\right)} \qquad (6)$$

As before, the ratio of the inside and outside radii will be near unity in most cases. Since the ratio of concentrations of CO_2 will range between 1 and 2 for typical ocean injections, the relative thickness of the hydrate is determined by the ratio of diffusivities in the hydrate and water phases.

It might be useful to compare diffusivities in polymers versus melts to estimate relative values. Diffusivities in liquids are about 10^{-4} to 10^{-5} cm^2/sec and diffusivities in solids are about 10^{-10} cm^2/sec (10). Using Equation 6, the estimated relative thickness would be in the range of 10^{-6} to 10^{-5} cm. This indicates that the thin layer of hydrates that initially forms on the outside of the drop should get thinner, although the absolute thickness of the hydrate depends on the drop radius.

Because of changing drop size as the CO_2 dissolves, tiny fissures or cracks may develop in the hydrate shell that may increase the effective diffusivity in the hydrate layer allowing a thicker hydrate shell. However, hydrate formation should be accelerated in these fissures because of the better contact between CO_2 and water. Such fissures would rapidly heal which means that the overall model should be reasonable. This has been observed in our laboratory.
If no hydrates are present, the gradient at the edge of the drop will increase by the factor C_0/C_H, assuming that diffusion is limiting. The absence of a shell will increase the dissolution rate by this same factor. For example, at 7.7°C, the equilibrium hydrate pressure is approximately 3.3 MPa. If solubility is linearly proportional to pressure (Henry's Law), CO_2 injected at 10 MPa (approximately 1000 m depth) would dissolve three times slower with the hydrate shell than without it. The time required will depend on the extent to which the equilibrium concentration of CO_2 at the system pressure exceeds the equilibrium CO_2 concentration in the presence of hydrates (the solubility of CO_2 in water at the hydrate equilibrium pressure). Simply put, the CO_2 dissolution rate will decrease by a factor of C_0/C_H due to hydrate formation.

The thickness of the shell is such a small fraction of the drop diameter that the buoyancy of the drop will not be affected by the hydrate, although the drag coefficient may be affected since the hydrate-covered drop may be somewhat more rigid.

Steady-State Saturated Reservoir

The main assumption in the steady-state infinite reservoir model is that the CO_2 concentration decreases with distance from the drop. A drop injected into CO_2-saturated water cannot dissolve but can form a layer of hydrates. Since hydrates are present, the water would be saturated at the hydrate equilibrium pressure and the CO_2, which is at a higher (hydrostatic) pressure, would still diffuse through the hydrate shell. However, the net flux would have to contribute entirely to the growth of the hydrate shell thickness at the hydrate-water interface. The growth of the hydrate caused by this flux can be determined from the following equation.

$$\frac{d\Delta r}{dt} = D_H \frac{C_0 - C_H}{\rho_H \Delta r} \tag{7}$$

where ρ_H is the density of the hydrate phase in moles of CO_2 hydrate per unit volume.

Based upon a solid-phase diffusivity of 10^{-10} cm^2/sec, and a hydrate thickness of 10^{-4} cm, the hydrate would thicken at the rate of 10^{-3} to 10^{-4} cm/hr. This equation can be integrated to give the thickness as a function of time as shown below.

$$\Delta r = \left[\Delta r_0^2 + D_H \frac{C_P - C_H}{\rho_H} t \right]^{1/2} \tag{8}$$

In this equation, t is the time and Δr_0 is the initial hydrate thickness which is not known but is likely to be small. As the shell thickens, the hydrate growth rate will decrease, but for typical rise times for CO_2 injected into the ocean (10-100 hrs), a hydrate thickness of greater than 10^{-2} to 10^{-1} cm would not be expected. Since the thickness has a square root dependency on the solid-state diffusivity of CO_2, uncertainties in this value are less critical in estimating the thickness of the hydrate shell.

No definitive experiments have been performed to demonstrate that the hydrate layer continues to thicken in CO_2 saturated water as predicted by Equation 8. It is difficult to perform such experiments because saturated water will form multiple hydrate nucleation sites. However, one could inject a CO_2 drop into saturated water and see if it is completely converted to hydrate.

CONCLUSION

It has been demonstrated that a very thin hydrate shell should form around drops of injected CO_2. If injected into unsaturated water, a stable hydrate thickness on the order of 10^{-2} to 10^{-4} times the radius of the drop will form. The hydrates can significantly retard the dissolution of the CO_2.

If injected into saturated water, the hydrate will form a thicker shell, possibly approaching 10^{-1} cm in thickness for growth periods in excess of 100 hours. Since the water is saturated with respect to hydrate-forming conditions, the hydrate shell serves only to slow the diffusion of CO_2 and thus prevent the formation of additional hydrate from the injected CO_2. Saturated conditions could occur in the vicinity of the injection. Under this scenario, additional hydrates could form on the hydrate-covered drop from the CO_2 dissolved in the water. This was the subject of an earlier paper (7).

In summary, in all cases addressed in this paper, the modeling results predict that a hydrate shell on a CO_2 drop will remain thin and the drop will disappear more slowly than predicted by conventional models that do not consider hydrate formation. The stabilization of the drop by the thin shell will make it more likely that the injected CO_2 will rise to unacceptably shallower depths before dissolution. Injection strategies that avoid or limit this phenomena will be required for effective sequestration. Such options have been previously discussed (7).

In salt water, a further complication exists. As hydrates form, dissolved salts are excluded from the solid and their concentration in the water builds up. Since the salinity of the water affects the hydrate equilibrium pressure and the solubility of CO_2, this effect should be accounted for. At steady state, there is no net hydrate formation and this affect can be neglected. However, if the shell is changing in thickness, the effect of salinity could be important.

DISCLAIMER

Reference in this report to any specific product, process, or service is to facilitate understanding and does not imply its endorsement or favoring by the United States Department of Energy.

REFERENCES

1. A Research Needs Assessment for the Capture, Utilization and Disposal of Carbon Dioxide from Fossil Fuel-Fired Power Plants, DOE Report DOE/ER-30194, July 1993 (available NTIS).
2. P. Englezos Ind. Eng. Chem. Res. **1993**, 32, 1251-1274.
3. R.P. Warzinski; A.V. Cugini; G.D. Holder Proc. Int. Conf. Coal Sci. **1995**, 2, 1931-1934.
4. R.P. Warzinski; C.-H. Lee; G.D. Holder J. Supercrit. Fluids **1992**, 5, 60-71.
5. H. Teng; C.M. Kinoshita; S.M. Masutani Chem. Eng. Sci. **1995**, 50(4), 559-564.
6. N. Nishikawa; M. Ishibashi; H. Ohta; N. Akutsu; M. Tajika; T. Sugitani; H. Kimuro Book of Abstracts, Second International Conference on Carbon Dioxide Removal, Kyoto, Japan; 1994, p 46.
7. G.D. Holder; A.V. Cugini; R.P. Warzinski Environ. Sci. Tech. **1995**, 29, 276-278.
8. Burruss as reported by E.D. Sloan, Jr. *in* International Conference on Natural Gas Hydrates; E.D. Sloan, Jr.; J. Happel; M.A. Hnatow, Eds.; Annals of the New York Academy of Sciences; Vol. 715; p 17.
9. G.D. Holder; S.P. Zetts; N. Pradhan Reviews in Chem. Eng. **1988**, 5(1), 1-70.
10. Perry's Chemical Engineers' Handbook, 6th ed.; R.H. Perry; D.W. Green; J.O. Maloney Eds.; McGraw Hill, New York, 1984; p 16-23 and p 3-258.

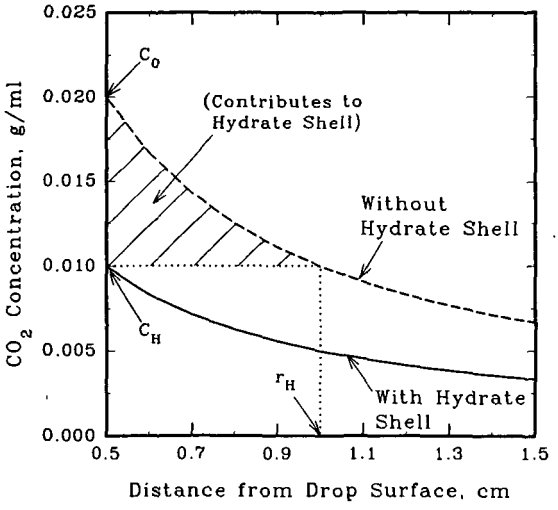

Figure 1. Concentration profiles around a CO_2 drop (0.5-cm radius) in the presence and absence of a hydrate shell in an infinite reservoir (arbitrary example).